Malaysian Journal of Analytical Sciences (MJAS)



Published by Malaysian Analytical Sciences Society

COMPARATIVE STUDY ON VISCOSITIES, STRESS RELAXATION, CURING AND MECHANICAL PROPERTIES OF SEPIOLITE AND SILICA FILLED NATURAL RUBBER COMPOSITES

(Kajian Perbandingan Mengenai Kelikatan, Kelonggaran Tekanan, Penyembuhan dan Sifat Mekanikal Komposit Getah Asli dengan Sepiolit dan Silika)

Nabil Hayeemasae^{1,2}, Ajaman Adair³, Abdulhakim Masa^{2,4}*

¹Department of Rubber Technology and Polymer Science, Faculty of Science and Technology

²Research Unit of Advanced Elastomeric Materials for BCG Economy, Faculty of Science and Technology

Prince of Songkla University, Pattani Campus, 94000 Pattani, Thailand

³Department of Cosmetic Science and Beauty, Faculty of Science Technology and Agriculture,

Yala Rajabhat University, 95000 Yala, Thailand

⁴Rubber Engineering & Technology Program,

International College, Prince of Songkla University,

90110 Hat Yai, Songkhla, Thailand

*Corresponding author: abdulhakim.m@psu.ac.th

Received: 1 November 2021; Accepted: 3 February 2022; Published: 28 April 2022

Abstract

In the present study, natural rubber composites filled with sepiolite and silica were prepared. The effects of the two fillers by loading (1–10 phr) on viscosities, stress relaxation, curing, and mechanical properties of the composites were investigated. Viscosity of rubber usually increased with filler loading about 7–22% with sepiolite and about 3–37% with silica, depending on filler content. Smaller rate of stress relaxation was found with sepiolite filler in comparison with silica filler. Furthermore, shorter curing cycle with greater crosslink density and hot temperature reversion resistance were achieved through the use of sepiolite filler in NR. Lorenz-Parks and Kraus models utilized for assessing rubber-filler interactions revealed stronger interactions of sepiolite filler with the rubber matrix. As a result of the good interactions between sepiolite filler and rubber matrix, larger reinforcement indexes and tensile strengths were achieved with sepiolite filler in comparison with silica filler. This was due to the higher aspect ratio of sepiolite (~5.32) compared to that of silica (~1.09) as demonstrated by SEM analysis. The highest tensile strength was achieved at 1 phr sepiolite loading which was about 17% improvement over unfilled sample.

Keywords: composites, fillers, rubber, sepiolite, silica

Abstrak

Komposit getah asli yang diisi dengan sepiolit dan silika telah disediakan dalam kajian ini. Kesan kedua-dua pengisi dengan memuatkan (1-10 phr) pada kelikatan, kelonggaran tekanan, tempoh pematangan dan sifat mekanikal komposit telah disiasat. Kelikatan getah biasanya meningkat dengan pengisi yang memuatkan dari 7-22% dengan sepiolite dan kira-kira 3-37% dengan silika, bergantung kepada kandungan pengisi. Kadar kelonggaran tekanan yang lebih kecil didapati dengan sepiolit berbanding

dengan pengisi silika. Juga, tempoh pematangan yang lebih pendek dengan ketumpatan sambung silang yang lebih tinggi dan rintangan perkembalian suhu panas dicapai dengan menggunakan pengisi sepiolit dalam getah asli. Model Lorenz-Parks dan Kraus yang digunakan untuk menilai interaksi pengisi getah mendedahkan interaksi yang lebih kuat dari pengisi sepiolit dengan matriks getah. Indeks pengukuhan yang lebih tinggi dan kekuatan tegangan dicapai dengan pengisi sepiolit daripada pengisi silika. Ini disebabkan oleh interaksi pengisi getah yang lebih baik yang timbul daripada nisbah aspek sepiolit yang lebih tinggi (~ 5.32) daripada silika (~ 1.09) seperti yang kemudiannya didedahkan oleh analisis SEM. Kekuatan tegangan tertinggi dicapai pada 1 phr pemuatan sepiolite iaitu kira-kira 17% peningkatan berbanding sampel yang tidak diisi.

Kata kunci: komposit, pengisi, getah, sepiolit, silika

Introduction

Generally, introducing one or more fillers is a strategy for improving the properties of natural rubber (NR). The use of a filler is convenient, effective, and relatively cheap for enhancing the properties of rubber [1, 2]. Among the different properties, modulus, tensile strength, tear strength, abrasion resistance, and service life of rubber can be improved, depending on size and shape of filler particles as well as the filler-matrix interactions [3, 4]. Various types of filler have been applied in rubber composites, and carbon black and silica are the most commonly used fillers in the rubber industries [5, 6]. Several studies have tested sepiolite filled rubber composites since sepiolite has unique needle-like particle shape with tunnel-like micropore channels, possibly improving the thermal, mechanical, and barrier properties of the composites [7-11].

Sepiolite belongs to nontoxic phyllosilicates, is abundant in the nature, and has a low cost. Regarding chemical structure, sepiolite comprises microcrystalline-hydrated magnesium silicate with the unit cell formula $Si_{12}Mg_8O_{30}(OH,F)_4$]. $(H_2O)_4 \cdot 8H_2O$ [11]. It is microfibrous with 2-10 µm particle length and tunnel-like micropore channels, providing efficient adsorption and high specific surface area for strong interaction with the rubber matrix. Comparative studies of sepiolite with other fillers, assessing reinforcing abilities, have been conducted recently [7, 9, 12-14]. Bokobza et al. [7, 9] investigated the relation of filler shape (silica particles and sepiolite fibers) with the mechanical properties of NR and styrene butadiene rubber (SBR), prepared by sol-gel process. They demonstrated that the sepiolite filler imparted more reinforcement in comparison with the spherical silica particles in NR. However, it had less interaction with

SBR because the sepiolite interacts less with SBR than NR, leading to poor interaction between the rubber and filler and poor dispersion in the SBR matrix. Bhattacharya et al. [12] investigated the impact of various nanofillers, namely, montmorillonite clay, sepiolite, hectorite, carbon nanofiber, and expanded graphite, and their dispersion methods on the properties of NR nanocomposites. They found that the mechanical and physical properties, including modulus, tear, and tensile strength, depended strongly on specific surface area, aspect ratio, filler volume fraction, and dispersion of filler. Lowe et al. [13] prepared NR nanocomposites reinforced with unmodified and modified clay and sepiolite. They observed that overall better properties were obtained for nanocomposites filled with clay. In case of sepiolite filler, the modified sepiolite exhibited relatively small improvements (only 3%) compared to the neat sepiolite. Winya and Hansupalak [14] compared the effects of sepiolite and silica on mechanical properties and thermal stability of NR/EPDM blend. They reported that both properties were similar for the two fillers, in the loading range investigated (0-12.5 phr), but the sepiolite was preferred over silica, as a lower loading achieved comparable mechanical and thermal properties.

Up to now, there is little work studying property changes of sepiolite and silica filled NR composites in the literature. The objective of the current study was to understand the effects of the two types of filler (i.e., sepiolite and silica) by small loading level on mechanical properties of NR composites. The study results are discussed considering certain properties, including viscosity, stress relaxation, curing, and tensile properties. The rubber-filler interactions are discussed based on Lorenz-Parks and Kraus models.

Materials and Methods

Materials

Table 1 summarizes the details of the various chemical ingredients utilized in compound preparation and their quantities expressed in part(s) per hundred parts of rubber (phr). All the ingredients were used as received.

Preparation of composites

The composites of NR with sepiolite or silica filler were prepared on a laboratory-sized two-roll mill with a 1.5 mm nip and a 12 cm guide. The chemical ingredients were added in the sequence displayed in

Table 2. NR was firstly masticated for 2 min, followed by incorporation of ZnO and stearic acid, and milled for 1 min. The filler (sepiolite or silica) was then added to the mix and milled for 9 min. Next, MBTS was fed to the mix and milled for 2 min. Finally, sulfur was added to the mix and milled for 1 min. After completion of the mixing with total mixing time of 15 min, the rubber compounds were then vulcanized through compression molding with a hydraulic press at 160 °C following their respective curing times (t₉₀) in order to obtain 1 mm thick vulcanized sheets.

Table 1. Formulation of the NR compounds

Chemical	Supplier
NR (Standard Thai Rubber graded 5L, STR 5L)	Chalong Concentrated Natural Rubber Latex Industry Company Limited, Songkhla, Thailand
Zinc oxide (ZnO)	Imperial Chemical Company Limited, Pathumthani, Thailand
Stearic acid	Global Chemical Company Limited, Samut Prakarn, Thailand
2,2'-Dithiobisbenzothiazole (MBTS)	Shanghai Rokem Industrial Company Limited, Shanghai, China
Sulfur	Siam Chemical Company Limited, Samut Prakan, Thailand
Sepiolite clay	Guangzhou Billion Peak Chemical Technology Company Limited, Guangzhou, China
Precipitated silica (Ultrasil VN3)	Evonik Industries AG, Essen, Germany

Table 2. Formulation of the NR compounds

Chemicals	Quanti	Mixing time	
	NR/sepiolite	NR/silica	(min)
NR	100	100	2
Stearic acid	1	1	1
ZnO	3	3	1
Sepiolite clay	0, 1, 3, 5, and 10	-	9
Silica	-	0, 1, 3, 5, and 10	9
MBTS	1.5	1.5	2
Sulfur	1.5	1.5	1
Total mixing tim	15		

Mooney viscosity and Mooney stress relaxation measurement

Mooney viscosity and Mooney stress relaxation of the different rubber composite samples were investigated through the use of a Mooney viscometer, MV 3000 Basic (MonTech, Germany), according to ASTM D1646. The tests were carried out at 100 °C using the large rotor. The stress relaxation was fit with the power law model in equations 1 and 2:

$$M = kt^a$$
, (1)

$$\log M = \log k + a \log t, \qquad (2)$$

where M refers to the torque during relaxation, k is a constant, t is the relaxation time, and the relaxation rate a denotes the slope visible in a log-log plot of M versus t.

Curing characteristics

The curing characteristics of the NR compounds, in terms of maximum torque (M_H), torque difference (M_H - M_L), cure time (t_{90}), and cure rate index (CRI), were determined at 160 °C through the use of a moving die rheometer (Montech MDR 3000 BASIC, Buchen, Germany). The CRI was defined by equation 3.

$$CRI = \frac{100}{t_{90}^{-t} s_1}$$
 (3)

Reversion resistance

The measurement of the reversion resistance of the composites at elevated temperature was performed using the percentage of reversion in the rubber compound after 300s, from the time at maximum torque (R_{300}), as shown in equation 4 [15, 16]:

$$R_{300} = \frac{M_H - M_{300}}{M_H} \times 100, \tag{4}$$

where M_{H} is the maximum torque in the curing curve and M_{300} is the torque at 300s after M_{H} .

Rubber-filler interactions

The extent of these filler-matrix interactions was estimated through the use of the Lorenz-Parks [17] and Kraus models [18]. The Lorenz-Parks model is as follows:

$$\frac{Q_f}{Q_g} = ae^{-z} + b, \qquad (5)$$

where Q is the amount of solvent absorbed, f and g indexes refer to filled and gum rubber vulcanizates, a and b are constants (the model parameters tuned to fit data), and z denotes the weight fraction of filler. The Q can be obtained via equation 6 [19]:

$$Q = \frac{\text{Swollen wt. - Dried wt.}}{\text{Original wt.}}.$$
 (6)

The Kraus equation is as follows:

$$\frac{V_{ro}}{V_{rf}} = 1 - m \left(\frac{f}{1 - f}\right),\tag{7}$$

where V_{ro} and V_{rf} refer to the volume fractions of elastomer in the solvent swollen gum vulcanizate and filled sample, f is the volume fraction of filler, and m is the rubber-filler interaction parameter. V_{rf} is expressed by the equation of Ellis and Welding [20], as follows:

$$V_{\rm rf} = \frac{(W_d - fW_0) / \rho_r}{(W_d - fW_0) / \rho_r + A_s / \rho_s},$$
 (8)

where W_d and W_0 are the deswollen and the initial weights of the composite samples, f is the volume fraction of filler in the composite, ρ_r is the density of rubber, A_s is the content of solvent absorbed, and ρ_s is the density of solvent. V_{ro} is given by equation 9:

$$V_{ro} = \frac{(W_d - W_f / \rho_r)}{(W_d - W_f / \rho_r + W_S / \rho_s)},$$
 (9)

where W_f denotes the weight of filler in the composite sample.

Tensile properties

The tensile properties including tensile strength, elongation at break, and reinforcement index (the ratio of the moduli at 300 and 100% elongations, or M300/M100, RI) of crosslinked NR composites were studied through the use of a universal tensile testing machine, LR5K Plus (LLOYD Instruments, UK) in accordance with ISO 37. The averages of five dumbbell-shaped specimens are reported, and the test was conducted at ambient temperature with a crosshead speed of 500 mm/min. The RI was defined by equation 10 [21-23]:

Reiforcement Index, RI =
$$\frac{M300}{M100}$$
 (10)

where M300 and M100 refer to the stresses at 100% and 300% strains, respectively.

Morphological test

The dispersion of sepiolite and silica fillers throughout the rubber matrix was investigated through the use of a scanning electron microscope (SEM; FEI Quanta 400 FEG, the Netherland). All composite specimens were immersed in liquid nitrogen and subsequently fractured before sputter-coating with gold in order to eliminate electrostatic charge buildup during examination. The SEM photomicrographs of cut surfaces were taken at magnification of 500x.

Results and Discussion

Mooney viscosity and Mooney stress relaxation measurement

The Mooney viscosities of the NR composite compounds filled with sepiolite or silica are shown in Figure 1. It is observed that in general the Mooney viscosity increased with filler loading. This is usually attributed to hydrodynamic effects, following the Guth and Gold equation [24].

$$\eta_{\text{rel}} = \frac{\eta_{\text{f}}}{\eta_{\text{H}}} = 1 + 2.5\phi + 14.1\phi^2 \tag{11}$$

where η_{rel} is the relative Mooney viscosity, η_f refers to the Mooney viscosity of filled rubber composite, η_u denotes the Mooney viscosity of neat rubber compound, and ϕ is the volume concentration of filler. As the filler loading increases, the viscosity should increase. However, a reduction of viscosity after adding 5 phr silica was observed, which was probably attributed to the formation of large silica aggregation as will be discussed later.

Figure 2 illustrates the Mooney stress relaxation rates of the composite compounds. The filler content had a great effect on the rate of relaxation, and the relaxation rates of sepiolite filled NR composites were slower than those of the silica filled ones. It has been reported that the choice of filler and its interactions with the polymer matrix considerably impacted the rate of stress relaxation. Interactions between filler particles and rubber chains hindered the molecular mobility, thus decreasing the relaxation rate [25, 26]. Considering the type of filler, composites filled with sepiolite relaxed slower than the silica filled ones. Since stronger interactions between filler and rubber matrix could better retard the relaxation rate as mentioned earlier, it is assumed that sepiolite gave stronger filler-matrix interactions than silica. The stronger filler-rubber interaction of sepiolite was attributed to the smaller size with higher aspect ratio of sepiolite dispersion in the rubber matrix as will be discussed later in the morphological observation part. The higher aspect ratio provided the higher surface area to interact with the rubber through chain entanglement and physical adsorption of rubber molecules onto the filler surfaces. It is well accepted that surface area is a major factor in the rubber composite structure. The larger the surface area of the filler is, the higher the possibility of filler-rubber contact takes place, resulting in efficient retardation of rubber molecules during relaxation.

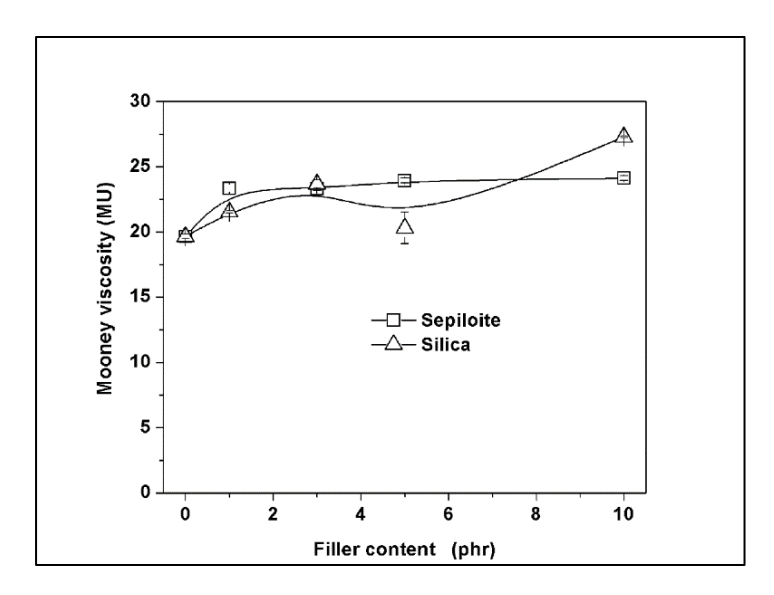


Figure 1. Mooney viscosities of NR compounds filled with sepiolite or silica

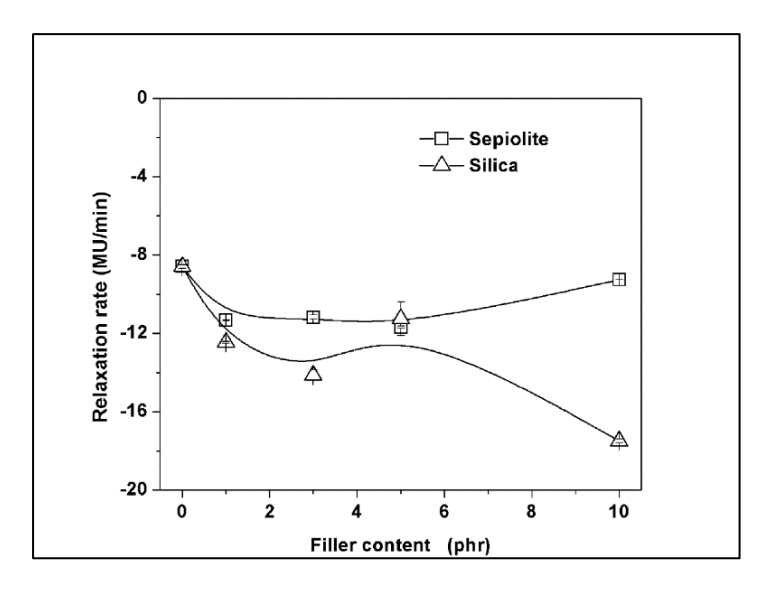


Figure 2. Mooney stress relaxation rates of NR compounds filled with sepiolite or silica

Curing characteristics

Curing properties in terms of M_H , M_H - M_L , t_{90} , and CRI, obtained from rheometric tests of the different rubber compounds, are presented in Figure 3(a)–Figure 3(d). It is noticed that the changes in curing properties were more pronounced for the sepiolite filled compounds in comparison with those for the silica filled ones. The M_H and M_H - M_L (Figures 3(a) and 3(b)) tended to increase with sepiolite loading, while they were approximately constant when silica was incorporated to

the NR compounds. It is well known that $M_{\rm H}$ and $M_{\rm H}$ are related to molecular rigidity and crosslink density, respectively, for rubber compounds. The higher molecular rigidity and crosslink density were achieved with sepiolite filler because of the larger aspect ratio and surface area for contacting with the rubber molecules. The adsorbed rubber chain fragments on filler surfaces forming physical interaction restrict the chain mobility in the rubbery matrix and serving as additional crosslinks in the

composites. Consequently, the rigidity and crosslink density of the composites were improved. It has been reported that large improvements in M_H and $M_{H^-}M_L$ for composites with small filler loadings are attributed to stronger rubber-filler interactions [27-29]. Therefore, stronger interactions of rubber and filler can be assumed for sepiolite compared to those for silica in filled NR compounds.

Considering t₉₀ of both sepiolite and silica filled compounds (Figure 3(c)), different phenomena are observed based on the filler type. Incorporation of sepiolite in NR tended to reduce t₉₀, while silica slightly prolonged it. A reduction of the t90 in sepiolite filled composites can be explained by the magnesium oxide (MgO) contained in the sepiolite structure. It is generally accepted that MgO is an activator of vulcanization reaction in rubber compounds, as it acts as a cation activating the crosslinking process at the diene backbone of the rubber [30]. On the contrary, the slight increase in t₉₀ noticed for the silica filled compounds was probably a result of the highly polar nature of silica, leading to the absorption of the curing ingredients, including ZnO, stearic acid, accelerators, and thereby resulting in a delayed curing process [31, 32].

The influence of metal oxide in sepiolite filled compounds on vulcanization process was later confirmed by increased CRI (Figure 3(d)), which indicated that curing reactions occurred faster with sepiolite filler than with silica filler. The CRI is a measure of rate of vulcanization based on the difference between cure time and scorch time. The higher the value of cure index, the faster the curing process [30].

Reversion resistance

Reversion resistances, R₃₀₀, for the composites with sepiolite or silica filler in NR vulcanizates were estimated by exposing the rubber composites to shear at an elevated temperature for a certain period of time. A larger R₃₀₀ indicates more reversion [15, 33]. Figure 4 illustrates the reversion resistances of NR composites filled with sepiolite and silica. It is observed that the filler type and loading had a

considerable effect on R₃₀₀ within the experimental range probably because of relatively small filler loading. However, a larger R₃₀₀ was seen for the silica filled NR composites, indicating that they had poorer reversion resistance in comparison with sepiolite filler. This can be because the greater sepiolite dispersion and better rubber-filler interactions improved the crosslink density of sepiolite filled NR composites. The better filler dispersion to gather with the higher overall crosslinking degree retarded the mobility of the rubber chains, and this enhanced the thermal stability of the rubber composites [8]. Furthermore, sepiolite itself could contribute to thermal stabilization and flame retardant properties of the filled polymer, as it served as a heat quencher and an initiator for formation of char on the polymer surface, inhibiting diffusion of oxygen [10].

Rubber-filler interactions

In order to evaluate the extent of interactions between rubber and filler, Lorenz-Parks and Kraus models were employed. Figure 5 presents Lorentz-Parks plot for the NR composites filled with sepiolite and silica. The value of rubber-filler interaction (Q_f/Q_g) generally reduced with sepiolite content but remained almost constant for the silica filled composites. Since the Q ascribed to the amount of solvent absorbed by rubber sample, the reduction of Q_f/Q_g was due to the better restricted diffusion of solvent molecules through the rubber matrix, resulting from greater extent of interaction between rubber and filler. The smaller value of Q_f/Q_g denotes stronger filler-matrix interactions [19, 28, 34, 35]. Since the Q_f/Q_g of sepiolite filled NR composites was below that of the silica filled composite at each loading level, the stronger rubberfiller interactions were achieved in the sepiolite filled composites. In contrast, the constant value of Q_f/Q_g in the composites filled with silica implies less interaction between silica and rubber matrix.

The rubber-filler interactions were further confirmed through the use of the Kraus model (plot of volume fraction ratio (V_{ro}/V_{rf}) versus volume ratio of filler (f/1-f)), and the results are displayed in Figure 6. It was observed that V_{ro}/V_{rf} decreased with filler loading. The negative slope in the plot of V_{ro}/V_{rf} versus f/1-f is an

indication of a good reinforcing effect [19, 28]. The negative slope was due to strong rubber-filler interaction, resulting from a reduction of the solvent uptake (solvent sorption) in the rubber composites. Consequently, the V_{rf} value decreases, resulting in a reduction in V_{ro}/V_{rf} value (V_{ro} is constant). More negative slope is noticed for the composites with sepiolite filler, implying that sepiolite was more effective in reinforcing the composite than the silica. Based on the Lorenz-Parks and Kraus models, it is confirmed that sepiolite provided stronger rubber-filler

interactions of the two fillers, leading to greater reinforcement within the range tested in the present study. The good interactions between sepiolite and rubber were attributed to the fact that the rubber chains can easily interact with the narrow channels in the sepiolite structure [9, 36]. Moreover, the larger specific surface area of sepiolite (364 m^2/g) [36] over silica (175 m^2/g) [37] may facilitate the rubber-filler interactions.

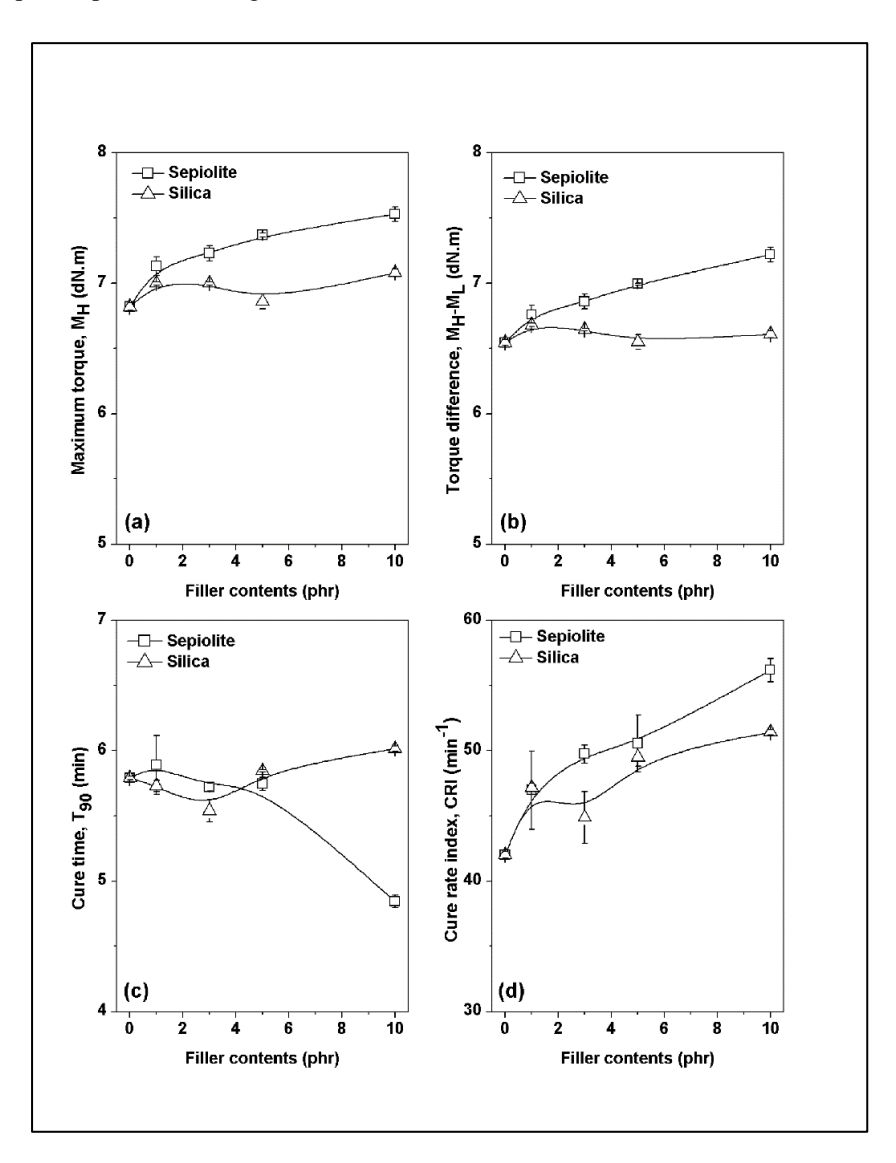


Figure 3. Curing properties in terms of (a) maximum torque, (b) torque difference, (c) cure time, and (d) cure rate index for the NR composites filled with sepiolite or with silica

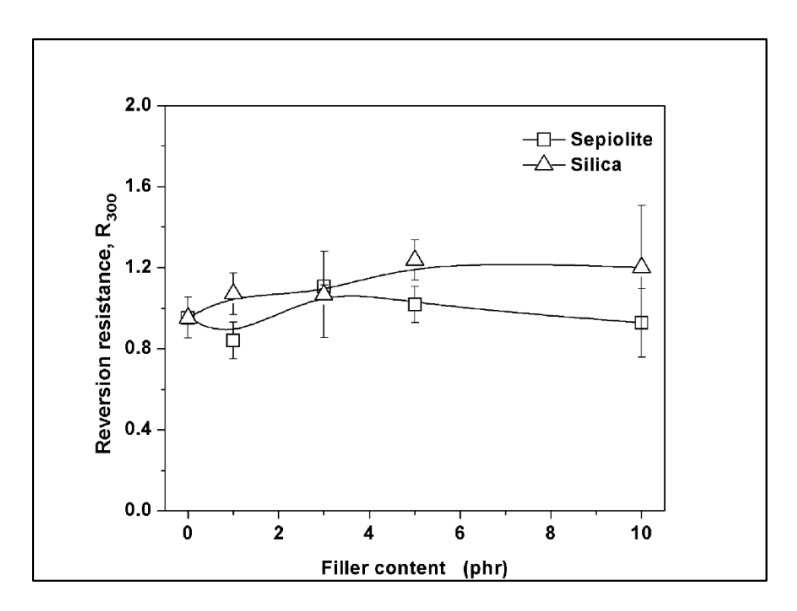


Figure 4. Reversion resistances of NR composites filled with sepiolite or with silica

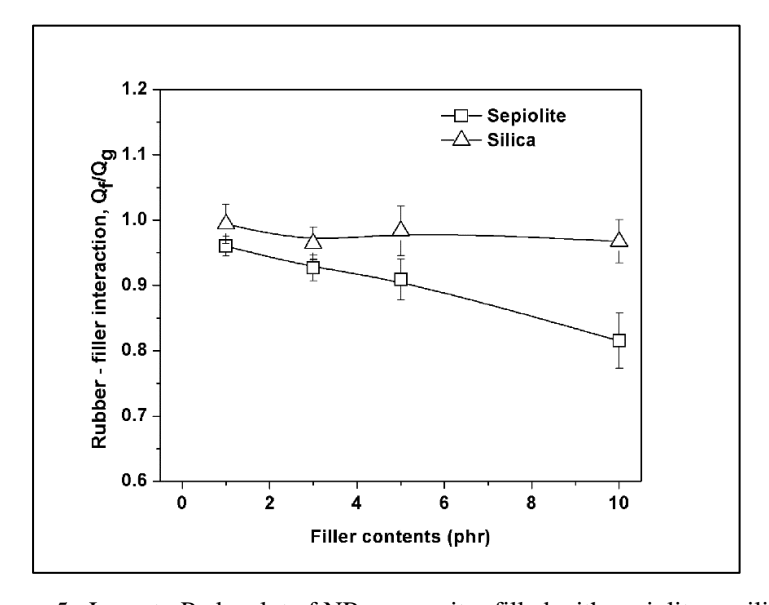


Figure 5. Lorentz-Parks plot of NR composites filled with sepiolite or silica

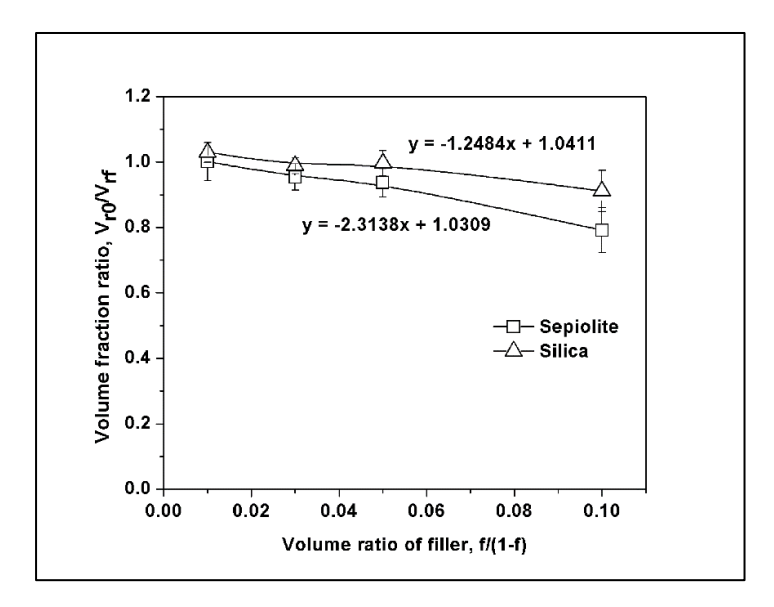


Figure 6. Kraus plot of NR composites filled with sepiolite or silica

Tensile properties

Figure 7 displays reinforcement index (M300/M100) for the NR composites filled with the two tested fillers. It is generally observed that the reinforcement index of sepiolite filled NR composite was greater than that of the silica filled composite. This was simply due to the stronger interactions between rubber and sepiolite filler, as previously discussed. The tubular-shaped with high specific surface area of sepiolite may act as stress transferring agent, which would increase reinforcing index. This finding is in agreement with previous literature [5, 7, 9, 38], reporting that sepiolite fibers provided more reinforcement than spherical silica particles due to their high aspect ratio. The aspect ratios of sepiolite and silica found in the current study were approximately 5.32 and 1.09, respectively, which are in line with the previous report [38].

Figure 8 displays the variation in tensile strength of NR composites filled with sepiolite and silica. It can be clearly noticed that incorporation of sepiolite provided slightly higher tensile strength than silica, because of the better rubber-filler interactions. The highest tensile strength was about 17% improvement over unfilled sample found at 1 phr sepiolite loading, probably due to the greatest rubber-filler interactions as previously suggested by the stress relaxation and filler-rubber

interaction results (Figures 2, 5, and 6). As a result of filler incorporation, the extensibility of rubber usually decreases due to either good rubber-filler interactions, restricting the movements of rubber chains, or poor filler dispersion, with agglomerates serving as stress concentration points. Thus, the elongation at break of composites reduced with filler loading, as presented in Figure 9. Similar observation was found in previous report [30]. The better rubber-filler interactions of sepiolite provided a slightly superior extension capability, particularly at low filler loadings.

In case of NR composites filled with silica, the highest tensile strength was found at 5 phr (about 12% over neat NR) which was considered to be optimum. Further increase in the silica incorporation slightly reduced the tensile strength because of the increment of silica aggregation, as will be discussed later in the morphological part. The aggregation of silica served as stress concentration point, resulting in a reduction of elongation at break. It is also found that the tensile strength of NR composites filled with sepiolite and silica was not much different due to relatively small filler loading. However, smaller loading of sepiolite required to obtain maximum tensile strength than silica would be benefited for preparation of rubber composite containing small filler loading.

Morphological property

Figure 10 presents the SEM micrographs of cryofractured surfaces of sepiolite (Figures 10(a) and 10(b)) and silica (Figures 10(c) and 10(d)) filled NR composites. It is noticed that the morphology of rubber composites comprises different sizes and shapes of filler dispersion, based on loading and type of filler. In the composites filled with sepiolite (Figures 10(a) and 10(b)), small size of filler with tubular-shaped was dispersed throughout the rubber matrix. The length (L) and diameter (D) of sepiolite in NR/Sepiolite 1 were about 1.34 - 3.15 μm and 0.34 - 0.91 μm, respectively. Meanwhile, they were about 2.45 - 5.50 µm and 0.45 -1.12 µm, respectively, in NR/Sepiolite 5. Thus, the average aspect ratios of rubber composites filled with 1 and 5 phr sepiolite were about 5.32 \pm 3.44 and 4.88 \pm 3.36, respectively. Less amount of tubular-shaped particulates was observed in sample containing 1 phr sepiolite due to small amount of sepiolite added. However, such dispersion is sufficient to assist the stress transfer to each other. Large size of sepiolite aggregation was seen when the sepiolite loading was up to 5 phr. Such dispersion would be responsible for a reduction in tensile strength and elongation at break.

Considering the composites filled with silica, the L and D of silica in NR/Silica 1 (Figure 10(C)) ranged within 0.46 - 3.02 μ m and 0.44 - 2.80 μ m, respectively, whereas they were within 1.34 - 6.72 μ m and 1.12 - 7.05 μ m, respectively, for NR/Silica 5 sample (Figure 10(D)), resulting in the aspect ratio of about 1.06±0.04 for NR/Silica 1 and 1.03 ± 0.2 for NR/Silica 5. It was also found that the size of silica dispersion increased with filler loading, suggesting that filler-filler interaction was preferred at high silica loading. Smaller aspect ratio of silica dispersion than those of sepiolite can be confirmed which was in well agreement with previous report [39].

Based on the SEM observation, it is clearly evident that the aspect ratio of sepiolite dispersion was greater than that of silica. The higher aspect ratio created larger surface area contact between rubber and filler, providing better stress transfer between the components. Therefore, the better restricted chain relaxation and the higher tensile properties were obtained with incorporation of sepiolite.

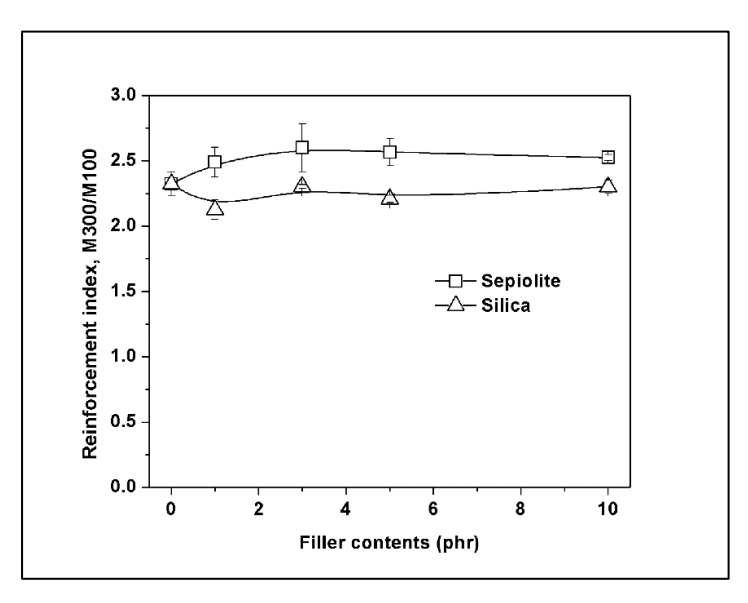


Figure 7. Reinforcement index (M300/M100) of NR composites filled with sepiolite or silica

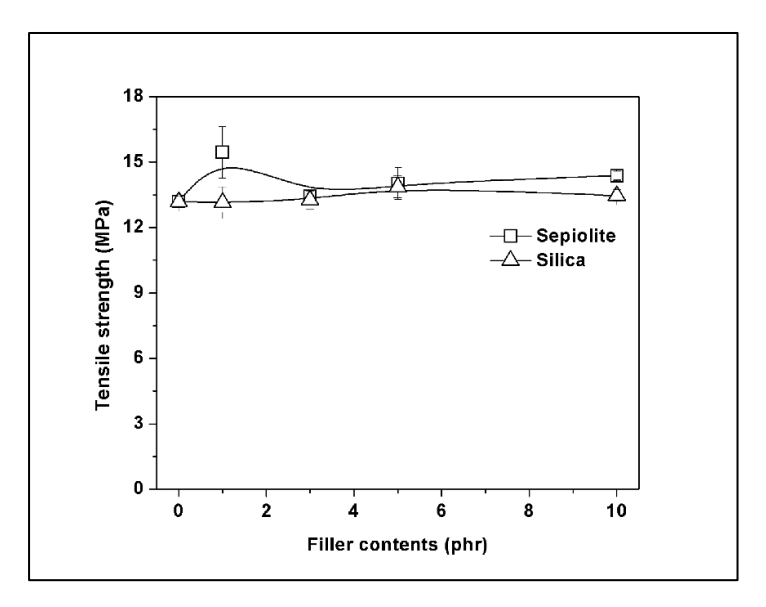


Figure 8. Tensile strength of NR composites filled with sepiolite or silica

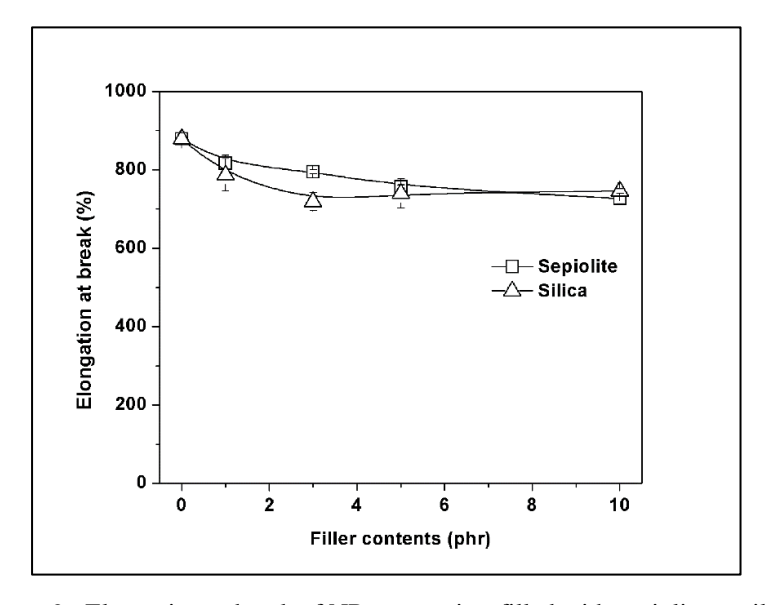


Figure 9. Elongation at break of NR composites filled with sepiolite or silica

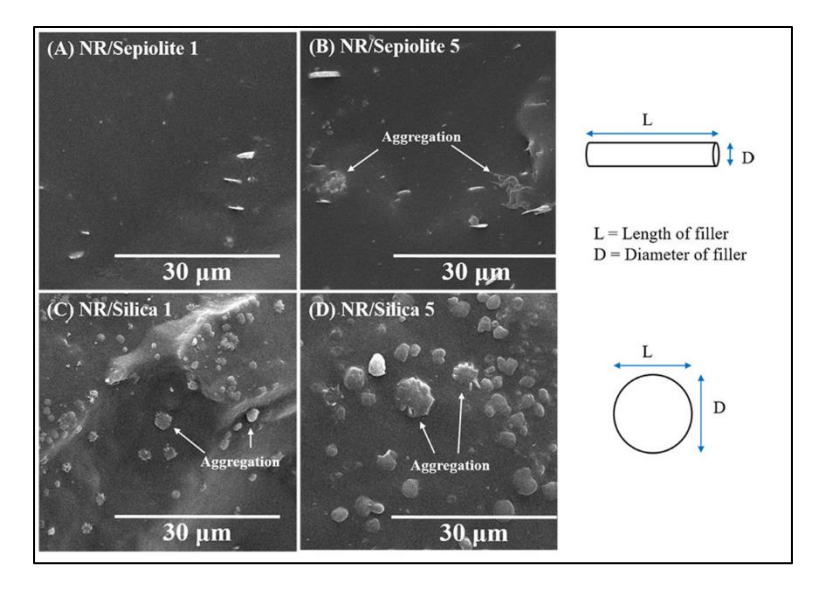


Figure 10. SEM micrographs of NR composites: (a) NR/Sepiolite 1 phr, (b) NR/Sepiolite 5 phr, (c) NR/Silica 1 phr, and (d) NR/Silica 5 phr at 500x

Conclusion

Composites of NR filled with sepiolite or with silica were prepared in the present study, and the influence of filler type and loading level on properties of the composites was investigated. From Mooney viscosity, stress relaxation, and rheometric tests, the results revealed that sepiolite filled NR exhibited a slower relaxation rate with larger torque difference and better reversion resistance than that with the silica filled compounds, suggesting better rubber-filler interactions than in silica filled composites. Increased addition of filler improved the viscosity of rubber by approximately 7 - 22% with sepiolite and approximately 3 - 37% with silica, depending on filler loading. The stronger rubber-filler interactions in the sepiolite filled composites were later confirmed through the use of the Lorenz-Parks and Kraus models. The greater extent of interaction between rubber and filler resulted in the greater restricted diffusion of solvent molecules through the rubber matrix. As a result of the good interactions between sepiolite filler and rubber matrix, larger reinforcement indexes and tensile strengths were achieved with sepiolite filler than with silica filler in the composites. This was due to the higher aspect ratio of sepiolite (~5.32) compared to that of silica (~1.09) as revealed by SEM analysis. The

highest tensile strength was achieved at 1 phr sepiolite loading which was about 17% improvement over unfilled sample.

Acknowledgement

This research was supported by Prince of Songkla University (Grant No. UIC6402030S).

References

- Chang, B. P. P., Gupta, A., Muthuraj, R. and Mekonnen, T. (2021). Bioresourced fillers for rubber composites sustainability: current development and future opportunities. *Green Chemistry*, 23: 5337-5378.
- Maslowski, M., Miedzianowska, J. and Strzelec, K. (2019). Natural rubber composites filled with crop residues as an alternative to vulcanizates with common fillers. *Polymers*, 11(6): 972.
- Bokobza, L. (2017). Mechanical and electrical properties of elastomer nanocomposites based on different carbon nanomaterials. *Journal of Carbon Research*, 3(2): 10.

- 4. Anand, A., Nussana, L., Sham Aan, M. P., Ekwipoo, K., Sangashetty, S. G. and Jobish, J. (2020). Synthesis and characterization of zno nanoparticles and their natural rubber composites. *Journal of Macromolecular Science, Part B*, 59(11): 697-712.
- Bokobza, L. (2019). Natural rubber nanocomposites: a review. *Nanomaterials*, 9(1): 12.
- 6. Roy, K., Debnath, S. C. and Potiyaraj, P. (2020). A critical review on the utilization of various reinforcement modifiers in filled rubber composites. *Journal of Elastomers and Plastics*, 52(2): 167-193.
- 7. Bokobza, L. and Chauvin, J. P. (2005). Reinforcement of natural rubber: use of in situ generated silicas and nanofibres of sepiolite. *Polymer*, 46(12): 4144-4151.
- 8. Chen, H., Zheng, M., Sun, H. and Jia, Q. (2007). Characterization and properties of sepiolite/polyurethane nanocomposites. *Materials Science and Engineering: A*, 445-446: 725-730.
- 9. Bokobza, L., Leroy, E. and Lalanne, V. (2009). Effect of filling mixtures of sepiolite and a surface modified fumed silica on the mechanical and swelling behavior of a styrene-butadiene rubber. *European Polymer Journal*, 45(4): 996-1001.
- Zhan, Z., Xu, M. and Li, B. (2015). Synergistic effects of sepiolite on the flame retardant properties and thermal degradation behaviors of polyamide 66/aluminum diethylphosphinate composites. *Polymer Degradation and Stability*, 117: 66-74.
- Zaini, N. A. M., Ismail, H. and Rusli, A. (2018). Thermal, flammability, and morphological properties of sepiolite filled ethylene propylene diene monomer composites. *Malaysian Journal of Analytical Sciences*, 22(5): 899-905.
- 12. Bhattacharya, M., Maiti, M. and Bhowmick, A. K. (2008). Influence of different nanofillers and their dispersion methods on the properties of natural rubber nanocomposites. *Rubber Chemistry and Technology*, 81(5): 782-808.
- 13. Lowe, D. J., Chapman, A. V., Cook, S. and Busfield, J. J. C. (2011). Natural rubber nanocomposites by in situ modification of clay.

- Macromolecular Materials and Engineering, 296(8): 693-702.
- 14. Winya, N. and Hansupalak, N. (2016). A comparison between the effects of sepiolite and silica on mechanical properties and thermal stability of NR/EPDM blend. MATEC Web of Conferences, 6: 04003.
- 15. Khang, T. H. and Ariff, Z. M. (2012). Vulcanization kinetics study of natural rubber compounds having different formulation variables. *Journal of Thermal Analysis and Calorimetry*, 109(3): 1545-1553.
- Hayeemasae, N. and Masa, A. (2020).
 Relationship between stress relaxation behavior and thermal stability of natural rubber vulcanizates. *Polímeros*, 30(2): e2020016.
- 17. Lorenz, O. and Parks, C. R. (1961). The crosslinking efficiency of some vulcanizing agents in natural rubber. *Journal of Polymer Science*, 50(154): 299-312.
- 18. Kraus, G. (1965). Interactions of elastomers and reinforcing fillers. *Rubber Chemistry and Technology*, 38 (5): 1070-1114.
- Swapna, V. P., Stephen, R., Greeshma, T., Sharan, D. C. and Sreekala, M. S. (2016). Mechanical and swelling behavior of green nanocomposites of natural rubber latex and tubular shaped halloysite nano clay. *Polymer Composites*, 37(2): 602-611.
- 20. Ellis, B. and Welding, G. N. (1964). Techniques of polymer science. society of the chemical industry, London: pp. 46-46.
- 21. Lee, J. Y., Kim, S. M. and Kim, K. J. (2015). Observation of interfacial adhesion in silica-nr compound by using bifunctional silane coupling agent. *Polymer Korea*, 39(2): 240-246.
- 22. Saramolee, P., Sahakaro, K., Lopattananon, N., Dierkes, W. K. and Noordermeer, J. W. (2015). Compatibilization of silica-filled natural rubber compounds by combined effects of functionalized low molecular weight rubber and silane. *Journal of Elastomers and Plastics*, 48(2): 145-163.
- 23. Mohamad Aini, N. A., Othman, N., Hussin, M. H., Sahakaro, K. and Hayeemasae, N. (2019). Hydroxymethylation-modified lignin and its effectiveness as a filler in rubber composites. *Processes*, 7(5): 315.

- Sajjayanukul, T., Saeoui, P. and Sirisinha, C. (2005). Experimental analysis of viscoelastic properties in carbon black-filled natural rubber compounds. *Journal of Applied Polymer Science*, 97(6): 2197-2203.
- Maria, H. J., Lyczko, N., Nzihou, A., Joseph, K., Mathew, C. and Thomas, S. (2014). Stress relaxation behavior of organically modified montmorillonite filled natural rubber/nitrile rubber nanocomposites. *Applied Clay Science*, 87: 120-128.
- Gabriel, D., Karbach, A., Drechsler, D., Gutmann, J., Graf, K. and Kheirandish, S. (2016). Bound rubber morphology and loss tangent properties of carbon-black-filled rubber compounds. *Colloid* and *Polymer Science*, 294: 501-511.
- Honorato, L., Dias, M. L., Azuma, C. and Nunes, R. C. R. (2016). Rheological properties and curing features of natural rubber compositions filled with Fluoromica ME 100. *Polimeros*, 26(3): 249-253.
- 28. Mondal, D., Ghorai, S., Rana, D., De, D. and Chattopadhyay, D. (2019). The rubber-filler interaction and reinforcement in styrene butadiene rubber/devulcanize natural rubber composites with silica-graphene oxide. *Polymer Composites*, 40(S2): E1559-E1572.
- Lopez-Manchado, M. A., Arroyo, M., Herrero, B. and Biagiotti, J. (2003). Vulcanization kinetics of natural rubber-organoclay nanocomposites.
 Journal of Applied Polymer Science, 89(1): 1-15.
- Masa, A., Krem-ae, A., Ismail, H. and Hayeemasae, N. (2020). Possible use of sepiolite as alternative filler for natural rubber. *Materials Research*, 23(4): e20200100.
- 31. Sridharan, H., Guha, A., Bhattacharyya, S., Bhowmick, A. K. and Mukhopadhyay, R. (2019). Effect of silica loading and coupling agent on wear and fatigue properties of a tread compound. *Rubber Chemistry and Technology*, 92(2): 326-349.

- 32. Ansarifar, M. A., Chugh, J. P. and Haghighat, S. (2000). Effects of silica on the sure properties of some compounds of styrene-butadiene rubber. *Iranian Polymer Journal*, 9(2): 81-87.
- 33. Kok, C. M. (1987). The effects of compounding variables on the reversion process in the sulphur vulcanization of natural rubber. *European Polymer Journal*, 23(8): 611-615.
- 34. Wu, X., Lin, T. F., Tang, Z. H., Guo, B. C. and Huang, G. S. (2015). Natural rubber/graphene oxide composites: effect of sheet size on mechanical properties and strain-induced crystallization behavior. *eXPRESS Polymer Letters*, 9(8): 672-685.
- 35. Ismail, H., Omar, N. F. and Othman, N. (2011). Effect of carbon black loading on curing characteristics and mechanical properties of waste tyre dust/carbon black hybrid filler filled natural rubber compounds. *Journal of Applied Polymer Science*, 121(2): 1143-1150.
- 36. Bhattacharya, M. and Bhowmick, A. K. (2008). Polymer-filler interaction in nanocomposites: New interface area function to investigate swelling behavior and Young's modulus. *Polymer*, 49(22): 4808-4818.
- 37. Kaewsakul, W., Sahakaro, K., Dierkes, W. K. and Noordermeer, J. W. (2013). Optimization of rubber formulation for silica-reinforced natural rubber compounds. *Rubber Chemistry and Technology*, 86(2): 313 329.
- 38. Locatelli, D., Pavlovic, N., Barbera, V., Giannini, L. and Galimberti, M. (2020). Sepiolite as reinforcing filler for rubber composites: from the chemical compatibilization to the commercial exploitation. *KGK Kautschuk Gummi Kunststoffe*, 73: 26-35.
- 39. Abdul Salim, Z. A. S., Hassan, A. and Ismail, H. (2018). A review on hybrid fillers in rubber composites. *Polymer-Plastics Technology and Engineering*, 57(6): 523-539.

Malaysian Journal of Analytical Sciences (MJAS)



Published by Malaysian Analytical Sciences Society

A SHORT REVIEW ON THE INFLUENCE OF THE PREPARATION METHOD ON THE PHYSICOCHEMICAL PROPERTIES OF Mg/Al HYDROTALCITE FOR GLUCOSE ISOMERIZATION

(Ulasan Ringkas Mengenai Pengaruh Kaedah Penyediaan Terhadap Sifat-Sifat Fizikokimia Mg/Al Hidrotalsit untuk Pengisomerisasi Glukosa)

Munirah Zulkifli^{1,2}, Noor Hidayah Pungot^{1,2}*, Nazrizawati Ahmad Tajuddin¹, Mohd Fadhlizil Fasihi Mohd Aluwi³, Nor Saliyana Jumali⁴, Zurina Shaameri^{1,2}

¹School of Chemistry and Environment, Faculty of Applied Sciences,
Universiti Teknologi MARA, 40450 Shah Alam, Selangor, Malaysia

²Organic Synthesis Laboratory, Institute of Science,
Universiti Teknologi MARA Puncak Alam Campus, 42300 Bandar Puncak Alam, Selangor, Malaysia

³Faculty of Industrial Sciences and Technology,
Universiti Malaysia Pahang, Lebuhraya Tun Razak, 26300 Gambang, Kuantan, Pahang, Malaysia

⁴ Department Chemistry, Kulliyyah of Science,
International Islam University Malaysia, 25200 Bandar Indera Mahkota, Kuantan, Pahang, Malaysia

*Corresponding author: noorhidayah977@uitm.edu.my

Received: 15 September 2021; Accepted: 3 February 2022; Published: 28 April 2022

Abstract

Hydrotalcite (Mg₆Al₂(OH)₁₆CO₃4H₂O) is a naturally occurring anionic clay with a layered crystal structure. Hydrotalcites is classified as heterogeneous catalysts that exhibit an excellent separation post-reaction. Furthermore, commercial hydrotalcites are environmentally friendly. Organically synthesised hydrotalcites have attracted numerous researchers. The compounds are crucial solid base materials for several organic reactions, such as the Aldol condensation, Knoevenagel, Claisen-Schmidt, and Michael addition reactions. The present review covers the synthesis of magnesium aluminide (MgAl) hydrotalcites with varying magnesium to aluminium (Mg/Al) molar ratios employed to prepare the catalyst. Additionally, the characterisation of MgAl hydrotalcites with X-ray diffraction (XRD), Brunauer-Emmett-Teller (BET), and scanning electron microscopy (SEM) are highlighted. The instruments were utilised to identify the physicochemical properties of the catalyst, including crystallinity, surface area, and morphology. The catalytic activity of MgAl hydrotalcite was explored in the isomerisation of glucose into fructose as a model reaction for the catalytic performance.

Keywords: MgAl hydrotalcite, Mg/Al molar ratio, physicochemical properties, catalytic activity

Abstrak

Hidrotalsit (Mg₆Al₂(OH)₁₆CO₃4H₂O) ialah tanah liat anionik yang wujud secara semula jadi dengan struktur kristal berlapis. Hidrotalsit dikelaskan sebagai pemangkin heterogen yang mempamerkan pemisahan selepas tindak balas yang sangat baik. Tambahan pula, hidrotalsit komersial adalah mesra alam. Hidrotalsit yang disintesis secara organik telah menarik ramai

Munirah et al: A SHORT REVIEW ON THE INFLUENCE OF THE PREPARATION METHOD ON THE PHYSICOCHEMICAL PROPERTIES OF Mg/Al HYDROTALCITE FOR GLUCOSE ISOMERIZATION

penyelidik. Sebatian tersebut merupakan bahan asas pepejal yang penting untuk beberapa tindak balas organik, seperti tindak balas kondensasi Aldol, Knoevenagel, Claisen-Schmidt, dan penambahan Michael. Ulasan semula ini meliputi sintesis magnesium aluminida (MgAl) hidrotalsit dengan pelbagai nisbah molar magnesium kepada aluminium (Mg/Al) digunakan untuk menyediakan mangkin. Selain itu, pencirian hidrotalsit MgAl dengan pembelauan sinar-X (XRD), Brunauer-Emmett-Teller (BET), dan mikroskop elektron pengimbasan (SEM) diserlahkan. Instrumen ini telah digunakan untuk mengenal pasti sifat fizikokimia mangkin, termasuk kehabluran, luas permukaan, dan morfologi. Aktiviti pemangkin hidrotalsit MgAl telah diterokai dalam pengisomeran glukosa kepada fruktosa sebagai tindak balas model untuk prestasi pemangkin.

Kata kunci: MgAl hidrotalsit, nisbah molar Mg/Al, sifat-sifat fizikokimia, aktiviti pemangkin

Introduction

Hydrotalcite is a magnesium-aluminium hydroxycarbonate, a naturally occurring mineral with the chemical composition Mg₆Al₂(OH)₁₆CO₃4H₂O that exhibits a layered crystal structure [1]. The layers consist of positively charged hydroxide layers, while the interlayers contain carbonate anions and water molecules, as displayed in Figure 1. The general hydrotalcites of $[M^{2+}_{(1-x)}M^{3+}_{x}(OH)_{2}]_{x+}(A_{x/n})^{n-}.yH_{2}O$, where M^{2+} M³⁺ are the metal components with divalent and trivalent cations, respectively, and An- is an interlayer anion [2]. Aluminium (Al) is partially substituted in magnesium hydroxide (Mg(OH)₂) and is a brucite structure in magnesium aluminide (MgAl) hydrotalcite, the typical representation of hydrotalcites [3]. The charge imbalance when a trivalent cation replaces the divalent is counterbalanced by the placement of available anions, such as CO₃²⁻, NO₃⁻, Cl⁻, SO₄²⁻, and OH⁻, in the interlayers along with water molecules [4].

The MgAl hydrotalcites are solid bases that exhibit potential catalytic activity and good stability under required reaction conditions [6]. Moreover, hydrotalcites possess two representative and prominent properties, the ability to capture and exchange organic and inorganic anions and the memory effect due to their unique structures [7]. The unique characteristics resulted in the wide range of applications of the compounds as anion exchangers, absorbing agents, stabilisers for polymers, catalysts, electroactive materials, and pharmaceuticals. Hydrotalcite is

classified as a heterogeneous catalyst with numerous advantages over homogeneous catalysts, including catalyst reusability, high purity by-products, and good separation and purification [8]. The wide applications of hydrotalcite catalysts have brought more functionality to the industry. Researchers in the scientific field generally employ hydrotalcite catalysts in organic synthesis reactions [9]. The catalysts are regarded as crucial solid base materials for various organic reactions, including Aldol condensation [10], Knoevenagel [11], Claisen-Schmidt [12], and Michael addition [13] reactions.

Numerous methods, such as co-precipitation, urea, solgel, and hydrothermal synthesis, could be utilised to prepare MgAl hydrotalcite [14, 15]. In this review, the preparation of MgAl hydrotalcite via co-precipitation, urea, and simple methods are discussed in detail. Furthermore, the current review highlights the characterisation of MgAl hydrotalcites with X-ray diffraction (XRD), Brunauer-Emmett-Teller (BET), and scanning electron microscopy (SEM). The instruments identified the physicochemical properties of the catalyst, including crystallinity, surface area, and morphology. The catalytic properties of MgAl hydrotalcite as base catalysts were confirmed by the isomerisation of glucose to fructose. The influence of the preparation method on the physicochemical properties and activity of MgAl hydrotalcites as solid base catalysts based on the characterisation results and the catalytic activities observed are discussed and compared.

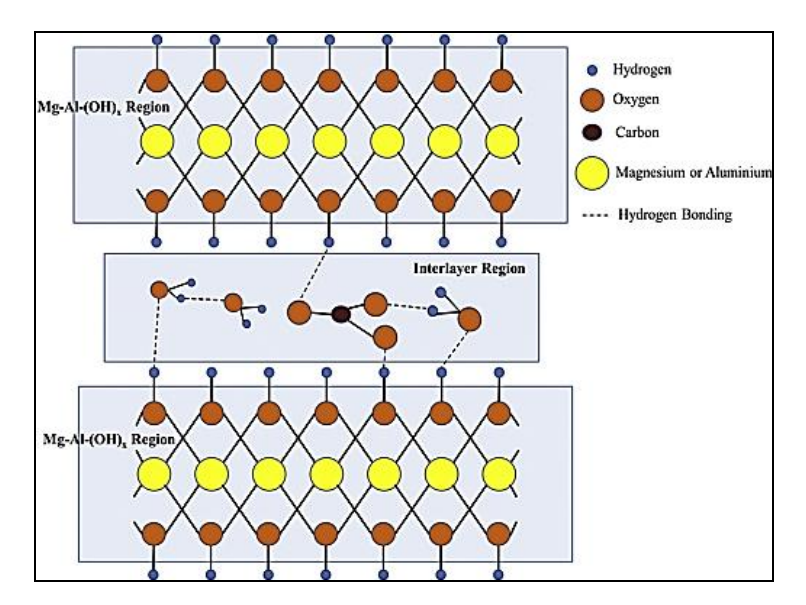


Figure 1. MgAl Hydrotalcite Structure [5]

Preparation of MgAl hydrotalcite catalyst

Researchers have employed numerous methods to synthesise MgAl hydrotalcite catalysts, such as coprecipitation, urea, and simple methods. techniques are applicable in the isomerisation of glucose into fructose. The most common method to prepare hydrotalcite catalyst is the co-precipitation method. The pH of the solution plays a vital role in the technique. If the pH of the solution utilised is low, not all ions would precipitate, while a high pH would result in the dissolution of the metallic ions present [5]. Consequently, it is essential to control the pH of the solution to obtain the hydrotalcite catalyst successfully. Park et al. [14] performed the preparation of MgAl hydrotalcite catalyst via the co-precipitation method by adding aqueous solution B, sodium hydroxide and sodium carbonate in distilled water dropwise into solution A that consisted Mg(NO₃)₂.6H₂O Al(NO₃)₃.9H₂O dissolved in distilled water. During the addition of solution B into solution A, the pH of the solution need to be maintained at approximately 9.5. The resulting solution was vigorously stirred at room temperature for 18 h before proceeding with the filtration process by washing it with distilled water several times. Subsequently, the solid product was dried overnight at 100 °C. The molar magnesium to aluminium (Mg/Al) ratio utilised in the study was

three. The report found that the ratio resulted in a promising catalyst for various base-catalysed reactions due to its excellent base catalytic properties.

The utilisation of varying Mg/Al molar ratios affected the catalytic performance of the MgAl hydrotalcites catalyst obtained [16]. Kang et al. prepared MgAl hydrotalcite via the co-precipitation method with different Mg/Al atomic ratios of from 0.5 to 3.5, which was dissimilar to the investigation by Park et al., where the only Mg/Al molar ratio employed was three. In a similar investigation to [14], Yu et al. reported synthesising fresh, calcined, and rehydrated MgAl hydrotalcite catalysts with the Mg/Al ratio of three [17]. The calcined MgAl hydrotalcite was prepared by calcining the synthesised MgAl hydrotalcite at 450 °C for 10 h in an airstream. In contrast, the rehydrated MgAl hydrotalcite was obtained by hydrating the calcined MgAl hydrotalcite in decarbonated water with vigorous stirring in an inert atmosphere at 60°C for a day followed by filtration and drying overnight at 80 °C.

Urea hydrolysis is one of the techniques employed to acquire MgAl hydrotalcite. The alternative precipitating agent utilised in the method is urea, while the co-precipitating technique employs Na₂CO₃ as the

Munirah et al: A SHORT REVIEW ON THE INFLUENCE OF THE PREPARATION METHOD ON THE PHYSICOCHEMICAL PROPERTIES OF Mg/Al HYDROTALCITE FOR GLUCOSE ISOMERIZATION

precipitating agent [5]. The MgAl hydrotalcite with Mg/Al = 3 was prepared by Park et al. [16] according to this procedure. A solution of Mg(NO₃)₂.6H₂O, Al(NO₃)₃.9H₂O, urea, and distilled water was added into a three-neck flask equipped with a condenser. The reaction was conducted at 95°C for two days, while the pH of the solution was measured every 15 min during the hydrolysis. After the reaction was completed, the resulting mixture was cooled in an ice bath for 30 minutes, filtrated, washed, and dried at 80 °C. Another method employed by the same researchers was the simple method. The technique was based on the hydration of metal oxides obtained by calcination of metal nitrates in the air at 450 °C for 10 h. Subsequently, suitable amounts of MgO and Al₂O₃ were dissolved in distilled water, and the resulting solution was aged at 60 °C for a week. A white precipitate was obtained after the solution was filtered and dried overnight at 80 °C. The method was simpler than the other two techniques as no particular controlled variables were involved with metal oxides [7].

Characterization of MgAl hydrotalcite catalyst

The formation of MgAl hydrotalcite was confirmed with various characterisation tools such as XRD, SEM, and BET. The XRD is one of the most common characterisation tools employed to confirm the layered structure of hydrotalcite. Park et al. [16] reported that the typical XRD pattern of MgAl hydrotalcite exhibits definite crystalline phases observable in fresh catalyst obtained from every method, attributing to the reflections of $2\theta = 11.6^{\circ}$ (003), 23.3° (006), 34.8° (009), 60.7° (110), and 62.0° (113), as shown in Figure 2. The results indicated that the MgAl hydrotalcite with Mg/Al = 3 retained the layered double hydroxide structures even though they are prepared differently. The XRD patterns in Figure 2(b) demonstrated a slight shift of the peaks at the (003) plane, depending on the preparation method employed. The observation was due to the different anions located in the interlayer spaces of the hydrotalcite procured from the three preparation techniques.

Figure 3 displays the XRD pattern of the MgAl hydrotalcite synthesised by Yu et al. [17]. Only the

synthesised and rehydrated MgAl hydrotalcites exhibited the characteristic hydrotalcite XRD peaks similar to the planes reported by Park et al. [16]. No XRD peaks corresponded to the layered structure of hydrotalcite in the calcined MgAl hydrotalcite due to the destruction of the structure by the calcination process. Conversely, the calcined MgAl hydrotalcite maintained the spinel structure of MgAl mixed oxide. Surprisingly, the rehydrated MgAl hydrotalcite preserved the layered structure of hydrotalcite, proving the memory effect of hydrotalcite.

Figure 3 exhibits the XRD peaks for (003) planes in the rehydrated MgAl hydrotalcite, which was much broader compared to the synthesised MgAl hydrotalcite. The observation was due to the exfoliation and vertical breaking of layers in the structure of hydrotalcite, resulting in a smaller crystallite size of the rehydrated MgAl hydrotalcite. A report demonstrated the XRD patterns of MgAl hydrotalcites synthesised with different Mg/Al atomic ratios between 0.5 and 3.5 (Figure 4). The catalysts with the Mg/Al atomic ratios of 0.5 and 1.5 were the least developed. The lower the Mg/Al atomic ratio, the more the peaks shifted towards higher values, attributing to a decreased d-spacing between the hydroxide layers, resulting in reduced distance between layers of MgAl hydrotalcite as the Al content was elevated [16].

The XRD peaks on the (003) plane were applied in the Scherrer equation to calculate the crystallite size of the MgAl hydrotalcites. Specific surface areas (S_{BET}) of the MgAl hydrotalcites were determined via the BET plot. Park et al. found that different preparation methods of MgAl hydrotalcite significantly impacted the crystallite size and S_{BET}. The MgAl hydrotalcite prepared via coprecipitation (HT P) demonstrated the smallest crystallite size and the highest S_{BET} compared to the urea (HT U) and simple (HT S) techniques (Table 1). Yu et al. [17] reported that the crystallite size of the synthesised (HT_A) and rehydrated MgAl (HT_R) hydrotalcites could be calculated as the catalysts prepared through the co-precipitation method but under different conditions retained their LDH structure. Nonetheless, the calcined MgAl (HT C) hydrotalcite did not produce results for crystallite as the structure of the catalyst was destroyed during the calcination process.

Kang et al. [16] concluded that as the Mg/Al atomic ratio decreased, the $S_{\rm BET}$ increased even at the Mg/Al ratio of 1.0 (Figure 4). Nonetheless, based on the XRD characterisation, the 1.0 sample exhibited lower $S_{\rm BET}$ due to the unsuccessful formation of layered structures. Additionally, the catalyst produced with the Mg/Al

ratio of 1.5 demonstrated the most significant $S_{\rm BET}$ and the smallest crystallite size. Consequently, the crystallite size was strongly affected by the preparation method as the growth of the hydrotalcite layers and the degree of layer stacking differed greatly depending on the preparation method. Resultantly, the surfaces of the active sites had different exposures to reactants, resulting in varying catalytic activities of the MgAl hydrotalcites [14].

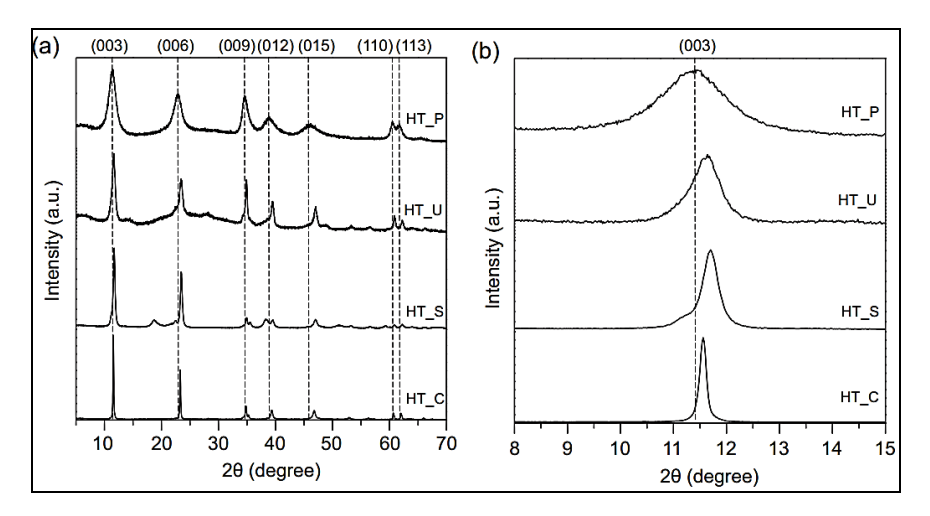


Figure 2. XRD patterns of MgAl hydrotalcite catalyst (HT_P = Co-precipitation, HT_U = Urea, HT_S = Simple & HT_C = Purchased from Sigma-Aldrich) [14]

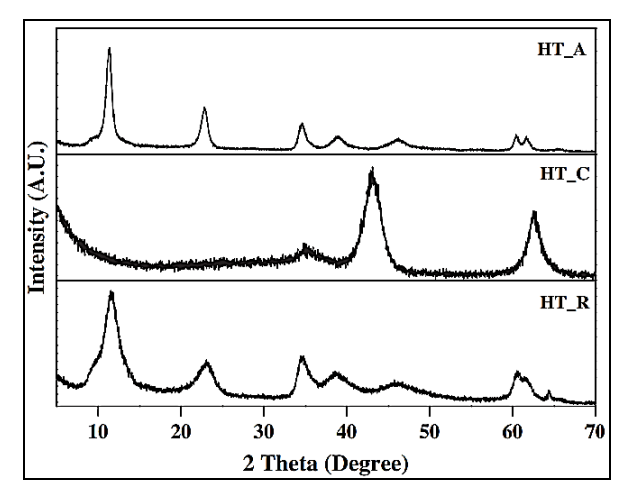


Figure 3. XRD patterns of MgAl hydrotalcite catalyst (HT_A = Synthesized MgAl hydrotalcite, HT_C = Calcined MgAl hydrotalcite & HT_R = Rehydrated MgAl hydrotalcite) [17]

Munirah et al: A SHORT REVIEW ON THE INFLUENCE OF THE PREPARATION METHOD ON THE PHYSICOCHEMICAL PROPERTIES OF Mg/Al HYDROTALCITE FOR GLUCOSE ISOMERIZATION

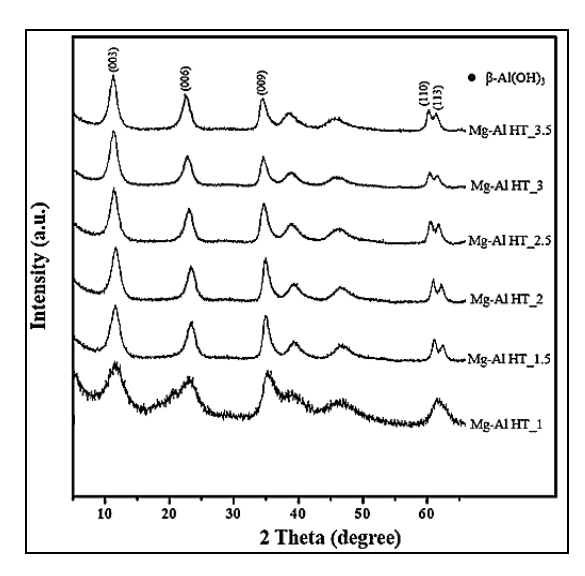


Figure 4. XRD patterns of MgAl hydrotalcite catalyst with different Mg/Al atomic ratio (1.0 – 3.5) [16]

Table 1. Crystallite size and specific surface areas of the Mg-Al hydrotalcite catalyst

Catalyst Used	Synthesis Method	Mg/Al Atomic Ratio	Crystallite Size (nm) (At (003) plane)	S _{BET} (m ² g ⁻¹)	Ref
Mg-Al	Co-precipitation (HT_P)	3.0	5.80	141.0	
	Urea (HT_U)	3.0	12.6	36.6	[14]
	Simple (HT_S)	3.0	21.3	1.3	
Mg-Al	Co-precipitation (HT_A)	3.0	9.9	68.9	
	(HT_C)	3.0	-	158.5	[17]
	(HT_R)	3.0	4.1	88.8	
Mg-Al	Co-precipitation (HT_1.0)	1.0	-	86.3	
	(HT_1.5)	1.5	3.9	204.5	
	(HT_2.0)	2.0	4.7	110.7	[16]
	(HT_2.5)	2.5	4.6	130.1	
	(HT_3.0)	3.0	4.7	109.0	
	(HT_3.5)	3.5	5.2	89.1	
Mg-Al	Co-precipitation (HT_1.0)	1.0	7.9	147	
	(HT_1.5)	1.5	8.4	131	
	(HT_2.0)	2.0	10.3	110	[18]
	(HT_3.0)	3.0	8.1	37	
	(HT_5.0)	5.0	6.8	23	

Upare et al. [18] reported XRD patterns for all the samples with rehydrated Mg/Al ratios from 1.0 to 5.0 (Figure 5). Based on the XRD characterisation, an increase of Mg/Al ratio was slightly shifted to a lower angle on the (003) plane at 2θ of 11.4° corresponding to the interlayer anion. This observation indicating that the interlayer spacing and unit cell parameter increased with Mg/Al ratio of the rehydrated hydrotalcite [18]. Additionally, the crystallite size increases from 7.9 to 10.3 nm as the rehydrated hydrotalcite with Mg/Al ratio increases from 1.0 to 3.0. Conversely, the crystallite size decreases from 10.3 to 6.8 nm as Mg/Al ratio decreases from 3.0 to 5.0.

Apart from XRD and BET analysis, SEM analysis also can be employed to confirm the structure of MgAl hydrotalcites and to prove the crystallite size calculated from the XRD analysis. The characteristic layered

structures of the synthesised MgAl hydrotalcites were composed of platelet-like particles that agglomerated in different ways depending on the preparation method, as shown in Figure 6. In particular, the HT_P MgAl hydrotalcite with the smallest crystallite size exhibited a sand-rose morphology (Figure 6(a)) [14]. Kang et al. [16] observed a similar sand-rose morphology, indicating that the co-precipitation method successfully produced the layered MgAl hydrotalcite structure (Figure 7). The findings might be due to the surfaces being easily exposed to reactants, which strongly affected the catalytic activity of the catalysts [14]. Consequently, Park et al. reported that MgAl hydrotalcites prepared according to the co-precipitation procedure could be expected to exhibit superior activity over other hydrotalcite catalysts in base-catalysed reactions [14].

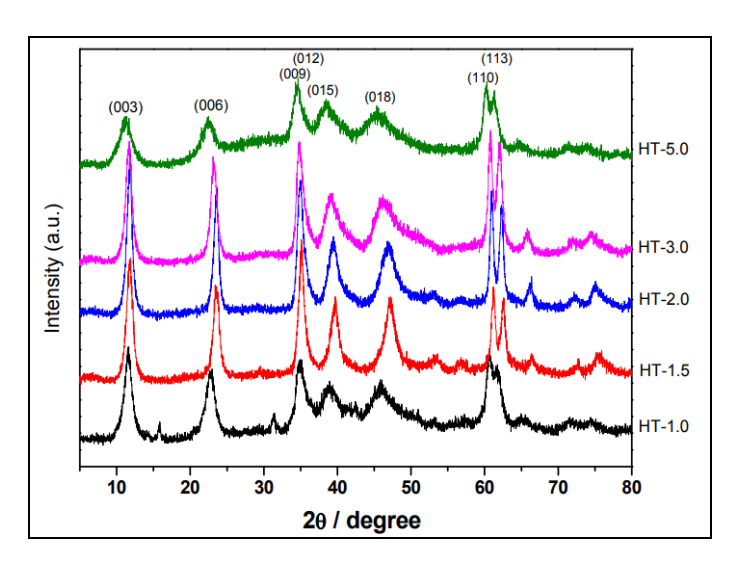


Figure 5. The XRD patterns of the rehydrated MgAl hydrotalcite catalyst synthesised with different Mg/Al atomic ratios (1.0–3.5) [18]

Munirah et al: A SHORT REVIEW ON THE INFLUENCE OF THE PREPARATION METHOD ON THE PHYSICOCHEMICAL PROPERTIES OF Mg/Al HYDROTALCITE FOR GLUCOSE ISOMERIZATION

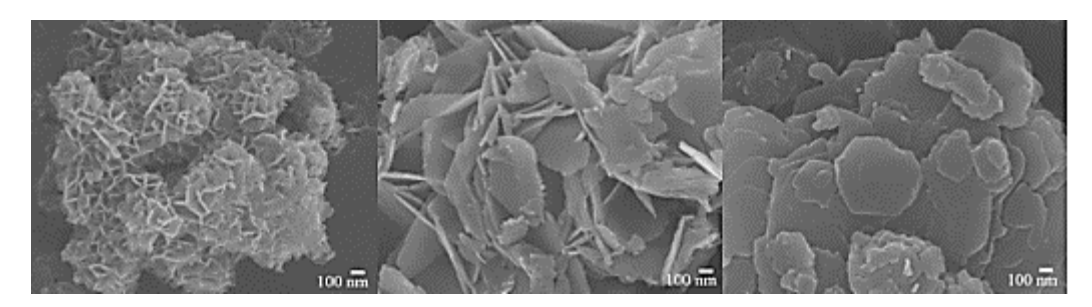


Figure 6. SEM images of (a) HT_P (b) HT_U (c) HT_S [14]

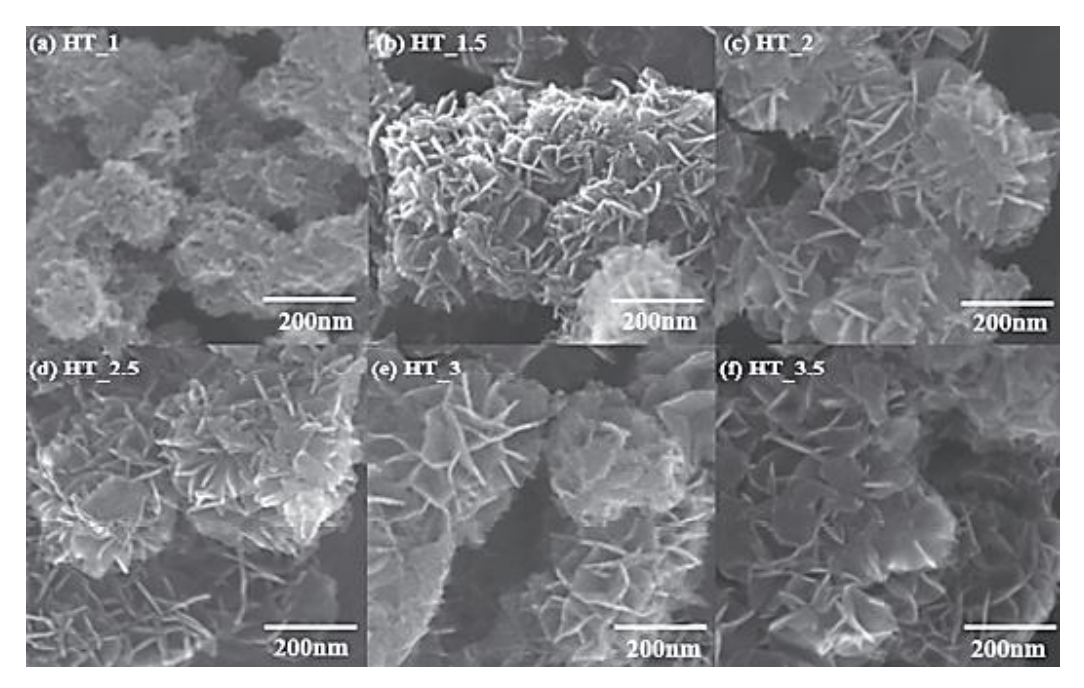


Figure 7. SEM images of MgAl hydrotalcite with different Mg/Al atomic ratio [16]

Catalytic reaction in the isomerization of glucose to fructose

Glucose isomerisation was employed as a model reaction to explore the catalytic activity of the synthesised MgAl hydrotalcites. The isomerisation of glucose into fructose is a critical step in biomass technologies [19]. Generally, conversion isomerisation of glucose into fructose was conducted in a batch-type glass reactor with glucose as the reactant, MgA1 hydrotalcite as the catalyst, dimethylformamide. The reaction was conducted at 100°C for 3 h. After the reaction was completed, the reactor was cooled in an ice bath, followed by filtrating

the resultant solution to separate the catalyst. Lastly, the filtrate was analysed with HPLC equipped with a UV-Vis detector. Table 2 tabulates the catalytic activity of the synthesised MgAl hydrotalcite as a solid base catalyst in the isomerisation of glucose into fructose, as reported by Park et al., Yu et al., and Kang et al. [14, 16, 17]. According to Park et al. [14], the MgAl hydrotalcite prepared by co-precipitation produced the highest fructose yield at 25% compared to the other methods. Moreover, since the method fabricated the smallest crystallite size with abundant surface base sites, numerous researchers utilised MgAl

hydrotalcite catalyst prepared with the co-precipitation technique to convert glucose into fructose [14].

Yu et al. [17] found that the highest fructose yield (30%) was obtained when the rehydrated MgAl hydrotalcite catalyst was employed. The results were due to the abundant and selective surface base sites for glucose isomerisation were produced during the rehydration process. Meanwhile, Kang et al. [16] studied the effects of Mg/Al with different ratios on the catalytic activity of MgAl hydrotalcite. They reported that the MgAl hydrotalcite with an Mg/Al ratio of 1.5 produced the highest fructose yield (42%). The increased catalytic activity of the MgAl hydrotalcite during the isomerisation of glucose into fructose was assumed to be due to the small crystallite size obtained by co-precipitation of Mg/Al with the molar ratio of 1.5. Theoretically, the larger the surfaces of the MgAl hydrotalcite exposed to the reactants, the catalyst would exhibit a better catalytic activity.

A report demonstrated by Upare et al. on glucose isomerization, 1-butanol was used as the solvent. It is noted to be very effective in preventing the formation of humin based on their previous study [18]. The

uniqueness of 1-butanol as a solvent for glucose isomerization showed that there is no leaching of Mg ions from the hydrotalcite catalyst compared to other solvents such as water, ethanol and dimethylformamide [18]. Notably, the rehydrated MgAl hydrotalcite catalyst with Mg/Al ratio of 2.0 is the excellent catalyst for the isomerization of glucose into fructose with the highest percent yield (51%). The fructose yield increased from Mg/Al ratio of 1.0 to 2.0, however, it decreased from Mg/Al ration of 2.0 to 5.0. These results showed that the high rehydrated Mg/Al ratio were not favourable in the formation of fructose [18].

Apart from using the combination of 1-butanol and hydrotalcite catalyst in glucose isomerisation, ethanol is one of the solvent used in this reaction. Yabuhita et al. found that the use of ethanol enhance the fructose yield and thus, obtained 50% yield which is quite higher compared to other results (Table 2). Furthermore, the removal of ethanol after the reaction is much simpler as its boiling point is quite low than water [20]. By having Mg/Al molar ratio of 3, Yabushita et al. [20] successfully acquired the formation of fructose within a short time.

Table 2. Recent studies on MgAl hydrotalcite for Isomerization of Glucose into Fructose

Synthesis Method	Mg/Al atomic ratio	Conditions	Conversion of glucose (%)	Selectivity of fructose (%)	Yield for fructose (%)	Ref
Co-precipitation			38	65	25	
Urea	3.0	At 100°C for	22	69	14	[14]
Simple		3 h	21	71	13	
Co-precipitation						
Synthesized HT			48	53	25	
Calcined HT	3.0	At 100°C for	75	32	23	[17]
Rehydrated HT		5 h	63	47	30	
Co-precipitation						
HT	1.0		25	98	24	
	1.5		62	71	42	
	2.0	At 100°C for	58	73	41	[16]
	2.5	5 h	55	70	39	
	3.0		48	81	40	
	3.5		47	79	38	

Munirah et al: A SHORT REVIEW ON THE INFLUENCE OF THE PREPARATION METHOD ON THE PHYSICOCHEMICAL PROPERTIES OF Mg/Al HYDROTALCITE FOR GLUCOSE ISOMERIZATION

Table 2 (cont'd).	Recent studies or	n MgAl hydrotalcite for	r Isomerization of	Glucose into Fructose

Synthesis Method	Mg/Al atomic ratio	Conditions	Conversion of glucose (%)	Selectivity of fructose (%)	Yield for fructose (%)	Ref
Co-precipitation						
Rehydrated	1.0		46	65	30	
(HT/1-Butanol)	•		59	83	49	
(,	2.0	At 120°C for	62	82	51	[18]
	3.0	5 h	66	70	46	
	5.0		72	58	42	
Co-precipitation						
(HT/Ethanol)	3.0	At 90°C for 2 h	61	83	50	[20]

Conclusion

Based on the comprehensive literature review, it could be concluded that the preparation method of MgAl hydrotalcite strongly influenced the growth and stacking of its layers and the type of anions intercalated during the formation of the layered structure. The unique characteristics of the MgAl hydrotalcites led to varied crystallite sizes and morphologies. The coprecipitation method was more favourable than the urea and simple methods to fabricate MgAl hydrotalcites with surfaces that consist of numerous basic sites. Furthermore, different Mg/Al molar ratios also affected the formation and catalytic activity of the synthesised MgAl hydrotalcite. The catalytic activity of the synthesised MgAl hydrotalcite was observed in the isomerisation of glucose into fructose. The MgAl hydrotalcite prepared via co-precipitation produced the highest fructose yield as its small crystallite size and sand-rose morphology result in significant exposure of its surface active sites to the reactants.

Acknowledgement

The authors acknowledge the generous support of Organic Synthesis Research Laboratory, Institute of Science (IOS), Universiti Teknologi MARA, Puncak Alam Campus and Faculty of Applied Sciences, Universiti Teknologi MARA (UiTM), Shah Alam as well as the financial support of the Ministry of Higher Education, Malaysia FRGS Grant [600-RMC/SRC/5/3 (024/2020)].

References

- 1. Dębek, R., Motak, M., Grzybek, T., Galvez, M. E. and Da Costa, P. (2017). A short review on the catalytic activity of hydrotalcite-derived materials for dry reforming of methane. *Catalysts*, 7(1): 32.
- Gomes, J. F. P., Puna, J. F. B., Gonçalves, L. M. and Bordado, J. C. M. (2011). Study on the use of MgAl hydrotalcites as solid heterogeneous catalysts for biodiesel production. *Energy*, 36(12): 6770-6778.
- Baskaran, T., Christopher, J. and Sakthivel, A. (2015). Progress on layered hydrotalcite (HT) materials as potential support and catalytic materials. RSC Advances, 5: 98853-98875.
- 4. Tsujimura, A., Uchida, M. and Okuwaki, A. (2007). Synthesis and sulfate ion-exchange properties of a hydrotalcite-like compound intercalated by chloride ions. *Journal of Hazardous Materials*, 143(1–2): 582-586.
- Sikander, U., Sufian, S. and Salam, M. A. (2017).
 A review of hydrotalcite based catalysts for hydrogen production systems. *International Journal of Hydrogen Energy*, 42: 19851-19868.
- 6. Delidovich, I. and Palkovits, R. (2015). Structure-performance correlations of Mg-Al hydrotalcite catalysts for the isomerization of glucose into fructose. *Journal of Catalysis*, 327: 1-9.

- Lee, G., Kang, J. Y., Yan, N., Suh, Y. W. and Jung, J. C. (2016). Simple preparation method for Mg–Al hydrotalcites as base catalysts. *Journal of Molecular Catalysis A: Chemical*, 423: 347-355.
- 8. Nur Fazira Edlina, I., Nazrizawati, A. T., Erma Hafiza, I. A. Z. and Noraini, H. (2020). MgAl mixed oxide derived alkali-free hydrotalcite for transesterification of waste cooking oil to biodiesel. *ASM Science Journal*, 13: 1-7.
- Nope, E., Sathicq, G., Martinez, J., Rojas, H., Luque, R. and Romanelli, G. (2018). Hydrotalcites in Organic Synthesis: Multicomponent Reactions. *Current Organic Synthesis*, 15(8): 1073-1090.
- Kikhtyanin, O., Kadlec, D., Velvarská, R. and Kubička, D. (2018). Using Mg-Al mixed oxide and reconstructed hydrotalcite as basic catalysts for aldol condensation of furfural and cyclohexanone. *ChemCatChem*, 10(6): 1464-1475.
- Jadhav, A. L. and Yadav, G. D. (2019). Clean synthesis of benzylidenemalononitrile by Knoevenagel condensation of benzaldehyde and malononitrile: Effect of combustion fuel on activity and selectivity of Ti-hydrotalcite and Znhydrotalcite catalysts. *Journal of Chemical Sciences*, 131(8): 79.
- Arias, K. S., Climent, M. J., Corma, A. and Iborra, S. (2016). Chemicals from biomass: Synthesis of biologically active furanochalcones by claisen–schmidt condensation of biomass-derived 5-hydroxymethylfurfural (HMF) with acetophenones. *Topics in Catalysis*, 59(13–14): 1257-1265.
- Mokhtar, M., Saleh, T. S. and Basahel, S. N. (2012). Mg-Al hydrotalcites as efficient catalysts for aza-Michael addition reaction: A green protocol. *Journal of Molecular Catalysis A:*

- Chemical, 353-354: 122-131.
- 14. Park, S., Kwon, D., Kang, J. Y. and Jung, J. C. (2019). Influence of the preparation method on the catalytic activity of Mg-Al hydrotalcites as solid base catalysts. *Green Energy and Environment*, 4(3): 287-292.
- Labuschagné, F. J. W. J., Wiid, A., Venter, H. P., Gevers, B. R. and Leuteritz, A. (2018). Green synthesis of hydrotalcite from untreated magnesium oxide and aluminum hydroxide. *Green Chemistry Letters and Reviews*, 11: 18-28.
- Kang, J. Y., Lee, G., Suh, Y. W. and Jung, J. C. (2017). Effect of Mg/Al atomic ratio of Mg-Al hydrotalcites on their catalytic properties for the isomerization of glucose to fructose. *Journal of Nanoscience and Nanotechnology*, 17(11): 8242-8247.
- Yu, S., Kim, E., Park, S., Song, I. K. and Jung, J. C. (2012). Isomerization of glucose into fructose over Mg-Al hydrotalcite catalysts. *Catalysis Communications*, 29: 63-67.
- Upare, P. P., Chamas, A., Lee, J. H., Kim, J. C., Kwak, S. K., Hwang, Y. K., and Hwang, D. W. (2020). Highly efficient hydrotalcite/1-butanol catalytic system for the production of the highyield fructose crystal from glucose. *ACS Catalysis*, 10(2): 1388-1396.
- Huang, H., Meng, X. G., Yu, W. W., Chen, L. Y. and Wu, Y. Y. (2021). High selective isomerization of glucose to fructose catalyzed by amidoximed polyacrylonitrile. *ACS Omega*, 6(30): 19860-19866.
- 20. Yabushita, M., Shibayama, N., Nakajima, K. and Fukuoka, A. (2019). Selective glucose-to-fructose isomerization in ethanol catalyzed by hydrotalcites. *ACS Catalysis*, 9(3): 2101-2109.

Malaysian Journal of Analytical Sciences (MJAS)



Published by Malaysian Analytical Sciences Society

OPTIMIZATION PARAMETERS FOR ELECTROPOLYMERIZATION OF MELAMINE IN DEEP EUTECTIC SOLVENT

(Pengoptimuman Parameter Elektropempolimeran Melamin Dalam Pelarut Eutektik Dalam)

Yeet Hoong Chang¹, Pei Meng Woi^{1,2}*, Yatimah Alias^{1,2}

¹Department of Chemistry, Faculty of Science ²University Malaya Centre for Ionic Liquids (UMCiL) University of Malaya, 50603 Kuala Lumpur, Malaysia

*Corresponding author: pmwoi@um.edu.my

Received: 15 September 2021; Accepted: 10 December 2021; Published: 28 April 2022

Abstract

Polymelamine is a new class of polymer that possess electrocatalytic behavior in dopamine (DA) detection. Our previous studies have successfully replaced the conventional acidic electrolyte to deep eutectic solvent (DES) has open the opportunity for a greener solvent in used. Herein we report the optimization process of melamine electropolymerize in DES- reline. Various electrochemical techniques have been employed to studies the ideal parameters. The optimum potential window, scan rate, and number of scan cycles were recorded as -0.20 V - 1.60 V, 50 mV s⁻¹ and five scan cycles, respectively. Cyclic voltammetry (CV) was employed in the electropolymerization of melamine to optimize the redox behavior of polymelamine film on electrode surface. The growing of polymer film which indicated by the increased of reduction current can be well-controlled by the slow scan rate and optimum scan cycles which leads to strong adhesion and uniform morphology. Amperometry sensing on DA was performed to study and compare the sensitivity and limit of detection for the polymers synthesized in varied parameters. A brief discussion on the principal polymerization factors that would affecting the electrocatalytic behavior of melamine is included.

Keywords: deep eutectic solvent, electropolymerization, melamine, optimization

Abstrak

Polimelamin adalah kelas polimer baharu yang mempunyai tingkah laku elektromangkin dalam pengesanan dopamin (DA). Kajian yang dilaporkan terdahulu menujukkan kerjayaan penggantian elektrolit berasid konvensional kepada pelarut eutektik (DES). Kerjayaan ini membuka peluang untuk pelarut yang lebih mesra alam digunakan. Dengan ini, kami melaporkan proses pengoptimum elektropolimerisasi melamin dalam DES-relin. Pelbagai teknik elektrokimia telah digunakan untuk mengkaji parameter yang terbaik. Julat keupayaan, kadar imbasan dan bilangan kitaran imbasan yang terbaik dicatat pada -0.20 V – 1.60 V, 50 mVs⁻¹ dan lima kitaran imbasan. Siklik voltametri (CV) telah digunakan dalam elektropolimerisasi melamin untuk mengoptimumkan tingkah laku elektropemangkinan lapisan polimelamin pada permukaan elektrod. Pertumbuhan lapisan polimer yang ditunjukkan dalam penainkkan arus penurunan boleh dikawal baik dengan kadar imbasan yang perlahan dan kitaran imbasan optimum untuk mencapai lekatan yang kuat dan morfologi yang seragam. Penderiaan amperometri pada DA telah dijalankan untuk mengkaji dan membandingkan kepekaan dan had pengesanan rendah untuk polimer yang disintesis dalam

parameter yang berbeza-beza. Perbincangan ringkas tentang faktor-faktor elektropolimerisasi yang mempengaruhi tingkah laku elektromangkin melamin telah disertakan.

Kata Kunci: pelarut eutektik dalam, elektropempolimeran, melamin, pengoptimuman

Introduction

Heretofore, the polymers such as polyisoprene, polystyrene, polythiophene, polyaniline, polypyrrole, formaldehyde resin and their by-products have been examined extensively as promising candidates in sensor development. A novel class of conducting polymer - polymelamine (PME) was proposed. PME is made from the nitrogen-rich melamine (1,3,5-Triazine-2,4,6-triamine) which is a heterocyclic organic compound. The synthesis methods of PME included chemical, electrochemical, photo-initiating, biocatalytic, and plasma polymerization. Among all, electropolymerization is commonly employed due to its advantages in facile engineer the morphology, thickness, density, and growing rate of the polymer. **PME** can be synthesized easily electropolymerization technique by oxidize the amino groups found in melamine. In the discipline of electrochemistry, PME has been employed as a stable matrix to enhance the effective immobilization of nanomaterials on it. It is also employed as electrochemical sensor owing to the existence of numerous active groups such as nitrogen and amine. PME and its offshoots were soon utilized extensively in sensing of different neurotransmitters, pharmaceutic particles, and toxic heavy metals [1-3]. Moreover, PME composited with nanocarbon demonstrated high specificity and exhibited exceptional catalytic reaction over broad extent of molarity [4].

Deep eutectic solvent (DES) draws great attention lately owing to their solvation potential, conductivity, simple synthesis method, cost effective and many are biodegradable [5]. DES are commonly applied in two principal fields: metal processing (metal electropolishing, metal dissolution, metal deposition) and as synthesis solvent [6-8]. Reline (a Type III DES) was employed as stimulant and reducing mediator for polymerization of hydrophilic monomer at temperature close to ambient [9]. Reline and glyceline (a Type III DES) were proposed to substitute typical aqueous

solution in free-radical polymerization of acrylamide [10]. The outcome shows the polymer synthesized has similar molecular mass compared to the polymer synthesized in aqueous solution. Moreover, polyaniline in DES demonstrated exceptional synthesized conductivity reported at 50 S cm⁻¹ [11]. The shows excellent reversibility polyaniline doping/dedoping mechanisms which indicated rapid charge transfer. Furthermore, Type I DES has effectively utilized as a cationic catalyst for epoxy resin curing [12].

Despite that, DES being the synthesis solvent particularly in the formation of polymers are rarely examined in terms of polymerization parameters. Conventionally, electropolymerization of melamine was conducted in acidic electrolyte [1]. Acidic electrolyte with pH less than two is the key for the growth and establishment of radical cations that required in rate-limiting step during electropolymerization of melamine. In accordance with our published work, we have successfully superseded the conventional acidic electrolyte with DES. PME synthesized in DES manifests excellent sensitivity, specificity, and stability [13]. In this work, we focus on the optimization of polymerization parameters, and discuss the effect of these parameters in polymerization of melamine. Reline is selected as study target due to the enlightenment of the novel perception asserted that chloride ion (Cl⁻) is the vital factor for PME formation [14]. Reline is a mixture of choline chloride and urea in 1:2 ratio, urea molecules offer plentiful positive hydrogen bonding spot to adopt the Cl- negative ion into their polar matrix [15]. PME synthesized in reline is then applied in electrochemical qualification and quantification of dopamine (DA).

Materials and Methods

Materials

Melamine monomer, choline chloride, ethylene glycol, urea, glycerol, dopamine (DA), potassium dihydrogen

phosphate (KH_2PO_4) and potassium hydrogen phosphate (K_2HPO_4) were purchased from Sigma Aldrich. Ultra-pure deionized (DI) water with a resistance of 18.3 M Ω cm (Merck Synergy) was used in all sample preparations. All the chemical reagents were of analytical grade and were used without further purification.

Instrumentation

The surface morphology of the bare and modified sensor was studied by using Horizontal Attenuated Total Reflectance-infrared spectroscopy (HATR-IR, PerkinElmer, Inc). All electrochemical experiments were carried out by Autolab potentiostat/galvanostat PGSTAT-302N with an ordinary three electrodes system, containing glassy carbon electrode (GCE) (ALS-Japan, diameter = 3.0 mm, surface area = 0.071cm²) as working electrode, a platinum braid wire (BASi, diameter = 1.0 mm, surface area = 0.008 cm^2) as counter electrode and sodium chloride (KCl) saturated Ag/AgCl (BASi) as the reference electrode. All the potential readings were referred to Ag/AgCl unless stated elsewhere. A pseudo reference electrode (Ag wire, BASi, diameter = 1.0 mm, surface area = 0.008 cm²) was employed for electrochemical polymerization of polymer in DES or mixtures. The referred reading of the pseudo wire with respect to the Ag/AgCl electrode was at + 90 mV. Amperometry analysis of DA was conducted at constant potential (0.20 V) in PBS (0.10 M, pH 7.0).

Preparation of deep eutectic solvent

Type III DES - reline was prepared by mixing choline chloride into urea, in 1:2 molar ratio. The mixture was heat under oil bath with control temperature from 55°C to 60°C until a clear solution was obtained. Reline was then set aside to cool down to ambient temperature prior served as supporting electrolyte for the electropolymerization of melamine.

Preparation of 0.10 mM melamine(reline) solution

A 10.0 mM of melamine was prepared by mixing 5.0 mg of melamine into 4.0 mL reline followed by ultrasonication for 30 minutes until a homogeneous

solution is achieved. The as-prepared melamine solution was named as melamine(reline).

Synthesis of PME(reline)/GCE

GCE was gently polished with $0.05~\mu M$ alumina slurry and then rinsed with DI water and ethanol a few times until a clean mirror-like surface was obtained. A clean GCE was then immersed into melamine(reline) solution and CV was scanned from the studied potential window at various scan rates for different number of cycles as part of the optimization studies. The fabricated PME(reline)/GCE was gently rinsed with DI to wash off the monomer residue and then set to dry in ambient condition before used.

Preparation of phosphate buffer solution

Phosphate buffer solution (PBS) was used as supporting electrolyte in amperometry sensing of DA. 27.2 g of KH_2PO_4 and 34.8 g of K_2HPO_4 were individually poured into 1.0 L volumetric flask and added with DI until meniscus line forming solution A (0.20 M) and B (0.20 M), respectively. PBS (0.10 M, pH 7.0) was prepared by mixing 39.0 mL solution A and 61.0 mL solution B follow diluted with DI to 200 mL. The pH value of the buffer solution was confirmed with pH meter (model pH 700, Eutech Instruments).

Preparation of DA stock solution

 $1000~\mu M$ of DA stock solution was prepared by adding 0.015~g DA into 100~mL volumetric flask and added DI until meniscus. DA solution was freshly prepared daily and kept in refrigerator at $4^{\circ}C$ before used for not more than 12~hours. A layer of aluminum foil was used to cover the stock solution to avoid contact with light.

Results and Discussion

Optimization of potential window for melamine electropolymerization

To understand the effect of applied potential window on the melamine electropolymerization process, repeated CV cycling tests were carried out on melamine dissolved in reline. To begin with the potential window investigation, parameters of melamine concentration, scan rate, scan cycles, and temperature were fixed at 10.0 mM, 50 mV s⁻¹, five scan cycles and 25°C, respectively. Figure 1 shows the

electropolymerization of melamine at fixed starting potential (-0.20 V) and ended with varied potentials: 1.20 V, 1.40 V, 1.60 V, and 1.80 V. The electropolymerization behavior of melamine in reline was different from the conventional electrolyte - H2SO4 as in previous literature [14]. In conventional electrolyte, a cathodic peak at around + 0.85 V was noticed owing to the coupling among the melamine molecules and carbonyl groups (C=O and/or C-O) from the DES instead of head-to-head linking of amine groups betwixt the melamine molecules [13]. Figure 1(c) illustrated an anodic peak at 1.20 V was observed for the electropolymerization of melamine from -0.20 to 1.60 V. The anodic peak was due to functionalization of melamine monomers with carbonyl groups (C=O) attributed from the reline and forming an electroactive PME functionalized DES. Likewise, an anodic peak at about 1.20 V was observed in Figure 1(b) for applied potential window -0.20 - 1.40 V, indicating the formation of PME. However, it noticed that the peak current was lower as compared to the electropolymerization of melamine at -0.20 to 1.60 V, indicating the limit of charge depository of polymer formed at -0.20 - 1.40 V. Noted that in Figure 1(a) and Figure 1(d), no anodic peak was observed with the applied potential. This is probably due to a narrow potential window restricts the charge depository ability of monomer during polymerization, while a wide potential window will lead to overoxidation of polymer, causing breakage of polymer chain [16]. From these, it was concluded that potential range from -0.20 V to 1.60 V is well suited to carry out the melamine electropolymerization for the PME formation.

To further verify how the tuning of potential window affecting the performance of PME in dopamine (DA)

sensing, all the PME/GCE electrodes synthesized in varied potential window were further tested in two aspects: sensitivity and limit of detection (LOD). In amperometry setting, DA is oxidised at potential 0.20 V [13]. Therefore, amperometry was scanning at fixed potential (0.20 V) with additional of DA with concentration ranging from 100 - 1200 µM in PBS (0.10 M, pH 7.0) as shown in Figure 2. Sensitivity and LOD were then calculated based on the amperometric results and summarized in Figure 3 and Table 1. Naming of PME was based on the maximum applied potential e.g., PME synthesized in reline with potential window applied at -0.20 - 1.20 V is named as PME(reline +1.20 V). Based on Figure 2, it was noticed that the amperometry result of PME(reline +1.60 V) recorded the highest current response as compared to the other PME. Figure 3(A) and (B) illustrated the calculated sensing sensitivity and LOD of DA at PME(reline), respectively. Noted that the sensing of DA at PME(reline +1.60 V) recorded the highest sensitivity and lowest LOD recorded at 0.044 $\mu A~\mu M^{-1}~cm^{-2}$ and 0.198 μM , respectively which are in line with amperometry result shown in Figure 2. The sensitivity line graph of over-potential showed increment from +1.20 V and reached maximum at +1.60 V. At the same time, LOD obey the opposite relationship and reaching the minimum LOD at +1.60 V. In case, further widen the potential window of PME(reline) to +1.80 V, the electrode sensing capability has reduced drastically where the LOD did not showed any improvement and has been increased 10-fold recorded at 2.070 µM compared to +1.60 V. The result justified the optimized potential window for electropolymerization of melamine is -0.20 V to +1.60 V.

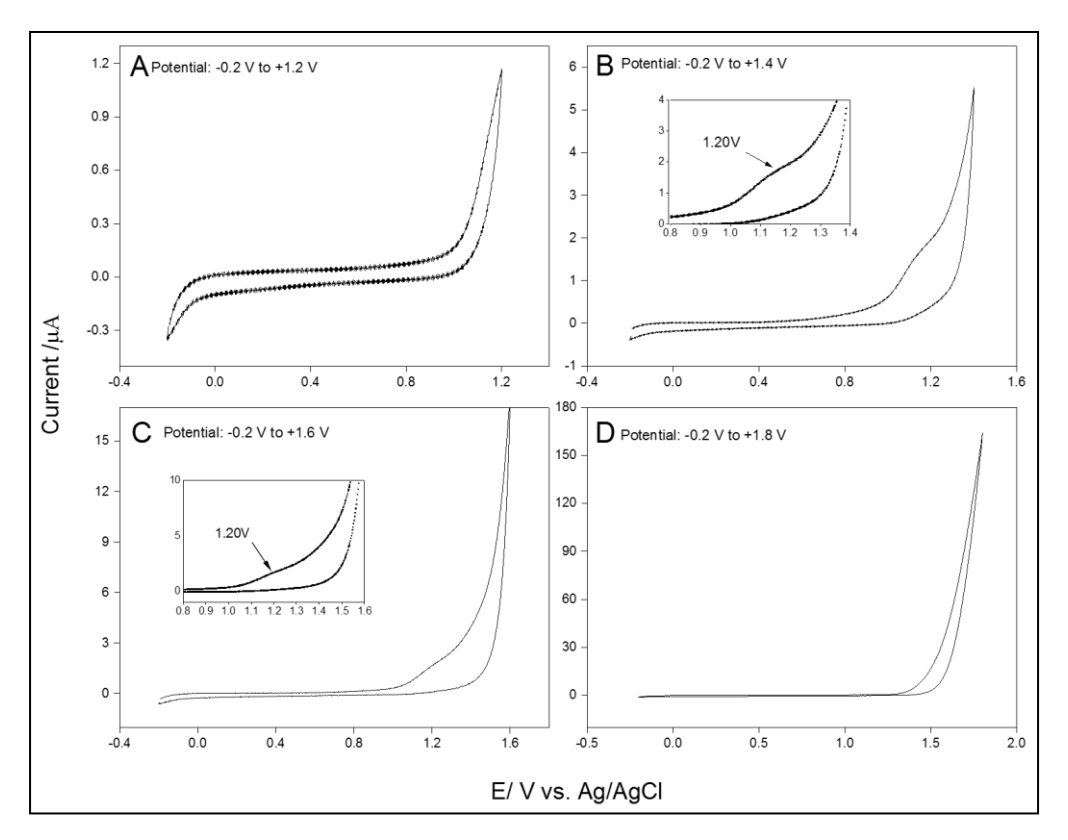


Figure 1. Electropolymerization of melamine (10.0 mM) in reline scanning with varied potential window a) -0.20 to 1.20 V, b) -0.20 to 1.40 V, c) -0.20 to 1.60 V, and d) -0.20 to 1.80 V at 50 mV s⁻¹ with five scan cycles

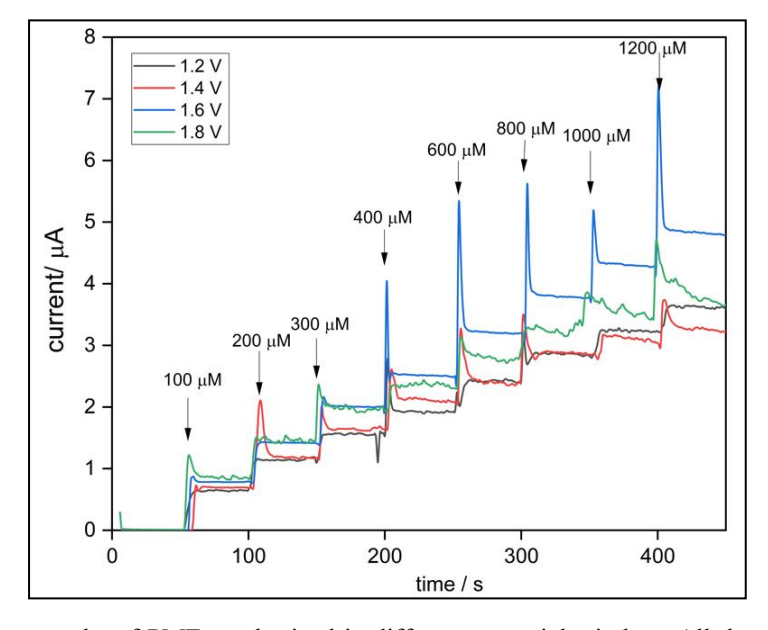


Figure 2. Amperometry results of PME synthesized in different potential window. All the amperometry test were scanned at a fixed potential (0.20 V) with additional of DA with concentration ranging from 100 - 1200 μ M in PBS (0.10 M, pH 7.0)

Chang et al: OPTIMIZATION PARAMETERS FOR ELECTROPOLYMERIZATION OF MELAMINE IN DEEP EUTECTIC SOLVENT

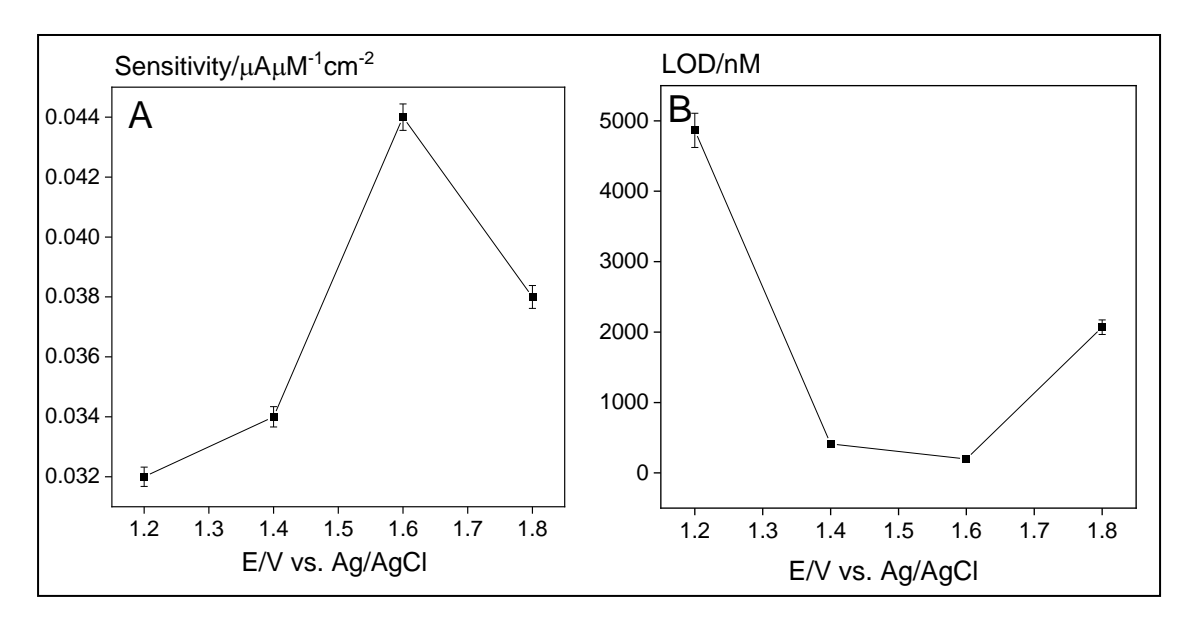


Figure 3. Graphs of (a) sensitivity and (b) LOD results versus varied potential window applied for electropolymerization of melamine in reline.

Table 1. Optimization studies for electropolymerization of melamine in reline, DA as model analyte; sensing with amperometry at 0.20 V vs Ag/AgCl: Effect of electropolymerization potential window, effect of scan rate and effect of scan cycles

Parameter Varied		Eutectic Solvent	Sensitivity / μ A μ M ⁻¹ cm ⁻²	LOD / μM
	1.2	reline	0.032	4.8640
Determinal (V)	1.4	reline	0.034	0.4110
Potential (V)	1.6	reline	0.044	0.1980
	1.8	reline	0.038	2.0700
	10	reline	0.035	0.4450
	25	reline	0.044	0.3260
Scan rate (mV s ⁻¹)	50	reline	0.044	0.1980
	75	reline	0.046	1.0770
	100	reline	0.045	0.7860
	3	reline	0.038	0.6800
G 1	5	reline	0.044	0.1980
Scan cycles	10	reline	0.039	1.1800
	15	reline	0.044	0.5680

Optimization of scan rate for melamine electropolymerization

Figure 4 illustrates the electropolymerization behavior of melamine in different scan rates. Scan rate determine the time taken to complete one polymerization cycle. In this study, the recorded voltammogram was not able to distinct any significant observation to relate the effect of scan rate on polymerization of melamine. Thus, these electrodes

prepared at 10, 25, 50, 75, and 100 mV s⁻¹ scan rates were analyzed using the amperometry technique to investigate the performance in DA sensing. Figure 5 displays the amperometry plot of PME whereas Figure 6 displays the calculated sensitivity and LOD based on the amperometry results obtained.

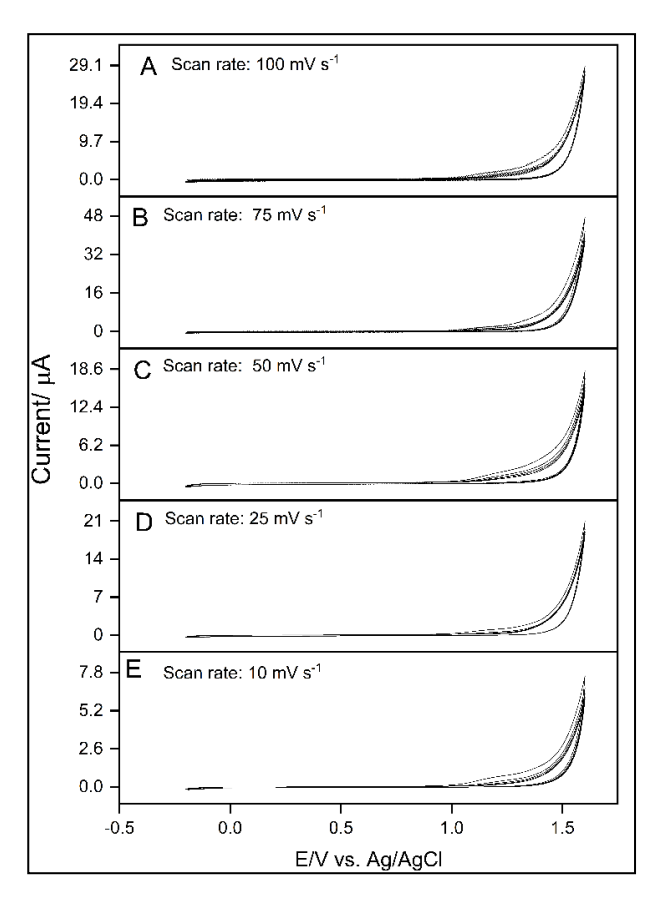


Figure 4. Electropolymerization of melamine (10.0 mM, -0.20- 1.60 V, five cycles) in reline scanning with varied scan rate (10, 25, 50, 75, and 100 mV s⁻¹)

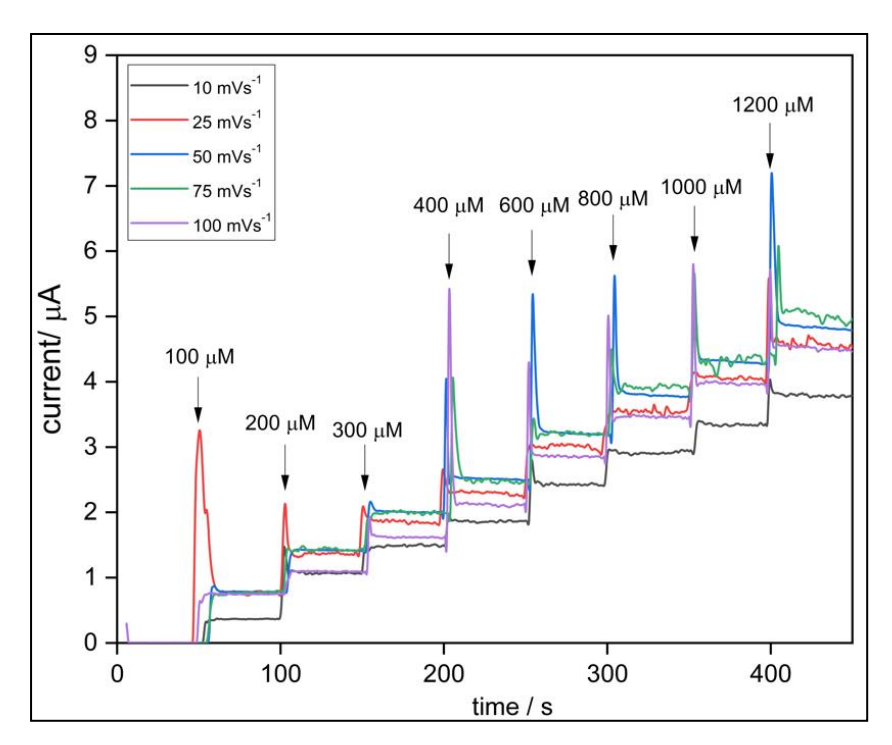


Figure 5. Amperometry results of PME synthesized in different scan rates. All the amperometry test were scanned at a fixed potential (0.20 V) with additional of DA with concentration ranging from 100 - 1200 μ M in PBS (0.10 M, pH 7.0)

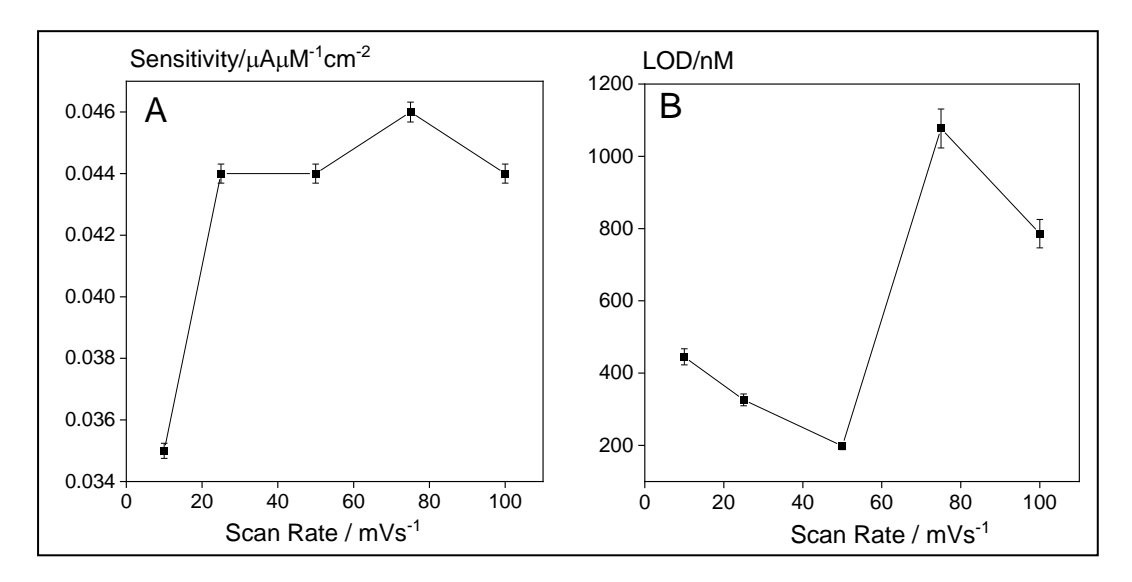


Figure 6. Graphs of (a) sensitivity and (b) LOD results versus varied scan rates applied for electropolymerization of melamine in reline

The result of amperometry sensing of DA at PME/GCE synthesized with varied scan rates are display in Figure 5. Based on Figure 5, the amperometry plots of PME(reline 75 mV s⁻¹) and PME(reline 50 mV s⁻¹) were very close to each other, unable to differentiate which scan rate gives the best outcome. Figure 6(a) and (b) show the fluttered of sensitivity and LOD of varied scan rates applied in electropolymerization of melamine (10.0 mM) in reline. The scan rate applied was varied from 10 to 100 mV s-1. PME(reline) synthesized with 10 mV s⁻¹ is named as PME(reline 10 mV s-1) in accordance to the scan rate applied. As shown, the PME(reline 50 mV s⁻¹) was selected as the ideal scan rate where the sensitivity and LOD reported at 0.044 µA µM⁻¹ cm⁻² and 0.198 µM, respectively. In this case, PME(reline 75 mV s⁻¹) and PME(reline 25 mV s⁻¹) demonstrated the excellent sensitivity at 0.046 μA μM⁻¹ cm⁻² and 0.044 μA μM⁻¹ cm⁻², respectively. However, both PME(reline 75 mV s⁻¹) and PME(reline 25 mV s⁻¹) showing much poorer sensing capability with LOD recorded at 1.077 µM and 0.326 µM, respectively as indicate in Table 1. It is noted that the change of polymerization scan rate affecting the LOD significantly. This is due to the low signal strength and high signal noise. Higher scan rate will result in branched polymer that have side chains growing out from the main chain. Branched polymer exhibits lower density and less packing where the analyte would be easily to move into the polymer cavity during the electrocatalytic activity, thus inducing flux of analyte molecules or ions at the electrode-electrolyte interface which result in a great fluctuation (noise) [17]. Whereas lower scan rate develops linear polymer which are very dense and compact, resulting there would be almost no channel for analyte to approach the electrode and hence reduced the signal strength and increased the LOD.

Optimization of scan cycles on melamine electropolymerization

Scan cycles influences the polymer film thickness and sensing characteristics. The optimum scan cycle was investigated using constant conditions i.e., 10.0 mM melamine in reline electrolyte at room temperature with CV scanned from -0.20 V - 1.60 V. The growing of polymer film was indicated from the increase of the reduction current. Figure 7 illustrates electropolymerization behavior of melamine in different scan cycle. Different scan cycles lead to different thickness of polymer on the surface of GCE. Unfortunately, the voltammogram could not show any significant result to relate the effect of scan cycle on polymerization behaviour of melamine as scan cycle are served to control the thickness the polymer film. Therefore, amperometry was employed to study the effect of polymer thickness on its sensing properties. Figure 8 shows the electrocatalytic performance of PME synthesized in different scan cycles. Scan cycles of five shows the steady increase of current with the increase of DA concentration, it also demonstrates the highest current response among all. Based on Figure 9(a) and (b), the optimum polymeric film can be obtained in five scan cycles, due to the sharp enhancement of sensitivity that has been recorded. When the scan cycles are increased to ten, it caused a minor decreased on LOD, further increasing of scan cycles to 15 attributed to a steeply decrease in sensitivity and raising of LOD. Such phenomenon was presumably due to excess polymer deposited on the GCE surface which blocking the electron transfer that needed for the DA oxidation process. As deduced from the higher charge transferred during polymerization, thin polymer films are usually superior in sensing studies due to better conductivity and easier in accessing analyte. Hence, five scan cycles were used for film formation.

Chang et al: OPTIMIZATION PARAMETERS FOR ELECTROPOLYMERIZATION OF MELAMINE IN DEEP EUTECTIC SOLVENT

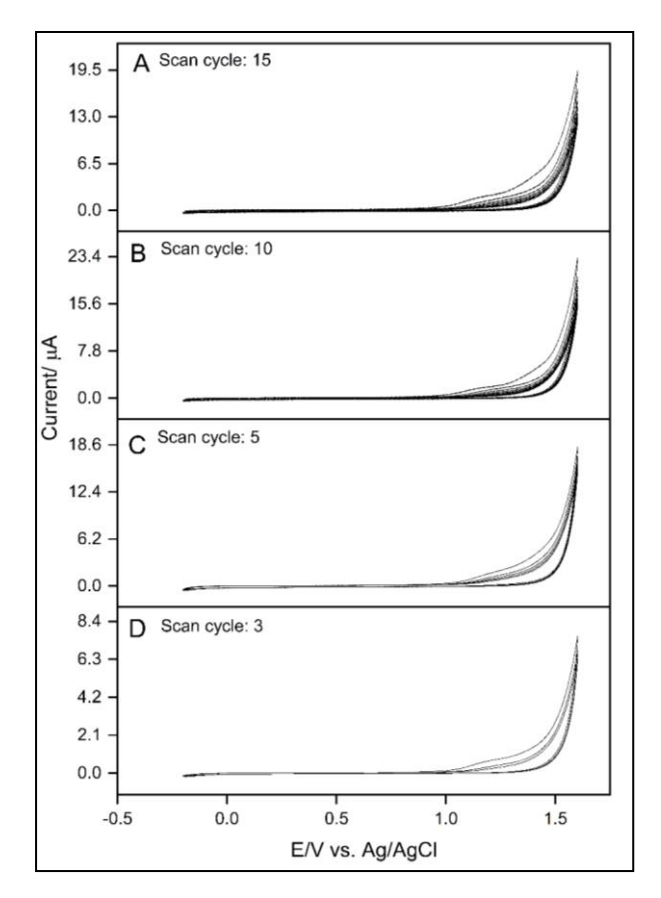


Figure 7. Electropolymerization of melamine (10.0 mM, -0.20- 1.60 V, 50 mV s^{-1}) in reline scanning with varied scan cycle (3, 5, 10 and 15)

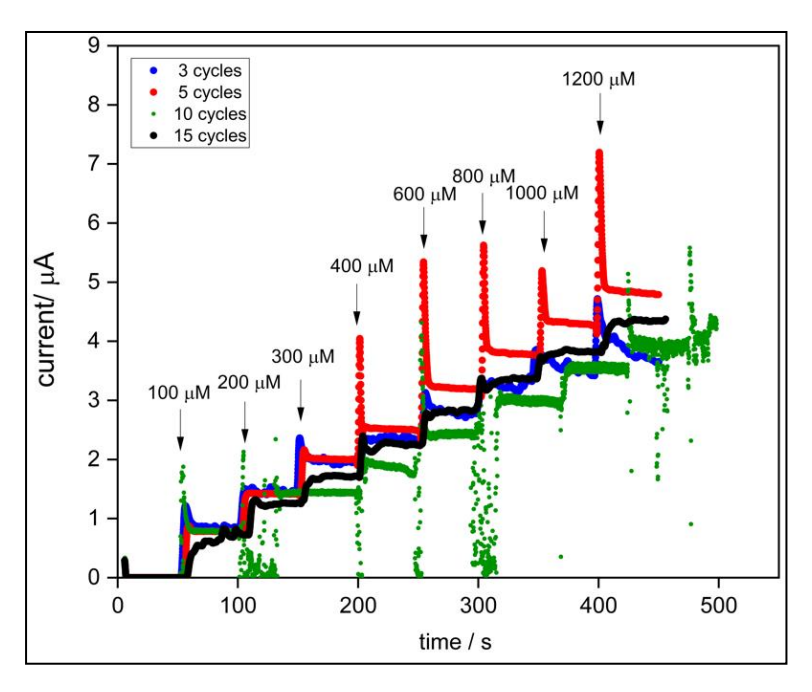


Figure 8. Amperometry results of PME synthesized in different scan cycles. All the amperometry test were scanned at a fixed potential (0.20 V) with additional of DA with concentration ranging from 100 - 1200 μ M in PBS (0.10 M, pH 7.0)

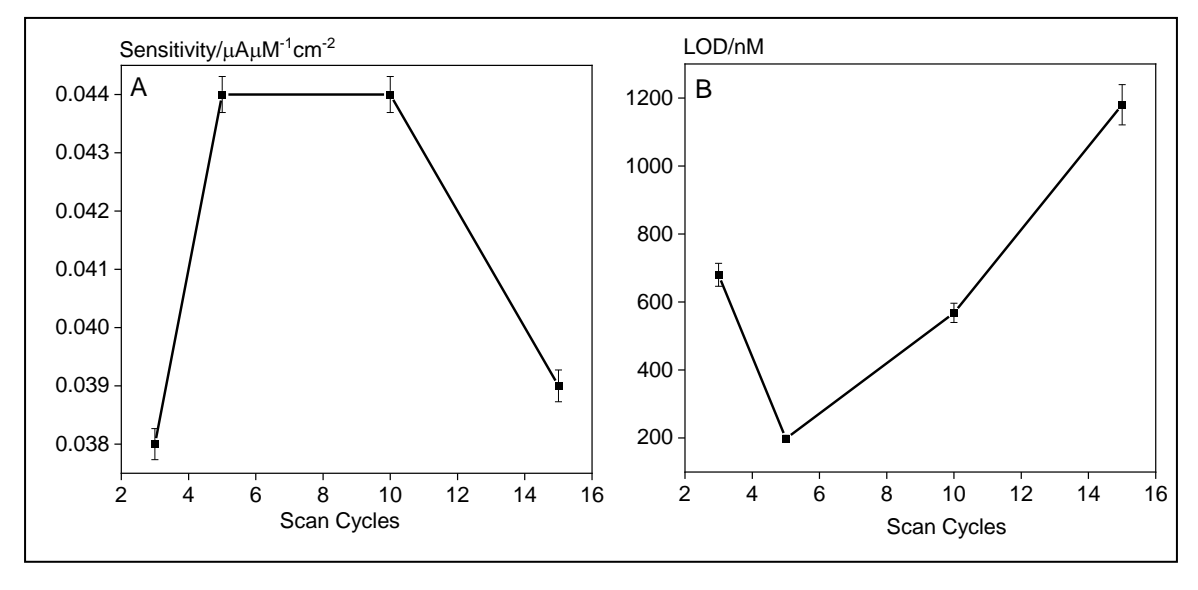


Figure 9. Graphs of (a) sensitivity and (b) LOD results versus varied scan cycles applied for electropolymerization of melamine in relin

Conclusion

Hereby reports the novel studies of optimization parameters for melamine electropolymerizes in DES, reline. Different parameters including potential window, scan rate, and number of scan cycles were manipulated in preparing PME in DES. Amperometry sensing on DA was conducted to compare the sensitivity and limit of detection for the PME prepared in different parameters. The optimum polymerization parameters for melamine were discovered as -0.20 V -1.6 V, 50 mVs⁻¹, and five scan cycles, respectively. The effect of each parameter on the electrocatalytic behavior of PME has been clarified. With the successful optimization, PME(reline)/GCE with high sensitivity and low limit of detection recorded at 0.044 μA μM^{-1} cm⁻² and 0.198 μM has achieved. Proportionally, contemporary potential polymers can be construct by manipulating the parameters accordingly.

Acknowledgement

This work is financially supported by Impact Oriented Interdisciplinary Research Grant IIRG013B-2019 and Frontier Research Grant FG030-17AFR by the Universiti Malaya.

References

- 1. Gupta, P. and Goyal, R. N. (2014). Polymelamine modified edge plane pyrolytic graphite sensor for the electrochemical assay of serotonin. *Talanta*, 120: 17-22.
- Kesavan, S., Kumar, D. R., Lee, Y. R. and Shim, J. J. (2017). Determination of tetracycline in the presence of major interference in human urine samples using polymelamine/electrochemically reduced graphene oxide modified electrode. Sensors and Actuators B: Chem, 241: 455-465.
- 3. Khosropour, H., Rezaei, B., Alinajafi, H. A. and Ensafi, A. A. (2021). Electrochemical sensor based on glassy carbon electrode modified by polymelamine formaldehyde/graphene oxide nanocomposite for ultrasensitive detection of oxycodone. *Microchimica Acta*, 188(1): 1.
- 4. Farida, A. N., Fitriany, E., Baktir, A., Kurniawan, F. and Harsini, M. (2019). Voltammetric study of

- ascorbic acid using polymelamine/gold nanoparticle modified carbon paste electrode. *IOP Conference Series: Earth Environmental Science*, 217: 012004.
- 5. Qin, H., Hu, X., Wang, J., Cheng, H., Chen, L. and Qi, Z. (2020). Overview of acidic deep eutectic solvents on synthesis, properties and applications. *Green Energy and Environment*, 5(1): 8-21.
- 6. Zante, G. and Boltoeva, M. (2020). Review on hydrometallurgical recovery of metals with deep eutectic solvents. *Sustainable Chemistry*, 1(3): 238-255.
- Cen, P., Spahiu, K., Tyumentsev, M. S. and Foreman, M. R. S. J. (2020). Metal extraction from a deep eutectic solvent, an insight into activities. *Physical Chemistry Chemical Physics*, 22(19): 11012-11024.
- 8. Paiva, A., Craveiro, R., Aroso, I., Martins, M., Reis, R. L. and Duarte, A. R. C. (2014). Natural deep eutectic solvents solvents for the 21st century. *ACS Sustainable Chemistry & Engineering*, 2(5): 1063-1071.
- Mendonça, P. V., Lima, M. S., Guliashvili, T., Serra, A. C. and Coelho, J. F. (2017). Deep eutectic solvents (DES): Excellent green solvents for rapid SARA ATRP of biorelevant hydrophilic monomers at ambient temperature. *Polymer*, 132: 114-121.
- Sánchez-Leija, R. J., Torres-Lubián, J. R., Reséndiz-Rubio, A., Luna-Bárcenas, G. and Mota-Morales, J. D. (2016). Enzyme-mediated free radical polymerization of acrylamide in deep eutectic solvents. RSC Advances, 6(16): 13072-13079.
- Fernandes, P. M. V., Campiña, J. M., Pereira, N. M., Pereira, C. M. and Silva, F. (2012). Biodegradable deep-eutectic mixtures as electrolytes for the electrochemical synthesis of conducting polymers. *Journal of Applied Electrochemistry*, 42(12): 997-1003.
- 12. Mąka, H., Spychaj, T. and Adamus, J. (2015). Lewis acid type deep eutectic solvents as catalysts for epoxy resin crosslinking. *RSC Advances*, 5(101): 82813-82821.

- 13. Chang, Y. H., Woi, P. M. and Alias, Y. B. (2021). Electrochemical characterization of melamine electropolymerized in deep eutectic solvents for selective detection of dopamine. *Electrocatalysis*, 12(3): 238-250.
- Chen, S., Liu, S., Wen, A., Zhang, J., Nie, H., Chen, J., Zeng, R., Long, Y., Jin, Y. and Mai, R. (2018). New insight into electropolymerization of melamine. I: Chloride promoted growth of polymelamine in different pH medium. *Electrochimica Acta*, 271: 312-318.
- 15. Migliorati, V., Sessa, F. and D'Angelo, P. (2019). Deep eutectic solvents: A structural point of view

- on the role of the cation. *Chemical Physics Letters*, 2: 100001.
- Li, R., Lin, C. W., Shao, Y., Chang, C., Yao, F. K., Kowal, M., Wang, H., Yeung, M., Huang, S. C. and Kaner, R. (2016). Characterization of aniline tetramer by MALDI TOF mass spectrometry upon oxidative and reductive cycling. *Polymers*, 8(11): 401.
- 17. Gabrielli, C., Huet, F. and Keddam, M. (1993). Fluctuations in electrochemical systems. I. General theory on diffusion limited electrochemical reactions. *The Journal of Chemical Physics*, 99: 7232.

Malaysian Journal of Analytical Sciences (MJAS) Published by Malaysian Analytical Sciences Societ

PREPARATION AND ADSORPTION STUDIES OF MOLECULARLY IMPRINTED POLYMER FOR SELECTIVE RECOGNITION OF TRYPTOPHAN

(Penyediaan dan Kajian Penjerapan Polimer Molekul Tercetak untuk Pengecaman Selektif Triptofan)

Nur Habibah Safiyah Jusoh¹, Faizatul Shimal Mehamod^{2*}, Noor Fadilah Yusof³, Abd Mutalib Md Jani⁴, Faiz Bukhari Mohd Suah⁵, Marinah Mohd Ariffin¹, Nur Asyigin Zulkefli¹

¹Faculty of Science and Marine Environment ²Advanced Nano Materials (ANoMA) Research Group, Faculty of Science and Marine Environment Universiti Malaysia Terengganu, 21030 Kuala Nerus, Terengganu, Malaysia ³School of Chemical and Energy Engineering, Faculty of Engineering, Universiti Teknologi Malaysia, 81310 Skudai, Johor Bahru, Malaysia. ⁴Faculty of Applied Sciences, Universiti Teknologi MARA, Perak Branch, Tapah Campus, 35400 Perak, Malaysia ⁵School of Chemical Sciences, Universiti Sains Malaysia, 11800 Minden, Pulau Pinang, Malaysia

*Corresponding author: fshimal@umt.edu.my

Received: 13 September 2021; Accepted: 18 December 2021; Published: 28 April 2022

Abstract

One of the effective technologies in molecular recognition is based on the molecular imprinting process. In this work, the polymers were prepared by bulk polymerization, using methacrylic acid and ethylene glycol dimethacrylate as the functional monomer and crosslinking agent, respectively. The polymers were characterized by Fourier transform infrared spectroscopy, scanning electron microscopy and surface area and porosity analyses. Several parameters influencing the adsorption efficiency of Tryptophan (Tryp) such as adsorbent dosage, contact time, pH of sample solution as well as selectivity and reproducibility study, have been evaluated. The Tryptophan-imprinted polymer (Tryp-IP) showed significantly higher removal efficiency and selective binding capacity towards Tryp compared to non-imprinted polymer (NIP). The adsorption isotherm demonstrated that the Tryp-IP followed Langmuir isotherm model, indicating the Tryp-IP owning the homogenous surface type of adsorbent. In contrast, the NIP fit with the Redlich-Peterson model, indicating that mechanism adsorption is a mixed type. The kinetic study revealed that pseudo-second order was the appropriate kinetic model for Tryp-IP and the adsorption kinetic of NIP appeared to fit with pseudo-first order.

Keywords: molecularly imprinted polymer, tryptophan, adsorption study

Abstrak

Salah satu teknologi yang efektif dalam pengecaman molekul adalah berdasarkan proses pencetakan molekul. Dalam kajian ini, polimer telah disediakan melalui pempolimeran pukal, masing-masing menggunakan asid metakrilik dan etilena glikol dimetakrilat sebagai monomer berfungsi dan agen tautsilang. Polimer dicirikan oleh spektroskopi inframerah transformasi Fourier, pengimbasan mikroskop elektron dan analisis luas permukaan dan keliangan. Beberapa parameter yang mempengaruhi kecekapan penjerapan Triptofan (Tryp) seperti dos penjerap, masa sentuhan, pH larutan sampel serta kajian selektiviti dan kebolehulangan telah dinilai. Polimer tercetak-

Nur Habibah Safiyah et al: PREPARATION AND ADSORPTION STUDIES OF MOLECULARLY IMPRINTED POLYMER FOR SELECTIVE RECOGNITION OF TRYPTOPHAN

Triptofan (Tryp-IP) menunjukkan kecekapan penyingkiran dan kapasiti pengikatan yang lebih tinggi terhadap Tryp berbanding polimer tidak dicetak (NIP). Isoterma penjerapan menunjukkan bahawa Tryp-IP mematuhi model isoterma Langmuir, ini menunjukkan Tryp-IP memiliki jenis penjerap permukaan homogen. Sebaliknya, NIP mematuhi model Redlich-Peterson, menunjukkan mekanisme penjerapan adalah jenis campuran. Kajian kinetik mendedahkan bahawa tertib pseudo-kedua adalah model kinetik yang sesuai untuk Tryp-IP dan kinetik penjerapan NIP kelihatan lebih sesuai dengan tertib pseudo-pertama.

Kata kunci: polimer tercetak molekul, triptofan, kajian penjerapan

Introduction

Tryptophan (Tryp) is one of the essential amino acids that is necessary for normal growth and it also acts as a precursor for several bioactive compounds such as nicotinamide (vitamin B6), serotonin, melatonin, tryptamine, kynurenine, and xanthurenic acids [1]. Tryp cannot be synthesized in the human body. However, it can be supplied via our dietary intake such as high protein food and fiber rich food like banana, soy, egg and rice. Even though the Tryp in the human body is relatively low, its potency is very significant. It is one of the amino acids capable of passing through the blood- brain barrier, which makes it very important for protein synthesis in our body [2]. Previous studies have shown that Tryp deficiency in the body can affect mood or cause depressive symptoms, whereas low serotonin levels contribute to increased anxiety and depression [3]. Since Tryp acts as a precursor for serotonin synthesis, the level of serotonin depends on the concentration of Tryp in the body [4]. From this point of view, it is crucial to determine the level of Tryp in the body to monitor this condition. At present, many technologies have been applied for the determination of Tryp, such as electrochemical sensors [5], highperformance liquid chromatography (HPLC) [6], solidphase extraction-liquid chromatographic-tandem mass spectrometric (XLC-MS/MS) [7] and tandem mass spectrometer [8]. These techniques are very selective and precise; however, they often require pre-treatment steps, expensive and complicated instruments, skilled operators and a lot more time [9]. For these reasons, attention has been focused on the adsorption method due to its low cost and ease of operation. The latest development of adsorbent material for determination and removal of Tryp/ Tryp derivatives such as polymeric resin [10], gold nanoparticles [11] and activated carbon [12], has shown outstanding results for the adsorptive capacity of Tryp.

In recent years, the low-cost adsorbent materials fabricated from molecular imprinting technology have attracted much attention due to the high selectivity and simple preparation method, which gives the technology a broad range of applications. Molecularly imprinted polymer (MIP) is an adsorbent from the imprinting technique with specific binding sites, shape and size towards the imprinted analyte called template. The molecular imprinting technique is a process that involves the polymerization reaction of functional monomers with the template molecule, thus allowing the formation of polymer networks to possess binding sites complementary with the template molecule [13]. MIP has several advantages which include low cost, ease of preparation, high stability and high selectivity and affinity. In addition, MIP is an insoluble substance with high durability under extreme pH conditions, organic solvents and high temperatures [14]. In general, many researchers favored the non-covalent approach due to the straightforward procedure, easy template removal as well as the fact that imprinted polymer can be used in various applications because most of the biomolecular interaction were non-covalent bond [15]. During pre-polymerization, functional monomers and template interaction are formed by self-assembly via non-covalent interactions, such as hydrogen bond, ionic interaction, hydrophobic interaction, and Van der Waals interaction [16]. Therefore, the present work highlights the application of MIP as a versatile material for selective determination of Tryp molecule. Tryptophan-imprinted polymer designated as Tryp-IP was prepared by bulk polymerization. Figure 1 shows a schematic for the formation of MIP for Tryp via the imprinting technique. The process involves methacrylic acid (MAA), ethylene glycol dimethacrylate (EGDMA) and azobisisobutyronitrile (AIBN) as the functional monomer, cross-linker and initiator, respectively. Once

the polymerization is complete, the removal of the template from the polymer matrix, leaves the cavities that are ideally complementary in terms of size, shape, and function to the template analyte. The corresponding non-imprinted polymer (NIP) was synthesized as a control sample.

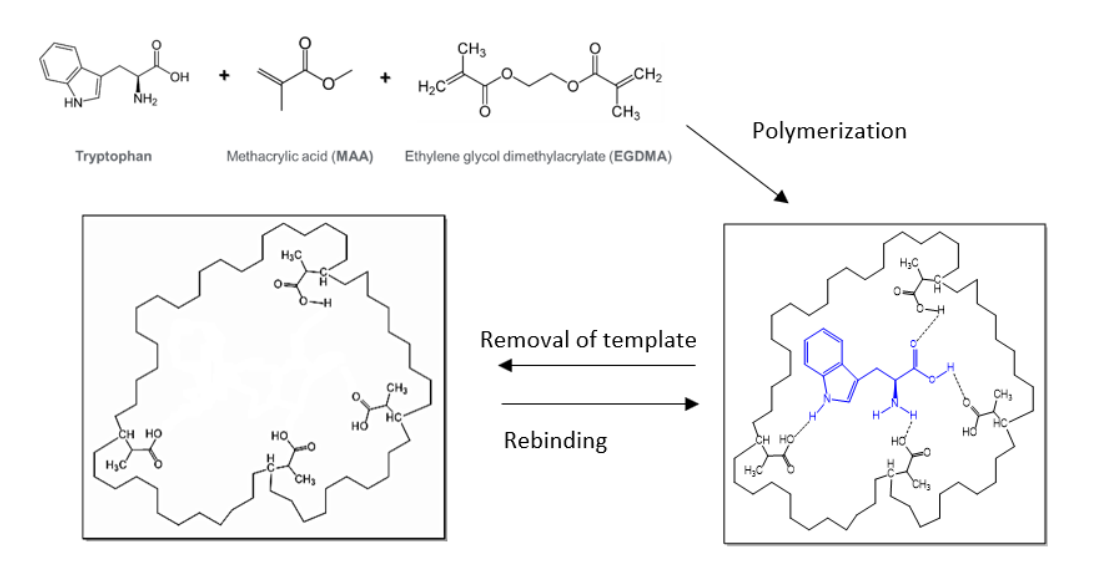


Figure 1. Schematic of the molecular imprinting process for Tryp

Materials and Methods

Materials

Tryptophan (Tryp), kynurenine (Kyn), tyrosine (Tyr), phenylalanine (Phe), methacrylic acid (MAA), ethylene glycol dimethacrylate (EGDMA), and azobisisobutyronitrile (AIBN) were purchased from Sigma Aldrich, Germany whereas methanol, acetic acid, sodium hydroxide (NaOH), hydrochloric acid (HCl) were supplied by R&M Chemicals, UK.

Preparation of Tryp-imprinted polymer

The preparation of Tryp-IP was carried out by the bulk polymerization method [17, 18]. Initially, Tryptophan (Tryp, 1 mmol) was dissolved in water/methanol (1:3 v/v). Then the functional monomer (MAA, 10 mmol), cross-linker (EGDMA, 30 mmol) and initiator; (AIBN) were added into the glass tube to allow the polymerization process to occur. Then, the mixture was stirred until homogeneous and purged with nitrogen gas before being placed in an oil bath at 60 °C for 48 hours. Upon completion of the polymerization reaction, the polymers obtained were crushed, ground, and sieved.

The polymers were treated with methanol and acetic acid in a 9:1 v/v ratio by Soxhlet extraction to remove the template molecules. The obtained polymers were stored at room temperature for further characterization. Finally, the non-imprinted polymer (NIP) as a control sample was prepared using the same method but in the absence of the template.

Characterization of the polymers

The polymers were characterized by attenuated total reflection-Fourier transform infrared spectroscopy (ATR-FTIR). The spectra were recorded from 500 cm⁻¹ to 4000 cm⁻¹. Then, the surface morphology of polymers was observed by Scanning Electron Microscopy (SEM). Each polymer was mounted on the stubs and coated with gold for protection from the electron beam. Next, the determination of the specific surface area, pore volume and pore diameter were performed by porosity analyzer using Bruner-Emmett-Teller (BET) and Barrett-Joyner-Halenda (BJH) technique.

Adsorption studies

The adsorption studies were conducted by batch rebinding experiment, which was performed in an aqueous medium [19]. First, 1 ppm of Tryp solution was prepared and mixed with a different mass of Tryp-IP (1, 3, 5, 7, 9 mg) while maintaining other parameters at optimal conditions. After the adsorption process, the Tryp solution was analyzed using a UV-Vis spectrometer to determine the remaining Tryp molecule by observing its final concentration. Then, the percentage removal and adsorption capacity of Tryp-IP towards Tryp was calculated using equations (1) and (2), respectively [20]:

% removal =
$$\frac{c_i - c_f}{c_i} \times 100$$
 (1)

$$Q_e = \frac{(c_i - c_f)V}{W}$$
 (2)

$$Q_e = \frac{(C_i - C_f)V}{W} \tag{2}$$

In the equations above, C_i and C_f are initial and final concentrations (mg/L) of Tryp solutions, respectively, O_e (mg/g) is the quantity of total adsorption of Tryp molecules, V (L) is the volume of the solution and W (g) is the weight of polymers.

The interaction and adsorption mechanism of Tryp-IP and Tryp were further studied by fitting equilibrium data into the isotherm models. The adsorption equilibrium data obtained were fitted into Langmuir, Freundlich and Redlich-Peterson isotherm models. Langmuir isotherm is often associated with adsorption on the surface of homogeneous sites within the adsorbent and occurs in a monolayer pattern. Nevertheless, Freundlich isotherms apply to adsorption processes that occur on heterogeneous surfaces. Redlich-Peterson isotherm is a three-parameter isotherm which combines Langmuir and Freundlich isotherms. The Langmuir, Freundlich and Redlich-Peterson equation can be written in the following linear form as stated in equations (3), (4) and (5), respectively

$$\frac{C_e}{Q_e} = \frac{1}{BQ_0} + \frac{C_e}{B} \tag{3}$$

$$\ln Q_e = \ln K_F + \frac{1}{n} \ln C_e \tag{4}$$

$$\ln \frac{C_e}{Q_e} = \beta \ln C_e - \ln A \tag{5}$$

In equations (3), (4) and (5), Qe is the equilibrium

adsorption capacity (mg/g), Ce is the equilibrium concentration of adsorbents at equilibrium (mg/L), and Qo is the maximum adsorption capacity of the adsorbents (mg/g). B (L/mg) is the Langmuir adsorption constant, while KF (mg/g) is the Freundlich adsorption equilibrium constants indicating the sorption capacity and 1/n represents the intensity of the adsorption. Meanwhile, A (Lg-1) is Redlich-Peterson isotherm constant and β is the exponent that lies between 0 and 1. The favorability of the Langmuir isotherm was expressed by a dimensionless constant called the separation factor (RL), as shown in equation (6).

$$RL = \frac{1}{1 + B(C_{\mathsf{a}})} \tag{6}$$

where RL values indicate the adsorption to be unfavorable when RL > 1, linear when RL = 1, favorable when 0 < RL < 1, and irreversible when RL =0 [21].

Adsorption kinetic study

Adsorption kinetics was studied to determine the kinetic behavior and rate-controlling step for the adsorption process of Tryp-IP. The experiments were conducted using 1 ppm of Tryp solution mixed with 9 mg of Tryp-IP. The kinetics of Tryp uptake by Tryp-IP were analyzed using a UV-Vis spectrometer. The time was set at 0 to 180 min. Two adsorption kinetic models, namely pseudo-first-order and pseudo-second-order, were tested and fitted into the adsorption kinetic data. The pseudo-first and pseudo-second order equations can be expressed in equations (7) and (8), respectively,

$$\ln(q_e - q_t) = \ln q_e - k_1 t \tag{7}$$

$$ln(q_e - q_t) = ln q_e - k_1 t$$
(7)
$$\frac{t}{q_t} = \frac{1}{k_2 q_e^2} + \frac{t}{q_e}$$
(8)

where q_t and q_e (mg/g) represent adsorption capacities at time and equilibrium, respectively, while k1 and k2 represent rate constants at equilibrium [22]. Furthermore, the favorability of kinetic models was calculated by standard deviation formula, Δq (%) and relative error, RE (%) as in the following equations:

$$\Delta q(\%) = \sqrt{\frac{[(Q_{e,exp} - q_{e,cal})/Q_{e,exp}]^2}{N-1}} \times 100$$
(9)
$$RE (\%) = \frac{|q_{e,cal} - Q_{e,exp}|}{Q_{e,exp}} \times 100$$
(10)

RE (%) =
$$\frac{|q_{e,exp}| - Q_{e,exp}|}{Q_{e,exp}} \times 100$$
 (10)

where N is the amount of data points fitted to the plot, $Q_{e,exp}$ and $q_{e,cal}$ (mg/g) are the experimental and calculated adsorption capacities, respectively. A lower Δq (%) gives the desired fitness of polymer to the kinetic model [20].

Effect of pH study

1 ppm of Tryptophan solution was prepared, and the pH was adjusted in the range of 4, 5, 7, 9, 11 and 13, by adding diluted HCl and NaOH. The experiment was carried out by mixing each solution with 9 mg of Tryp-IP. An independent analyte solution was analyzed and the optimum pH for optimum adsorption was determined.

Effect of selectivity study

In the selectivity study, the molecular structural analogues of Tryptophan; kynurenine, tyrosine and phenylalanine were tested for the binding performance with Tryp-IP. Firstly, 1 ppm of analyte concentrations were prepared separately and mixed with 9 mg of Tryp-IP. Then, the solutions were analyzed using UV-Vis spectrometer. The distribution coefficient (kd) was calculated based on the equation 11.

$$k_{d} = \frac{(C_{i} - C_{f})}{C_{f}} \left(\frac{V}{W}\right) \tag{11}$$

where k_d is the concentration ratio between two solutions, C_i and C_f are initial and final concentrations of each compound, respectively. V (L) is the volume of the solution and W (g) is the weight of polymers [23]. The adsorption capacity of the polymer increases as the value of k_d increases. Selectivity coefficient (k), which indicates the selectivity of Tryp over the competitive compounds was calculated based on the equation 12 below:

$$k = \frac{k_d(Tryp)}{k_d(Kyn/Tyr/Phe)}$$
 (12)

Relative selectivity coefficient (k') was determined by comparing the ratio of Tryp-IP and NIP as equation 13 below:

$$k' = \frac{k \text{ (Tryp-IP)}}{k \text{ (NIP)}} \tag{13}$$

Reproducibility study

A reproducibility study was explored to evaluate the practical application of the prepared adsorbent. Firstly, 1 ppm of Tryp solution was mixed with nine sets of Tryp-IP (9 mg) at the optimal time taken. Then, each solution was evaluated by UV- Vis spectrometer and its adsorption capacity were calculated.

Results and Discussion

FTIR characterization

Figure 2 shows the FTIR spectra of Tryp, Tryp-IP before and after template removal and the NIP. From the Tryp spectrum in Figure 2(a), a peak at 3400 cm⁻¹ and 3012 cm⁻¹ were observed, indicating a peak for NH stretching from the indole group and alkene C-H stretching, respectively. The IR peaks obtained at 1654 cm⁻¹ and 1575cm⁻¹ show the COO-NH asymmetric stretching vibrations, respectively [9]. Due to the high cross-linking agent, all polymers show similar vibration peaks with almost the same IR spectrum. Based on Figure 2(b), the IR broad peaks obtained around 3471 cm⁻¹ - 3275 cm⁻¹ show a strong interaction between the NH group of Tryp and the O-H group of the MAA monomer through hydrogen bonding [24]. The aromatic stretching of C-H appeared at 2985 cm⁻¹ at a lower intensity indicating the presence of Tryp in the polymer. After removal of Tryp Figure 2(c), the IR spectrum showed the complete disappearance of Tryp characteristic. The intensity of C=O from MAA at 1724 cm⁻¹ increased. In comparison with Figure 2(b), the C=O absorption peak shifted from 1716 cm⁻¹ to 1724 cm⁻¹, indicating the rupture of the hydrogen bond. In Figure 2(d), the IR spectrum for NIP is expected to be similar to Tryp-IP after the template is removed, where the C-H stretching vibration of MAA appeared at 2985 cm⁻¹. The schematic from Figure 1 is used to confirm all the functional groups present in the polymers for the FTIR spectra.

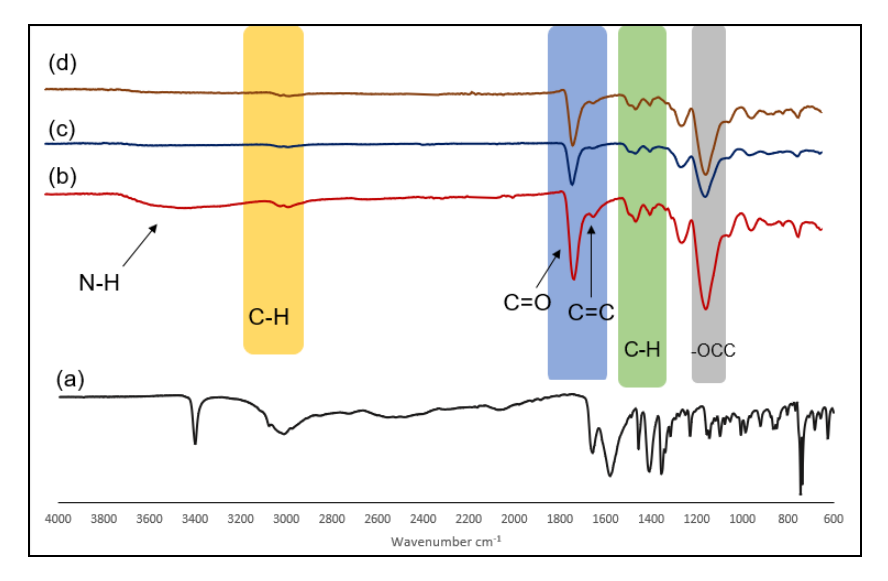


Figure 2. FTIR spectrum of (a) Tryp, (b) Tryp-IP before and (c) Tryp-IP after removal of the template and (d) NIP

SEM analysis

Figures 3(a) and 3(b) show the SEM micrographs for Tryp-IP and NIP, respectively. Bulky particles with the size in the range of a few microns is observed. This morphological feature is typical for polymers synthesized by the bulk polymerization approach. Furthermore, agglomeration is observed in Tryp-IP and NIP, and this is expected due to the high molar ratio of monomer to cross-linker (10:30) used in this study [24, 25]. Based on previous studies, bulk polymerization using the optimum molar ratio (4:20) can give a morphological image in heterogeneous irregular shapes and sizes due to

crashing, grinding, and sieving processes [26]. Besides, the molar ratio of the cross-linker played a significant role in controlling the morphology of the polymer where it can form a rigid surface of the primary particles, which makes it difficult to agglomerate [27]. As in a previous study reported in the literature, the polymer morphology changes when the cross-linker ratio exceeds the optimum level within the polymer structure, resulting in the hard segment and a reduction in the polymer matrix binding sites [24].

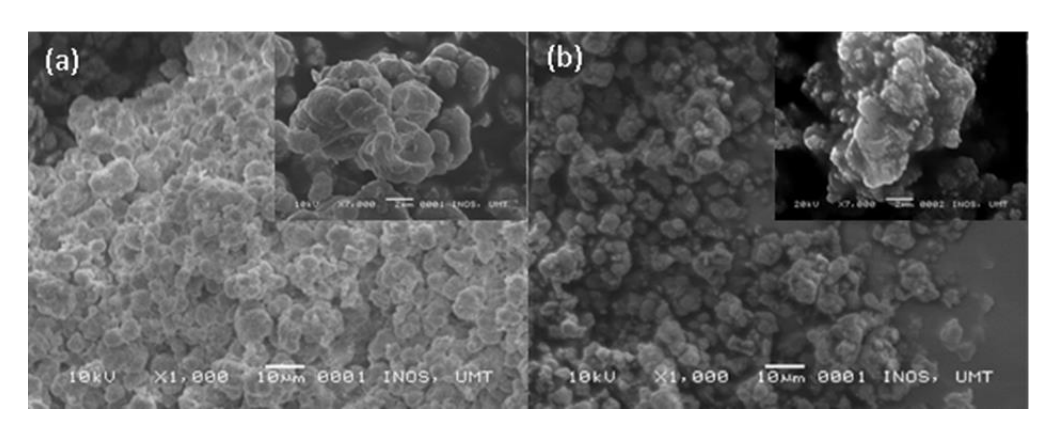


Figure 3. SEM micrograph of (a) Tryp-IP and (b) NIP

BET surface area analysis and porosity

BET analysis was carried out to determine the specific surface area and porosity properties of the Tryp-IP and NIP. Table 1 shows the results of surface area, pore volume and pore diameter of the polymers. The average pore diameters of Tryp-IP and NIP were in the range of 2–50 nm, indicating that both polymers have a mesoporous structure [20, 28]. However, Tryp-IP has larger a surface area and slightly larger total pore volume than the NIP. The increased surface area in Tryp-IP reflects the effect

of the imprinting process, which occurred when the presence of the Tryp as a template during MIP synthesis resulted in the formation of pores or imprinted cavities [29, 30]. Based on previous studies, high molar ratios of monomers to the cross-linker resulted in non-specific interactions, while low ratios lead to inadequate functional sites [31]. Consequently, the agglomeration of the polymers particle resulted in the reduction of surface area and the number of active sites of polymers.

Table 1. BET surface area, pore volume and pore diameter

Polymer	Surface area (m² g-1)	Pore volume (cm ³ g ⁻¹)	Pore diameter (nm)
Tryp-IP	6.4519	0.022482	13.94
NIP	4.0351	0.016078	15.94

Adsorption isotherm study

The effect of the mass polymer was investigated to get the optimum mass for Tryp-IP. Based on Figure 4, it was observed that the percentage removal of Tryp increased with the increase of polymer mass. The maximum percentage removal achievable by Tryp-IP and NIP were 82% and 70%, respectively. An increase in polymer mass appears to increase the number of active sites and surface area for Tryp adsorption [32, 33]. Due to the absence of a template during the NIP synthesis, the non-specific cavities are formed, thus lower percentage removal of NIP than Tryp-IP. Based on Figure 4, the percentage removal increased until it reached the optimum level at 5 mg, indicating that all cavities were filled with Tryp molecules. However, a previous study agreed that a further increase in polymer mass could lead to adsorbent aggregation resulting in a decrease in the adsorption sites [34]. Hence, an increase in polymer mass does not increase the adsorption of Tryp.

Figure 5 is the isotherm models used in this study to fit the experimental data to predict the adsorption mechanism. Based on the isotherm parameter in Figures 5(a) and 5(b), the adsorption mechanism for Tryp-IP followed the Langmuir isotherm model and

NIP followed the Redlich-Peterson isotherm which gave the highest R² value. The Langmuir isotherm was described as monolayer adsorption of Tryp onto Tryp-IP. The possible way for monolayer adsorption is for the adsorption to take place on the homogenous surface of the polymer matrix [35]. The similar observation was reported by the adsorption of D-Tryp onto polymer matrix [36]. To further strengthen the important features of the Langmuir isotherm model, the dimensionless constant separation factor (RL) was calculated [37]. RL values were found in the range of 0.017-0.009, which confirms adsorption of Tryp onto Tryp-IP was good. For the NIP, the data was fitted to the Redlich-Peterson model which, incorporates the features of both Langmuir and Freundlich isotherm. This can be applied as a homogeneous and heterogeneous system due to its versatility [38]. The parameters calculated for the three isotherms are tabulated in Table 2. From the data obtained, the maximum adsorption capacity for Tryp onto Tryp-IP was found to be 0.98 mg/g, which was seven times lower than the NIP (7.325 mg/g). The similar finding was reported by Hasanah et.al, which might be due to the non-specific recognition sites in NIP and therefore, made it swells better in polar solvent [39].

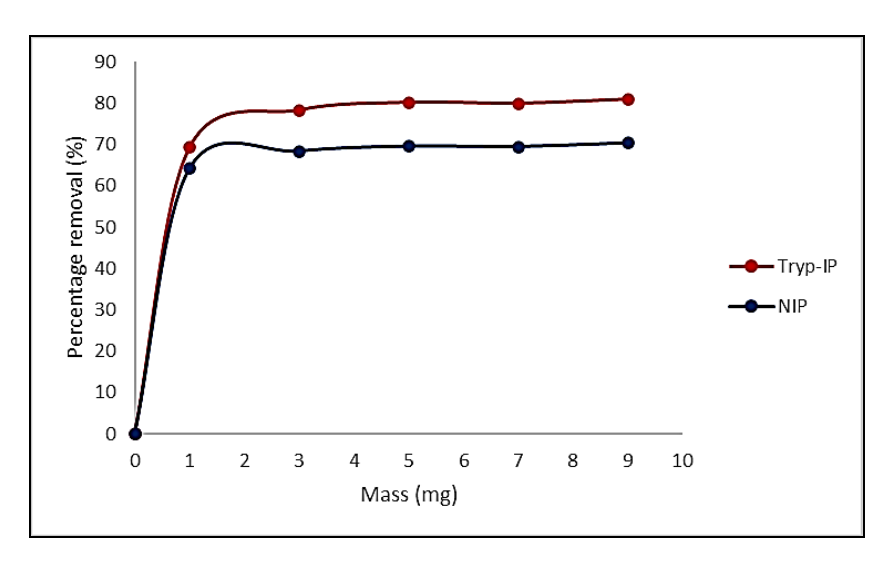


Figure 4. Effect of mass polymer on adsorption Tryp by Tryp-IP and NIP

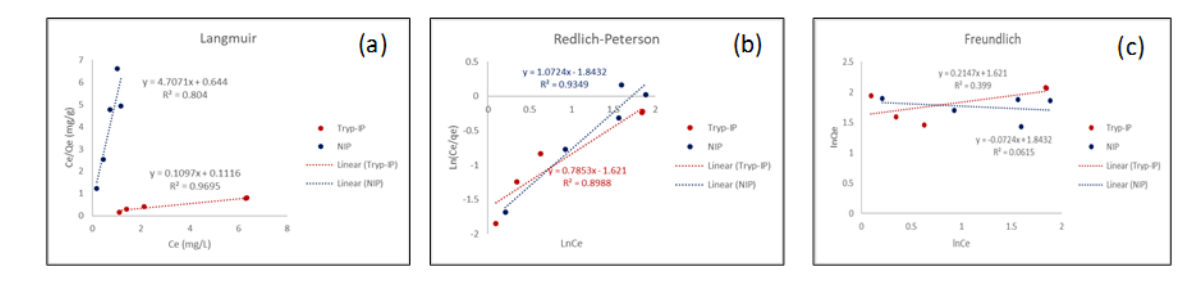


Figure 5. Adsorption isotherms of Tryp-IP and NIP using models (a) Langmuir (b) Redlich-Peterson (c) Freundlich

Redlich-Peterson Freundlich Langmuir Polymer \mathbb{R}^2 Q_0 В ß A \mathbb{R}^2 1/n $\mathbf{K}_{\mathbf{F}}$ \mathbb{R}^2 Tryp-IP 0.98 9.116 0.9695 0.7853 5.058 0.8988 0.2147 5.058 0.399

6.3167

0.9349

1.0724

Table 2. Isotherm parameter for adsorption of Tryp by Tryp-IP and NIP

Adsorption kinetic study

7.325

NIP

The effect of contact time on the binding capacity of polymers is important to evaluate the binding efficiency in adsorption studies. It has been observed that the adsorption of Tryp onto the polymer surface increases with prolonging the contact time up to achieve equilibrium [40]. In Figure 6, initially, the

0.212

0.804

adsorption rate of Tryp onto the polymeric surface was accelerating due to the abundant number of empty adsorption sites that can be accessed and less mass transfer resistance which allowed the active sites to capture the target analyte. However, with the progress of time, the number of active sites decreases, the imprinted cavities are gradually filled

-0.0724

6.3167

0.0615

with Tryp and the mass transfer resistance of Tryp to the active sites increases. Thus, the adsorption rate decreases and the removal percentage decreases slowly [41]. Finally, the adsorption equilibrium was reached within 120 min for Tryp-IP and 150 min for NIP. There is no change in the percentage removal if the time is prolonged because the polymer binding sites have been occupied with the Tryp. Therefore, it could be observed that Tryp-IP exhibited slightly higher percentage removal and faster mass transfer than the NIP, which could be attributed to the imprinting effect of Tryp [35, 42].

The adsorption mechanism was further evaluated by two of the most widely used kinetic models which is pseudo-first order kinetics, and pseudo-second order kinetic models. The results shown in Table 3 indicates that the R^2 value of Tryp-IP is most fitted with pseudo-second order (R^2 =0.9698) whereas the R^2 value for pseudo-first order is 0.2195. In the pseudo-second-order model, the theoretical and experimental adsorption capacity values were in good agreement. Therefore, the pseudo-second-order

adsorption mechanism is predominant and the ratelimiting step at the surface involving a chemisorption process between Tryp and cavities of Tryp-IP [38].

Moreover, the values of Δq and RE were found to be low compared to pseudo-first order which means the accuracy and validity of the kinetic model were better equipped with pseudo second order. However, NIP appeared to be more suitable with pseudo-first order with the highest R^2 value (0.9107). It was expected that the rate of adsorption is proportional to the number of unused sites and the rate-limiting step was physisorption [39]. As in the case of Tryp-IP where Δq and RE values of NIP were exceedingly low for pseudo-first-order compared to pseudo-second order, these values indicate the accuracy of this kinetic model. Furthermore, the adsorption capacity Q_e (Table 3) for Tryp-IP (10.0336) was lower than NIP (11.3958). This result is due to the absence of specific recognition sites in the NIP, thus leading to the physical adsorption and random interaction of the Tryp molecule with the functional group of MAA in the polymer chain [43].

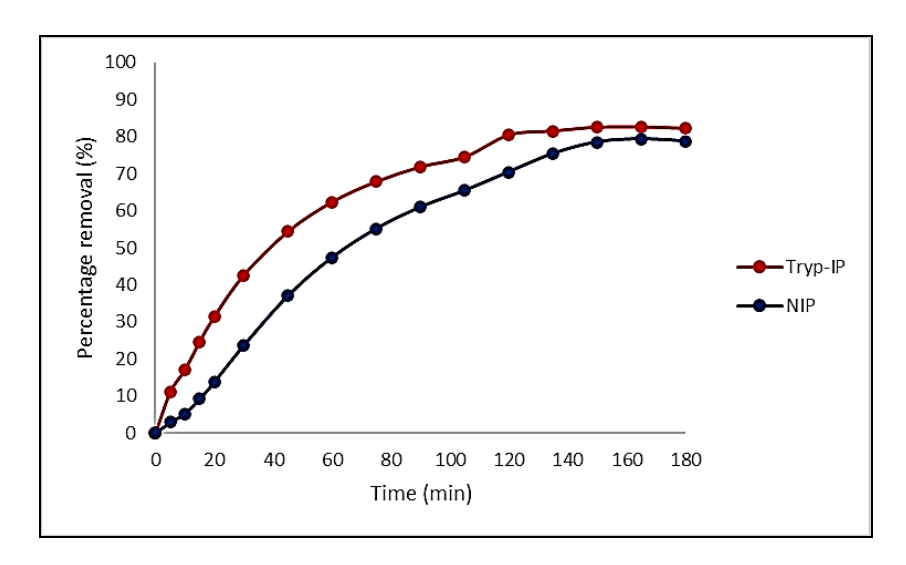


Figure 6. Effect of contact time on adsorption Tryp by Tryp-IP and NIP

Kinetic Parameters							
Polymer	Model	y = mx + c	Q _e (mg/g)	Qe (mg/g)	Δ q (%)	RE (%)	R ²
Tryp-IP	Pseudo-first-order Pseudo-second-order	y = -0.0223x + 1.909 y = 8.0813x + 2.902	10.0336	6.746 12.3001	8.464 5.826	32.78 22.56	0.2196 0.9698
NIP	Pseudo-first-order Pseudo-second-order	y = -0.017x + 2.478 y = 0.0353x + 7.9307	11.3958	11.9174 28.3286	1.18 38.37	4.58 149	0.9107 0.3772

Table 3. Kinetic parameter for adsorption of Tryp by Tryp-IP and NIP

Effect pH study

The pH of the adsorption medium is the most critical parameter influencing the adsorption capacity [29]. In this analysis, a pH of 4-13 has been selected. Figure 7 shows that the highest percentage removal was obtained when the pH is in acidic condition and the percentage removal decreases as the pH increases (base condition). This condition might be due to the interaction of hydrogen bonding between the surface of the carboxylic group of MAA and the functional group of

Tryp. As shown in Figure 7, the highest percentage removal of Tryp appeared when the pH became acidic. This observation occurred as a result of the zwitterionic Tryp and the large electronegativity of the oxygen atom of the carbonyl group in the polymers [43]. However, when the pH value becomes basic, Tryp exists as an anion and diffuses very slowly into the polymer surface [44]. Therefore, pH 5 was chosen as the optimal pH throughout this study.

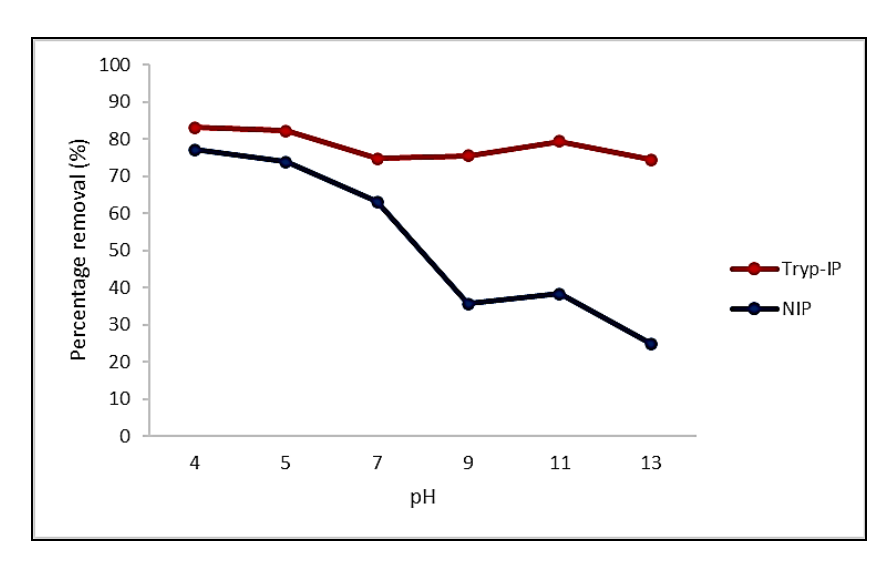


Figure 7. Effect of pH on adsorption Tryp by Tryp-IP and NIP

Effect of selectivity study

To study the selectivity of Tryp-IP and NIP, the recognition of Tryp was compared with tyrosine, phenylalanine and kynurenine as potential interferences. Table 4 shows the k_d values of each molecule in the Tryp-IP and the NIP. According to the

Table 4, Tryp has higher k_d values compared to the other molecules in the Tryp-IP, which means that high specific recognition ability for Tryp is associated with a unique complementary form of the binding sites [42]. In contrast with the NIP, tyrosine gave a higher k_d value compared to Tryp. This is due to the non-specific

cavities existing in the NIP. Furthermore, the k values indicate that the polymer has selective behavior for the template in the presence of other molecules. The larger the k values, the higher the selectivity of the polymer towards the template compared to the other molecule [23]. For the Tryp-IP, the k values are higher than for the NIP, which means that Tryp-IP has selective behavior for Tryp as calculated in Equation 12. In

order to show the efficiency of Tryp-IP for selective separation of Tryp against NIP, the k' values were calculated according to Equation 13. The larger the k' values the more selective is the Tryp-IP against NIP for the template toward the other molecules [41]. It can be concluded that the Try-IP has greater molecular recognition towards its template molecule.

	Tryp-IP		NIP		k'
	k_d	K	k_d	k	
Tryptophan	1.5751	-	1.2175	-	-
Kynurenine	0.7495	2.1015	0.8407	1.4482	1.451112
Tyrosine	0.5309	3.958	1.3346	0.9123	4.338485
Phenylalanine	0.8392	4.7168	0.7567	1.609	2.93151

Table 4. Selectivity study constant for Tryp-IP and NIP

Effect of the reproducibility study

The reproducibility performance of the Tryp-IP was evaluated by comparing the adsorption capacity for each adsorption process of Tryp-IP. The result in Figure 8 revealed that the percentage removal of Tryp did not show a significant change (80% to 83%) for each repeated usage. The Tryp-IP can be

used at least nine times while maintaining its percentage removal of more than 80%, reflecting the excellent precision and reproducibility of the proposed polymer. Therefore, Tryp-IP showed good stability and could maintain its adsorption capacity at a constant value.

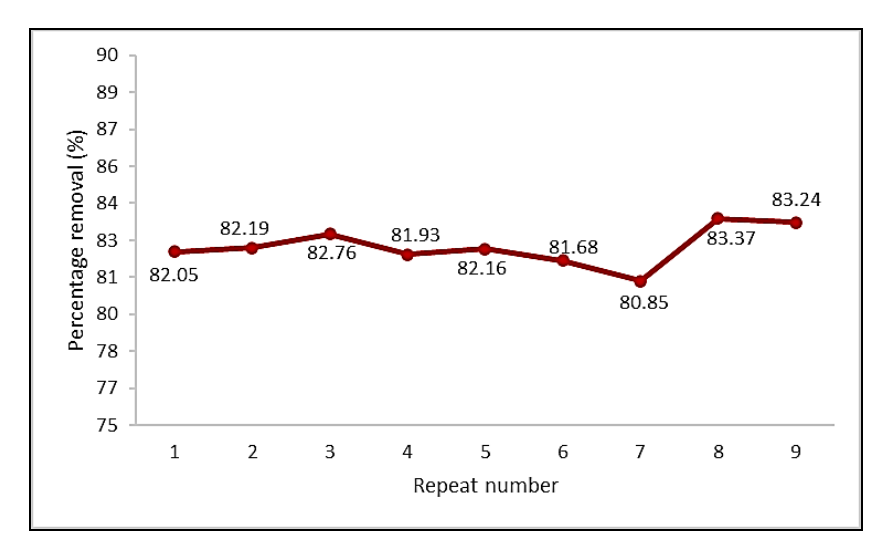


Figure 8. Effect of reproducibility of Tryp-IP

Conclusion

In this study, Tryp-IP and NIP were successfully synthesized through bulk polymerization and used as an adsorbent for tryptophan detection. FTIR, SEM, and BET were used to analyze the physical and chemical characterizations, which revealed evidence of chemical interaction, surface morphology, and cavities of the polymer matrix; all of which are responsible for the binding ability of the polymer. Hence, the adsorption studies have revealed that Tryp-IP has a greater removal percentage, selectivity, and stability than the NIP.

Acknowledgments

We would like to thank the Ministry of Higher Education Malaysia for the project funding support under Fundamental Research Grant Scheme (FRGS/1/2018/STG01/UMT/02/6 – Vot: 59493) and Universiti Malaysia Terengganu.

References

- Friedman, M. (2018). Analysis, nutrition, and health benefits of tryptophan. *International Journal of Tryptophan Research*, 11: 1178646918802282.
- Richard, D. M., Dawes, M. A., Mathias, C. W., Acheson, A., Hill-Kapturczak, N. and Dougherty, D. M. (2009). L-tryptophan: basic metabolic functions, behavioral research and therapeutic indications. *International Journal of Tryptophan Research*, 23(2): 45-60.
- 3. Lindseth, G., Helland, B. and Caspers, J. (2015). The effects of dietary tryptophan on affective disorders. *Archives of Psychiatric Nursing*, 29(2): 102-107.
- 4. Jenkins, T. A., Nguyen, J. C. D., Polglaze, K. E. and Bertrand, P. P. (2016). Influence of tryptophan and serotonin on mood and cognition with a possible role of the gut-brain axis. *Nutrients*, 8(1): 56.
- Sundaresan, R., Mariyappan, V., Chen, S.-M., Keerthi, M. and Ramachandran, R. (2021). Electrochemical sensor for detection of tryptophan in the milk sample based on MnWO₄ nanoplates encapsulated RGO nanocomposite. *Colloids and*

- Surfaces A: Physicochemical and Engineering Aspects, 625: 126889.
- Capuron, L., Ravaud, A., Neveu, P. J., Miller, A. H., Maes, M. and Dantzer, R. (2002). Association between decreased serum tryptophan concentrations and depressive symptoms in cancer patients undergoing cytokine therapy. *Molecular Psychiatry*, 7(5): 468-473.
- de Jong, R. A., Nijman, H. W., Boezen, H. M., Volmer, M., Klaske, A., Krijnen, J., van der Zee, A. G. J., Hollema, H. and Kema, I. P. (2011). Serum tryptophan and kynurenine concentrations as parameters for indoleamine 2, 3-dioxygenase activity in patients with endometrial, ovarian, and vulvar cancer. *International Journal of Gynecologic Cancer*, 21(7): 1320-1327.
- 8. Onesti, C. E., Boemer, F., Josse, C., Leduc, S., Bours, V. and Jerusalem, G. (2019). Tryptophan catabolism increases in breast cancer patients compared to healthy controls without affecting the cancer outcome or response to chemotherapy. *Journal of Translational Medicine*, 17(1): 1-11.
- 9. Tian, Y., Deng, P., Wu, Y., Ding, Z., Li, G., Liu, J. and He, Q. (2019). A simple and efficient molecularly imprinted electrochemical sensor for the selective determination of tryptophan. *Biomolecules*, 9(7): 294.
- Jiao, P., Wei, Y., Zhang, M., Zhang, X., Zhang, H. and Yuan, X. (2021). Adsorption separation of 1-tryptophan based on the hyper-cross-linked resin XDA-200. ACS Omega, 6(3): 2255-2263.
- Lee, D., Hussain, S., Yeo, J. and Pang, Y. (2021). Adsorption of dipeptide L-alanyl-L-tryptophan on gold colloidal nanoparticles studied by surfaceenhanced Raman spectroscopy. Spectrochimica Acta Part A: Molecular and Biomolecular Spectroscopy, 247: 119064.
- 12. Belhamdi, B., Merzougui, Z., Laksaci, H. and Trari, M. (2019). The removal and adsorption mechanisms of free amino acid 1-tryptophan from aqueous solution by biomass-based activated carbon by H₃PO₄ activation: regeneration study. *Physics and Chemistry of the Earth, Parts A/B/C*, 114: 102791.

- 13. Mehamod, F. S., KuBulat, K., Yusof, N. F. and Othman, N. A. (2015). The development of molecular imprinting technology for caffeine extraction. *International Journal of Technology*, 6(4): 546-554.
- Samarth, N. B., Kamble, V., Mahanwar, P. A., Rane, A. V. and Abitha, V. K. (2015). A historical perspective and the development of molecular imprinting polymer-A review. *Chemistry International*, 4: 202-210.
- 15. Mujahid, A. and Dickert, F. L. (2016). Molecularly Imprinted polymers: principle, design, and enzyme-like catalysis. *Molecularly Imprinted Catalysts: Principles, Syntheses, and Applications*, pp. 79-101.
- 16. Zhang, H., Ye, L. and Mosbach, K. (2006). Non-covalent molecular imprinting with emphasis on its application in separation and drug development. *Journal of Molecular Recognition:* An Interdisciplinary Journal, 19(4), 248-259.
- 17. Yusof, N. F., Mehamod, F. S., Kadir, M. A. and Suah, F. B. M. (2018). Characteristics of adsorption isotherm and kinetic study for newly prepared Co2+-imprinted polymer linkage with dipicolinic acid. *IOP Conference Series: Materials Science and Engineering*, 440(1): 012005.
- 18. Yusof, N. F., Mehamod, F. S. and Suah, F. B. M. (2018). The effect of RAFT polymerization on the physical properties of thiamphenicol-imprinted polymer. *E3S Web of Conferences*, 67(12): 03050.
- Abdul Hamid, N. S., Naseeruteen, F., Wan Ngah, W. S., Yusof, N. F., Mehamod, F. S. and Mohd Suah, F. B. (2020). Synthesis of chitin-ionic liquid beads as potential adsorbents for methylene blue. *Malaysian Journal of Chemistry*, 22(2): 98-110.
- Yusof, N. F., Mehamod, F. S. and Suah, F. B. M. (2019). Fabrication and binding characterization of ion imprinted polymers for highly selective Co2+ ions in an aqueous medium. *Journal of Environmental Chemical Engineering*, 7(2): 103007.
- 21. Ayawei, N., Ebelegi, A. N. and Wankasi, D. (2017). Modelling and interpretation of adsorption isotherms. *Journal of Chemistry*, 2017: 3039817.
- 22. Alveroglu, E., Balouch, A., Khan, S., Mahar, A. M., Jagirani, M. S. and Pato, A. H. (2021).

- Evaluation of the performance of a selective magnetite molecularly imprinted polymer for extraction of quercetin from onion samples. *Microchemical Journal*, 162: 105849.
- 23. Fareghi, A. R., Moghadam, P. N., Khalafy, J., Bahram, M. and Moghtader, M. (2017). Preparation of a new molecularly imprinted polymer based on self-crosslinkable cellulose acrylate in aqueous solution: A drug delivery system for furosemide. *Journal of Applied Polymer Science*, 134(48): 45581.
- 24. Prabakaran, K., Jandas, P. J., Luo, J., Fu, C. and Wei, Q. (2021). Molecularly imprinted poly (methacrylic acid) based QCM biosensor for selective determination of L-tryptophan. *Colloids and Surfaces A: Physicochemical and Engineering Aspects*, 611: 125859.
- Azodi-Deilami, S., Abdouss, M. and Seyedi, S. R. (2010). Synthesis and characterization of molecularly imprinted polymer for controlled release of tramadol. *Central European Journal of Chemistry*, 8(3): 687-695.
- 26. Wang, L., Zhi, K., Zhang, Y., Liu, Y., Zhang, L., Yasin, A. and Lin, Q. (2019). Molecularly imprinted polymers for gossypol via sol–gel, bulk, and surface layer imprinting—a comparative study. *Polymers*, 11(4): 602.
- Xia, Q., Yun, Y., Li, Q., Huang, Z. and Liang, Z. (2017). Preparation and characterization of monodisperse molecularly imprinted polymer microspheres by precipitation polymerization for kaempferol. *Designed Monomers and Polymers*, 20(1): 201-209.
- Madikizela, L. M., Zunngu, S. S., Mlunguza, N. Y., Tavengwa, N. T., Mdluli, P. S. and Chimuka, L. (2018). Application of molecularly imprinted polymer designed for the selective extraction of ketoprofen from wastewater. *Water SA*, 44(3): 406-418.
- Hasanah, A. N., Susanti, I., Marcellino, M., Maranata, G. J., Saputri, F. A. and Pratiwi, R. (2021). Microsphere molecularly imprinted solid-phase extraction for diazepam analysis using itaconic acid as a monomer in propanol. *Open Chemistry*, 19(1): 604-613.

- 30. Yusof, N. F., Mehamod, F. S., & Suah, F. B. M. (2020). Adsorptive removal of bis (2-ethylhexyl) phthalate using an imprinted polymer: isotherm and kinetic modelling. *International Journal of Environmental Analytical Chemistry*, 2020: 1-12.
- Song, S., Wu, A., Shi, X., Li, R., Lin, Z. and Zhang, D. (2008). Development and application of molecularly imprinted polymers as solid-phase sorbents for erythromycin extraction. *Analytical* and *Bioanalytical Chemistry*, 390(8): 2141-2150.
- Albadarin, A. B., Mangwandi, C., Ala'a, H., Walker, G. M., Allen, S. J. and Ahmad, M. N. M. (2012). Kinetic and thermodynamics of chromium ions adsorption onto low-cost dolomite adsorbent. *Chemical Engineering Journal*, 179: 193-202.
- 33. Gomes, C., Sadoyan, G., Dias, R. and Costa, M. R. P. F. N. (2017). Development of molecularly imprinted polymers to target polyphenols present in plant extracts. *Processes*, 5(4): 72.
- 34. Mor, S., Chhoden, K. and Ravindra, K. (2016). Application of agro-waste rice husk ash for the removal of phosphate from the wastewater. *Journal of Cleaner Production*, 129: 673-680.
- 35. Bakhtiar, S., Bhawani, S. A. and Shafqat, S. R. (2019). Synthesis and characterization of molecular imprinting polymer for the removal of 2-phenylphenol from spiked blood serum and river water. *Chemical and Biological Technologies in Agriculture*, 6(1): 1-10.
- 36. Jin, Y., Liu, C. C., Sun, X. H., Lee, K. J., Jung, Y. A. and Row, K. H. (2012). Adsorption isotherms of tryptophan enantiomer on d-tryptophan molecular imprinted polymer. *Asian Journal of Chemistry*, 24(6): 2461-2466.
- 37. Hameed, B. H., Ahmad, A. L. and Latiff, K. N. A. (2007). Adsorption of basic dye (methylene blue) onto activated carbon prepared from rattan sawdust. *Dyes and Pigments*, 75(1): 143-149.
- 38. Kumar, V. (2019). Adsorption kinetics and isotherms for the removal of rhodamine B dye and Pb²⁺ ions from aqueous solutions by a hybrid ion-exchanger. *Arabian Journal of Chemistry*, 12(3): 316-329.

- 39. Hasanah, A. N., Dwi Utari, T. N. and Pratiwi, R. (2019). Synthesis of atenolol-imprinted polymers with methyl methacrylate as functional monomer in propanol using bulk and precipitation polymerization method. *Journal of Analytical Methods in Chemistry*, 2019: 9853620.
- 40. Yusof, N. F., Mehamod, F. S., Jusoh, N., Amin, K. A. M. and Suah, F. B. M. (2017). Ion-imprinted polymer-based on picolinic acid as a co-functional monomer for highly selective sorption of Cu(II) ions in an aqueous solution. *AIP Conference Proceedings*, 1885: 020017.
- 41. Abouzarzadeh, A., Forouzani, M., Jahanshahi, M. and Bahramifar, N. (2012). Synthesis and evaluation of uniformly sized nalidixic acid—imprinted nanospheres based on precipitation polymerization method for analytical and biomedical applications. *Journal of Molecular Recognition*, 25(7): 404-413.
- 42. Pan, J., Li, L., Hang, H., Ou, H., Zhang, L., Yan, Y. and Shi, W. (2013). Study on the nonylphenol removal from aqueous solution using magnetic molecularly imprinted polymers based on fly-ash-cenospheres. *Chemical Engineering Journal*, 223: 824-832.
- 43. Kong, Y., Zhao, W., Yao, S., Xu, J., Wang, W. and Chen, Z. (2010). Molecularly imprinted polypyrrole prepared by electrodeposition for the selective recognition of tryptophan enantiomers. *Journal of Applied Polymer Science*, 115(4), 1952-1957.
- 44. Monier, M., Abdel-Latif, D. A. and Nassef, H. M. (2015). Preparation of 1-tryptophan imprinted microspheres based on carboxylic acid functionalized polystyrene. *Journal of Colloid and Interface Science*, 445: 371-379.

Malaysian Journal of Analytical Sciences (MJAS) Published by Malaysian Analytical Sciences Societ



THE CHEMICAL PROPERTIES AND ANTI-ACNE ACTIVITY DETERMINATION of Swietenia macrophylla SEED EXTRACTS

(Penentuan Ciri Kimia dan Aktiviti Anti-Jerawat Ekstrak Biji Swietenia Macrophylla)

Non Daina Masdar¹, Noor Hafizah Uyup¹, Zamzila Erdawati Zainol², Muhammad Akmal Roslani², Siti Nur Syarifa Anuar¹, Muhamad Azhar Zulkafle³*

¹Department of Chemistry ²Department of Marine ³Department of Biology Faculty of Applied Sciences, Universiti Teknologi MARA, Perlis Branch, Arau Campus, 02600 Arau, Perlis, Malaysia

*Corresponding author: azharz@uitm.edu.my

Received: 7 October 2021; Accepted: 18 December 2021; Published: 28 April 2022

Abstract

Acne is a common skin disorder usually treated using antibiotics and drugs. However, until today, dermatologists struggle to treat acne resistance towards topical treatment over a long period. One of the solutions is using natural bioactive compounds from plant extracts. In this work, Swietenia macrophylla seeds oil, rich in active compounds, was used to inhibit acne-causing bacteria, i.e., Propionibacterium acnes, Staphylococcus aureus, and Staphylococcus epidermidis. The seed powder sample was extracted using the Soxhlet extraction method in three different solvents for six hours and ten cycles. The seed extracts were analysed using a gas chromatography-mass spectrophotometer (GC-MS), and a disc diffusion assay was performed to analyse the antibacterial activities. The heavy metal analysis was determined by inductively coupled plasma atomic emission spectroscopy (ICP-OES). The results show that bioactive compound yields are 37-72%. Eugenol and isoeugenol compounds are the main constituents in the oil extracts with 98% and 97% quality. The compounds also demonstrated inhibitory activities towards all tested bacteria, with inhibition zones between 11 and 22 mm on 30 µg tetracycline discs. These compounds without isolation work also showed inhibitory activity against all bacteria tested with inhibition zones ranging from 11 to 21 mm.

Keywords: Swietenia macrophylla, acne, natural treatment, Propionibacterium acne, Staphylococcus epidermidis

Abstrak

Jerawat adalah penyakit kulit biasa dan selalunya dirawat menggunakan antibiotik dan ubat-ubatan. Namun, sehingga hari ini, pakar dermatologi masih belum dapat merawat ketahanan jerawat terhadap rawatan permukaan dalam jangka masa panjang. Salah satu penyelesaiannya adalah menggunakan sebatian bioaktif semula jadi dari ekstrak tumbuhan. Dalam kajian ini, minyak biji Swietenia macrophylla yang kaya dengan sebatian aktif, digunakan untuk merencat bakteria penyebab jerawat iaitu Propionibacterium acnes, Staphylococcus aureus, dan Staphylococcus epidermidis. Sampel serbuk biji diekstrak menggunakan kaedah pengekstrakan Soxhlet dalam tiga jenis pelarut berbeza selama enam jam dan sepuluh kitaran. Analisis hasil ekstrak dijalankan menggunakan kromatografi gas-spektrofotometer jisim (GC-MS) dan asai cakera resapan dilakukan untuk menganalisis aktiviti antibakteria. Analisis logam berat pula ditentukan melalui spektrometri pancaran optikal-plasma gandingan aruhan (ICP-OES). Hasil kajian menunjukkan bahawa hasil sebatian bioaktif ialah 37-72%. Sebatian eugenol dan isoeugenol merupakan sebatian utama dalam sampel ekstrak minyak dengan kualiti 98% dan 97%. Sebatian tanpa kerja pengasingan ini juga menunjukkan aktiviti perencatan terhadap semua bakteria yang diuji dengan zon perencatan berjulat antara 11 hingga 21 mm.

Kata kunci: Swietenia macrophylla, jerawat, rawatan semula jadi, Propionibacterium acne, Staphylococcus epidermidis

Introduction

IntroductionAcne is a specific skin disease in dermatology. The skin problem occurs in pre-pubertal individuals, teenagers, and adults. It usually occurs in 14 to 17 years old girls and 16 to 19 years old boys. Those affected would experience distressing selfesteem and social relationships due to the inflammatory lesions and scarring effects [1]. Several factors that trigger acne include genetics, gender, youth, stress, and smoking habit [2]. The proliferation of bacteria such as Propionibacterium acnes in clogged pores causes the problem to worsen, especially when the body releases enzymes to break down the sebum, causing inflamed pores [3]. The main goal of acne treatment is to control the existing acne lesions, prevent permanent scarring, and reduce the disorder. According to Vora et al. [4], acne may be treated by topical and systemic therapies, such as antibiotics, comedolytic agents, and antiinflammatory drugs such as clindamycin, salicylic acid, and isotretinoin.

The use of natural products or non-drug treatments is preferable and acceptable due to organic awareness of remedial solutions. Moreover, natural products, especially skincare, are safer than synthetic products [5]. Even though various herbal products such as orange peel, neem, jojoba oil, and turmeric are used for acne treatment, the research on natural medication continues due to the tolerance resistance of P. acnes towards the commercially available antibiotics [6-7]. Swietenia macrophylla is a common plant species that grows wildly in Malaysia. It is known as the "sky fruit" or tunjuk langit, as the fruits seem to point upwards to the sky (Figure 1). Swietenia macrophylla is abundant in more than 40 countries, including Brazil, Bolivia, Mexico, Guatemala, Peru, and other central American countries [8]. In Malaysia, the locals usually consume the S. macrophylla seeds to treat high blood pressure, diabetes, increase blood

circulation, and relieve body pain [9]. The *S. macrophylla* seeds are also widely used in healthcare and skincare products [10]. Due to the numerous pharmacological activities of *S. macrophylla* extract, *including* antimicrobial, anti-inflammatory, antioxidant, antidiabetic, antifungal, and antimalaria [11], the *S. macrophylla* extract is suitable to be explored and utilised in an acne treatment regime.



Figure 1. Photo image of *Swietenia macrophylla* tree and seeds (insert)

Hence, this study explored the properties of seed extract as the novel ingredient for acne treatment. The Soxhlet extraction method was performed to investigate the extraction yield in three different extraction solvent systems (methanol, ethyl acetate, and methanol: ethyl acetate mixture). The bioactivities of the extracts were analysed using a gas chromatography-mass spectrophotometer (GC-MS), and the heavy metals elements were determined using the inductive coupled plasma optical emission spectrometry (ICP-OES). A biochemical test and the disc diffusion assay method were conducted to determine the antibacterial activity against *P. acnes, Staphylococcus aureus, and Staphylococcus epidermidis.*

Materials and Methods

Material and reagents

Tetracycline (30 µg) was purchased from Sigma Chemicals (St. Louis, MO, USA), Mueller Hinton agar (MHA), Mueller Hinton broth, nutrient agar (NA) and nutrient broth used for the determination of antibacterial activity were purchased from Merck (M) Sdn. Bhd. and Thermo Fisher Scientific (M) Sdn. Bhd. All chemicals and solvents used in the experiment were analytical grades with above 98% purity. The reagents were supplied by the Chemistry Laboratory 2 and 4, UiTM Perlis Branch. The methanol, ethyl acetate, and 1:1 ratio of methanol: ethyl acetate mixtures were prepared and used to extract the *S. macrophylla* seeds sample. *P. acnes, S. aureus*, and *S. epidermidis* were obtained from the Biology Laboratory, UiTM Perlis Branch.

Preparation of Swietenia macrophylla samples extract

The *S. macrophylla* seeds were collected from the trees in Jitra, Kedah. The seeds were washed with tap water to remove dust and other inert materials. The cleaned samples were air-dried for two days. Then, the samples were ground into powder using an electrical blender. About 5.0 g of powdered seed sample was mixed with 150 mL of extraction solvent (methanol, ethyl acetate, and methanol-ethyl acetate mixture) and extracted using the Soxhlet apparatus for 6 h. The filtrate was then concentrated using a rotary evaporator to remove the solvent, and the yield percentage was expressed in w/w% and stored in a vacuum desiccator for further analysis. The yield percentage was calculated using the following equation:

% yield =
$$[M_1 - M_0] \times 100$$
 (1)

where M_1 = mass of sample (g) and M_o = mass of the extract (g)

The chemical properties of SME

The chemical properties of SME were analysed using a GC-MS (Model Agilent 6890 equipped with 5MS, 30 m \times 0.25 mm i.d. capillary column coated with 0.25 μ m film and coupled with Agilent Chemstation software of NIST/Wiley Library). A volume of 0.1 mL samples extracts was derivatised with 100 μ L N, O-

Bis(trimethylsilyl)trifluoroacetamide (BSTFA) for 30 min in a sealed 2 mL vial. Then $0.1~\mu L$ of derivatised samples were analysed by the GC-MS, and the data was recorded, according to Hashim et al. [11].

The elemental analysis was determined using the ICP-OES (Model Thermo Scientific ICAP6000 Series). The multi-element of the standard solution was prepared from a 10-ppm stock solution in different concentrations at 0.01 ppm, 0.1 ppm, 1.0 ppm, and 10 ppm. Approximately 0.5 g of sample was digested with 8 mL of 65% nitric acid and 2 mL of concentrated hydrogen peroxide in microwave digestion. The sample was treated in the microwave digester for 15 min at 180 °C of 500 W. The treated sample mixture was cooled and diluted to 10 times concentration with distilled water prior to ICP-OES analysis.

The antibacterial analysis

The MHA and NA media were prepared according to the manufacturer's instructions. Approximately 38.0 and 28.0 g of the MHA and NA powders were weighed to prepare 1000 mL agar and poured into conical flasks. The powder was dissolved in distilled water and continuously stirred until homogenised. The agar solution was sterilised using an automatic autoclave at 121 °C for 15 min. The agar was cooled to 45 to 50 °C before being poured into sterile Petri dishes. These agars were stored upside down in a chiller of 4 to 8 °C before being used.

The bacteria were subcultured by the streaking method. The inoculation loop was sterilised and cooled for a few seconds before dipping into the bacterial solution and streaked in a zigzag motion on the agar. This method was repeated three times for each bacterium. The inoculating loop was sterilised each time before subculturing the bacteria. The agar plates of *S. aureus* and *S. epidermidis* were incubated at 37 °C for 18 to 24 h in an inverted position [12].

The *P. acnes* was subcultured using a different method since it is a facultative anaerobic. It grows best under limited oxygen (0-20%), and the growth rate was reduced at high oxygen concentration [14]. The cultured plate was incubated under anaerobic

conditions [13], i.e., inside a candle jar to provide a suitable condition for the *P. acnes* to grow at 37 °C for 72 h [15]. The biochemical tests involved were the catalase, the methyl red/Voges-Proskauer (MR-VP), and Gram staining to identify the desired bacterial interaction activities.

The catalase test was performed according to Habib et al. [16], whereby *S. aureus* and *S. epidermidis* were streaked onto MHA, and *P. acnes* was streaked onto NA to obtain bacterial colonies. The plates were incubated for 24 h and 72 h, respectively. Each bacterial colony was mixed with 2 to 3 drops of 3% hydrogen peroxide, where the formation of bubbles indicated positive results.

The methyl red (MR) and Voges-Proskauer (VP) test utilised the MR-VP broth. The MR-VP broth was prepared according to the manufacturer's recommendation. About 17g of broth powder was weighed to prepare 1000 mL MR-VP broth and sterilised at 121 °C for 15 min. The MR-VP broth was then incubated at 37 °C for 24 h and 48 h, respectively, for the VP and MR tests. The VP and MR test method. Approximately 1 mL of MR-VP broth was poured into test tubes. The VP test involved the addition of each bacterial colony, 0.6 mL of 5% α naphthol, and 0.2 mL of 40% of potassium hydroxide to test tubes. Meanwhile, the MR test involved the addition of five drops of methyl red to test tubes containing bacterial colonies. Then, the test tubes were shaken gently and left undisturbed for 10 to 15 min. The colour changes from yellow to red of the sample showed a positive result.

The Gram staining test method was performed according to Shinkafi and Ndanusa [17]. A loopful of bacteria was heat-fixed onto a slide. A drop of crystal violet, followed by the decolouriser, iodine, and safranin, was added onto the bacteria on the slide for 1 min and was washed off with distilled water. The slide was blotted to dry before being observed under the light microscope at 100× magnifications and recorded.

The disc diffusion assay method to test antibacterial activities was performed according to Park et al. [14]. Approximately 100 µL of each bacterial suspension was used and spread on MHA using a sterile cotton swab (for S. aureus and S. epidermidis) and NA (for P. acnes). Each disc impregnated with antibiotics was gently pressed down to ensure that the disc was completely in contact with the agar surface and did not fall when inverted. The streptomycin antibiotic disc was used as a positive control, while the extraction solvent, i.e., methanol, ethyl acetate, and 1:1 ratio of methanol: ethyl acetate mixture, was used as the negative control. The experiment was done in triplicate for each bacterium. The plates were incubated at 37 °C for 24 h (S. aureus and S. epidermidis) and 37 °C for 72 h in a candle jar to retain the anaerobic condition for P. acnes. The antibacterial activity was measured based on the diameter of the inhibition growth zone.

Results and Discussion

The S. macrophylla seed was extracted using the Soxhlet extraction method in three different solvent systems; methanol aqueous, ethyl acetate, and 1:1 methanol-ethyl acetate mixture. Table 1 shows that the 1:1 ratio of methanol-ethyl acetate solvent mixture produces the highest percentage of crude oil extract (72.68%), followed by ethyl acetate (67.55%) and aqueous methanol (37.65%). All solvents used can extract the crude oil in 6 h extraction time. Do et al. mentioned that methanol solvent is generally more efficient in extracting lower molecular weight polyphenols [18]. In this experiment, the combination of methanol-ethyl acetate organic solvent facilitates a suitable extraction of all soluble compounds in both solvents. According to Nawaz et al., using a combination of polar and nonpolar solvents can increase the excellent quality of extraction yield from the bean and other legume seeds [19]. Furthermore, Che Sulaiman et al. reported that the extraction yield of organic samples is also dependent on the extraction times, extraction temperatures, and solvent ratios [20].

 3.40 ± 0.18

 3.67 ± 0.49

Solvent Types	Mass of Dried Powder (g)	Mass of Oil Crude Extract (g)	% Yield
Methanol	5.07 ± 0.02	1.90 ± 0.45	37.65

 5.04 ± 0.02

 5.04 ± 0.03

Table 1. Percentage Yield of Swietenia macrophylla Seed's Extract in a different solvent

The phytochemical compounds the S. in macrophylla seed extract were analysed using GC-MS analysis. About 13 compounds were successfully identified in the methanol extract, 20 in the ethyl acetate extract, and 12 in the 1:1 methanol-ethyl acetate mixture as terpenoids, flavonoids, and limonoids. The compounds obtained strongly depended on the nature of extracting solvent due to different antioxidant compounds that vary their chemical characteristics and polarities. The most extracted compounds were reported in ethyl acetate, methanol, and 1:1 methanolethyl mixture due to the semipolar-polar compounds [21]. The number of extracted compounds in the 1:1 methanol-ethyl acetate extract is less than ethyl acetate alone because the elution strength of ethyl acetate decreased due to the polarisation effect of methanol. The extraction process yielded seven compounds in methanol extract, five compounds in ethyl acetate extract, and two compounds in the 1:1 methanol-ethyl acetate mixture, with more than 80% quality compared to the GC-MS reference library software (Table 2). In Table 2 show that silane methoxytrimethyl-, disiloxane hexamethyl, and 2,2,2-trifluoro-N-(trimethylsilyl)- are the major bioactive compound present in S. macrophylla seed extract, with the under peak percentage area of more than 23.57%. A previous study by Azhari et al. [22] stated that several compounds of limonoids such as phenol, 2-methoxy-4-(1-propenyl)-, and eugenol were also found in S. macrophylla seed extract using the maceration method. In this work, compounds such as phenol, 2-methoxy-4-(1propenyl)-, (E)-(isoeugenol), silane, [2-methoxy-4-(1propenyl) phenoxy] trimethyl- (isoeugenol), and eugenol are present in the sample. As reported in previous works, these compounds possess effective antifungal and antibacterial activities [23-25].

Ethyl Acetate

Methanol: Ethyl Acetate

According to Sharma et al. [26], phytocompounds present in chloroform and methanol seed extracts are responsible for the varied antioxidant and antimicrobial activities.

67.55

72.68

The concentration of arsenic (As), lead (Pb), cadmium (Cd), nickel (Ni), mercury (Hg), and copper (Cu) in *S. macrophylla* seed powder was analysed using ICP-OES. Table 3 shows the result of heavy metal concentration in the crude oil extract sample. Only low concentrations of mercury are detected in the sample, i.e., 0.080 ppm. The result revealed that the *S. macrophylla* seed powder is low in heavy metal content. Hence, it is considered a safe ingredient in medication or cosmetic products. According to the U.S. Food and Drug Administration (USFDA) limits regulation, the accepted concentration of mercury must be less than 1 ppm (1 mg/kg), i.e., safe to be used as new constituents in products [31].

The images of catalase test (CT), Voges Proskauer (VP), and Gram staining test (GST) of Gram-positive bacteria (S. aureus, S. epidermidis, and P. acnes [facultative anaerobic bacteria]), are shown in Figures 2 - 4. Figure 2 shows a positive CT result, whereby bubbles are observed at 10 min observation. The finding is similar to the study by Mustafa [30], Kallstrom et al. [31], and Cauich-Sanchez et al. [32]. The catalase acts as a catalyst in breaking down the hydrogen peroxide into water and oxygen to form an oxygen bubble produced by the bacteria. The VP test was conducted to measure the production of acetyl methyl carbinol, as shown in Figure 3. S. aureus and P. acnes show positive results, where the color of the solution change to red. In contrast, the colour of the S. epidermidis solution remains unchanged. This result

Non Daina et al: THE CHEMICAL PROPERTIES and ANTI-ACNE ACTIVITY DETERMINATION of Swietenia macrophylla SEED EXTRACTS

is similar to Shinkafi and Ndanusa [17], whereby the colour change from light yellow to slightly red in the *S. aureus* and *P. acnes* tests indicated positive results. Whereas the colour of the solution in the *S. epidermidis* tube did not change, indicating a negative result. Further validation analysis for *S. aureus*, *S. epidermidis*, and *P. acnes* were carried out using the methyl red (MR) test (Figure 4). The unchanged colour of the MR solution of *S. aureus* and *P. acnes* indicates *positive* results. On the contrary, the colour

of the *S. epidermidis* solution changed from light yellow to red. The researcher also stated that *S. aureus* and *P. acnes* showed negative results when the colour of the MR solution remained unchanged. This is contradictory to *S. epidermidis*, which showed positive results when the light-yellow solution slightly changed to red. The purpose of the MR test is to determine the ability of the bacteria to oxidise glucose and produce a high concentration of acidic products.

Table 2. Phytocompounds in SME in different extraction solvents by using GC-MS

Retention Time (min)	Area (%)	Name of Compound	Bioactivity	Solvent
1.300	45.76	Silane, methoxytrimethyl-	NR	
1.545	23.57	Disiloxane, hexamethyl-	NR	
4.409	0.34	Benzene-1-ethyl-3-methyl-	NR	
4.540	0.16	Benzene-1,3,5-trimethyl-	NR	Methanol
4.723	0.12	Benzene, 1-ethyl-2-methyl-	NR	
4.997	0.57	Benzene, 1,2,3-trimethyl-	NR	
5.535	0.18	Benzene, 1,2,3-trimethyl-	NR	
1.923	25.84	Disiloxane, hexamethyl-	NR	
2.414	34.13	Acetamide, 2,2,2-trifluoro-N- (trimethylsilyl)-	NR	
13.205	0.11	Phenol, 2-methoxy-4-(1-propenyl)-, (E)-	Antifungal [21],	
13.239	0.15	Eugenol	Antibacterial, Anti- inflammatory [22], Antioxidant [23]	Ethyl acetate
14.988	0.12	Silane, [2-methoxy-4-(1-propenyl) phenoxy] trimethyl-	Antifungal [20]	
1.631	2.77	Silane, methoxytrimethyl-	NR	Methanol:
5.660	0.15	Benzene, 1,2,4-trimethyl-	NR	ethyl acetate (1:1)

NR - Activity of compound is not reported

Table 3. Heavy metal concentration in Swietenia macrophylla seed's powdered sample using ICP-OES

Heavy Metal	Concentration (ppm)
As	0
Pb	0
Cd	0
Ni	0
Hg	0.080
Cu	0

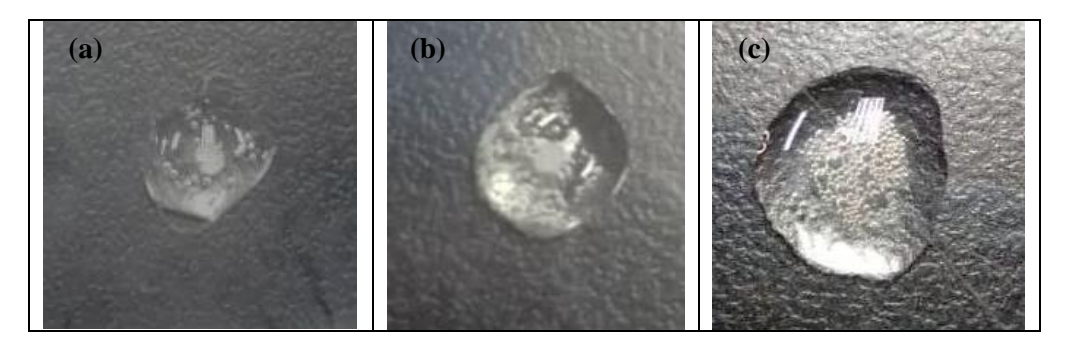


Figure 2. The photo images of catalase test of (a) S. aureus, (b) S. epidermidis, and (c) P. acnes

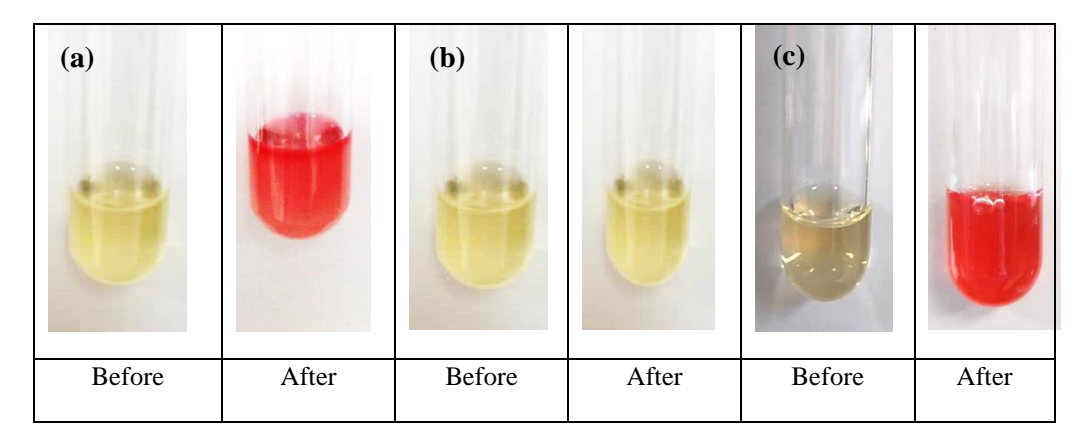


Figure 3. The photo images of Voges Proskauer (VP) test of (a) S. aureus (b) S. epidermidis (c) P. acnes

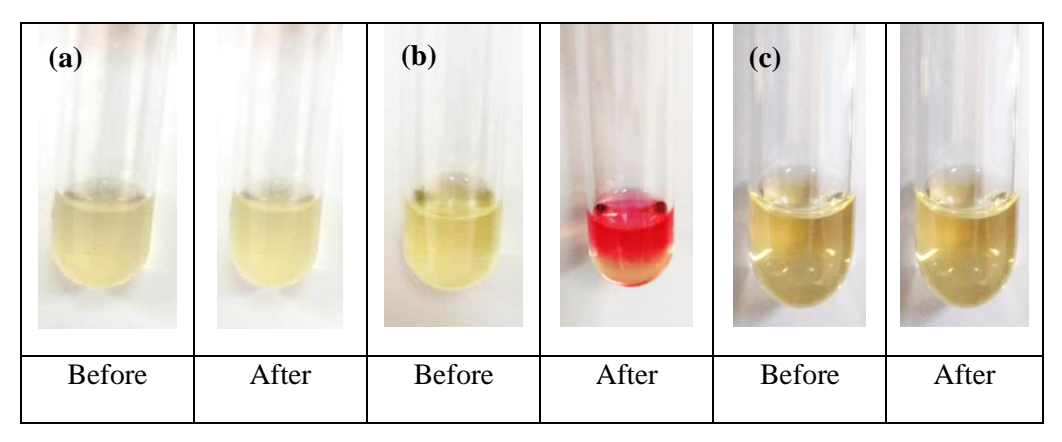


Figure 4. Photo images of methyl red (MR) test of (a) S. aureus, (b) S. epidermidis, and (c) P. acnes

The Gram-staining analysis was performed to determine the Gram-positive and Gram-negative bacteria based on the bacterial cell wall colour using an Olympus CKX53 inverted microscope (Figure 5). The Gram-positive bacteria, i.e., S. aureus, epidermidis, and P. acnes, were observed in this analysis. The results showed that the bacteria appear violet with aggregated grape-like clusters under 100× magnification [16]. In contrast, the P. acnes is visualised as violet with a rod-like bacillus structure [33], as shown in Figure 5(c). According to Panawala [34], the bacteria appear violet under the microscope due to the thick peptidoglycan cell wall and teichoic acid composition.

The inhibition zones of the three bacteria species were determined using the disc diffusion assay method, as shown in Figure 6 and Table 4. The disc assay method is a rapid determination of antibacterial activity by measuring the diameter of the inhibition zone that resulted from the diffusion of the phytochemical compound into the medium surrounding the disc [35]. Table 4 shows the inhibition zone category and bacterial inhibition zone in 30-disc tetracycline concentration (μ g/disc).

The inhibition of bacteria towards the sample extract was expressed as susceptible, intermediate, and resistant according to international standards (ISO 20776-1). Susceptible is when the bacteria are inhibited *in vitro* by a drug concentration with high therapeutic

properties. Meanwhile, intermediate is when the bacteria are inhibited in vitro by a drug with uncertain therapeutic effects. For resistance, the bacteria are inhibited in vitro by a drug with a high chance of therapeutic failure [36].

Figure 6 shows *P. acnes* is minimally inhibited in the methanol and 1:1methanol-ethyl acetate extracts. In comparison, the inhibition zone of the *S. aureus* is more prominent than in tetracycline (antibiotic control). Table 4 shows the results of the inhibition zone of the bacteria tested. *S. aureus* is susceptible in methanol and 1:1 methanol-ethyl acetate extracts, as the zone of inhibition more than 19.00 ± 0.00 mm, while *S. epidermidis* is resistant towards ethyl acetate and 1:1 methanol-ethyl acetate extracts at 13.00 ± 1.00 mm and 13.00 ± 2.31 , respectively.

Meanwhile, *P. acnes* exhibits resistant, intermediate, and susceptible properties in 1:1 methanol-ethyl acetate, methanol, and ethyl acetate extract respectively. Aditi and Hossain [37] reported that *S. aureus* acquired resistance easily, a good bio-indicator model for surveillance studies of antimicrobial resistance [38]. *S. aureus* and *P. acnes* in ethyl acetate extraction solvent showed a more significant inhibition zone but slightly lower inhibition of *S. epidermidis*. In a nutshell, for antibacterial activity, all extracts showed a high therapeutic capability towards *S. aureus* and *P. acnes* but are less effective against *S. epidermidis*.

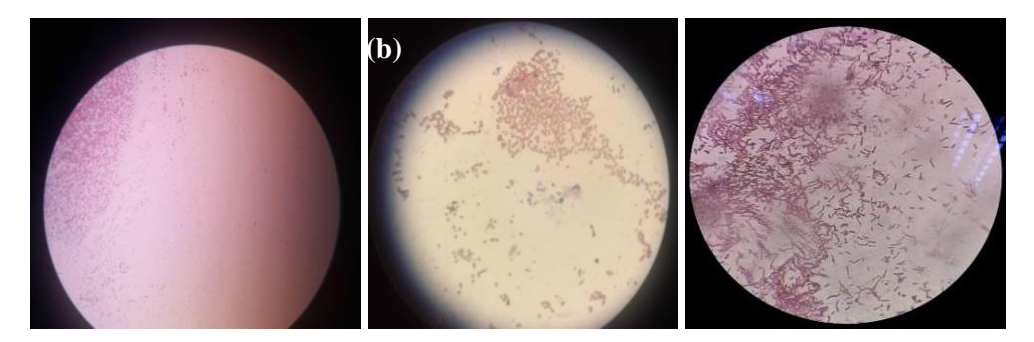


Figure 5. Photo images of Gram Staining Test in 100X Magnifications of (a) S. aureus (b) S. epidermidis, and (c) P. acnes

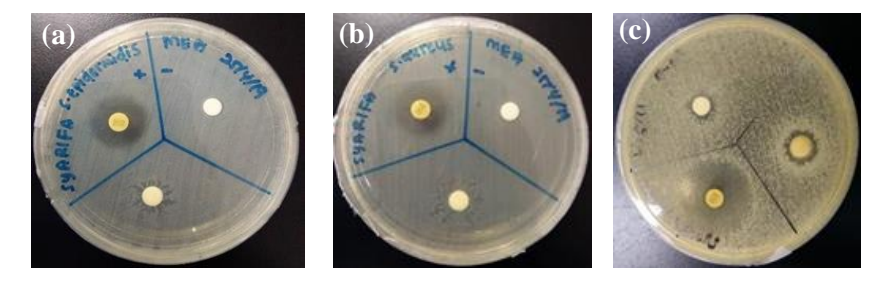


Figure 6. Inhibition zone photo images of the test discs (a) *S. epidermidis*, (b) *S. aureus*, and (c) *P. acnes* of SME in 1:1 methanol-ethyl acetate mixture

Table 4. Inhibition zone category in tetracycline and inhibition zone on bacterial growth activities in different extraction solvent

Antibiotic	Inhibition zone (Category)			
Tetracycline (control) in 30-disc (μg/disc)	S. aureus (± n) 18.33 ± 0.58	S. epidermidis (\pm n) 18.67 \pm 0.58	P. acnes (± n) 21.33 ± 1.53	
Sample in the different extraction solvent	Inhibition zone (Bacterial Growth)			
Methanol Ethyl acetate Methanol: Ethyl acetate (1:1)	20.67 ± 6.03 16.67 ± 6.66 21.67 ± 11.72	18.67 ± 14.15 13.00 ± 1.00 13.00 ± 2.31	16.33 ± 5.69 19.00 ± 4.36 11.00 ± 1.73	

^{*}R- resistant (≤14 mm), I- intermediate (15-18 mm), S-susceptible (≥19 mm) [9]

Conclusion

The properties of *S. macrophylla* seeds in three different extraction solvents were successfully determined. Three new compounds, phenol, 2-methoxy-4-(1-propenyl)-, (E)-Eugenol; and silane, [2-methoxy-4-(1-propenyl) phenoxy] trimethyl, were

successfully extracted from *S. macrophylla* seeds using ethyl acetate solvent. The highest extraction yield is obtained in the 1:1 methanol-ethyl acetate mixture (72.68%), followed by ethyl acetate (67.55%) and methanol (37.65%). From the disc diffusion assay, *S. epidermidis and P. aureus* are susceptible towards

^{*}The values were presented in mean \pm SD, where n=3

methanol and 1:1 methanol-ethyl acetate extracts. In contrast, *P. acnes* is susceptible towards ethyl acetate extract. The result showed that *S. macrophylla* seeds extract is an effective ingredient for treating acne due to positive inhibition towards three acne-causing bacteria and is considerably low in heavy metal contents.

Acknowledgement

The authors are sincerely grateful to UiTM Perlis Branch, Arau Campus, to provide the research facilities. High appreciation also goes to the Frontier Applied Science and Technology research group (FAST) for completing this work.

References

- Zaghloul, S. S., Cunliffe, W. J. and Goodfield, M. J. D. (2005). Objective assessment of compliance with treatments in acne. *British Journal of Dermatology*, 152(5): 1015-1021.
- 2. Fox, L., Csongradi, C., Aucamp, M., Du Plessis, J. and Gerber, M. (2016). Treatment modalities for acne. *Molecules*, 21(8): 1-20.
- 3. Savage, A. E. O. (1985). *United States Patent*, 19(54): pp. 19.
- Vora, J., Srivastava, A. and Modi, H. (2018). Antibacterial and antioxidant strategies for acne treatment through plant extracts. *Informatics in Medicine Unlocked*, 13: 128-132.
- 5. Afsar, Z. and Khanama, S. (2016). Formulation and evaluation of polyherbal soap and sanitiser. *International Research Journal of Pharmacy*, 7(8): 54-46
- 6. Platsidaki E. and Dessinioti C. (2018). Recent advances in understanding *Propionibacterium acnes* (*Cutibacterium acnes*) in acne. F1000Research, 7(F1000 Faculty Rev:1953).
- 7. Tan, A. U., Schlosser B. J. and Paller, A.S. (2017). A review of diagnosis and treatment of acne in adult female patients. *International Journal of Women's Dermatology*, 4(2): 56-71.
- 8. Eid, A. M. M., Elmarzugi, N. A. and El-Enshasy, H. A. (2013). A review on the phytopharmacological effect of *Swietenia macrophylla*. *International Journal of Pharmacy and Pharmaceutical Sciences*, 5(3): 47-53.

- 9. Suliman, M. B. (2018). Preliminary phytochemical screening and thin layer chromatography analysis of *Swietenia Macrophylla King* methanol extracts. *Chemistry of Advanced Materials*, 3(1): 1-7.
- Durai, M., Balamuniappan, G. and Geetha, S. (2016). Phytochemical screening and antimicrobial activity of leaf, seed and central-fruit-axis crude extract of Swietenia macrophylla King. Journal of Pharmacognosy and Phytochemistry, 181(53): 181-186.
- Hashim, M. A., Yam, M. F., Hor, S. Y., Lim, C. P., Asmawi, M. Z. and Sadikun, A. (2013). Antihyperglycaemic activity of *Swietenia macrophylla king (meliaceae)* seed extracts in normoglycemic rats undergoing glucose tolerance tests. *Chinese Medicine* (United Kingdom), 8(1): 1-8.
- Wu, Q., Li, Y., Hu, H., Wang, M., Wu, Z. and Xu, W. (2012). Rapid identification of *Staphylococcus* aureus: FISH versus PCR methods. *Laboratory* Medicine, 43(6): 276-280.
- 13. Naghdi, N. and Ghane, M. (2017). A comparison of culture and PCR methods for identifying *Propionibacterium* acnes in lesions isolated from patients with acne. *Turkish Journal of Medical Sciences*, 47(3): 967-972.
- 14. Park, J., Lee, J., Jung, E., Park, Y., Kim, K., Park, B., Jung, K., Park, E., Kim, J. and Park, D. (2004). In vitro antibacterial and anti-inflammatory effects of honokiol and magnolol against Propionibacterium sp. European Journal of Pharmacology, 496(1): 189-195.
- Nirmal, N. P. and Panichayupakaranant, P. (2014).
 Anti-propionibacterium acnes assay-guided purification of brazilin and preparation of brazilin rich extract from *Caesalpinia sappan* heartwood. *Pharmaceutical Biology*, 52(9): 1204-1207.
- 16. Habib, F., Rind, R., Durani, N., Latif Bhutto, A., Buriro, R. S., Tunio, A., Aijaz, N., Lakho, S., Ghulam, B. and Shoaib, M. (2015). Morphological and cultural characterization of *Staphylococcus aureus* isolated from different animal species. *Journal of Applied, Environmental and Biological Sciences*, 5(2): 15-26.

- 17. Shinkafi, S., and Ndanusa, H. (2013). Antibacterial activity of citrus lemon on acne *vulgaris* (pimples). *International Journal of Science Inventions Today*, 2(5): 397-409.
- Do, Q. D., Angkawijaya, A. E., Tran-Nguyen, P. L., Huynh, L. H., Soetaredjo, F. E., Ismadji, S. and Ju, Y. H. (2014). Effect of extraction solvent on total phenol content, total flavonoid content, and antioxidant activity of *Limnophila aromatica*. *Journal of Food and Drug Analysis*, 22(3): 296-302.
- 19. Nawaz, H., Shad M. A., Rehman, A. N., Andaleeb, H. and Ullah, N. (2020). Effect of solvent polarity on extraction yield and antioxidant properties of phytochemicals from bean (*Phaseolus vulgaris*) seeds. *Brazilian Journal of Pharmaceutical Sciences*, 56: 17129.
- 20. Che Sulaiman I. S. and Basri, M. (2017). Effects of temperature, time, and solvent ratio on the extraction of phenolic compounds and the antiradical activity of *Clinacanthus nutans* Lindau leaves by response surface methodology. *Chemistry Central Journal*, 11(1): 54.
- Akbar A., Soekamto N. H., Firdaus and Bahrun (2021) Antioxidant of n-hexane, ethyl acetate and methanol extracts of *Padina* sp. with DPPH method. *Earth and Environmental Science* 800: 012019.
- Azhari, Nour, H., Mohammed, Sulieman, B., Mashitah, Yousf, M. and Adam, M. M. (2016). Bioassay-guided isolation and identification of antifungal compounds from seeds of Swietenia macrophylla King. Australian Journal of Basic and Applied Sciences, 10(17): 55-62.
- 23. Aquirre-Becerra H., Pineda-Noeto S. A., Garciatrejo J.F., Guevara-Gonzalez R. G., Feregrino-Perez A. A., Alerez-Mayorga B. L. and Rivera-Pastrana D. M. (2020). Jacaranda flower (*Jacarand mimosifolia*) as alternaive for antioxidant and antimicrobial use. *Heliyon*, 6(12): e05802.
- Eid A., Elmarzugi N. and El-Enshasy H. (2013). A review on the phytopharmacological effect of Swietenia macrophylla. International Journal of Pharmacy and Pharmaceutical Sciences, 5: 47-53.

- Moghadamtousi S. Z., Goh B. H., Chan C. K., Shabab T. and Kadir, H. A. (2013). Biological activities and phytochemicals of *Swietenia* macrophylla King. Molecules, 18: 10465-10483.
- 26. Sharma S., Kumari A., Dhatwalia J., Guleria I., Lal S., Upadhyay N., Kumar V. and Kumar A., (2021), Effect of solvents extraction on phytochemical profile and biological activities of two *Ocimum* species: A comparative study. *Journal of Applied Research on Medicinal and Aromatic Plants*, 25(2021): 100348.
- 27. Koeduka, T. (2014). The phenylpropene synthase pathway and its applications in the engineering of volatile phenylpropanoids in plants. *Plant Biotechnology*, 2014: 14-0801.
- 28. Nejad, S. M., Özgüneş, H. and Başaran, N. (2017). Pharmacological and toxicological properties of eugenol. *Turkish Journal of Pharmaceutical Sciences*, 14(2): 201.
- Bendre, R. S., Rajput, J. D., Bagul, S. D. and Karandikar, P. S. (2016). Outlooks on medicinal properties of eugenol and its synthetic derivatives. *Natural Product Chemistry Research*, 4(3): 1-6.
- 30. Mustafa, H. S. I. (2014). *Staphylococcus aureus* can produce catalase enzyme when adding to human WBCs as a source of productions in human plasma or serum in the laboratory. *Open Journal of Medical Microbiology*, 04: 249251.
- 31. Kallstrom, G., Chang, T., Albertson, M., Morilla, D., Fisher, M. A. and Eberly, B. (2011). Recovery of a catalase-negative *Staphylococcus epidermidis* strain in blood and urine cultures from a patient with pyelonephritis. *Journal of Clinical Microbiology*, 49(11): 4018-4019.
- 32. Cauich-Sanchez, P., Alatriste-Mondragon, F., Garcia-Cano, E. and Aquino-Santiago, C. (2001). Identification of anaerobic nonsporeforming grampositive bacilli by biochemical tests and gas-liquid chromatography. *Revista Latinoamericana de Microbiologia*, 43(1): 27-35.
- 33. Rolf, L. (2011). Propionibacterium acnes and its phages department of clinical sciences. Department of Clinical Sciences, Lund University: pp. 1-85.

- 34. Kuntom, A. and Kifli, (1998). Properties of soaps derived from distilled palm stearin and palm kernel fatty acids. *Journal of Surfactants and Detergents*, 1(3): 329-334.
- 35. Panawala, L. (2017). Difference between gram positive and gram-negative bacteria. *Epediaa*, 3: 1-13.
- 36. Tenover F. C. (2019). Antimicrobial susceptibility testing. *Encyclopedia of Microbiology (Fourth Edition)*: pp. 166-175.
- 37. Rodloff, A., Bauer, T., Ewig, S., Kujath, P. and Müller, E. (2008). Susceptible, intermediate, and resistant the intensity of antibiotic action. *Deutsches Aerzteblatt Online*, 105(39): 657-662.
- 38. Aditi, F. Y., Rahman, S. S. and Hossain, M. M. (2017). A study on the microbiological status of mineral drinking water. *The Open Microbiology Journal*, 11: 31.
- Hepp, N. M., Mindak, W. R., Gasper, J. W., Thompson, C. B. and Barrows, J. N. (2014). Survey of cosmetics for arsenic, cadmium, chromium, cobalt, lead, mercury, and nickel content. *Journal Cosmetic Sciences*, 65(3): 125.

Malaysian Journal of Analytical Sciences (MJAS)



Published by Malaysian Analytical Sciences Society

ESTIMATION OF METHANE PRODUCTION VIA ANAEROBIC CO-DIGESTION OF FOOD WASTE AND SLUDGE BY BIOCHEMICAL METHANE TEST

(Anggaran Pengeluaran Metana Melalui Pencernaan Bersama Anaerobik Sisa Makanan dan Enap Cemar oleh Ujian Potensi Metana Biokimia)

Nur Anisah Abdul Latif¹, Zuhaida Mohd Zaki², Khor Bee Chin³, Faeiza Buyong¹*

¹Faculty of Applied Sciences, Universiti Teknologi MARA, 40450 Shah Alam, Selangor, Malaysia ²Faculty of Civil Engineering, Universiti Teknologi MARA, 13500 Permatang Pauh, Pulau Pinang, Malaysia ³Indah Water Konsortium Sdn. Bhd., Damansara Height, 50490 Kuala Lumpur, Malaysia

*Corresponding author: faeiza@uitm.edu.my

Received: 28 December 2021; Accepted: 27 February 2022; Published: 28 April 2022

Abstract

Biochemical methane potential (BMP) tests are extensively used in many studies related to anaerobic co-digestion (AcoD) to evaluate biogas production and determine the potential methane yield between various substrates at specific retention times and parameters. AcoD is a process of mixing two or more substrates in a digester that could help to improve the methane yield as compared to mono-digestion with the same substrates. This study evaluates the methane production efficiency via AcoD of food waste and thickened sludge by using the BMP tests. The substrates used for this study were wastes from non-dairy creamer, coffee, and mixed food waste with sludge. Additionally, thickened sludge as an inoculum was used for the BMP test. The samples characterisation was analysed according to standard and HACH methods. The thickened sludge was set up at a ratio of 1:1 as a control, while the food wastes sample with sludge was set up at a ratio of 1:2. The initial pH was adjusted in a range of 6.5-7. The BMP test setup was done using a 125mL serum bottle in triplicates for 31 days in an incubator at 37°C. The results showed that the highest methane production of the BMP was from thickened sludge itself which is 18.275 ± 3.3 mL CH₄/gVS, followed by non-dairy creamer waste with thickened sludge, mixed food waste with sludge and coffee waste with thickened sludge which are 17.865 ± 6.2 mL CH₄/gVS, 17.825 ± 0.05 mL CH₄/gVS and 14.797 ± 0.01 mL CH₄/gVS respectively. In conclusion, the pre-treatments process is highly recommended in order to improve biogas production.

Keywords: anaerobic co-digestion, biochemical methane potential, experimental methods, food wastes, methane production

Abstrak

Ujian potensi metana biokimia (BMP) digunakan secara meluas dalam banyak kajian berkaitan penghadaman bersama anaerobik (AcoD) untuk menilai pengeluaran biogas dan menentukan potensi hasil metana antara pelbagai substrat pada masa dan parameter pengekalan tertentu. AcoD merupakan suatu proses mencampurkan dua atau lebih substrat dalam pencerna yang boleh meningkatkan hasil metana berbanding mono-pencernaan dengan substrat yang sama. Kajian ini bertujuan menilai kecekapan pengeluaran metana oleh AcoD bagi sisa makanan dan enap cemar pekat menggunakan ujian BMP. Substrat yang digunakan

Nur Anisah et al: ESTIMATION OF METHANE PRODUCTION VIA ANAEROBIC CO-DIGESTION OF FOOD WASTE AND SLUDGE BY BIOCHEMICAL METHANE TEST

untuk kajian ini ialah sisa daripada krimer bukan tenusu, kopi, dan sisa makanan yang bercampur dengan enap cemar. Enap cemar pekat digunakan untuk ujian BMP sebagai inokulum. Pencirian sampel dianalisis mengikut kaedah standard dan HACH. Enap cemar yang menebal telah disediakan dalam nisbah 1:1 sebagai kawalan, manakala sampel sisa makanan dengan enap cemar disediakan dalam nisbah 1:2. Nilai pH awal diselaraskan dalam julat 6.5–7. Persediaan ujian BMP dilakukan menggunakan botol serum 125mL sebanyak tiga kali ganda selama 31 hari dalam inkubator pada suhu 37°C. Hasil kajian menunjukkan bahawa pengeluaran metana BMP tertinggi adalah daripada enap cemar pekat itu sendiri, iaitu 18.275 \pm 3.3 mL CH4/gVS, diikuti sisa krimer bukan tenusu dengan enap cemar pekat, sisa makanan bercampur dengan enap cemar, dan sisa kopi dengan enap cemar pekat, masing-masing 17.865 \pm 6.2 mL CH4/gVS, 17.825 \pm 0.05 mL CH4/gVS, dan 14.797 \pm 0.01 mL CH4/gVS. Kesimpulannya, proses pra-rawatan amat disyorkan untuk meningkatkan pengeluaran biogas.

Kata kunci: pencernaan bersama anaerob, potensi metana biokimia, kaedah eksperimen, sisa makanan, penghasilan metana

Introduction

The amount of sewage sludge is continuously increasing as a surplus of the wastewater treatment process due to increased population. The higher percentage of households connected to the main wastewater treatment plants (WWTPs) also contributes to the higher production of sewage sludge [1, 2]. Nevertheless, improper handling and untreated sewage sludge may lead to environmental impacts and public health problems. This is because sewage sludge is characterised by its high concentrations of solids and organic matter, with the presence of nutrients, organic and inorganic pollutants and pathogens that create odour problems. Nowadays, there are several alternative techniques which are applied for sewage sludge disposal, such as incineration, landfills, compost, recycling, and anaerobic digestion (AD). AD is a proven technology and one of the most feasible techniques applied for the treatment of sewage sludge in many countries due to its lower operational cost, reduced chemical oxygen demand (COD), decreased pollutants discharged into the environment, and production of energy-rich biogas [3, 4, 5].

Besides that, anaerobic digestion (AD) is also known as the most efficient process for the treatment of municipal solid waste and wastewater sludge [6, 7]. In general, anaerobic digestion (AD) is the process in which organic waste such as bio-waste, animal manure, sludge, crops, and other biomasses are biologically degraded in the absence of oxygen and converted into a form of biogas and other organic compounds as end products [6, 7]. The food waste also can be characterised by its high percentage of

biodegradability, moisture content around (> 70%), volatile solids (> 95%), with numerous amounts of lipids [8] that will enhance the AD performance. Other than that, the methane gas obtained from the AD process can be used to generate electricity and for heating purposes. Sewage sludge is characterised by its high concentration of solids and organic matter, with the presence of nutrients, organic and inorganic pollutants, and pathogens. According to Appels et al., [6], fuels can be produced by using sewage sludge. It can also be used as an inoculum in the anaerobic digestion process by considering its characteristics. Thus, anaerobic co-digestion (AcoD) is the process of mixing two or more substrates in a digester that could improve methane production from 25% to 400% as compared to the mono-digestion [9-13] of the same substrates [14,15].

Non-dairy creamer (NDC) and coffee are from the food and beverages industry. However, the NDC contains no lactose. It is a substitute product for milk or cream in the form of a liquid or powder which produces high water dissolved fat emulsion that is made up from vegetable oil (30% hydrogenated coconut or palm oil) for the purpose of reducing the amount of milk or replacing the milk powder in oatmeal, baked goods, coffee and others [16]. Huang et al.,[17] stated that NDC is made up of 60-65% glucose or corn syrup, 2-5% sodium caseinate, stabilisers, and emulsifiers [18], and it contains about 1.2% of minerals, 8.5% of protein, 32.5% of fat, and the highest percentage is carbohydrate at 58%. The liquid waste and sewage sludge are the by-products of the NDC industry. The improper processing of the NDC wastewater will affect the environment. The sewage sludge and wastewater from NDC contain high organic matter such as proteins, lipids, and carbohydrates [19-21] While the coffee processing effluent is highly acidic, has high chemical oxygen demand (COD), and also contains a high amount of organic matter and suspended solids [22-23], the foul odour and eutrophication occurs due to the dark brown colour of the effluent which was produced from the coffee processing plants due to the decomposition of lignin (humic acid, tannin) with different macromolecules such as caffeine and polyphenols (melanoidins). Cardenas et al., [24] cited that melanoidins consist of ligands (polysaccharides, tannins), which hardly degrade biologically [25]. Thus, AD is considered as an alternative method to treat both NDC and coffee waste.

In addition to that, AD can be applied experimentally via the biochemical methane potential (BMP) test by determining the biodegradability of waste biomass and wastewater and also the methane potentiality [26]. The BMP experimental test is usually suitable for small-scale (batch) analysis (lab-work) which is costly, and time-consuming, with analysis within 20 to >100 days [27] compared to the BMP theoretical test. Several

parameters influence the determination of BMP experimental tests such as the inoculum-substrate ratio, pH, temperature, retention time, chemical oxygen demand (COD), total solids (TS), moisture content, volatile solids (VS), and others [28]. The objective of this study is to evaluate the methane production via anaerobic co-digestion of food waste and sludge by using the BMP experimental method.

Material and Methods

Sample collection

Substrate and inoculum

Food waste samples as substrates (coffee, non-dairy creamer waste and mixed food waste) were obtained from the food manufacturing industry and the IWK sludge (thickened) was used as inoculum. All food wastes and thickened sludge were supplied by Indah Water Konsortium Sdn. Bhd (IWK), whose WWTP plant is located at IWK Sewage Treatment Plant, Kuala Lumpur. Then, the collected samples were degassed or pre-incubated to deplete the residual biodegradable organic material present in them [29]. Table 1 presents the setup of substrates used for this study.

Table 1.	Substrates	for	BMP.	and	S/I rat	tio

Inoculum & Substrates	Label	Substrate/inoculum Ratio, S/I	
Thickened sludge (inoculum)	IWK Sludge	1:1	
Non-dairy creamer waste + inoculum	Co-digestion 1	1:2	
Coffee waste + inoculum	Co-digestion 2	1:2	
Mixed food wastes + inoculum	Co-digestion 3	1:2	

Analytical method

Sample characterization

The characterisations of the substrate (food waste) and inoculum (thickened sludge) conducted for this study are the moisture content, Volatile Matter, pH, temperature, Total Solid (TS) and Volatile Solid (VS), chemical oxygen demand (COD), alkalinity and volatile fatty acid (VFA). Thus, all these parameters were measured according to the Standard Methods [30] except for the alkalinity and VFA, which used the HACH method. About 200mL of the sample was

placed in a 500 mL beaker. The pH meter was calibrated first at pH 4, 7 and 10, and then the pH of the samples was measured by using the pH meter (Orion Star A111 pH meter). In order to do that, moisture and TS were determined by drying the samples at 105 °C overnight and for 4 hours at a constant weight [30]. While the previous sample from the moisture content and TS was heated by furnace at 550 °C for 2 hours and 15 minutes to measure the volatile matter and VS. Chemical oxygen demand (COD) was performed by using and preparing the high

range COD standard reagents (200-15000 mg/L), blank, and samples. Each sample was diluted by 1:10 time's dilution, and about 2.0 mL of the sample was filled into the high range COD reagent vial. Thus, the samples were placed into the COD reactor within 2 hours at 150 °C. Then, the readings of the COD were analysed by using the spectrophotometer.

However, for alkalinity, the digital titration cartridge, sulfuric acid 1.600±0.008 N was used (based on the HACH method procedure). About 10mL of the sample volume was titrated with a digital titration cartridge, and the titration was stopped at a pH 4.5. Then, the counter (at the digital titrator) showed the digits for the first endpoint, and the digits were multiplied with the digit multiplier (x10) for samples in the range of 1000-4000 (mg/L as CaCO₃). Thus, the exact volume (mg CaCO₃/L) total alkalinity was recorded. Lastly, for the VFA test method, about 0.5 mL of deionized water and samples (the filtrate or supernatant) were placed separately on a sample cell. An amount 1.5 mL of ethylene glycol was added to each sample cell, and then it was swirled, followed by adding 0.2 mL of 19.2N sulfuric acid. Then, the sample cell was boiled for 3 minutes. The sample cell was immersed into cool water at 25 °C (until the cells feel cold). 0.5 mL of Hydroxylamine hydrochloride solution, 2.0 mL of 4.5N sodium hydroxide standard solution, 10 mL of ferric chloride sulfuric acid solution, and 10 mL of deionized water was added to each sample cell and the cell was inverted to mix. 10 mL of the blank solution and prepared sample were transferred to a clean sample

cell. The sample cell was inserted into the cell holder and the results were shown in mg/L HOAC.

Sample preparation

BMP experimental test

The BMP experimental test was performed in 125 mL serum bottles for the AD process [31] with a working volume of 70% and 30% remaining for the gas production as shown in Figure 1 [32]. Food waste samples such as coffee and non-dairy creamer were used as a substrate, while the IWK sludge (thickened sludge) was an inoculum. The initial pH was adjusted at a range of 6.5-7. After mixing and adding the samples into the serum bottle, the nitrogen gas was purged immediately in the headspace of the bottles for 3 minutes to remove the presence of air, which creates an anaerobic condition in the system [33], prior to sealing the serum bottles. All serum bottles were placed into an incubator at 37 °C, which is the optimum temperature for microbial activities [34] within the retention period of 31 days [35]. Every batch of AD was set up according to a 1:1 ratio for control and a 1:2 ratio of food waste to sludge. The serum bottles were placed into a rotary shaker once a day for 15 minutes to ensure the mixtures were well shaken. All experiments were performed in triplicate. An inoculum filled with water, with no substrate added, was used as a blank assay for the background of the methane yield. The gas sample produced was abstracted from the serum bottle and was then analysed by Gas Chromatography (GC) Agilent 7890A (30m x 32 μ m x 0.25 μ m).

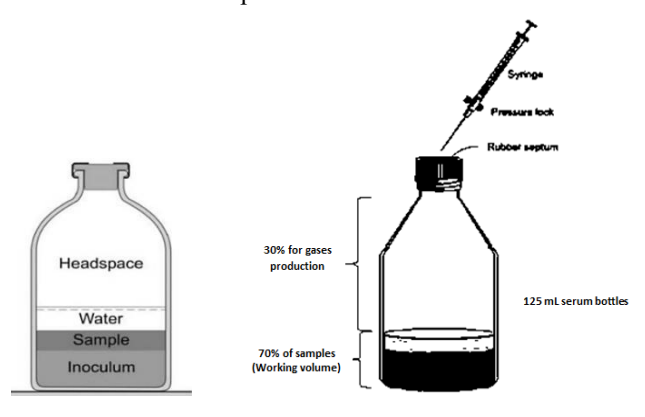


Figure 1. 125 mL of serum bottles set up [31]

Results and Discussion

Sample characterization

The results of the characterization of all samples are summarized in Table 2. The pH for non-dairy creamer waste (NDC), coffee waste, thickened sludge, and mixed food waste with sludge was in the range of slightly neutral to alkaline. The highest pH observed was in coffee waste. During the methanogenesis stages of AD, the methanogenic bacteria are highly sensitive to pH, so the optimum pH for methanogenic bacteria activities is within a range of 6.8-7.2 [36-37], as supported by Lusk [38]. The digester should be maintained at a pH near 7.0 to enhance biogas production, while a low pH would create the accumulation of volatile fatty acids (VFA) which results in the inhibition of the digestion process [39-40]. For a proximate analysis, the information on the moisture content (MC), volatile matter (VM) and others were obtained, which is important to determine the potentiality and suitability of the biomass [41]. From the results in Table 2, the MC for all raw samples is more than 90%, which shows that the water content of each sample was high, which means the raw materials have sufficient MC for anaerobic digestion, as the moisture content of the food waste in the substrate is between 95 - 97% from his study [42]. The volatile matter (VM) for all the samples was in the range of 66-80%. Thus, the fraction of VM for all the samples showed its potential to produce higher biogas production [43-44]. The thickened sludge and mixed food waste produced the higher chemical oxygen demands (COD) with 18790 \pm 96.44, and 12,516 \pm 92.38 mg/L respectively. According to Treagust [45], the COD of coffee wastewater reaches up to 50,000 mg/L. Toxic chemicals such as tannis, alkaloids (caffeine) and polyphenolics can be found in coffee wastewater in small amounts. The COD values

measured the oxygen needed to oxidize all organic material present within substances [46]. The higher the COD values, the higher the potential of substances to produce methane.

The total solids (TS) of the substrates mainly started from < 7%. TS measures the suspended and dissolved solids in water. Coffee waste has the greater TS value, with 7.32%, compared to others. Volatile solids (VS), are described as the organic matter present in the wastewater which is important for AD performances that would enhance the higher production of methane. The VS value for food waste and sludge is at a range of 40-70%. Alkalinity is a very important parameter in the AD process. Alkalinity helps to avoid the failure of the digester and causes the inhibition of methanogenic bacteria activities by preventing the pH drop. The alkalinity of NDC, coffee waste, thickened sludge, and mixed food waste with sludge was 900 ± 1.48 , 794.83 \pm 1.56, 3012.5 \pm 1.75 and 3337.5 \pm 0.89 mg CaCO₃/L. Volatile fatty acid (VFA) is another option to justify the availability of the raw materials used in AD for the production of methane. Like other common factors of AD such as pH, alkalinity, and COD, the VFA gives information on the process status [47]. The hydraulic loading, temperature, and organic loading might affect the concentration of VFA. According to Yu et al. [48], the accumulation of VFA will interrupt the digester buffer capacity, leading to acidification and the failure of system performance by inhibiting the methanogenic bacteria activities. Thus, the VFA readings for all the samples were 6510 \pm 25.39, 2410.33 \pm 27.94, 211 \pm 23.81, and 707.33 \pm 57.66 mg/L which represents the NDC, coffee waste, thickened sludge, and mixed food waste with sludge. There are many studies on the effects of VFA content that might affect AD efficiency.

Parameters	Non-Dairy Creamer waste (NDC)	Coffee waste	Mixed Food waste with sludge	Thickened sludge
pH	7.46 ± 0.01	11.55 ± 0.08	7.07 ± 0.03	7.09 ± 0.03
Moisture Content (%)	99.34 ± 0.02	90.05 ± 0.03	95.53 ± 0.02	96.21 ± 0.01
Volatile Matter (%)	80.03 ± 1.82	73.59 ± 1.18	66.07 ± 2.08	68.97 ± 0.002
Chemical Oxygen Demands (mg/L)	8400 ± 52.92	7843.33 ± 32.15	12516.67 ± 92.38	18790 ± 96.44
Total Solid (%)	0.68 ± 0.18	7.32 ± 0.02	4.49 ± 0.03	4.11 ± 0.06
Volatile Solid (%)	70.84 ± 0.08	44.68 ± 0.002	67.11 ± 0.06	69.18 ± 0.001
Alkalinity (mg CaCO ₃ /L)	900 ± 1.48	794.83 ± 1.56	3337.5 ± 0.89	3012.5 ± 1.75
Volatile Fatty Acids, VFA (mg/L)	6510 ± 25.39	2410.33 ± 27.94	707.33 ± 57.66	211 ± 23.81

BMP experimental test

The BMP experimental test was performed in 125 mL serum bottles for the AD process [31] with a working volume of 70% and 30% remaining for the gas production as shown in Figure 1. Constant BMP experimental results were achieved for all samples after the retention time of 31 days for the anaerobic digestion process took place. The BMP assays are assumed to be finished when the daily production is less than 1% or when the cumulative graph shows a constant trend of methane production which indicates the organic substances are fully degraded. The microorganisms no longer have enough nutrients for digestion purposes. Figure 2 shows the methane production of co-digestion 1, co-digestion 2, codigestion 3, and thickened sludge. The lag phase, which is the time of adaptation for inoculum to a new environment or medium, stopped around 7 days, in this study. According to the curves in Figure 2, it can be observed that the methane production was initially slow, but continuously increased at around 20 days. There was a constant production of methane from day 20 until day 31. Thus, it took almost 20 days for all the methane to be produced from the substrates. It can be seen that the highest methane production was from the thickened sludge which is 18.275 ± 3.3 mL CH₄/gVS, followed by the non-dairy creamer waste with sludge (co-digestion 1) that is 17.865 ± 6.2 mL CH₄/gVS and mixed food waste with sludge (co-digestion 3) at 17.825 ± 0.05 mL CH₄/gVS. While, the lowest methane production is from coffee waste with sludge (co-digestion 2) which is 14.797 ± 0.01 mL CH₄/gVS.

Co-digestion 2 shows the lowest production of methane compared to co-digestions 1 and 3. The coffee waste itself is characterized as lipids, cellulose, lignin-rich biomasses. Lignin (humic acid, tannin) has different macromolecules such as caffeine and polyphenols (melanoidins). Cardenas et al.,2009 [24] cited that, melanoidins consist of ligands (polysaccharides, tannins), which hardly degrade biologically [24]. The cellulose and lignin make the lignocellulosic biomass a great prospect for biogas production through AD. However, it is still considered difficult for it to be degraded and digested. Somehow, the study also highlighted that lower methane potentials of about 0.16 - 0.35 CH₄ m3/kg VS of food waste are richlignocellulosic fractions and have low lipids content, such as fruit and vegetable residues and brewery waste. Moreover, the coffee waste shows that the highest pH, which is 11.55 ± 0.08 , is very alkaline. It will affect biogas productivity. As mentioned before, it has been proved that the optimum pH for methanogenic bacteria activities is within a range of 6.8-7.2, which will give a

significant effect on biogas yield [36-37]. Co-digestion 1 shows that the second-highest methane yield is 17.865 ± 6.2 mL CH₄/gVS. This is because NDC contains high organic matter with about 1.2% minerals, 8.5% protein, 32.5% fat, and the highest percentage is carbohydrates (58%) [18-21]. Protein and carbohydrate-rich substrates are considered to be easily degradable, and lipids have less of a hydrolysis rate [48]. Thus [42, 49], higher methane yields can be achieved from food wastes rich in lipids, such as easily degradable carbohydrates.

The reading of the methane yields for co-digestion 3 (mixed food waste with sludge) is slightly similar to co-digestion 1 which is 17.825 ± 0.05 mL CH₄/gVS. The COD of co-digestion 3, which is 12516.67 ± 92.38 mg/L, is higher compared to co-digestion 1 and co-digestion 2. However, the COD for the thickened sludge, which is 18790 ± 96.44 mg/L, shows the highest yield compared to the others. This shows that

most of the organic matter is contained in both codigestion 3 and the thickened sludge. It can be summarised from Figure 2, that the solely thickened sludge has the potential to produce a higher methane yield without adding any substrate. As we informed, the mixed food waste with sludge consists of coffee and non-dairy creamer waste. Thus, there is the mixing of protein, carbohydrates, and lipids with lignin groups of waste within it. These can act as a reason for the lower methane yield of co-digestion 3 compared to the inoculum which is solely thickened sludge. Therefore, the pre-treatment to the substrate is suggested either by biological, chemical, or thermal treatments to improve the substrate's potential in producing methane. This study has proven different substrates have different characteristics, as can be seen in the proximate analysis of the raw materials. Thus, pre-treatment approaches can be taken to enhance the efficiency of methane generation.

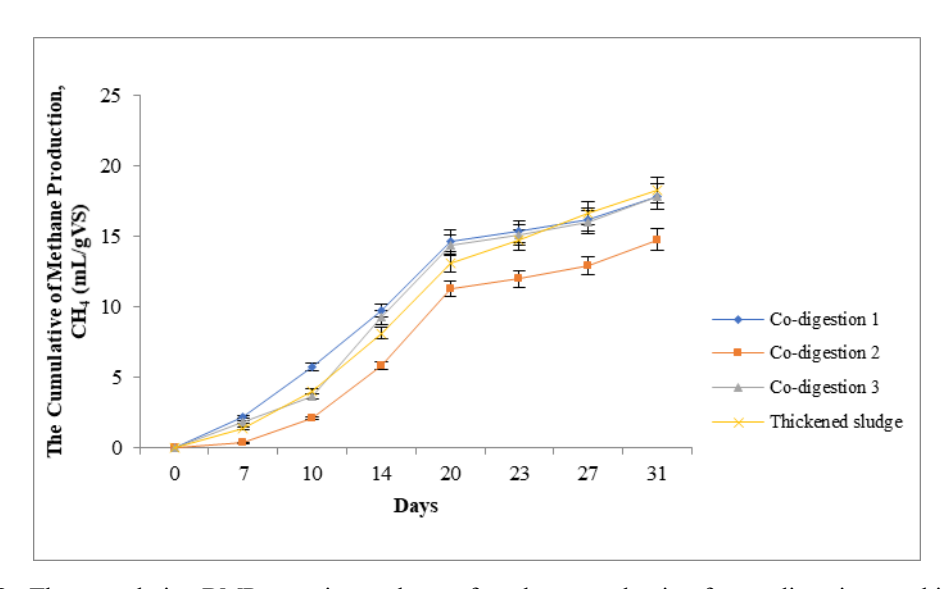


Figure 2. The cumulative BMP experimental test of methane production for co-digestions and inoculum

Conclusion

The NDC and coffee industry play an important role by providing good handling and processing wastewater management in order to achieve and maintain environmental stability. Nevertheless, the BMP experimental test results indicate that there is a potential for a single inoculum (thickened sludge), and

the co-digestion of different wastes such as coffee waste, non-diary creamer waste, and the sample of mixed food waste with sludge would produce a methane yield within the 31 days of the AD process. However, it is also possible to inhibit the AD process if the nutrients are imbalanced. For further observation, an effective and environmentally friendly pre-

treatments process is highly recommended to improve biogas production.

Acknowledgements

The authors would like to thank Universiti Teknologi MARA and IWK for awarding the grant ((100-RMC 5/3/SRP PRI (026/2020)). Special appreciation to the Faculty of Applied Sciences, UiTM, and IWK for providing the facilities to conduct this study.

References

- Werther, J. and Ogada, T. (1999). Sewage sludge combustion. *Progress Energy Combustion*, 25: 55-116
- Appels, I., Baeyens, J., Degrève, J. and Dewil, R. (2008). Principles and potential of the anaerobic digestion of waste-activated sludge. *Progress Energy Combustion*, 34: 755-781.
- 3. Appels, L., Degrève J., Van der Bruggen, B., Van Impe, J., and Dewil, R. (2010). Influence of low temperature thermal pre-treatment on sludge solubilisation, heavy metal release and anaerobic digestion. *Bioresource Technology*, 101: 5743-5748.
- Angelidaki, D., Karakashev, D.J. Batstone, C.M, Plugge, A.J.M. (2011). Stams, biomethanation and its potential. *Methods in Enzymology*, 494: 327-351.
- Ward, A. J., Hobbs, P. J., Holliman, P. J. and Jones, D. L. (2008). Optimization of the anaerobic digestion of agricultural resources. *Bioresource Technology*, 99: 7928-7940.
- 6. Appels, L., Joost, L., Degrève, J., Helsen, L., Lievens, B. and Willems, K. (2011). Anaerobic digestion in global bio-energy production: potential and research challenges. *Renewable Sustainable Energy Reviews*, 15: 4295-4301.
- 7. Nasir, I. M., Tinia, I. M. G. and Rozita, O. (2012). Production of biogas from solid organic wastes through anaerobic digestion: a review. *Applied Microbiology Biotechnology*, 95: 321-329.
- 8. Zhang, J., Wang, Q., Zheng, P. and Wang, Y. (2014). Anaerobic digestion of food waste stabilized by lime mud from paper-making process. *Bioresource Technology*, 170: 270-277.

- Astals, S., Nolla-Ardevol, V. and Mata-Alvarez, J. (2013). Thermophilic co-digestion of pig manure and crude glycerol: process performance and digestate stability. *Journal of Biotechnology*, 166: 97-104.
- Chen, J. H., Lin, C. C. and Wang, K. S. (2013). Potential of methane production by thermophilic anaerobic co digestion of pulp and paper sludge with pig manure. *Journal Biobased Material Bioenergy*, 7: 300-304.
- 11. Giuliano, A., Bolzonella, D., Pavan, P., Cavinato, C. and Cecchi, F. (2013). Co-digestion of livestock effluents, energy crops and agro-waste: Feeding and process optimization in mesophilic and thermophilic conditions. *Bioresource Technology*, 128: 612-618.
- 12. Astals, S., Ariso, M., Galí, A. and Mata-Alvarez, J. (2011). Co-digestion of pig manure and glycerine: experimental and modelling study. *Journal Environmental Management*, 92: 1091-1096.
- Fraizer, R. S., Hamilton, D. and Ndegwa, P. M. (2011). Anaerobic digestion: biogas utilization and cleanup. Oklahoma Cooperative Extension Service.
- 14. Cavinato, C., Fatone, F., Bolzonella, D., Pavan, P. (2010). Thermophilic anaerobic co-digestion of cattle manure with agro-wastes and energy crops: comparison of pilot and full scale experiences. *Bioresource Technology*, 101:545-50.
- 15. Shah, F. A., Mahmood, Q., Rashid, N., Pervez, A., Raja, I. A and Shah, M. M. (2015). Co-digestion, pretreatment and digester design for enhanced methanogenesis. *Renewable Sustainable Energy Reviews*, 42: 627-642.
- 16. Dedin, F., Rosida, Mulyani, T. and Reshita Septalia, L. (2016). A comparative study of nondairy cream based on the type of leguminosae protein source in terms of physico chemical properties and organoleptic. Agriculture and Agricultural Science Procedia, 9: 431-439.
- 17. Huang, X., Lee, E. J. and Ahn, D.U. (2019). Development of non-dairy creamer analogs/mimics for an alternative of infant formula using egg white, yolk, and soy proteins. *Asian-Australasian Journal of Animal Sciences*, 32(6): 881-890.

- 18. Ramesh, C.C, Kilara, A. and Shah, N. P. (2008). Dairy processing and quality assurance. 1st Edition., Wiley Blackwell Publishing, A. John Wiley and Sons Inc., New York.
- 19. Dewi, E. R. S., Legowo, A. M. and Izzati, M. (2016). Absorption of organic compounds by *Saccharomyces cerevisiae* on industrial waste media. *International Journal of Applied Environmental Science*, 11(1): 27-36.
- Dewi, E. R. S., Legowo, A. M., Izzati, M. and Purwanto (2016). Kinetic growth of Saccharomyces cerevisiae in non dairy creamer wastewater medium. *Journal of Environmental* Studies, 2(1): 1-5.
- 21. Triyaswati, D. and Ilmi, M. (2020). Lipase-producing filamentous fungi from non-dairy creamer industrial waste. *Microbiology and Biotechnology Letters*, 48(2): 167–17.
- 22. Navitha, K. and Kousar, H. (2018). A comparative study on the potential of *Aspergillus niger* and *Aspergillus favus* for the treatment of coffee processing effluent. *International Journal Environmental Ecology Family and Urban Studies*, 8(4):17-22.
- Sahana, M., Srikantha, H., Mahesh, S. and Swamy, M.M. (2018). Coffee processing industrial wastewater treatment using batch electrochemical coagulation with SS and Fe electrodes and its combinations recovery and reuse of sludge. *Water Science Technology*, 78: 279-289.
- Cardenas, A., Zayas, T., Morales, U. and Salgado, L. (2009). Electrochemical oxidation of wastewaters from the instant coffee industry using a dimensionally stable RuIrCoOx anode. ECS Transactions, 20(1): 291-299.
- Péerez, T.Z., Geissler, G. and Hernandez, F. (2007). Chemical oxygen demand reduction in coffee wastewater through chemical flocculation and advanced oxidation processes. *Journal Environmental Sciences*, 19: 300-305.
- 26. Remigi, E.U., Buckley, C.A. (2006). Co-digestion of high strength/toxic organic effluents in anaerobic digesters at wastewater treatment works; water research commission: Pretoria, South Africa.
- 27. Da Silva, C., Astals, S., Peces, M., Campos, J. L. and Guerrero, L. (2018). Biochemical methane

- potential (BMP) tests: Reducing test time by early parameter estimation. *Waste Management*, 71: 19-24.
- 28. Raposo, M. M. M., Castro, M. C., Belsley, M. and Fonseca, A. M. C. (2011). Push pull bithiophene azo-chromophores bearing thiazole and benzothiazole acceptor moieties: Synthesis and evaluation of their redox and nonlinear optical properties. *Dyes Pigments*, 91:454-465.
- Yan (2014). Romania to develop national strategy to reduce food waste: Minister. Access from http://news.xinhuanet.com/english/world/2014-04/01/c 133230744.htm [Accessed date 03.09.14]
- APHA (1998). Standard methods of examination of water and wastewater. 20th ed. American Water Works Association, Water Pollution Control Federation, American Public Health Association, Washington DC.
- 31. Angelidaki, I., Alves, M., Bolzonella, D., Borzacconi, L., Campos, J. L., Guwy, A. J. and van Lier, J. B. (2009). Defining the biomethane potential (BMP) of solid organic wastes and energy crops: a proposed protocol for batch assays. *Water Science and Technology*, 59(5): 927-934.
- 32. Ramatsa, I., Sibiya, N. and Huberts, R. (2014). Effect of nutrients addition during anaerobic digestion of potato peels and maize husk. *International Conference on Chemical, Environmental & Metallurgical Engineering,* 2014: pp. 15-16.
- 33. Ebner, J. H., Labatut, R. A., Lodge, J. S., Williamson, A. A. and Trabold, T. A. (2016). Anaerobic co-digestion of commercial food waste and dairy manure: Characterizing biochemical parameters and synergistic effects. Waste Management, 52: 286-294.
- 34. Sibiya, N. T., Edison, M. and Habtom, B. T. (2014). Effect of temperature and pH on the anaerobic digestion of grass silage. *International Conference on Chemical Engineering & Advanced Computational Technologies*, 2014: 198-201.
- 35. Nielfa, A., Cano, R. and Fdz-Polanco, M. (2015). Theoretical methane production generated by the co-digestion of organic fraction municipal solid waste and biological sludge. *Biotechnology Reports*, 5, 14-21.

Nur Anisah et al: ESTIMATION OF METHANE PRODUCTION VIA ANAEROBIC CO-DIGESTION OF FOOD WASTE AND SLUDGE BY BIOCHEMICAL METHANE TEST

- 36. Turovskiy, I. S. and Mathai, P.K. (2006). Wastewater sludge processing. New York: Wiley
- 37. Cioabla, A. E., Ionel, I., Dumitrel, G.-A. and Popescu, F. (2012). Comparative study on factors affecting anaerobic digestion of agricultural vegetal residues. *Biotechnology for Biofuels*, 5(1): 39.
- Lusk, P. (1999). Methane recovery from animal manures the current opportunities casebook. National Renewable Energy Laboratory, NREL/SR-580-25145.
- 39. Parkin, G. F. and Owen, W. F. (1986). Fundamentals of anaerobic digestion of wastewater sludges. *Journal of Environmental Engineering*, 112: 867-920.
- Pearse, L.F., Heittiaratchi, J.P. and Kumar, S. (2018). Towards developing a representative biochemical methane potential (BMP) assay for landfilled municipal solid waste-a review. *Bioresource Technology*, 254: 312-324.
- 41. Brito, J. O., Barrichello, L. E. G. and Trevisan, J. F. (1978). Condicoes climaticas e suas influencias sobre a producao de resinas de pinheiros tropicais, Piracicaba, 16: 37-44
- 42. Labatut, R., Angenent, L.T. and Scott, N., (2011). Biochemical methane potential and biodegradability of complex organic substrates. *Bioresource Technology*, 102(3): 2255-2264.
- 43. Vassilev, S., Baxter, D., Andersen, L. and Vassileva, C. (2010). An overview of the chemical composition of biomass. *Fuel*, 89: 913-933.
- 44. Demiral, I. and Ayan, E.A. (2011). Pyrolysis of grape bagasse: Effect of pyrolysis conditions on the product yields and characterization of the liquid product. *Bioresource Technology*, 102: 3946-3951.
- Treagust, J. (1994). Coffee waste water treatment.
 B.Sc. (Hons.) dissertation. Cranfield, United Kingdom: Cranfield University.
- 46. Watershed Protection Plan Development Guidebook (2015). Description of commonly considered water quality constituents [Access date 10 October 2015].
- 47. Boe, K., Batstone, D. J. and Angelidaki, I. (2007). An innovative online VFA monitoring system for the anerobic process, based on headspace gas

- chromatography. *Biotechnology and Bioengineering*, 96(4): 712-721.
- 48. Mata-Alvarez, J., Dosta, J., Romero-Güiza, M., Fonoll, X., Pecesa, M. and Astals, S., (2014). A critical review on anaerobic co-digestion achievements between 2010 and 2013. *Renewable Sustainable Energy Review*, 36: 412-427.
- 49. Meng, Y., Li, S., Yuan, H., Zou, D., Liu, Y., Zhu, B., Chufo, A., Jaffar, M. and Li, X., (2015). Evaluating biomethane production from anaerobic mono- and co-digestion of food waste and floatable oil (FO) skimmed from food waste. *Bioresource Technology*, 185: 7-13.

Malaysian Journal of Analytical Sciences (MJAS)



Published by Malaysian Analytical Sciences Society

POTENTIAL APPLICATIONS OF CONDUCTING POLYMER/TUNGSTEN DISULFIDE COMPOSITES: A MINI REVIEW

(Aplikasi Potensi Konduktif Polimer/ Tungsten Disulfida komposit: Ulasan Mini)

Siti Nor Atika Baharin¹, Nur Solehah Samsudin¹, Nur Farahin Suhaimi¹, Kavirajaa Pandian Sambasevam^{1,2*}

¹Advanced Material for Environmental Remediation (AMER) Research Group, Faculty of Applied Sciences, Universiti Teknologi MARA, Cawangan Negeri Sembilan, Kampus Kuala Pilah, 72000 Kuala Pilah, Malaysia ²Electrochemical Material and Sensor (EMaS) Group, Universiti Teknologi MARA,40450 Shah Alam, Selangor, Malaysia

*Corresponding author: kavirajaa@live.com

Received: 22 July 2021; Accepted: 4 January 2022; Published: 28 April 2022

Abstract

Recent works on many types of synergistic conducting polymers/tungsten disulfide (CP/WS₂) composites are thoroughly covered in this mini review. Data were gathered from over 60 scientific research papers from all over the world and published within the last decade (2012-2021). CPs are as versatile materials because of their remarkable advantages over other traditional materials. These advantages include wide and adjustable electrical conductivity, high mechanical flexibility, high capacitance, and low manufacturing cost. However, CPs do possess limitations in terms of stability, processability, and mechanical strength. As a result, CPs are frequently integrated with inorganic fillers such as metal sulfide. WS₂ has garnered significant attention among metal sulfides when combined with CPs, where it improves chemical/thermal stability and provide good processability to the CPs/WS₂ composites. Hydrothermal procedures and solvothermal techniques were all mentioned and discussed as relevant synthesis methods. As a result, hybridized CP/WS₂ composites have shown prospects in terms of functionality and applicability. Sensors, energy storage, and electrical applications are among the areas that experienced enhanced performance by using CP/WS₂. A brief discussion of the mechanisms underlying these successful applications is also included. This mini review is meant to provide readers with information on CP/WS₂ and, as a result, instill interest in new research topics.

Keywords: conducting polymer, tungsten disulfide, sensors, supercapacitors, photocatalyst

Abstrak

Terdapat banyak jenis komposit yang terdiri daripada konduktif polimer/tungsten disulfida (CP/WS₂) telah dibincangkan di dalam ulasan mini ini. Data yang telah dikumpulkan telah diperolehi dari lebih 60 penyelidikan saintifik dari seluruh dunia selama sepuluh tahun sebelumnya. CP merupakan bahan kimia yang serba boleh kerana mempunyai kelebihan yang luar biasa berbanding bahan tradisional yang lain, termasuk kekonduksian elektrik yang luas dan boleh laras, fleksibiliti mekanikal yang tiggi, kapasitans yang tinggi dan kos pembuatan yang rendah. Walau bagaimanapun, CPs mempunyai batasan dari segi kestabilan, kebolehkerjaan dan kekuatan mekanikal. Oleh itu, CP sering digunakan bersama dengan pengisi bukan organik seperti sulfida logam. Di antara sulfida logam, WS₂ telah mendapat perhatian yang signifikan jika digabungkan dengan CP kerana dapat meningkatkan kestabilan kimia/haba serta menambahbaik ciri-ciri pemprosesan dalam komposit CP/ WS₂. Antara kaedah sintesis yang relevan yang telah dibincangkan dalam kajian mini ini adalah proses hidrotermal dan teknik solvotermal.

Hasilnya, komposit CP/WS₂ yang dihibridisasi telah menunjukkan penningkatan dari segi fungsi dan kebolehgunaan. Penggunaan CP/WS₂ dalam bidang sensor, penyimpanan tenaga dan aplikasi elektrik dapat meningkatkan keupayaan mereka. Perbincangan ringkas mengenai mekanisme aplikasi yang berjaya turut disertakan. Akhir sekali, tujuan kajian mini ini adalah untuk memberi maklumat kepada pembaca mengenai CP/WS₂ dan menarik minat mereka untuk menghasilkan suatu kajian penyelidikan yang baharu.

Kata kunci: konduktif polimer, tungsten disulfida, pengesan, superkapasitor, fotomangkin

Introduction

Conducting polymers (CPs) are a unique class of materials with a π -conjugated system that corresponds to its electrical conductivity. The success of CPs as synthetic metals was discovered in the late seventies by Hideki Shirakawa and his team by accidental addition of excess halides in the reaction medium of polyacetylene. Since then, CPs were widely studied upon in terms of their significant properties such as large conducting mechanisms, electrical properties, adjustable electrochemical properties, and easy processing. Currently, the CPs family consists of polyacetylene (PA), polyaniline (PANI), polypyrrole (PPy), poly(phenylene vinylene) (PPV), poly(3,4ethylene dioxythiophene) (PEDOT), polyfuran (PF), and other polythiophenes (PTh) and its' derivatives [1]. Due to their fascinating properties, CPs have received widespread attention from both the industrial community and researchers, especially in the study of supercapacitors, sensors, fuel cells, and photocatalysis for their wide range of applications. Figure 1 summarizes far-famed CPs that correspond to their applications.

Although CPs have become the interest of many communities, they still possess a few drawbacks such as high recycling instability [2], high defect sites from poor temperature tolerance [3], slow exchange of ions [4], and inconsistent solubility [5]. Therefore, enormous effort has been undertaken to incorporate various types of filler such as carbon materials, polymers and inorganic compounds into the CPs' matrix to enhance its properties. Particularly, in recent decades, many attempts were made to produce CPsinorganic hybrid materials, where the integration of inorganic fillers into CPs may enhance the stiffness, toughness, and dimension stability of the resulting hybrid materials [6]. Among the inorganic fillers,

transition metal dichalcogenides (TMDC) were the most favored due to considerable bandgaps in the range of 1-2eV, which is applicable for sensing, nanoelectronics, and photonics [7]. Considering metal sulfides are a class of TMDC, it is an excellent candidate to improve the CPs' properties in terms of conductivity, thermal stability [8], capacitance activity, and cyclic stability[9]. This is because by supplying electrons or withdrawing electrons to or from the transition state of reaction, the transition metal retains a good source of electrons from the partially filled dsubshell. CPs eventually have more free-moving electrons obtained from metal sulfide and therefore exhibits better electrical conductivity. In a study reported by Ramesan 2013, it was found that when PPy and cadmium sulfide (CdS) were combined, the nanocomposite's alternating current conductivity was greater than pristine PPy. Meanwhile, the highest generated direct current electrical conductivity was obtained when a higher amount of CdS were added [10].

In addition, metal sulfide is outstanding because it generates excellent characteristics due to its twodimensional (2D) structure that exhibits tunable band gaps in the visible to near-infrared spectrum [11] and exceptional physicochemical properties [12]. Among the metal sulfides, tungsten disulfide (WS₂) possesses considerable advantages too, which is comparable to other existing metal sulfides. Tungsten is a d-block element from period 6 and sulfur is a p-block element from period 3. Interestingly, the band-gap of WS₂ changed from an indirect band-gap of 1.4 eV to a direct band-gap of 20 eV when a 2D material was isolated by a simple mechanical exfoliation technique from the bulk material. Due to the wide bandgap, WS₂ is seen as an interesting material for many areas of application, especially in the industry of solid lubricant, lithium-ion battery, catalytic degradation, and electronic devices. By considering the pros and cons of both CPs and WS₂, numerous synthetic approaches have been developed with different morphologies, structures, and properties to satisfy the demands of different applications. WS₂ has been investigated with several types of CPs such as PANI, PPy and PEDOT. In the past decade, CP/ WS₂ composites have been found to have potential in several applications such as in supercapacitors,

electronic components and sensors and actuators. However, a simple search in the SCOPUS database with a combined search string specifically on CPs and WS_2 only resulted in less than 50 papers, indicating that more extensive research is needed to cultivate and promote the CP/WS $_2$ binary composites. Therefore, this mini-review is an attempt to scrutinize the potential applications of CP/WS $_2$ composites and its benefits.

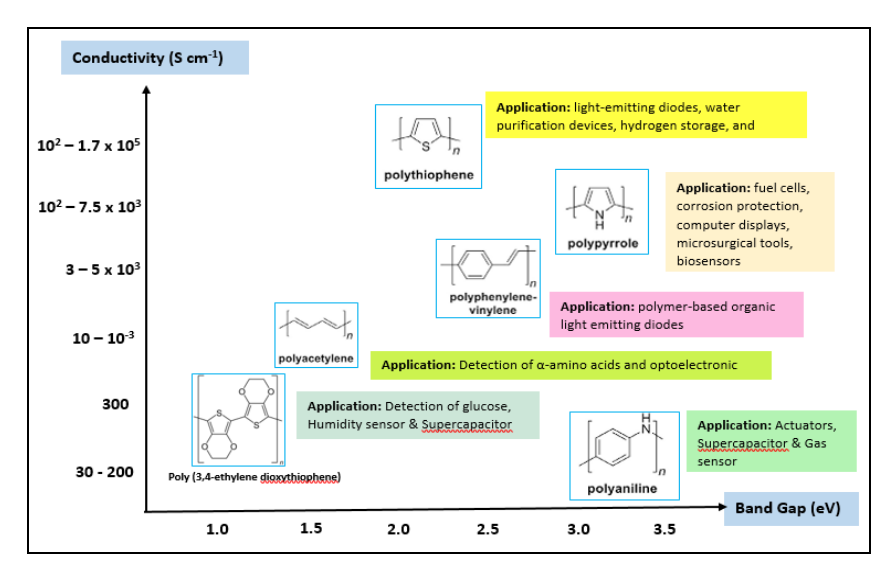


Figure 1. Various types of CPs assigned to a specific range of conductivity and band gap including their existing applications

Brief history of tungsten disulfide composites

Tungsten disulfide (WS₂) or also known as tungstenite is an inorganic compound which is composed of tungsten and sulfur with a molar mass of 247.98 g/mol. In the past, WS₂ has shown great potential for a high-temperature solid lubricant used in space as jotted in the National Aeronautics and Space Administration (NASA) record (History of Tungsten Disulfide (WS₂), 2018). The idea was initiated due to inefficient spacecraft mechanisms which cannot be inspected or maintained after launched. It was discovered that some parts of the spacecraft were not well-lubricated. On top of that, any satellite components that are subject to sliding wear must be properly lubricated to withstand the requirements of the mission. In that sense, WS₂ became the promising candidate due to its anti-friction

properties that attributed by its crystal structure, which consists of hexagonal close-packed atomic tungsten layers sandwiched between two hexagonally closed atomic layers of sulfur. Weak Van der Waals forces that hold two adjacent sulfur layers allow them to slide for lubrication purposes [13]. Progressively, the success of WS2 as a layered structure has expanded due to their interesting anisotropic behavior, great diversity in other physical properties and its advantages for various applications when added to base oil under specific laboratory test conditions. The composition of WS₂ with folded triple-layer of S-W-S sheets enables the atoms within each triple layer to be held by potential carbon-carbon bond. Each bond is clenched by weak Van der Waals interactions. This anisotropic nature of WS2 therefore opens an opportunity to be

incorporated into different types of polymer matrices, resulting in high strength moduli and a good ability for shock absorption [14].

Synthesis method of WS₂

The synthesis of WS₂ composite usually involves multiple steps. Pristine WS₂ must be prepared prior to the integration with a specific CP. Then, WS₂ can be utilised to synthesise CP/WS₂ composite commonly via chemical oxidative method [15]. Every synthetic route for metal disulfide (MS₂) synthesis offers different outputs. The synthesised material can be tailored in order to develop various functions and applications for the metal sulfide [16]. For WS₂, every type of synthetic methods conducted possess several pros and cons depending on the processes involved. Hydrothermal and solvothermal syntheses are a few of the existing methods to synthesise WS₂ that have different synthetic route and its own significance.

Hydrothermal synthesis

Hydrothermal synthesis has been reported as an appealing method due to its simple procedure and productivity. Due to its advantages of low temperature, large-scale development and simple synthesis, it is an environmentally friendly technique for the preparation of various nanostructures [17]. In addition, hydrothermal method leads to the development of nanoscale products under supercritical pressure, which is cumbersome via classical routes. In this method, sodium thiosulfate and hydroxylamine sulfate are the important chemical ingredients. Hydroxylamine sulfate not only acts as the source of sulfur, but is also utilised as a strong acid to establish an acidic state for the nanoparticles that may form. Moreover, WS2 can also be produced with a chrysanthemum-like nanostructure via hydrothermal synthesis. According to Tang et al. [18], the addition of pluronic and cetyltrimethyl ammonium bromide (CTAB) significantly affect the growth and final morphology of the WS2. The resulted self assembled chrysanthemum-like nanostructures were grown prior to a fast nucleation of amorphous primary particles and slow aggregation of nanosheets [19]. Prominently, this method is interesting since large-scale metal sulfide composite can be achieved via this technique. However, this method is limited to

aqueous precursors which might restrict the control over certain optimisations like temperature, reaction time, and type of solvent.

Solvothermal synthesis

Typically, solvothermal synthesis is a technique for preparing a variety of materials such as ceramics, polymers, metals and semiconductors. It might imitate the hydrothermal synthesis method but what differentiate both of them is the precursor type. Both hydrothermal and solvothermal synthesis use aqueous and non-aqueous precursor solution, respectively [20]. This method may adjust certain experimental parameters including temperature of reaction, time of reaction, type of solvent, type of surfactant, and type of precursor to ensure precise control of the size, distribution of shape and crystallinity of the nanostructure product. Focusing on WS2, one step exfoliation-restacking technique is invalid to be employed even though WS2 has similar chemical structure with MoS₂. The reason why this restacking technique makes the WS2 layered nanocomposites difficult to obtain is because the precursor does not have optimum concentration. Hence, the solvothermal method is used to increase the amount of lithium introduced in WS2 in order to improve processability [21].

Applications of conducting polymer/tungsten disulfide

The electrical properties of polymeric materials have piqued researchers' attention in the field of solid-state electronics. Generally, CPs by nature reveal poor electrical conductivity due to the absence of free moving electrons to enable the conduction process. However, when the CPs undergoes doping treatment with oxidizing or reducing agent, they can exhibit reasonable conductivity [22]. As a result of the presence of both the polymer and the filler material, a range of inorganic materials may be integrated into CPs with improved characteristics. Metal sulfide appears to be a superior alternative for making hybrid CP composites than metal oxide and other carbon derivatives. Metal sulfide is not only inexpensive and abundant in nature, but it also performs well in faradic redox reactions, making it useful in the fuel cell

business. When it comes to the WS₂ nanostructure, the weak Van der Waals interactions indicate that it is anisotropic, and it is well known for its high strength moduli and shock absorption capabilities [14]. However, WS₂ has a drawback in the form of short cycle stability, which causes the capacitance to rapidly degrade. As a result, including WS₂ into CP matrices might be a promising method to improve the stability and combine favourable physical properties of both organic and metallic components while retaining capacitance in a single composition [23].

Polyaniline/Tungsten Disulfide (PANI/WS2)

Since PANI is one of the most promising CP with enhanced properties, researchers actively synthesize and analyze the PANI composites in numerous applications. A lot of papers were published on the preparation of conducting composites of PANI, such as PANI/TiO₂, PANI/ZrO₂, PANI/Fe₃O₄, PANI/MoO₃, PANI/zeolite, PANI/WO₃, PANI/MnO₂ and PANI/WS₂ from metal sulfide groups [24]-[31]. Despite many papers have been published regarding PANI composites, PANI/WS2 are still lagging in terms of research and have limited source of information. Only a few reports were found using PANI/WS2 in the fabrication of micro supercapacitor microrobots and its incorporation with chlorin e6 (Ce6) to give a triplesynergistic strategy in tumor treatment [32]. In a study by Stejskal et al. [33] PANI/WS2 was fabricated through in situ polymerisation. The flake-like semiconducting particles of WS₂ were coated with a thin film of PANI during the oxidation of aniline. In addition, scanning electron microscopy (SEM) analysis of PANI/WS2 revealed a porous nature and seems to be robust, where the WS₂ particles interlinked the PANI nanorods. This is probably due to the fact that, WS₂ naturally exists as a stack layered material, where the incorporation of PANI provides additional strength to the whole structure.

Humidity sensors

Humidity is another critical parameter that significantly affects the operation of electronic components in the determination of geographical distribution and the maximum intensity of precipitation, biosphere and surface hydrology. Measurements of humidity or

moisture level in the human body could be beneficial in evaluating a variety of physiological and metabolic conditions. Since low humidity has adverse effects on human health, the existence of humidity sensor is important in interpreting the growth, repair and aging mechanisms to regulate internal body conditions [34]. Manjunatha et al. [31] reported on the preparation of PANI/WS₂ composite by in situ polymerisation technique and demonstrated an excellent humidity sensing compare to pure WS2 as reported by Guo et al [35]. Typically, PANI/WS₂ exhibits enhanced humidity sensing properties due to its porous nature. The porous nature is of paramount interest for the adsorption of water molecules, which is also an important aspect in developing humidity sensors. Consequently, the agglomerated flower-like structure with highly microporous nature of PANI/WS2 is assumed to have an important role in the humidity sensing behaviour of the composite. Typically, the water vapour could find its way through micropores of PANI/WS2 to react and give response in the sensing mechanism. Figure 2 shows a uniform distribution of WS2 micro-sized sheets in the matrix of PANI from the observation of a field emission scanning electron microscope (FESEM) micrograph of the composite with magnification 12kx.

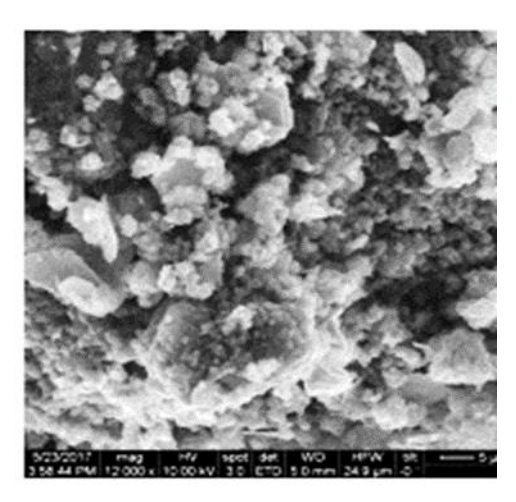


Figure 2. Field emission scanning electron micrograph of the PANI/WS₂ composite with 12000x magnification [31]

Ammonia gas sensor

The application of gas sensors in industries of environmental analysis, automotive, medical applications and indoor air quality controls have been developed for more than a decade ago due to the enforcement of the Occupational Safety and Health (OSHA) regulations against volatile hazardous gases [36]. Among the hazardous gases, ammonia (NH₃) has received major attention in the field of gas sensors due to its abundance in chemicals manufacturing industries and applied in diverse areas around the world [37]. Hybrid PANI/WS₂ composite promises a synergetic effect for NH₃ gas detection. The mechanism of NH₃ gas sensing by PANI/WS2 can be proposed based on electron donation concept. Complementary to each other, PANI is a p-type conducting polymer with a linear conjugation of π -electronic system, while WS₂ is an n-type semiconductor whose band gap increases with the decrease in the number of stacked layers. The fact that NH₃ could donate electrons to the p-type PANI resulted in a decrease in the hole-transport concentration and next, deprotonation reaction caused the resistance of PANI to incline. Consequently, PANI/WS2 showed high selectivity towards NH3 gas with long term stability and repeatability [38]. The

magnificent sensing capability of PANI/WS₂ sensor in humid environments and at room temperature makes it a suitable candidate for environmental monitoring devices [39].

Supercapacitor

Self-propelled supercapacitor device based on WS₂ nanoparticles-polyaniline/platinum (PANI/Pt) microrobot design opened a new insight that it can act as an on-demand reconfigurable device owing to its superior capacitance of 14000 µFcm⁻² with energy density and power density of 0.07 mWhm⁻² and 120 mWm⁻², respectively [40]. Due to great capacitance result exerted by this microbot, it is expected to be proficient for on-demand construction and adjustment of the electronic devices. The fabrication of this autonomous WS₂NPs-PANI/Pt self-propelled microsupercapacitor for on-site electronics delivery in the circuit involved an electrodeposition process using cyclopore polycarbonate membrane as a template. WS₂NPs-PANI/Pt micromotors (u-motor) fabrication process is shown in Figure 3.

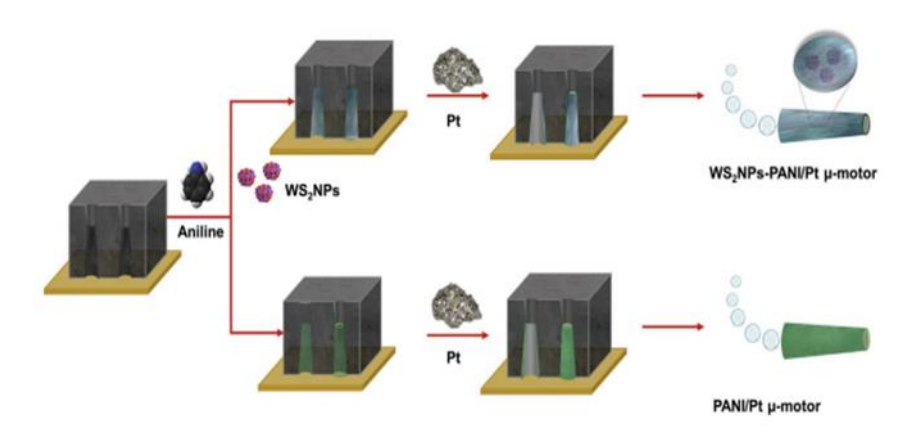


Figure 3. Schematic representation of WS₂NPs-PANI/Pt μ-motor fabrication process. Reproduced with permission from ACS [40].

Polypyrrole/Tungsten Disulfide (PPy/WS₂)

The integration between PPy and WS₂ nanocomposites exhibited a conductivity higher than the pristine WS2 at ambient temperature [37]. In addition, WS₂ coated with PPy has benefit of wettability. In simple words, wettability is the ability of surface to reduce the surface tension of the liquid that is in contact with it and allow the liquid to spread over the surface and wet [41]. Wettability is important in adhesion as it provides quality for adhesive bonding and coating. Besides, synthesis of PPy/WS2 can be steered by in-situ oxidative polymerization. The oxidation of pyrrole yields water-insoluble pyrrole oligomers that is further adsorbed on an immersed surfaces and continually grow the PPy chains. Typically, the process started with adsorption where the PPy patches are reinforced into chain colonies and are then grown slowly, resulting in uniform brush-like coating on the entire film [42] to the extent whenever the substance are still available, additional PPy globules will continuously be produced. The PPy globules are produced on hydrophilic PPy films or in surrounding aqueous phase and the globules stick to the film surface. In this context, the deposition of CPs are hydrophilic or hydrophobic surface dependent [43]. The product therefore generally consists of two phases which involve a thin polymer film deposited on the substrate and globular PPy. These two phases were demonstrated by the morphology analysis where, at a composition of 23.7 wt.% of PPy content, WS2 flakes readily become coated with PPy. Furthermore, the appearance of additional PPy globules was due to the increment of the PPy content up to 38.3%. The idea of uniform PPy coating on WS₂ is due to the different hydrophobicity of pyrrole oligomers in conjunction to the fact that WS2 is mildly hydrophilic [41].

Hydrogen evolution reaction

Hydrogen evolution reaction (HER) is basically a water splitting technology which found importance in energy storage based on hydrogen evolution. The combination of PPy and WS₂ seems to be a promising composite in the HER catalytic process due to the enhanced conductivity and wettable properties of this composite.

Stejskal and co-workers [41] prepared PPy/WS₂ in various ratio of pyrrole monomer. The study revealed that excess of PPy globules would block the active edges of WS₂ in HER, despite of improved conductivity. However, a significant result was attained upon physical mixing of the PPy and WS₂ as a result of proton abundancy which was responsible for capacitive charging process in HER.

In Vivo drug release

Traditional drug delivery medications, such as oral administration and injections, tend to deliver greater drug concentrations than necessary, which may cause side effects in patients. Therefore, externally controlled drug delivery systems are of special relevance for study because they enable for drug delivery control from outside the body [44]-[46]. Particular interest on PPy functionalized WS₂ was paid by Hsiao and co-workers [47] since the composite possesses excellent synergistic properties to fine-tune the electrical properties to enable an electrically active nanocarrier system for an effective drug delivery to the target organ. The study revealed that a large quantity of anticancer drug, such as 5-fluorouracil (5-FC), be effectively delivered (90%) in the presence of electrical stimulation. They also successfully reported could that no toxic effect was evident in the electrical stimulation of PPy/WS₂.

Poly (3,4-ethylenedioxythiophene: Poly (Styrene Sulfonate)/Tungsten Disulfide (PEDOT: PSS/WS₂)

Poly(3,4-ethylenedioxythiophene): poly(styrene sulfonate)/tungsten disulfide, PEDOT:PSS/WS₂ is one of the ternary CPs composites as a potential material in thermoelectric applications due to its various benefits such as adjustable electrical conductivity and solution processability [49, 50]. PSS is a polymer surfactant, which enhances the dispersion and stability of PEDOT in water and other solvents [50]. PEDOT:PSS is well-known in the thermoelectric field for its excellent mechanical flexibility, low thermal conductivity, water solubility and processability [51]. As PEDOT:PSS went through a small treatment via direct vacuum filtration, the composite has been enhanced with high

electrical conductivity. Since then, research related with incorporation of inorganic nanostructures with PEDOT:PSS to enhance the thermoelectric performances has been expanding [49].

The introduction of PEDOT:PSS into WS2 resulted in a composite that facilitated the charge carriers to move along the polymer chains, which effectively improved the charge transfer within the composite [52]. The fabrication technique was utilized due to the poor conductivity of WS2, where the lateral transfer of electrons along the lamella structure of the WS2 nanostructures were blocked, making the electron transfer inefficient. PEDOT:PSS also acts as spacers to avoid restacking of WS2 and provide plenty of channels to enhance the charge transport. Moreover, synthesized the PEDOT:PSS/WS2 thin film synthesized may easily be peeled off and transferred to another substrate, resulting in more potential applications. Therefore, stronger performing thermoelectric composite such as PEDOT:PSS/WS2 carries better properties rather than the pristine PEDOT:PSS and pristine WS₂ [52].

Schottky diodes

In a study by Ortiz et al. [53], PEDOT:PSS/WS₂ Schottky nano-diode was constructed through heterojunction of a hole transporting CP with an n-type semiconductor. In order to fabricate this composite, individual PEDOT:PSS was synthesized electrospinning while the mono- and multi-layer WS2 flakes were synthesized via chemical vapor deposition (CVD). These combination methods are developed from a previous research that implemented electrochemical polymerization techniques [54]. The previous experiment demonstrated poor device operation due to undesirable chemical reactions with the inorganic semiconductor. In terms of performance, the equations in standard thermionic emission model of a Schottky junction were used and from there it exerts an ideality parameter of 1.9 and a barrier height of 0.58 eV. Far from being ideal, the high ideality parameter measured value for this device may be contributed by the recombination of hole and electrons at the interface or the presence of interface states at the CP/WS2 interface. Even so, upon large surface to volume ratio of the film, semiconductor carrier density is tunable via

a back-gate bias and the reversible change of barrier height makes it potentially useful as a sensor [53].

Supercapacitor

In the organic semiconducting family, PEDOT has triggered worldwide interest owing to its development as pioneer for electronically conducting polymers (ECPs). However, the fact that PEDOT has outstanding electrochemical properties is still insufficient for it to meet the needs of practical applications. To overcome the problem, WS2 has been incorporated into PEDOT to accelerate its applications in the fields of various devices, especially for the supercapacitors [55]. Nevertheless. to excel as high-performance supercapacitors, PEDOT/WS2 may need to form a ternary composite with another compound. The combination of the three components in nanoscale creates a synergistic effect and higher potential in the faradaic processes Xia et al. [34]. For instance, a recent study in the electrical field by Liang et al. [56]reported that the use of poly(3,4-ethyleenedioxythiophene)poly(ethylene glycol)-tungsten disulfide (PEDOT-PEG-WS₂) as ternary compounds exhibited good performance as a supercapacitor. PEDOT-PEG-WS₂ nanocomposite was prepared via electrochemical selfassembly of PEDOT and WS2 nanosheets in the presence of PEG.

This ternary composite has resulted in a unique threedimension interpenetrating porous network (3D-IPN) in nano-/micro scale. The addition of 5% PEG surfactant has effectively stabilized the WS2 nanosheets that coexist with additional electrolytes. 3D-IPN materials has gained attention for its high-volume ions transport system and utilization of limited space that allows enhancement of energy storage capacity. Moreover, the 3D-IPN confined to metal-organic framework helps to build and verify automotive hydrogen storage systems that will allow hydrogenfueled vehicle platforms to meet customer specifications. The optimization of PEDOT-PEG-WS₂ nanocomposite has been developed from the WS2 contents and CV cycles adjustment. Based on their CV area and specific capacity of each sample, it was found that the as-prepared PEDOT-PEG-WS2 nanocomposite has reached maximum specific capacity by adding 2.7% WS₂ in solution and 50 electrodeposition cycles.

Other than that, electrochemical properties of the engineered 3D IPN-PEDOT-PEG-WS₂ nanocomposite were recognized and compared with PEDOT-PEG [56].

Organic photovoltaic cells

OPV is an electrical device that converts light directly into electricity by photovoltaic cells, which combine physical and chemical phenomenon. The great characteristics such as low cost, light weight, flexible and scalability through roll-to-roll coating processes make OPV is great for green technology. The performance of OPV can be improved by a few ways including device structure optimization, conversion of light to suitable absorbance wavelengths and synthesis of new short band-gap polymers. PEDOT:PSS is familiar in hole-extraction layers (HEL) which works as buffer layers between the active layer and electrode. Recently, researchers have discovered that MoS₂ based OPVs utilizing PEDOT:PSS HEL, possesses better performance due to increased hole extraction and light absorption [57]. This finding has opened a venue for WS₂ to replace traditional MoS₂ as HEL in OPVs since it is structurally similar to MoS₂ with some expectation to enhance device performance equally or better. Surprisingly, a study by Lin and co-workers [58] exhibited excellent results of the OPV device performance through the implementation of an WS2

HEL layer combined with the indium tin oxide (ITO) anode, PEDOT:PSS layer, poly (3-hexylthiophene) (P3HT) and phenyl-C61-butyric acid methyl ester (PCBM) [58]. In this study, WS₂ nanosheets were obtained by a simple ultra-sonication method and were uniformly spin coated on a ITO/glass as visualized in Figures 4 (a) and (b). Next, the hole-extraction efficiency of WS₂ was amplified by a UV-ozone treatment which at the same time empowered the OPV device.

In another study by Le and co-workers [59], the effect of WS2 upon UVO treatment was investigated by introducing WS2 into CP composites such as PEDOT:PSS, P3HT:PCBM and lithium fluoride/aluminum (LiF/Al) [59]. As expected, the change in work function of WS2 due to UVO treatment enhanced its hole-extraction properties. The power conversion efficiency (PCE) of the OPV with WS₂/PEDOT:PSS was 3.07%, which is superior compared to the OPV with only PEDOT:PSS layer of 2.87%. Therefore, the study agreed on a deduction that high PCE resulted from the efficiency of charge separation and collection processes WS₂/PEDOT:PSS.

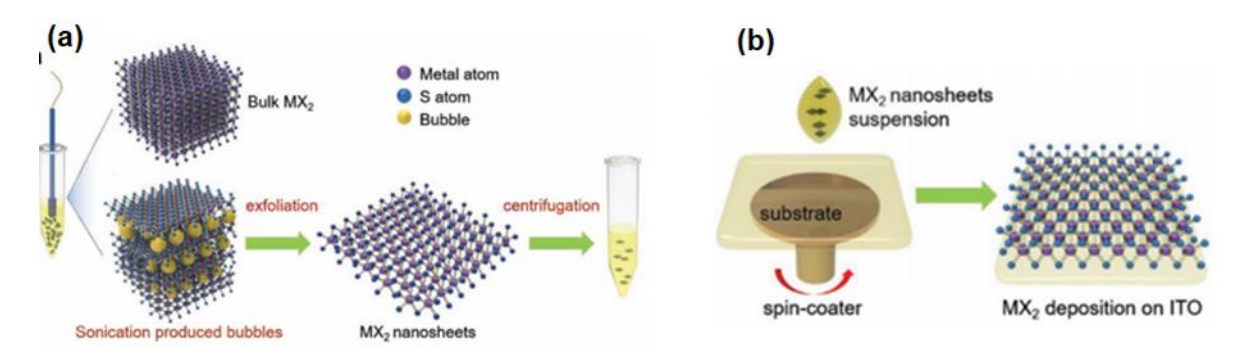


Figure 4. (a) Sonication assisted liquid exfoliation to prepare WS₂ and (b) deposition of WS₂ or MoS₂ onto ITO substrate via spin coating technique

Polyfluorene/ Tungsten Disulfide (PFO/ WS₂)

Polyfluorene (PFO) is an attractive material for display applications such as light source in organic light

emitting diodes (LED) due to efficient blue light emission, good solubility and high mobility. Light absorption of PFO in the UV region falls approximately at 380 nm. Beyond the desired blue emission at 425 nm, a green component close to 530 nm can either be attributed to intermolecular interactions or oxidation-induced keto defects that cause aggregates to form [60]. According to Luccio et al. [61], even though the energy emission is low, the removal of the inter-chain interaction enhanced the color purity and luminescence stability of PFO/WS₂. Considering WS₂, both fullerene-like nanoparticles (F-WS₂-NP) and nanotube (WS₂-NT) structures work differently. F-WS₂ is more into lubricating fluids, self-lubricating coatings and medical devices. Meanwhile, WS₂-NT is great at improving the mechanical properties of CP composites [61]. With respect to that, the addition of inorganic nanomaterial like WS₂

ensures color emission tunability. Not to mention, the exhibited optical and electrical properties of PFO/WS₂ depends on the number of WS₂ layer present [61]. The surface morphology of PFO has a smooth appearance at a glance as shown in Figure 5 (a). Meanwhile, SEM images of PFO/WS₂ nanocomposite films showed high dispersion of WS₂ nanotubes upon various WS₂ concentration from 10 wt.% to 50 wt.% as displayed in Figure 5 (b–d). It is observed that the dispersion of the WS₂-NT is quite homogeneous for all the concentrations investigated, even though some nanotube agglomerates remain. This finding suggests a further study is needed either on the purification of nanotubes or the preparation of the blend.

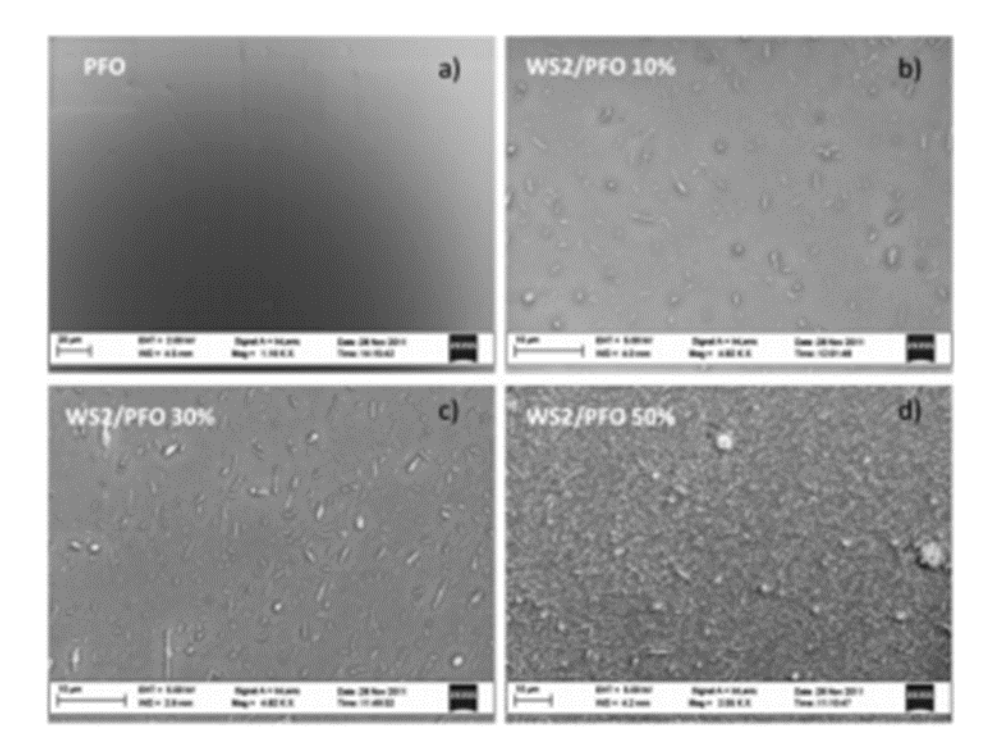


Figure 5. Scanning electron microscope images of a) bare PFO, and PFO/WS₂ nanocomposites at b) 10 wt.% c) 30 wt.% and d) 50 wt.% [61].

Organic light-emitting diode

An organic light-emitting diode (OLED) is a light emitting diode in which organic layers are responsible for light emission. The light emitted by OLED follows the basic principal of electroluminescence in which a material acts in response to the electrical field applied across it [62]. In context of CP/WS₂, PFO has recorded

an investigation where PFO matrix and WS₂ nanotubes were combined to prepare PFO/WS₂ blends with various loadings of 10 wt.%, 30 wt.%, and 50 wt.%. The fabrication of these homogeneously dispersed PFO/WS₂ composites were influenced by two major steps including the WS₂ nanotube purification and the blend preparation. An optimization on the threshold

voltage has recorded the highest voltage of 4.7 V when 30% of WS₂ was integrated with PFO, and surprisingly the threshold voltage depreciated at 50% of WS₂ and recorded 4.1 V which was almost similar to pure PFO. Compared to pure PFO, the devices containing the nanocomposites has poor efficiency. This is because the electrical data exhibited that the PFO/WS₂ nanocomposite device of WS₂ showed fluctuated performances with increasing wt.%. Such

unsynchronized data of threshold voltage and efficiency of the tailored material might be contributed by several factors such as unbalanced charges and electrode interfaces. It also could be due to the change of the device working point or total applied power [61]. Table 1 summarizes various CPs/WS2 composites with its respective summary on desired applications and advantages.

Table 1. Summary of CP/WS₂ in various application and their significant advantages

Conducting Polymer/WS ₂	Application	Advantage	Remarks	Ref.
PANI/WS ₂	Dye sensitized solar cell (DSSC)	Higher conversion efficiency of WS ₂ compare to platinum counter-electrode. Relatively cheaper cost compares to platinum.	Nano-sheets of WS ₂ and nano-rods of PANI were used in the investigation.	[63]
	Supercapacitor	The higher composition of PANI in the WS ₂ matrix has enhanced the supercapacitor performance.	Conductivity: 65.7 S/m; Specific capacitance: 441 at 0.5A/g.	[64]
	Supercapacitor	Exhibited excellent electrochemical properties and high frequency response.	High capacitance of 180 μFcm ⁻² at 1 ₂ 0 Hz. Potential use in energy storage device.	[65]
	Sensor	The sensor showed an excellent result under humid environment which can be utilized in the respiratory gases.	Ammonia sensor	[39]
PPy/WS ₂	Drug release	Biocompatible Non-invasive electrically stimulating drug release system	5-fluorouracil (anticancer drug)	[47]
	Potential use in medium-frequency devices such as humidity and gas sensors.	Excellent operation in terms of AC conductivity and dielectric properties.	PPy with 40 wt% of WS ₂ possessed highest conductivity of 5.081 x 10 ⁻³ S/cm.	[66]

Siti Nor Atika et al: POTENTIAL APPLICATIONS OF CONDUCTING POLYMER/TUNGSTEN DISULFIDE COMPOSITES: A MINI REVIEW

Table 1 (cont'd). Summary of CP/WS₂ in various application and their significant advantages

Conducting Polymer/WS ₂	Application	Advantage	Remarks	Ref.
PPy/WS ₂	Humidity sensor	Excellent long term-stability.	Response/recovery = 52/58 s, respectively.	[67]
			Long term stability up to 60 days at 55 and 95% relative humidity.	
PEDOT/WS ₂	Electrochemical sensor	WS ₂ has enhanced the denseness and smoothness of PEDOT morphology. The ternary composite of SWCNT/WS ₂ -PEDOT showed good linear response in the range of $0.00_2 - 0.9 \mu\text{M}$ with low LOD of 0.7nM in the Vitamin B ₂ detection.	The study involves molecularly imprinted polymer of WS ₂ -PEDOT in the presence of Vitamin B ₂ as the template.	[68]
	Supercapacitor	The supercapacitor showed long-term stability up to 5000 cycles by retaining 83.3% of initial areal capacitance.	Hybrid material of ternary composites consist of PEDOT, MeOH, PEG and WS ₂ were prepared using simple coelectrodeposition method.	[69]
	Schottky diode	Novel material of PEDOT/WS ₂ used for the first time in nano-diodes. The perfect ambient tolerance of the diode makes it an ideal candidate for gas or light sensors.	The combination of PEDOT and WS ₂ has resulted in rectification ratio of 1 ₂ and a turn-on voltage of 1.4 V.	[53]
	Miniature- supercapacitor	Simple and cost-effective fabrication of WS ₂ /PEDOT:PSS ternary composite. Improved flexibility in the miniaturized supercapacitor.	The WS ₂ /PEDOT:PSS supercapacitor recorded a high conductivity of 44 S/cm, high areal specific capacitance of 86 mFcm ⁻² , and 107% capacitance retention after 5000 cycles.	[70]

					t advantages

Conducting Polymer/WS ₂	Application	Advantage	Remarks	Ref.
Polythiophene/WS ₂ (PTh/WS ₂)	Functionally designed PTh/WS ₂	Shown good magnetic effect which could find potential use in microwave absorbing materials.	Modified liquid phase oxidative polymerization that controls interface PTh-based layered material.	[71]
	Functionally designed coating method for Pth/WS ₂	Electro-conductivity and mechanical properties of WS ₂ has been enhanced via the tailor-made functionalization.	Potential use in drug release control.	[72]
PFO/WS ₂ Organic Light Emitting Diodes		PFO with 30% of WS ₂ showed a threshold voltage of 4.7 V when 30% of WS ₂ .	PFO/WS ₂ has been tested for the first time as OLED and it opens the door for new avenues for this composite material.	[61]

Conclusion

A widespread overview of CP composites has been studied in the context of their properties and existing applications. WS2-based CPs offer a very broad and promising field of research, not only due to its enhanced properties but also because of the chances to achieve multifunctional nano systems from the synergic effect between CP and WS2. In this minireview, CP/WS₂ composite showed the performance as energy storage material followed by electronic components and sensors. CP/WS2 is a great choice for energy storage since it shows high capacitive behaviour even in a micro-sized supercapacitor. As a matter of fact, this material composite deserves a place in electronic and biomedical industries. Based on the findings and limitation of this research, some improvement can be made on low energy emission by PFO/WS2. As abovementioned, WS2 nanotubes were not fully homogenous in the PFO matrix. Henceforth, future research might consider nanotube purification in the fabrication of PFO/WS2. Besides, CP/WS2 can also consider more formation of ternary compounds

inspired from the PEDOT-PEG-WS₂ composite. This is because the initiative of using ternary compound can strengthen the connection between CP and inorganic filler, thus exhibiting remarkable performance in supercapacitors due to better electrons transport.

Acknowledgement

The authors would like to thank Fundamental Research Grant Scheme (FRGS) [FRGS/1/2019WAB05/UITM/02/5] for the financial assistance.

References

- Das, T. K. and Prusty, S. (2012). Review on conducting polymers and their applications. *Polymer - Plastics Technology and Engineering*, 51(14): 1487-1500.
- Mohd Norsham, I. N., Baharin, S. N. A., Raoov, M., Shahabuddin, S., Jakmunee, J. and Sambasevam, K. P. (2020). Optimization of waste quail eggshells as biocomposites for polyaniline in ammonia gas detection. *Polymer Engineering and Science*, 60(12): 1-13.

- 3. Sambasevam, K. P., Mohamad, S. and Phang, S.-W. (2015). Enhancement of polyaniline properties by different polymerization temperatures in hydrazine detection. *Journal of Applied Polymer Science*, 132(13): 41746.
- Kumar, R., Singh, S. and Yadav, B. C. (2016). Conducting polymers: Synthesis, properties and applications conducting polymers. *International Advanced Research Journal In Science, Engineering and Technology*, 2(11): 110-124.
- 5. Kaur, G., Adhikari, R., Cass, P., Bown, M. and Gunatillake, P. (2015). Electrically conductive polymers and composites for biomedical applications. *RSC Advances*, 5(47): 37553-37567.
- Yu, M., Huang, R., He, C., Wu, Q. and Zhao, X. (2016). Hybrid composites from wheat straw, inorganic filler, and recycled polypropylene: morphology and mechanical and thermal expansion performance. *International Journal of Polymer Science*, 2016: 1-12.
- Huo, N., Yang, S., Wei, Z., Li, S. S., Xia, J. B. and Li, J. (2014). Photoresponsive and gas sensing field-effect transistors based on multilayer WS₂ nanoflakes. *Scientific Reports*, 4: 1-9.
- 8. Ajibade, P. A. and Mbese, J. Z. (2014). Synthesis and characterization of metal sulfides nanoparticles/poly(methyl methacrylate) nanocomposites. *International Journal of Polymer Science*, 2014: 1-8.
- Abdel Maksoud, M. I. A., Fahim, R. A., Shalan, A. E., Abd Elkodous, M., Olojede, S. O., Osman, A. I., Farrell, C., Al-Muhtaseb, A. H., Awed, A. S., Ashour, A. H. and Rooney, D. W. (2021). Advanced materials and technologies for supercapacitors used in energy conversion and storage: a review. *Environmental Chemistry Letters*, 19(1): 375-439.
- Ramesan, M. T. (2013). Synthesis, characterization, and conductivity studies of polypyrrole/copper sulfide nanocomposites. *Journal of Applied Polymer Science*, 128(3): 1540-1546.
- 11. Ahmad, H., Kamarudin, S. K., Minggu, L. J. and Kassim, M. (2015). Hydrogen from photo-catalytic water splitting process: A review. *Renewable and*

- Sustainable Energy Reviews, 43: 599-610.
- Ke, X., Dai, K., Zhu, G., Zhang, J. and Liang, C. (2019). In situ photochemical synthesis noblemetal-free NiS on CdS-diethylenetriamine nanosheets for boosting photocatalytic H₂ production activity. *Applied Surface Science*, 481: 669-677.
- Takahashi, A., Tetuko, J. and Hashimoto, K. (2018). Evaluation of friction characteristics and low friction mechanism of tungsten disulfide for space solid lubricant at elevated temperature in a vacuum. *Proceedings of the 44th Aerospace Mechanisms Symposium*, 2018: pp. 113-126.
- 14. Sade, H. and Lellouche, J. (2018). Preparation and characterization of WS₂@SiO₂ and WS₂@PANI core-shell nanocomposites. *Nanomaterials*, 8(3): 156
- 15. Li, H., Yu, C., Chen, R., Li, J. and Li, J. (2012). Novel ionic liquid-type Gemini surfactants: Synthesis, surface property and antimicrobial activity. *Colloids and Surfaces A: Physicochemical and Engineering Aspects*, 395: 116-124.
- Chandrasekaran, S., Yao, L., Deng, L., Bowen, C., Zhang, Y., Chen, S., Lin, Z., Peng, F. and Zhang, P. (2019). Recent advances in metal sulfides: from controlled fabrication to electrocatalytic, photocatalytic and photoelectrochemical water splitting and beyond. *Chemical Society Reviews*, 48(15): 4178-4280.
- 17. Ashraf, W., Fatima, T., Srivastava, K. and Khanuja, M. (2019). Superior photocatalytic activity of tungsten disulfide nanostructures: role of morphology and defects. *Applied Nanoscience*, 1(1): 1-15.
- 18. Tang, G., Tang, H., Li, C., Li, W. and Ji, X. (2011). Surfactant-assisted hydrothermal synthesis and characterization of WS₂ nanorods. *Materials Letters*, 65(23–24): 3457-3460.
- Cao, S., Liu, T., Hussain, S., Zeng, W., Pan, F. and Peng, X. (2014). Synthesis and characterization of novel chrysanthemum-like tungsten disulfide (WS₂) nanostructure: structure, growth and optical absorption property. *Journal of Materials Science: Materials in Electronics*, 26(2): 809-814.

- Zhang, D., Liu, T., Cheng, J., Liang, S., Chai, J., Yang, X., Wang, H., Zheng, G. and Cao, M. (2019). Controllable synthesis and characterization of tungsten disulfide nanosheets as promising nanomaterials for electronic devices. *Ceramics International*, 45(9): 12443-12448.
- 21. Sun, S., Li, Z. and Chang, X. (2011). Synthesis and structural characterization of tungsten disulfide nanomaterials. *Materials Letters*, 65(19-20): 3164-3166.
- 22. Ramesan, M. T. (2013). Synthesis, characterization, and properties of new conducting polyaniline/copper sulfide nanocomposites. *Polymer Engineering and Science*, 2013: 1-8.
- 23. Flores, A., Naffakh, M., Díez-Pascual, A. M., Ania, F. and Gómez-Fatou, M. A. (2013). Evaluating the reinforcement of inorganic fullerene-like nanoparticles in thermoplastic matrices by depth-sensing indentation. *Journal of Physical Chemistry C*, 117(40): 20936-20943.
- 24. Li, S., Liu, A., Yang, Z., Zhao, L., Wang, J., Liu, F., You, R., He, J., Wang, C., Yan, X., Sun, P., Liang, X., and Lu, G. (2019). Design and preparation of the WO₃ hollow spheres@ PANI conducting films for room temperature flexible NH₃ sensing device. *Sensors and Actuators B: Chemical*, 289: 252-259.
- Ma, Y., Qiao, M., Hou, C., Chen, Y., Ma, M., Zhang, H. and Zhang, Q. (2015). Preparation of polyaniline (PANI)-coated Fe₃O₄ microsphere chains and PANI chain-like hollow spheres without using surfactants. *RSC Advances*, 5(125): 103064-103072.
- Shyaa, A. A., Hasan, O. A. and Abbas, A. M. (2015). Synthesis and characterization of polyaniline/ zeolite nanocomposite for the removal of chromium(VI) from aqueous solution. *Journal of Saudi Chemical Society*, 19(1): 101-107.
- Prasanna, B. P., Avadhani, D. N., Muralidhara, H. B., Chaitra, K., Thomas, V. R., Revanasiddappa, M. and Kathyayini, N. (2016). Synthesis of polyaniline/ZrO₂ nanocomposites and their performance in AC conductivity and electrochemical supercapacitance. *Bulletin of Materials Science*, 39(3): 667-675.
- 28. Khademian, M. and Eisazadeh, H. (2015).

- Preparation and characterization emulsion of PANI-TiO₂ nanocomposite and its application as anticorrosive coating. *Journal of Polymer Engineering*, 35(6): 597-603
- 29. Jiang, Feiran, Li, W., Zou, R., Liu, Q., Xu, K., An, L. and Hu, J. (2014). MoO₃/PANI coaxial heterostructure nanobelts by in situ polymerization for high performance supercapacitors. *Nano Energy*, 7: 72-79.
- Ghani, S. A. and Young, H. C. (2010). Conductive polymer based on polyaniline-eggshell powder (PANI-ESP) composites. *Journal of Physical Science*, 21(2): 81-97.
- 31. Manjunatha, S., Chethan, B., Ravikiran, Y. T. and Machappa, T. (2018). Room temperature humidity sensor based on polyaniline-tungsten disulfide composite. *AIP Conference Proceedings*, 1953.
- 32. Wang, J., Pang, X., Tan, X., Song, Y., Liu, L., You, Q., Sun, Q., Tan, F. and Li, N. (2017). A triple-synergistic strategy for combinational photo/radiotherapy and multi-modality imaging based on hyaluronic acid-hybridized polyaniline-coated WS₂ nanodots. *Nanoscale*, 9(17): 5551-5564.
- 33. Stejskal, J., Mrlík, M., Plachý, T., Trchová, M., Kovářová, J. and Li, Y. (2017). Molybdenum and tungsten disulfides surface-modified with a conducting polymer, polyaniline, for application in electrorheology. *Reactive and Functional Polymers*, 120: 30-37.
- 34. Xia, X., Hao, Q., Lei, W., Wang, W., Sun, D. and Wang, X. (2012). Nanostructured ternary composites of graphene/Fe₂O₃/polyaniline for high-performance supercapacitors. *Journal of Materials Chemistry*, 22(33): 16844-16850.
- 35. Guo, H., Lan, C., Zhou, Z., Sun, P., Wei, D. and Li, C. (2017). Transparent, flexible, and stretchable WS₂ based humidity sensors for electronic skin. *Nanoscale*, 9(19): 6246-6253.
- Kim, S. J., Hwang, I. S., Kang, Y. C. and Lee, J. H. (2011). Design of selective gas sensors using additive-loaded In₂O₃ hollow spheres prepared by combinatorial hydrothermal reactions. *Sensors*, 11(11): 10603-10614.

- 37. Xu, B. H., Lin, B. Z., Chen, Z. J., Li, X. L. and Wang, Q. Q. (2009). Preparation and electrical conductivity of polypyrrole/WS₂ layered nanocomposites. *Journal of Colloid and Interface Science*, 330(1): 220-226.
- 38. Jha, R. K., Wan, M., Jacob, C., & Guha, P. K. (2018). Ammonia vapour sensing properties of in situ polymerized conducting PANI-nanofiber/WS₂ nanosheet composites. *New Journal of Chemistry*, 42(1): 735-745.
- 39. Liu, G., Zhou, Y., Zhu, X., Wang, Y., Ren, H., Wang, Y., Gao, C. and Guo, Y. (2020). Humidity enhanced ammonia sensing of porous polyaniline/tungsten disulfide nanocomposite film. *Sensors and Actuators B: Chemical*, 323: 128699.
- Mayorga-Martinez, C. C., Moo, J. G. S., Khezri, B., Song, P., Fisher, A. C., Sofer, Z. and Pumera, M. (2016). Self-propelled supercapacitors for ondemand circuit configuration based on WS₂ nanoparticles micromachines. *Advanced Functional Materials*, 26(36): 6662-6667.
- 41. Stejskal, J., Acharya, U., Bober, P., Hajná, M., Trchová, M., Mičušík, M., Omastová, M., Pašti, I. and Gavrilov, N. (2019). Surface modification of tungsten disulfide with polypyrrole for enhancement of the conductivity and its impact on hydrogen evolution reaction. *Applied Surface Science*, 492(5): 497-503.
- Kapralova, V. M., Sapurina, I. Y. and Sudar', N. T. (2018). Variation in the conductivity of polyaniline nanotubes during their formation. Semiconductors, 52(6): 816-819.
- Stejskal, J., Sapurina, I. and Trchová, M. (2010).
 Polyaniline nanostructures and the role of aniline oligomers in their formation. *Progress in Polymer Science*, 35(12): 1420-1481.
- 44. Hailemeskel, B. Z., Addisu, K. D., Prasannan, A., Mekuria, S. L., Kao, C. Y. and Tsai, H. C. (2018). Synthesis and characterization of diselenide linked poly(ethylene glycol) nanogel as multi-responsive drug carrier. *Applied Surface Science*, 449: 15-22.
- 45. Timko, B. P. and Kohane, D. S. (2012). Materials to clinical devices: Technologies for remotely triggered drug delivery. *Clinical Therapeutics*, 34(11): S25-S35.

- Wu, S. Y., Chou, H. Y., Yuh, C. H., Mekuria, S. L., Kao, Y. C. and Tsai, H. C. (2018). Radiation-sensitive dendrimer-based drug delivery system. Advanced Science, 5(2): 1700339.
- 47. Hsiao, P. F., Anbazhagan, R., Tsai, H.-C., Rajakumari krishnamoorthi, Lin, S.-J., Lin, S.-Y., Lee, K.-Y., Kao, C.-Y., Chen, R.-S. and Lai, J.-Y. (2020). Fabrication of electroactive polypyrroletungsten disulfide nanocomposite for enhanced in vivo drug release in mice skin. *Materials Science and Engineering: C*, 107: 110330.
- 48. Bubnova, O., Khan, Z. U., Malti, A., Braun, S., Fahlman, M., Berggren, M. and Crispin, X. (2011). Optimization of the thermoelectric figure of merit in the conducting polymer poly(3,4-ethylenedioxythiophene). *Nature Materials*, 10(6): 429-433.
- 49. Jiang, Fengxing, Xiong, J., Zhou, W., Liu, C., Wang, L., Zhao, F., Liu, H. and Xu, J. (2016). Use of organic solvent-assisted exfoliated MoS₂ for optimizing the thermoelectric performance of flexible PEDOT:PSS thin films. *Journal of Materials Chemistry A*, 4(14): 5265-5273.
- Sun, K., Zhang, S., Li, P., Xia, Y., Zhang, X., Du, D., Isikgor, F. H. and Ouyang, J. (2015). Review on application of PEDOTs and PEDOT:PSS in energy conversion and storage devices. *Journal of Materials Science: Materials in Electronics*, 26(7): 4438-4462.
- 51. Wei, Q., Mukaida, M., Kirihara, K. and Ishida, T. (2014). Experimental studies on the anisotropic thermoelectric properties of conducting polymer films. *ACS Macro Letters*, 3(9): 948-952.
- 52. Wang, T., Liu, C., Wang, X., Li, X., Jiang, F., Li, C., Hou, J. and Xu, J. (2017). Highly enhanced thermoelectric performance of WS₂ nanosheets upon embedding PEDOT:PSS. *Journal of Polymer Science, Part B: Polymer Physics*, 55(13): 997-1004.
- 53. Ortiz, D. N., Vedrine, J., Pinto, N. J., Naylor, C. H. and Charlie Johnson, A. T. (2016). Monolayer WS₂ crossed with an electro-spun PEDOT-PSS nano-ribbon: Fabricating a Schottky diode. *Materials Science and Engineering B: Solid-State Materials for Advanced Technology*, 214: 68-73.

- 54. Kim, M. S., Yun, S. J., Lee, Y., Seo, C., Han, G. H., Kim, K. K., Lee, Y. H. and Kim, J. (2016). Biexciton emission from edges and grain boundaries of triangular WS₂ monolayers. ACS Nano, 10(2): 2399-2405.
- 55. Li, Y., Niu, J., Xue, T., Duan, X., Tian, Q., Wen, Y., Lu, X., Xu, J., Lai, L., Chang, Y., Li, Z., Zhao, X. and Chen, Y. (2020). Multifunctional porous nanohybrid based on graphene-like tungsten disulfide on poly(3,4-ethoxylenedioxythiophene) for supercapacitor and electrochemical nanosensing of quercetin. *Journal of The Electrochemical Society*, 167(4): 047512.
- Liang, H., Zhang, B. Q. and Song, J. M. (2019).
 Synthesis of textured tungsten disulfide nanosheets and their catalysis for benzylamine coupling reaction. *ChemCatChem*, 11(24): 6288-6294.
- 57. Gu, X., Cui, W., Li, H., Wu, Z., Zeng, Z., Lee, S. T., Zhang, H. and Sun, B. (2013). A solution-processed hole extraction layer made from ultrathin MoS₂ nanosheets for efficient organic solar cells. *Advanced Energy Materials*, 3(10): 1262-1268.
- 58. Lin, Y., Adilbekova, B., Firdaus, Y., Yengel, E., Faber, H., Sajjad, M., Zheng, X., Yarali, E., Seitkhan, A., Bakr, O. M., El-Labban, A., Schwingenschlögl, U., Tung, V., McCulloch, I., Laquai, F. and Anthopoulos, T. D. (2019). 17% efficient organic solar cells based on liquid exfoliated WS₂ as a replacement for PEDOT:PSS. Advanced Materials, 31(46): 1902965.
- Le, Q. Van, Nguyen, T. P. and Kim, S. Y. (2014).
 UV/ozone-treated WS₂ hole-extraction layer in organic photovoltaic cells. *Physica Status Solidi Rapid Research Letters*, 8(5): 390-394.
- Fukumaru, T., Toshimitsu, F., Fujigaya, T. and Nakashima, N. (2014). Effects of the chemical structure of polyfluorene on selective extraction of semiconducting single-walled carbon nanotubes. *Nanoscale*, 6(11): 5879-5886.
- Di Luccio, T., Borriello, C., Bruno, A., Maglione, M. G., Minarini, C. and Nenna, G. (2013). Preparation and characterization of novel nanocomposites of WS₂ nanotubes and polyfluorene conductive polymer. *Physica Status Solidi (A) Applications and Materials Science*,

- 210(11): 2278-2283.
- 62. Zou, S. J., Shen, Y., Xie, F. M., Chen, J. De, Li, Y. Q. and Tang, J. X. (2020). Recent advances in organic light-emitting diodes: Toward smart lighting and displays. *Materials Chemistry Frontiers*, 4(3): 788-820.
- 63. Ahmad, M. S., Rahim, N. A., Syed shahabuddin, Mehmood, S. and Khan, A. D. (2021). Effect of WS₂ nano-sheets on the catalytic activity of polyaniline nano-rods based counter electrode for dye sensitized solar cell. *Physica E: Low-Dimensional Systems and Nanostructures*, 126: 114466.
- 64. Gopalakrishnan, K., Sultan, S., Govindaraj, A. and Rao, C. N. R. (2015). Supercapacitors based on composites of PANI with nanosheets of nitrogendoped RGO, BC 1.5 N, MoS₂ and WS₂. *Nano Energy*, 12: 52-58.
- 65. De Adhikari, A., Shauloff, N., Turkulets, Y., Shalish, I. and Jelinek, R. (2021). Tungstendisulfide/polyaniline high frequency supercapacitors. *Advanced Electronic Materials*, 7(6): 2100025.
- 66. Sunilkumar, A., Manjunatha, S., Ravikiran, Y. T., Revanasiddappa, M., Prashantkumar, M. and Machappa, T. (2021). AC conductivity and dielectric studies in polypyrrole wrapped tungsten disulphide composites. *Polymer Bulletin*, 2021: 1-17.
- 67. Sunilkumar, A., Manjunatha, S., Machappa, T., Chethan, B. and Ravikiran, Y. T. (2019). A tungsten disulphide–polypyrrole composite-based humidity sensor at room temperature. *Bulletin of Materials Science*, 42(6): 271.
- 68. Zhang, Z., Xu, J., Wen, Y. and Wang, T. (2018). A highly-sensitive VB₂ electrochemical sensor based on one-step co-electrodeposited molecularly imprinted WS₂-PEDOT film supported on graphene oxide-SWCNTs nanocomposite. *Materials Science and Engineering: C*, 92: 77-87.

- 69. Liang, A., Cai, Y., Wang, J., Xu, L., Zhou, W., Xue, Z., He, Y., Xu, J. and Duan, X. (2021). Coelectrodeposited porous poplar flower-like poly(hydroxymethyl-3,4-ethylenedioxythiophene)/ PEG/WS₂ hybrid material for high-performance supercapacitor. *Journal of Electroanalytical Chemistry*, 891: 115261.
- 70. Liang, A., Li, D., Zhou, W., Wu, Y., Ye, G., Wu, J., Chang, Y., Wang, R., Xu, J., Nie, G., Hou, J. and Du, Y. (2018). Robust flexible WS₂/PEDOT:PSS film for use in high-performance miniature supercapacitors. *Journal of Electroanalytical Chemistry*, 824: 136-146.
- 71. Ben Ishay, R., Harel, Y., Lavi, R. and Lellouche, J.-P. (2016). Multiple functionalization of tungsten disulfide inorganic nanotubes by covalently grafted conductive polythiophenes. *RSC Advances*, 6(92): 89585-89598.
- Raichman, D., Ben-Shabat Binyamini, R. and Lellouche, J. P. (2016). A new polythiophenedriven coating method on an inorganic INT/IF-WS₂ nanomaterial surface. *RSC Advances*, 6(6): 4490-4504.

Malaysian Journal of Analytical Sciences (MJAS) Published by Malaysian Analytical Sciences Society



DIASTEREOSELECTIVE REDUCTION OF ENDOCYCLIC β -ENAMINO ESTER: AN APPROACH TO PREPARE DIASTEREOPURE MULTISUBSTITUTED PYRROLIDINE β-AMINO ESTERS

(Penurunan Diastereoselektif Terhadap Ester β-Enamino Endosiklik: Satu Pendekatan untuk Menyediakan Ester β-Amino Pirolidin Multi-Penukarganti Diastereotulen)

Ayisy Amirul Afti^{1*}, Nor Saliyana Jumali¹, Mohd Fazli Mohammat², Zurina Shaameri², Ahmad Sazali Hamzah²

¹ Department of Chemistry, Kulliyyah of Science, International Islamic University Malaysia, 25200 Kuantan, Pahang, Malaysia. ² Organic Synthesis Research Laboratory, Institute of Science (I.O.S), Universiti Teknologi MARA, 42300 Bandar Puncak Alam, Selangor, Malaysia.

*Corresponding author: ayisy.aaba@live.iium.edu.my

Received: 26 November 2021; Accepted: 27 February 2022; Published: 28 April 2022

Abstract

A set of chiral multi-substituted pyrrolidine diastereomers containing β -amino ester moiety (5a-c) were successfully synthesized from 4-carbethoxy-3-hydroxy-2-oxo-5-phenyl-3-pyrroline (1). The key intermediate endocyclic β-enamino ester (4) was prepared by methylamination of precursor 1, followed by acid-catalyzed reduction of 4 using sodium cyanoborohydride to obtain target products (5) with moderate diastereoselectivity. Other exploration on the reduction of 4 includes the use of sodium triacetoxyborohydride in acetic acid and catalytic hydrogenation which are subsequently compared with the aforementioned approach in terms of selectivity. Several plausible reaction mechanisms have been proposed based on experimental data.

Keywords: pyrrolidine; β-enamino ester; diastereoselective reduction; catalytic hydrogenation; sodium cyanoborohydride.

Abstrak

Satu set diastereomer pirolidin multi-penukarganti kiral yang mengandungi bahagian ester β-amino (5a-c) telah berjaya disintesis daripada 4-karbetoksi-3-hidroksi-2-okso-5-fenil-3-pirolin (1). Perantara utama, ester β-enamino endosiklik (4), telah disediakan melalui metilaminasi pendahulu 1. Kemudian, penurunan bagi 4 yang dimangkinkan oleh asid menggunakan natrium sianoborohidrid menghasilkan produk sasaran 5 dengan diastereoselektiviti yang sederhana. Tatacara lain untuk menurunkan 4 termasuk penggunaan natrium triasetoksiborohidrid dalam asid asetik dan penghidrogenan mangkin telah dibandingkan dengan kaedah terdahulu dari sudut selektiviti. Di sini, kami menghuraikan beberapa mekanisme tindakbalas yang munasabah daripada hasil eksperimen ini.

Kata kunci: pirolidin; ester β-enamino; penurunan diastereoselektif; penghidrogenan mangkin; natrium sianoborohidrid.

Introduction

β-enamino esters **A** are recognized as versatile building blocks in the synthesis of various interesting alkaloids [1] including bi- and tricyclic heterocycles such as pyrrolopyrimidines [2], pyrroloquinolines [3], indoles [4], pyrrolizidines and indolizidines [5, 6] (Figure 1). The multifunctionality of these compounds resides in the simultaneous presence of a nitrogen atom, a carbon-carbon double bond, C=C (which when reduced, gives rise to one or two chiral centre(s) and enhances the nucleophilicity of the nitrogen via the localization of its lone pair electrons) and an ester group for further chain extension or ring closure [7, 8].

Owing to their role as key intermediates for synthesizing naturally occurring compounds (Figure 2), this class of functional group has been of crucial interest to researchers especially for the chemistry of its enantio- and diastereoselective reductions.

Excellent enantioselectivity of catalytic hydrogenation over palladium hydroxide, Pd(OH)₂ enables the preparation of (+)-calvine, an alkaloid piperidine isolated from coccinellid beetles of the genus *Calvia*

[9]. Hydrogenations in the presence of 10% platinum on carbon (Pt/C) and 10% palladium on carbon (Pd/C) offers high diastereoselectivity to reduce β -enamino esters with exocyclic C=C in the asymmetrical syntheses of (+)-laburnine and (+)-tashiromine, respectively. While the ones with endocyclic double bond can be reduced using platinum dioxide-catalyzed hydrogenation with a large diastereomeric excess (d.e. = 90%) as described in the synthetic approach of constructing (-)-isoretronecanol [10, 11].

Apart from that, chemical reduction by sodium triacetoxyborohydride, NaBH(OAc)₃ in acetic acid provides greater diastereoselectivity for enamino esters with endocyclic C=C rather than their exocyclic and acyclic counterparts [10], while in the presence of magnesium iodide (MgI₂), near quantitative yield can be achieved [12]. Sodium cyanoborohydride, NaBH₃CN is a versatile reducing agent known for its ability to yield diastereopure β -amino esters as mentioned in the preparation of (±)-lythrancepine (II) and (III) [8].

Figure 1. Bi- and tricyclic alkaloids derived from β-enamino esters

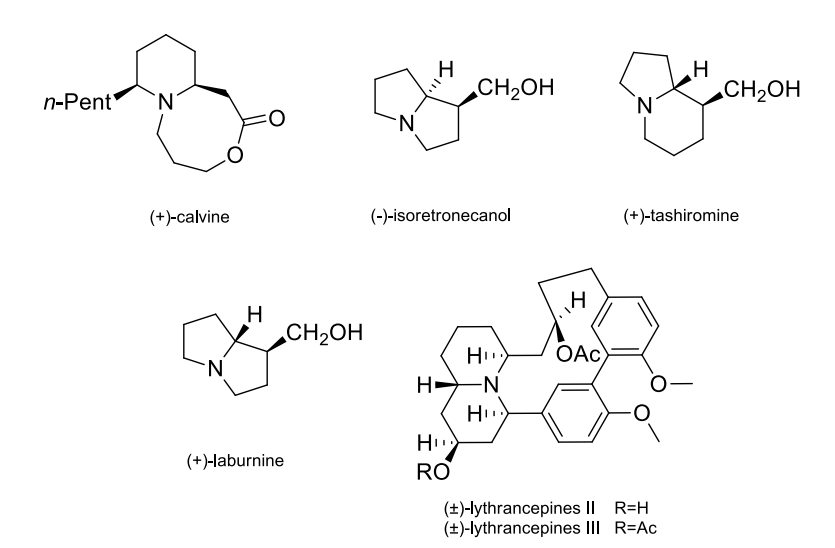


Figure 2. Naturally occurring compounds derived from selective reductions of β -enamino esters

Notably, some studies report that catalytic hydrogenations portray superior selectivity over chemical reductions when involving exocyclic and acyclic β -enamino esters [10, 13]. To our knowledge, there is yet any reported work that specifically discusses the chemistry behind the reduction of endocyclic β -enamino esters – i.e. comparison between the two approaches.

Ergo, in this short study, we describe an experiment to reduce β -enamino ester (4) containing endocyclic C=C. The procedures explored include hydrogenation with either 10% Pd/C or 20% Pd(OH₂)/C along with reduction using either NaBH(OAc)₃ in acetic acid or NaBH₃CN in acidic medium. Different approaches are believed to have distinct stereochemical controls and effectiveness over the reduction protocols.

Materials and Methods

All reagents and solvents were supplied by R&M Chemicals, Merck KgaA and Acros Organics. The reactions were monitored by TLC on silica gel 60 F254 plates, Merck (layer thickness 0.25 mm) and visualized with UV light (254 and 365 nm) and KMnO₄ solution as the staining reagent. For product purification using column chromatography, Merck silica gel (230-400 mesh particle size) was used. Infrared spectra were recorded on Varian 3100 Excalibur Series FT-IR

spectrometer in the range of 4000-400 cm $^{-1}$. 1 H-, 13 C- and 2D NMR spectra were captured on JEOL-400 (1 H 400 MHz, 13 C 101 MHz) NMR spectrometer.

Multicomponent reaction (MCR) to synthesize 4-carbethoxy-3-hydroxy-2-oxo-5-phenyl-3-pyrroline (1)

The method was adapted from literature [15]. Sodium diethyl oxalacetate (5.01 g, 24 mmol), benzaldehyde (2.4 mL, 24 mmol) and aqueous ammonia (8.0 mL, 119 mmol) were suspended in ethanol (70 mL) and refluxed. After an hour and 15 minutes, the reflux was stopped and once the mixture cooled down to room temperature, it was added to an ice bath. The mixture was acidified with concentrated HCl until it reached pH 2 while being constantly stirred. The resulting precipitate was filtered by suction and washed with distilled water. The solid was dried under vacuum overnight to give the product, 4-carbethoxy-3-hydroxy-2-oxo-5-phenyl-3-pyrroline, as a white solid (Yield: 2.67 g, 42%).

Analytical data: FT-IR (ATR) \bar{v} (cm⁻¹) 3370 (O-H), 3311 (N-H), 2994 (C-H), 1689 (C=O); ¹H-NMR (400 MHz, CD₃OH) δ (ppm) 7.32-7.22 (m, 5H, ArH), 5.23 (s, 1H, ArC<u>H</u>NH), 4.10-4.01 (m, 2H, OCH₂), 1.06 (t, J = 7.1 Hz, 3H, CH₃); ¹³C-NMR (101 MHz, CD₃OH) δ (ppm) 167.4 (C=C-OH), 163.5 (O-C=O), 155.0

(NHC=O), 137.4 (ArC-CH), 128.2 (ArCH), 127.9 (ArCH), 127.1 (ArCH), 114.0 (C=C-C=O), 60.1 (OCH₂), 57.3 (ArCHNH), 13.0 (CH₃).

Leuckart reaction to synthesize 3-amino-4-carboethoxy-2-oxo-5-phenyl-3-pyrroline (2)

The method was adapted from literature [2]. To a suspension of 4-carbethoxy-3-hydroxy-2-oxo-5-phenyl-3-pyrroline (1) (2.01 g, 8 mmol) in ethanol (40 mL), ammonium formate (1.03 g, 16 mmol) was added while stirring. After heating under reflux for 24 hours with TLC monitoring, the mixture was left to cool to room temperature. The solvent was evaporated under reduced pressure and the crude product was purified using column chromatography (petroleum ether/ethyl acetate: 2/1) to yield the product, 3-amino-4-carboethoxy-2-oxo-5-phenyl-3-pyrroline, as a white solid (Yield: 1.23 g, 62%).

Analytical data: TLC (Petreoleum ether/ethyl acetate : 2/1, $R_f = 0.26$); FT-IR (ATR) \bar{v} (cm⁻¹) 3482 (N-H), 3385 (N-H), 3278 (N-H), 2965 (C-H), 1718 (conj. C=O), 1679 (C=O), 1625; ¹H-NMR (400 MHz, CD₃OH) δ (ppm) 7.28-7.19 (m, 5H, ArH), 5.16 (s, 1H, ArCHNH), 4.57 (s, 2H, NH₂), 4.06-3.99 (m, 2H, OCH₂), 1.07 (t, J = 7.1 Hz, 3H, CH₃); ¹³C-NMR (101 MHz, DMSO-d₆) δ (ppm) 167.3 (O-C=O), 164.8 (NHC=O), 147.4 (C=C-NH₂), 140.3 (ArC-CH), 128.6 (ArCH), 128.0 (ArCH), 127.7 (ArCH), 103.3 (C=C-C=O), 59.3 (OCH₂), 57.8 (ArCHNH), 14.7 (CH₃).

Hydrogenation of 3-amino-4-carboethoxy-2-oxo-5-phenyl-3-pyrroline (2) over 10% Pd/C

This is our in-house method [19]. To a stirred solution of 3-amino-4-carboethoxy-2-oxo-5-phenyl-3-pyrroline (2) (0.50 g, 2.03 mmol) in acetic acid (50 mL), 10% Pd/C (0.30 g, 0.26 mmol) was added slowly. The reaction mixture was stirred vigorously under hydrogen atmosphere at 1 atm with TLC monitoring. After 22 hours, the reaction was stopped and the catalyst was filtered through Celite. The solvent was removed from the filtrate under reduced pressure to give a white solid. From TLC, FT-IR and NMR characterization experiments, it was concluded that the starting material 2 was recovered.

Analytical data: TLC (Petreoleum ether/ethyl acetate : 2/1, $R_f = 0.26$); FT-IR (ATR) \bar{v} (cm⁻¹) 3482 (N-H), 3385 (N-H), 3278 (N-H), 2965 (C-H), 1718 (conj. C=O), 1679 (C=O), 1625; ¹H-NMR (400 MHz, DMSO-*d*6) δ (ppm) 9.10 (s, 2H, NH₂), 7.27-7.12 (m, 5H, ArH), 6.46 (s, 1H, NHC=O), 5.06 (s, 1H, ArC<u>H</u>NH), 3.91 (qt, J = 11.0, 3.5 Hz, 2H, OCH₂), 0.98 (t, J = 7.1 Hz, 3H, CH₃); ¹³C-NMR (101 MHz, DMSO-d₆) δ (ppm) 167.3 (O-C=O), 164.8 (NHC=O), 147.4 (C=<u>C</u>-NH₂), 140.3 (Ar<u>C</u>-CH), 128.6 (ArCH), 128.0 (ArCH), 127.7 (ArCH), 103.3 (C=<u>C</u>-C=O), 59.3 (OCH₂), 57.8 (ArCHNH), 14.7 (CH₃).

Synthesis of 4-carboethoxy-3-methylamino-2-oxo-5-phenyl-3-pyrroline (4)

The method was adapted from literature [2]. To a suspension of 4-carbethoxy-3-hydroxy-2-oxo-5-phenyl-3-pyrroline (1) (1.94 g, 8 mmol) in ethanol (40 mL), aqueous methylamine (40%) (1.4 mL, 16 mmol) was added while stirring. After heating under reflux for 24 hours with TLC monitoring, the mixture was left to cool to room temperature. After cooling in an ice bath, the resulting white crystals were filtered to give the product, 4-carboethoxy-3-methylamino-2-oxo-5-phenyl-3-pyrroline, as white crystals (Yield: 1.41 g, 69%).

Analytical data: TLC (Ethyl acetate, $R_f = 0.83$); FT-IR (ATR) \bar{v} (cm⁻¹) 3351 (N-H), 2980 (C-H), 1698 (C=O), 1667 (C=O), 1633; ¹H-NMR (400 MHz, CDCl₃) δ (ppm) 7.30-7.20 (m, 5H, ArH), 6.48 (s, 1H, CH₃NH), 5.14 (s, 1H, ArCHNH), 4.04-3.93 (m, 2H, OCH₂), 3.34 (s, 3H, CH₃NH), 1.71 (s, 1H, CH₃NH), 1.03 (t, J = 7.1 Hz, 3H, CH₃); ¹³C-NMR (101 MHz, CDCl₃) δ (ppm) 167.9 (O-C=O), 166.6 (NHC=O), 147.1 (C=C-NHCH₃), 138.9 (ArC-CH), 128.4 (ArCH), 128.1 (ArCH), 127.4 (ArCH), 104.8 (C=C-C=O), 59.5 (OCH₂), 57.9 (ArCHNH), 30.2 (NHCH₃), 14.1 (CH₃).

Hydrogenation of 4-carboethoxy-3-methylamino-2-oxo-5-phenyl-3-pyrroline (4) over 10% palladium on carbon (Pd/C)

This is our in-house method [19]. To a stirred solution of 4-carboethoxy-3-methylamino-2-oxo-5-phenyl-3-pyrroline (4) (0.50 g, 1.92 mmol) in acetic acid (10 mL), 10% Pd/C (0.20 g, 0.19 mmol) was added

slowly. The reaction mixture was stirred vigorously under hydrogen atmosphere at 1 atm with TLC monitoring. After 24 hours, the reaction was stopped and the catalyst was filtered through Celite. The solvent was removed from the filtrate under reduced pressure and the residue was purified by column chromatography (gradient elution) to yield the diastereomers of 4-carbethoxy-3-methylamino-2-oxo-5-phenylpyrrolidine as yellow oils; *cis-trans* **5a** (Yield: 51.9 mg, 10.3%), *all-trans* **5b** (Yield: 22.9 mg, 4.5%) and *all-cis* **5c** (Yield: 48.3 mg, 9.6%).

Analytical data: FT-IR (ATR) \bar{v} (cm⁻¹) 3395 (N-H), 3200 (N-H), 2981 (C-H), 1698 (C=O), 1646 (C=O); cis-trans **5a**: TLC (Ethyl acetate, $R_f = 0.53$); ¹H-NMR (400 MHz, CD₃OH) δ (ppm) 7.38-7.28 (m, 5H, ArH), 4.98 (d, J = 4.8 Hz, 1H, H-5), 4.57 (s, 1H, CH_3N_H), 4.19-4.16 (dq, 2H, OCH₂), 3.60 (d, J = 8.4 Hz, 1H, H-3), 3.31 (m, 1H, H-4), 2.45 (s, 3H, CH_3NH), 1.24 (t, J =7.6 Hz, 3H, CH₃); ¹³C-NMR (101 MHz, CD₃OH) δ (ppm) 176.0 (NHC=O), 171.1 (O-C=O), 140.4 (ArC-CH), 128.8 (ArCH), 128.1 (ArCH), 125.8 (ArCH), 61.4 (C-3), 60.8 (OCH₂), 58.0 (C-5), 53.9 (C-4), 34.0 (NHCH₃), 13.2 (CH₃). all-trans 5b: TLC (Ethyl acetate, $R_f = 0.13$); ¹H-NMR (400 MHz, CD₃OH) δ (ppm) 7.40-7.31 (m, 5H, ArH), 4.73 (d, J = 8.2 Hz, 1H, H-5), 4.22-4.11 (m, 2H, OCH₂), 3.95 (d, J = 9.6Hz, 1H, H-3), 3.01 (dd, J = 9.8, 8.5 Hz, H-4), 2.51 (s, 3H, CH₃NH), 1.18 (t, J = 7.3 Hz, 3H, CH₃); ¹³C-NMR (101 MHz, CD₃OH) δ (ppm) 175.6 (NHC=O), 173.4 (O-C=O), 140.0 (ArC-CH), 128.6 (ArCH), 128.3 (ArCH), 126.4 (ArCH), 62.7 (C-4), 61.4 (OCH₂), 58.2 (C-3), 55.4 (C-5), 32.2 (NHCH₃), 13.1 (CH₃). all-cis **5c**: TLC (Ethyl acetate, $R_f = 0.31$); ¹H-NMR (400 MHz, CD₃OH) δ (ppm) 7.38-7.29 (m, 5H, ArH), 5.11 (d, J = 6.4 Hz, 1H, H-5), 4.05 (d, J = 6.9 Hz, 1H, H-3),3.86 (t, J = 6.9 Hz, 1H, H-4), 3.73-3.67 (m, 1H, OCH₂), 3.57-3.51 (m, 1H, OCH₂), 2.63 (s, 3H, CH₃NH), 0.71 $(t, J = 7.1 \text{ Hz}, 3H, CH_3); ^{13}\text{C-NMR} (101 \text{ MHz},$ CD₃OH) δ (ppm) 174.6 (NHC=O), 169.4 (O-C=O), 136.6 (ArCH), 128.2 (ArCH), 126.3 (ArCH), 61.3 (C-3), 60.7 (OCH₂), 56.8 (C-5), 51.2 (C-4), 33.6 (NHCH₃), 12.5 (CH₃).

Hydrogenation of 4-carboethoxy-3-methylamino-2-oxo-5-phenyl-3-pyrroline (4) over 20% palladium hydroxide on carbon (Pd(OH)₂/C)

This method was adapted from our in-house method [19]. To a stirred solution of 4-carboethoxy-3methylamino-2-oxo-5-phenyl-3-pyrroline (4) (0.50 g, 1.92 mmol) in acetic acid (10 mL), 20% Pd(OH)₂/C (0.13 g, 0.19 mmol) was added slowly. The reaction mixture was stirred vigorously under hydrogen atmosphere at 1 atm with TLC monitoring. After 24 hours, the reaction was stopped and the catalyst was filtered through Celite. The solvent was removed from the filtrate under reduced pressure and the residue was purified by column chromatography (gradient elution) to yield the diastereomers of 4-carbethoxy-3methylamino-2-oxo-5-phenylpyrrolidine as yellow oils; cis-trans 5a (Yield: 11.4 mg, 2.2%), all-trans 5b (Yield: 0.7 mg, 0.1%) and all-cis 5c (Yield: 10.3 mg, 2.0%).

Analytical data: FT-IR (ATR) \bar{v} (cm⁻¹) 3358 (N-H), 3193 (N-H), 2982 (C-H), 1698 (C=O), 1646 (C=O); cis-trans **5a**: TLC (Ethyl acetate, $R_f = 0.43$); ¹H-NMR (400 MHz, CDCl₃) δ (ppm) 7.34-7.25 (m, 5H, ArH), 6.58 (s, 1H, CH₃NH), 4.98 (d, J = 3.7 Hz, 1H, H-5), 4.21-4.12 (m, 2H, OCH₂), 3.58 (d, J = 8.2 Hz, 1H, H-3), 3.27 (dd, J = 4.1 Hz, H-4), 2.46 (s, 3H, CH₃NH), 1.23 (t, J = 7.1 Hz, 3H, CH₃); ¹³C-NMR (101 MHz, CDCl₃) δ (ppm) 175.1 (NHC=O), 170.8 (O-C=O), 140.5 (ArC-CH), 129.2 (ArCH), 126.0 (ArCH), 125.7 (ArCH), 61.3 (C-3), 60.7 (OCH₂), 57.6 (C-5), 54.1 (C-4), 35.4 (NHCH₃), 14.1 (CH₃). all-trans **5b**: TLC (Ethyl acetate, $R_f = 0.11$); ¹H-NMR (400 MHz, Acetone-d₆) δ (ppm) 7.38-7.30 (m, 5H, ArH), 4.71 (d, J = 8.4 Hz, 1H, H-5), 4.15-4.12 (m, 2H, OCH₂), 3.60 (d, J = 9.6 Hz, 1H, H-3), 2.80 (m, 1H, H-4), 2.40 (s, 3H,CH₃NH), 1.16 (t, J = 7.2 Hz, 3H, CH₃); ¹³C-NMR (101 MHz, Acetone-d₆) δ (ppm) 173.8 (NHC=O), 172.0 (O-C=O), 141.2 (ArC-CH), 128.7 (ArCH), 128.2 (ArCH), 126.4 (ArCH), 64.4 (C-3), 60.8 (OCH₂), 57.8 (C-5), 57.6 (C-4), 33.9 (NHCH₃), 13.6 (CH₃). all-cis **5c**: TLC (Ethyl acetate, $R_f = 0.26$); ¹H-NMR (400 MHz, CDCl₃) δ (ppm) 7.33-7.29 (m, 3H, ArH), 7.18-7.16 (m,

2H, ArH), 6.64 (s, 1H, CH₃N<u>H</u>), 5.00 (d, J = 9.6 Hz, 1H, H-5), 4.10 (d, J = 9.1 Hz, 1H, H-3), 3.81-3.76 (m, 1H, H-4), 3.73-3.61 (m, 2H, OCH₂), 2.15 (s, 3H, C<u>H₃</u>NH), 0.93 (t, J = 7.3 Hz, 3H, CH₃); ¹³C-NMR (101 MHz, CDCl₃) δ (ppm) 175.3 (NHC=O), 169.7 (O-C=O), 137.7 (Ar<u>C</u>-CH), 128.8 (ArCH), 127.2 (ArCH), 126.9 (ArCH), 61.2 (C-4), 59.4 (C-3), 57.6 (C-5), 52.1 (OCH₂), 31.1 (NHCH₃), 13.8 (CH₃).

Reduction of 4-carboethoxy-3-methylamino-2-oxo-5-phenyl-3-pyrrolines (4) by sodium triacetoxy-borohydride (NaBH(OAc)₃)

The method was adapted from literature [9]. A solution of NaBH(OAc)₃ was prepared by the addition of sodium borohydride (NaBH₄) (0.73 g, 19 mmol) to glacial acetic acid (5.6 mL, 96 mmol) at 0 °C and the mixture was stirred for 30 minutes at room temperature with some evolution of hydrogen gas. Then, 4-carboethoxy-3-methylamino-2-oxo-5-phenyl-3-pyrroline (4) (1.01 g, 4 mmol) in acetonitrile (25 mL)

pyrroline (4) (1.01 g, 4 mmol) in acetonitrile (25 mL) was transferred into the previous mixture. The resulting mixture was stirred vigorously for 48 hours before being neutralized by saturated Na₂CO₃ solution. Upon extraction by dichloromethane, the organic phase was washed with brine and dried over anhydrous MgSO₄. The solvent was removed from the organic phase *in vacuo* to give a white solid. From TLC, FT-IR and NMR characterization experiments, it was concluded that the starting material 4 was recovered.

Analytical data: TLC (Ethyl acetate, $R_f = 0.79$); FT-IR (ATR) \bar{v} (cm⁻¹) 3351 (N-H), 2980 (C-H), 1698 (C=O), 1667 (C=O), 1633; ¹H-NMR (400 MHz, CDCl₃) δ (ppm) 7.30-7.21 (m, 5H, ArH), 6.43 (s, 1H, CH₃NH), 5.14 (s, 1H, ArCHNH), 4.04-3.93 (m, 2H, OCH₂), 3.35 (s, 3H, CH₃NH), 1.70 (s, 1H, CH₃NH), 1.03 (t, J = 7.1 Hz, 3H, CH₃); ¹³C-NMR (101 MHz, CDCl₃) δ (ppm) 167.9 (O-C=O), 166.6 (NHC=O), 147.1 (C=C-NHCH₃), 138.9 (ArC-CH), 128.4 (ArCH), 128.1 (ArCH), 127.4 (ArCH), 104.8 (C=C-C=O), 59.5 (OCH₂), 57.9 (ArCHNH), 30.2 (NHCH₃), 14.1 (CH₃).

Reduction of 4-carboethoxy-3-methylamino-2-oxo-5-phenyl-3-pyrroline (4) by sodium cyanoborohydride (NaBH₃CN)

The method was adapted from literature [8]. Traces of bromocresol green was added to 4-carboethoxy-3methylamino-2-oxo-5-phenyl-3-pyrroline (4) (1.00 g, 4 mmol) in methanol (20 mL) while stirring followed by NaBH₃CN (0.97 g, 15 mmol). Dilute MeOH-HCl mixture was added dropwise until the colour of the reaction mixture turned yellow. More MeOH-HCl was added to the mixture periodically to maintain the yellow colour (pH ~4) with TLC monitoring. After 24 hours, the reaction was quenched by dropwise addition of 0.1 N NaOH solution (saturated with NaCl) until the mixture turned blue. The crude product was extracted by ethyl acetate and the organic phase was washed with brine and dried over anhydrous MgSO₄. The solvent was evaporated under vacuum and the residue was purified by column chromatography elution) to give the diastereomers of 4-carbethoxy-3-methylamino-2-oxo-5-phenylpyrrolidine; all-trans **5b** (Yield: 174.7 mg, 34.7%) and *all-cis* **5c** (Yield: 97.6 mg, 19.4%).

Analytical data: FT-IR (ATR) \bar{v} (cm⁻¹) 3391 (N-H), 3306 (N-H), 2977 (C-H), 1718 (C=O), 1698 (C=O); all-trans **5b**: TLC (Ethyl acetate, $R_f = 0.49$); ¹H-NMR (400 MHz, CDCl₃) δ (ppm) 7.37-7.31 (m, 5H, ArH), 6.42 (s, 1H, CH₃NH), 4.78 (d, J = 8.2 Hz, 1H, H-5), 4.18-4.16 (m, 2H, OCH₂), 3.84 (d, J = 9.6 Hz, 1H, H-3), 3.06 (t, J = 8.9 Hz, 1H, H-4), 2.16 (s, 3H, CH_3NH), 1.20 (t, J = 7.1 Hz, 3H, CH₃); ¹³C-NMR (101 MHz, CDCl₃) δ (ppm) 173.9 (NHC=O), 171.7 (O-C=O), 139.5 (ArC-CH), 129.0 (ArCH), 128.7 (ArCH), 126.5 (ArCH), 63.6 (C-3), 61.7 (OCH₂), 57.9 (C-5), 55.9 (C-4), 31.1 (NHCH₃), 14.1 (CH₃). all-cis **5c**: TLC (Ethyl acetate, $R_f = 0.26$); ¹H-NMR (400 MHz, CDCl₃) δ (ppm) 7.33-7.29 (m, 3H, ArH), 7.18-7.16 (m, 2H, ArH), 6.64 (s, 1H, CH_3NH_2), 5.00 (d, J = 9.6 Hz, 1H, H-5), 4.10 (d, J = 9.1 Hz, 1H, H-3), 3.81-3.76 (m, 1H, H-4), 3.73-3.61 (m, 2H, OCH₂), 2.15 (s, 3H, CH₃NH), 0.93 (t, J = 7.3 Hz, 3H, CH₃); ¹³C-NMR (101 MHz, CDCl₃) δ (ppm) 175.3 (NHC=O), 169.7 (O-C=O), 137.7 (ArC-CH), 128.8 (ArCH), 127.2 (ArCH), 126.9 (ArCH), 61.2 (C-4), 59.4 (C-3), 57.6 (C-5), 52.1 (OCH₂), 31.1 (NHCH₃), 13.8 (CH₃).

Results and Discussion

4-carbethoxy-3-hydroxy-2-oxo-5-phenyl-3-pyrroline (1) were prepared through one-pot multicomponent reaction (MCR) by refluxing equimolar sodium diethyl oxalacetate and benzaldehyde with excess aqueous ammonia in ethanol as developed by Metten et. al. (Scheme 1) [15]. The product was more stable in the enol rather than the keto form, consistent with previous findings [16-19]. The moderate yield was compromised for the ease of the purification process and overall facile procedure.

Afterwards, treatment of **1** with ammonium formate gave enamino ester **2** with a good yield via Leuckart reaction (Scheme 2) [2,3]. Hydrogenation of **2** in the presence of 10% Pd/C in acetic acid for 22 hours was ineffective, recovering the starting material. To our

best knowledge, there is yet to be a report on a successful reduction of primary enamino esters such as **2**. Wang and co-workers described that the enamino group has to be protected prior to the hydrogenation to gain successful conversions [20]. Other works of literature suggested that there should be at least one substituent on the enamino functionality for the procedure to work [7-13]. Perhaps, the conjugated π system and alternating intramolecular hydrogen bonding form very stable 6-membered resonance structures (Figure 3) therefore preventing interaction with the metal catalyst.

However, methylamination of 1 in the presence of formic acid afforded secondary β -enamino ester (4), which was then reacted through four different reduction systems (Scheme 3).

Scheme 1. Synthesis of 4-carbethoxy-3-hydroxy-2-oxo-5-phenyl-3-pyrroline (1) via one-pot MCR

HO HO NH₄

EtOH

Reflux

$$H_2N$$
 H_2 , Pd/C

 H_2N
 $AcOH$
 H_2N
 $AcOH$
 H_3
 $AcOH$
 H_4
 H_2
 H_4
 H_5
 H_4
 H_5
 H_5

Scheme 2. Amination of 1 and the attempt to catalytically hydrogenate 2 over Pd/C

Ayisy Amirul Afti et al: DIASTEREOSELECTIVE REDUCTION OF ENDOCYCLIC β -ENAMINO ESTER: AN APPROACH TO PREPARE DIASTEREOPURE MULTISUBSTITUTED PYRROLIDINE β -AMINO ESTERS

Figure 3. Intramolecular hydrogen bonding and the resonance structures of 2.

* The absolute configuration was not determined. Thus, both possible enantiomers are displayed.

Scheme 3. Methylamination of 1 and various reduction protocols of 4.

Pd/C hydrogenation of 4 displayed diastereoselectivity (d.r. = 42 : 19 : 39) of three separable mixtures of β-amino ester diastereomers (5ac) with low yields (4 to 10%) (Table 1). Hydrogenation of 5 in the presence of Pd(OH)₂ on charcoal was more diastereoselective (d.r. = 51:3:46) than Pd/C but afforded an even poorer yield (0.1 to 2.2%) of isomers (5a-c). Both catalytic processes involved the syn addition of hydrogens onto the double bond resulting in a nearly equivalent d.r. of 5a (cistrans) and 5c (all-cis) products with a minor anti addition causing the formation of **5b** (all-trans) product, in agreement with one of our previous findings [17].

The treatment with sodium borohydride, NaBH4 and acetic acid to form insitu sodium triacetoxyborohydride, NaBH(OAc)₃ failed to reduce compound 4. On the other hand, reduction using sodium cyanoborohydride (NaBH3CN) in acidic medium gained the mixture of 5b and 5c diastereomers, giving superior stereochemical control (d.r. = 64 : 36) than catalytic hydrogenations, with better yields. Deustch et. al. observed similar diastereomeric selectivities when reducing acyclic βenamino ester derivatives by the same protocol [8].

Table 1. Stereoselective reduction of 4

Doducing A cont	Isol	Diastereomeric ratio		
Reducing Agent —	5a	5b	5c	(d.r.)**
Pd/C, H ₂	10.3	4.5	9.6	42:19:39
$Pd(OH)_2/C, H_2$	2.2	0.1	2.0	51:3:46
NaBH(OAc) ₃	-	-	-	-
NaBH ₃ CN	-	34.7	19.4	64:36

^{*}Isolated yield of each diastereomeric product obtained after purification by column chromatography.

All resulting diastereomers were studied through nuclear magnetic resonance (NMR) experiments to assign their configurations. For instance, Nuclear Overhauser Effect Spectroscopy (NOESY) correlation between the hydrogen at C-4 (3.01 ppm) and aryl proton (7.35 ppm) in **5b** (all-trans) product confirmed that both the hydrogen and the phenyl ring are on the same side (Figure 4) whereby in 5c (all-cis) product, the correlation between the hydrogens at C-4 (3.86 ppm) and C-5 (5.11 ppm) were observed, indicating their close proximities to each other. This claim is supported by the low proton NMR (¹H-NMR) chemical shift value of the hydrogen on C-4 of 5b compared to that of 5c due to the anisotropic effect of being near the phenyl ring. Moreover, 5b diastereomer showed significantly higher values of $J_{4,5}$ coupling constant than 5c (Table 2).

Alternatively, the assignment of *cis*-configuration between protons on C-4 and C-5 of **5c** isomer can be further proven by another anisotropy experienced by protons of its ester moiety indicated by their lower chemical shift values in comparison to those of **5a** (*cistrans*) and **5b** diastereomers. On another note, the NOESY correlation between the hydrogen on C-4 (3.01 ppm) with methylamine proton (2.51 ppm) of **5b** led to the notion that the protons on C-3 and C-4 were *trans* to each other while for **5a**, its C-4 proton (3.35 ppm) correlated with the one on C-3 (3.60 ppm) thus they were assigned as *cis*.

The mechanistic pathway that we proposed for these catalytic hydrogenations is displayed in Scheme 4. Syn addition of hydrogens on either side of the C=C of the enamino ester caused both the methylamine and ester groups to be on the same side. These structural changes

^{**}Diasteremeric ratio (d.r.) was determined based on the isolated yield after column chromatography.

gave rise to steric clashes between the ester and phenyl ring that determined which conformer was more favourable. The steric strain in 5c (ester and phenyl groups located near to each other) contributed to a slightly lower yield compared to the thermodynamic product 5a (the groups were on opposite sides).

Anti addition of hydrogens by metal-catalysed hydrogenation was initiated by the formation of an enolate intermediate through the protonation of one of the prochiral centres which are C-3 in **5b**, the less hindered site (Scheme 4). The following step involved the addition of another hydrogen on C-4 selectively to form a stable conformer whereby the ester group and phenyl ring were situated on different planes (lower steric strain) thus resulting in the *trans*-position between the hydrogens on C-3 and C-4 [10].

NaBH₃CN reduction began with a rate-determining step of acid protonation on C-4 of **4** from either side of the C=C of the enamino ester, thus forming respective iminium intermediates (Scheme 5) [21]. Then, an attack by cyanoborohydride from the less crowded site (away from the phenyl ring) restored the nitrogen lone pair electrons. The reagent selectively favoured the formation of **5b** over **5c** due to the greater strain between ester and phenyl groups in **5c**, consequently causing the latter to be less energetically stable.

The poor yield of Pd(OH)₂ hydrogenation compared to Pd/C and the unsuccessful reduction by NaBH(OAc)₃ can be explained by the bulkiness of the reagent structures causing severe steric hindrance that antagonized the reactions.

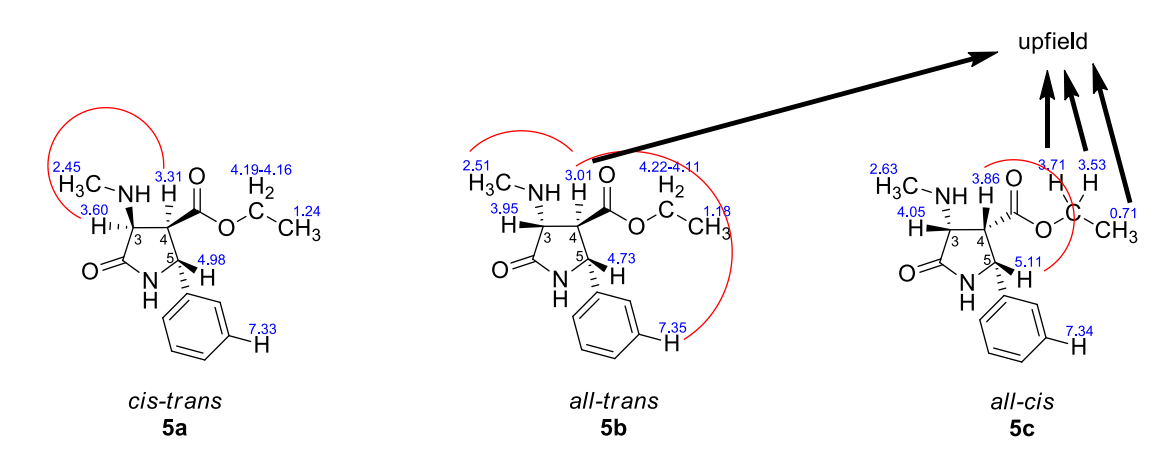
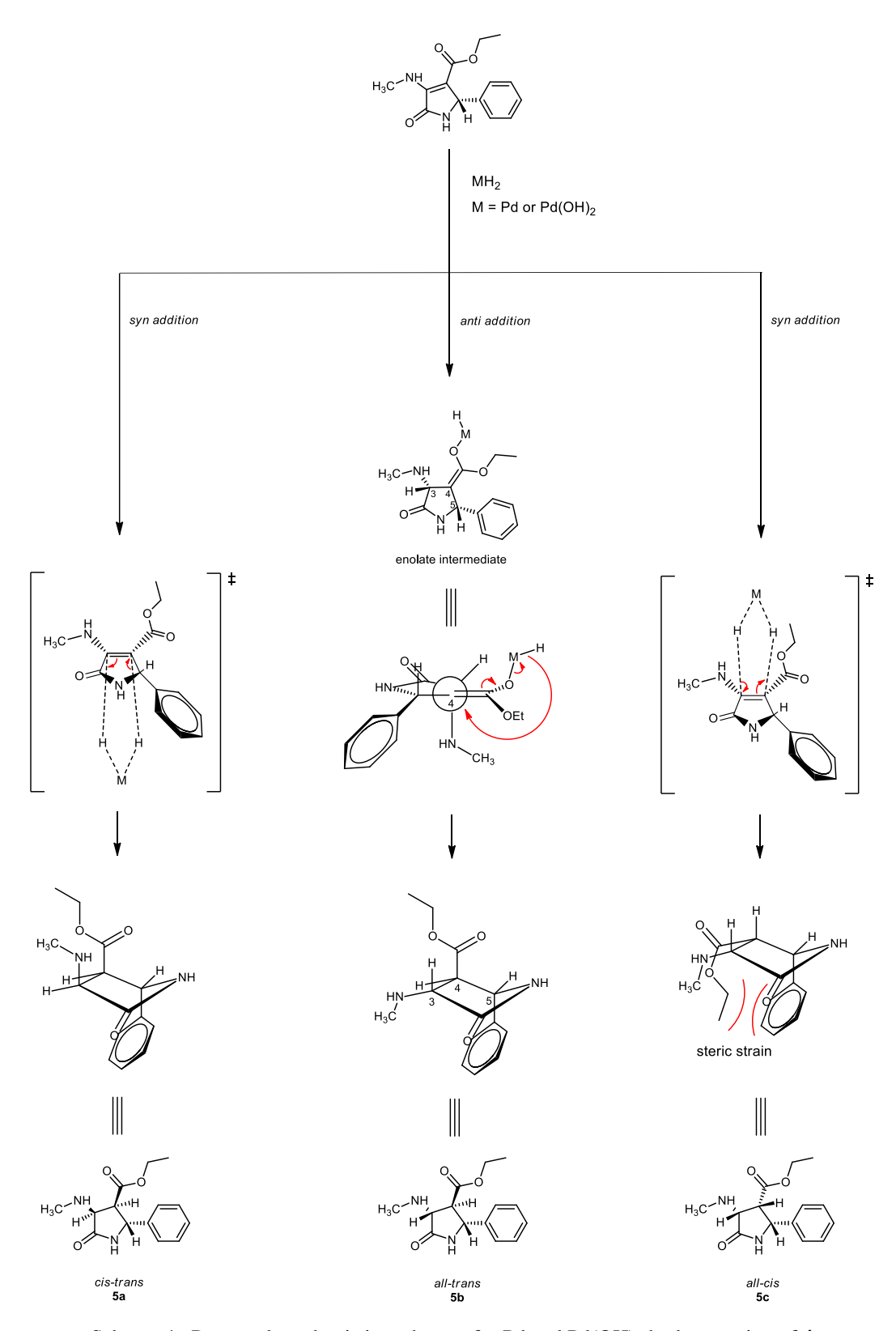


Figure 4. ¹H-NMR shift values and NOESY correlations of diastereomers 5a-c

Table 2. Selected ¹H-NMR data for diastereomers **5a-c** in methanol-d₄

Compound —	Sh	ift value, δ (pp	m)	Coupling constant, J (Hz)		
	Н-3	H-4	Н-5	Н-3	H-4	H-5
5a	3.60	3.35	4.99	8.4	_*	4.8
5b	3.95	3.01	4.73	9.6	8.5	8.2
5c	4.05	3.86	5.11	6.9	6.9	6.4

^{*}H-4 of 5a showed a multiplet pattern



Scheme 4. Proposed mechanistic pathways for Pd and Pd(OH)₂ hydrogenation of 4

Ayisy Amirul Afti et al: DIASTEREOSELECTIVE REDUCTION OF ENDOCYCLIC β-ENAMINO ESTER: AN APPROACH TO PREPARE DIASTEREOPURE MULTISUBSTITUTED PYRROLIDINE β-AMINO ESTERS

Scheme 5. Plausible reaction mechanism for reduction of 4 by NaBH₃CN.

Conclusion

Overall, the stereochemical control for this class of functional group depends strongly on the position of the ester group in regards to the phenyl ring after the protonation/reduction steps i.e. if they are on the same plane, the lower the preference for the formation of said diastereomer. This brief experiment shows that endocyclic β -enamino ester (4) can be reduced with excellent diastereoselectivity by NaBH₃CN (d.r. = 64:

36), in addition to its moderate turnover percentage (54.1%). Hydrogenations on Pd and Pd(OH)₂ surfaces suffered from poor selectivities (d.r. = 42:19:39 and d.r. = 51:3:46, respectively) and yields (0.1 to 10.3%) with unexpected anti additions of hydrogens while NaBH(OAc)₃ reduction recovered the starting material. Nevertheless, we have successfully employed some of these reduction strategies to prepare chiral

cyclic β -amino ester with satisfying diastereomeric purity.

Acknowledgement

We would like to thank University Teknologi MARA (UiTM) for providing the facilities to conduct the research and International Islamic University Malaysia (IIUM) along with the Malaysian Ministry of Higher Education (MoHE) for the financial support (FRGS/1/2017/STG01/UIAM/03/2 [Project ID: 11794]).

References

- 1. Xin, D., & Burgess, K. (2014). A Chemoselective Route to β-Enamino Esters and Thioesters. *Organic Letters*, 16(8), 2108-2110.
- Southwick, P. L., & Hofmann, G. H. (1963). Compounds in the pyrrolo[3,4-d]pyrimidine series. Syntheses based on 2, 3-dioxopyrrolidines. *The Journal of Organic Chemistry*, 28(5), 1332-1336.
- 3. Madhav, R., Dufresne, R. F., & Southwick, P. L. (1973). The preparation of derivatives 9-oxo-2,3,4,9-tetrahydro-1*H*-pyrrolo[3,4-*b*]quinoline and 7-oxo-7,9,10,11-tetrahydro-8*H*-benzo[*h*]pyrrolo [3,4-*b*]quinoline. *Journal of Heterocyclic Chemistry*, 10(2), 225-228.
- Jia, Z., Nagano, T., Li, X., & Chan, A. S. (2013). Iodide-Ion-Catalyzed Carbon—Carbon Bond-Forming Cross-Dehydrogenative Coupling for the Synthesis of Indole Derivatives. *European Journal* of Organic Chemistry, 2013(5), 858-861.
- David, O., Fargeau-Bellassoued, M. C., & Lhommet, G. (2002). A short and convenient synthesis of chiral heterocyclic β-enamino esters from halogeno acetylenic esters. *Tetrahedron Letters*, 43(19), 3471-3474.
- Calvet, S., David, O., Vanucci-Bacqué, C., Fargeau-Bellassoued, M. C., & Lhommet, G. (2003). Chiral heterocyclic β-enamino esters: convenient synthesis and diastereoselective reduction. *Tetrahedron*, 59(33), 6333-6339.
- 7. Hart, D. J., Hong, W. P., & Hsu, L. Y. (1987). Total synthesis of (±)-Lythrancepine II and (±)-Lythrancepine III. *The Journal of Organic Chemistry*, 52(21), 4665-4673.

- 8. Deutsch, H. M., Ye, X., Shi, Q., Liu, Z., & Schweri, M. M. (2001). Synthesis and pharmacology of site specific cocaine abuse treatment agents: a new synthetic methodology for methylphenidate analogs based on the Blaise reaction. *European Journal of Medicinal Chemistry*, 36(4), 303-311.
- 9. Calvet-Vitale, S., Vanucci-Bacqué, C., Fargeau-Bellassoued, M. C., & Lhommet, G. (2005). Stereocontrolled reduction of chiral pyrrolidine and piperidine β-enamino esters: formal enantioselective synthesis of (+)-calvine. *Tetrahedron*, 61(32), 7774-7782.
- 10. David, O., Blot, J., Bellec, C., Fargeau-Bellassoued, M. C., Haviari, G., Célérier, J. P., & Gardette, D. (1999). Enamino ester reduction: A short enantioselective route to pyrrolizidine and indolizidine alkaloids. Synthesis (+)laburnine,(+)-tashiromine, and (-)isoretronecanol. The of Journal Organic Chemistry, 64(9), 3122-3131.
- 11. Haviari, G., Célérier, J. P., Petit, H., & Lhommet, G. (1993). Asymmetric synthesis with chiral hydrogenolysable amines. A short synthesis of (-)-isoretronecanol. *Tetrahedron letters*, *34*(10), 1599-1600.
- 12. Zhang, X., Mi, N., Liu, H., & Liu, Y. (2019). An approach to highly efficient reduction of β-enamino esters: A convenient synthesis of β-amino esters. *Journal of Chemical Research*, 43(5-6), 196-200.
- 13. Cimarelli, C., & Palmieri, G. (1996). Stereoselective reduction of enantiopure β-enamino esters by hydride: a convenient synthesis of both enantiopure β-amino esters. *The Journal of Organic Chemistry*, *61*(16), 5557-5563.
- 14. Furukawa, M., Okawara, T., Noguchi, Y., & Terawaki, Y. (1979). Asymmetric syntheses of β-amino acids by the reduction of enamines. *Chemical and Pharmaceutical Bulletin*, 27(9), 2223-2226.
- 15. Metten, B., Kostermans, M., Van Baelen, G., Smet, M., & Dehaen, W. (2006). Synthesis of 5-aryl-2-oxopyrrole derivatives as synthons for highly substituted pyrroles. *Tetrahedron*, 62(25), 6018-6028.

Ayisy Amirul Afti et al: DIASTEREOSELECTIVE REDUCTION OF ENDOCYCLIC β-ENAMINO ESTER: AN APPROACH TO PREPARE DIASTEREOPURE MULTISUBSTITUTED PYRROLIDINE β-AMINO ESTERS

- 16. Mohammat, M. F., Najim, N., Mansor, N. S., Sarman, S., Shaameri, Z., Zain, M. M., & Hamzah, A. S. (2011). Synthesis and bioactivity of some 2oxo-5-aryl-3-hydrazone and 2-oxo-5-aryl-4hydrazone pyrrolidine derivatives. ARKIVOC: Online Journal of Organic Chemistry.
- 17. Mohammat, M. F., Mansor, N. S., Shaameri, Z., & Hamzah, A. S. (2015). Diastereoselective Reduction of 2,3-Dioxo-4-carboxy-5-substituted Pyrrolidines Using NaBH₄/AcOH and Heterogenous Hydrogenation Reactions. *Journal of the Korean Chemical Society*, 59(1), 31-35.
- Rashid, F. N. A. A., Mohammat, M. F., Shaameri, Z., & Hamzah, A. S. (2019). Synthesis of novel 3,4-fused pyrazolidinone γ-lactam bicyclic moieties from 2,3-dioxo-4-carboxy-5-(substituted) pyrrolidines. *Organic Communications*, 12(3), 121-131.

- Rashid, F. N. A. A., Mohammat, M. F., Bouchamma, F. E., Shaameri, Z., & Hamzah, A. S. (2020). Facile Reduction of β-Enamino Oxopyrrolidine Carboxylates Mediated by Heterogeneous Palladium Catalyst. *Russian Journal of Organic Chemistry*, 56(6), 1082-1088.
- 20. Wang, G. T., Chen, Y., Wang, S., Gentles, R., Sowin, T., Kati, W., ... & Kempf, D. (2001). Design, synthesis, and structural analysis of influenza neuraminidase inhibitors containing pyrrolidine cores. *Journal of medicinal chemistry*, 44(8), 1192-1201.
- Borch, R. F., Bernstein, M. D., & Durst, H. D. (1971). Cyanohydridoborate anion as a selective reducing agent. *Journal of the American Chemical Society*, 93(12), 2897-2904.

Malaysian Journal of Analytical Sciences (MJAS)



Published by Malaysian Analytical Sciences Society

CHROMIUM (VI) ANALYSIS IN EFFLUENTS USING LIQUID-LIQUID EXTRACTION COUPLED WITH FLAME ATOMIC ABSORPTION SPECTROMETRY

(Analisis Kromium (VI) dalam Efluen Menggunakan Pengekstrakan Cecair-Cecair Bersama Spektrometri Serapan Nyalaan Atom)

Nguyen Cong-Hau¹, Le-Thi Anh-Dao¹, Nguyen Thanh-Nho¹*, Le-Thi Huynh-Mai², Le Nhon-Duc³, Do Minh-Huy¹

¹Faculty of Environmental and Food Engineering, Nguyen Tat Thanh University, Ho Chi Minh City, Vietnam ²Faculty of Chemistry, University of Science, Vietnam National University Ho Chi Minh City, Vietnam ³Warrantek Joint Stock Company, Testing Center, Can Tho City, Vietnam

*Corresponding author: ntnho@ntt.edu.vn

Received: 1 September 2021; Accepted: 10 January 2022; Published: 28 April 2022

Abstract

Simple sample preparation was investigated and developed to selectively determine Cr(VI) in wastewater samples or effluents based on the liquid-liquid extraction principle using tetrabutylammonium hydrogensulfate (TBAHS) as the ion-pair reagent in an acidic medium. TBAHS was prepared in an organic solvent to improve the extraction efficiency. The extracted Cr(VI) in the organic phase endured the acid digestion, and its atomic absorption was measured at 357.9 nm. The influences of several working parameters, namely, organic solvents (methyl isobutyl ketone-MIBK, dichloromethane-DCM, and chloroform), pH values (lower than 1.0, 1.0, 2.0, and 3.0) in the aqueous phase, TBAHS concentrations in the organic solvent (0.02, 0.04, 0.05, and 0.06 mol L⁻¹), extraction duration (from 3 to 30 minutes), number of extraction cycles (single or repeated extraction), sample preservation duration at ambient temperature, and co-existence of Cr(III) in the sample matrices, were investigated to discover the optimized working parameters. The results showed that dichloromethane (DCM) was the most effective extraction solvent. The most favorable conditions for complex formation were determined as follows: a pH of around 1.0 to 3.0; 0.05 mol L⁻¹ TBAHS prepared in DCM, triple extraction, and a shaking duration of 15 minutes for each extraction cycle. The calibration curve was linear in the range of 0.05, 0.10, 0.20, 0.40, 0.60, 0.90, 1.2, 1.5 and 2.0 mg L^{-1} , and the regression equation was y =0.1068x + 0.0012 with $R^2 = 0.9994$, exhibiting goodness of linearity. The method detection and quantification limit values were estimated to be 0.012 mg L^{-1} and 0.04 mg L^{-1} , respectively. The repeatability (RSD_r = 0.71%) and reproducibility (RSD_R = 1.1%) were favorable according to the requirements presented in Appendix F of AOAC (2016) for analytical method validation. The proposed method was applied to real wastewater samples and spiked samples, showing very low Cr(VI) concentrations for most samples and proper recoveries (91.1-109%).

Keywords: Cr(VI), Cr(III), liquid-liquid extraction, TBAHS, dichloromethane, DCM, ion-pair reagent

Abstrak

Penyediaan sampel yang mudah telah dikaji dan dibangunkan bagi penentuan terpilih Cr(VI) di dalam air sisa atau efluen berdasarkan prinsip pengekstrakan cecair-cecair menggunakan tetrabutylammonium hidrogensulfat (TBAHS) sebagai reagen pasangan ion di dalam medium berasid. TBAHS telah disediakan dalam pelarut organik bagi tujuan meningkatkan keberkesanan pengekstrakan. Cr(VI) yang telah diekstrak di dalam fasa organik melalui penghadaman asid, dan serapan atom telah diukur pada 357.9 nm. Pengaruh parameter seperti pelarut organik (metil isobutil keton-MIBK, diklorometana-DCM, dan klorofom), nilai pH (dibawah 1.0, 1.0, 2.0 dan 3.0) di dalam fasa akues, kepekatan TBAHS di dalam pelarut organik (0.02, 0.04, 0.05, dan 0.06 mol L-1), tempoh pengekstrakan (dari 3 hingga 30 minutes), bilangan kitaran pengekstrakan (pengekstrakan tunggal atau ulangan), tempoh pengawetan sampel pada suhu sekitar, dan kehadiran bersama Cr(III) dalam matrik sampel turut dikaji untuk penentuan parameter kerja yang optimum. Hasil kajian menunjukkan diklorometana (DCM) paling efektif sebagai pelarut pengekstrakan. Keadaan paling baik untuk penghasilan kompleks ditentukan seperti berikut: pH antara 1.0 hingga 3.0; 0.05 mol L-1 TBAHS disediakan dalam DCM, tiga kali pengekstrakan, dan masa goncangan ialah 15 minit bagi setiap kitaran pengekstrakan. Lengkung kalibrasi adalah linear pada julat 0.05 hingga 2.0 mg L^{-1} , dan persamaan regresi ialah y = 0.1068x + 1.0068x + $0.0012 \text{ dan } R^2 = 0.9994. \text{ Had pengesanan dan kuantifikasi telah dihitung masing-masing pada} \quad 0.012 \text{ mg } L^{-1} \text{ and } 0.04 \text{ mg } L^{-1}.$ Kebolehulangan (RSD_r = 0.71%) dan kebolehhasilan semula (RSD_R = 1.1%) adalah baik berdasarkan keperluan yang dinyatakan dalam Appendix F of AOAC (2016) bagi validasi kaedah analisis. Kaedah yang dicadang ini telah digunapakai bagi analisis sampel air sisa sebenar dan sampel yang dipaku, ia menunjukkan kepekatan Cr(VI) yang rendah dan perolehan semula yang baik (91.1-109%).

Kata kunci: Cr(VI), Cr(III), pengekstrakan cecair-cecair, diklorometana, reagen pasangan ion

Introduction

Chromium (Cr) has been known as the non-essential and toxic element for human beings and animals despite existing in trace quantities [1, 2]. The emission of Cr into the environment is mainly derived from metallurgical, electroplating, pigments, etc. The two most common species of chromium are Cr(III) and Cr(VI), whereby Cr(VI) exhibits remarkably high toxicity due to its higher solubility and flexibility than Cr(III) [3, 4], 100 times more toxic than Cr(III). Many studies have indicated death risks from lung cancers during working and direct exposure to Cr(VI). Moreover, Cr(III) is considered an essential micronutrient and is responsible for blood glucose control and lipid metabolism in mammals. Because of their toxicity differences, the determination of total Cr concentrations did not provide enough reliable and accurate information to evaluate the toxicity potentials toward the environment. Additionally, the selective determination of Cr species has helped the scientists to recognize their origins and behaviors to find adequate solutions to remove these exposed pollutants from the environment. Modern instrumental methods using ICP-OES or ICP-MS coupled with liquid chromatography have met the requirements for direct analysis of Cr species in various sample matrix due to their selectivity

and sensitivity [5, 6]. However, such methods are costly and not easily equipped in many laboratories. Therefore, another cheap, convenient, simple, and effective analytical method by using selective solvent or liquid-liquid extraction techniques (LLE) and measured on the Flame-Atomic Absorption Spectrometry (F-AAS) analysis, a common instrument for metal(loid)s quantification in various environmental laboratories, should be developed for Cr(VI) detection in complicated sample matrices such as wastewater.

For trace analysis of metal ions, solvent extraction has become a popular technique to serve the analyte enrichment and/or matrix removal purposes. Moreover, such techniques allow to easy control of the volumes of the aqueous and organic phases, which makes them possible to be coupled with any potentially suitable analytical methods for determining various metal ions. Typically, the volume of organic solvent used in the extraction is smaller than that of the sample volumes, resulting in higher enrichment factors and lower method limits of detection and quantification. At the industrial scale, solvent extraction has been utilized in chemical industries for the purification of chemical elements and/or for the separation and concentration of metals of interest [7, 8]. However, for the analytical

method development, the single application of organic solvents is usually faced with a lack of selectivity. Therefore, in order to enhance the selectivity of the LLE, complexing agents in organic solvents could be used. The separation of Cr(III) and Cr(VI) using ionexchange and/or complex reagents in organic solvent have gained considerable interests among the scientists since the last few decades, e.g., zephyramine [9], bis(2ethyl hexyl phosphoric acid) in benzene [10], diphenyl carbazide with isoamyl alcohol [11], and 4-methyl-3pentene-2-one [12]. In 2009, Kalidhasan and Rajesh published the determination of Cr(VI) based on the LLE using tetrabutylammonium iodide (TBAI) as an ion-pair reagent in methyl isobutyl ketone (MIBK) used as the extraction solvent [8]. The ion-pair complex was back-extracted using ascorbic acid to convert Cr(VI) into free Cr(III) before spectrophotometric measurement for quantification purposes. The extraction of Cr(VI) using TBAB as the ion-pair reagent in dichloromethane was performed with 95% recovery [13].

As an emerging country with rapid development in industrialization and urbanization, Vietnam has been facing the risk of serious water pollution, as the heavy metals discharged from industrial activities have identified as a threat to public health and the safety of the ecosystem. Notably, the wastewater from the mechanical, electronic, dyeing, and tanning industries, etc., potentially has high concentrations of heavy metals, e.g., Cr, and in many cases, may exceed the permitted levels. In the present study, we employed the liquid-liquid extraction (LLE) tetrabutylammonium sulfate (TBAHS) as the ion-pair reagent prepared in the extraction solvent of dichloromethane to separate Cr(VI) from the effluents into the organic phase before measuring the quantity using Flame Atomic Absorption Spectrometry (F-AAS). The preparation of TBAHS in the organic solvent instead of in water aimed to assist the chemical reaction between the analyte and the complexing agent, then to increase the extraction yield for quantification purposes. The parameters related to the LLE namely the concentrations of ion-pair reagent, extraction pH and solvents, reaction duration, numbers of extraction cycles (repeated extraction), and sample preservation as the co-existence of Cr(III), were evaluated to discover the optimized analytical conditions for real wastewater application. Moreover, in this current study, the ion-pair reagent was prepared in the extraction organic solvent instead of in the aqueous phase to increase the extraction efficiency, minimize the interferences of co-existing ions and substances, and improve the recovery of the proposed analytical method for quantification purposes.

Materials and Methods

Chemicals and reagents

All chemicals and reagents, including a stock solution of 1000 mg L⁻¹ chromium (III), methyl isobutyl ketone (MIBK), dichloromethane (DCM), and chloroform, were of the analytical grade and purchased from Merck (Germany). A stock solution of 1000 mg L⁻¹ chromium (VI) solution was prepared from potassium dichromate (≥ 99.9%, Merck, Germany). Working standard solutions of Cr(VI) were prepared daily by appropriate dilution of the 1000 mg L⁻¹ stock solution using deionized water (DIW, Millipore, USA) before each of 0.05 \mathbf{L}^{-1} Ion-pair reagents mol use. tetrabutylammonium hydrogensulfate (TBAHS) in extraction solvents namely dichloromethane (DCM), methyl isobutyl ketone (MIBK), and chloroform were prepared by dissolving 7.608 g of TBAHS in 500 mL of each of these solvents to obtain three different solutions used as the extraction solvent. Sulfuric acid of 1.0 mol L⁻¹ was prepared by properly diluting the concentrated sulfuric acid in DIW. The Cr(VI) standard solution of 1.0 mg L-1 was prepared and used for evaluating the effects of various analytical parameters in the LLE, including types of organic solvents, pH index in the aqueous phase, ion-pair reagent concentrations in the extraction organic solvent, shaking duration per each extraction cycle, and the numbers of extraction cycles (single or repeated extraction). For the assessment of sample preservation at the ambient temperature, primarily due to the effects of Cr(III) co-existence, Cr(III) and Cr(VI) standard solutions were spiked into real wastewater samples to obtain the concentrations of both species at 1.0 mg L^{-1} .

Liquid-liquid extraction

The single factor experiment of the standard solution was used for optimizing the liquid-liquid extraction (LLE). The LLE was set up as follows: 1.00 mL of 10 mg L-1 Cr(VI) was added to 40 mL glass vial with a cap. The solution pH was adjusted to different investigated values, namely below 1.0, 1.0, 2.0, and 3.0 using 1.0 mol L⁻¹ sulfuric acid and sodium hydroxide solutions. Then, 5.00 mL of TBAHS with various concentrations of 0.02, 0.04, 0.05, and 0.05 mol L^{-1} in the extraction organic solvents was added to the sample liquids to carry out the LLE. Three different organic solvents of methyl isobutyl ketone or MIBK, dichloromethane or DCM, and chloroform were investigated to discover the most suitable extraction solvent. The extraction was carried out by shaking the sample glass vial for a certain duration (3, 5, 10, 15, 20, 25, and 30 minutes). Single, double, and triple extractions were evaluated to find out the number of repeated extractions required for the highest recovery. All the organic phases were collected and transferred to another glass vial before being evaporated to the volume of around 1 mL by gentle heating at 60-70 °C. Next, approximately 1 mL of concentrated nitric acid was added. The mixture was continued to heat until the volume observed was nearly 0.3-0.5 mL (do not heat to dry). Finally, the residue in the reaction vial was dissolved carefully in DIW and transferred to a 10-mL volumetric flask. The solution was filtered through a 0.45-µm membrane before measurement at 357.9 nm on an atomic absorption spectrometer.

Flame atomic absorption spectrometry for determining Cr(VI)

Cr(VI) determination after LLE was performed on a flame atomic absorption spectrometer (AA-6650 Shimadzu, Japan), equipped with a chromium hollow cathode lamp, an air-acetylene flame atomizer. The wavelength, lamp current, and spectral bandwidth used were 357.9 nm, 10 mA, and 0.5 nm, respectively. The burner height was 12 mm and the gas flow rate were 3.0 L min⁻¹. The background correction using a Deuterium lamp was applied for all measurements. The calibration curve was developed based on the linear relationship between the Cr(VI) standard concentrations (i.e., 0.05, 0.10, 0.20, 0.40, 0.60, 0.90,

1.2, 1.5 and 2.0 mg $L^{-1})$ prepared in 0.5% (v/v) nitric acid and the respective absorbance. The method limits of detection and quantification (MLD and MLQ) were determined by simultaneously analyzing 11 blank samples using the optimized LLE and F-AAS measurement. The estimated average concentration value (\overline{x}) and standard deviation (SD) were calculated to apply in the following relationships [14, 15]: MLD = \overline{x} + 3SD and MLQ = 10/3*MLD. The repeatability and reproducibility were evaluated by calculating %RSDr and %RSDR for intra-day (six replicates, n = 6) and inter-day (three separate days). The trueness of the method was evaluated based on the recovery of the spiked samples.

Application of the proposed method to determine Cr(VI) in real effluent samples

A total number of 10 wastewater samples or effluents were randomly collected from several industrial parks around Ho Chi Minh City, based on ISO 5667-3:2003 [16] and ISO 5667-10:2020 [17]. The effluents were collected from the wastewater drain pipes of textile and electronics factories. The samples were contained in acid-washed polyethylene bottles, filtered through a 0.45-um membrane (GE Whatman Membrane Filters, GF/F), and stored at freezing conditions (-10 °C) until further analysis. These samples were analyzed by the proposed analytical method using the LLE procedure for the selective determination of Cr(VI). Besides, the Cr(VI) standard solution was spiked to these collected effluents to carry out the recovery test based on the real sample matrices, which aimed to assess the matrix effects on the analytes of interest.

Results and Discussion

Effects of extraction solvents

There are two possible ways for the extraction of Cr(VI) from the aqueous phase to the organic phase. A common approach is the formation of an ion-pair complex in the aqueous phase, using an ion-pair reagent in water. The formed complex was extracted using a suitable organic solvent. However, the produced $TBA^+-HCrO_4^-$ ion-pair complex is less polar, and therefore poorly interactive with water. The molecule has a large molecular size, and thus is less stable in water, lowering extraction efficiency. Another

approach is to prepare the ion-pair reagent in organic solvents and carry out the LLE between aqueous and organic phases. In the present study, to enhance the extraction efficiency and minimize the interferences of co-existing ions and substances, the later approach was applied, i.e., the TBAHS was prepared in organic solvents, then used for LLE. The formation of an ionpair complex could happen at the interface between the aqueous and organic phases (mostly in the aqueous phase) due to shaking effects. Such affects allow for the analyte of interest to be transferred into the organic solvent due to the stronger interaction formed by the ion-pair complex with organic solvents [8]. In the present study, three organic solvents were investigated for their potential use as extraction solvents, i.e., MIBK, DCM, and chloroform. The extraction yield (%) of Cr(VI) in the solvents (i.e., performing a single extraction within 10 minutes) is presented in Figure 1.

In descending order, the highest yield was obtained in DCM (97.4%), followed by chloroform (70.9%), and MIBK (26.9%). The differences in extraction yields could be due to the differences in the polarity of these solvents, of which MIBK has a relatively high polarity,

and thus was less effective for extraction of Cr(VI). Meanwhile, DCM (polarity index of 3.1) and chloroform (polarity index of 4.1) are less polar than MIBK [18, 19], thus exhibiting higher extraction efficiency. Between DCM and chloroform, the former exhibited a better extraction efficiency, which may be due to the lower polarity and larger size of DCM molecules that allow for more favorable solvation for the ion-pair complex. The ion-pair complex is large in size, held by relatively weak electrostatic forces (Figure 3) but possesses enough stability to be effectively extracted to the organic phase [20]. Due to the large size of the formed complex, the organic solvents with larger molecule sizes may provide favorable conditions for better extraction yields than that of smaller molecule sizes under the same working parameters. Comparing between CCl₄ and CHCl₃ as the extraction solvent, CCl₄ with lower polarity was reported to perform higher extraction efficiency [21, 22]. Therefore, in this current study, an ion-pair reagent of TBAHS was prepared in DCM as a lower polar extraction solvent for further experiments and investigations to assure the highest extraction yield.

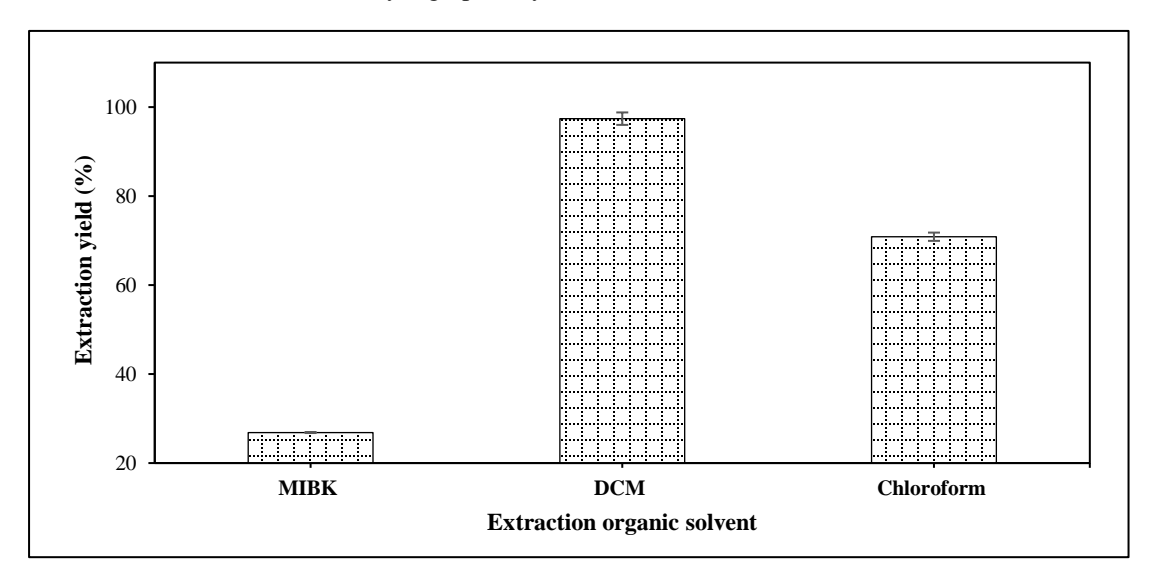


Figure 1. The Cr(VI) extraction efficiency using different extraction organic solvents

Effects of pH index in the aqueous phase

Depending on pH, predominant speciation of chromium could be changed to reach chemical equilibrium, which typically includes the formation of

chromate (CrO_4^{2-}), dichromate ($Cr_2O_7^{2-}$), hydrogen chromate ($HCrO_4^{-}$), chromic acid (H_2CrO_4), hydrogen dichromate ($HCr_2O_7^{-}$), trichromate ($Cr_3O_{10}^{2-}$), and tetrachromate ($Cr_4O_{13}^{2-}$) [23, 24]. For instance, $HcrO_4^{-}$,

Cr₂O₇²⁻, and H₂CrO₄ dominated the acid medium [25]. The different chromium species in water remarkably influence the extraction efficiency. The effects of pH on the extraction efficiency were investigated in the pH range from under 1.0 to 3.0. The extraction yield at different pH values is presented in Figure 2.

The results showed that the Cr(VI) ion quantitatively formed an ion-pair complex with TABHS at all the investigated pH, resulting in the extraction yields higher than 90%. Extraction yields generally remained unchanged within the ranges of pH tested in this current study (i.e., from less than 1.0 to 3.0). This phenomenon could be attributed to Cr(VI) mostly existing as $HCrO_4^-$ in the medium with a pH < 4.0, whereby the association was well-formed due to the big radius of $HCrO_4^-$ [26]. The TBA^+ - $HCrO_4^-$ ion

association was formed in the interaction between the two phases (mostly in the aqueous phase) according to the following schematic representation (Figure 3). Therefore, the favorable pH for complex formation may vary in a relatively wide range, and pH adjustment in the sample preparation was not strictly (from very acidic, pH lower than 1.0, to pH of 3.0) [8, 20]. At pH > 4, lower extraction efficiency has been reported in previous publications, e.g., Ouejhani et al. [7], Baig et al. [21], and Kalihasan et al. [20]. The lower extraction yield of Cr(VI) in the alkaline medium could be explained due to the presence of dominant species, the CrO₄²⁻ and its potential hydrolysis [27]. In the present study, we did not investigate the extraction at high alkaline pH. The pH around 1.0 was chosen for further experiments and investigations due to the easy and convenient adjustment.

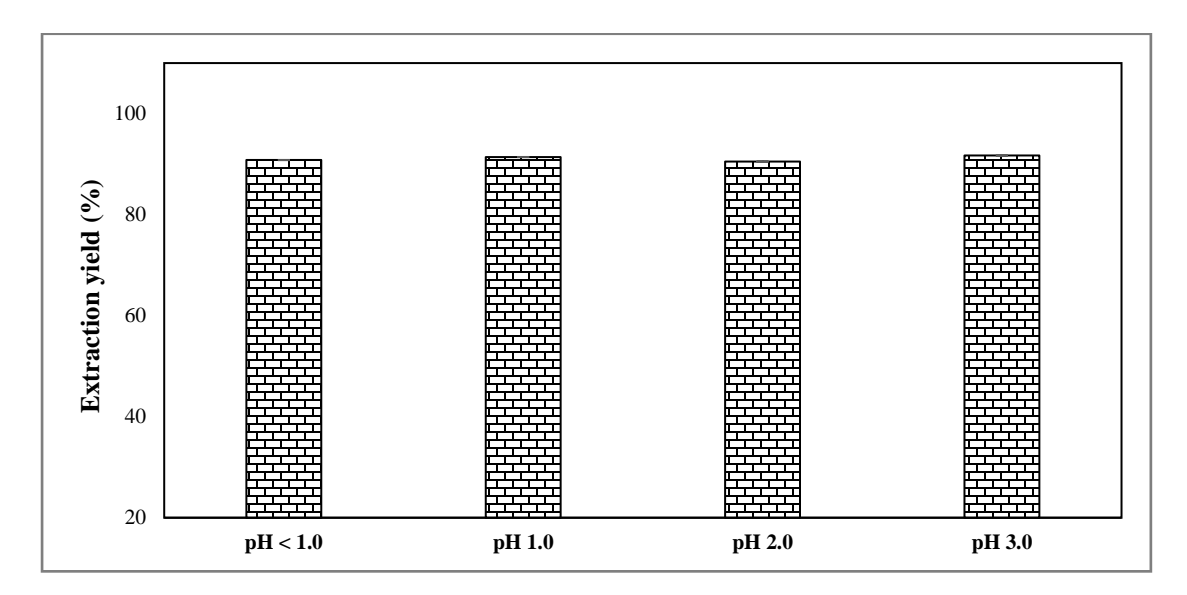


Figure 2. The Cr(VI) extraction efficiency at different pH

Figure 3. The chemical reaction for the formation of the ion-pair association

Effects of ion-pair reagent-TBAHS concentrations in DCM

As mentioned before, the ion-pair reagent of TBAHS was prepared in DCM to maximize the extraction efficiency [13]. The effects of TBAHS concentrations on the recovery were assessed, and the results are presented in Figure 4. It has been known that the formation of the ion-pair complex happens at the interface between two phases. However, the lower TBAHS concentration in the organic phase could lead to the lower concentrations of TBAHS as the ion-pair reagent at the interface, hence ineffective complexation between TBAHS and Cr(VI). Therefore, higher TBAHS concentrations were required to provide high TBAHS contents for favorable for ion-pair formation.

Moreover, as shown in Figure 4, the chemical equilibrium was shifted forward to form the ion-pair complex when the concentrations of reactants (TBAHS) were higher. The increasing recovery as the concentration of TBAHS in DCM was increased was observed as the lowest (67.1%) and highest (103%) recovery was obtained at 0.02 mol L⁻¹ and 0.05 mol L⁻¹, respectively. The TBAHS concentration of 0.04 mol L⁻¹ resulted in relatively lower recovery (98.5%) and poorer precision (%RSD of 1.2%) than that of 0.05 mol L⁻¹ (recovery of 103% and %RSDs of 0.68%). Based on the results, the 0.05 mol L⁻¹ TBAHS in DCM was used for further experiments to ensure the most favorable recovery and precision.

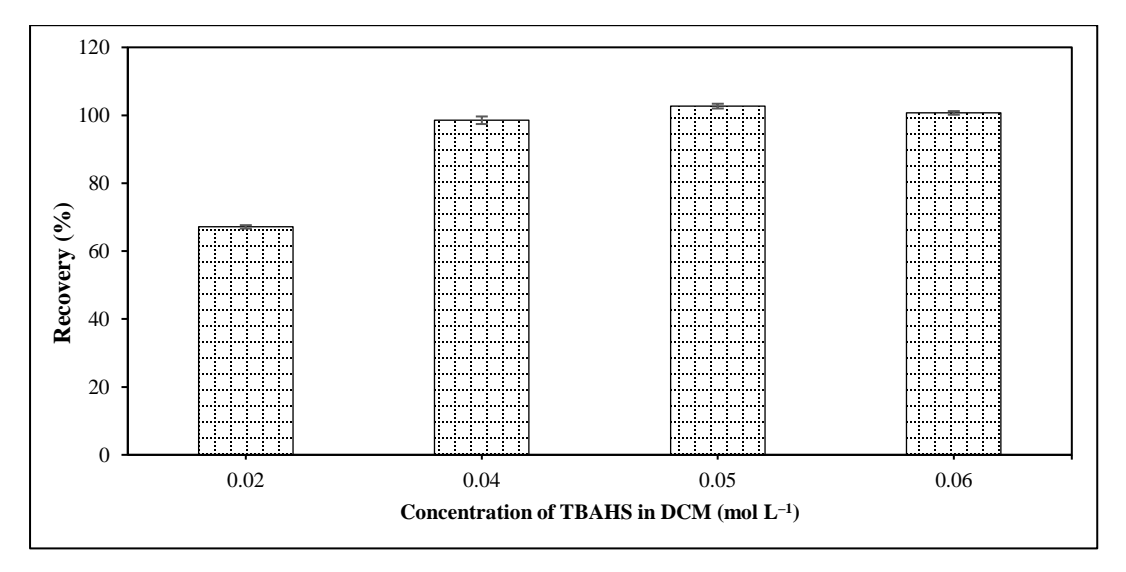


Figure 4. The extraction efficiency of Cr(VI) at different TBAHS concentrations in DCM

Effects of shaking duration and numbers of extraction cycles

During the extraction period, the shaking activity increases the interaction between Cr(VI) in the aqueous phase (wastewater samples) and the ion-pair reagents in the organic phase (DCM) at the interface of the two phases, and thus increases the chances for the formation of the ion-pair complex in the organic phase. The effects of shaking duration on the Cr(VI) recoveries are illustrated in Figure 5, which indicates that the longer shaking duration led to higher

recoveries (i.e., 80.4% to 101%). We suggest that it is necessary to apply sufficient shaking for a certain duration to equilibriate the complex formation via a chemical reaction in the complicated wastewater matrices. In the present study, the recoveries mostly remained unchanged in the extraction performed for more than 15 minutes for each extraction cycle. Therefore, 15 minutes was determined as the shaking duration for each cycle of the extraction. In addition, to ensure the quantitative extraction of Cr(VI), the number of extraction cycles (i.e., repeated extraction)

Nguyen et al: CHROMIUM (VI) ANALYSIS IN EFFLUENTS USING LIQUID-LIQUID EXTRACTION COUPLED WITH FLAME ATOMIC ABSORPTION SPECTROMETRY

was investigated. Double and triple extraction procedures were compared for their respective recoveries. The results showed higher recovery in triple

than double extractions (i.e., 89.6% and 104%, respectively), which reflected the high partition coefficient of the complex in the organic phase.

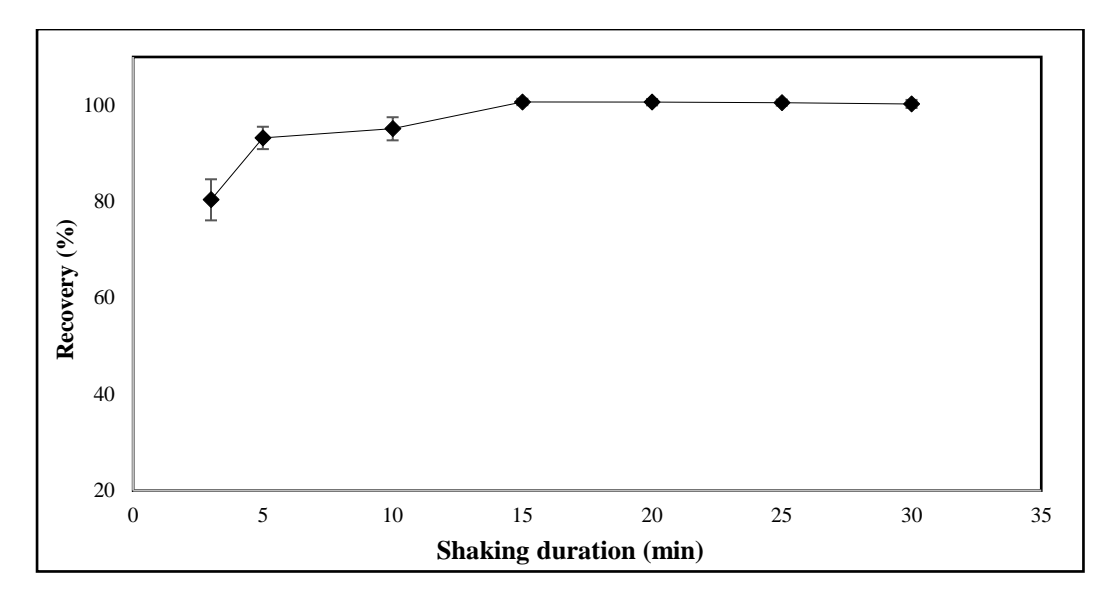


Figure 1. The variability of Cr(VI) recoveries at different shaking duration values (from 3 to 30 minutes), using 5.0 mL of DCM containing 0.05 mol L^{-1} TBAHS for 1.00 mg L^{-1} Cr(VI) standard solution

Effect of sample preservation on Cr(VI) analysis

The effects of sample matrices were investigated to obtain the most favorable sample preservation conditions at the ambient temperature. Cr(III) and Cr(VI) standard solutions were spiked into the real wastewater samples with free chromium to obtain the concentrations of 1.0 mg L⁻¹ for both species to calculate the recoveries of Cr(VI) at different preservation duration values at the ambient temperature. The sample preparation for Cr(VI) analysis was carried out based on the optimized conditions, as shown in Figure 6.

The filtered sample solution endured FAAS measurement at 357.9 nm for quantification purposes. The results in Figure 7 showed that the immediate

extraction within an hour resulted in no significant changes in the concentration of Cr(VI) as compared to its initial concentration, while the longer preservation duration resulted in lower recoveries (53.0% and 35.3% for 24-and 48-hour preservation, respectively). The result could be due to the presence of organic matters in the wastewater that may reduce Cr(VI) into Cr(III) [28, 29] and/or the presence of other substances that may interfere in the formation of Cr(VI) and the ion-pair reagent complexes. Therefore, to ensure reliable and accurate results, the wastewater samples should be analyzed right after being transported to the laboratory (within around one hour) or preserved at freezing temperature to minimize the conversion of Cr(VI) into Cr(III).

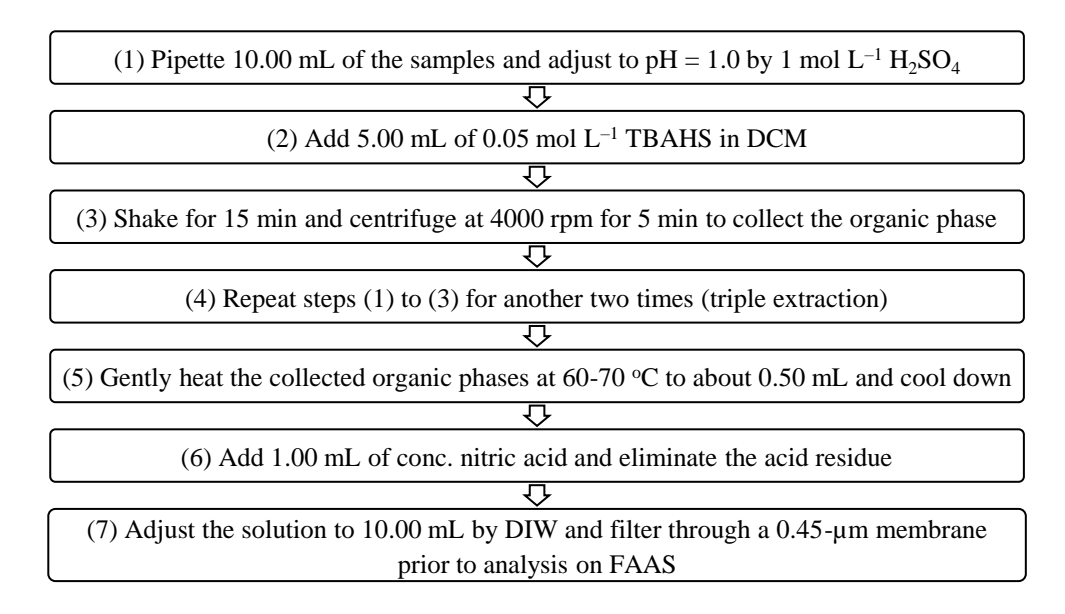


Figure 6. Optimized preparation procedure for Cr(VI) analysis

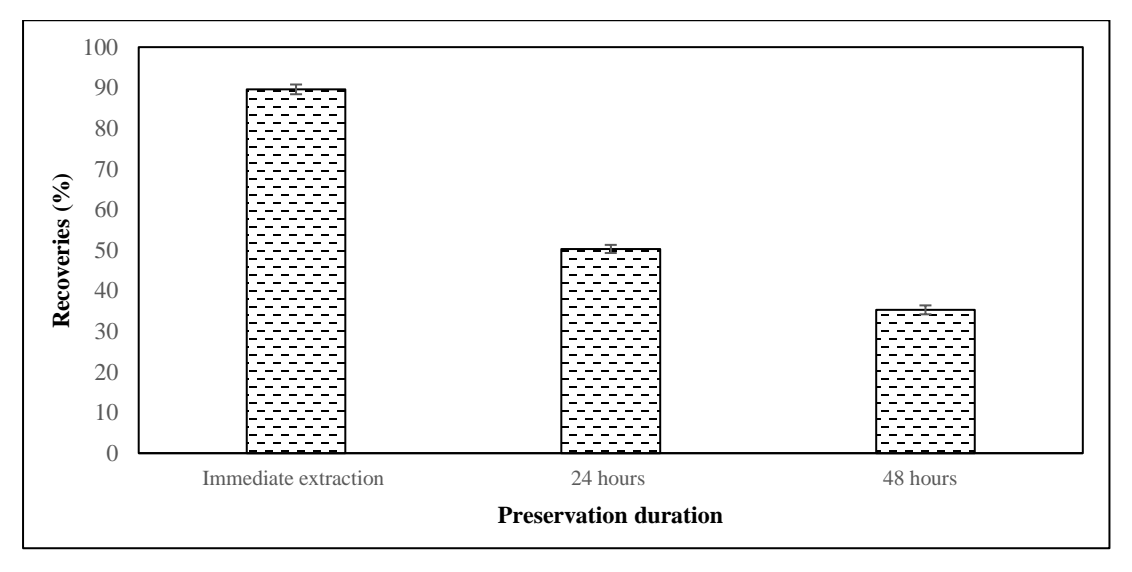


Figure 7. Recoveries of Cr(VI) in spiked samples with the co-existence of Cr(III) at different preservation duration values

Analytical method performance for analyzing Cr(VI)

The selective determination of Cr(VI) in wastewater following LLE with ion-pair reagent using FAAS was evaluated. The results are presented in Table 1. The estimated MDL and MQL were lower than regulated values in QCVN 24: 2009/BTNMT (National

Technical Regulation on Industrial Wastewater) for industrial wastewater disposed to domestic and non-domestic water sources (0.05 and 0.1 mg L^{-1}) [30]. Therefore, the analytical method could be applied for industrial wastewater control and management of Cr(VI) content. The calibration curve was established based on the linear relationship between the chromium

concentrations and their atomic absorption values, which exhibited goodness of linearity ($R^2 = 0.9994$). The RSD_r and RSD_R were used to evaluate the repeatability (within one day) and reproducibility (for three separate days) of the proposed analytical method,

which proved favorable according to the Appendix F of AOAC (2016) [31]. Besides, the recoveries varied from 91.1 to 109%, demonstrating the result accuracy obtained via the proposed method.

Table 1. Parameters for analytical method performance

Regression Equation	\mathbb{R}^2	MDL (mg L ⁻¹)	MQL (mg L ⁻¹)			Recoveries (%)
y = 0.1068x + 0.0012	0.9994	0.012	0.040	0.71	1.1	91.1-109

The variability of Cr(VI) in the effluents

The sample preparation for Cr(VI) analysis in real wastewater samples or effluents was carried out based on the optimized procedure in Figure 6. The results of Cr(VI) analysis in real effluent samples are shown in Table 2. Most of the wastewater samples exhibited remarkably low Cr(VI) (i.e., below MQL values of 0.040 mg L⁻¹). The highest Cr(VI) in wastewater was determined as 0.37 mg L⁻¹. The Cr(VI) standard solution was spiked into all these samples for the

recovery test, which demonstrated favorable recovery values (91.1-109%) according to the Appendix F of AOAC (2016) [31]. The recovery test was conducted to examine the matrix effects (mostly from the co-existing ions and organic matters present in wastewater). Therefore, the obtained high recoveries obtained in the test demonstrated the effectiveness of the LLE using the ion-pair reagent (TBAHS) for selective determination of Cr(VI) in complicated sample matrices.

Table 2. Analytical results of Cr(VI) in wastewater samples and recovery tests

Sample code	Cr(VI) (mg L ⁻¹)	Spiked Cr(VI) (mg L ⁻¹)	Recoveries (%)	RSD for Recoveries (%)
S1	n.d	1.00	96.8	1.6
S2	n.d	1.00	91.1	2.1
S3	0.37	1.00	109	1.1
S4	n.d	1.00	102	1.8
S5	0.22	1.00	94.3	1.8
S6	n.d	1.00	95.3	1.8
S7	n.d	1.00	99.7	1.7
S8	n.d	1.00	96.8	1.1
S9	0.18	1.00	96.2	1.1
S10	n.d	1.00	96.8	1.4

n.d: not detected

Conclusion

The proposed analytical method for determining Cr(VI) in wastewater or effluents demonstrated its

good sensitivity and selectivity. The measurement was performed on an inexpensive and common technique of FAAS following the liquid-liquid extraction with TBAHS as the ion-pair reagent. The TBAHS was prepared in the organic solvent to improve the extraction efficiency due to the low potential of interferences. Dichloromethane (DCM) was found to be the most favorable organic solvent for the extraction process. Various analytical parameters related to the extraction procedure were investigated to discover the optimized working parameters, including 0.05 mol L⁻¹ TBAHS as the ion-pair reagent in DCM, aqueous sample with pH index in the range of around 1.0 to 3.0 (i.e., before the extraction), triple extraction cycle or triple extraction, and 15 minutes of shaking duration for each cycle. The calibration curve was established using a standard solution with a concentration ranging from 0.05 to 2.0 mg L⁻¹ based on the linear relationship between Cr concentrations and the respective atomic absorption values at the wavelength of 357.9 nm. The method limit of detection and quantification values were estimated as 0.012 mg L^{-1} and 0.040 mg L^{-1} , respectively. This proposed analytical method could serve as a simple and low-cost procedure to determine the severely low concentrations of Cr(VI) in wastewater samples or effluents, which indicated proper recoveries (91.1-109%) for spiked samples based on the Appendix F of AOAC (2016). Moreover, the LLE approaches coupled with the addition of ionpair reagents may be applied for quantitative and qualitative analysis of other ion metals for trace analysis purposes.

Acknowledgment

The authors would like to express our gratitude and appreciation to Nguyen Tat Thanh University and University of Science, Vietnam National University Ho Chi Minh City, Vietnam for their assistance and support throughout this study.

References

- Ali, H., Khan, E. and Ilahi, I. (2019). Environmental chemistry and ecotoxicology of hazardous heavy metals: environmental persistence, toxicity, and bioaccumulation. *Journal* of Chemistry, 2019 (6730305): 1-14.
- 2. Tchounwou, P. B., Yedjou, C. G., Patlolla, A. K. and Sutton, D.J. (2012). Heavy metal toxicity and the environment. Springer.

- 3. Saha, R., Nandi, R. and Saha, B. (2011). Sources and toxicity of hexavalent chromium. *Journal of Coordination Chemistry*, 64(10): 1782-1806.
- 4. Oliveira, H. (2012). Chromium as an environmental pollutant: Insights on induced plant toxicity. *Journal of Botany*, 2012(375843): 1-8.
- 5. Jia, X., Gong, D., Xu, B., Chi, Q. and Zhang, X. (2016). Development of a novel, fast, sensitive method for chromium speciation in wastewater based on an organic polymer as solid phase extraction material combined with HPLC–ICP-MS. *Talanta*, 147: 155-161.
- Séby, F. and Vacchina, V. (2018). Critical assessment of hexavalent chromium species from different solid environmental, industrial and food matrices. *Trends in Analytical Chemistry*, 104: 54-68
- Ouejhani, A., Dachraoui, M., Lalleve, G. and Fauvarque, J.-F. (2003). Hexavalent chromium recovery by liquid-liquid extraction with tributylphosphate from acidic chloride media. *Analytical Sciences*, 19(11): 1499-1504.
- 8. Kalidhasan, S. and Rajesh, N. (2009). Simple and selective extraction process for chromium (VI) in industrial wastewater. *Journal of Hazardous Materials*, 170(2-3): 1079-1085.
- 9. Noro, J., Maruyama, K. and Komatsu, Y. (2002). Separation of chromium (III) and chromium (VI) by the combination of solvent and ion exchange methods. *Analytical Sciences/Supplements Proceedings of IUPAC International Congress on Analytical Sciences*, 2001: 1333-1336.
- Islam, F. and Biswas, R. (1979). The solvent extraction of chromium (III) with bis-(2-ethyl hexyl) phosphoric acid in benzene and other solvents. *Journal of Inorganic and Nuclear Chemistry*, 41(2): 229-233.
- 11. Gardner, M. and Comber, S. (2002). Determination of trace concentrations of hexavalent chromium. *Analyst*, 127(1): 153-156.
- Shinde, V. and Khopkar, S. (1970). Extraction of chromium (VI) with 4-methyl-3-pentene-2-one and subsequent photometric determination as diphenylcarbazide complex. Fresenius' Zeitschrift für analytische Chemie, 249(4): 239-241.

Nguyen et al: CHROMIUM (VI) ANALYSIS IN EFFLUENTS USING LIQUID-LIQUID EXTRACTION COUPLED WITH FLAME ATOMIC ABSORPTION SPECTROMETRY

- 13. Venkateswaran, P. and Palanivelu, K. (2004). Solvent extraction of hexavalent chromium with tetrabutyl ammonium bromide from aqueous solution. *Separation and Purification Technology*, 40(3): 279-284.
- Konieczka, P. and Namiesnik, J. (2016). Quality assurance and quality control in the analytical chemical laboratory: A practical approach, CRC Press.
- Ellison, S. L., Barwick, V. J. and Farrant, T. J. D. (2009). Practical statistics for the analytical scientist: A bench guide, Royal Society of Chemistry.
- 16. ISO 5667-3:2003 (2003). Water quality-Sampling-Part 3: Guidance on the preservation and handling of water samples.
- 17. ISO 5667-10:2020 (2020). Water quality-Sampling-Part 10: Guidance on sampling of waste waters.
- 18. Wypych, G. (2001). Handbook of solvents, ChemTec Publishing.
- 19. Polarity Index. https://macro.lsu.edu/howto/solvents/polarity%20index.htm. [Assess online 20 December 2020].
- 20. Kalidhasan, S., Ganesh, M., Sricharan, S. and Rajesh, N. (2009). Extractive separation and determination of chromium in tannery effluents and electroplating waste water using tribenzylamine as the extractant. *Journal of Hazardous Materials*, 165(1-3): 886-892.
- 21. Baig, J. A., Kazi, T. G., Elci, L., Afridi, H. I., Khan, M. I. and Naseer, H. M. (2013). Ultratrace determination of Cr (VI) and Pb (II) by microsample injection system flame atomic spectroscopy in drinking water and treated and untreated industrial effluents. *Journal of Analytical Methods in Chemistry*, 2013: 629495
- 22. Sereshti, Khojeh, V. and Samadi, S. (2011). Optimization of dispersive liquid–liquid microextraction coupled with inductively coupled plasma-optical emission spectrometry with the aid

- of experimental design for simultaneous determination of heavy metals in natural waters. *Talanta*, 83(3): 885-890.
- 23. Tandon, R., Crisp, P., Ellis, J. and Baker, R. (1984). Effect of pH on chromium (VI) species in solution. *Talanta*, 31(3): 227-228.
- 24. Kalidhasan, S. and Rajesh, N. (2009). Simple and selective extraction process for chromium (VI) in industrial wastewater. *Journal of Hazardous Materials*, 170(2-3): 1079-1085.
- 25. Sperling, M., Xu, S. and Welz, B. (1992). Determination of chromium (III) and chromium (VI) in water using flow injection on-line preconcentration with selective adsorption on activated alumina and flame atomic absorption spectrometric detection. *Analytical Chemistry*, 64(24): 3101-3108.
- Palmer, C. D. (1994). Natural attenuation of hexavalent chromium in ground water and soils: Superfund Technology Support Center for Ground Water.
- 27. Leśniewska, B., Jeglikowska, A. and Godlewska-Żyłkiewicz, B. (2016). Chromium speciation in wastewater and sewage by solid-phase extraction using a new diphenylcarbazone-incorporated resin. *Water, Air, & Soil Pollution*, 227(8): 1-10.
- 28. Zhang, L. and Lay, P. A. (1996). EPR Spectroscopic studies of the reactions of Cr (VI) with l-ascorbic acid, l-dehydroascorbic acid, and 5, 6-O-isopropylidene-l-ascorbic acid in water. 1 Implications for chromium (VI) genotoxicity. *Journal of the American Chemical Society*, 118(50): 12624-12637.
- 29. Xu, X.-R., Li, H.-B., Li, X.-Y. and Gu, J.-D. (2004). Reduction of hexavalent chromium by ascorbic acid in aqueous solutions. Chemosphere, 57(7): 609-613.
- 30. QCVN 24:2009/BTNMT (2009). National Technical Regulation on Industrial Wastewater.
- 31. Appendix F of AOAC (2016). Guidelines for Standard Method Performance Requirements.

Malaysian Journal of Analytical Sciences (MJAS)



Published by Malaysian Analytical Sciences Society

KAFFIR LIME OIL QUALITY GRADING USING NON-LINEAR SUPPORT VECTOR MACHINE WITH DIFFERENT KERNELS

(Penentuan Kualiti Minyak Limau Purut Dengan Menggunakan Mesin Vektor Sokongan Bukan Linear Dengan Kernel Berbeza)

Nor Syahira Jak Jailani^{1*}, Zuraida Muhammad², Nor Salwa Damanhuri², Muhd Hezri Fazalul Rahiman¹, Mohd Nasir Taib¹

¹College of Engineering, Universiti Teknologi MARA, 40450 Shah Alam, Selangor, Malaysia ²College of Engineering, Universiti Teknologi MARA, 13500 Permatang Pauh, Pulau Pinang, Malaysia

*Corresponding author: norsyahira_jakjailani@yahoo.com

Received: 23 September 2021; Accepted: 5 February 2022; Published: 28 April 2022

Abstract

Nowadays, Kaffir lime oil is one of the highly demand in the industries and sold with various market prices. But sometime the most expensive price of kaffir lime oil does not guarantee the best quality of this oil. Currently, kaffir lime oil quality grading is based only on human sensory evaluation such as smell and visual which accompanying with confusion and inconsistent result. This is due to human sensory evaluations have limitations such as easily fatigue and unable to manage mass products of the oil in time. This paper presents the classification of significant chemical compound of kaffir lime oil in the oil quality grading by using Non-Linear Support Vector Machine (NSVM). The objective of this study is to classify the quality of kaffir lime oil whether it is high or low in quality only by tuning the two different kernels into NSVM. This project has used up to 90 samples of kaffir lime oil data from various high to low quality to prepare NSVM with two different kernels. The implementation of this project was performed by using MATLAB version R2020A. The result appeared NSVM model with RBF kernel is better than NSVM model with Polynomial kernel. It was discovered that RBF kernel was able to generate 100% accuracy, specificity, precision, and sensitivity compared to Polynomial kernel. Since the finding and outcome were effective and significant, thus this study contributes a lot of benefits for future study especially in kaffir lime field.

Keywords: non-linear support vector machine, radial basis function, polynomial, kaffir lime oil, high/low quality

Abstrak

Saat ini, minyak limau purut mendapat permintaan tinggi di industri, dan dijual dengan harga yang berbeda di pasar. Tetapi harga minyak limau purut yang mahal tidak menjamin kualiti tinggi minyak ini. Pada masa ini, penilaian kualiti minyak limau purut berdasarkan penilaian deria seperti hidung dan mata menimbulkan kekeliruan dan hasil yang tidak konsisten. Ini kerana penilaian deria mempunyai batasan dan mudah letih dan tidak dapat menangani banyak sampel sekaligus. Oleh itu, kajian inimembentangkan klasifikasi sebatian kimia yang penting dalam minyak limau purut untuk gred kualiti minyak dengan

Nor Syahira et al: KAFFIR LIME OIL QUALITY GRADING USING NON-LINEAR SUPPORT VECTOR MACHINE WITH DIFFERENT KERNELS

menggunakan Mesin Vektor Sokongan Bukan Linear (NSVM). Objektif kajian ini adalah untuk mengklasifikasikan kualiti minyak limau purut sama ada berkualiti tinggi atau rendah dengan menyesuaikan dua kernel yang berbeza ke dalam NSVM. Projek ini menggunakan 90 sampel data minyak limau purut dari berkualiti tinggi hingga rendah untuk melatih NSVM dengan kernel yang berbeza. Pelaksanaan projek ini dilakukan dengan menggunakan MATLAB versi R2020A. Hasilnya menunjukkan model NSVM dengan kernel RBF lebih baik daripada model NSVM dengan kernel Polinomial. Didapati kernel RBF mampu menghasilkan ketepatan, kekhususan, ketepatan, dan kepekaan 100% berbanding dengan kernel Polinomial. Penemuan dan hasil ini berkesan dan signifikan sekali gus akan mendorong dan memberi banyak faedah untuk kajian masa depan terutama dalam bidag limau purut

Kata kunci: mesin vektor sokongan bukan linear, fungsi asas radial, polinomial, minyak limau purut, kualiti tinggi/rendah

Introduction

Kaffir lime oil or scientifically known as Citrus Hystrix which is originate from Rutacae family can be found in most Asian Countries. It was widely consumed in Asian dishes and other few industries such as aromatherapy, medicines, and fragrances. Despite all, Kaffir lime oil can also be obtained from its peels and Currently, the oil quality grading was leaves. performed manually based on human sensory evaluation. It was observed based on the physical properties of the samples. Human experienced and perception on the oil long-lasting aroma, color and odor is the only method to classify the quality of the oil. Natural sensory quality evaluation method like this produces less accuracy and subjective as it may vary from everyone. Usually, the result performed by natural sensory train grader were not consistent since it may vary to each other and the process itself take a high time consuming in the procedure [1-3]. Many researchers encountered that essential oil can be classified based on their chemical compound. This method of classification is more accurate compared to the human sensory evaluation [4]. The chemical compounds of essential oil need to be analyzed in order to classify the grading of their quality [5].

The quality of kaffir lime oil can be determined based on their abundances of major chemical compound. Many researchers found the major chemical compound of kaffir lime oil was monoterpene components. The monoterpene components discovered were Citronellal, Limonene, β -pinene, α -pinene and Sabinene [6-9] Besides that, caryophyllene was also identified by Ngan et al., researcher from Vietnam [10] and terpinene-4-ol was found by Hongatanaworkit &

Buchbauer as another major compounds of kaffir lime oil [11].

Furthermore, to overcome the inconsistent result of classifying oil grading and the amount time consuming, this project proposed a latest technique of classifying major compounds in Kaffir lime essential oil using Non-Linear Support Vector Machine (NSVM) to perform the automated grading. A SVM is a method in supervised learning that usually used for classification. SVM is used to overcome the problem of classification and regression with linear or non-linear data [12, 13]. However, NSVM will be applied when the data consumed can't be easily separated with linear line. Therefore, the kernels ought to be used to make nonseparable data into separable data. Kernels is used to map out the data from the vector input into the high dimension vector space [12]. In this project, the RBF kernel and polynomial were choosing to be tuning into NSVM. The abundance percentages (%) of major compounds act as an input and will be supplied to NSVM model develops by kernel. The output will determine the quality of kaffir lime oil whether it is low or high in quality. Hence, the oil quality and grading of kaffir lime will be classified by using an automated intelligent nonlinear support vector machine (NSVM) which regards to their chemical compounds and reduce the time-consuming during grading processes.

Materials and Methods

Sample preparations

The 90 samples data of kaffir lime oil that contains high and low in quality were used in this study that contains high and low quality. These data were obtained from 15 samples kaffir lime oil before applying synthetic data. 12 samples of kaffir lime oil obtained in the market with different various brands. All 12 brands kaffir lime oil was sent to Forest Research Institute Malaysia (FRIM) to extract the chemical compound by applying gas chromatographymass spectrometry (GC-MS). It was found kaffir lime oil has almost 96 chemical compounds. Another three samples kaffir lime oil data get from previous researcher[7, 9, 14].

Z-score technique

The Z-score technique was utilised to group the data and assign an explicit grouping to the data population sample in this study. Previous studies have used Z-score approaches to establish a specific set, with Z-score being a widely used application for standardising data and calculating a factor score. Thus, the Z-score technique was applied to identify the significant chemical compound of kaffir lime oil [4]. In this

technique, the two significant chemical compounds of kaffir lime oil were found, which were β-pinene, limonene, linalool, citronellal, and terpinene-4-ol. The five chemical compounds were used as a marker compound for the NSVM classification method. Table 1 shows samples kaffir lime oil was used in this project and its significant chemical abundance (%). There are 11 HIGH samples and 4 LOW samples of kaffir lime oil. Samples AA, AB and AC got from previous researcher that were extract directly from kaffir lime, so they were labelled as a high quality. Another. 8 samples HIGH kaffir lime oils are traded as high quality by certified trader and some of them were published as high-quality kaffir lime oil

The quality of kaffir lime oil was determined based on its chemical abundance (%). The higher the abundance(%) of this chemical, the higher quality of kaffir lime oil [6, 8, 15–17].

Table 1. Significant Kaffir lime chemical constituents used for classification (Group' 1' for HIGH quality and '2' for LOW quality

	Abundance (%)					
	β-pinene	Limonene	Linalool	Citronellal	Terpinen-4-ol	Group
AA	16.8	19.8	1	7.8	2.8	1
AB	8.974	28.649	0.541	8.29	0.47	1
AC	9.321	26.446	0.687	6.63	1.0541	1
WS	1.42	0.52	7.19	60.06	0.99	1
FF	0.6	0.46	5.68	54.73	0.62	1
T	18.13	22.7	0.44	0	11.15	1
SS	0.56	0.37	7.4	79.39	0	1
SE	10.47	15.06	1.85	28.32	5.98	1
S	16.37	24.39	0.38	0	10.84	1
NL	1.16	0.42	7.35	60.65	0.85	1
DE	16.19	23.01	0.8	4.45	9.93	1
SP	0	16.8	2.48	0	0	2
C	0.19	18.49	2.14	0	0	2
В	0	0	12.38	51.05	0	2
LL	2.19	50.61	7.14	0	0	2

Synthetic data

All 15 data was added with synthetic data to become 90 samples data to increase the performances classification method[18]. Synthetic data was created by adding the SNR signal to the original input-output data. The synthetic data equations can be represented as follows, as recommended by Sevgi [19]:

$$Ysynthetic = Y_{NSVM} + Y_{SNR}$$
 (1)

The original NSVM input-output data is Y_{NSVM} , and the SNR signal or random noise is Y_{SNR} . The trend of the original data and original data with synthetic data should be the same. The calculation minimum, maximum and median of synthetic data are done to support the trend similarity.

Data pre-processing

Data pre-processing done for this experiment consists of a holdout cross-validation strategy for splitting data. The data is divided into ratios 80%:20% for training data and for testing data that was recommended by the authors [5, 20-22], which were for training data set it has 72 samples while the testing data has 18 samples. The ratio is applied in that manner due to the higher number of the training data collected, hence the higher accuracy results appeared on the model [22]. On the other hand, the difference between these two data sets is that the training data is used in model creation while the test data is performed as the model output prediction.

Build the NSVM classifier model

In the real world, data is rarely linearly separable. Most are non-linear. NSVM is modified by entering the kernel functions into SVM. There are a few types of kernel functions of NSVM: polynomial, quadratic, RBF, and sigmoid [23]. When using NSVMs in practice, it's especially vital to pick the correct kernel parameters. Thus, this experiment will test two different kernels to find the best kernel for modelling the quality kaffir lime oil grading. The two different kernels are the Polynomial kernel and RBF kernel. In general, the RBF kernel is a good starting point. This kernel nonlinearly maps samples into a higherdimensional space to handle the case where the relationship between class labels and attributes is nonlinear, unlike the linear kernel[24]. The polynomial kernel is selected because this kernel gives 100% accuracy for agarwood oil grading in a previous study [20] compared to the RBF kernel that is given only 89.5% [25].

The compounds gathered from the 90 samples of kaffir lime oil were used to train NSVM with Polynomial kernel and RBF kernel. The abundances (%) of the chemical compounds act as input, and this input were fed into NSVM model development, and hence the output is set to be either '1' or low '2' quality. All the analytical work was performed automatically by using MATLAB software version R2020A. Figure 1 shows the flowchart of NSVM modelling.

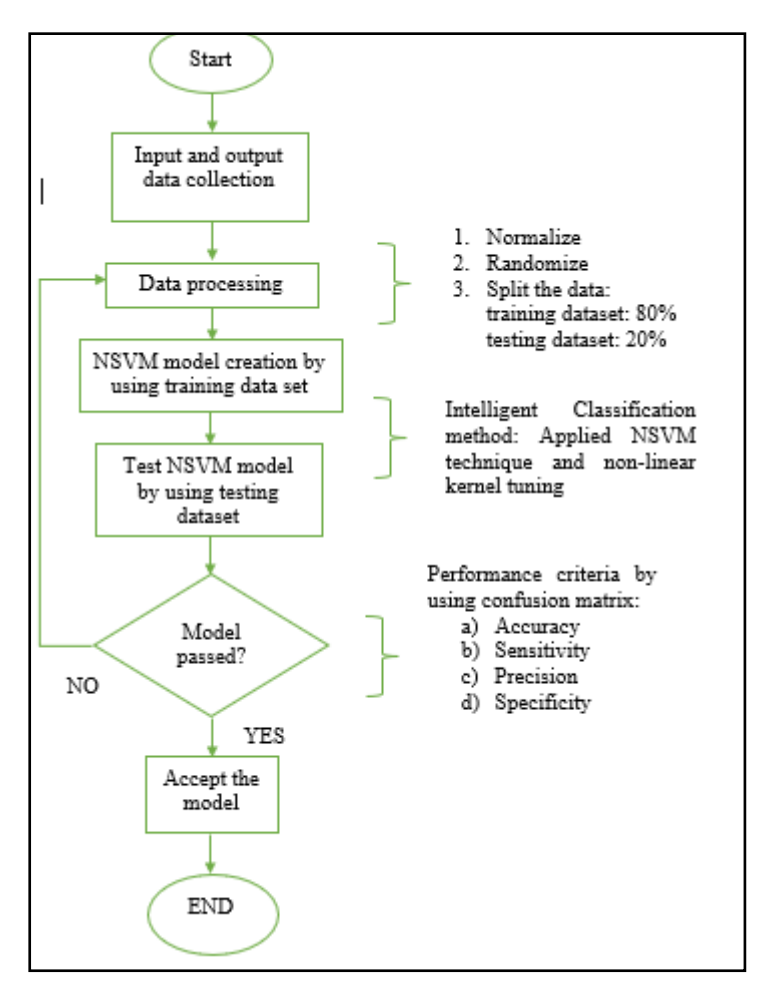


Figure 1. Flowchart NSVM modelling

Performance's measure

The performances for NSVM modelling were measured by using the confusion matrix. Other than that, measurements such as accuracy, sensitivity, specificity, precision, and Mean Absolute Error (MAE) would also be used to obtain more granular and precise model-building results. The accuracy (ACC) is defined as the effectiveness of the classifier. The calculation of the accuracy is as follows [29]:

$$ACC = (TP+TN)/(TP+FN+FP+TN)$$
 (2)

Sensitivity (SENS) is defined as the rate of a true positive. The effectiveness of a classifier to identify the high quality of kaffir lime is as follow [29]:

$$SENS=TP/(TP+FN)$$
 (3)

The specificity (SPEC) is interpreted as the rate of the negative. The effectiveness of a classifier to identify the low quality of kaffir lime is as follows [29]:

$$SPEC=TN/(TN+FP) \tag{4}$$

Precision (PREC) is interpreted how often it is correct when it predicts high quality of kaffir lime oil as follow:

$$PREC=TP/(TP+FP)$$
 (5)

Results and Discussion

The confusion matrix result is shown in Table 2 for the polynomial kernel and Table 3 for the RBF kernel. Where TP (True positive): Classified as HIGH quality and the actual was HIGH quality, FP (False positive): Classifies as HIGH quality but the real is LOW quality, FN (False negative): classified as HIGH quality, but the actual was LOW quality and TN (True negative): classified as LOW negative and the actual is LOW quality. From the result in table 2 and table 3, the value of TP for Polynomial and RBF were 14 and the value of FN for both kernels is also the same, which is 0. FP value for table 1 was 4, while FP value in table 2 was 0. TN value in table 1 was 0 while TN value in table 2 was 4. This result shows that RBF kernel is better than the polynomial kernel because the best model does not have value of FP and FN.

Table 4 shows the comparison performances between the polynomial kernel with RBF kernel. It is clearly showing that RBF kernel is way better than polynomial. RBF kernel can reach up to 100% of its accuracy, sensitivity, specificity, precision, and 0% mean absolute error (MAE) compared to the polynomial kernel which only manage to achieve 100% in its sensitivity, 66.78% accuracy precision, and 0% specificity, and 0.22 for MAE. In general, the lower the MAE, the better a model's ability to match a dataset. We may compare the MAE of two distinct models to see which one delivers a better fit to a dataset when comparing them.

Table 2. Confusion matrix for polynomial

Data Class N=18	Classified as HIGH	Classified as LOW
actual HIGH	TP=14	FP=4
actual LOW	FN=0	TN=0

Table 3. Confusion matrix for RBF

Data Class N=18	Classified as HIGH	Classified as LOW
actual HIGH	TP=14	FP=0
actual LOW	FN=0	TN=4

Table 4. Confusion performances between polynomial kernel and RBF kernel

Performances	Polynomial (%)	RBF (%)
Accuracy	66.78	100
Sensitivity	100	100
Specificity	0	100
Precision	66.78	100
MAE	0.22	0

Conclusion

This paper has successfully evaluated the Kaffir lime oil quality either high or low by tuning in polynomial kernel and radial basis function (RBF) kernel into NSVM. The result shows RBF kernel was able to produce 100% in its accuracy, specificity, precision, and sensitivity compared to Polynomial kernel which was able only to produce 77.78% in its accuracy, 100% sensitivity, 0% specificity and 77.78% precision. Hence it is also can be concluded that RBF kernel parameter better than polynomial for kaffir lime oil grading classification. Since the finding and outcome were effective and significant, thus this study contributes a lot of benefits for future study especially in kaffir lime field.

Acknowledgements

A highly appreciate this research funder, the Malaysia Ministry of Higher Education's Fundamental Research Grant Scheme (FRGS-RACER). This research was supported by FRGS Grant no 600-IRMI/FRGS-RACER 513(115/2019) for my financial support. The authors wish to thank Universiti Teknologi MARA, Cawangan Pulau Pinang and Faculty of Electrical Engineering, Universiti Teknologi MARA, Cawangan Pulau Pinang for their endless technical assistance.

References

- Abas, M. A., Zubir, N. S. A., Ismail, N., Yassin, I. M., Ali, N. A. M., Rahiman, M. H. F. and Taib, M. N. (2017). Agarwood oil quality classifier using machine learning. *Journal of Fundamental and Applied Sciences*, 9(4): 62-76.
- Haron, M. H., Taib, M. N., Ismail, N., Mohd Ali, N. A. and Tajuddin, S. N. (2019). Statistical analysis of agarwood oil compounds based on GC-MS data. 9th IEEE Control System Grad. Research Colloquium: pp. 27-30.
- Azah, M. N., Husni, S. S., Mailina, J., Sahrim, L., Majid, J. A. and Faridz, Z. M. (2013). Classification of agarwood (gaharu) by resin content. *Journal of Tropical Forest Science*, 2013: 213-219.
- Ismail, N., Azah, M. A. N., Jamil, M., Rahiman, M. H. F., Tajuddin, S. N. and Taib, M. N. (2013). Analysis of high quality agarwood oil chemical

- compounds by means of SPME/GC-MS and Z-score technique. *Malaysian Journal of Analytical Sciences*, 17(3): 403-413.
- Jantan, H., Yassin, I. M., Zabidi, A., Ismail, N. and Ali, M. M. (2017). Differentiation of agarwood oil quality using support vector machine (SVM). *Journal Engineering Applied Sciences*, 12(15): 3810-3812.
- Mohd Sauid, S. and Aswandi, F. A. (2018). Extraction methods of essential oil from kaffir lime (*Citrus hystrix*): A review. *Malaysian Journal* of Chemical Engineering and Technology, 1: 56-64.
- Kasuan, N., Muhammad, Z., Yusoff, Z., Fazalul Rahiman, M. H., Taib, M. N. and Haiyee, Z. A. (2013). Extraction of *Citrus hystrix* DC (kaffir lime) essential oil using automated steam distillation process: analysis of volatile compounds. *Malaysian Journal of Analytical Sciences*, 17: 359-369.
- 8. Haiyee Z. A. and Winitkitcharoen, C. (2012). Extraction of volatile oil from kaffir lime leaves (*Citrus hystrix*) using pressurize liquid extraction. *International Journal Food, Nutrition Public Health*, 5: 201-210.
- Muhammad, Z., Yusoff, Z. M. and Nordin, M. N. N. (2013). Steam Distillation with induction heating system: analysis of kaffir lime oil compound and production yield at various temperatures. *Malaysian Journal of Analytical Sciences*, 17(2): 340-347.
- Ngan, T. T. K., Hien, T. T., Tien, L. X., Anh, T. T., Quan, P. M., Cang, M. H. and Toan, T. Q. (2019). Physico-chemical profile of essential oil of kaffir lime (*Citrus hystrix* DC) grown in An Giang Province, Vietnam. *Asian Journal Chemistry*, 31(12): 2855-2858.
- 11. Hongatanaworkit, T. and Buchbauer, G. (2007). Chemical composition and stimuating effect of *Citrus hystrix* oil on human. *Flavour Fragrance Journal*, 22(4): 443-449.
- 12. Dewi, C. and Basuki, A. (2018). Identifying citronella plants from UAV imagery using support vector machine. *Telkomnika*, 16(4): 1877–1885.

- 13. Windha Mega, P. D. and Haryoko (2019). Optimization of parameter support vector machine (SVM) using genetic algorithm to review go-jek's services. 4th International Conference Information Technology, Information System, and Electrical Engineering, 6: 301-304.
- Zakiah, M. Y., Zuraida, M., Nurhani, K., Mohd, H. F. R. and Mohd, N. T. (2013). Effect of temperature on kaffir lime oil by using hydrodiffusion steam distillation system. *Malaysian Journal of Analytical Sciences*, 17(2), 326-339.
- Lubinska-Szczygieł, M., Różańska, A., Namieśnik, J., Dymerski, T., Shafreen, R. B., Weisz, M., ... & Gorinstein, S. (2018). Quality of limes juices based on the aroma and antioxidant properties. *Food Control*, 89: 270-279.
- An, T. N. T., Ngan, T. T. K., Van, C. K., Anh, H. L. T., Minh, L. V. and Ay, N. V. (2021, March). The major and minor components of Kaffir Lime (Citrus hystrix DC) essential oil in the steam distillation process. In IOP Conference Series: Materials Science and Engineering, 1092(1): 012082.
- 17. Jailani, N. S. J., Muhammad, Z., Rahiman, M. H. F. and Taib, M. N. (2021). Analysis of kaffir lime oil chemical compounds by gas chromatographymass spectrometry (GC-MS) and Z-Score technique. In 2021 IEEE International Conference on Automatic Control & Intelligent Systems: pp. 110-113.
- 18. Ismail, N., Rahiman, M. H. F., Taib, M. N., Ali, N. A. M., Jamil, M. and Tajuddin, S. N. (2014). Application of ANN in agarwood oil grade classification. In 2014 IEEE 10th International Colloquium on Signal Processing and its Applications: pp. 216-220.
- 19. Sevgi, L. (2007). Synthetic radar-Signal environment: Computer generation of signal,

- noise, and clutter. *IEEE Antennas and Propagation Magazine*, 49(5): 192-198.
- Ismail, N. S., Ismail, N., Rahiman, M. H. F., Taib, M. N., Ali, N. A. M. and Tajuddin, S. N. (2018, October). Polynomial tuned kernel parameter in SVM of agarwood oil for quality classification. In 2018 IEEE International Conference on Automatic Control and Intelligent Systems: pp. 77-82.
- 21. Ariffin, B. M., Ismail, N., Ali, N. A. M., Rahiman, M. H. F., Tajuddin, S. N. and Taib, M. N. (2018). Multilayer perceptron (MLP) tuned kernel parameter in support vector machine (SVM) for agarwood oil compounds quality classification. *J. Tomography System and Sensors Application*, 1(1): 1-15.
- 22. Raif, M. A. A., Ismail, N., Ali, N. A. M., Rahiman, M. H. F., Tajuddin, S. N. and Taib, M. N. (2019). Quadratic tuned kernel parameter in Non-linear support vector machine (SVM) for agarwood oil compounds quality classification. *Indonesia Journal Electronic Engineering Computer Science*, 17(3): 1371-1376.
- 23. Patle, A. and Chouhan, D. S. (2013). SVM kernel functions for classification. In *2013 International Conference on Advances in Technology and Engineering*, pp. 1-9.
- Apostolidis-Afentoulis, V. and Lioufi, K. I. (2015). SVM classification with linear and RBF kernels: pp. 1-7.
- 25. Kamarulzaini, K. A. A., Ismail, N., Rahiman, M. H. F., Taib, M. N., Ali, N. A. M. and Tajuddin, S. N. (2018). Evaluation of RBF and MLP in SVM kernel tuned parameters for agarwood oil quality classification. In 2018 IEEE 14th International Colloquium on Signal Processing & Its Applications, pp. 250-254.

Malaysian Journal of Analytical Sciences (MJAS)





DIRECT CATALYTIC CONVERSION OF CELLULOSE INTO FORMIC ACID BY SUPPORTED PHOSPHOTUNGSTIC ACID CATALYST

(Penukaran Terus Selulosa Kepada Asid Formik Menggunakan Pemangkin Asid Fosfotungstik yang Disokong)

Nor Liyana Zakira Zabidi Adil @ Zaibidai Adil, Farah Wahida Harun, Syaza Azhari, Lailatun Nazirah Ozair, Shikh Mohd Shahrul Nizan Shikh Zahari, Tengku Shafazila Tengku Saharuddin*

Faculty of Science and Technology, Universiti Sains Islam Malaysia, Bandar Baru Nilai, 71800 Nilai, Negeri Sembilan

*Corresponding author: shafazila@usim.edu.my

Received: 15 August 2021; Accepted: 11 January 2022; Published: 28 April 2022

Abstract

This study aims to prepare phosphotungstic acid supported on hydrotalcite (PTA-HT) for one-pot hydrothermal cellulose conversion into formic acid (FA). In this study, different percentages of PTA on HT (1, 5, 10, 15, 20, 25, and 33%) were prepared and the catalytic activity was observed for two different parameters such as time (1 to 5 hours) and reaction temperature (160 to 240 °C). The prepared catalysts were characterized using Fourier transform infrared (FTIR), X-ray powder diffraction (XRD), Brunauer-Emmet-Teller (BET) and field emission scanning electron microscopy-energy dispersive X-ray spectrometry (FESEM-EDX), while the production of FA was determined using ultra high-performance liquid chromatography (UHPLC). To avoid bias, raw PTA and calcined HT were compared with varying percentages of supported PTA. PTA-HT was successfully prepared through the impregnation method as confirmed by XRD, FTIR, BET and FESEM-EDX. According to the results, the optimum condition for cellulose conversion into formic acid was when 25% PTA-HT was applied at 220 °C for 4 hours, with a 30% cellulose conversion and 18 % FA yield. Due to the acidity and redox properties of PTA, it has been demonstrated that PTA-HT increased the catalytic activity by two-fold when compared to calcined HT alone (8%). The significance of this finding opens new suggestion of bifunctional catalyst in cellulose conversion into FA.

Keywords: catalyst, cellulose, formic acid, hydrothermal, phosphotungstic acid

Abstrak

Tujuan kajian ini adalah untuk menyediakan asid fosfotungstik yang disokong dengan oleh hidrotalsit (PTA-HT) bagi proses hidroterma penukaran selulosa kepada asid formik. Di dalam kajian ini, perbezaan peratus PTA ke atas HT (1, 5, 10, 15, 20, 25 dan 33%) telah disediakan dan aktiviti pemangkinan telah dijalankan terhadap dua parameter iaitu masa (1 jam hingga 5 jam) dan suhu (160 hingga 240 °C). Pemangkin yang telah disediakan diperincikan menggunakan inframerah transformasi Fourier (FTIR), pembelauan sinar-X (XRD), Brunauer-Emmet-Teller (BET) and mikroskopi imbasan pancaran medan-spektrometri tenaga serakan sinar-X (FESEM-EDX) manakala asid formik yang terhasil ditentukan menggunakan kromatografi cecair berprestasi ultra tinggi (UHPLC). Bagi mengelakkan keputusan yang berat sebelah dalam kajian, PTA tulen dan HT yang dikalsin telah dibandingkan dengan perbezaan peratus PTA yang disokong. PTA-HT yang telah disediakan melalui kaedah

impregnasi dicirikan oleh XRD, FTIR, BET dan FESEM-EDX. Berdasarkan keputusan, keadaan yang paling optimum bagi penukaran selulosa kepada asid formik adalah apabila 25% PTA-HT digunakan pada 220 °C selama 4 jam dengan menghasilkan 30% penukaran selulosa dan 18% penghasilan asid formik. Oleh kerana ciri-ciri asid dan redoks yang dimiliki oleh PTA, keputusan kajian telah menunjukkan bahawa PTA yang disokong oleh HT meningkatkan aktiviti pemangkin sebanyak dua kali ganda berbanding HT yang telah dikalsin yang hanya menghasilkan 8% asid formik. Kepentingan kajian ini akan membuka cadangan baru terhadap penggunaan pemangkin dwifungsi dalam penukaran selulosa kepada asid formik.

Kata kunci: pemangkin, selulosa, asid formik, hidroterma, asid fosfotungstik

Introduction

Biomass is a great alternative for carbon sources in the production of platform chemicals as biomass originated from plants and animals [1]. Numbers of researches focused on forestry and agricultural residues as it is non-edible to address food competition issues such as wood [2], corncob waste [3] and rice husk [4]. Plant biomass is made up of three main constituents: cellulose, hemicellulose and lignin. Among these constituents, cellulose has the highest percentage and play important structural function for plant cell walls [5, 6]. Cellulose is a polymer that is highly crystalline due to rigid intermolecular bonds of hydrogen to hydroxyl group and oxygen with nearby glycosidic rings [7, 8]. Glycosidic bonds of cellulose causes difficulty in depolymerizing cellulose, which required highly reactive catalyst and rigorous experimental conditions. In converting cellulose, many techniques have been studied such as pretreatment of cellulose using ball-milling [9], addition of oxidant [10], Fenton reaction [11-13], hydrolysis [14, 15], ozonation [2] and oxidation [16]. A successful cellulose conversion provides production of important chemicals such as formic acid [17-19], lactic acid [20, 21], levulinic acid [22] and acetic acid [23]. Industries have been eyeing formic acid (FA) due to its nontoxicity, noncorrosive, easy handling and readily biodegradable qualities [24]. Formic acid is the most basic form of carboxylic acid and is commonly used as a byproduct in a variety of applications such as agriculture [25], cosmetics [26], textile [27] and pharmaceuticals [28].

Mineral acids such as hydrochloric acid, sulfuric acid and phosphoric acid have previously been used as acid catalysts for cellulose conversion due to their strong acidity and low cost, but these catalysts are highly corrosive [29-33]. Therefore, improvement had been

made to convert cellulose using solid acid catalyst such as heteropoly acid [16], zirconia, zeolite and montmorillite [34]. The advantageous of using solid catalyst is that it is less corrosive, easier to handle, and separates the catalyst from the reaction medium. Among all catalysts, heteropoly acid (HPA) catalyst appears to be the most promising due to its strong Bronsted acidity and redox property [35] that able to hydrolyze and oxidize cellulose into FA. Nevertheless, drawbacks of homogenous HPA are low thermal stability, low surface area and easily soluble in polar solvent [35]. Supporting HPA on a suitable support is one way to heterogenized HPA, which can improve product yield, selectivity, and reduce HPA's drawbacks by providing more active sites and making it more porous [14, 22, 35, 36]. In addition, hydrotalcite (HT), a potential support material with a high surface area and basic properties that may aid in the catalytic conversion of cellulose, is one such material that has been widely used-in flame retardance, neutralizing additives, a base catalyst for cellulose conversion and adsorbent [37-40]. Therefore, in this work, cellulose conversion into FA by different percentages of PTA (H₃PW₁₂O₄) supported with HT (Mg₆Al₂CO₃(1₆)·4H₂O) were investigated to see the effects of temperature, time and PTA amount towards the production of FA.

Materials and Methods

Materials

All reagents were analytical grade and used without further purification such as hydrotalcite (Sigma-Aldrich), microcrystalline cellulose and ethanol 99.5% (Systerma) while formic acid 98-100% HPLC grade, tungstophsphoric acid hydrate, orthophosphoric acid and potassium dihydrogen phosphate were purchased from Merck.

Preparation of catalyst

The catalyst preparation starts with the reconstruction pathway in which commercial HT was calcined at 450 °C for 4 hours under nitrogen gas to remove carbonate ions. This step is to allow anions from raw PTA solution to enter into the empty interlayer region later [41]. The raw PTA was dissolved into deionized water to the desired amount (1, 5, 10, 15, 20, 25 and 33% by w/w%). Meanwhile, calcined HT was dissolved in another beaker. Subsequently, dissolved PTA was added dropwise into calcined HT solution. At this step, calcined HT will reconstruct into its original shape with new interlayer anions from PTA. This is because calcined HT regains its original structure when exposed to the aqueous solution [42]. Then, the mixture was stirred for 4 hours to ensure that PTA and calcined HT until both solutions were well-mixed. Lastly, the mixture was dried overnight to remove the water from the mixture forming a solid containing PTA and calcined HT.

Catalytic experiment

Cellulose conversion was conducted in a 100 mL hydrothermal reactor in which the contents of catalyst and cellulose fed were 0.1 g and 0.05 g respectively. Then, about 50 mL of deionized water was added. The reactor was tightened and placed inside an oven. Once reaction temperature and time were up, the cellulose conversion started. As soon as the required temperature and time were reached, the liquid product was filtered using a syringe filter and the solid residue was filtered using a vacuum pump. Cellulose conversion was calculated according to Equation 1. The concentration of FA was analyzed using the UHPLC system (1290 Infinity, Agilent Technologies) using Zorbax SB C18 column with an internal diameter of 21.2mm and 5µm particle size. The UHPLC system was connected with a DAD detector measuring at 210 nm. 10 mM phosphate buffer with pH adjusted to pH 2 was prepared, filtered and degassed. The concentration of FA from the sample was identified by comparing the retention times with standards. Standards calibration was used for FA quantification. The yield of FA was calculated using Equation 2 [43].

$$Cellulose conversion = \frac{Cellulose fed - (Solid residue - Catalyst)}{Cellulose fed} \times 100\%$$
(1)

Formic acid yield =
$$\frac{\text{Liquid product}}{(\text{Stoichiometric coefficient FA from glucan})} \times 100$$
(2)

Catalyst characterization

Nitrogen adsorption was done to differentiate specific surface area, pore size distribution and pore volume of PTA-HT, raw PTA, calcined HT and raw HT using Brunner-Emmet-Teller (BET) model Flex Micromeritics. BET analysis started with degassing the sample to remove unwanted adsorbed molecules inside the sample pore. The thermal condition of degassing is prior to thermal gravimetric analysis to ensure that the sample was not destroyed during degassing. After degassing, the sample was placed inside the sample tube and liquid nitrogen was filled inside the dewar and placed below the sample tube for BET analysis. Then, phase characterization was carried out by X-ray diffraction (XRD) model Mini Flex 600, Rigaku with Cu Ka 1.54 (40 kV, 40 mA) X-ray radiation source at angle range 3^{θ} to 90^{θ} . In order to identify the crystalline phase compositions, the diffraction patterns were matched with Crystallography Open Database (COD). Chemical functional groups identification was carried out using Fourier Transform Infrared (FTIR) model Nicolet™ iS50 FTIR Spectrometer, Thermo Scientific. FTIR sample was grind using pestle and mortar until it become fine and thin. The sample analysis started after placing the sample onto the detector and background scanning was done. Then, surface morphology of sample was confirmed by Field Emission Scanning Electron Microscope (FESEM) model JSM-IT 800 FESEM, Joel with accelerating voltage 20 kV. Sample was coated with platinum using JEOL Smart Coater. The FESEM images were paired with Energy Dispersive X-ray Analysis (EDX) model Ultimax 45

Oxford to confirm the presence of elemental composition of each sample.

Results and Discussion

Catalytic activity

Three parameters were investigated to find the best conditions for FA production from cellulose using the PTA-HT catalyst: reaction time, temperature, and amount of PTA. The influence of reaction time towards FA production is displayed in Figure 1. To determine the best reaction time, the temperature and amount of PTA were kept constant at 180 °C and 5%, respectively. From the results, FA yield increased gradually from 0.08% to 0.22% between 1 to 3 hours of the reaction time. The value then increased slightly to 0.24% at 4 hours and remained constant until 5 hours. In the case of cellulose degradation, a longer reaction time allowed higher degradation rates ranging from 15% to 42% and does not achieve a plateau. From the result, it is observed that reaction condition for both cellulose degradation and FA yield at 180 °C is very mild although the reaction time varies from 1 hour to 5 hours. This can be seen when the reaction time was prolonged to 5 hours the cellulose degradation is slightly increased from 30 to 44% while FA vield remain constant as shown in Figure 1. Degradation of cellulose can be done independently without the presence of catalyst as reported in previous journal [44]. However, high temperature of water was required range 320 to 400 °C but cellulose was able to degrade into cellobiose, glucose and fructose [44]. Another study of cellulose degradation without presence of catalyst also observed the same trend where at 180°C degradation products such as acids, furans and sugar were not detectable with only 12% cellulose converted [45]. Meanwhile, as shown in Figure 1, our experiment shows that at 180 °C, cellulose degradation increases as reaction time prolonged and FA was detectable and reached a plateau at 4 hours reaction time. The production of FA which may cause by the presence of 5% PTA-HT that enhance cellulose degradation. This is because PTA contains tungsten ions and oxygen ions that does have an effect on hydrolysis and oxidation. Although

hydrolysis mainly took place in a high temperature water medium, the production of the targeted product requires oxidation of cellulose where PTA provide additional oxygen located at bridging and terminal oxygen atom. However, the reaction time, water temperature and acidic strength of PTA was only able to hydrolyse cellulose but this condition is not enough to produce more FA. Hence, to improve this, we further with the next condition at 4 hours reaction time with the same amount of PTA to determine the suitable temperature and amount of PTA on HT catalyst.

Subsequently, the effect of reaction temperature on FA production was examined by varying the reaction temperature from 160 to 280 °C. As illustrated in Figure 2, a noticeable increment can be seen towards cellulose degradation from 9% to nearly 50% with prolonged temperature. FA yield also showed better improvement with a maximum yield of 13.36% at 240 °C. However, a very slight change in FA yield was observed between 220 °C (13.05 %) and 240 °C (13.36%). From the graph, the trend of FA yield started to decrease at 250 to 280 °C although cellulose degradation increases. The suggested mechanism pathway started with cellulose undergoes hydrolysis which form glucose [46]. The glucose further dehydrated into hydroxymethylfurfural (HMF) where later rehydrated into levulinic acid and decomposed into FA [47]. It is reasonable to speculate that higher temperature promotes degradation of cellulose as stated in [48] where cellulose can be degraded without the presence of acid at high temperature. However, previous journal [45] only highlighted the production of monosaccharides but our study proved that with the presence of PTA it enhances cellulose degradation route until FA was produced at suitable temperature. This occurs due to Brönsted acidity of PTA that highly protonate ions during reaction took place. Although, production of FA was a success, FA is an unstable compound which can easily decomposed into CO₂ [43][9]. Hence, selecting 220°C as our reaction temperature is reasonable to avoid decomposition of FA.

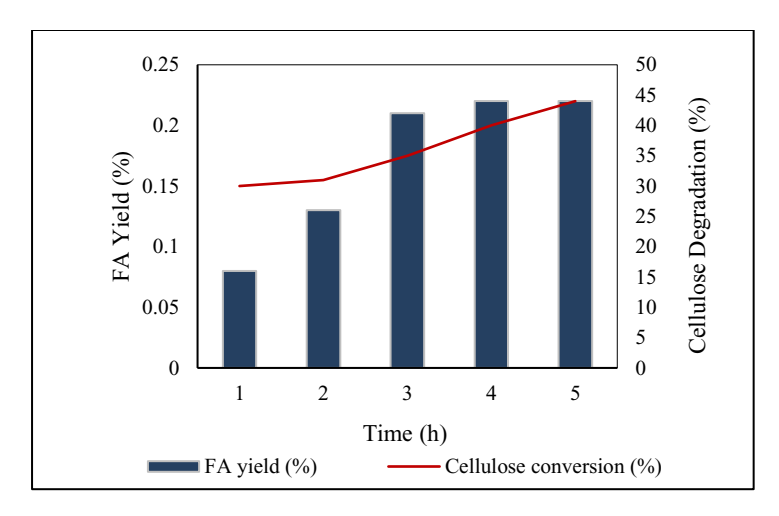


Figure 1. Effect of reaction time on cellulose conversion and FA yield by PTA-HT catalyst. Reaction condition: 0.05 g cellulose, 0.1 g PTA-HT, the temperature at 180 °C and PTA loading on HT is 5%

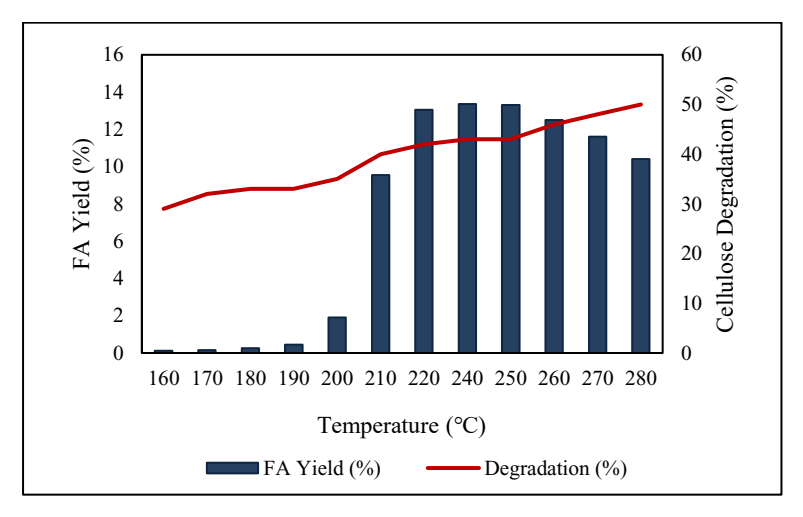


Figure 2. Effect of reaction temperature on cellulose conversion and FA yield by PTA-HT catalyst. Reaction condition: 0.05 g cellulose, 0.1 g PTA-HT, 5% PTA-HT and 4 hours reaction time

The influence of PTA amount supported on calcined HT was displayed in Figure 3. This investigation was compared with blank experiment where catalyst was not included during cellulose degradation. In Figure 3, although cellulose was degraded in blank experiment, FA yield was not obtained. However, other reactors that contained PTA-HT yielded FA. This phenomenon is possible to occur due to PTA criteria that is highly protonic acid which speed up the cellulose degradation [41]. Hence, FA can be obtained in 4 hours under 220 °C water temperature. A factor that allows

hydrolysis to happen in blank experiment is when water medium is heated to high temperature but as observed our solid acid catalyst improves the hydrolysis rate and react further to form FA. Furthermore, the degradation rate in blank experiment was lesser as compared when PTA-HT was presence. The formation of FA occurred due to cascade reaction in which dehydration and rehydration took place before FA was formed. So as Brönsted acid was placed in the medium, hydrogen ions were highly dissociated which speed up dehydration of glucose into HMF which later

rehydrate into FA [44]. From our experiment, FA production depends on the acidic strength of our catalyst as FA yield increase with increasing amount of PTA but the FA yield was inconsistent. However, FA yield drops drastically to 0.08% when 33% of PTA-HT was placed in reaction medium while highest yield of FA (18%) was observed with 25% amount of PTA. To our surprise, calcined HT alone produce 8% FA which initially function as catalyst support.

Based on previous literature, calcined HT contains medium-strong Lewis basic O²⁺-Mnⁿ⁺ pairs and isolated O²⁻ as strong basic sites which promote production of FA compared with uncalcined HT that contain weak basic sites [49]. After cellulose was hydrolyze, glucose was not dehydrated into HMF instead isomerizes into fructose and retro-aldol forming glycolic acid. Then, dehydrated into lactic acid which later degraded into FA [50,51, 38]. From this, we understand that two possible routes occurred during FA production as illustrated in Scheme 1. PTA and HT

when combined together consist of both acid and base Having Brönsted acid feature increase degradation rate of cellulose while the basic site of calcined HT hindered decomposition of FA into carbon dioxide. 25 % PTA-HT was chosen to further investigate and characterize its properties in relation to the catalytic reaction. 25% PTA-HT was compared with calcined 25% PTA-HT to observe any difference in FA production. Cellulose degradation from calcined 25% PTA-HT was better than blank and calcined HT. The FA yield decreased drastically when PTA loading are more than 25%. This might happen due to leaching of PTA. Another similar study, compared uncalcined tungsten-based zirconia and calcined tungsten-based zirconia reported the same result [52]. From Figure 4, the UHPLC result shows the formation of FA together with other by-products that was obtained during FA production. Although other by-products were obtained, FA peak is one of the highest compared to the others.

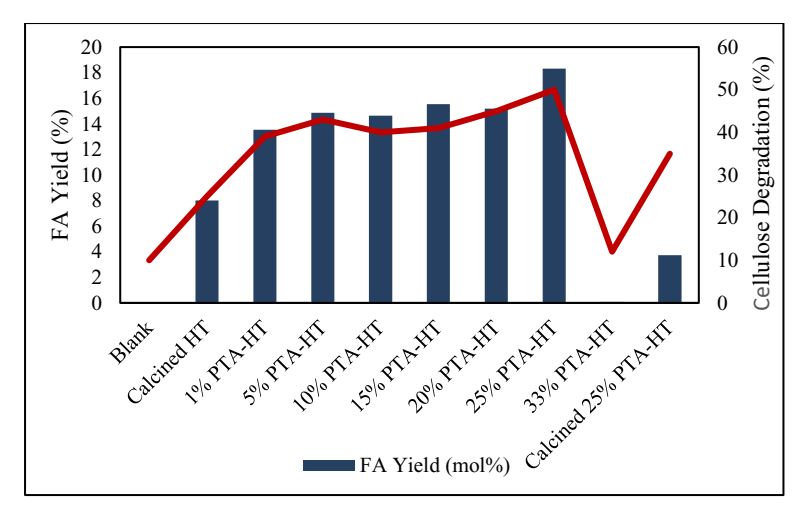


Figure 3. Effect of percentage PTA loading on HT on cellulose conversion and FA yield by PTA-HT catalyst. Reaction condition: 0.05 g cellulose, 0.1 g PTA-HT and temperature at 220 °C

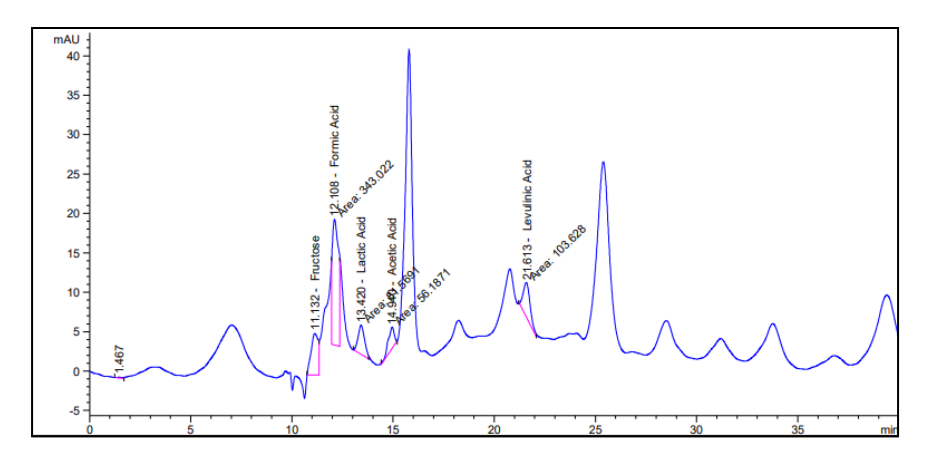


Figure 4. HPLC analysis of cellulose degradation with 0.1g 25% PTA-HT, 4 hours reaction time at 220 °C

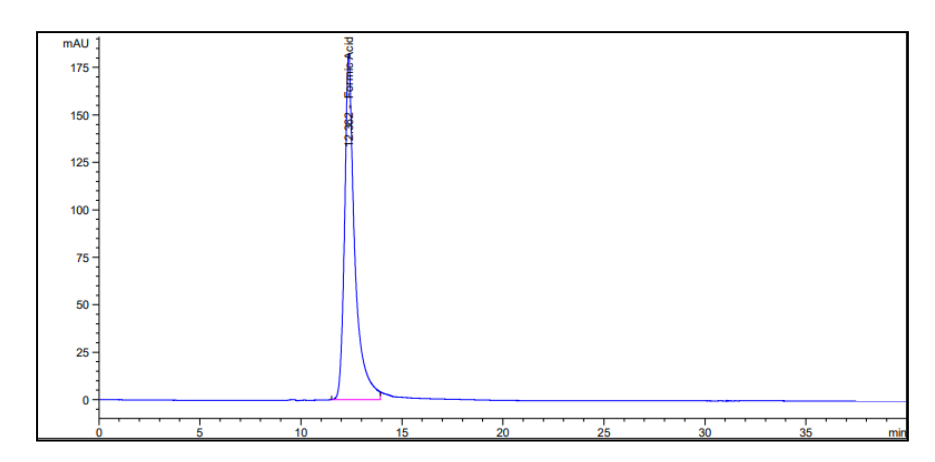
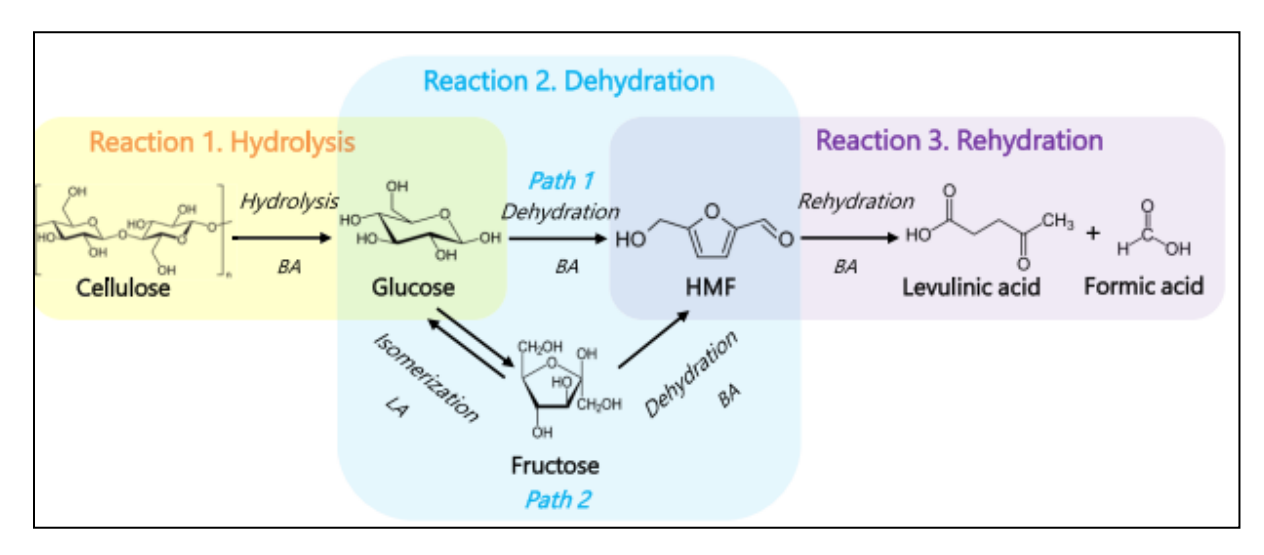


Figure 5. HPLC result for standard FA



Scheme 1. Mechanism pathway of cellulose degradation into FA [51]

Nitrogen adsorption-desorption analysis

BET measurement has been carried out on raw HT, raw PTA, calcined HT and 25% PTA-HT. The objective of this test is to evaluate the significance of impregnating PTA with calcined HT. One of the drawbacks implementing PTA as homogenous catalyst is because of its low surface area and difficulty to reuse. Hence, having large surface area and porous catalyst support can overcome this. Few journals have reported supported PTA with zirconia, activated carbon and carbon foam but as far as our knowledge there is no PTA supported with calcined HT for cellulose degradation study. As shown in Table 1, raw PTA have

the lowest specific surface area as compared to 25% PTA-HT. The main reason to calcined HT is to provide larger surface area and porous surface to support PTA and open more active sites during cellulose degradation. If raw HT was not calcined and impregnated with PTA, we assumed that our catalyst will not be well supported as the surface area for raw HT is small compared to calcined HT. The specific surface area of 25% PTA-HT was significantly lesser than calcined HT is because PTA was deposited inside the pores of calcined HT. Hence, it is important to calcined HT so that the surface area is still larger despite being deposited with PTA.

Table 1. BET analysis of raw HT, calcined HT and 25% PTA-HT

Sample	Specific Surface Area (m²/g)	
Raw HT	10.63	
Raw PTA	3.91	
Calcined HT	206.62	
25% PTA-HT	163.39	

XRD analysis

XRD patterns of raw HT ($2\theta = 11.58^{\circ}$, 23.31° , 34.42° , 34.80°, 35.30°, 39.32°, 46.71°, 52.84°, 56.32°, 60.65° and 61.98°) and raw PTA ($2\theta=6.89$ °, 8.62°, 9.33°, 9.5°, 10.97°, 11.66°, 16.09°, 17.41°, 17.83°, 18.60° and 19.46°) showed the typical crystalline structure of Mg-Al layered double hydroxides and phosphotungstic acid respectively. Meanwhile, the XRD peak of calcined HT showed significant difference as crystallinity of raw HT was destructed and formed amorphous mixed oxide phase. This can be seen at $2\theta=26.55^{\circ}$, 29.54° , 39.52° and 62.32° that showed an appearance of MgAl₂O₄ (spinel) (COD Card No. 5000120). Calcination of HT also gave rise to weak and broad peaks that correlated to MgO known as periclase (COD Card No. 9013246) at $2\theta = 34.78^{\circ}$, 43.29° , 60.70° and 79.03° . As shown in Figure 6, XRD peak of 25 % PTA-HT showed the presence of MgO at $2\theta = 38.39$ °, MgAl₂O₄ ($2\theta = 43.01$ °,

 62.95° and 79.77°) and $(2\theta=18.59^{\circ}, 28.66^{\circ}, 34.79^{\circ})$ and 47.24°). This phenomenon is related to calcination of HT that will generate mixed oxide and surface defects. Hence, after calcination of HT at 450 °C for 4 hours, original structure of HT lost water and carbonate ions [53]. Removing water and carbonate ions that located at interlayer region will allow incorporation of PTA in MgO framework. Therefore, it is observed that 25% PTA-HT peak follows calcined HT peak. From Figure 4, cellulose peak was observed in sample 25% PTA-HT after reaction because this sample was only separated from liquid product using vacuum filter. Although most peaks appear in 25% PTA-HT after reaction sample, there is missing peak of periclase which might cause from leaching due to reaction condition. However, most of the peaks are maintained in 25% PTA-HT after reaction sample.

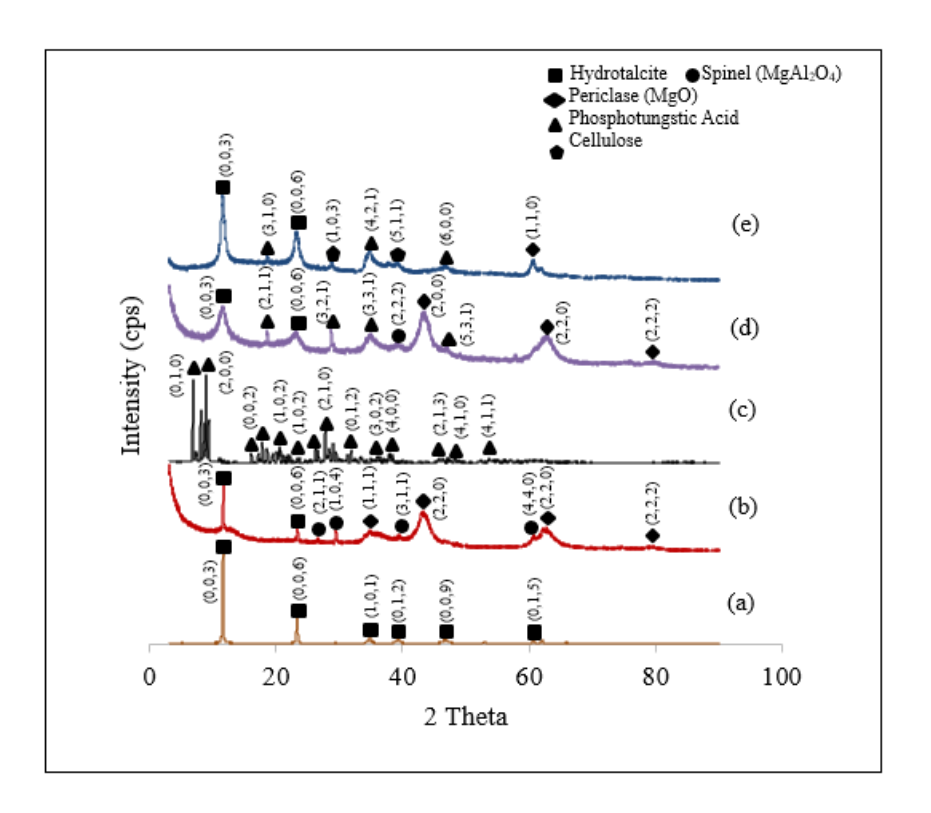


Figure 6. XRD patterns of (a) Raw HT, (b) Calcined HT, (c) Raw PTA, (d) 25% PTA-HT and (e) 25% PTA-HT after reaction

Infrared spectroscopy

IR spectroscopy was used to confirm the presence of PTA after impregnated with calcined HT. As shown in Figure 7, raw PTA was observed to have significant peaks of Keggin HPA at 1071 cm⁻¹ (P-O), 970 cm⁻¹ (W=O), 899 cm⁻¹ (W-O-W) and 729 cm⁻¹ (W-O-W) that attributed to stretching vibrational peaks of Keggin anions [54]. The peaks were not obvious because for 25% PTA-HT only 0.025g of PTA impregnated with 0.1g calcined HT. In the case of raw HT, peaks observed at low peaks range between 900-500 cm⁻¹ corresponded to metal hydroxides such as Mg(OH)₂ and Al(OH)₃ [55]. Meanwhile, peaks near 937 cm⁻¹

were caused by Mg-O and Al-O. The characteristic peak of raw HT is at 1359 cm⁻¹ which is the carbonate and 3403 cm⁻¹ for O-H group [56]. The disappearance peaks of metal hydroxides and weak peak of O-H at 3442 cm⁻¹ in calcined HT is due to loss of water [57, 58]. IR spectra for 25% PTA-HT, showed the appearances of P-O (1003 cm⁻¹), W=O (801 cm⁻¹), W-O-W (700 cm⁻¹) and Mg-O and Al-O (501 cm⁻¹ to 532 cm⁻¹) peaks, which indicated the successful impregnation between PTA and HT. This result can be confirmed with XRD analysis and EDX analysis that can show elements present in the sample.

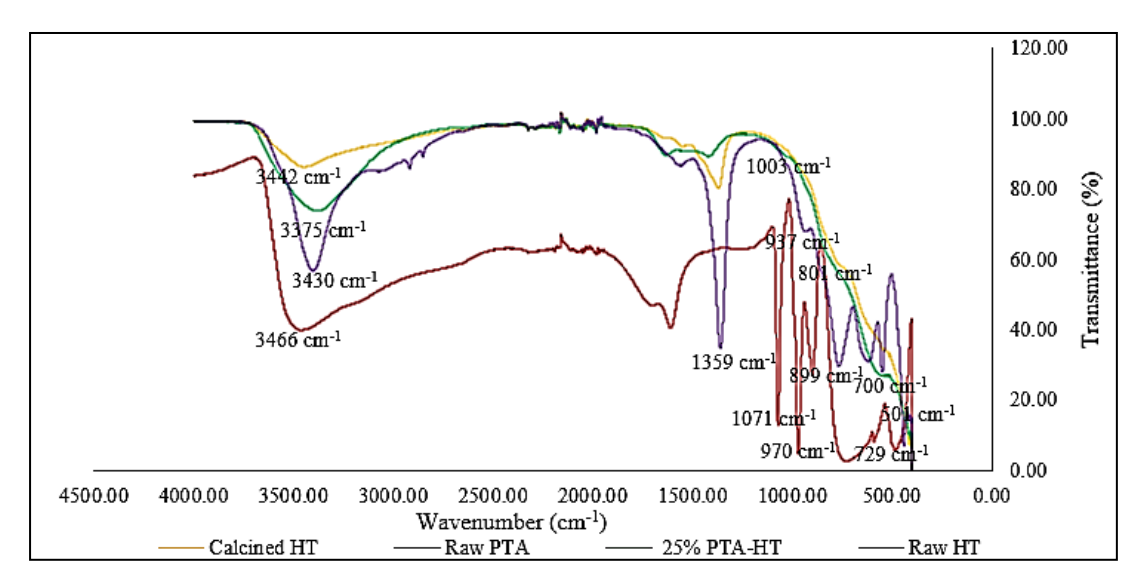


Figure 7. FTIR spectra of raw PTA, raw HT, calcined HT and 25% PTA-HT

FESEM-EDX analysis

FESEM was used to characterize the surface morphology of calcined HT and 25% PTA-HT as shown in Figure 8. Both calcined HT and 25% PTA-HT displayed a similar pattern of particles with irregular shapes. This is because small amount of PTA was impregnated with calcined HT which does not provide any distinguish pattern between calcined HT and 25% PTA-HT. Hence, EDX analysis is important for us to detect the presence of PTA incorporated with calcined HT that can be observed in Figures 9 and 10. As reported before, phosphorus-based HPAs are slightly more acidic than silicon-based HPAs [58]. The importance of tungsten (W) and oxygen (O) inside PTA is their proton affinity which contribute to its

acidic site. As shown in Figure 7, the presence of tungsten (W), phosphorus (P) and oxygen (O) indicated the core elements of PTA. Calcination of HT remove carbonate and water at the interlayer and formed mixed oxide where only magnesium (Mg), aluminum (Al) and oxygen were present in Figure 8. The empty interlayer region will be filled with PTA elements and regains its original structure. The unlabeled peaks were carbon tape used for imaging. Both EDX results showed high intensity of Mg, O and Al peaks which shows that calcined HT is more dominant in 25% PTA-HT. Hence, there is no significant difference between FESEM images and FTIR results. Although, calcined HT was dominant the amount of PTA far important towards FA production.

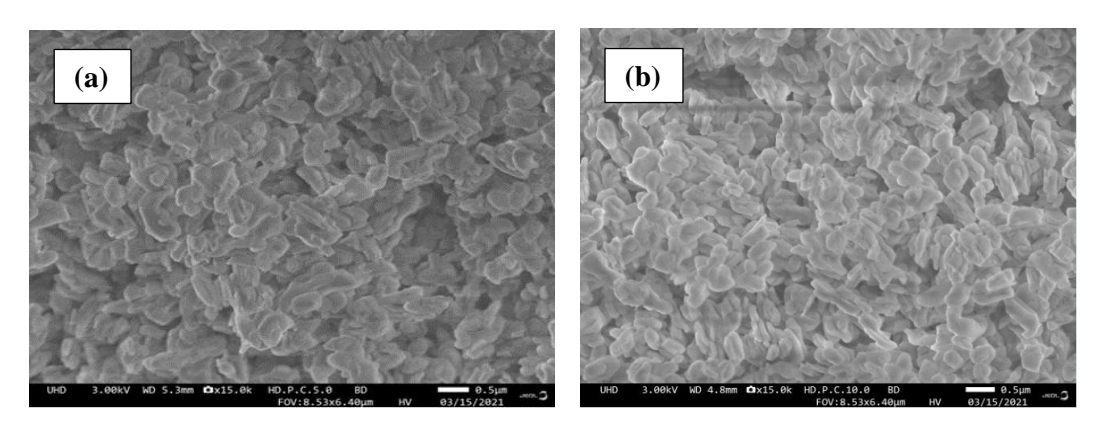


Figure 8. FESEM image of (a) calcined HT and (b) 25% HTA-PTA

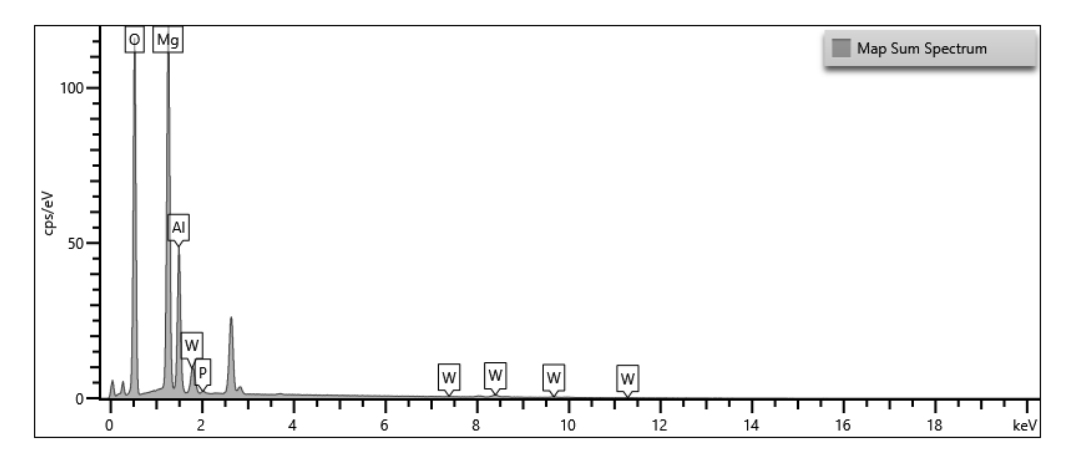


Figure 9. EDX analysis of 25% PTA-HT. Core elements belong to PTA were tungsten (W), phosphorus (P) and oxygen (O). Meanwhile, magnesium (Mg) and aluminum (Al) belong to HT

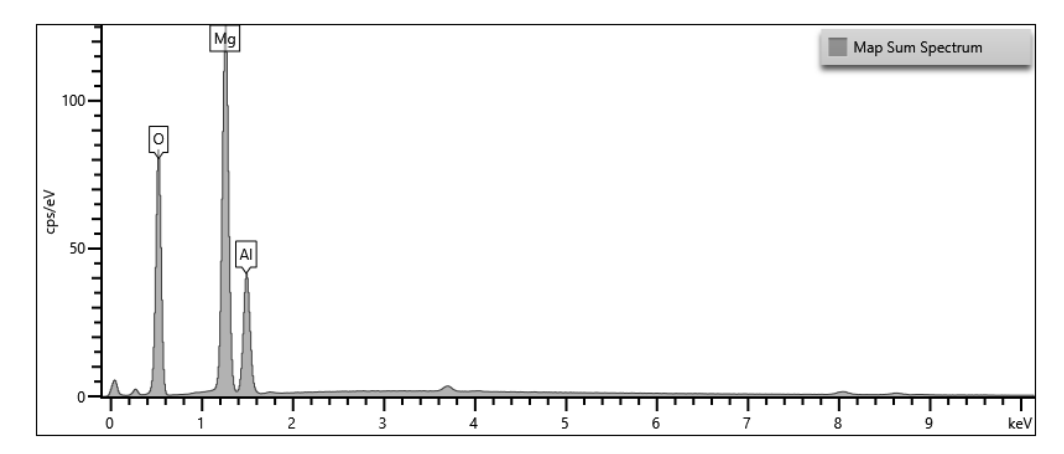


Figure 10. EDX analysis of calcined HT. Core elements belong to calcined HT were magnesium (Mg) and aluminum (Al) belong to HT

Conclusion

From our results, the FA production follows two possible routes contributed by Brönsted acid of PTA and basicity of calcined HT. The basicity of calcined HT may also promote formation of FA while performs well as catalyst support. Although calcined HT is dominant in the catalyst, acidity of PTA plays major role in degrading cellulose into FA. As reported, at optimum condition, 18% FA was yielded together with 30% cellulose degradation which was two times higher than calcined HT alone. To conclude this, the temperature and acidity of catalyst influence the cellulose degradation into FA. However, suitable temperature acidity is required to avoid decomposition of FA. Meanwhile, reaction time have minimal effect towards FA yield. The cellulose degradation can be done independently in water medium but regards to temperature and acid catalyst, the reaction was enhanced. Through catalyst characterization, PTA was successfully impregnated with calcined HT as proved from our results. According to the finding, FA was successfully produced in moderate amounts. Optimum condition for FA yield was as follows: 220°C, 4 hours with 25% catalyst loadings.

Acknowledgement

Authors thank Fundamental Research Scheme Grant (FRGS/1/2019/STG01/USIM/03/1) from Ministry of Education Malaysia for the financial support and Universiti Sains Islam Malaysia for laboratory facilities.

References

- Foong, S. Y., Liew, R. K., Yang, Y., Cheng, Y. W., Yek, P. N. Y., Mahari, W. A. W., ... and Lam, S. S. (2020). Valorization of biomass waste to engineered activated biochar by microwave pyrolysis: progress, challenges, and future directions. *Chemical Engineering Journal*, 389: 124401.
- Mamleeva, N. A., Autlov, S. A., Bazarnova, N. G. and Lunin, V. V. (2016). Degradation of polysaccharides and lignin in wood ozonation. *Russian Journal of Bioorganic Chemistry*, 42(7): 694-699.

- Ribeiro, L. S., de Melo Órfão, J. J. and Pereira, M. F. R. (2017). Simultaneous catalytic conversion of cellulose and corncob xylan under temperature programming for enhanced sorbitol and xylitol production. *Bioresource Technology*, 244: 1173-1177.
- Scapin, E., Rambo, M. K. D., Viana, G. C. C., Marasca, N., Lacerda, G. E., Rambo, M. C. D. and Fernandes, R. D. M. N. (2019). Sustainable production of furfural and 5-hidroximetilfurfural from rice husks and soybean peel by using ionic liquid. *Food Science and Technology*, 40: 83-87.
- 5. Dalena, F., Basile, A. and Rossi, C. (Eds.). (2017). *Bioenergy systems for the future: Prospects for biofuels and biohydrogen*. Woodhead Publishing.
- Tursi, A. (2019). A review on biomass: importance, chemistry, classification, and conversion. *Biofuel Research Journal*, 6(2): 962-979.
- 7. Nur, N. D., Nur, W. M. Z., Ahmad, H. M., Nor, M. A. and Sheikh, A. I. S. M. G. (2020). Study on the oxidation and properties of dihydroxyl cellulose using different amounts of sodium periodate. *Malaysian Journal of Analytical Sciences*, 24(6): 830-837.
- 8. Prasad, S. and Ingle, A. P. (2019). Impacts of sustainable biofuels production from biomass. In *Sustainable Bioenergy*, Elsevier. pp. 327-346.
- Wattanapaphawong, P., Sato, O., Sato, K., Mimura, N., Reubroycharoen, P. and Yamaguchi, A. (2017). Conversion of cellulose to lactic acid by using ZrO₂–Al₂O₃ catalysts. *Catalysts*, 7(7): 221.
- Hou, Y., Lin, Z., Niu, M., Ren, S. and Wu, W. (2018). Conversion of cellulose into formic acid by Iron(III)-catalyzed oxidation with O₂ in acidic aqueous solutions. ACS Omega, 3(11): 14910-14917.
- 11. Zhang, M. H., Dong, H., Zhao, L., Wang, D. X. and Meng, D. (2019). A review on Fenton process for organic wastewater treatment based on optimization perspective. *Science of the Total Environment*, 670: 110-121.

- 12. Morone, A., Mulay, P. and Kamble, S. P. (2019). Removal of pharmaceutical and personal care products from wastewater using advanced materials. *Pharmaceuticals and Personal Care Products: Waste Management and Treatment Technology*, 2019: 173-212.
- 13. Ma, J., Zhang, K., Huang, M., Hector, S. B., Liu, B., Tong, C., ... and Zhu, Y. (2016). Involvement of Fenton chemistry in rice straw degradation by the lignocellulolytic bacterium *Pantoea ananatis* Sd-1. *Biotechnology for Biofuels*, 9(1): 1-13.
- 14. Awudu, F. (2018). Hydrolysis of Cellulose and Biomass using Blue Molybdenum (Doctoral dissertation, East Tennessee State University).
- Gromov, N. V., Medvedeva, T. B., Rodikova, Y. A., Babushkin, D. E., Panchenko, V. N., Timofeeva, M. N., ... and Parmon, V. N. (2020). One-pot synthesis of formic acid via hydrolysis–oxidation of potato starch in the presence of cesium salts of heteropoly acid catalysts. *RSC Advances*, 10(48): 28856-28864.
- Cheng, C., Wang, J., Shen, D., Xue, J., Guan, S., Gu, S. and Luo, K. H. (2017). Catalytic oxidation of lignin in solvent systems for production of renewable chemicals: A review. *Polymers*, 9(6): 240.
- 17. Albert, J. (2017). Selective oxidation of lignocellulosic biomass to formic acid and high-grade cellulose using tailor-made polyoxometalate catalysts. *Faraday Discussions*, 202: 99-109.
- Chen, X., Liu, Y. and Wu, J. (2020). Sustainable production of formic acid from biomass and carbon dioxide. *Molecular Catalysis*, 483: 110716.
- Voß, D., Dietrich, R., Stuckart, M. and Albert, J. (2020). Switchable catalytic polyoxometalate-based systems for biomass conversion to carboxylic acids. ACS Omega, 5(30), 19082-19091.
- Doungsri, S., Rattanaphanee, P. and Wongkoblap,
 A. (2019). Production of lactic acid from cellulose using solid catalyst. In MATEC Web of Conferences, 268: 07006).
- Sun, Y., Shi, L., Wang, H., Miao, G., Kong, L., Li,
 and Sun, Y. (2019). Efficient production of lactic acid from sugars over Sn-Beta zeolite in water: catalytic performance and mechanistic

- insights. Sustainable *Energy & Fuels*, 3(5): 1163-1171.
- 22. Ramli, N. A. S. and Amin, N. A. S. (2015). Fe/HY zeolite as an effective catalyst for levulinic acid production from glucose: characterization and catalytic performance. *Applied Catalysis B: Environmental*, 163: 487-498.
- 23. Bhorodwaj, S. K. and Dutta, D. K. (2011). Activated clay supported heteropoly acid catalysts for esterification of acetic acid with butanol. *Applied Clay Science*, 53(2): 347-352.
- 24. Hietala, J., Vuori, A., Johnsson, P., Pollari, I., Reutemann, W. and Kieczka, H. (2016). Formic acid. *Ullmann's Encyclopedia of Industrial Chemistry*, 1: 1-22.
- Ricke, S. C., Dittoe, D. K. and Richardson, K. E. (2020). Formic acid as an antimicrobial for poultry production: A review. *Frontiers in Veterinary Science*, 2020: 563.
- 26. Johnson Jr, W., Heldreth, B., Bergfeld, W. F., Belsito, D. V., Hill, R. A., Klaassen, C. D., ... and Andersen, F. A. (2016). Safety assessment of formic acid and sodium formate as used in cosmetics. *International Journal of Toxicology*, 35(2): 41S-54S.
- 27. Kos, L., Michalska, K., Żyłła, R. and Perkowski, J. (2014). Effect of formic acid on pollutant decomposition in textile wastewater subjected to treatment by the Fenton method. *Fibres & Textiles in Eastern Europe*, 22, 135-139.
- del Barrio, M. A., Hu, J., Zhou, P. and Cauchon, N. (2006). Simultaneous determination of formic acid and formaldehyde in pharmaceutical excipients using headspace GC/MS. *Journal of Pharmaceutical and Biomedical Analysis*, 41(3): 738-743.
- 29. Higgins, F. J. and Ho, G. E. (1982). Hydrolysis of cellulose using HCl: a comparison between liquid phase and gaseous phase processes. *Agricultural Wastes*, 4(2): 97-116.
- Goldstein, I. S., Pereira, H., Pittman, J. L., Strouse,
 B. A. and Scaringelli, F. P. (1983, January).
 Hydrolysis of cellulose with superconcentrated hydrochloric acid. In *Biotechnol. Bioeng. Symp.*; (United States), 13: No. CONF-830567.
 North Carolina State Univ., Raleigh.

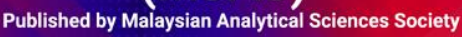
- Dussán, K. J., Silva, D. D., Moraes, E. J., Arruda, P. V. and Felipe, M. G. (2014). Dilute-acid hydrolysis of cellulose to glucose from sugarcane bagasse. *Chemical Engineering Transaction*, 38: 433-438.
- 32. Alcañiz-Monge, J., El Bakkali, B., Trautwein, G. and Reinoso, S. (2018). Zirconia-supported tungstophosphoric heteropolyacid as heterogeneous acid catalyst for biodiesel production. *Applied Catalysis B: Environmental*, 224: 194-203.
- 33. Anggorowati, H., Jamilatun, S., Cahyono, R. B. and Budiman, A. (2018). Effect of hydrochloric acid concentration on the conversion of sugarcane bagasse to levulinic acid. In *IOP Conference Series: Materials Science and Engineering*, 299(1): p. 012092.
- 34. Huang, P. and Yan, L. F. (2017). Efficient degradation of cellulose in its homogeneously aqueous solution over 3D metal-organic framework/graphene hydrogel catalyst. *Chinese Journal of Chemical Physics*, 29(6): 742.
- 35. Sivasubramaniam, D., Amin, N. A. S., Ahmad, K. and Ramli, N. A. S. (2019). Production of ethyl levulinate via esterification reaction of levulinic acid in the presence of ZrO₂ based catalyst. *Malaysian Journal of Analytical Sciences*, 23(1): 45-51.
- Demesa, A. G., Laari, A., Sillanpää, M. and Koiranen, T. (2017). Valorization of lignin by partial wet oxidation using sustainable heteropoly acid catalysts. *Molecules*, 22(10): 1625.
- 37. Zhang, Z., Wang, B., Zhang, Y., Zhang, G. and Wang, Y. (2019). Study on the synthesize, characterization, and conductive performance of nickelzircomolybdnum heteropoly acid salt with Keggin structure. *Advances in Polymer Technology*, 2019: 501593.
- Guarin, C., Gavila, L., Constanti, M. and Medina, F. (2018). Impact of cellulose treatment with hydrotalcites in hydrothermal catalytic conversion. *Chemical Engineering Science*, 179: 83-91.
- 39. Ziyat, H., Naciri Bennani, M., Hajjaj, H., Mekdad, S. and Qabaqous, O. (2018). Synthesis and characterization of crude hydrotalcite Mg-Al-

- CO₃: study of thymol adsorption. *Research on Chemical Intermediates*, 44(7): 4163-4177.
- 40. Li, T., Miras, H. N. and Song, Y. F. (2017). Polyoxometalate (POM)-layered double hydroxides (LDH) composite materials: design and catalytic applications. *Catalysts*, 7(9): 260.
- 41. Omwoma, S., Chen, W., Tsunashima, R. and Song, Y. F. (2014). Recent advances on polyoxometalates intercalated layered double hydroxides: From synthetic approaches to functional material applications. *Coordination Chemistry Reviews*, 258: 58-71.
- 42. Sasaki, M., Fang, Z., Fukushima, Y., Adschiri, T. and Arai, K. (2000). Dissolution and hydrolysis of cellulose in subcritical and supercritical water. *Industrial & Engineering Chemistry Research*, 39(8): 2883-2890.
- 43. Paksung, N., Pfersich, J., Arauzo, P. J., Jung, D. and Kruse, A. (2020). Structural effects of cellulose on hydrolysis and carbonization behavior during hydrothermal treatment. *ACS Omega*, 5(21): 12210-12223.
- 44. De Guzman, D. and De Leon, R. (2021). Preliminary optimization and kinetics of SnCl₂-HCl catalyzed hydrothermal conversion of microcrystalline cellulose to Levulinic acid. *Journal of Renewable Materials*, 9(1): 145.
- 45. Wang, K., Liu, Y., Wu, W., Chen, Y., Fang, L., Li, W. and Ji, H. (2020). Production of levulinic acid via cellulose conversion over metal oxide-loaded MOF catalysts in aqueous medium. *Catalysis Letters*, 150(2): 322-331.
- 46. Li, X., Lu, X., Nie, S., Liang, M., Yu, Z., Duan, B., ... and Si, C. (2020). Efficient catalytic production of biomass-derived levulinic acid over phosphotungstic acid in deep eutectic solvent. *Industrial Crops and Products*, 145: 112154.
- Lauermannová, A. M., Paterová, I., Patera, J., Skrbek, K., Jankovský, O. and Bartůněk, V. (2020). Hydrotalcites in construction materials. *Applied Sciences*, 10(22): 7989.

- 48. Gromov, N. V., Taran, O. P., Delidovich, I. V., Pestunov, A. V., Rodikova, Y. A., Yatsenko, D. A., ... and Parmon, V. N. (2016). Hydrolytic oxidation of cellulose to formic acid in the presence of Mo-VP heteropoly acid catalysts. *Catalysis Today*, 278: 74-81.
- Guarin, C., Gavila, L., Constanti, M. and Medina, F. (2018). Impact of cellulose treatment with hydrotalcites in hydrothermal catalytic conversion. *Chemical Engineering Science*, 179: 83-91.
- 50. Delidovich, I. and Palkovits, R. (2015). Structure—performance correlations of Mg—Al hydrotalcite catalysts for the isomerization of glucose into fructose. *Journal of Catalysis*, 327: 1-9.
- Tulaphol, S., Hossain, M. A., Rahaman, M. S., Liu, L. Y., Phung, T. K., Renneckar, S., ... and Sathitsuksanoh, N. (2019). Direct production of levulinic acid in one pot from hemp hurd by dilute acid in ionic liquids. *Energy & Fuels*, 34(2): 1764-1772.
- 52. Dandach, A., Vu, T. T. H., Fongarland, P. and Essayem, N. (2019). ZrW catalyzed cellulose conversion in hydrothermal conditions: Influence of the calcination temperature and insights on the nature of the active phase. *Molecular Catalysis*, 476: 110518.
- 53. Tian, J., Wang, J., Zhao, S., Jiang, C., Zhang, X. and Wang, X. (2010). Hydrolysis of cellulose by the heteropoly acid H₃PW₁₂O₄₀. *Cellulose*, 17(3): 587-594.
- Xiaohua, C., Jie, R., Changlong, X., Zhang, K., Changchao, Z. H. A. N., and Jian, L. A. N. (2013). Preparation, characterization of Dawson-type

- heteropoly acid cerium (III) salt and its catalytic performance on the synthesis of n-butyl acetate. *Chinese Journal of Chemical Engineering*, 21(5): 500-506.
- 55. Julianti, N. K., Wardani, T. K., Gunardi, I. and Roesyadi, A. (2017). Effect of calcination at synthesis of Mg-Al hydrotalcite using coprecipitation method. *The Journal of Pure and Applied Chemistry Research*, 6(1): 7.
- 56. Jia, Y., Fang, Y., Zhang, Y., Miras, H. N. and Song, Y. F. (2015). Classical Keggin intercalated into layered double hydroxides: facile preparation and catalytic efficiency in Knoevenagel condensation reactions. *Chemistry—A European Journal*, 21(42): 14862-14870.
- 57. Liu, G., Yang, J. and Xu, X. (2020). Synthesis of hydrotalcite-type mixed oxide catalysts from waste steel slag for transesterification of glycerol and dimethyl carbonate. *Scientific Reports*, 10(1): 1-14.
- 58. Roohollahi, G. and Ehsani, M. (2019). An investigation into the effect of hydrotalcite calcination temperature on the catalytic performance of mesoporous Ni-MgO-Al₂O₃ catalyst in the combined steam and dry reforming of methane. *Iranian Journal of Oil and Gas Science and Technology*, 8(4): 64-84.
- Bardin, B. B., Bordavekar, S. V., Neurock, M. and Davis, R. I. (1998). Analysis of kegging-type heteropoly compounds evaluated by catalytic probe reaction sorption microcalorimetry and density functional quantum chemical calculations. *Journal Physical Chemistry*, 102: 10817-10825.

Malaysian Journal of Analytical Sciences (MJAS)





THE PREPARATION AND APPLICATION OF ZINC SULFIDE AS PHOTOCATALYST FOR WATER REMEDIATION: A MINI REVIEW

(Penyediaan dan Aplikasi Zink Sulfida sebagai Pemangkin Cahaya untuk Rawatan Air: Ulasan Ringkas)

Kavirajaa Pandian Sambasevam, Jamilin Rashida Adnan, Izyan Najwa Mohd Norsham, Siti Nor Atika Baharin*

Advanced Material for Environmental Remediation (AMER) Research Group,
Faculty of Applied Sciences,

Universiti Teknologi MARA, Cawangan Negeri Sembilan, Kampus Kuala Pilah, 72000 Kuala Pilah, Negeri Sembilan, Malaysia

*Corresponding author: atikabaharin@uitm.edu.my

Received: 2 September 2021; Accepted: 7 March 2022; Published: 28 April 2022

Abstract

ZnS has gained attention as an effective photocatalyst for the photocatalytic degradation method in wastewater treatment. Photocatalysis is believed to be a promising solution to solve the problem of water pollution and remove organic pollutants. Apart from other photocatalysts such as ZnO, TiO₂ and MoS₂, ZnS is a developing photocatalyst in this degradation method due to its large bandgap energy. This review paper comprehensively considered the preparation (hydrothermal, solvothermal, low temperature, green synthesis, solid-state reaction, and microwave-assisted synthesis) of ZnS, application, and some challenges that have been faced by photocatalytic degradation methods. The adsorption and photocatalytic properties of ZnS depend on the different morphology and size formed by different methods. ZnS modification presents higher decomposition efficiency in removing organic pollutants.

Keywords: metal disulfide, organic pollutants, photocatalytic degradation, sustainable water management

Abstrak

ZnS mendapat perhatian sebagai pemangkin cahaya yang terbaik untuk melakukan rawatan terhadap air yang tercemar. Fotokatalisis dipercayai sebagai penyelesaian dalam menyelesaikan masalah air yang tercemar dan menyingkirkan pencemaran semulajadi yang terdapat di dalam air. Selain daripada pemangkin cahaya seperti ZnO, TiO₂ dan MoS₂, ZnS dijadikan sebagai pemangkin cahaya dalam kaedah pemulihan air kerana ZnS mempunyai tenaga jurang pita yang tinggi. Kertas kajian ini merangkumi cara penyediaan (hidroterma, solvoterma, teknik suhu rendah, sintesis hijau, tindak balas keadaan pepejal, dan sintesis berteraskan gelombang mikro) ZnS, aplikasi dan beberapa cabaran yang perlu di hadapi dalam proses rawatan air. Ciriciri penyerapan dan fotokatalitik ZnS bergantung kepada perbezaan struktur permukaan dan saiz yang terbentuk dari perbezaan penyediaan. Pengubahsuaian ZnS menunjukkan kecekapan penguraian yang tinggi kepada pencemaran semulajadi.

Kata kunci: logam disulfida, pencemar organik, penyingkiran fotokatalitik, pengurusan lestari air

Introduction

Filtration, chemical precipitation, ion exchange adsorption, electro deposition and membrane system are several conventional methods of water treatment. However, they exhibit slow and non-destructive effects on some organic contaminants [1]. Application of advanced oxidation methods such as photodegradation is significant due to their complete degradation without leaving any by-product behind. Photocatalysis has been widely studied because it requires an exceptionally simple procedure to generate free radicals that can degrade organic pollutants [2]. Photocatalytic study can be defined as the ability of some materials to speed up a certain reaction as a catalyst in combination with light including sunlight, UV and visible light. The term 'photocatalytic' designated reactions accelerated by light but maintaining the same course as the thermal reactions [3]. Photocatalytic activity is influenced by the crystal structure, particle size, band gap, dispersibility and hydroxyl of the catalyst. Photocatalytic degradation is a study that is still currently developing. Semiconductor photocatalysts play an important role in photocatalytic activities. Various studies were widely carried out by many researchers around the globe. Among all semiconductors, titanium dioxide (TiO2) is the most frequently used photocatalyst in study and research regarding oxidation of organic pollutants. However, its high potential for charge recombination has become a limiting factor of TiO2 for sunlight photocatalytic applications [4].

Meanwhile, the single semiconductor which is the photocatalyst only consists of one medium of photocatalyst to degrade organic pollutant that shows ineffective degradation rates, such as bismuth vanadate (BiVO₄), zinc oxide (ZnO) and cadmium selenide (CdSe) [5]. ZnS is a II-VI semiconductor material that exhibits a high excitation energy which is approximately 40 meV. ZnS also has a band gap energy of 3.7 eV and ZnS can be used as semiconductor photocatalyst to degrade pollutants due to its non-toxic nature, highly negative reduction potential of excited electrons and high rate of

formation of electron-hole pairs that leads to higher conduction band position in aqueous media [6,7]. A study reported that ZnS is an important inorganic material for various applications such as solar cell, field effect transistor, photoconductors, sensors, light-emitting materials and optical coating [8]. Moreover, ZnS is chosen to be a photocatalyst because of its direct wide band gap (e.g., = $3.7 \, \text{eV}$), good mechanical stability, highly efficient conductivity, and high electron transfer ability, aside from the ZnS nanoparticle having a high rate of success when doped with the polyaniline matrix [6,5]. Thus, this mini review aimed to examine the recent preparation technique of ZnS and its application as a photocatalyst in water remediation.

Fundamental of photocatalytic degradation

Photocatalytic degradation technology is one of the advanced oxidation processes (AOP) that involves semiconductor photocatalyst and oxygen to produce radicals in which the activity is influenced by the crystal structure, particle size, band gap, dispersibility and hydroxyl of the catalyst. The basic principle of photocatalyst activation mechanism can be seen in Figure 1. During this reaction, these photons contribute to the excitation of electrons (e-) on the surface of photocatalyst in the valence band when the energy of the photons is higher than the band gap which makes the e⁻ rise up into the conduction band and causes the production of a hole (h⁺) in the valence band. These separated holes and electrons can recombine and release the absorbed energy to form heat. The excited electrons that are now in the conduction band (e-CB) will react with oxygen (O₂) to form superoxide radicals (O₂-) or hydroperoxide radicals (HO₂). Next, these reactive oxygen species will be used for the degradation of pollutants into water (H2O) and carbon dioxide (CO₂). O₂- can be further used again in secondary degradation steps where these reactions could result in the oxidation of water molecules at the positive hole in the valence band (h+VB) that produces hydroxyl radicals (OH) and hydrogen ions (H⁺). Lastly, the OH would react with pollutants and result in H₂O and CO₂ [9,10].

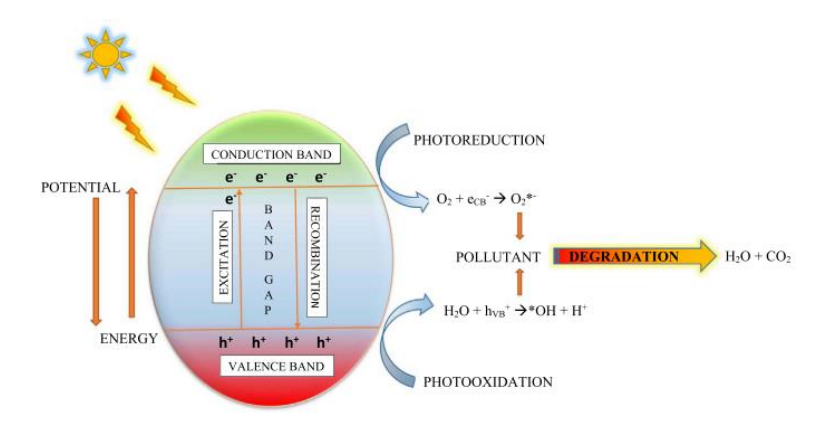


Figure 1. Basic principle of photocatalysis [9]

Many studies have been carried out to test a variety of sources and mostly focused implementation of UV light because this light provides enough photons to generate electron hole pairs within the catalyst. Thus, it could perform efficiently in the production of radicals and the oxidative degradation of the toxic and dangerous pollutants [11]. Photocatalytic processes can use artificial UV lamps and sunlight as the radiation source in photocatalysis. Mostly used artificial UV lamps that were mercury lamps that can be divided into low pressure, medium pressure and high pressure. Moreover, sunlight also has been used in this reaction as nearly 4 to 5% of the sunlight that reaches the surface of earth is in the range of 300 to 400 nm. ZnS is powerful as a photocatalyst in UV range compared to visible range [12]. Furthermore, sunlight has its own limitation because of its graphical variation when compared with artificial UV lamps [13]. Munawaroh and co-author stated that zinc oxide/graphene oxide (ZnO/GO) had high adsorption

capacity and GO addition made the band gap narrower, which prevented the recombination of electron and led to high electron transfer on the ZnO [14]. The photocatalytic activity of ZnO/GO is performed in different irradiation times which are 15, 30, 45 and 60 minutes and the maximum wavelength is 665 nm. Figure 3 shows that UV light is involved to activate the photocatalytic properties of the material to form radical species that lead to degradation of the methylene blue dve into green compounds. From Figure 2, it is proven that the longer the contact time, the more electrons would be excited which contribute to production of more h⁺. Mechanisms (1) to (6) show the formation of h⁺ which contributes to formation of hydroxyl radicals in the photocatalytic degradation. More production of h⁺ would increase the photocatalytic degradation. The percent efficiency of degradation based on formula (7) in methylene blue with ZnO/GO 1:2 is 94.05% [14].

Excitation: Photon
$$(hv)$$
 + Semiconductor \rightarrow $e^ _{CB}$ + h^+ $_{VB}$ (1)

Recombination: e^- + h^+ \rightarrow energy (2)

Oxidation of H_2O : H_2O + h^+ $_{VB}$ \rightarrow \bullet OH + H^+ (3)

Reduction of adsorbed O_2 : O_2 + $e^ \rightarrow$ O_2 \bullet^- (4)

Reaction with H^+ : O_2 \bullet^- + H^+ \rightarrow \bullet OOH (5)

Electrochemical reduction: \bullet OOH + \bullet OOH \rightarrow H_2O_2 + O_2 (6)

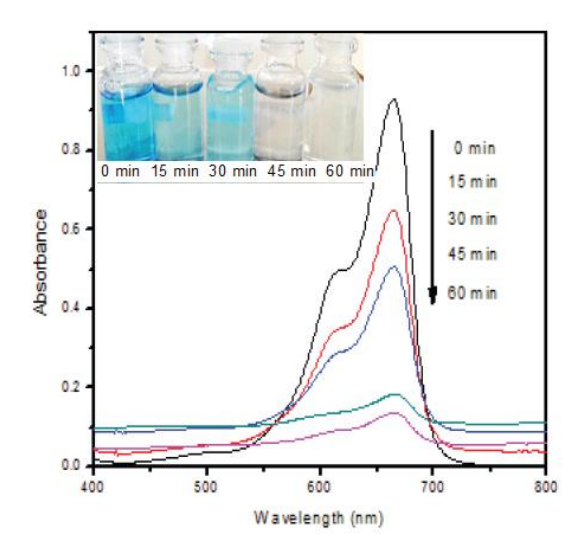


Figure 2. UV-vis spectra of methylene blue with ZnO/GO (1:2) and under UV illumination [14]

Preparation of zinc sulfide

In general, ZnS can be synthesised via various methods such as solution-phase reaction, hydrothermal, solvothermal, exfoliation, high pressure autoclave processes, physical vapour deposition (PVD) and chemical vapour deposition (CVD). ZnS can be easily synthesised with the aid of autoclave at high pressure and low temperature without the need of a catalyst [15]. At ambient conditions, ZnS possess two crystal structures which are zinc blend (cubic) and wurtzite (hexagonal), meanwhile at high pressure "rock salt" crystalline shape can be achieved but only in case of nanostructures of ZnS [15].

Hydrothermal method

Hydrothermal method refers to the heterogeneous reactions for synthesising inorganic materials in an aqueous media above ambient temperature and pressure which is used to obtain nanoparticles, generally at relatively high temperature which is around 200°C by using an autoclave reactor and high pressure. In order to get the desired size and shape of ZnS, a capping agent is applied to control the size and shape of ZnS such as surfactants, ligands, dendrimers and polymers [16]. In hydrothermal synthesis, this capping agent is used to control the nanometre size of ZnS. Thioglycolic acid (TGA) is a common capping

agent that has been studied for synthesising ZnS. It is ZnO/ZnS nanocable, ZnS/organic composite nanoribbons and ZnS nanotube arrays have been successfully synthesised by using TGA. In the previous study, TGA was used to prevent the chalcogenide nanocrystal accumulation which is known as stability agents. Thus, TGA is a perfect choice during the hydrothermal process as a capping agent for self-assembly and crystal growth of ZnS crystal to cluster. In this process, the temperature of 105°C is maintained during the autoclave for 7 hours. Based on the transmission electron microscopy (TEM) and selected area electron diffraction (SAED) in the range of 50 to 150 nm as shown in Figure 3, the morphology of ZnS crystal forms some loose spheres by accumulation of small particles. Most of the organic molecules are degraded because of the temperature that took place during the process. The ZnS nanocluster is formed at the final process due to only a part of the TGA molecule which is diffused into the ZnS nanoparticle. The SAED pattern also shows sharp rings of (1 1 1), (2 2 0) and (3 1 1) planes of cubic zinc blended ZnS that corresponded to the XRD study Figure. 4. The size of the nanocrystals based on the Scherrer formula (D= $0.89\lambda/\beta \cos \theta$), estimated from the full width at half maxima (FWHM) of the (1 1 1) diffraction peak is about 4 nm for synthesised nanoparticles which are much smaller than the spherical diameters. This indicates that the clusters are formed from nanocrystal mass assembly. It is fair to assume that the TGA-assisted hydrothermal process provides a great opportunity to scale-up other chalcogenides morphology preparation [17]. Based on a previous study, a composite of SnO₂/ZnS prepared by hydrothermal method at 180°C showed the highest photocatalytic activity to degrade RhB [18]. The

photocatalytic degradation of 95% is reached at the 1 g/L SnO₂/ZnS dosage with 10 mg/L initial RhB concentration, 4.59 initial solution pH and 23°C. The photocatalytic degradation of the RhB really fitted to the first-order kinetic model and it is also showing the decrease of initial RhB concentration with the increase of SnO₂/ZnS dosage. The composited SnO₂/ZnS that are prepared by hydrothermal method also showed a stable performance during 5 runs of reuse [18].

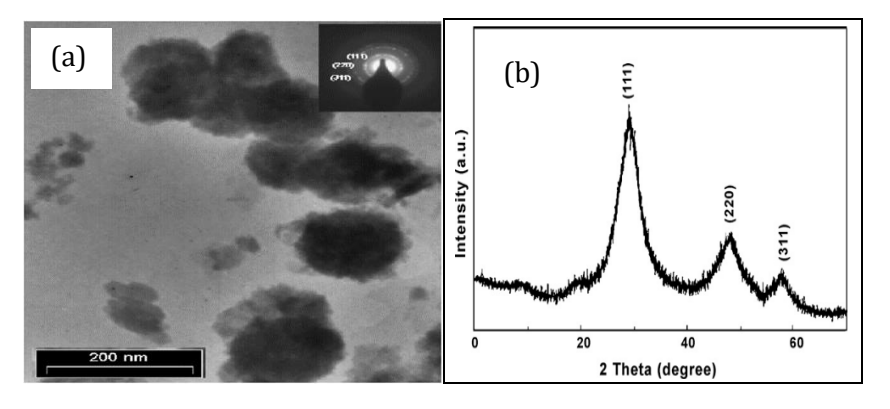


Figure 3. (a) TEM image of ZnS nanocluster; (b) Figure 4 XRD pattern of as-prepared ZnS nanocluster [17]

Solvothermal method

Solvothermal process refers to a heterogeneous reaction involving the thermal decomposition of metal complexes using the solvent mineraliser either by boiling the contents in an inert atmosphere or in a sealed vessel (autoclave). Solvothermal method including possesses advantages energy consumption and simple and also some disadvantages including need for expensive autoclaves and Teflon liners in stainless steel, which can lead to safety problems during reaction processes and impossibility of studying in-situ reactions due to their closed system [19]. Unlike hydrothermal route which needs a surfactant, toxic template or capping agent to control the size of ZnS morphology, solvothermal method is without surfactant and needs propylene glycol solvent at 140 °C for 12 hours to produce the ZnS nanoplates. The SEM image in Figure 4 (a) of ZnS exhibits flower-like morphology and a large amount of quasi hexagonal plates which were produced via solvothermal method.

However, in the solvothermal method, the right choice of temperature is crucial. As can be seen in Figure 4 (b), higher temperature at 160 °C yielded non-uniform and amorphous nature of ZnS. Obviously, this condition via solvothermal technique did not favour the synthesis of ZnS. This is due to the decreasing crystallisation temperature which can be attributed to a slight increase in photocatalytic activity, hence temperatures higher than 140 °C mostly do not support this method [20]. Song and co-worker carried out the preparation of a ternary photocatalyst of zinc cadmium sulphide by this method which was synthesised at a maintained temperature of 120-140 °C for 3 hours [21]. The methylene blue (MB) was degraded by the photocatalytic activity of zinc cadmium sulphide. 0.4 g zinc cadmium sulphide photocatalyst was dispersed in 250 mL of MB solution. In this study, after a 1-hour reaction time, at 120 °C the photocatalytic activity showed the best photocatalytic activity compared to 140 and 130 °C as shown in Figure 5 below due to 120 °C being the lowest temperature so it is suitable for the solvothermal method.

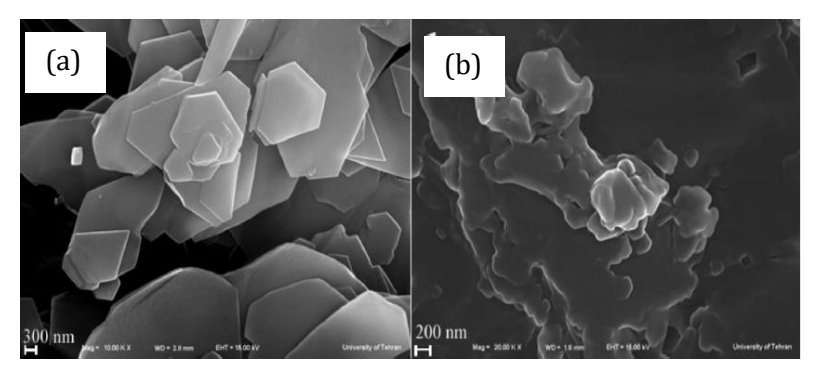


Figure 4. SEM image of as-synthesized product in propylene glycol for 12 hours: (a) 140 °C and (b) 160 °C [20]

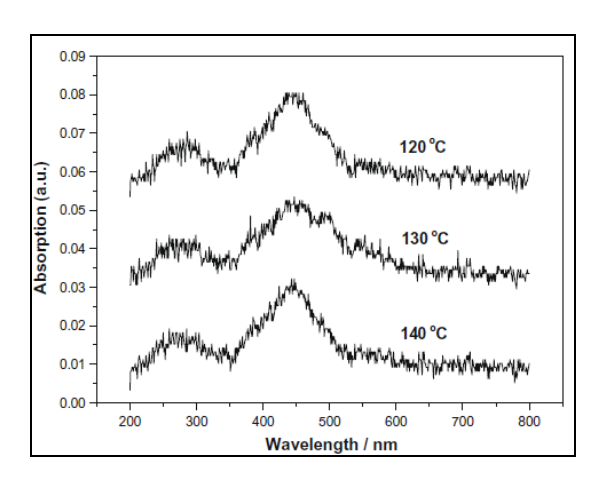


Figure 5. UV-vis absorbance spectra of sample treated at 120-140 °C [21]

Low temperature method

This method basically involves low temperature (below 100°C) by a chemical reaction that occurs between zinc ions and reduces sulphide ions in ethanol as a reaction medium. This method requires a strong reducing agent to have a better control reaction such as hydrazine hydrate to have better control to convert elemental sulphur (S₈) to reactive sulphide ions (S²⁻) by in-situ reduction. The sulphide ions then react on impulse with zinc ions, since zinc chloride and elemental sulphur were used separately as sources of zinc and sulphur [22]. Low temperature method exhibited preferable characteristics as it is less toxic, less time consuming, low cost and needs low temperature without any solvent release, low waste and environmentally friendly [22]. The less time consumption can be observed when the reduction of S₈ into S²- took place in a very short time. The reaction can be represented in Equation (7) [20].

Equation (7) showed a rapid process as it only takes a few seconds (30-40 seconds) of the elemental sulphur reduction to happen. The concentration of zinc before and after reaction was calculated to know the yield of the reaction by using an ICP-OES spectrometer. The reading of the ICP-OES spectrometer showed 99% consumption of zinc precursor in the reaction which means a very high conversion yield of the precursor to the final product was obtained. Study of the reaction time impact showed that longer reaction times lead to agglomeration of less particles to bigger ones. Hence, the reaction time should be adjusted to form the particles as soon as hydrazine hydrate has been added. Figure 6 (a) shows UV-Vis absorption spectra of ZnS

quantum dots at 60 °C with different reaction times of 2, 3, 5, 7 and 12 minutes which displayed that the size of ZnS quantum dots were almost the same and that longer time which was up to 60 minutes at 60 °C did not influenced the particle size with absorption peak at ~257 nm. Meanwhile, Figure 6 (b) shows UV-Vis absorption spectrum of ZnS quantum dots at 120 °C for 60 minutes. An absorption peak at 277 nm was

observed which is red shifted as compared to the absorption peak at 60 °C, displaying an increase in size [22]. The photocatalytic activity of ZnS synthesised by this method can be observed on the removal of MB with a photocatalyst of ZnS under UV irradiation. This study showed that ZnS succeeded in achieving removal efficiency of 75% during photocatalytic degradation of MB [23].

$$ZnCl_2 + \frac{1}{8S} + N_2H_2.H_2O \xrightarrow{C_2H_5OH,60\,^{\circ}C} ZnS + 2HCl + N_{2(g)}H_{2(g)} + H_2O$$
(7)

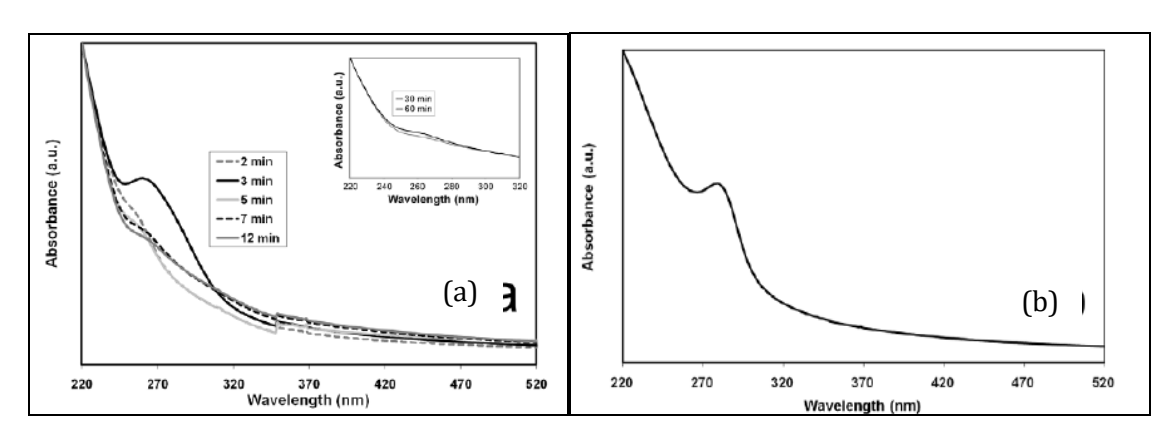


Figure 6. (a) UV-Vis absorption spectrum of ZnS quantum dots at 60 °C for reaction time 2, 3, 5, 7, 12 minutes (a) at 60 °C for reaction time 30 and 60 minutes (b) at 120 °C for 60 minutes [22]

Green synthesis method

Green synthesis method is a biological synthesis of nanoparticles that basically uses plants or plant extract which is low cost, nontoxic and environmental friendly method. A study on glucose was used as both stabilizer and capping agent while latex solution prepared from Jatropha curcas L. In the Jatropha curcas L there were curcacycline A (an octapeptide), curcain (an enzyme) and curcacyline B (a nanopeptide) equipped inside as a potential stabilizing and reducing agent [24,25]. Glucose is a monosaccharide that present in the plants with five hydroxyl groups are arranged in its own manners along its six-carbon backbone and it is renewable, natural, large quantity and biodegradable. Glucose is used in this method while zinc nitrate and sodium sulfide as zinc and sulphur source respectively. In this method, the resulting solution was heated at 70 °C up to 6 hours. The final product of this synthesis, can be observed in the Equation (8). The ZnS that obtained via this method, exhibited crystallinity peak at 28.38°, 47.73° and 56.50° as shown in Figure. 7. The peaks were assigned to the cubic of ZnS as (1 1 1), (2 2 0) and (3 1 1). The broad peaks in XRD indicated the formation of nanoparticles. Thus, it proved that ZnS nanoparticles successfully synthesized by green method by using glucose as capping agent [24].

This method can be observed in its photocatalytic activity in a study by Kannan et al. (2020) involving ZnS that had been synthesised using plant extract of *Tridax procumbens* (T:ZnS). Biosynthesised T:ZnS (40 mL) nanoparticles displayed high surface area which was 131.84 m²/g and also exhibited larger pore size which was 12.15 nm. This high surface area was able to promote more active sites, hence increasing the photocatalytic ability to degrade MB achieved 98% of degradation efficiency under visible light irradiation.

$$Zn(NO_3)_2 + Na_2S \xrightarrow{Glucoss} ZnS + 2NaNO_3$$
 (8)

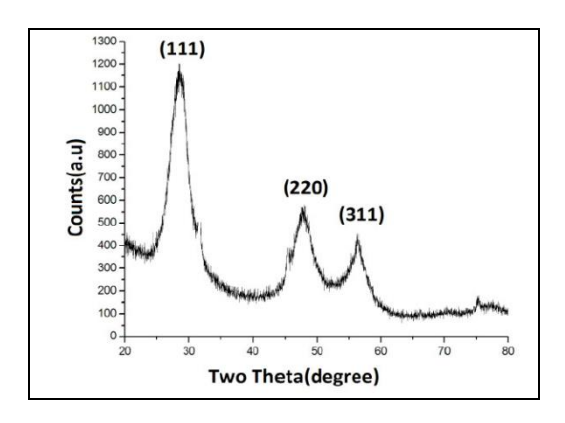


Figure 7. XRD spectra of ZnS nanoparticles [23]

Solid-state reaction method

Solid state reaction method is a simple reaction for the preparation of ZnS nanorods. This method utilises simple techniques such as melting or grinding together the starting materials or simply applying heat to a mixture of starting materials and also without any metal catalyst, solvent or templates. The nanoparticles were prepared by one-step, typically solid-state reaction of zinc chloride and sodium sulphide as zinc and sulphide sources, respectively which will be ground with mortar and pestle at ambient temperature

in sodium chloride flux. This method, however, needs high temperatures because it involves precursors to synthesise nanotubes by using a furnace at 800 °C for 2 hours for the heat treatment sample. Figure 8 shows XRD spectra of final nanoparticle ZnS nanorods fabricated by annealing precursor ZnS nanoparticle in sodium chloride flux. The synthesised ZnS nanorods have changed from cubic to hexagonal structure via solid state reaction method [27].

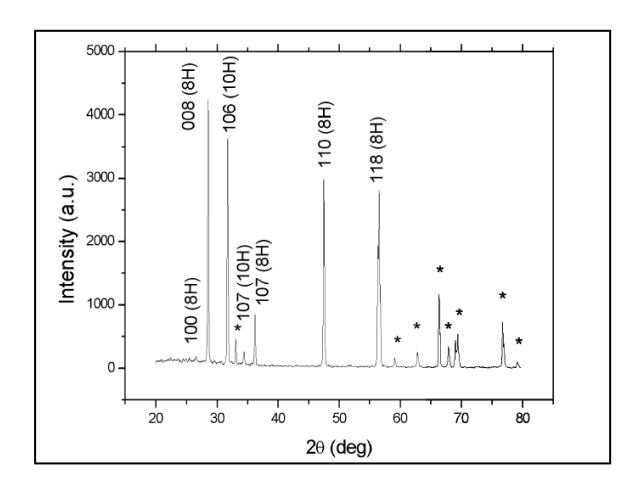


Figure 8. XRD spectra of final nanoparticle ZnS nanorods fabricated by annealing precursor ZnS nanoparticle in sodium chloride [27]

The photocatalytic performance is known to be dependent on the crystallinity, morphology and surface area that are able to enhance the recombination of photogenerated electron-hole pairs. Jothibas et al. (2018) showed the photocatalytic activity of ZnS doped with nickel (Ni) that was synthesised by this method. The ZnS doped Ni was used to degrade the MB. It proved the MB concentration decreases in the presence of ZnS doped Ni due to destruction of the homo and hetero-poly aromatic ring present in the MB or the fast degradation of the dye [27].

Microwave assisted synthesis method

Microwave (MW) assisted synthesis is a heating method that uses ionic liquids (ILs) as MW absorbing medium to synthesise the highly crystalline ZnS quantum dots (QDs). Imidazolium or phosphonium cations together with many types of anions ranging from simple anions including halides to more complex ones included bis(trifluoromethanesulphonyl) amide based, are two types of ionic liquids that were used in this method. The QDs that were synthesised as the final product were less than 5 nm in size and of wurtzite ZnS type. MW irradiation basically is a heating method where the dielectric heating mechanism involves bipolar polarisation and ionic conduction that allows for faster reactions with higher yields and higher purities without high vacuum requirements [22]. ILs are considered as friendly environmental media that can be replaced with other volatile and toxic organic solvent. It is also exhibiting some properties of high polarity, high thermal stability, high ionic conductivity and a good solvent for both electrolyte and organic compounds. Hence MW assisted with IL method that produced via 'green' synthesis route to produce the nanoparticles [23]. The microwave-assisted synthesis method to produce ZnS nanoballs with an average diameter of 41.9 nm was composited with graphene nanosheets (GNS) [29]. These ZnS nanoballs are made up of many small self-assembled ZnS crystals with an average size of 3 nm. 0.20 g of ZnS-GNS composite was used to degrade the MB, resulting in the intensity of the adsorption peaks of MB which gradually diminished with increasing exposure time and finally disappeared after about 32 minutes. This showed a complete degradation of MB as no new absorption peaks appeared in the visible and UV region.

Zinc sulfide as photocatalyst in photodegradation of organic pollutant

Overall, from the syntheses listed above, they show that photocatalytic performance of photocatalysts can be influenced by their crystallinity, morphology, size and surface area. Morphology-controlled synthesis are increasing in popularity because of the structure that decides the characteristics. Different sizes, morphology and structure of materials exhibited different properties. Scale quantisation of particles with semiconductors resulted in dramatic shifts of other essential properties of the materials. Firstly, the quantisation of the scale affects the electronics characteristics of the semiconductor particle, with ultra-small crystallites made up of a few molecular units maintaining their subtle HOMOs (Highest Occupied Molecular Orbitals) and LUMOs (Lowest Unoccupied Orbital Molecular Orbitals). Next, chemical and physical properties which are dedicated to electronic properties of the semiconductor really depend on the size of the nanoparticles. The band gap of the semiconductor becomes larger as the particle size decreases and is related to an absorption shift at shorter wavelengths hence, the level of valence band is shifted to lower energy while conduction band are strongly shifted to higher energies. To summarise, Table 1 represents comparable methods of ZnS preparation, properties and their degradation efficiency towards degradation of pollutants.

On the other hand, many methods have been developed remove organic pollutants including photodegradation with ZnS usage of as semiconductor/photocatalyst. the Among semiconductors/photocatalysts mentioned above, degradation efficiency of ZnS also can be enhanced as in binary and ternary photocatalysts.

Table 1. Methods of preparation, properties, and their degradation efficiency

Methods of Preparation	Particle Size and Shape	Pollutants	Source of Light	Degradation Efficiency	References
Hydrothermal	Clearly observed lattice fringes indicate that the particles are crystalline.	Methyl Orange (MO)	UV lamp	70% in 120 min	[30]
Solvothermal	The shape and size are uniform and it is observed that all the nanorods are well dispersed.	Rhodamine B	UV lamp	98% in 90 minutes	[31]
Solid-state reaction	The orbital composition of well-defined particles, which has spherical shapes	MO	Visible	88% in 75 minutes	[32]
Green synthesis	Revealed the crystal structures and obvious atomic planes for single particles .	Phenanthrene	Visible	82% in 90 minutes	[33]
Microwave assisted	Looked like agglomerated spherical clusters with particle size	4-chlorophenol	UV lamp	100%	[34]

Binary photocatalyst

Binary photocatalyst of ZnS is when ZnS is composited with another filler for example graphene. This composite (ZnS-graphene) can result in new properties of photocatalysts. The photocatalytic activity of ZnS-graphene was observed by degrading methylene blue (MB) in water [29]. This study used a graphene nanosheet and the UV-Vis spectrum in the range of 300 to 800 nm is given in Figure 9. The characteristic absorption peak of methylene blue solution at 663 nm was selected as the parameter monitored to detect the methylene blue concentration. Figure 13 shows the evolution of absorption spectra of MB in the presence of 0.20 g ZnS-graphene

composites. It was found that the intensity of the absorption peaks aligned directly to MB which gradually declined with increasing exposure time and finally vanished after about 32 minutes. There were no new absorption peaks pop up in the visible and ultraviolet region, showing the complete degradation of MB. In addition, the photocatalytic activity of ZnS-graphene can be observed to degrade 4-nitrophenol (4-NP) [34]. The declining of absorption peak intensity of nitrophenolate ion with ZnS-graphene was recorded over time under simulated light to observe the photocatalytic activity of the composite toward reduction of 4-NP.

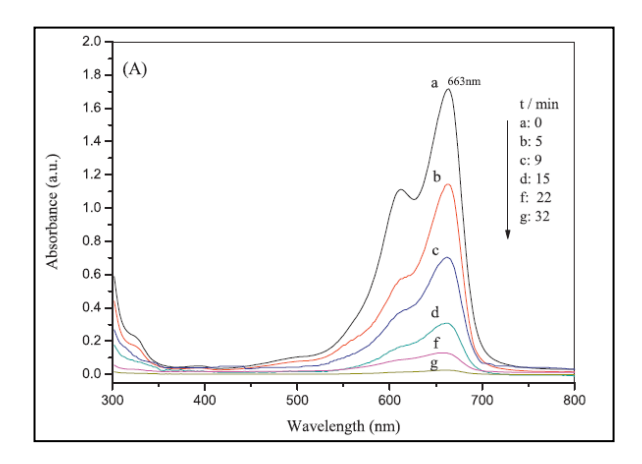


Figure 9. Absorption spectra of a solution of MB with ZnS-graphene [29]

The reduction efficiency of ZnS-graphene and ZnS was compared under simulated solar light illumination as indicated in Figure 10 (a) and (b) respectively. The time used for illumination was 70 minutes to achieve 87% of reduction efficiency with the composite while it was only 34% with single ZnS under similar experimental conditions. Hence, based on formula (10) of reduction rate constant, k shows the results of pseudo-first order reduction kinetics of 4-NP where the k of ZnS is 6 × 10⁻³ min⁻¹ while ZnS-graphene composite is 30 × 10⁻³ min⁻¹. This shows that ZnS-

graphene composite results in better efficiency compared to ZnS and 5 times higher k than ZnS because of its synergistic effect between reduced graphene oxide and ZnS where graphene is responsible for an efficient photo-induced charge separation and transportation [35]. Then, the photo-induced electrons generated in the ZnS nanorod high-band gap pass from its conduction bands to the 4-NP LUMO level through the graphene sheets and reduce the 4-NP to 4-aminophenol [35].

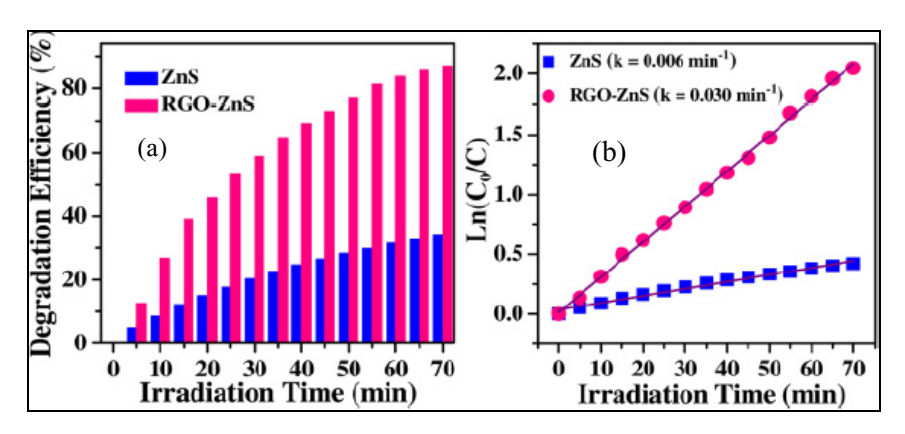


Figure 10. (a) The comparison of the reduction efficiency versus irradiation time over ZnS and ZnS-graphene (b) Plot of In (C_0/C) for the photocatalysis of 4-NP solution with ZnS and ZnS-graphene composite [35]

Ternary photocatalyst

Ternary photocatalyst is a photocatalyst that has a three-system photocatalysis; for example, reduced graphene oxide-ZnS-TiO₂ (rGO-ZnS-TiO₂). photocatalytic activity of ternary photocatalysts of rGO-ZnS-TiO2 nanocomposite can be observed on its application for crystal violet dye (CV) removal [36]. This combination is proven to be an effective photocatalyst for the treatment of wastewater. Through this study, the result showed that almost 97% CV dye was removed by adsorption and photodegradation at temperature of 35 °C with initial dye concentration of 50 ppm and nanocomposite amount of 0.4 g/L. The study was carried out with varied loadings of catalyst to decide the optimal amount of rGO-ZnS-TiO₂ nanocomposite prepared with the aid of ultrasonic irradiation. Based on Figure 11, the overall photocatalytic degradations are 94.83%, 97.02% and 96.30% obtained for 0.3 g/L, 0.4 g/L and 0.5 g/L of rGO-ZnS-TiO₂ nanocomposite respectively. The results also showed that the quantity of nanocomposite increased from 0.3 g/L to 0.4 g/L. The degradation of CV was also increased from 94.83% to 97.02% independently and continuous increase in the loading of rGO-ZnS-TiO2 nanocomposite at 0.5 g/L exhibited a marginal decline in the degradation, which was meant to be at 96.30%. rGO-ZnS-TiO₂ nanoparticles displayed strong adsorption abilities and the excessive adsorption reduced the photocatalytic activity. Hence, the distribution of impudent loaded nanocomposite will hinder the UV light irradiation and the restriction can result in an efficient usage of light resulting in declining photocatalytic degradation of CV dye. So, the result concluded that the optimal dose of rGO-ZnS-TiO₂ is 0.4 g/L with the aid of ultrasonic illumination to obtain effective degradation of CV dye [36].

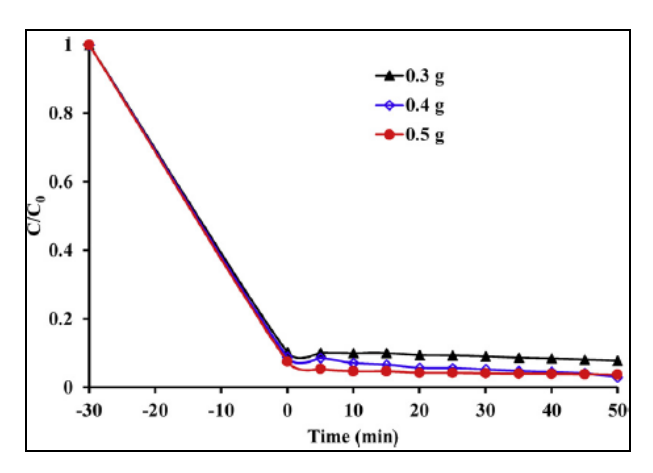


Figure 11. The effect of catalyst loading on degradation of CV dye [36]

Table 2. Comparison between binary and ternary ZnS composites in photocatalytic degradation

Types of ZnS Photocatalyst	Pollutants	Source of Light	Degradation Efficiency	References
Binary				
ZnS-graphene	methylene blue (MB)	UV light	98%	[29]
RGO-ZnS	4-nitrophenol	Solar Light	87%	[35]
Cadmium-ZnS	Methyl Orange	Visible light	90%	[32]
ZnS layers of ZnS(en)x complex	Chromium IV	Hg lamp	99%	[37]
Ternary				
rGO-ZnS-TiO ₂	crystal violet dye	UV light	97%	[36]
ZnS-TiO ₂ /RGO	Methylene blue	Visible light	90%	[38]
ZnO/reduced graphene oxide (rGO)/polyaniline (PANI)	Methyl Orange	Visible Light	100%	[39]
ZnO-ZnS@Pani	2-chlorophenol	Visible Light	87%	[40]
Ag ₂ S–ZnS loaded on cellulose	Rhodamine B	Visible light	95%	[41]

Conclusion

Based on the overall review towards the application of ZnS, it can be concluded that ZnS can be successfully composited with conducting polymers and other photocatalysts. ZnS was able to be prepared through various preparations and methods resulting in different sizes and morphologies based on their SEM and TEM images. It is also proven that different sizes and morphologies of ZnS would result in different reactions of ZnS towards photocatalytic studies. The smaller the size of ZnS, the better the photocatalytic degradation of organic pollutants. Moreover, ZnS can also act as a photocatalyst in different forms including single semiconductor, binary photocatalyst and ternary photocatalyst. Ternary photocatalysts proved to be the better photocatalytic as three media compositions increased the photocatalytic behaviour of ZnS. This is because ternary photocatalysts improved the electric properties of the photocatalyst, hence improving the photocatalytic degradation of organic pollutants. Last but not least, it can be proven on the basis of the analysis that ZnS exhibited a strong photocatalytic activity to degrade organic contaminants such as

organic dye and nitrophenols. Future studies can explore whether ZnS is able to act as a photocatalyst which is a composite with conducting polymer. Conducting polymer is widely used in applications such as sensors because of its characteristics including ease of synthesis, low density and conducting properties. Conducting polymers show potential as it can greatly increase conductivity has the advantages of conventional organic polymers including strength, plasticity, toughness and flexibility. It is believed that composited photocatalysts with conducting polymer increase the effectiveness of degradation because of the increasing appropriate surface of the photocatalyst.

References

 Dehghanifard, E., Jafari, A. J., Kalantary, R. R., Mahvi, A. H., Faramarzi, M. A. and Esrafili, A. (2013). Biodegradation of 2, 4-dinitrophenol with laccase immobilized on nano-porous silica beads. *Iranian Journal of Environmental Health Science* and Engineering, 10(1): 25.

- Anjum, M., Oves, M., Kumar, R. and Barakat, M. A. (2017). Fabrication of ZnO-ZnS@ polyaniline nanohybrid for enhanced photocatalytic degradation of 2-chlorophenol and microbial contaminants in wastewater. *International Biodeterioration and Biodegradation*, 119: 66-77.
- 3. Ayodhya, D. and Veerabhadram, G. (2018). A review on recent advances in photodegradation of dyes using doped and heterojunction based semiconductor metal sulfide nanostructures for environmental protection. *Materials Today Energy*, 9: 83-113.
- 4. Salah, N., Hameed, A., Aslam, M., Babkair, S. S., and Bahabri, F. S. (2016). Photocatalytic activity of V doped ZnO nanoparticles thin films for the removal of 2-chlorophenol from the aquatic environment under natural sunlight exposure. *Journal of Environmental Management*, 177: 53-64.
- Das, M. and Sarkar, D. (2017). One-pot synthesis of zinc oxide-polyaniline nanocomposite for fabrication of efficient room temperature ammonia gas sensor. *Ceramics International*, 43(14): 11123-11131.
- 6. Allahyeran and Mehrizad (2017). Comparison between different d-dimer cutoff values to assess the individual risk of recurrent venous thromboembolism: Analysis of results obtained in the DULCIS study. *International Journal of Laboratory Hematology* 38(1): 42-49.
- Lai, K., Wei, W., Yingtao, Z., Meng, G., Ying, D. and Baibiao, H. (2012). Effects of oxygen vacancy and n-doping on the electronic and photocatalytic properties of Bi₂MO₆ (M=Mo, W). *Journal of Solid State Chemistry* 187:103-108.
- Goswami, M., Sahoo, S., Meikap, A. K. and Ghosh, R. (2011). Characterization, optical and dc electrical properties of polyaniline-zinc sulphide nanocomposite. In *International Conference on Nanoscience, Engineering and Technology*, 2011: 314-318.
- 9. Bora, L. V. and Mewada, R. K. (2017). Visible/solar light active photocatalysts for organic effluent treatment: Fundamentals, mechanisms and parametric review. *Renewable and Sustainable Energy Reviews*, 76: 1393-1421.

- Byrne, C., Subramanian, G. and Pillai, S. C. (2018). Recent advances in photocatalysis for environmental applications. *Journal of Environmental Chemical Engineering*, 6(3): 3531-3555.
- Al-Hamdi, Abdullah, M., Uwe, R. and Mika, S. (2017). Tin dioxide as a photocatalyst for water treatment: A review. *Process Safety and Environmental Protection* 107:190-205.
- 12. Mahvelati-Shamsabadi, T. and E. K. Goharshadi. (2017). Photostability and visible-light-driven photoactivity enhancement of hierarchical ZnS nanoparticles: The role of embedment of stable defect sites on the catalyst surface with the assistant of ultrasonic waves. *Ultrasonics Sonochemistry*, 34: 78-89.
- 13. Umar, M. and Aziz, H. A. (2013). Photocatalytic degradation of organic pollutants in water. *Organic Pollutants-Monitoring, Risk and Treatment*, 8: 196-197.
- Munawaroh, H., Sari, P. L., Wahyuningsih, S. and Ramelan, A. H. (2018) The photocatalytic degradation of methylene blue using graphene oxide (GO)/ZnO nanodrums. *In AIP Conference Proceedings*, 2014: p. 020119.
- 15. Majhi, M., Choudhary, R. B., and Maji, P. (2017). HCl protonated polymeric PANI-ZnS nanocomposites and measurement of their robust dielectric, optical and thermal performance. *Optik*, 136: 181-191.
- 16. Varanda, L. C., de Souza, C. G. S., Perecin, C. J., de Moraes, D. A., de Queiróz, D. F., Neves, H. R. and da Silva, T. L. (2019). Inorganic and organic–inorganic composite nanoparticles with potential biomedical applications: Synthesis challenges for enhanced performance. In *Materials for Biomedical Engineering*: pp. 47-99.
- 17. Salavati-Niasari, M., Fatemeh, D. and Mehdi, M. (2009). Synthesis and characterization of ZnS nanoclusters via hydrothermal processing from [Bis(Salicylidene)Zinc(II)]. *Journal of Alloys and Compounds* 470(1–2): 502-506.

- 18. Hu, L., Feiyan, C., Pengfei, H., Lianpei, Z. and Xing, H. (2016). Hydrothermal synthesis of SnO2/ZnS nanocomposite as a photocatalyst for degradation of rhodamine b under simulated and natural sunlight. *Journal of Molecular Catalysis A: Chemical*, 411: 203-213.
- 19. Lee, G. J. and Wu, J. J. (2017). Recent developments in ZnS photocatalysts from synthesis to photocatalytic applications -A review. *Powder Technology*, 318: 8-22.
- Shakouri-Arani, M. and Salavati-Niasari, M. (2014). Synthesis and characterization of wurtzite ZnS nanoplates through simple solvothermal method with a novel approach. *Journal of Industrial and Engineering Chemistry*, 20(5): 3179-3185.
- Song, L., Zhang, S., Chen, B., Ge, J. and Jia, X. (2010). Fabrication of ternary zinc cadmium sulfide photocatalysts with highly visible-light photocatalytic activity. *Catalysis Communications*, 11(5): 387-390.
- Shahid, R., Toprak, M., Soliman, H. and Muhammed, M. (2012). Low temperature synthesis of cubic phase zinc sulfide quantum dots. *Open Chemistry*, 10(1): 54-58.
- 23. Guo, J., Khan, S., Cho, S. H., and Kim, J. (2019). Preparation and immobilization of zinc sulfide (ZnS) nanoparticles on polyvinylidene fluoride pellets for photocatalytic degradation of methylene blue in wastewater. *Applied Surface Science*, 473: 425-432.
- Senapati, U. S., Jha, D. K. and Sarkar D. (2013).
 Green synthesis and characterization of ZnS nanoparticles. *Research Journal of Physical Sciences*, 1(7): 2320-4796.
- Hudlikar, M., Shreeram, J., Mayur, D. and Kisan, K. (2012). Latex-mediated synthesis of ZnS nanoparticles: Green synthesis approach. *Journal* of Nanoparticle Research, 14(5): 865.
- 26. Kannan, S., Subiramaniyam, N. P. and Sathishkumar, M. (2020). A novel green synthesis approach for improved photocatalytic activity and antibacterial properties of zinc sulfide nanoparticles using plant extract of Acalypha indica and Tridax procumbens. Journal of

- Materials Science: Materials in Electronics, 31(12): 9846-9859.
- Lan, C., Kunquan, H., Wenzhong, W. and Guanghou, W. (2003). Synthesis of ZnS nanorods by annealing precursor ZnS nanoparticles in NaCl flux. Solid State Communications, 125(9): 455-58.
- Jothibas, M., Manoharan, C., Jeyakumar, S. J., Praveen, P., Punithavathy, I. K. and Richard, J. P. (2018). Synthesis and enhanced photocatalytic property of Ni doped ZnS nanoparticles. *Solar Energy*, 159: 434-443.
- Hu, H., Wang, X., Liu, F., Wang, J. and Xu, C. (2011). Rapid microwave-assisted synthesis of graphene nanosheets–zinc sulfide nanocomposites:
 Optical and photocatalytic properties. Synthetic Metals, 161(5-6): 404-410.
- 30. Boulkroune, R., Sebais, M., Messai, Y., Bourzami, R., Schmutz, M., Blanck, C., ... and Boudine, B. (2019). Hydrothermal synthesis of strontium-doped ZnS nanoparticles: structural, electronic and photocatalytic investigations. *Bulletin of Materials Science*, 42(5): 1-8.
- 31. Chen, Y., Yin, R. H. and Wu, Q. S. (2012). Solvothermal synthesis of well-disperse ZnS nanorods with efficient photocatalytic properties. *Journal of Nanomaterials*, 2012: 560310.
- 32. Suganya, S., Jothibas, M. and Jeyakumar, S. J. (2019). Solid state synthesis of cadmium doped ZnS with excellent photocatalytic activity and enhanced visible light emission. *Journal of Materials Science: Materials in Electronics*, 30(8): 7916-7927.
- 33. Abbasi, M., Rafique, U., Murtaza, G. and Ashraf, M. A. (2018). Synthesis, characterisation and photocatalytic performance of ZnS coupled Ag2S nanoparticles: A remediation model for environmental pollutants. *Arabian Journal of Chemistry*, 11(6): 827-837.
- 34. Wang, W., Lee, G. J., Wang, P., Qiao, Z., Liu, N. and Wu, J. J. (2020). Microwave synthesis of metal-doped ZnS photocatalysts and applications on degrading 4-chlorophenol using heterogeneous photocatalytic ozonation process. *Separation and Purification Technology*, 237: 116469.

Sambasevam et al: THE PREPARATION AND APPLICATION OF ZINC SULFIDE AS PHOTOCATALYST FOR WATER REMEDIATION: A MINI REVIEW

- Ibrahim, S. K., Chakrabarty, S., Ghosh, S. and Pal, T. (2017). Reduced graphene oxide–zinc sulfide composite for solar light responsive photo current generation and photocatalytic 4-nitrophenol reduction. *ChemistrySelect*, 2(1): 537-545.
- 36. Kale, D. P., Deshmukh, S. P., Shirsath, S. R. and Bhanvase, B. A. (2020). Sonochemical preparation of multifunctional rGO-ZnS-TiO₂ ternary nanocomposite and its application for CV dye removal. *Optik*, 208: 164532.
- 37. Hernández-Gordillo, A., García-Mendoza, C., Alvarez-Lemus, M. A. and Gómez, R. (2015). Photocatalytic reduction of Cr(VI) by using stacked ZnS layers of ZnS (en) x complex. *Journal of Environmental Chemical Engineering*, 3(4): 3048-3054.
- 38. Qin, Y. L., Zhao, W. W., Sun, Z., Liu, X. Y., Shi, G. L., Liu, Z. Y., ... and Ma, Z. Y. (2019). Photocatalytic and adsorption property of ZnS-

- TiO₂/RGO ternary composites for methylene blue degradation. *Adsorption Science & Technology*, 37(9-10): 764-776.
- 39. Wu, H., Lin, S., Chen, C., Liang, W., Liu, X. and Yang, H. (2016). A new ZnO/rGO/polyaniline ternary nanocomposite as photocatalyst with improved photocatalytic activity. *Materials Research Bulletin*, 83: 434-441.
- 40. Anjum, M., Oves, M., Kumar, R. and Barakat, M. A. (2017). Fabrication of ZnO-ZnS@ polyaniline nanohybrid for enhanced photocatalytic degradation of 2-chlorophenol and microbial contaminants in wastewater. *International Biodeterioration & Biodegradation*, 119: 66-77.
- 41. Kumar, T. K. M. and Kumar, S. K. (2019). Visible-light-induced degradation of rhodamine B by nanosized Ag₂S-ZnS loaded on cellulose. *Photochemical & Photobiological Sciences*, 18(1): 148-154.

Malaysian Journal of Analytical Sciences (MJAS)



Published by Malaysian Analytical Sciences Society

PREPARATION OF EXTRACTED MAGNETITE FROM AN INDUSTRIAL WASTE MILL MODIFIED BY CETYL TRIMETHYL AMMONIUM BROMIDE FOR CADMIUM ION REMOVAL FROM AQUEOUS SOLUTION

(Penyediaan Magnetit daripada Sisa Buangan Sisik Besi yang Dimodifikasikan oleh Setil Trimetil Ammonium Bromida untuk Menyerap Kadmium Ion daripada Larutan Akues)

Nur Asyikin Ahmad Nazri^{1,2*}, Raba'ah Syahidah Azis^{2,3}, Hasfalina Che Man⁴, Ismayadi Ismail²

¹Centre of Foundation Studies, Cawangan Selangor,
Universiti Teknologi MARA, 43800 Dengkil, Selangor, Malaysia

²Material Synthesis and Characterization Laboratory (MSCL), Institute of Advanced Technology (ITMA)

³Department of Physics, Faculty of Science

⁴Department of Biological and Agricultural Engineering, Faculty of Engineering
Universiti Putra Malaysia, 43400 Serdang, Selangor, Malaysia

*Corresponding author: asyikin2750@uitm.edu.my

Received: 9 September 2021; Accepted: 18 December 2021; Published: 28 April 2022

Abstract

This work, using a batch study, revealed the performance of modified magnetite millscales with a cationic surfactant [cetyl trimethyl ammonium bromide (CTAB)] (Fe₃O₄/CTAB MNS) in cadmium ion removal from aqueous solution. The self-assembly method was employed to modify Fe₃O₄ with CTAB. As prepared Fe₃O₄ limited the modification method to *ex situ*. Therefore, a heterocoagulation method was used to self-assemble CTAB on Fe₃O₄. The prepared magnetic nanosorbents (MNSs) were used in batch adsorption to optimize cadmium adsorption. In addition, characterization with Fourier transform infrared spectroscopy (FTIR) and transmission electron microscopy (TEM) revealed new characteristics of that modified Fe₃O₄ that contributed to the enhancement of the adsorption efficiency (*Q*) to reach 21.6 mg/g. The higher removal percentage shown by Fe₃O₄/CTAB MNS was 89%, which confirmed the successful modification. Therefore, Fe₃O₄ modified with CTAB has higher potential to be used as magnetic nanosorbent owing to lower cost of production with compatible adsorption capacity.

Keywords: stabilized magnetite, magnetic nanosorbents, cadmium solution, cation polymer, cetyl trimethyl ammonium bromide

Abstrak

Kajian ini mendedahkan prestasi skala magnetit yang diubah suai dengan surfaktan kationik (setil trimetil ammonium bromida (CTAB)) (Fe₃O₄ / CTAB), digunakan sebagai penyingkiran ion kadmium dari larutan akues melalui kajian kumpulan. Kaedah pemasangan diri digunakan untuk mengubah Fe₃O₄ dengan CTAB. Fe₃O₄ yang telah disiapkan telah membatasi kaedah modifikasi menjadi *ex situ*. Oleh itu, kaedah heterokoagulasi digunakan untuk memasang CTAB pada Fe₃O₄. Penjerap nano magnetik yang disiapkan (MNS) digunakan dalam penjerapan kumpulan untuk mengoptimumkan penjerapan kadmium. Selain itu, pencirian dengan spektroskopi infra merah transformasi Fourier (FTIR), dan mikroskopi elektron transmisi (TEM) telah

Nur Asyikin et al: PREPARATION OF EXTRACTED MAGNETITE FROM AN INDUSTRIAL WASTE MILL MODIFIED BY CETYL TRIMETHYL AMMONIUM BROMIDE FOR CADMIUM ION REMOVAL FROM AQUEOUS SOLUTION

mengungkapkan ciri-ciri baru Fe₃O₄ yang dimodifikasi yang menyumbang kepada peningkatan kecekapan penjerapan (*Q*) menjadi 21.6 mg/g. Peratusan penyingkiran yang lebih tinggi yang ditunjukkan oleh Fe₃O₄ / CTAB MNS adalah 89% yang membuktikan pengubahsuaian berjaya. Oleh itu, dapat disimpulkan bahawa modifikasi dengan CTAB berpotensi lebih tinggi untuk digunakan sebagai penjerap nano magnetik kerana melibatkan kos pengeluaran yang lebih rendah dengan kapasiti penjerapan yang serasi.

Kata kunci: magnetit stabil, penjerap nano magnetik, larutan kadmium, polimer kation, setil trimetil ammonium bromida

Introduction

Contamination of water is a serious global issue that must be addressed. Contaminated water greatly affects the human well-being. Even if people do not directly drink the contaminated water, it may still cause harm to seafood through the spread of contaminants. Cadmium is a nonessential metal with a high exchange factor. Zinc deficiency increases the risk of Cd poisoning. Zinc acts as an antidote to the toxic effects of Cd. The use of foods and grains (developed in soil polluted by superphosphate compost and sewage slime), the use of refined food sources (exposed to cadmium at specific locations such as cadmium coating on iron and copper), and the consumption of plastics have contributed to an increase in zinc deficiency. Workers at the production line of battery anodes and semiconductors are particularly vulnerable to Cd poisoning. [1].

Cd is a heavy metal; it is a highly harmful industrial and environmental pollutant. It is not biodegradable and accumulates throughout the food chain as a result of plant uptake in polluted soils, which poses a serious health risk to humans. In Malaysia, the maximum allowed Cd concentration in drinking water is 0.005 mg/L. Cd toxicity has been reported by many researchers [2, 3, 4]. Any significant level of Cd in the body causes rapid poisoning and liver damage. Renal tubule failure is the cause of kidney disease [5]. Cd is also harmful to endocrine organs, especially the pituitary gland. Cd-containing compounds are strong carcinogens [6]. According to Hotz et al. [7], there is substantial evidence regarding the carcinogenicity of Cd and Cd compounds in humans. Renal dysfunction, bone degeneration, liver damage, and blood damage have all been linked to chronic exposure to high levels of Cd [5-7].

Ion exchange, membrane filtration, chemical reduction and precipitation, adsorption on activated carbon, nanotechnology treatments, electrochemical removal, and advanced oxidation processes are some of the traditional treatment techniques for removing heavy metal contaminants from the environment or wastewater effluents [4, 8-10]. Unfortunately, many of these traditional techniques have significant drawbacks such as low selectivity, high cost, partial removal, high energy consumption, or the production of large amounts of toxic waste. As a result, the demand for safe, less expensive, and more efficient technologies to remove heavy metals from polluted water has prompted research into low-cost alternatives to commercially available methods [10].

Currently, adsorption is widely accepted as a viable and cost-effective approach for heavy metal wastewater treatment. The adsorption process is versatile in terms of design and operation, and it typically produces high-quality treated effluent. Adsorbents can also be renewed using an appropriate desorption procedure because adsorption is sometimes reversible. Thus, extensive research was conducted to identify the best adsorbents that are low-cost, mass-produced in large quantities, and have a simple and rapid separation process, ensuring that this technology can replace the traditional method of removing heavy metals in wastewater treatment [6, 9].

Owing to their unique features, nanometer-sized materials have recently attracted considerable interest among mainstream researchers. These materials have been used in various areas including biotechnology, design, biomedical science, natural science, and materials science. The use of nanoparticles (NPs) as

effective adsorbents for heavy metals removal is gaining popularity among scientists [10]. Compared to micrometer-sized particles, NPs have a considerably larger surface area to volume ratio and a shorter diffusion path, which results in high extraction limit, fast extraction of elements, and high extraction efficiency.

Mill scale waste is a by-product of steel production that occurs during the hot rolling process. The annual output exceeds a million tonnes, and it may contribute to ground contamination [11]. Thus, repurposing mill scale in various applications may help to reduce waste and transform it into a useful agent. Mill scale contains 50% of wurtzite (FeO), 10% of hematite (Fe₂O₃), and 40% of magnetite (Fe₃O₄) [12]. Fe₃O₄ is a metal oxide that behaves as an amphoteric solid, allowing protonation and deprotonation on the surface to produce surface charge. This property is interesting for studying the adsorption mechanism of heavy metals on Fe₃O₄ because Fe₃O₄ easily reacts with the surrounding particles. Therefore, each year [13-16], several synthetic approaches for extracting magnetite from mill scales have been published. Furthermore, magnetite nanoparticles are receiving more attention owing to their superior magnetic properties and high specific surface area. To extract high purity magnetite from mill scale waste, Azis et al. developed a magnetic separation process. Specifically, 1 T of external magnetic field has been used for the extraction [12-14].

High-energy ball milling (HEBM) is a straightforward approach for size reduction. This approach decreases the size of particles from micrometer to nanometer size. However, nano-sized magnetite is unstable and readily oxidizes to form a new composite that does not exhibit the unique high magnetization behavior. Furthermore, because magnetite has a stronger magnetic force, the agglomeration is higher among the particles [11-15].

Therefore, the modification of the surface process may help to reduce the agglomeration problems and the unstable state of Fe₃O₄ NPs. CTAB is a cationic polymer that can self-assemble with other composites

[16,17]. Previously, CTAB-modified Fe₃O₄ NPs have been used in removing dye. Faraji et al. believed that CTAB was essential in the dye adsorption mechanism. Therefore, they added CTAB into the dye solution, and CTAB was expected to coat Fe₃O₄ during the batch adsorption experiment; finally, the particles were separated together using an external magnetic field [18].

In this work, Fe₃O₄ was magnetically extracted from mill scale waste and underwent HEBM to become nano-sized. Then, the prepared Fe₃O₄ was coated with CTAB using an ultrasonication bath. The obtained product was used in batch adsorption to remove Cd ions from an aqueous solution. An equilibrium study was performed to evaluate the relevance of using the obtained material at an industrial scale. Thus, the obtained adsorption capacity of the particles, which was enhanced after coating with CTAB, indicates the potential of using the obtained material in removing heavy metals.

Materials and Methods

Sample preparation (adsorbent)

The first step of extraction was to remove the impurities from raw millscales collected at a steel factory in Malaysia. The manual removal of impurities (e.g., stones, sand, dust, or pieces of plastic) that may contaminate the samples was also performed. Then, approximately 100 g of MS flakes was crushed using conventional milling (Pascal Engineering, UK) for 24 h under dry conditions, 700 rpm speed, and 10:1 BRP. The first separation method was impurity magnetic separation (IMS) used to extract the magnetic particles from the RM. The iron oxides (IO) powder was placed inside a glass tube (with a stopper at the bottom) with deionized water (DI) (at room temperature of 22-24 °C) with the presence of a 1 T external field, as shown in Figures 1 and 2. Then, the tube was manually shaken for 10-15 min. Separation II: The Curie Temperature Separation Technique (CTST) was then used to remove stronger magnetic components from the magnetic powder. Separations I and II of waste mill scales were carried out in the same way as previously reported by Azis et al. [12]. CTST's magnetite (Fe₃O₄) Nur Asyikin et al: PREPARATION OF EXTRACTED MAGNETITE FROM AN INDUSTRIAL WASTE MILL MODIFIED BY CETYL TRIMETHYL AMMONIUM BROMIDE FOR CADMIUM ION REMOVAL FROM AQUEOUS SOLUTION

output was dried in an oven at 120°C for 24 h. The magnetite powder was processed for 8 h on a SPEX

8000D milling machine with a 10:1 ball-to-powder (BPR) ratio.

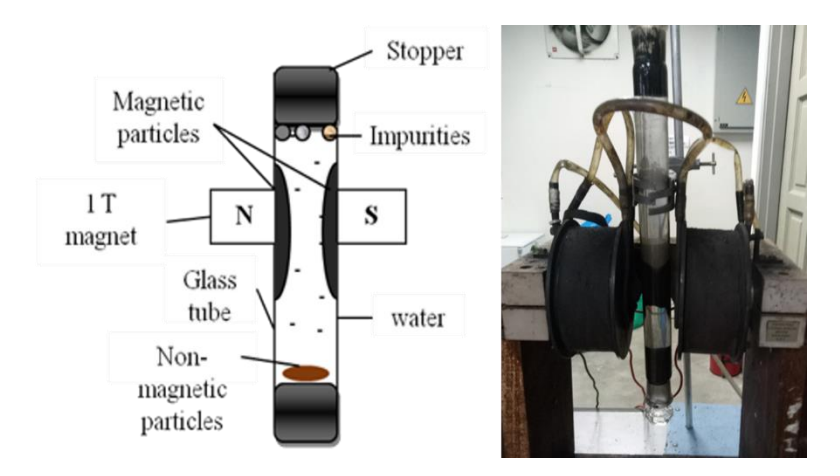


Figure 1. Set up for impurity magnetic separation

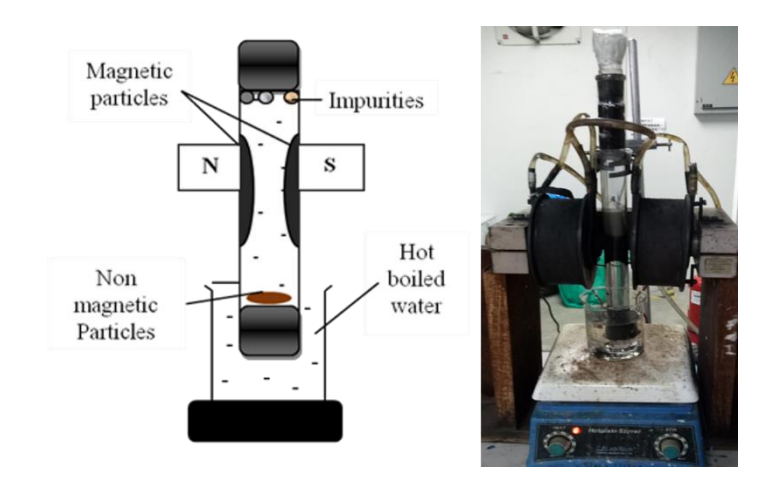


Figure 2. Set up for the curie temperature separation technique

Fe₃O₄/CTAB magnetic nanosorbents

CTAB with a 0.02 M concentration was prepared by mixing the CTAB powder with deionized water and stirred for 30 min in an ultrasonication bath. Then, 20 ml of CTAB solution at a concentration of 0.20 M was mixed with 1.0 g of magnetite extracted from millscales. After 30 min of mixing, an external magnetic field was applied to the mixture, and the collected magnetite coated with CTAB was dried in an oven for 24 h at 60 °C. A summary of the modification

method is shown in Figure 3. Next, agitation by sonication in an ultrasonic bath for 20 min was performed. The pH to perform this was at optimum for the CTAB, which has a higher positivity and the highest negativity potential for MNPs (via zeta potential analysis). The pH was then adjusted by using NaOH and nitric acid using the titration method. This step was performed to increase the dispersity of Fe₃O₄ NPs in the CTAB. The Fe₃O₄/CTAB was then magnetically separated using an external magnetic field

to separate the modified magnetic NPs from the residue, as shown in Figure 3. The modified magnetic NPs were collected and then rinsed twice before being dried overnight in the oven at 60 °C. The dried samples were then ground using a mortar to obtain a fine

powder of modified magnetic NPs. The surface modification of magnetic NPs using CTAB is summarized in Figure 3, the method was adjusted from previous works [16, 18, 19].

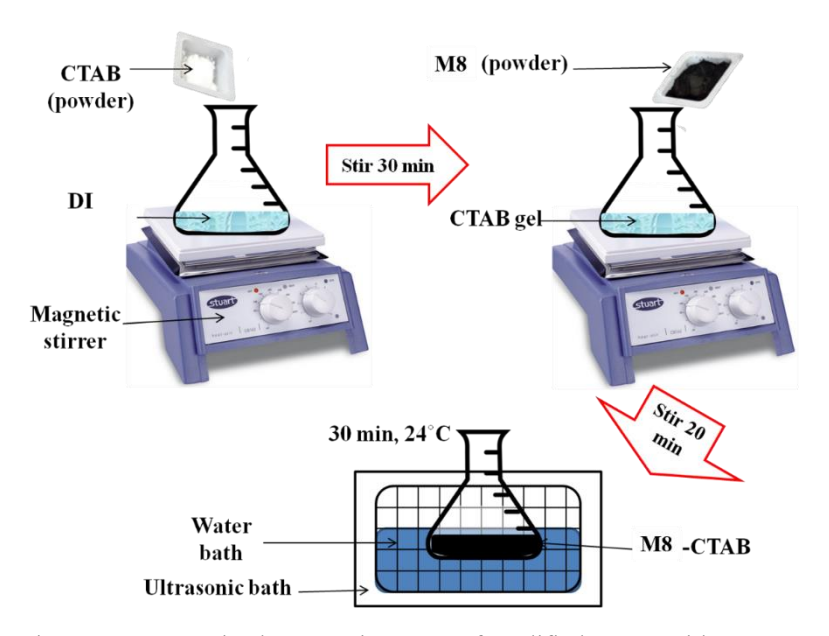


Figure 3. Summarized preparation steps of modified MNPs with CTAB

Adsorbate

All the compounds used to prepare the reagent solutions were of analytical reagent grade. The stock solution of cadmium nitrate (Cd(NO₃)₂) (99%, Sigma-Aldrich, UK) (3 mg/L) was prepared by dissolving a weighed quantity of the respective Cd(NO₃)₂ in deionized water. The concentration of the metal solution and pH used in this work were 3 mg/L with pH 7, respectively. The pH of the solution was adjusted by using sodium hydroxide (NaOH) and nitric acid (HNO₃).

Batch adsorption experiment

The 100 mL of Cd solution was mixed with 10 mg of Fe₃O₄ nanoparticle adsorbent and placed in a vibrator bath (variable speed reciprocal vibrator (model HY-8)) with a fixed 160 rpm for 5, 10, 15, 20, 25, 30, 35, and 40 min of contact time. All adsorption tests were performed in a vibrator at room temperature (22-25 °C)

using accurately weighed amounts of adsorbents in a covered bottle with adsorbate solutions of specific concentrations. The pH of the solution was adjusted from 1 to 10. The adsorption capacity at any time, Q_t (mg g⁻¹), was calculated according to the following Equation 1:

$$Q_{t} = \frac{C_{o} - C_{t}}{m}V \tag{1}$$

where C_0 and C_t (mgL/1) are the initial and residual Cd ions concentrations at any time (min), respectively. The volume of Cd ion solution was V (mL), and the mass of dry adsorbent was m (mg). Equation 2 was used to calculate the adsorption capacity at equilibrium:

$$Q_e = \frac{C_o - C_e}{m} V \tag{2}$$

Removal efficiency and adsorption capacity

The removal percentage of metal ions refers to the percentage of metal ions removed from the initial metal concentration solutions. Equation 3 was used to calculate the removal efficiency of Cd²⁺ from the aqueous solution.

$$Cd \% Re \, m \, oval = \frac{c_o - c_e}{c_o} \times 100\% \tag{3}$$

Sample characterization

Structural and phase composition

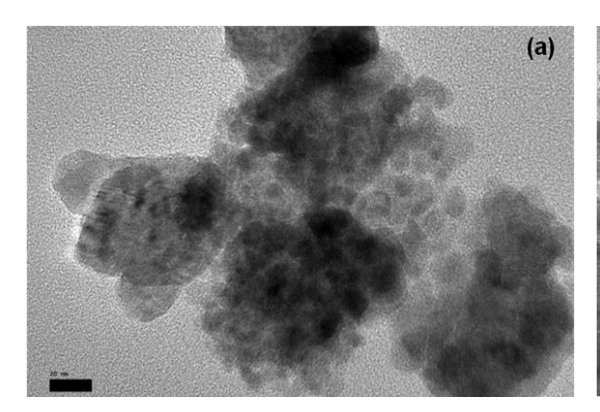
A JEM JEOL 2100 HR transmission electron microscope was used to examine the sample morphology, particle size, and atom arrangement (HR-TEM). Spectroscopic analysis using the infrared FTIR spectrometer was performed by recording infrared spectra (200-4000 cm⁻¹) (Thermo Nicolet, Model Nicolet 6700). Atomic adsorption spectroscopy (AAS) is a technique for determining the concentration of heavy metals in a solution.

Results and Discussion

Morphology analysis

Figure 4a shows the HR-TEM images, which show that aggregation occurred between the Fe₃O₄ nanoparticles that were a range of 5-20 nm in size. The particle sizes

increased after coated with CTAB. The result is in agreement with previous works [21, 18]. The nanoparticles aggregated with higher dispersity, indicating good connectivity between the grains due to the higher magnetic forces and subjected to the modification process. The agglomeration was reduced after coated with CTAB [17]. Figure 4b shows images of Fe₃O₄ and Fe₃O₄/CTAB nanosorbents with a scale of 20 nm. Table 1 represent the average value of Fe₃O₄ and Fe₃O₄/CTAB MNS. The average size of the particles was calculated by using Image J. In total, 200 particles were used to determine the average particles. Clearly, the modified Fe₃O₄ was a larger size due to the presence of the CTAB layer on the particles. However, this result was in contrast with the previous publication, considering agglomerations [16-19]. The smaller size is due to the measurement of the real sizes of the particles without the occurrence of agglomeration.



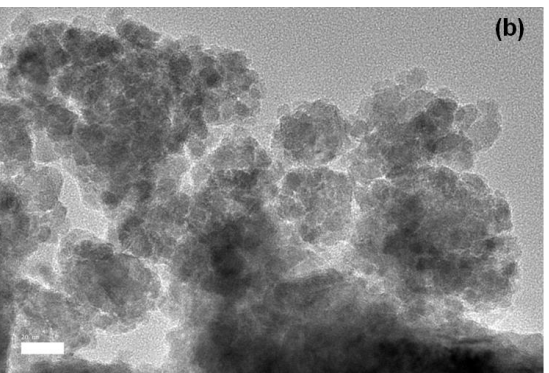


Figure 4. Fe₃O₄ extracted from (a) millscales waste and (b) Fe₃O₄/CTAB

Table 1. HR-TEM particle sizes

Adsorbent	HR-TEM Particle Size, d_{TEM} (nm)		
Fe ₃ O ₄	13.10		
Fe ₃ O ₄ /CTAB	15.26		

Phase analysis

Figure 5 shows the XRD spectrum of Fe₃O₄, and Fe₃O₄/CTAB MNS. As shown, diffraction peaks of all samples after HEBM completely correspond to standard pattern characteristic peaks of the magnetite hexagonal inverse spinel structure (JCPDS: 98-005-9302) 220 (30.1), 113 (35.45), 004 (43.07), 333 (56.97), 044 (62.47). As can be seen from the spectra,

the main peaks which correspond to hkl (113) were observed to be broader as the milling time increased. The spectrum after modified with CTAB not showing any phase changes indicated that the modification process preserve the phase. In addition, it proved that the core shell of the MNS is still Fe₃O₄. This finding is in agreement with the previous report [18].

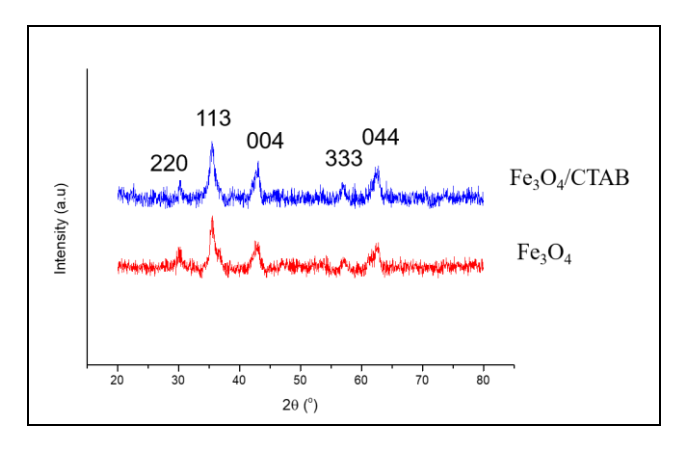


Figure 5. XRD spectrum of Fe₃O₄, and Fe₃O₄/CTAB MNS

Optical analysis

Figure 6 shows the FTIR spectrum of Fe₃O₄, Fe₃O₄/CTAB, and pure CTAB. CTAB's IR spectrum (Figure 6) contains a band at 3420 cm⁻¹, which could be attributed to the ammonium moiety's vibrations. Two distinct CH bands vibrations of the –CH₂ group in CTAB are responsible for the peaks at 2918 and 2848 cm⁻¹. The asymmetric and symmetric stretching vibrations of N⁺–CH₃ are represented by the bands at

1630 and 1467 cm $^{-1}$, respectively, while the out-of-plane –CH vibration of CH $_3$ is represented by the band at 960 cm $^{-1}$. Br $^-$ could be represented by the band at 720 cm $^{-1}$. The signal at 566 cm $^{-1}$ in the FTIR spectrum of Fe $_3$ O $_4$ /CTAB MNS (Figure 5) reflects Fe-O of Fe $_3$ O $_4$. The electrostatic interaction between Fe $_3$ O $_4$ surface hydroxyl groups and the ammonium moiety in CTAB (OH....N $^+$) could account for the bandwidth at 3430 cm $^{-1}$ [16-18].

Nur Asyikin et al: PREPARATION OF EXTRACTED MAGNETITE FROM AN INDUSTRIAL WASTE MILL MODIFIED BY CETYL TRIMETHYL AMMONIUM BROMIDE FOR CADMIUM ION REMOVAL FROM AQUEOUS SOLUTION

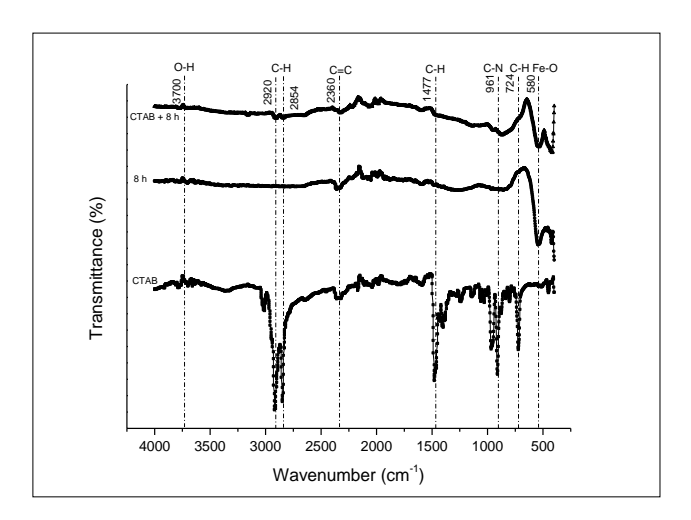


Figure 6. FTIR spectrum of Fe₃O₄ extracted from millscale waste and Fe₃O₄/CTAB MNS

Figure 7 shows magnetic behavior of the magnetic nanosorbents (MNS). The M-H curve indicated that both MNS are ferromagnetic materials with 50 and 28 emu/g. In addition, magnetic hysteresis loops measured at room temperature. The magnetization values observed in nanostructure materials are smaller than

the corresponding bulk materials, assuming that is no changes in ionic configurations occurred. The reduction and lack of saturation after that are likely related to the smaller particle size and high surface areas, which could lead to some spin canting [12].

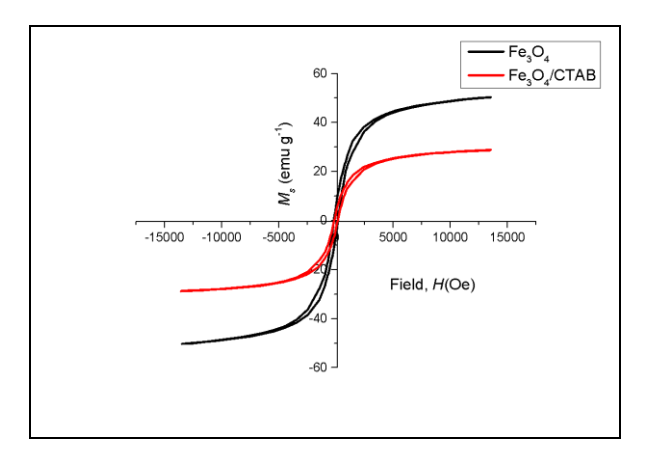


Figure 7. M-H hysteresis of Fe₃O₄ extracted from millscale waste and Fe₃O₄/CTAB MNS

Figure 8 shows that the formation of vesicular Fe₃O₄/CTAB. The coating showed self-assembly when the pH was 7. At that pH, CTAB had a higher positivity; meanwhile, Fe₃O₄ showed a higher negative surface charge. Therefore, it electrostatically self-assembled to form a vesicle [16]. The formation of the vesicle provided new surface charge for the nanoparticles. The new surface charge caused the

repulsive force to increase. This is visible in the HR-TEM images showing that nanoparticles with higher dispersity formed. However, when more than a bilayer micelle already formed, the excess CTAB reacted on the surface, and the hydrophobic side formed a new layer. Therefore, when we added more CTAB, it did not increase the surface area; in fact, the surface area likely decreased [22].

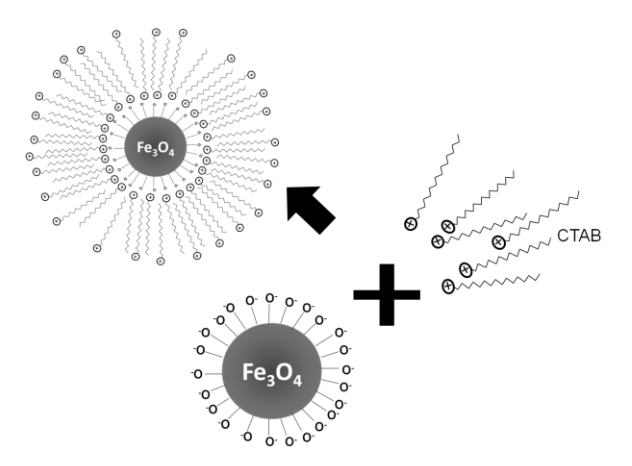


Figure 8. Schematic mechanism of the coating process of Fe₃O₄/CTAB MNS

Adsorption equilibrium studies Effect of contact time

The influence of contact time on the adsorption capacity of Cd ions on Fe₃O₄/CTAB is shown in Figure 9. For the adsorption of Cd ions, the adsorption amount, Q_t , grew rapidly at first and then reached equilibrium in approximately 10 to 15 min. The increase in driving force produced by the concentration gradient of cations in solution and the presence of a considerable number of active sites on the surface of Fe₃O₄/CTAB MNS could be attributed

to the fast adsorption rate in the incipient stage [13]. In the adsorption of Cd ions, a contact duration of 15 min was adequate to achieve equilibrium for $Fe_3O_4/CTAB$ MNS. The adsorption capacity of Fe_3O_4 is 10.01 mg/g; meanwhile, that of $Fe_3O_4/CTAB$ MNS is 21.6 mg/g.

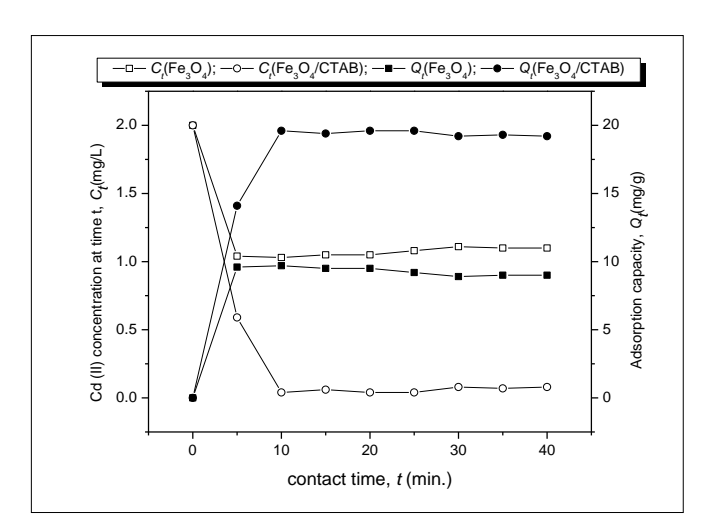


Figure 9. Effect of contact time on the adsorption capacity and concentration at equilibrium of Fe_3O_4 and $Fe_3O_4/CTAB$ MNS

Effect of solution pH

According to the findings of a previous paper [14], adsorption can occur at various pH values. The pH setting would aid in the optimal uptake of Cd ions. As a result, the influence of solution pH on Cd ion adsorption onto Fe₃O₄/CTAB was investigated in the pH range of 1 to 10, as shown in Figure 8. For both modified and unmodified MNS, no adsorption was detected at pH values of 1 and 2, while half Cd ion absorption was recorded at pH 3 (>50%). Despite this, the adsorption capacity of the solution gradually increased from 3 to 6 and plateaued between pH 6 and 10. The ion exchange was responsible for the rapid increase in adsorption before pH 6. As a result, chemisorption, mainly ion exchange, is used exclusively for adsorption. The increase in adsorption after pH 6 could be due to electrostatic repulsion between H₃O⁺ ions and cationic Cd ions, which cause Cd ions to be attracted to the Fe₃O₄/CTAB's negative surface charge. Van der Waal forces create an increase

in the amount of Cd ions on a solid's surface (including dipole-dipole, dipole-induced dipole, London forces, and possibly hydrogen bonding). The increase can be explained as shown in Figure 6, where active hydroxyls can be found on the adsorbent surface based on FTIR data. These findings corroborate the intensity change in the IR spectra, as shown in Figure 10 [19]. As a result, the Q was highest at pH 9 for Fe₃O₄/CTAB MNS with 20.19 mg/g; meanwhile, 10.03 mg/g of Cd was removed by Fe₃O₄ MNS.

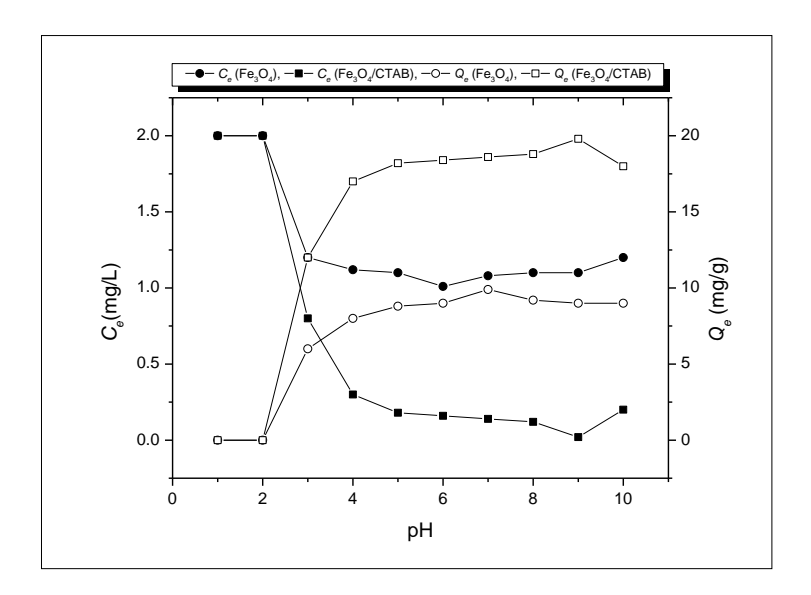


Figure 10. Effect of pH on the adsorption capacity and concentration at equilibrium of Fe₃O₄/CTAB MNS

Effect of initial Cd2+ concentration

One of the criteria utilized to examine the equilibrium of magnetic nano-adsorbents is initial concentration.

The initial metal ion concentration serves as a driving factor for breaking through the mass transfer barrier between the adsorbent and the adsorbate medium. The Fe₃O₄/CTAB MNS was first studied for its ability to remove metal ions from aqueous solutions. For the different beginning concentrations, the solution concentrations were 1, 2, 3, 4, and 5 mg/L, with an adsorbent dosage of 10 mg as the constant, as shown in Figure 11. For model Cd ions solutions with starting concentrations of 1 to 5 mg/L, the removal percentage approached 95%. As a result, increasing the concentration of Cd ions reduced the efficiency of Cd

ion removal slightly. Furthermore, once equilibrium is reached, it will no longer be able to adsorb the other ions. This same pattern was discovered in a few other published studies [21, 22, 23].

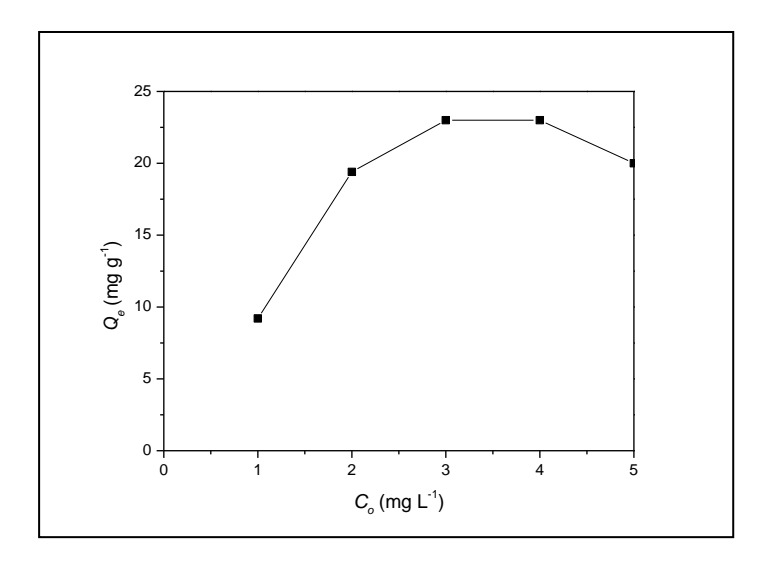


Figure 11. Effect of initial concentration on the adsorption capacity of the adsorption of Cd by using Fe₃O₄/CTAB

Conclusion

In this study, Fe₃O₄/CTAB MNS was prepared via the self-assembly method. The confirmation of success was supported by the characterization via FTIR and HR-TEM images before and after coating. Then, the Fe₃O₄/CTAB MNS was used as an adsorbent for removal of Cd ions from aqueous solution. The Fe₃O₄/CTAB MNS showed excellent performance in removing Cd ions from aqueous solution, which was evaluated by the equilibrium studied. The affecting parameters were studied, and the results showed that the presence of CTAB significantly affected the removal efficiency of the Cd ions. Due to the higher dispersity and magnetically assisted separability of the Fe₃O₄/CTAB MNS, high adsorption capacities could be obtained in a very short time. The reported data should be useful for the design and fabrication of an

economically viable treatment process using batch or stirred tank reactors for Cd ion adsorption. This work involved a valuable contribution where the usage of millscales successfully lowered the production cost of the MNS.

Acknowledgement

This work was supported by Universiti Putra Malaysia Grants (Putra Impact Grants (UPM/700-/2/GPPI/2017/954160) and Putra Initiative Grants (GP-IPS/2017/9580600). Thanks to Falcon for proofing this manuscript.

Nur Asyikin et al: PREPARATION OF EXTRACTED MAGNETITE FROM AN INDUSTRIAL WASTE MILL MODIFIED BY CETYL TRIMETHYL AMMONIUM BROMIDE FOR CADMIUM ION REMOVAL FROM AQUEOUS SOLUTION

References

- 1. Mahmood, Q., Asif, M., Shaheen, S., Hayat, M. T. and Ali, S. (2019). Cadmium contamination in water and soil. In *Cadmium toxicity and tolerance in plants*. Academic Press: pp. 141-161.
- 2. Pyrzynska, K. (2019). Removal of cadmium from wastewaters with low-cost adsorbents. *Journal of Environmental Chemical Engineering*, 7(1): 102795.
- Ciesielczyk, F., Bartczak, P. and Jesionowski, T. (2016). Removal of cadmium (II) and lead (II) ions from model aqueous solutions using sol–gelderived inorganic oxide adsorbent. *Adsorption*, 22(4): 445-458.
- 4. Ali, A. H. (2013). Comparative study on removal of cadmium (II) from simulated wastewater by adsorption onto GAC, DB, and PR. *Desalination and Water Treatment*, 51(28-30): 5547-5558.
- Farhan, A. S. and Jasim, S. T. (2020). Cadmium toxicity and some target organs: A review. Al-Anbar Journal of Veterinary Sciences, 13(2): 17-26.
- Riaz, U., Aslam, A., uz Zaman, Q., Javeid, S., Gul, R., Iqbal, S., ... and Jamil, M. (2021). Cadmium contamination, bioavailability, uptake mechanism and remediation strategies in soil-plantenvironment system: a critical review. *Current Analytical Chemistry*, 17(1): 49-60.
- 7. Järup, L. and Åkesson, A. (2009). Current status of cadmium as an environmental health problem. *Toxicology and Applied Pharmacology*, 238(3): 201-208.
- 8. Cui, L., Chen, T., Yin, C., Yan, J., Ippolito, J. A. and Hussain, Q. (2019). Mechanism of adsorption of cadmium and lead ions by iron-activated biochar. *BioResources*, 14(1): 842-857.
- Carolin, C. F., Kumar, P. S., Saravanan, A., Joshiba, G. J. and Naushad, M. (2017). Efficient techniques for the removal of toxic heavy metals from aquatic environment: A review. *Journal of Environmental Chemical Engineering*, 5(3): 2782-2799.
- Dubey, S., Banerjee, S., Upadhyay, S. N. and Sharma, Y. C. (2017). Application of common nano-materials for removal of selected metallic species from water and wastewaters: A critical

- review. *Journal of Molecular Liquids*, 240: 656-677.
- Gaballah, N. M., Zikry, A. F., Khalifa, M. G., Farag, A. B., El-Hussiny, N. A. and Shalabi, M. E. H. (2013). Production of iron from mill scale industrial waste via hydrogen. *Open Journal of Inorganic Non-metallic Materials*, 3(3): 6.
- Hashim, M., Saiden, N. M., Daud, N. and Shahrani, N. M. M. (2015). Study the iron environments of the steel waste product and its possible potential applications in ferrites. In Advanced Materials Research, 1109: 295-299.
- 13. Shahid, M. K., Phearom, S. and Choi, Y. G. (2018). Synthesis of magnetite from raw mill scale and its application for arsenate adsorption from contaminated water. *Chemosphere*, 203: 90-95.
- 14. Shahid, M. K., Phearom, S. and Choi, Y. G. (2019). Adsorption of arsenic (V) on magnetite-enriched particles separated from the mill scale. *Environmental Earth Sciences*, 78(3): 1-11.
- Hosseinzadeh, M., Seyyed Ebrahimi, S. A., Raygan, S. and Masoudpanah, S. M. (2016). Removal of cadmium and lead ions from aqueous solution by nanocrystalline magnetite through mechanochemical activation. *Journal of Ultrafine Grained and Nanostructured Materials*, 49(2): 72-79.
- Elfeky, S. A., Mahmoud, S. E. and Youssef, A. F. (2017). Applications of CTAB modified magnetic nanoparticles for removal of chromium (VI) from contaminated water. *Journal of Advanced Research*, 8(4): 435-443.
- 17. Saksornchai, E., Kavinchan, J., Thongtem, S. and Thongtem, T. (2018). Simple wet-chemical synthesis of superparamagnetic CTAB-modified magnetite nanoparticles using as adsorbents for anionic dye Congo red removal. *Materials Letters*, 213: 138-142.
- 18. Faraji, M., Yamini, Y., Tahmasebi, E., Saleh, A. and Nourmohammadian, F. (2010). Cetyltrimethylammonium bromide-coated magnetite nanoparticles as highly efficient adsorbent for rapid removal of reactive dyes from the textile companies' wastewaters. *Journal of the Iranian Chemical Society*, 7(2): S130-S144.

- Elfeky, S. A., Mahmoud, S. E. and Youssef, A. F. (2017). Applications of CTAB modified magnetic nanoparticles for removal of chromium (VI) from contaminated water. *Journal of Advanced Research*, 8(4): 435-443.
- 20. Chaki, S. H., Malek, T. J., Chaudhary, M. D., Tailor, J. P. and Deshpande, M. P. (2015). Magnetite Fe₃O₄ nanoparticles synthesis by wet chemical reduction and their characterization. *Advances in Natural Sciences: Nanoscience and Nanotechnology*, 6(3): 035009.
- 21. Xu, W., Liu, Z., Fang, J., Zhou, G., Hong, X., Wu, S., ... and Cen, C. (2013). CTAB-assisted hydrothermal synthesis of Bi₂Sn₂O₇ photocatalyst and its highly efficient degradation of organic dye under visible-light irradiation. *International Journal of Photoenergy*, 2013: 234806.
- 22. Nikoobakht, B., & El-Sayed, M. A. (2001). Evidence for bilayer assembly of cationic surfactants on the surface of gold nanorods. *Langmuir*, 17(20): 6368-6374.
- 23. Ehrampoush, M. H., Miria, M., Salmani, M. H., & Mahvi, A. H. (2015). Cadmium removal from aqueous solution by green synthesis iron oxide

- nanoparticles with tangerine peel extract. *Journal* of Environmental Health Science and Engineering, 13(1): 1-7.
- 24. Taleb, K., Markovski, J., Veličković, Z., Rusmirović, J., Rančić, M., Pavlović, V and Marinković, A. (2019). Arsenic removal by magnetite-loaded amino modified nano/microcellulose adsorbents: Effect of functionalization and media size. Arabian Journal of Chemistry, 12(8): 4675-4693.
- 25. Aydın, H., Yerlikaya, Ç. and Uzan, S. (2012). Equilibrium and kinetic studies of copper (II) ion uptake by modified wheat shells. *Desalination and Water Treatment*, 44(1-3): 296-305.
- 26. Hao, Y. M., Man, C. and Hu, Z. B. (2010). Effective removal of Cu (II) ions from aqueous solution by amino-functionalized magnetic nanoparticles. *Journal of Hazardous Materials*, 184(1-3): 392-399.
- Cantu, Y. (2017). Remediation of trivalent and hexavalent chromium ions from aqueous solutions using titanium dioxide polymorphs. The University of Texas Rio Grande Valley: pp. 1576-1580.

Malaysian Journal of Analytical Sciences (MJAS)



Published by Malaysian Analytical Sciences Society

THERMAL DECOMPOSITION OF CALCIUM CARBONATE IN CHICKEN EGGSHELLS: STUDY ON TEMPERATURE AND CONTACT TIME

(Penguraian Kalsium Karbonat dalam Kulit Telur Ayam: Kajian Mengenai Suhu dan Masa)

Nadia Razali¹, Nurriswin Jumadi^{1,2}*, Adlin Yasmin Jalani¹, Nurhanim Zulaikha Kamarulzaman¹, Khairul Faizal Pa'ee³

¹Section of Environmental Engineering Technology

²Section of Process Engineering Technology

³Section of Food Engineering Technology

Universiti Kuala Lumpur – MICET, 78000 Alor Gajah, Melaka, Malaysia

⁴Kolej Komuniti Jelebu,

71600 Kuala Klawang, Negeri Sembilan, Malaysia

*Corresponding author: nurriswin@s.unikl.edu.my

Received: 13 September 2021; Accepted: 3 February 2022; Published: 28 April 2022

Abstract

Within the context of a circular economy, the recycling or valorisation of eggshells, which are typically discarded in landfills, represents an opportunity. The primary compound in eggshells is calcium carbonate (CaCO₃), which can be decomposed into calcium oxide (CaO) by calcination. This study examined the calcination conditions (temperature and contact time) for the optimum CaCO₃ decomposition rate. The eggshell samples were pre-treated to eliminate dirt and unnecessary biological substance, ground into powder and sieved. The primary physical and chemical characteristics of eggshell powder were studied, including colour changes, mass loss, bulk density, moisture content, pH, thermal properties, and identification of chemical bonds and compounds in a molecule. This study evaluated the physical and chemical properties of the synthesised CaCO₃ from eggshells, moisture content, bulk density, pH, FTIR, and XRD. The results showed significant differences in the samples' colour transition at various temperatures and contact times based on the physical observation. The TGA analysis showed that eggshell powder decomposed at a temperature range of 600–900 °C. The FTIR results reported that for the calcine samples, the grey powder consists of CaCO₃, while the solid white powder consists of metal oxide content. Similar seven diffraction peaks were observed in the XRD analysis for calcination at 900 °C and industrial CaO (32.25, 37.41, 53.92, 64.18, 67.41, 79.70, and 88.58). The eggshell powder calcined at the temperature of 900 °C and contact time of 3 h was identified as an ideal condition for the decomposition of raw eggshell powder based on FTIR and XRD analyses. Both results showed that CaO corresponded to the wavelength spectrum and diffraction analysis of the sample.

Keywords: calcium carbonate, calcium oxide, eggshell, calcination

Abstrak

Dalam konteks ekonomi kitaran, terdapat peluang untuk mengitar semula kulit telur yang biasanya dibuang di tempat pembuangan sampah. Sebatian utama dalam kulit telur ialah kalsium karbonat dan ia boleh diuraikan kepada kalsium oksida melalui proses pengkalsinan. Kajian ini dilakukan untuk mengkaji keadaan kalsinasi (suhu dan masa pembakaran) yang sesuai

Nadia et al: THERMAL DECOMPOSITION OF CALCIUM CARBONATE IN CHICKEN EGGSHELLS: STUDY ON TEMPERATURE AND CONTACT TIME

bagi kadar penguraian kalsium karbonat yang optimum. Sampel kulit telur diproses terlebih dahulu untuk membuang kotoran dan sisa biologi yang tidak diperlukan dan seterusnya dikisar menjadi serbuk serta diayak. Ciri-ciri fizikal dan kimia utama serbuk kulit telur seperti perubahan warna, kehilangan jisim, ketumpatan, kandungan lembapan, pH, sifat terma, dan mengenal pasti ikatan kimia dan sebatian dalam molekul telah dikaji. Untuk mengkaji ciri-ciri fizikal dan kimia sintesis kalsium karbonat daripada kulit telur, ujian kandungan lembapan, ketumpatan pukal, pH, FTIR, and XRD dilaksanakan. Daripada pemerhatian fizikal, hasil menunjukkan terdapat perbezaan dalam perubahan warna sampel pada pelbagai suhu dan masa pembakaran. Analisis TGA menunjukkan serbuk kulit telur terurai pada julat suhu 600°C hingga 900°C. Hasil FTIR melaporkan bahawa warna kelabu sampel terkalsin terdiri daripada kalsium karbonat sementara serbuk putih terdiri daripada kandungan oksida logam. Terdapat tujuh puncak difraksi yang serupa yang dilaporkan dalam analisis XRD untuk kalsinasi pada suhu 900 °C dan kalsium oksida (32.25, 37.41, 53.92, 64.18, 67.41, 79.70, dan 88.58). Pengkalsinan serbuk kulit telur pada suhu 900 °C selama 3 jam dikenal pasti sebagai keadaan yang sesuai untuk penguraian serbuk kulit telur mentah berdasarkan analisis FTIR dan XRD. Kedua-dua hasil menunjukkan terdapat kalsium oksida berdasarkan spektrum gelombang dan analisis difraksi sampel.

Kata kunci: kalsium karbonat, kalsium oksida, kulit telur, kalsinasi

Introduction

Poultry egg is a cost-effective food source due to its high protein and nutritional content [1]. The egg from a chicken or hen (Gallus gallus domesticus, Linnaeus, 1758) is now a global mass-production industry. Quail, duck, goose, turkey, and ostrich eggs are popular choices. Both white and yellow yolks contain aqua, protein, glucose, fat, and ash, but the proportions of these components differ in every egg breed [2]. Essential lipids, proteins, minerals, and low-calorie sources are also found in eggs. Egg products are utilised in various food industrial applications, including thickening, binding, leavening, glazing, and garnishing [3]. A three-layered structure makes up an eggshell: cuticle, spongeous, and lamellar layers. The cuticle layer is the outermost layer, mainly made up of proteins. Protein fibres coupled to calcium carbonate (CaCO₃) crystals form a matrix made up of spongey and lamellar layers. CaCO3 accounts for 94% of the eggshell, followed by calcium phosphate (1%), magnesium carbonate (1%), and organic matter (4%) [4]. The eggshell and albumen are two thin eggshell membranes primarily of collagen, alkynes, alkanes, amines, protein amides, and carboxylic acids [5].

Approximately 8 million tons of eggshell wastes are produced annually worldwide [6]. Meanwhile, in Malaysia, 70,686 tons of eggshell waste are produced by various industries [7]. Eggshell waste is listed in the European Union regulation as hazardous waste, and this regulation leads to elevated costs of disposal management [8-11]. In America, companies spend

millions of dollars annually to dispose of eggshells in landfills, and the capacity is reached by the fillings [12]. The majority of eggshells are usually disposed to landfills without being treated as eggshells are considered unusable and have no commercial value [13]. However, there have been many studies utilising eggshells in various applications, such as agricultural green chemicals [13, 14, 15], a low-cost catalyst for biodiesel production [16], biofilter in wastewater treatment [17], construction materials [18, 19, 20], biomedical [21], health supplements [22], and craft [23, 24]. [25] studied the effects of eggshell powder as a supplementary material to produce recycled paper.

Various researchers have studied calcined eggshell powder (CESP) waste as a source of calcium oxide (CaO). [26] studied calcined eggshells as a catalyst in biodiesel production, [27] reported the characterisation of nano-CaO based on eggshell waste, [28] studied the CaO sorbents from chicken eggshells for enhanced carbon dioxide (CO₂) capture, [29] utilised calcined eggshells to formulate mortar for building restoration, [30] studied the effects of calcined eggshells as biomaterials for the preparation of linear low-density polyethene, [31] examined the effects of calcined eggshell catalyst in the transesterification of waste cooking oil, and [32] identified the thermoluminescence properties of CaO powder obtained from chicken eggshells.

The calcination process can decompose CaCO₃ to CaO. Calcination is a technique for extracting volatile

chemicals from solids by heating them to a high temperature, oxidising a portion of the mass, or making them brittle [33]. Calcination is frequently thought of as a purifying method. CaCO3 is calcined using two methods: combustion with CO₂/oxygen gas (O₂) or steam [34]. The process produces a completely decomposed substance depending on the temperature selected. CaCO₃ completely decomposed at the temperature range of 500-900 °C [35]. Research by [36] identified that seashell calcination at the temperature of 800 °C produced a higher amount of CaO based on Fourier transform infrared (FTIR) spectroscopy, scanning electron microscopy (SEM), energy-dispersive X-ray spectroscopy (EDX), and thermal gravimetric analysis (TGA) tests. Although seashells and eggshells are made of CaCO₃, their structure is different. It can be seen through their surface morphology. According to [37], the SEM image for seashell (cockle) is platy-shaped. On the other hand, the eggshell is porous and fibril [38]. Furthermore, based on the TGA result, the thermal decomposition of ESP and seashell varied. [39] established that the decomposition of raw eggshell powder (RESP) was in the range of 600-850 °C, while according to [40], the decomposition of cockle was in the range of 500-700 °C. [41] indicated that calcination was highly dependent on temperature, heating rate, and particle size. [39] identified no significant differences in the weight variation of eggshell powder samples during calcination. It was observed that the optimum operating conditions for the decomposition of CaCO₃ samples were 900 °C with a heating rate of 20 °C/min and particle size of 0.3 mm. Therefore, it is established

that the best temperature for CaCO₃ calcination is 800 °C and above.

Researchers have recently studied CaO derived from eggshells for new green chemistry and catalyst by dependence on limestone. reducing However, variations in calcination temperatures and contact hours have been reported. Therefore, this study aimed at finding the ideal conditions in the calcination process for converting CaCO3 from chicken eggshells to CaO. The experiments were conducted based on two parameters: contact time (h) and temperature (°C). The primary physical and chemical characteristics of eggshell powder were studied, including colour changes, mass loss, bulk density, moisture content, pH value, thermal properties, and identification of chemical bonds and compounds in a molecule.

Materials and Methods

Raw materials

Chicken eggshells were collected from local food truck vendors. The eggshells were instantly washed with gentle soap and tap water after being collected as preparation for cleaning treatment. The eggshells were boiled for 30 min [42]. This process is vital to avoid biological contamination and decaying of the eggshells. Next, the eggshells were cleaned by running tap water, air-dried for 24 h at room temperature, and stored in a dark-coloured container [43, 44]. The chicken eggshell samples were ground using an electrical powder grinder (SY-25) 2,000 W to obtain RESP. Then, the RESP was sieved with a 500-µm mesh to eliminate granular sizes. Figure 1 shows the pre-treated eggshells and ground eggshell powder.



Pre-treated eggshells



Raw eggshell powder

Figure 1. Preparation of chicken eggshells samples

Material's thermal stability and the fraction of volatile components - Thermogravimetric analysis

TGA was performed using a Shimadzu TGA-50 thermobalance. In this study, approximately 8 g of eggshell powder was heated at 50–950 °C in a nitrogen atmosphere with a flow rate of 20 mL/min and a heating rate of 25 °C/min [45].

Calcination of chicken eggshell

The eggshell powder samples were placed in closed porcelain crucibles and calcined in a chamber furnace

(Carbolite ELF 11/14B) according to the eight experiment sets as shown in Table 1. Two parameters were varied to examine the calcination process (i.e., temperature (°C) and contact time (h)) with a constant weight RESP (i.e., 20 g). Each calcination protocol was done in triplicates. To avoid a reaction with moisture and atmospheric air, the CESP was stored in flasks and placed atop a desiccator after calcination [46].

Table 1. Calcination parameters

No.	Sample Code	Parameter			
		Temperature (°C)	Contact Time (hour)		
1	CESP T ₆₀₀₋₃	600	3		
2	CESP T ₆₀₀₋₄	600	4		
3	CESP T ₇₀₀₋₃	700	3		
4	CESP T ₇₀₀₋₄	700	4		
5	CESP T ₈₀₀₋₃	800	3		
6	CESP T ₈₀₀₋₄	800	4		
7	CESP T ₉₀₀₋₃	900	3		
8	CESP T ₉₀₀₋₄	900	4		

Results and Discussion

Thermogravimetric analysis

TGA is carried out to determine the thermal stability of a material and its fraction of volatile components by monitoring the weight change that occurs as a sample is heated at a constant rate. Based on Figure 2, four reaction steps occurred in this experiment.

The first step showed that 1.13% mass decreased at midpoint 84.23 °C. The temperature range at step 1 can be considered as eliminating moisture of the sample.

[48] supported this statement, stating that biomass drying is conducted in the range of 40–200 °C. Referring to [49], the slight decrease of mass in the second step was due to the decomposition of organic matter in the range of 200–600 °C. The RESP started to decompose from CaCO₃ to CaO and released CO₂ at 600 °C and ended at 850 °C in step 3. A slight mass loss in step 4 at 950 °C can be referred to as the end of the reaction.

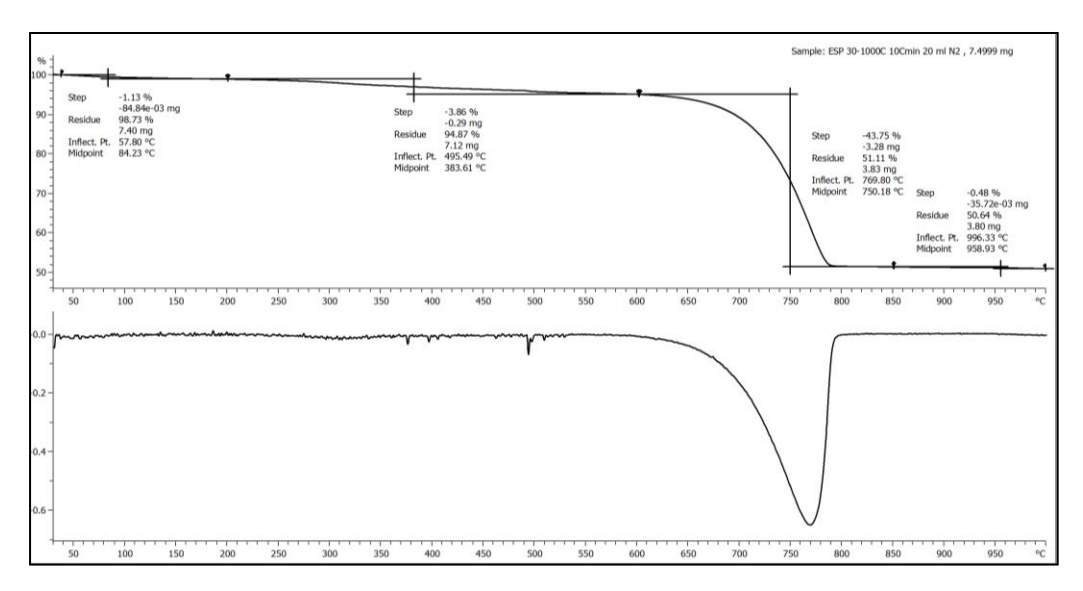


Figure 2. Thermogravimetric analysis of RESP

Calcination process

Calcination is the process of decomposing CaCO₃ by burning the compound at high temperatures. The catalysts were completely decomposed at the temperature range of 500–900 °C [39]. The optimum temperature for the calcination of CaCO₃ from cockle shell was 900 °C for 2 h with a particle size of 0.3 mm under inert conditions [41]. [13] supported this statement and reported that the suitable temperature and time for complete decomposition in the calcination of CaCO₃ from duck eggshells were 900 °C and 1 h, respectively. [50] and [40] argued that calcite fully decomposed to form CaO at 800 °C. Based on these studies, three conditions may affect the calcination process. In this study, CaO is derived from eggshell powder, as shown in Equation 3.

$$CaCO_{3(s)} \rightarrow CaO_{(s)} + CO_{2(g)}$$
 (3)

The primary characteristics of CESP were studied and recorded, including physical observation (colour changes), moisture content, bulk density, and average mass loss. Based on the TGA result in Figure 2, the RESP decomposed in the temperature range of 600–850 °C. Therefore, the range of calcination temperature in this study was chosen from 600 °C to 900 °C. By referring to Table 2, as the temperature increases, the bulk density value decreases, and consequently, the

mass loss increases. From the result, it shows that calcination temperature affected the reduction in mass for eggshell powder. Different colour changes were observed between uncalcined and calcined samples. The colour of the uncalcined eggshell is light brown based on its original colour. In comparison, a perfect CESP should be solid white. Based on the result, low calcination temperatures produced dark or grey colour, whereas at high calcination temperatures, solid white colour was obtained. More metal oxide (solid white powder) was produced for higher calcination temperatures. [51] stated that the higher temperature would produce a higher amount of metal oxide and the colour would become whiter. [41] established the optimum temperature of 900 °C for CaCO₃ decomposition. High temperatures are required for CESP to produce perfect CaO. The dark powder obtained at low temperatures indicates that eggshell powder has not completely decomposed.

Compared to other manipulated variables, the samples calcined at different contact times showed a massive percentage of mass loss. This could be explained by the longer calcination duration, which resulted in greater mass loss [52]. The colour transition for different contact times is presented in Table 2. Even though the samples of eggshell powder were calcined at the same temperature and weight, the calcination result was

Nadia et al: THERMAL DECOMPOSITION OF CALCIUM CARBONATE IN CHICKEN EGGSHELLS: STUDY ON TEMPERATURE AND CONTACT TIME

affected by the contact time. The formation of dark grey powder at low contact time was due to a lack of heat distribution. The grey powder at the inner part of the sample showed that the heat was not well distributed to the whole part of the sample. Therefore, increasing the calcination period is one of the significant ways to improve the formation of metal oxide. [13] stated that higher temperature and longer calcination time produced better CaO quality.

Moisture loss occurred during calcination, which corresponds to the loss of water and/or gas of the eggshell powder. In this study, the moisture loss percentages of CESP in all conditions were too insignificant, and therefore, could be ignored. [54] stated that the decomposition of volatile materials (e.g., water and organic matter) occurred in the temperature range of 30–400 °C. There were no changes in the acidity of RESP and dark powder. Meanwhile, the acidity for solid white powder changed to alkali. Therefore, if the amount of dark powder is more

significant than solid white powder, the sample can be considered as CaCO₃.

The bulk density values of eggshell powder calcined with different parameters are tabulated in Table 2. The solid white powder of CESP T₉₀₀₋₃ and CESP T₉₀₀₋₄ showed a softer and more refined texture. [13] reported that calcination at 900 °C for 1 h reduced the particle size of the samples. According to Equation 2, density is inversely proportional to volume. The bulk density decreased as the particle size increased [53]. The volume depends on the particle size of the samples.

The pH of RESP changed to alkali when it was calcined at high temperatures. The alkalinity value increased as the temperature and contact time increased. The samples of CESP₇₀₀₋₄ to CESP₉₀₀₋₄ showed an alkaline pH value of 12.70–13.26, indicating the presence of CaO. The result is correlated with previous findings, where the calcination temperature of 700 °C produced sufficient CaO and achieved the critical value of an alkaline solution [54].

Bulk Moisture Mass Loss Sample **Physical Observation Content Density** pН (%)(%)(g/ml) Uncalcined N/A 0.451 2.47 7.00 CESP T₆₀₀₋₃ 0.84N/A 1.38 9.36 CESP T₆₀₀₋₄ 0.83 N/A 1.41 10.84

1.13

N/A

1.36

11.64

Table 2. Calcination of ESP with different parameters

CESP T₇₀₀₋₃

Table 2 (cont'd). Calcination of ESP with different parameters

Sample	Physical Observation	Mass Loss (%)	Moisture Content (%)	Bulk Density (g/ml)	pН
CESP T ₇₀₀₋₄		0.98	N/A	1.33	12.70
CESP T ₈₀₀₋₃		2.19	N/A	1.38	12.67
CESP T ₈₀₀₋₄		2.99	N/A	1.33	12.85
CESP T ₉₀₀₋₃		11.00	N/A	3.00	12.96
CESP T ₉₀₀₋₄		11.43	N/A	3.33	13.26

Compounds identification

The FTIR analysis can be divided into three broad regions. The first region is from 4000 cm⁻¹ to 3000 cm⁻¹, which represents hydrogen bonding. The second region, which is from 3000 cm⁻¹ to 1500 cm⁻¹, shows functional groups. Meanwhile, the third region reveals the existence of biominerals. Based on physical observation and pH values in Table 2, chemical characterisation was conducted for the selected samples of CESP T₇₀₀₋₄, CESP T₈₀₀₋₃, CESP T₈₀₀₋₄, CESP T₉₀₀₋₃, and CESP T₉₀₀₋₄. Sufficient CaO content produced from the calcination of eggshells will make the pH value reach the critical value of 12.7 [56]. Therefore, the FTIR analysis identifies the functional groups present in the eggshells calcined at 900 °C with different contact times.

Figure 3 below presents the FTIR spectra for CESP at various temperatures and contact times. Small sharp peaks were detected at 874 cm⁻¹ and 1417 cm⁻¹ for CESP T₇₀₀₋₃, CESP T₇₀₀₋₄, CESP T₈₀₀₋₃, and CESP T₈₀₀₋₄. The bands at both wavelength indicated CaCO₃ in the tested samples [55,56]. Another strong peak was observed at 2516 cm⁻¹ due to the presence of CaCO₃ [57]. According to [7], the observable peaks in the range of 713–875 cm⁻¹ can be associated with the presence of CaCO₃. The observation by [58] for the band at 1430 cm⁻¹ was attributed to the stretching vibration of CaCO₃. Meanwhile, the bands at 875 cm⁻¹ and 715 cm⁻¹ strongly corresponded to CaCO₃ [59]. The lowest band represents the weak band to indicate CaCO₃.

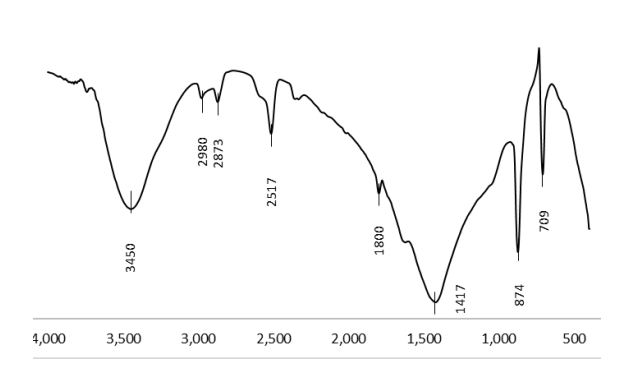
Nadia et al: THERMAL DECOMPOSITION OF CALCIUM CARBONATE IN CHICKEN EGGSHELLS: STUDY ON TEMPERATURE AND CONTACT TIME

Sharp peaks were observed at 707 cm⁻¹ and 709 cm⁻¹. The wavenumber increased as the transmittance increased intensely at the peak of 874 cm⁻¹. Both peaks are associated with in-plane deformation and out-plane deformation modes of eggshell powder in the presence of CaCO₃, as described by [7]. The sharp, strong band detected at 1560 cm⁻¹ is attributed to the oxidation process [60].

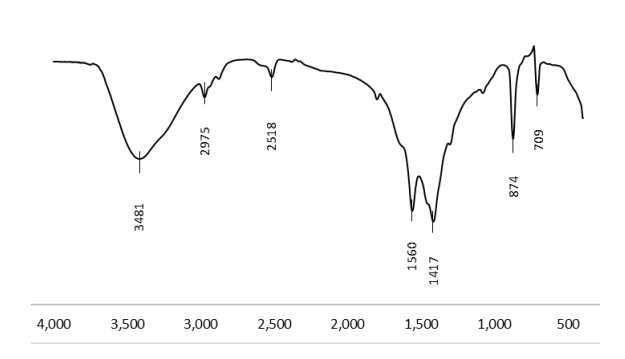
An amine group was present at the band of 1055 cm⁻¹. According to [61], the presence of the functional groups of amines and amides was observed due to the chemical composition of fibrous proteins. As referred to [62], CESP T₉₀₀₋₃ showed a medium-sized peak at 1052 cm⁻¹ corresponding to the stretching of both C-O

in the C-OH bond. The peaks at 1424 cm⁻¹ and 1422 cm⁻¹ indicated the presence of OH bonding. The existence of hydroxide might be due to exposure to the atmosphere during calcination [63]. Another significant peak was detected at 2361 cm⁻¹ in regard to the presence of O=C=O bonds. The presence of O=C=O bonds indicated the carbonation of CaO, as shown in Equation 4 [64].

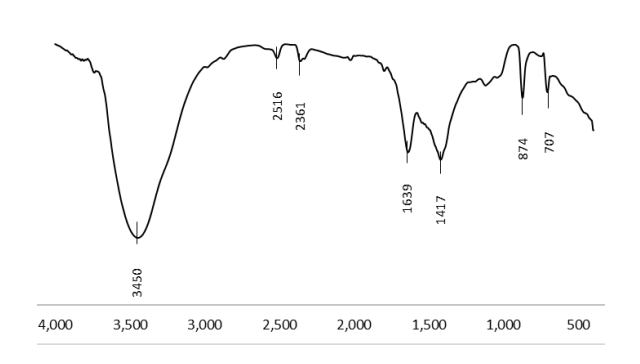
$$Ca(OH)^2 + CO_2 \rightarrow CaCO_3 + H_2O$$
 (4)



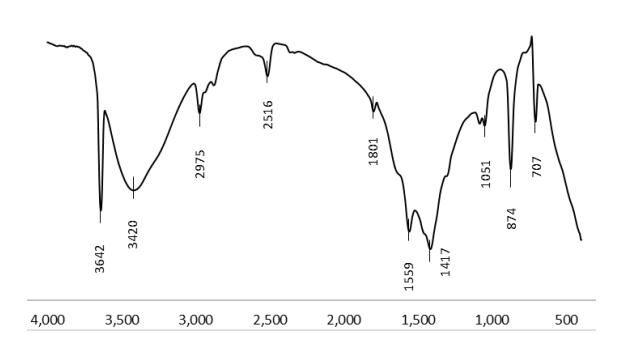
(a) CESP T₇₀₀₋₃



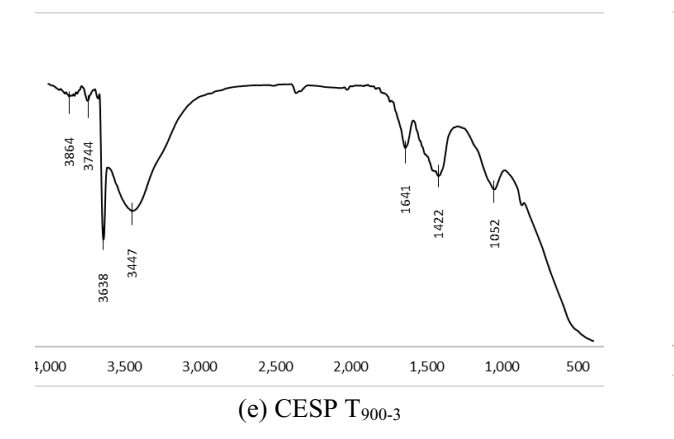
(b) CESP T₇₀₀₋₄



(c) CESP T₈₀₀₋₃



(d) CESP T₈₀₀₋₄



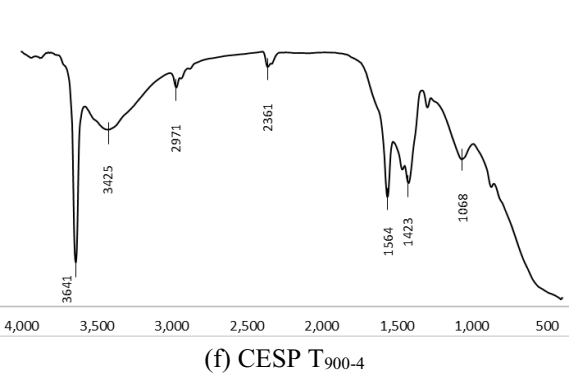


Figure 3. The FTIR spectra for CESP at different contact times and temperatures

The XRD analysis was carried out to identify CaO in CESP at different temperatures. Figure 4 illustrates the results of XRD analysis for RESP and CESP at 900 °C (CESP T_{900-3}), 700 °C (CESP T_{700-3}), and industrial CaO as a reference. The intensity of CaCO₃ showed the primary compound of RESP. The diffraction showed both distinct components of CaO and CaCO₃ for CESP T_{700-3} . Thus, the intensity of CaCO₃ decreased compared to RESP. At 700 °C, incomplete

decomposition of CaCO₃ occurred, based on the diffraction pattern (c). A similar study by [53] claimed that CaO was absent at 700 °C. CESP T_{700-3} showed a different peak pattern of CaO than CESP T_{900-3} and industrial CaO. Meanwhile, CESP T_{900-3} showed seven diffraction peaks similar to the diffraction peaks of industrial CaO. The simplified XRD analysis is shown in Table 3.

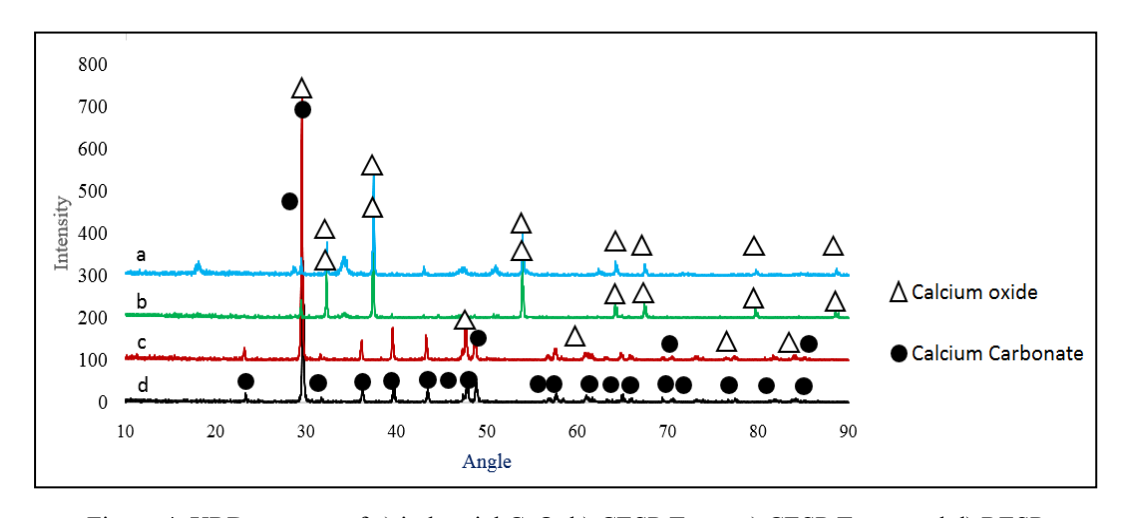


Figure 4. XRD patterns of a) industrial CaO, b) CESP T₉₀₀₋₃, c) CESP T₇₀₀₋₃, and d) RESP

Sample	Compound				Angle (2θ))		
CESP T ₇₀₀₋₃	CaCO ₃	28.78	47.25	62.73	71.79	84.88	-	-
	CaO	29.52	47.67	60.84	77.45	84.02	-	-
CESP T ₉₀₀₋₃	CaO	32.25	37.41	53.92	64.18	67.41	79.70	88.58
Industrial CaO	CaO	32.33	37.45	56.97	64.24	67.47	79.78	88.66

Table 3. X-ray diffraction results for CaO and CaCO3 from synthesised eggshell powder

Conclusion

Different calcination temperatures and contact times were applied in the calcination of eggshell waste to decompose CaCO₃ into CaO. Based on physical inspection, higher temperature and increased contact time produced white powder, which was later identified as CaO. Among the studied calcination conditions, the best conditions were the temperature of 900 °C and the contact time of 3 h. The CaO synthesized from eggshells can be used in various applications, such as in the laboratory (gas absorber), construction (lime putty and cement production), soil stabiliser, medicinal purposes, and others. Hence, it is believed that calcined chicken eggshells can be an alternative source of CaO to reduce the dependency on limestone resources.

Acknowledgement

An industrial research fund partially supported this research under the MRT-SSP-V208-Second Tier ICP Agreement 2019 (Grant Number: ICP/MTDC/2019). We would like to thank our colleagues from Universiti Kuala Lumpur – MICET and Universiti Teknikal Melaka Malaysia, who provided insight and expertise that greatly assisted the research.

References

- 1. Miranda, J.M., Anton, X., Redondo-Valbuena, C., Roca-Saavedra, P., Rodriguez, J.A. and Lamas, A. (2015). Egg and egg-derived foods: Effects on human health and use as functional foods. *Nutrients*, 7: 706-729.
- 2. Godbert, S.R., Guyot, N. and Nys, Y. (2019). The golden egg: Nutritional value, bioactivities, and emerging benefits for human health. *Nutrients*, 11(684): 1-26.

- 3. Laca, A., Paredes, B., Rendueles, M. and Díaz, M. (2014). Egg yolk granules: Separation, Characteristics, and Applications in The Food Industry. *LWT Food Science and Technology*, 59(1): 1-5.
- 4. Rivera, E.M., Araiza, M., Brostow, W., Castano, V.M., Diaz-Estrada, J.R., Hernandez, R. and Rodriguez, J.R. (1999). Synthesis of hydroxyapatite from eggshells. *Materials Letter*, 41: 128-134.
- 5. Park, S., Choi, K.S., Lee, D., Kim, D., Lim, K.T., Lee, K.H., Seonwoo, H. and Kim. J. (2016). Eggshell membrane: Review and impact on engineering. *Biosystem Engineering*, 151: 446-463.
- De Angelis, G., Medeghini, L., Conte, A.M. and Mignardi, S. (2017). Recycling of eggshell waste into low-cost adsorbents for Ni removal from wastewater. *Journal of Cleaner Production*, 164: 1497-1506.
- Carvalho, J., Araujo, J. and Castro, F. (2011). Alternative low-cost adsorbent for water and wastewater decontamination derived from eggshell waste: an overview. Waste Biomass Valor, 2: 157-167.
- 8. Laca, A., Laca, A. and Díaz, M. (2017). Eggshell waste as catalyst: A review. *Journal of Environmental Management*, 197: 351-359.
- 9. Quina, M., Soares, M.A. and Quinta, F.R. (2017). Applications of industrial eggshells as a valuable anthropogenic resource. *Resources Conservation and Recycling*, 123: 176-186.
- Ummartyotin S. and Manuspiya, H. (2018). A critical review of eggshell waste: An effective source of hydroxyapatite as photocatalyst. *Journal* of Metals, Materials, and Minerals, 28(1): 124-135.

- 11. Sonenklar, C. (1999). Famous for Egg Waste. The PennState news. The Pennsylvania State University. https://news.psu.edu/story/140891/1999/09/01/research/famous-egg-waste. [Access online 1 September 1999]
- 12. Arabhosseini, A. and Faridi, H. (2018). Application of eggshell wastes as valuable and utilizable products: A review. *Resource Agriculture Engineering*, 64: 104-114.
- 13. Tangboriboon, N., Kunanuruksapong, R. and Sirivat, A. (2012). Preparation and properties of calcium oxide from eggshells via calcination. *Materials Science-Poland*, 30(4): 313-322.
- 14. Ok, Y.S., Lee, S.S., Jeon, WT., Oh, S.E., Usman, A.R.A. and Moon, D.H. (2011). Application of eggshell waste for the immobilization of cadmium and lead in contaminated soil. *Environ Geochem Health* 33: 31-39.
- 15. Yasar, F. (2019). Biodiesel production via waste eggshell as a low-cost heterogeneous catalyst: Its effects on some critical fuel properties and comparison with CaO. *Fuel*, 255(1): 115828.
- 16. Bashir, A.S.M. and Manusamy, Y. (2015). Characterization of raw eggshell powder (ESP) as a good bio filler. *Journal of Engineering Research and Technology*, 2(1): 56-60.
- 17. Ahmad, R., Rohim, R. and Ibrahim, N. (2015). Properties of waste eggshell as calcium oxide catalyst *Applied Mechanics and Materials*, 754: 171-175.
- 18. Karthick, J., Jeyanthi, R. and Petchiyammal, M. (2014). Experimental study on usage of egg shell as partial replacement for sand in concrete. *International Journal of Advanced Research in Education Technology*, 1(1): 7-10.
- 19. Gabol, N.A., Memon, F.A., Jawaduddin, M. and Zardari, Z.H. (2019). Analysis of eggshell powder as a partial replacing material in concrete. *International Journal of Modern Research in Engineering & Management*, 2(9): 22-31.
- 20. Razali, N., Azizan, M.A., Pa'ee, K.F., Razali, N. and Jumadi, N. (2020). Preliminary studies on calcinated chicken eggshells as fine aggregates replacement in conventional concrete. *Materials Today: Proceedings*, 31(1): 354-359.
- Abdulrahman, I., Tijani, H.I., Mohammed, B.A., Saidu, H., Yusuf, H., Jibrin, M.N. and Mohammed, S. (2014). From garbage to biomaterials: An overview on eggshell-based hydroxyapatite. *Journal of Materials*, 2014: 1-6.
- 22. Bartter, J., Diffey, H., Yeung, Y.H., O'Leary, F., Häsler, B., Maulaga, W. and Alders, R. (2018). Use of chicken eggshell to improve dietary

- calcium intake in rural sub-saharan Africa. *Maternal & Child Nutrition*, 14(3): 1-10.
- 23. Hitchcock, R.K. (2012). Ostrich eggshell jewelry manufacturing and use of ostrich products among San and Bakgalagadi in the Kalahari. *Botswana Notes and Records*, 44: 93-105.
- 24. Zoran. A. (2018). The ostrich eggshell beads craft of the Ju/'hoansi: A reflection on modern craft theories. *Craft Research*, 9(2): 229-253.
- Abdullah, M., Soo, K. Y., Raofuddin, D.N.A, Sukor, M.Z., Roslan, A., Ilyas, S.M.M. and Yasin, M.H. (2018). An evaluation of eggshell waste/waste paper mechanical properties as composite paper. *International Journal of Engineering & Technology*, 7: 239-241.
- Sulaiman S., and Talha N.S. (2018) Technique to produce catalyst from egg shell and coconut waste for biodiesel production. In: Amid A., Sulaiman S., Jimat D., Azmin N. (eds) *Multifaceted Protocol* in *Biotechnology*.
- 27. Mosaddegh, E. and Hassankhani, A. (2014). Preparation and characterization of nano-cao based on eggshell waste: Novel and green catalytic approach to a highly efficient synthesis of pyrano[4,3-b] pyrans. *Chinese Journal Catalyst*, 35: 351-356.
- 28. Sacia, E.R., Ramkumar, S., Phalak, N. and Fan, L.S. (2013). Synthesis and regeneration of sustainable CaO sorbents from chicken eggshells for enhanced carbon dioxide capture. *ACS Sustainable Chemical Engineering*, 1: 903-909.
- 29. Beck, K., Brunetaud, X., Mertz, J.D. and Al-Mukhtar, M. (2010). The use of eggshell lime and tuffeau powder to formulate an appropriate mortar for restoration purposes. *Geological Society London Special Publications*, 331(1): 137-145.
- Jirimali, H.D., Chaudhari, B.C., Khanderay, J.C., Joshi, S.A., Singh, V., Patil, A.M. and Gite, V.V. (2018). Waste eggshell-derived calcium oxide and nanohydroxyapatite biomaterials for the preparation of LLDPE polymer nanocomposite and their thermomechanical study. *Polym-Plast Technology Engineering*, 57: 804-811.
- 31. Tan, Y.H., Abdullah, M.O., Nolasco-Hipolito, C. and Zauzi, N.S.A. (2017). Application of RSM and Taguchi methods for optimizing the transesterification of waste cooking oil catalyzed by a solid ostrich and chicken-eggshell derived CaO. *Renew Energy*, 114(Part B): 437-447.

- 32. Nagabhushana, K.R., Lokesha, H.S., Reddy, S.S., Prakash, D., Veerabhadraswamy, M., Bhagyalakshmi, H. and Jayaramaiah, J.R. (2017). Thermoluminescence properties of CaO powder obtained from chicken eggshells. *Radiation Physics Chemistry*, 138: 54-59.
- 33. Britannica, T. Editors of Encyclopedia. Calcination. Encyclopedia Britannica. Retrieved Oct 04, 2016, from https://www.britannica.com/technology/calcinatio n. [Access online 4 October 2016].
- 34. Lin. S., Kiga. T., Wang. Y. and Nakayama. K. (2011). Energy analysis of CaCO₃ calcination with CO₂ capture. *Energy Procedia*, 4: 356-361.
- 35. Al-Fatesh, A.S.A. and Fakeeha, A.H. (2012). Effects of calcination and activation temperature on dry reforming catalysts. *Journal of Saudi Chemical Society*, 16: 55-61.
- 36. Nordin, N., Hamzah, Z., Hashim, O., Kasim, F.H., and Abdullah, R. (2015). Effect of temperature in calcination process of seashells. *Malaysian Journal of Analytical Sciences*, 19(1): 65-70.
- 37. Dampang, S., Purwanti, E., Destyorini, F., Kurniawan, S. B. K., Abdullah, S. R. S. and Imron, M. (2021). Analysis of optimum temperature and calcination time in the production of CaO using seashells waste as CaCO₃ source. *Journal of Ecological Engineering*, 22(5): 221–228.
- 38. Aina, S., Plessis, B. D., Mjimba, V. and Brink, H. (2021). Eggshell valorization: Membrane removal, calcium oxide synthesis, and biochemical compound recovery towards cleaner productions. *Biointerface Research in Applied Chemistry*, 12(5): 5870-5883.
- 39. Razali, N., Musa, F. A. M., Jumadi, N. and Jalani, A. Y. (2021). Production of calcium oxide from eggshell: Study on calcination temperature, raw weight and contact time. *RSU International Research Conference*, 2021: 624-637.
- Hussein, A. I., Ab-Ghani, Z., Mat, A. N. C., Ab-Ghani, N. A., Husein, A. and Rahman, I. A. (2021). Synthesis and characterization of spherical calcium carbonate nanoparticles derived from cockle shells. *Applied Science*, 10: 7170.
- 41. Mohamad, S.F.S, Mohamad, S. and Jemaat, Z. (2016). Study of calcination condition on decomposition of calcium carbonate in waste cockle shell to calcium oxide using thermal gravimetric analysis. ARPN *Journal of Engineering and Applied Sciences*, 11(16): 9917-9921.

- 42. Islam, K.N., Bakar, M.Z.B.A., Ali, M.E., Hussein, M.Z.B., Noordin, M.M., Loqman, M.Y., Miah, G., Wahid, H. and Hashim, U. (2013). A novel method for the synthesis of calcium carbonate (aragonite) nanoparticles from cockle shells. *Powder Technology*, 235: 70-75.
- 43. Ali, M. and Badawy W. Z. (2017). Utilization of eggshells by-product as a mineral source for fortification of bread strips. *Journal of Food and Dairy Sciences*, 8(11): 455-459.
- 44. Oulego, P., Laca, A., Calvo, S. and Díaz, M. (2019). Eggshell-supported catalysts for the advanced oxidation treatment of humic acid polluted wastewaters. *Water*, 12(100): 1-18.
- 45. Yahya, N., Tahir, S.M. and Rosli, N.H.M. (2019). Green eggshell/polypropylene biocomposite. *International Journal of Recent Technology and Engineering*, 8: 2277-3878.
- Castro, L.D.S., Barañano, A.G., Pinheiro, C.J.G.L, Menini, L. and Pinheiro, P.F. (2019). Biodiesel production from cotton oil using heterogeneous CaO catalysts from eggshells prepared at different calcination temperatures. *Green Process Synthesis*, 8: 235-244.
- 47. Gatea, A.A., Kouzani, A.Z., Kaynak, A., Khoo, S.Y., Norton, M. and Gates, W. (2018). Soil bulk density estimation methods: A review. *Pedosphere*, 28(4): 581-596.
- 48. Jewiarz, M., Wrobel, M., Mudryk, K. and Szufa, S. (2020). Impact of the drying temperature and grinding technique on biomass grindability. *Energies*, 13(3392): 1-22.
- 49. Queirós, M.V.A., Bezerra, M.N. and Feitosa, J.P.A. (2017). Composite superabsorbent hydrogel of acrylic copolymer and eggshell: Effect of biofiller addition. *Journal Brazillian Chemical Society*, 2017: 1-9.
- 50. Loy, C.W., Matori, K.A., Way F.L., Schmid, S., Zainuddin, N., Wahab, Z.A., Alassan, Z.N. and Zaid, M.H.M. (2016). Effects of calcination on the crystallography and nonbiogenic aragonite formation of ark clamshells under ambient conditions. *Advances in Materials Science and Engineering*. 2016: 1-8.
- 51. Mohadi, R., Anggraini, K., Riyanti F. and Lesbani, A. (2016). Preparation of calcium oxide (CaO) from chicken eggshells. *Sriwijaya Journal of Environment*, 1(2): 32-35.
- 52. Krähenbühl, M., Etter, B. and Udert, K.M. (2015). Pre-treated magnesite as a source of low-cost magnesium for producing. *Science of The Total Environment*, 542: 1155-1161.

- 53. Zhang, S. (2015). Relationship between particle size distribution and porosity in dump leaching. Thesis of Doctor of Philosophy. The University of British Columbia.
- 54. Shao, W.C., and Dong, Y.W. (2020). A study on physicochemical properties and formaldehyde adsorption and degradation of purifying air quality by modified biocalcium. *International Journal of Environmental Science and Development*, 7(11): 327-335.
- Rujitanapanich, S., Kumpapan, P. and Wanjanoi, P. (2014). Synthesis of hydroxyapatite from oyster shell via precipitation. *Energy Procedia*, 56: 112-117.
- 56. Yao, C., Xie, A., Shen, Y., Zhu, J. and Li, T. (2013). Green synthesis of calcium carbonate with unusual morphologies in the presence of fruit extracts. *Journal Chilean Chemical Society*, 58(4): 2235-2238.
- 57. Daskalakis, M.I., Magoulas, A., Kotoulas, G., Catsikis, I., Bakolas, A., Karageorgis, A.P., Mavridou, A., Doulia, D., Rigas, F. (2013). Pseudomonas, pantoea and cupriavidus isolates induce calcium carbonate precipitation for biorestoration of ornamental stone. *Journal of Applied Microbiology*, 115: 409-423.
- 58. Veerasingam, S. and Venkatachalapathy, R. (2014). Estimation of carbonate concentration and characterization of marine sediment by fourier transmission infrared spectroscopy. *Infrared Physics and Technology*, 66: 136-140.
- Reyes, J., Gutiérrez, R., Centeno, G., Treviño,
 D., Bartolo, P., Quintana, P., Azamar, J.A., and
 Pérez, T. (2008). Chemical characterization of
 Crusts Formed in Mortars of Historical

- Buildings in San Francisco de Campeche City, Mexico. *Historical Mortars Conference*, 2008: pp. 1-11.
- 60. Pardo, F.N., Barrera, G.M., Hernández, A.L.M., Castaño, V.M., Armenta, J.L.R., Rodríguez, F.M. and Santos C.V. (2013). Effects on the thermomechanical and crystallinity properties of nylon 6,6 electrospun fibres reinforced with one dimensional (1d) and two-dimensional (2d) carbon. *Materials*, 8: 3494-3513.
- 61. Tsai, T.Y., Coumar, M.S., Hsu, T., Hsieh, H.P., Chien, C.H., Chen, C.T., Chang, C.N., Lo, Y.K., Wu, S.H., Huang, C.Y., Huang, Y.W., Wang, M.H., Wu, H.Y., Lee, H.J., Chen, X., Chao, Y.S., and Jiaang, W. (2006). Substituted pyrrolidine-2,4-dicarboxylic acid amides as potent dipeptidyl peptidase IV inhibitors. *Bioorganic & Medicinal Chemistry Letters*. 16(12): 3268-3272.
- 62. Nandiyanto, A.B.D., Oktiani, R. and Ragadhita, R. (2019). How to read and Interpret FTIR spectroscope of organic material. *Indonesian Journal of Science & Technology*, 4(1): 97-118.
- 63. Zaman, T., Mostari, M. S., Mahmood, M. A. and Rahman, M. S. (2018). Evolution and characterization of eggshell as a potential candidate of raw material. *CerâMica*, 64(370): 236-241.
- 64. Habte, L., Khan, M.D., Shiferaw, N., Farooq, A., Lee, M.H., Jung, S.H. and Ahn, J.W. (2020). Synthesis, characterization, and mechanism study of green aragonite crystals from waste biomaterials as a calcium supplement. *Sustainability*, 12(5062): 1-10.

Malaysian Journal of Analytical Sciences (MJAS) Published by Malaysian Analytical Sciences Society



DEVELOPMENT AND OPTIMIZATION OF A RAPID RESOLUTION LIQUID CHROMATOGRAPHY METHOD FOR CYANIDIN-3-O-GLUCOSIDE IN RAT **PLASMA**

(Pembangunan dan Pengoptimuman Kaedah Kromatografi Cecair Resolusi Pantas untuk Sianidin-3-O-Glukosida Klorida di dalam Plasma Tikus)

Nadiratul Asyikin Sauji¹, Wan Amir Nizam Wan Ahmad¹, Liza Nordin², Ruzilawati Abu Bakar³*

¹Biomedicine Program, School of Health Sciences ²Department of Physiology, School of Medical Sciences ³Department of Pharmacology, School of Medical Sciences Universiti Sains Malaysia, 16150 Kubang Kerian, Kelantan, Malaysia

*Corresponding authors: ruzila@usm.my

Received: 16 January 2022; Accepted: 15 March 2022; Published: 28 April 2022

Abstract

The growing interest in anthocyanins in plants has brought about the importance of investigating their pharmacological properties. Sensitive and specific analytical methods are required to accurately analyze the anthocyanins present in samples. One of the anthocyanins found in plants is cyanidin-3-O-glucoside. The objective of this study was to develop and optimize a rapid resolution liquid chromatography (RRLC) method for cyanidin-3-O-glucoside determination in rat plasma. Spectrophotometric analysis was performed to determine the best ultraviolet (UV) absorbance wavelength. Liquid-liquid extraction (LLE) and solidphase extraction (SPE) methods were compared to determine the best extraction method for cyanidin-3-O-glucoside in rat plasma samples. The effects of varying the type and proportion of organic solvents, the type and concentration of buffer solutions, flow rates, column temperatures, and UV wavelengths were examined. The optimized chromatographic method for RRLC analysis of cyanidin-3-O-glucoside was a mobile phase composition of 0.1% trifluoroacetic acid aqueous solution and acetonitrile in a ratio of 81:19, respectively, with a 0.5 mL/min flow rate, at 30°C column temperature and 525 nm detection wavelength. SPE was our choice of final extraction method. Our findings revealed that the optimized RRLC method can be used to determine cyanidin-3-O-glucoside in rat plasma.

Keywords: rapid resolution liquid chromatography, method development, cyanidin-3-o-glucoside, rat plasma

Abstrak

Kajian antosianin dalam rosel yang semakin meluas mengetengahkan kepentingan analisis sebatian tersebut untuk mengkaji ciriciri farmakologinya. Kaedah analisis yang sensitif dan spesifik diperlukan untuk menganalisis antosianin yang terdapat dalam sampel dengan tepat. Salah satu antosianin yang terdapat dalam tumbuhan ialah sianidin-3-O-glukosida. Objektif kajian ini adalah untuk membangunkan dan mengoptimumkan kaedah kromatografi cecair resolusi pantas (RRLC) untuk sianidin-3-Oglukosida di dalam plasma tikus. Analisis spektrofotometri dilakukan untuk memilih penyerapan ultraungu yang terbaik. Kaedah pengekstrakan cecair-cecair (LLE) dan pengekstrakan fasa pepejal (SPE) juga dijalankan untuk menilai kaedah pengekstrakan

terbaik bagi antosianin daripada sampel plasma tikus. Kesan mempelbagaikan jenis dan peratusan pelarut organik, jenis dan kepekatan larutan penimbal, kadar aliran fasa bergerak, suhu turus dan panjang gelombang pengesan ultraungu telah diuji. Kaedah pengoptimuman kromatografi menunjukkan komposisi fasa bergerak bagi larutan akueus asid trifluoroasettik 0.1% dan asetonitril dalam nisbah 81:19, dengan kadar aliran 0.5 mL/min, pada suhu turus 30°C dan panjang gelombang pengesanan 525 mm adalah sesuai untuk analisis sianidin-3-O-glukosida. Kaedah SPE dipilih sebagai kaedah pengekstrakan terbaik kerana ia menghasilkan puncak kromatogram yang lebih baik berbanding kaedah LLE. Kesimpulannya, kaedah RRLC yang dibangunkan dalam kajian ini boleh digunakan untuk menentukan sianidin-3-O-glukosida dalam plasma tikus.

Kata kunci: kromatografi cecair resolusi pantas, pembangunan kaedah, sianidin-3-O-glukosida, plasma tikus

Introduction

Anthocyanins are polyphenolic pigments that belong to the flavonoid group and are present in the vacuolar sap of the epidermal tissues of flowers and fruits [1, 2]. These compounds are responsible for various colors of plant organs, such as fruits, flowers, and leaves, and they are also present in vegetables [1]. One of the anthocyanins found in plants is cyanidin-3-O-glucoside [3]. The ever-increasing evidence about anthocyanins has drawn many researchers to investigate more about these plant flavonoids. The increasing importance of elucidating their health -promoting properties has raised the need for specific tasks for their determination methods.

The development of a combined extraction method spectrophotometric and chromatographic methods is regarded as having the most significant impact on the analysis of anthocyanins [3, 4]. Although liquid chromatography has been the most employed technique to identify or quantify anthocyanins [5], an advanced and improved method of high-performance liquid chromatography (HPLC), such as rapid resolution liquid chromatography (RRLC), is currently applied in anthocyanin research, as it offers better separation and identification of specific components of anthocyanins. Therefore, the objective of this study was to develop and optimize an RRLC method for cyanidin-3-Oglucoside in rat plasma. Spectrophotometric analysis was performed to determine the appropriate UV absorbance. Both liquid-liquid extraction (LLE) and solid-phase extraction (SPE) methods were performed to determine the best extraction method for cyanidin-3-O-glucoside chloride in the rat plasma sample. We tested the effects of varying the type and percentage of organic solvents, the type and concentration of buffer solutions, flow rates, and column temperatures.

Materials and Methods

Chromatographic equipment

The chromatographic system and machine consisted of the Agilent Technologies 1200 Series system consisted of a binary pump, an autosampler, thermostat column compartment, variable wavelength detector and a vacuum degasser (Agilent Technologies, Santa Clara, California, USA). The analytical column was Agilent Reverse Phase EC-C18 (4.6 x 150 mm I. D, particle size 2.7 μ m) (Agilent Technologies, Santa Clara, California, USA). The guard column was Agilent Reverse Phase EC-C18 2.7 μ m (4.6 x 5 mm) (Agilent Technologies, Santa Clara, California, USA).

Chemicals and reagents

All chemicals were HPLC grade. Acetonitrile (ACN), 5-sulfosalicylic acid dihydrate, ethyl acetate, methyl tert-butyl ether (MTBE), methanol (MeOH), formic acid (CH₂O₂), phosphoric acid (H₃PO₄), hydrochloric acid (HCL) and trifluoroacetic acid (TFA) were from Merck® (Darmstadt, Germany). Diethyl ether was from Fisher Chemical (Massachusetts, USA).

Drug standard and internal standard

The drug standard, cyanidin-3-O-glucoside chloride was purchased from ChemFaces (catalogue no. CFN99740) (CAS no. 7084-24-4). The internal standard, cyanidin-3,5-O-diglucoside chloride was also purchased from ChemFaces (catalogue no. CFN92138) (CAS no. 2611-67-8).

Standard stock solutions of cyanidin-3-O-glucoside chloride ($100~\mu g/ml$) and internal standard, cyanidin-3,5-O-diglucoside chloride ($100~\mu g/ml$) were prepared by dissolving 1 mg of each compound in 10 ml MeOH, respectively. The solutions were then stored at -20°C in clear vials and were protected from light with aluminum foils. The working cyanidin-3-O-glucoside chloride and internal standard solutions were prepared fresh daily by diluting the stock solutions with the mobile phase. The concentration of working solution for internal standard and cyanidin-3-O-glucoside chloride used for the optimization of chromatographic conditions were 250 ng/ml and 500 ng/ml, respectively.

Preparation of plasma standard and samples

The rats used in this study were approved by the USM Institutional Animal Care and Use Committee (USM IACUC) [USM/IACUC/2019/(118)(1000)] and supplied by the Animal Research and Service Centre (ARASC), Health Campus, USM Kelantan, Malaysia. Rats' blood was collected and stored in heparin blood tubes before being centrifuged to separate the plasma. Then, the rat plasma was stored at -80 °C within 8 hours of collection.

The fresh-frozen rat plasma was allowed to thaw naturally on the bench at room temperature for approximately 45-60 minutes. It was then vortexed for a few seconds to ensure uniform distribution. The plasma standard was prepared in the same ratio with different volumes for each extraction method.

Spectrophotometry analysis

The spectrophotometric analysis of cyanidin-3-O-glucoside chloride and the internal standard were performed on a Cary 100 UV-visible spectrophotometer. Dilutions of aliquots of standard stock solution (100 ug/mL) of both cyanidin-3-O-glucoside chloride and internal standard were carried out with 0.1% HCL in 75% MeOH to reach the concentration range 10 ug/mL and 50 ug/mL. The wavelength of range 300 to 700 nm was selected for the quantitation of cyanidin-3-O-glucoside chloride and internal standard.

Optimization of chromatographic conditions

We followed the RRLC optimisation guideline provided by Agilent Technologies to equilibrate the column and detector with 10 column volumes of the mobile phase prior to use (1-5 mL) depending on column size [6]. The approximate time to equilibrate the instrument was 20 minutes to 45 minutes or until the pressure pump reading was stabilized. The column of RRLC should be equilibrated each time before use and need to be performed when run for the new solvent of different mobile phases. The pressure pump was maintained at 147 bar during the equilibration process. The effect of varying the type and percentage of organic solvents, type and concentration of buffer solutions, flow rates, column temperatures and ultraviolet wavelengths were tested.

Optimization of extraction methods

Liquid-liquid extraction (LLE) and solid-phase extraction (SPE) methods were carried out to decide which extraction method is more suitable to be used in extracting the cyanidin-3-O-glucoside chloride from rat plasma. The method which demonstrated the best extraction results of cyanidin-3-O-glucoside chloride and internal standard would be chosen for further testing.

Liquid-liquid extraction

The LLE method was performed by referring to a study conducted by Banaszewski et al. [7]. In this method, 50 μL of working cyanidin-3-O-glucoside chloride and internal standard solutions were added to the $500 \, \mu L$ of rat plasma. The freshly prepared plasma standard was then acidified to pH 2 with CH₂O₂ because anthocyanin is more stable at low pH and then extracted with 1.5 mL of ACN. The sample was then centrifuged at 10,000 rpm for 15 minutes at a temperature of 4 °C. After that, they were re-extracted with 1.5 mL MeOH. The extracts were then pooled and the supernatants were collected. Then, the supernatants underwent an evaporation process in the pre-heated water bath at 35 °C, in vacuo using a vacuum pump. Next, they were reconstituted in 250 µL of mobile phase and centrifuged at 10,000 rpm for 30 minutes at 4 °C. Lastly, the samples were transferred to the amber vials and immediately analyzed by RRLC. We also

compared different extraction solvents to extract the anthocyanin from plasma such as diethyl ether, ethyl acetate and MTBE using the same procedure.

Solid-phase extraction

The SPE method was carried out by referring to a study conducted by Harada et al. [8]. The cartridge was firstly conditioned, by washing with 1 to 2 mL of MeOH and then equilibrated with the same volume of 0.1% TFA aqueous solution. The plasma standards were prepared by mixing 200 µL of cyanidin and internal standard working solutions of selected concentrations into 2 mL of the thawed plasma, followed by vortexing the solution for 5 seconds. Then, the plasma standard was subsequently mixed with 2 mL of 0.1% TFA aqueous solution and 100 μL of 20% sulfosalicylic acid aqueous solution. After that, it was vortex-mixed and centrifuged at 4000 x g for 20 minutes at 4 °C. The supernatant then was further treated in the conditioned and equilibrated Sep-Pak C18 cartridge. Next, the cartridge was rinsed with 2 mL of 0.1% TFA solution and subsequently purged

with air. The dried cartridge was then eluted with 2 mL of MeOH and evaporated to dryness using a vacuum pump at a temperature below 40 °C (35 - 37°C). The resultant dry residue then was dissolved in 50 μL of 0.1% TFA aqueous solution. Afterwards, it was centrifuged at 6000 rpm for 15 minutes at 10 °C using an Ultrafree®-MC centrifugal filter (Merck, Germany). Lastly, the solution was subjected to RRLC for analysis.

Results and Discussion

Spectrophotometry analysis

The UV absorbances of cyanidin-3-O-glucoside chloride and cyanidin-3,5-O-diglucoside chloride were measured using Cary 100 UV-visible spectrophotometer (Varian, California, USA). Spectrophotometry analysis of both cyanidin-3-Oglucoside chloride and cyanidin-3,5-O-diglucoside chloride showed that the maximum absorption was 524 nm, as shown in Figure 1. Thus, UV absorbance was used throughout the study.

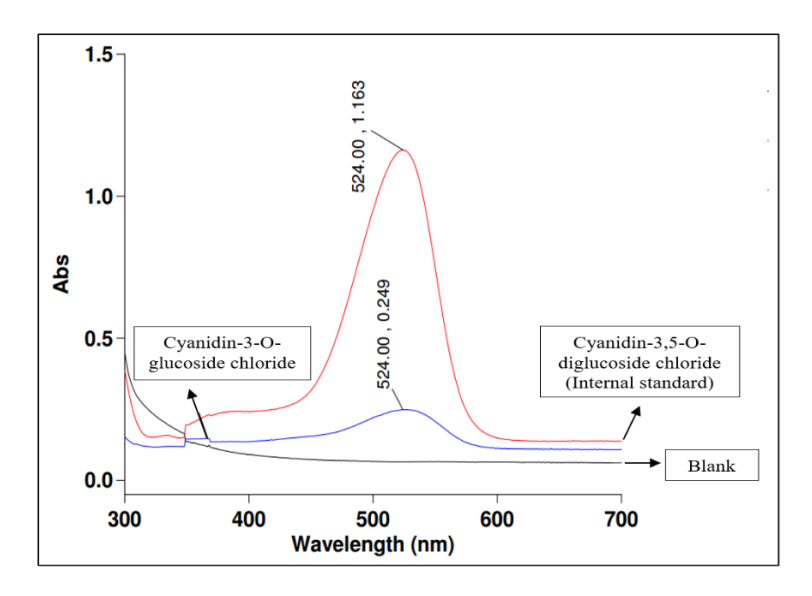


Figure 1. Spectrophotometry of the blank sample, cyanidin-3-O-glucoside chloride and cyanidin-3,5-O-diglucoside chloride (internal standard)

Absorption spectroscopy, especially UV-Vis spectroscopy, has been extensively utilized to identify anthocyanins and has revealed a lot about the structural properties and identification of these molecules [9].

From the results, the absorption peak of both cyanidin-O-glucoside chloride and the internal standard emerged at a wavelength of 524 nm. Using UV-Vis spectroscopy, absorption peaks emerged at

wavelengths of 266 nm and 530 nm, indicating that the extract contains anthocyanin compounds [10]. UV-Vis spectrophotometer demonstrated that absorption at an absorption maxima (λ_{max}) 536 nm was the specification of anthocyanins [11]. A typical UV-Vis spectrum of anthocyanin exhibits two basic absorbance clusters [9]. The first one is at 260–280 nm (UV area) and the second at 490–550 nm (VIS region) (visible region), in which the λ_{max} in the visible range is typically measured at 510–520 nm. The typical absorption bands of anthocyanins are in the 490 to 550 nm region of the visible spectra [12].

Optimization of chromatographic conditions: Type and concentration buffer solutions

Three different buffer solutions were investigated: 5% CH₂O₂ aqueous solution, 1% H₃PO₄ aqueous solution, and 0.1% TFA aqueous solution with acetonitrile (ACN) as the organic solvent. Each of the solvents was prepared with different concentrations according to the manufacturer's datasheet, as well as based on respective previous studies [8, 13]. The column temperature, mobile phase flow rate, and wavelength signal were kept constant. Among the three buffer solutions, the mobile phase of 0.1% TFA aqueous solution and ACN showed faster retention time and good peak shapes, with the least peak tailing. Thus, this combination of solvents was selected.

One of the factors that affects the retention of substances in RRLC is the mobile phase composition [14]. Buffers are usually used in mobile phases to hold and adjust the pH constant. The pH of the mobile phase is kept constant because it is always freshly prepared before RRLC analysis. The acid is used to improve the chromatographic peak shape and to provide a source of protons in reversed-phase LC/MS [15]. In this method, we also utilized isocratic elution, as it offers greater simplicity, lower cost, simpler instrumentation, and no need for column re-equilibration between consecutive injections [16].

The percentage of organic solvents

We investigated three ratios of TFA:ACN: 90%:10%, 85%:15%, and 81%:19%. The column temperature, wavelength signal, and mobile phase flow rate were

kept constant. The ratio combination was determined based on the previous literature on anthocyanins [8]. Among the three ratios tested, only the 81%:19% composition showed the presence of peaks. The chromatograms of the other two ratios did not generate any peaks, possibly due to differences in the percentage of ACN used. The higher the percentage of acetonitrile, the faster the retention time for anthocyanins. Hence, the 81%:19% TFA:CAN combination was chosen because it also exhibited a faster retention time and good peak shapes.

Optimization of type of organic solvents

The selection of proper organic solvents is also important for retaining substances in RRLC. The two organic solvents tested, ACN and MeOH, are the most commonly used solvents in RRLC. We tested ACN and MeOH in combination with a 0.1% TFA aqueous solution. The column temperature, mobile phase flow rate, wavelength signal, and percentage of organic solvent in the mobile phase were kept constant.

The results showed that using ACN as an organic solvent generated peaks in the chromatogram, while there was no peak when MeOH was used. This could be due to the elution strength of the organic solvents. ACN has a higher elution strength than MeOH [17]. Thus, at the same percentage of organic solvent in the mobile phase, which was 19% for ACN and MeOH, we observed shorter retention times for the analytes with ACN than with MeOH. ACN has a lower viscosity than MeOH [18]. Hence, with increasing column temperature, the pressure also tends to decrease as the viscosity of the solvent decreases. ACN is also often used because of its low UV cut-off wavelength, which is lower than that of MeOH (190 nm and 205 nm for ACN and MeOH, respectively) [19]. Thus, ACN was chosen for further investigation, as the chromatogram showed peaks of cyanidin-3-O-glucoside chloride and an internal standard.

Optimization of flow rates

Another chromatographic parameter that affects chromatographic separation is the flow rate. Three different mobile phase flow rates 0.5, 0.8, and 1.0 ml/min were investigated. The percentage of organic

solvent in the mobile phase, column temperature, and injection volume were kept constant. An increase in the flow rate will decrease the retention factor, thereby resulting in rapid analysis [20]. A flow rate of 0.5 mL/min was chosen, as it displayed a good retention time of about 4 min, good area counts, and good peak shape. Although the peaks at other flow rates were generated at a shorter retention time, they were not chosen, as the increase in the flow rate caused a reduction in the peak area. Increased flow rates may shorten retention time, but they may contribute to band broadening and a decrease in the column's efficiency [20].

Optimization of column temperatures

One of the important chromatographic conditions is column temperature, as it is an important variable in LC separation [21]. The column temperature was optimized at three different temperatures: 30, 35, and 40°C. The percentage of organic solvent in the mobile phase, wavelength signal, and mobile phase flow rate were kept constant. The column temperature of 30°C was chosen because it gave the best peak area ratio, as recommended by the manufacturer.

Higher column temperatures can affect column pressure due to their effect on lowering mobile phase viscosities. Thus, a desirable lower systemic pressure will be produced. This, in return, allows a lower linear

velocity for the chromatographic system and thus produces a sharper peak [22]. In this study, although column temperatures of 35 and 40°C generated shorter retention times, the column temperature of 30°C was selected because it also gave fast retention time and better peak shape without compromising the peak area. Further, a lower column temperature is preferable to sustaining the stability of cyanidin, as a higher temperature would result in a faster degradation rate of anthocyanins [23]. High temperatures could also be detrimental to the column's packing when used over a prolonged time [22].

Final chromatographic conditions

We performed the detection of cyanidin-3-O-glucoside chloride and internal standard cyanidin-3,5-O-diglucoside chloride at 525 nm with the ratio of mobile phase at 81:19 (0.1% TFA:ACN) (v/v). The mobile phase flow rate was set at 0.5 ml/min. The column temperature was set at 30°C. Using the column chromatographic conditions described above, the average retention times for cyanidin-3-O-glucoside chloride and cyanidin-3,5-O-diglucoside chloride were 4.4 min and 3.2 min, respectively, with a total run time of 10 min and a stop time of 5 min (Figure 2).

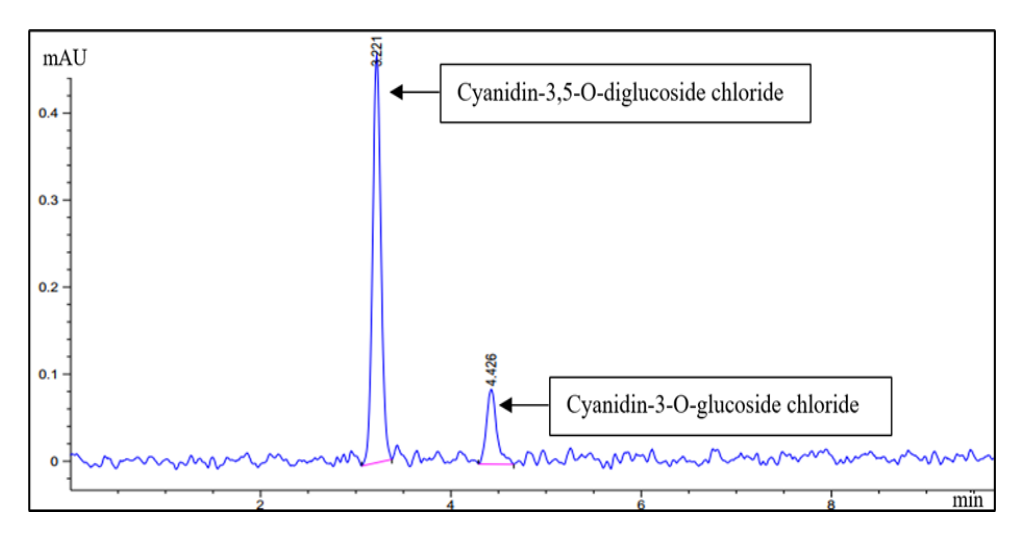


Figure 2. Chromatograms of standard solutions of cyanidin-3-O-glucoside chloride (3.221 min) and the internal standard, cyanidin-3,5-O-diglucoside chloride (4.426 min)

Optimization of liquid-liquid extraction method

The optimized chromatographic condition was applied for the analysis of plasma samples using the LLE method.

Effect of using different extracting solvents

The percentage recoveries of compounds extracted using different solvents were calculated (Table 1). The acetonitrile was chosen as the extracting solvent

because both the percentage recoveries of analyte and internal standard were higher than those of the other solvents. The internal standard was used in this test to aid in quantification of analytes (anthocyanin) and improve the accuracy and precision of the method. Internal standard is used to compare the peak area of target analytes to the peak area of internal standard to obtain the peak area ratio.

Table 1. Percentage recoveries of cyanidin-3-O-glucoside chloride and cyanidin-3,5-O-diglucoside chloride by liquid-liquid extraction method when different extracting solvents were used

Solvent	Recovery for cyanidin-3- O-glucoside chloride (%)	Recovery for cyanidin-3,5-O-diglucoside chloride (%)
Acetonitrile (ACN)	72.85	119.05
Diethyl ether (Et ₂ O)	No peak seen	No peak seen
Ethyl acetate (EtAc)	66.72	38.85
Methyl tert-butyl ether (MTBE)	110.46	44.85

Optimization of solid-phase extraction method

The optimized chromatographic conditions were also applied for the analysis of the plasma samples using SPE.

Selection of final extraction method

The chromatograms of cyanidin-3-O-glucoside chloride for both the LLE and SPE methods were analyzed at concentrations of 500 ng/mL and 1000 ng/mL respectively. The recovery percentage of cyanidin-3-O-glucoside chloride from LLE was slightly better than that of SPE (72.85% and 68.36%, respectively). However, the chromatogram generated from the SPE method demonstrated better peak shapes for cyanidin-3-O-glucoside chloride and the internal standard compared to the chromatogram of the LLE method. In addition, the chromatogram of the SPE method showed less peak tailing compared to the LLE method. The chromatogram of the SPE method also exhibited similar retention times for cyanidin-Oglucoside chloride and internal standard prior to extraction. Hence, we chose SPE as the final extraction method, as it yielded more favorable results than LLE

in the extraction cyanidin-O-glucoside chloride in rat plasma based on the results of RRLC analysis (Figure 3).

Extraction is a critical step in sample preparation, as the presence of endogenous impurities in biological fluids might cause interference in anthocyanin analysis. SPE and LLE are among the extraction methods used for anthocyanins, with increasing selectivity or specificity and improved recoveries and reproducibility [24]. In this experiment, we performed both methods to determine the most suitable extraction method for cyanidin-3-O-glucoside chloride.

LLE offers an advantage as an extraction method, in that the technique is relatively cheaper than SPE. However, this method requires costly and hazardous organic solvents, which are undesirable for health and disposal reasons [25]. LLE also requires a lengthy analysis period, which can give rise to the possible degradation of anthocyanins. By contrast, SPE techniques can overcome many of the problems associated with LLE, such as incomplete phase

separations, less-than-quantitative recoveries, and the use and disposal of large and expensive quantities of organic solvents [25]. The only drawback of the SPE compared to the LLE technique is that the cost of the equipment required for SPE is higher than for LLE. Another advantage of SPE is that this technique can be used not only in preparing liquid samples and extracting semi-volatile or non-volatile analytes but also for solids that are pre-extracted into solvents [25].

From our results, although the percentage recoveries of anthocyanin from the LLE method were slightly better than those from the SPE method, we also considered other factors. The chromatographic peak shapes obtained with the SPE method were better than those obtained with LLE. An optimum chromatographic peak shape is important to ensure more accurate quantitation

of analytes. Abnormal peak shapes, such as peak tailing, generate imprecise results. The chromatograms of SPE displayed lesser peak tailing than those of LLE. Peak tailing is one of the common chromatographic peak shape distortions [26], which can occur for several reasons, including the purity of the packing material, a quality that can influence the peak shape [27]. Contaminants in the material can enhance secondary interactions, which lead to peak tailing. Thus, using an extraction method that employs a sample cleanup procedure will offer better results [26]. Here, the SPE method involved a filtration step that used an Ultrafree-MC 0.45 µm filter unit before RRLC analysis. Therefore, given its chromatogram results and advantages compared to LLE, the SPE method was adopted as the extraction method in this study.

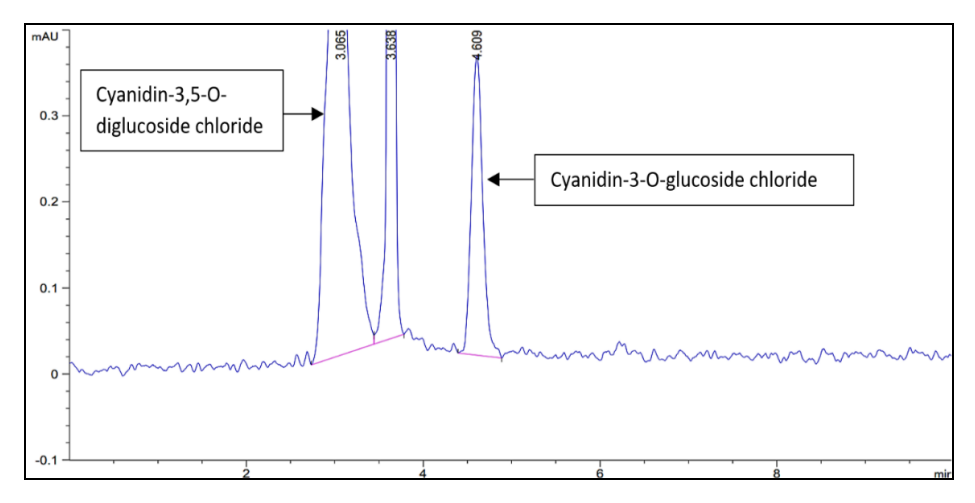


Figure 3. Chromatogram of cyanidin-3-O-glucoside chloride (4.609 min) and internal standard, cyanidin-3,5-O-diglucoside chloride (3.065 min) at concentration 1000 ng/mL following SPE method

Conclusion

We successfully determined cyanidin-3-O-glucoside chloride in rat plasma using RRLC analysis. The spectrophotometry analysis showed that the maximal absorbance of the compound was in the absorption range reported in the previous literature. The optimization of chromatographic conditions demonstrated that the mobile phase composition of 0.1% TFA aqueous solution and ACN in the ratio of 81:19%, respectively, with a flow rate of 0.5 ml/min, at

30°C column temperature and detection wavelength of 525 nm, were suitable for RRLC analysis of cyanidin-3-O-glucoside chloride. SPE was selected as the final extraction method for cyanidin-3-O-glucoside chloride and its internal standard.

Acknowledgement

The research was financially supported by the Ministry of Agriculture's Herbal Research Grant

Scheme (HRGS) (project: NH1015S020; 304.PPSK.6150169.K123).

References

- 1. Wallace, T. C. and Giusti, M. M. (2015). Anthocyanins. *Advances in Nutrition*, 6(5): 619-622.
- 2. Passeri, V., Koes, R. and Quattrocchio, F. (2016). New challenges for the design of high value plant products: stabilization of anthocyanins in plant vacuoles. *Front Plant Science*, 7: 1-9.
- 3. Riaz, G. and Chopra, R. (2018). A review on phytochemistry and therapeutic uses of *Hibiscus sabdariffa L. Biomedicine & Pharmacotherapy*, 102: 575-586.
- 4. Rubinskiene, M., Jasutiene, I., Venskutonis, P. R. and Viskelis, P. (2005). HPLC determination of the composition and stability of blackcurrant anthocyanins. *Journal of Chromatographic Science*, 43(9): 478-482.
- Hapsari, B. W., Manikharda and Setyaningsih, W. (2021). Methodologies in the analysis of phenolic compounds in roselle (*Hibiscus sabdariffa L.*): Composition, biological activity, and beneficial effects on human health. *Horticulturae*, 7(2): 1-36.
- Angelika, G.-H., Frank, M., & Gotenfels, C. (2009). Agilent 1200 series rapid resolution LC and rapid resolution LC/MS optimization guide. Access from https://www.agilent.com/cs/library/usermanuals/public/1200SeriesRRLC-Optimize Guide_ebook.pdf. [Access online 11 July 2021].
- Banaszewski, K., Park, E., Edirisinghe, I., Cappozzo, J. C. and Burton-Freeman, B. M. (2013). A pilot study to investigate bioavailability of strawberry anthocyanins and characterize postprandial plasma polyphenols absorption patterns by Q-TOF LC/MS in humans. *Journal of Berry Research*, 3(2): 113-126.
- 8. Harada, K., Kano, M., Takayanagi, T., Yamakawa, O. and Ishikawa, F. (2004). Absorption of acylated anthocyanins in rats and humans after ingesting an extract of *Ipomoea batatas* purple sweet potato tuber. *Bioscience*, *Biotechnology and Biochemistry*, 68(7): 1500-1507.
- 9. Saha, S., Singh, J., Paul, A., Sarkar, R., Khan, Z. and Banerjee, K. (2021). Anthocyanin profiling

- using UV-Vis spectroscopy and liquid chromatography mass spectrometry. *Journal of AOAC International*, 103 (1): 23-39.
- Dwilistiani, D., Darwis, D. and Santoni, A. (2015). Characterization of cyanidin 3-(6-acetylglucoside)-5-(3"-coumaryl-6"- malonylglucoside) compound from cinnamon bud leaves (*Cinnamomum burmanni* (Ness & T. Ness) Blume) by HPLC-DAD-ESI-MS. *Journal of Chemical and Pharmaceutical Research*, 7 (47): 519-523.
- Nuryanti, S., Matsjeh, S., Anwar, C. and Raharjo, T. J. (2012). Isolation anthocyanin from roselle petals (*Hibiscus sabdariffa L*) and the effect of light on the stability. *Indonesian Journal of Chemistry*, 12(2): 167-171.
- 12. Prior, R. L. and Wu, X. (2012). Analysis methods of anthocyanins. In Z. Xu & L. R. Howard (Eds.), *Analysis of Antioxidant-Rich Phytochemicals*, John Wiley & Sons, New Jersey: pp. 149-180.
- 13. Durst, R. W. and Wrolstad, R. E. (2005). Separation and characterization of anthocyanins by HPLC. In *Current Protocols in Food Analytical Chemistry*, John Wiley & Sons, New Jersey: pp. 33-45.
- Deineka, V. I., Deineka, L. A. and Saenko, I. I. (2015). Regularities of anthocyanins retention in RP HPLC for "water-acetonitrile-phosphoric acid" mobile phases. *Journal of Analytical Methods in Chemistry*, 2015 (2015): 1-6.
- 15. Guzzetta, A. (2001). Reverse phase HPLC basics for LC/MS. Access from http://www.ionsource.com/tutorial/chromatography/rphplc.htm. [Access online 18 July 2021].
- 16. Ukić, Š., Rogošić, M., Novak, M., Šimović, E., Tišler, V. and Bolanča, T. (2013). Optimization of IC separation based on isocratic-to-gradient retention modeling in combination with sequential searching or evolutionary algorithm. *Journal of Analytical Methods in Chemistry*, 2013 (1): 1-11.
- 17. Gilar, M., Jaworski, A. and McDonald, T. S. (2014). Solvent selectivity and strength in reversed-phase liquid chromatography separation of peptides. *Journal of Chromatography A*, 1337(1): 140-146.

Nadiratul Asyikin et al: DEVELOPMENT AND OPTIMIZATION OF A RAPID RESOLUTION LIQUID CHROMATOGRAPHY METHOD FOR CYANIDIN-3-O-GLUCOSIDE IN RAT PLASMA

- 18. Chua, Y. A., Abdullah, W. Z., Yusof, Z. and Gan, S. H. (2019). Validation of HPLC and liquid-liquid extraction methods for warfarin detection in human plasma and its application to a pharmacokinetics study. *ASM Science Journal*, 12(2019): 1-10.
- 19. Yabré, M., Ferey, L., Somé, I. T. and Gaudin, K. (2018). Greening reversed-phase liquid chromatography methods using alternative solvents for pharmaceutical analysis. *Molecules:* A Journal of Synthetic Chemistry and Natural Product Chemistry, 23(5): 1065-1089.
- Afsah-Hejri, L., Jinap, S., Arzandeh, S. and Mirhosseini, H. (2011). Optimization of HPLC conditions for quantitative analysis of aflatoxins in contaminated peanut. *Food Control*, 22(3–4): 381-388
- 21. Dolan, J. W. (2002). The importance of temperature. *LC GC Europe*, 20(6): 524-530.
- 22. Chua, Y. A., Abdullah, W. Z. and Gan, S. H. (2012). Development of a high-performance liquid chromatography method for warfarin detection in human plasma. *Turkish Journal of Medical Sciences*, 42 (5): 930-941.
- Liu, Y., Liu, Y., Tao, C., Liu, M., Pan, Y. and Lv, Z. (2018). Effect of temperature and pH on stability of anthocyanin obtained from blueberry. Journal of Food Measurement and Characterization, 12(3): 1744-1753.

- 24. Martín, J., Navas, M. J., Jiménez-Moreno, A. M. and Asuero, A. G. (2017). Anthocyanin pigments: Importance, sample preparation and extraction. In M. Soto-Hernandez, M. Palma-Tenango and M. R. Garcia-Mateos (Eds.), *Phenolic Compounds Natural Sources, Importance and Applications*, Intech Open, London: pp. 117-152.
- Garcia-Salas, P., Morales-Soto, A., Segura-Carretero, A. and Fernández-Gutiérrez, A. (2010).
 Phenolic-Compound-extraction systems for fruit and vegetable samples. *Molecules*, 15(12): 8813-8826.
- Crawford Scientific. (2017). Peak tailing in HPLC. Access from https://www.crawfordscientific.com/ chromatography-blog/post/peak-tailing-in-hplc. [Access online 19 July 2021].
- 27. Denoulet, B. (2020). The perfect peak shape: Five solutions to peak tailing problems. Access from https://www.barts-blog.net/the-perfect-peak-shape-five-solutions-to-peak-tailing-problems/.[Access online 19 July 2021].

Malaysian Journal of Analytical Sciences (MJAS)





CHEMICAL CHARACTERISATION OF BIOCHAR FROM OIL PALM FROND FOR PALM OIL MILL SECONDARY EFFLUENT TREATMENT

Analisis Sifat Kimia Biochar Daripada Pelepah Kelapa Sawit Untuk Rawatan Air Sisa Sekunder Kilang Pemprosesan Kelapa Sawit

Nadia Razali and Nurhanim Zulaikha Kamarulzaman*

Section of Environmental and Polymer Engineering Technology, Malaysian Institute of Chemical and Bioengineering Technology (MICET, Universiti Kuala Limpur, 78000 Alor Gajah, Melaka, Malaysia

*Corresponding author: nurhanim.kamarulzaman@s.unikl.edu.my

Received: 15 September 2021; Accepted: 3 February 2022; Published: 28 April 2022

Abstract

The oil palm frond (OPF) biomass contains chemical characteristics, which makes it a potential alternative adsorbent in wastewater treatment applications. In this study, the OPF sample was produced as biochar by using a top-lit updraft (TLUD) gasifier. The maximum temperature of this process was 750°C and it yielded 20% w/w of biochar. The Brunauer–Emmett–Teller (BET) surface area for the OPF biochar was 248.08 m²/g with an average pore size of 4.3 nm and categorised as mesoporous adsorbent. The OPF biochar had a high carbon content of more than 70%, which was desirable for the alternative adsorbent. It was discovered that the aromatic ring and aliphatic functional group was detected in the biochar based on the Fourier Transform Infrared (FTIR) analysis which was commonly found in biochar produced at temperatures above 500°C. Based on the result obtained from the adsorption test, the OPT biochar could provide a maximum removal of 64.65% of COD, with an initial COD of 3960 mg/L. This study has found that the OPF biochar is suitable to be used as an alternative adsorbent for wastewater applications.

Keywords: biochar, oil palm frond, adsorption, palm oil mill effluent

Abstrak

Pelepah kelapa sawit (OPF) mempunyai sifat kimia yang berpotensi sebagai bahan penjerap alternatif dalam aplikasi rawatan air sisa. Dalam kajian ini, sampel OPF digunakan sebagai bahan mentah untuk menghasilkan biochar dengan menggunakan *gasifier top-lit updraft* (TLUD). Suhu maksimum process ini adalah 750°C dan 20% w/w biochar telah dihasilkan. Luas permukaan Brunauer–Emmett–Teller (BET) untuk biochar OPF adalah 248.08 m²/g dengan ukuran purata saiz pori 4.3 nm dan diketagorikan sebagai penjerap mesoporos. Biochar OPF mempunyai kandungan karbon yang tinggi melebihi daripada 70%, yang merupakan ciri-ciri yang dikehendaki untuk penjerap alternatif. Berdasarkan analisis spektroskopi inframerah transformasi Fourier (FTIR), kumpulan organik alifatik dan cincin aromatik dikesan didalam bahan ini. Kumpulan organik ini biasanya ditemui dalam biochar yang dihasilkan pada suhu melebihi 500°C. Berdasarkan hasil kajian yang diperolehi daripada ujian penjerapan, biochar OPT mampu memberikan menyingkirkan 64.65% COD daripada air sisa kilang kelapa sawit yang mempunyai COD awal sebanyak 3650 mg/L. Kajian ini mendapati bahawa biochar OPF wajar digunakan sebagai penjerap altenatif untuk rawatan sisa pepejal.

Kata kunci: biochar, pelepah kelapa sawit, penjerapan, sisa efluen kilang kelapa sawit

Introduction

Crude palm oil (CPO), palm kernel oil (PKO), and palm kernel cake (PKC) are the primary interests in palm oil industry. In 2020, there were 5.87 million hectares of palm oil plantations in Malaysia. The production of crude palm oil (CPO) in the same year was 19.14 million tonnes [1]. A total of 80 million tonnes of biomass are generated annually in Malaysia, with the majority from the palm oil industry [2, 3]. Biomass generated by the palm oil industry are mainly produced from the harvesting of fresh fruit bunch (FFB) at the plantation, and the processing of FFB in mills. These biomasses include mesocarp fibre (MF), empty fruit bunch (EFB), palm shell (PS), oil palm fronds (OPF), oil palm leaflet (OPL), oil palm trunk (OPT), and palm mill effluent (POME). The presence of wastes creates a disposal problem, which requires the implementation of a robust management strategy.

POME is one of the wastes generated from the palm oil industry. POME is brownish wastewater generated from the processing of FFB; it has a high amount of organic contaminants and requires proper treatment before it can be discharged into any water body. Anaerobic and aerobic digestion treatments are the common treatments used to remove the organic contaminants in the wastewater, but both treatments are not sufficient to comply with the standard set by the Department of Environment (DOE) Malaysia, as shown in Table 1 [4]. The final discharge of POME from the biological treatment or palm oil secondary effluent (POMSE) usually remains high in chemical oxygen demand (COD) and biochemical oxygen demand (BOD), with an average of 800 mg/L and 200 mg/L respectively. Furthermore, it is also dark in colour, which is higher than the standard set by the DOE [5]. This is due to the presence of lignin, carotene, humic acids and other organic compounds that are recalcitrant to biological treatments [6]. Another treatment that should be implemented to polish the biologically treated POME, ensuring that it complies with environmental legislation, is the

adsorption technique, a technology that can be applied to biologically treat POME as a polishing method. The key benefits of this technology are that it is easy to design, and it has a minimal initial investment. Natural resources such as biomass, silica, and zeolite can be used to make the adsorbent [7, 8].

Table 1. Environmental Quality (Industrial Effluent)
Regulation 2009

Parameter	Unit	Standard		
		A	В	
COD	mg/L	80	200	
BOD ₅	mg/L	20	50	
Colour	ADMI	100	200	
TSS	mg/L	50	100	

The biomass from this industry has the potentials to be converted into valuable products. The potentials include using OPT as building materials, OPF as the precursor for ethanol production, OPS as an aggregate in lightweight cement, MF as a growing media for tissue culture, POME as a substrate for methane generation, and OPL and EFB as mulch in plantation [3, 9]. Some biomass, such as PKS and EFB, have critical functions as fuel sources for mills and to maintain soil conditions [10, 11]. However, there is still a significant amount of biomass that are unutilised, and measures should be taken to improve its functionalities. In recent years, there is an increasing amount of literature on the conversion of palm oil biomass into biochar. Biochar is a carbon-rich material produced from the thermochemical process. The pyrolysis process is the common thermochemical process utilised to produce biochar. However, scarce attention has been paid to gasification as a thermochemical process to produce biochar.

Gasification is defined as a thermochemical process to convert carbonaceous feedstock into syngas (a mixture of hydrogen, carbon dioxide, and methane), tar, and biochar at high temperatures (≥ 500°C) in oxygendeficit conditions [12, 13]. So far, this method has only been applied for the generation of energy [14]. Most of the literature on the gasification process only focus on the optimisation of process parameters and the quality of gas produced from this process [15, 16]. The solid product of gasification, i.e., biochar, receives less attention. In general, biochar is known as an effective carbon sequestration strategy due to its recalcitrant properties. Therefore, biochar produced from the gasification process might have the same potentials as biochar produced from other thermochemical processes, i.e., fast pyrolysis, and hydrothermal process. The characteristics of biochar are dependent on the properties of biomass, the conditions of the process, and the type of reactor used for the thermochemical process.

Most literature on biochar are more focused on carbon sequestration and soil conditioner. The potential of biochar is not only limited to carbon sequestration and soil application, but it also has the potential to be used in other applications especially in water application. However, there are limited studies done on the application of biochar in water and wastewater treatment. In a study on the application of biochar as an alternative adsorbent, Huggins et al. [17] found that biochar from the gasification process could reduce phosphate, COD, and nitrogen ammonia in brewery wastewater. Kearn et al. [18] proved that biochar produced from the gasification process could remove trace organic contaminants from drinking water. Similarly, Kaetzl et al. [19] found that biochar was found to reduce both organic and inorganic contaminants from a municipal wastewater. Overall, many studies highlighted that biochar was effective in eliminating organic and inorganic pollutants from water and wastewater [16-23] This could be due to the high porosity of biochar or the presence of other chemical species that aids the adsorption process [12, 25].

The utilisation of biochar produced from the gasification process in wastewater application is an interesting topic to be studied. This paper will focus on biochar produced from gasification by using top-lit

updraft (TLUD) gasifier and oil palm frond (OPF), which were used as the raw materials in this study. The characteristics of the biochar and its performance to treat biologically treated POME will be evaluated.

Materials and Methods Source and preparation of biomass

The raw material used in this study was oil palm frond (OPF). The OPF was obtained from a local plantation located in Tampin, Negeri Sembilan. Figure 1 shows the structure of OPF. The structure of the OPF consists of the top section, middle section, and basal. Only the basal part of the frond was used in this study as it was easier for real-life application. The OPF was chopped using a mechanical chopper with the particle size ranging from 1–4 mm and rinsed with tap water to remove any impurities. The OPF was then dried in a vacuum oven for 24 hours to avoid rotting.

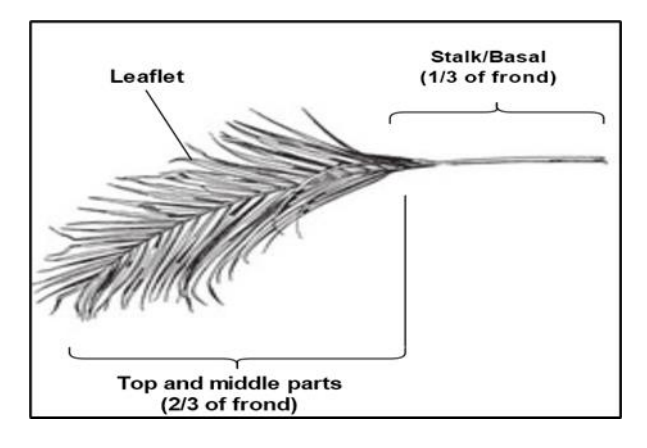


Figure 1. Structure of OPF

Gasification of oil palm frond

The top-lit updraft gasifier (TLUD) was used to produce OPF biochar, as illustrated in Figure 2. Before the gasification process, the raw OPF was sieved to ensure that the particle of the OPF was uniformed. The uniformity of the size of feedstock was vital to ensure that the feedstock was fully charred, and to achieve a good airflow through the reactor body. The dried OPF was weighed before it was filled into the gasifier. The dried OPF was then placed into the gasifier about ¾ of the reactor body (approximately 600 g of dried OPF). A small piece of paper or wood was used as rekindling. The kindling was lighted, and it would burn strongly.

The fan of the gasifier was turned on to provide air to assist the gasification process. The temperature of the process was monitored for quality control and assurance. The dried OPF was burnt from top to bottom until a bluish flame was formed. The blue flame was an indicator that the OPF was fully gasifier. The fan was then turned off and the gasifier was allowed to cool. The OPF biochar was then sprayed with some water to remove any ash and fine. The biochar was cooled until it was cool enough for handling.

The OPF biochar produced was weighted and the percentage of yield of the biochar was calculated using Equation 1.

$$\text{\%Yield} = \frac{W_1 - W_2}{W_1} \times 100$$
 (1)

where W_1 is a weight of biomass and W_2 is a weight of biochar.

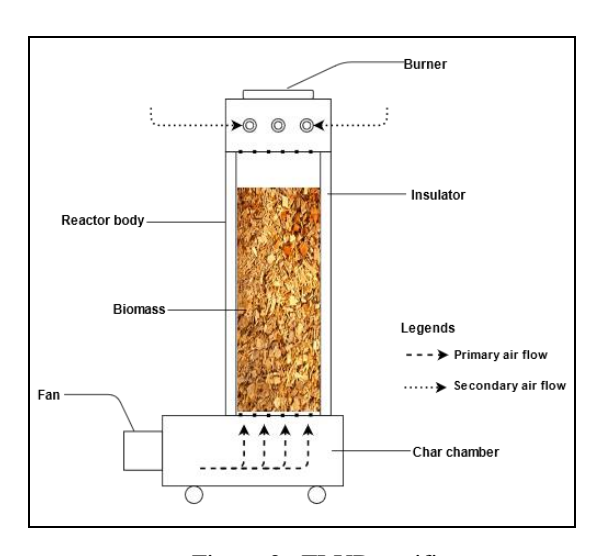


Figure 2. TLUD gasifier

Characterisation of OPF pH of biochar

pH is an indicator of the acidity and basicity of the biochar. The pH of biochar can be a good indicator to understand the oxygen complexes and functional groups on the surface of biochar. The OPF biochar was soaked in the deionised water (ratio of 1:25% wt./v solid to water ratio) for one hour with agitation [26].

The pH of the slurry was then tested with a pH meter (Mettler Toledo).

Proximate analysis and ultimate analysis of raw material and biochar

There were three components of proximate analysis which were moisture content, ash content, and volatile matter. The proximate analysis of raw OPF was done using National Renewable Energy Laboratory (NREL) method for all three analyses. On the other hand, the proximate analysis of biochar was done using the ASTM method (ASTM D2867-09, ASTM D5832-98, and ASTM D2866-04).

The ultimate analysis of both raw OPF and OPF biochar was carried out using a CHNS analyser. This analysis was done to quantify the content of carbon, hydrogen, nitrogen, and sulphur in both samples. All four elements were analysed simultaneously.

Scanning electron microscopy analysis and Brunauer–Emmett–Teller surface area analysis

Scanning electron microscopy (SEM) analysis of raw OPF and OPF biochar was carried out using Scanning Electron Microscope SEM (FEI Quanta 450). BET analysis was used to determine the surface area of biochar in this study. The BET analysis was conducted using a BET Surface analyser (Micromeritic) with N_2 gas adsorption at 77 K in relative pressure from 0.05 to 0.2. The samples were degassed for 2 hours at 200 °C.

Fourier transform infrared analysis

FTIR analysis was done to determine the functional groups of the biochar. This analysis is vital to gain an understanding of the chemical characteristic of biochar and the adsorption mechanism of biochar. Before conducting the FTIR analysis, the OPF biochar was ground into powder and dried in an oven overnight to remove any residual moisture in the biochar. The sample was then mixed with potassium bromide (KBr) with a ratio of 1:2000 (1 part sample: 2000-part KBr). The mixture was then pressed into a pellet form by using a hydraulic presser. The pellet was finally analysed using the FTIR analyser (Nicolet 5700, FTIR, Thermo Fisher Scientific, and Waltham, MA, USA).

Adsorption test

The batch adsorption test was conducted to determine the applicability of OPF biochar as an adsorbent for wastewater treatment. The adsorbate used in this study was palm oil mill secondary effluent (POMSE). POMSE is the effluent generated after the biological treatment of POME. It is high in chemical oxygen demand. (COD). Method No.8006 was used to measure the COD of POMSE before and after treatment. The measurement of COD was conducted using the APHA potassium dichromate method. The measurement was carried out in HACH COD high range vials by using DR900 spectrophotometer and HACH COD reactor (Model: 45600).

Next, the batch adsorption test was conducted using 100 ml of POMSE. The OPF biochar was added to the conical flask containing 100 ml of POMSE. The mixture of the OPF biochar and POMSE was then shaken for 24 hours at 150 rpm using an incubator shaker. The samples were withdrawn at a fixed time interval. The adsorbent was separated from samples by filtration. The filtrates were then analysed for COD. The number of COD adsorbed per unit mass of the adsorbent (qe) was calculated according to the following Equation 2 and the adsorption yield was calculated by using Equation 3.

$$q_e = (C_0 - C) \times \frac{V}{m}$$
 (2)

%COD removal =
$$\frac{c_0 - c}{c_0} \times 100$$
 (3)

where, q_e is the number of COD adsorbed per gram of adsorbent (mg/g); C_0 and C are the initial and final COD concentrations (mg/L), respectively; V is the volume of POMSE (L); and m is the mass of biochar (g).

Results and Discussion

Gasification of OPF

The main products of the gasification process usually consist of syngas, bio-oil, and biochar. The quantity biochar product derived from the gasification process is usually lower compared to other types of thermochemical processes such as pyrolysis, hydrothermal and torrefaction. For this study, the yield

of OPF biochar was 20%. The same yield of biochar was obtained by Nsamba et al.[26] using the same gasification system. The biochar obtained from the gasification process is usually lower than other thermochemical processes i.e., fast pyrolysis because of the partial oxidation of carbon into carbon monoxide and other flue gasses [27, 28]. Other than partial oxidation of carbon in the biomass, the release of volatile matter from the polymeric backbone of carbonaceous feedstock also contributed to the yield of the biochar. Apart from that, the temperature of the gasification that is usually ≥ 500 °C is good to produce high porosity biochar [29, 30]. In this study, the range of maximum temperature of the gasification process for OPF biochar was 750 °C by controlling the speed of the fan that improved the air supply. Studies on the effect of temperature on the properties of biochar in past studies found that the surface area of the biochar increased as the temperature thermochemical increased [31, 32]. Increasing the surface area of the biochar contributed to better performance of biochar as an adsorbent as it can remove more pollutants from wastewater. This trend can be seen in earlier studies using orange peel biochar for removal of cadmium from aqueous solution; maximum removal of cadmium was obtained when the orange peel biochar was produced at a temperature of 700 °C, which was then used as an adsorbent [33]. Other studies showed a similar trend in the removal of chromium from aqueous solution [34, 35]. These findings suggest that gasification biochar has the potential to be used as an adsorbent.

Characterisation of OPF biochar pH of biochar

The pH for OPF biochar in this study is alkaline (pH=8) which is similar to the literature where most biochar is best produced at temperatures higher than 400 °C [29, 30, 36, 37]. The alkaline pH of OPT biochar is correlated to the presence of basic functional groups on the surface of biochar, as shown in Figure 4. Generally, raw biomass has a high number of acidic functional groups. Figure 4 illustrates the presence of acidic functional group in the raw OPF that corresponded to the carboxylic acid functional group. However, the band of the functional group diminished

after the gasification process. The reduction of the acidic functional groups was aligned to the reduction of volatile matter of biomass as the temperature of the process increased.

Apart from the reduction of acidic functional groups, the alkalinity of OPF biochar was contributed by the formation of the aromatic and aliphatic functional group. The peak of the functional groups can be seen at the band of 1200–1600 cm⁻¹. The same findings can be seen in a study conducted by Usman et al. [38] on the production of biochar from the date palm waste. Other studies had established that the pH of biochar increased when the temperature of thermochemical increased [38-40]. The presence of alkaline metal contributed to the alkalinity of biochar [12, 42].

Proximate analysis and ultimate analysis

Table 2 shows the proximate analysis and ultimate analysis for both raw material and biochar. Generally, the value of each component changed after the gasification process. Table 2 shows that the volatile matter decreased sharply from 86.49% in raw OPF to 15.57%. This was due to the conversion of volatile matter into more condensed aromatic structures and/or may burn out which might help in the development of the porous structure of biochar [43]. The raw OPF had high volatile matter (86.49%), which was a good indicator that the biomass is suitable to be used as a feedstock for the thermochemical process. The percentage of volatile matter obtained in this study is closed to those obtained from other studies [11, 31, 11, 31].

Ash content is a vital indicator to determine the suitability of the biomass as feedstock for the thermochemical process. The ash content of the raw OPF in this study is 0.92%, which aligned with previous studies [11, 31, 44]. The ash content of the biochar is higher than the raw OPF due to the accumulation of inorganic material in the biomass after the volatilisation of carbon, oxygen, and hydrogen [45]. The fixed carbon content is significantly increased from 12.59% in raw OPF to 68.34% in OPF biochar. The ash content of OPF biochar is 13 times greater than raw OPF; similar trend can be observed in other studies [28, 36, 38, 46].

Table 2 provides the Carbon (C), Hydrogen (H), Nitrogen (N), Sulphur (S) and Oxygen (O) content of both raw OPF and OPF biochar. The C and N content of the OPF biochar was significantly higher compared to its original biomass. On the other hand, the O and H content of the biochar is lower than its original biomass. This may be due to the breakdown of carbon and functional groups of the biomass during the gasification which led to the formation of aromatic functional groups [47]. The O/C and H/C ratio of the biochar is found to be lower than the biomass, which indicated the formation of aromatic functional and reduction of hydrophilicity of the biochar [47], [48].

Table 2. Proximate analysis and ultimate analysis

Proximate Analysis (%w/w)	Raw OPF	OPF Biochar		
Moisture content	9.95	3.71		
Ash content	0.92	12.38		
Volatile matter	86.49	15.57		
Fixed carbon	12.59	68.34		
Ultimate analysis (%w/w)				
Carbon (C)	41.87	76.97		

TE 11 0	1	D .		1 1.1	1 .
Table 3 (conf d)	Provimate	analyete a	and ultimate	analyete
Table 5 (com u,	. I IOAIIIIaic	anary sis a	ma unimaic	anarysis

Proximate Analysis (%w/w)	Raw OPF	OPF Biochar
Hydrogen (H)	6.00	2.50
Nitrogen (N)	0.33	0.76
Sulphur (S)	0.70	0.39
Oxygen (O)	51.10	19.38
O/C ratio	0.92	0.19
H/C ratio	1.72	0.39
pH	-	8
Porous characteristics		
BET surface area, m ² /g	-	248.08
Pore Volume, cm ² /g	-	0.23
Average pore size, nm	-	4.3

Scanning electron microscopy analysis and Brunauer–Emmett–Teller surface area analysis

SEM analysis was performed to analyse the morphology of raw biomass and biochar. Figure 3 shows the morphology of raw material and biochar. Figure 3 demonstrates a significant change in the surface of OPF and OPL before and after the gasification process. In Figure 3 (a), the surface of OPF is very rough and less pore is visible whereas in Figure 3 (b) the surface of the OPF biochar is smoother than raw OPF. More pores were visible for OPF biochar. The formation of pores in the biochar are caused by the release of volatile matter, decomposition of cellulose and hemicellulose, which resulted in the complex structure of biochar with multiple diameters of pore [47, 49].

BET and BJH analysis were done on the OPF biochar to analyse its surface area and characteristics of pores. Table 2 provides the BET surface area, pore volume and average pore size of OPF biochar. The BET surface area of OPT biochar was 248.08 m²/g with an average pore size of 4.3 nm. The OPF biochar can be classified in the mesopore category as the average pore size of OPF biochar fell within the range of 2–50 nm. When compared to other studies, the surface area and pore volume of OPF biochar found to be higher than other studies which, on average pores, are lower than

150 m²/g [44, 50, 51]. Compared to commercial activated carbon (AC), the AC has a larger surface area and smaller average pore size which leads to high affinity to low molecular weight compound but is less efficient in the removal of high molecular weight compound. The high molecular weight compounds are commonly present in wastewater after biological treatments as refractory pollutants. A study conducted by An et al. [52] proved that a mesoporous lignite adsorbent was effective in removing refractory pollutants from biologically treated coal gasification wastewater. The result of this study is aligned to the findings from other studies using the same type of wastewater, similar to the research by Gai et al. [53] and Xu et al. [54]. The OPF biochar appears to have the potential to be used as alternative adsorbent to improve the characteristics of biologically treated wastewater.

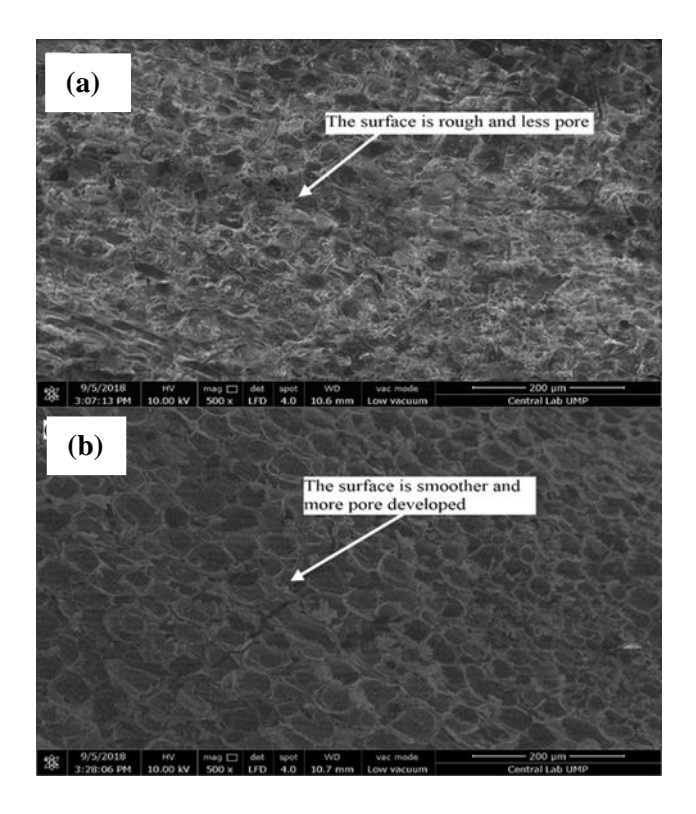


Figure 3. (a) raw OPF (b) OPF biochar

Fourier transform infrared analysis

FTIR analysis was done to determine the functional group of the biochar's. Figure 4 compares the FTIR spectra of both raw materials and biochar produced in the gasification process. Overall, the spectra between raw OPF and OPF biochar is different. In Figure 4, the peak between 3200-3600 cm⁻¹ corresponded to the – OH group with stretch vibration and carboxylic acid functional group. The presence of broad –OH in the raw OPF which attributed to the moisture content and hydroxyl functional group found in lignin, hemicellulose, and cellulose [54], [55]. The intensity of the peak decreased after the gasification process. The reduction of the intensity of the peak indicated that the removal of moisture and volatile matter contributed to the porous structure of the biochar [39], [56].

There is a peak within the band of 2800-3000 cm⁻¹ which corresponded to the saturated aliphatic C–H functional group. This functional group is associated with the methylene functional group in cellulose [54, 56]. The peak within the band of 1700-1800 cm⁻¹ represents the C=O acetyl group associated with the ester functional group in hemicellulose [55, 57]. This band diminished after the gasification process due to the integration of cellulose and hemicellulose. There are some peaks within the band of 1600-1700 cm⁻¹ in both biomass and biochar. These bands correlated with the carboxylic acid functional group. However, the peaks diminished after the gasification process is aligned with the alkaline pH of the biochar.

The intensity of the peak within the band of 1500-1600 cm⁻¹ is abated. The peaks within this band correlated to the aromatic hydrocarbon functional group of lignin

C-C stretching vibration in the aromatic ring [55, 56]. The peaks within the band of 1000-1500 cm⁻¹ corresponded to the aliphatic and aromatic functional groups. The intensity of the peaks was reduced in the OPF biochar. This might be due to the partial decomposition of lignin in the raw biomass. The presence of aromatic aliphatic functional groups in the biochar will provide the active sites to assist the adsorption process and contributes to the hydrophobicity of the biochar. This can be seen in the study conducted by Liu et al. [57] on the role of

functional groups in the adsorption of bisphenol A (BPA) on activated carbon. The study revealed that the modified AC provided 10% higher removal of BPA compared to commercial AC. This was due to the decrease of acidic functional groups in the modified AC and stronger hydrophobicity than commercial AC which leads to better BPA adsorption and more water molecule exchange, which aligns with the findings by Sidik et al. [58] on the OPL adsorbent with enhanced hydrophobicity.

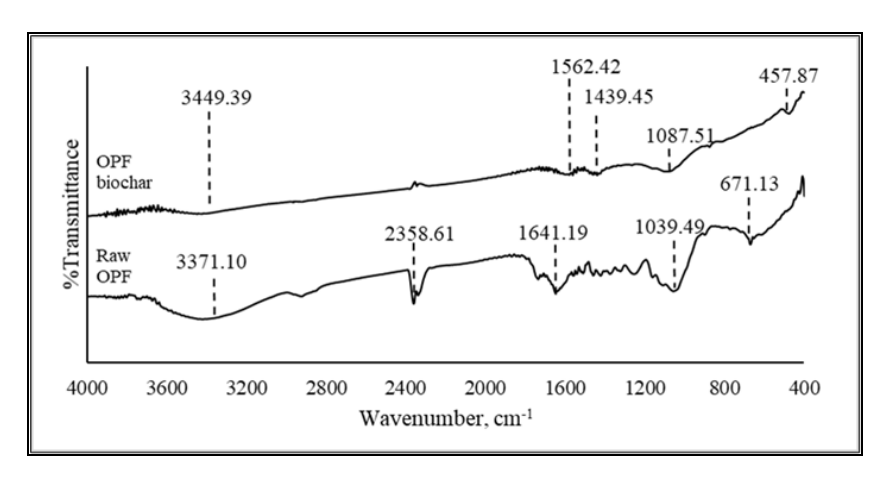


Figure 4. FTIR spectra of raw OPF and OPF biochar

Adsorption test

The wastewater used in this study was palm oil secondary effluent (POMSE) obtained from a local palm mill in Selangor. The POMSE is the effluent generated from the biological treatment of raw POME and it was still high in COD. This is a common problem faced by palm oil mill operators [59]. The high COD in the POMSE was contributed by the presence of macromolecules, such as fulvic acid and humic acid [60]. The initial concentration of COD is 3960 mg/L and the experiment was conducted in batch modes. Figure 5 and Figure 6 show the reduction of COD from POMSE by using OPF biochar as an adsorbent. As shown in Figure 5, there is a significant reduction of COD from POMSE. After 30 minutes of contact time with OPF biochar, the COD of POMSE is reduced from 3960 mg/L to 2100 mg/L. The COD of POMSE continuously reduced as the contact time with the OPF biochar increased.

From Figure 6, the maximum removal of COD is 64%, in which it is achieved after 24 hours of contact time. When compared to other studies, the biochar produced in this study can provide better removal of pollutants than other alternative adsorbent which on average can only provide 55% removal of pollutants [44]. Other than that, the performance of the OPF biochar in this study was comparable to the coconut-based activated carbon produced in the study conducted by Parveen et al. [61]. After 24 hours of contact time, the removal of COD from POMSE is constant. This is due to the unavailability of active adsorption sites on the OPF biochar [62], [63]. By comparing to the research conducted by Razali et al. [64] using oil palm trunk (OPT) biochar, the OPF biochar provided better removal of COD than OPT biochar. This might be due to the differences in characteristics of the biochar. In comparison, the surface area of the OPF biochar is higher than the OPT biochar. Other than the surface area, the OPF biochar has a higher pore volume

compared to OPT biochar which is in line with the surface area of the biochar.

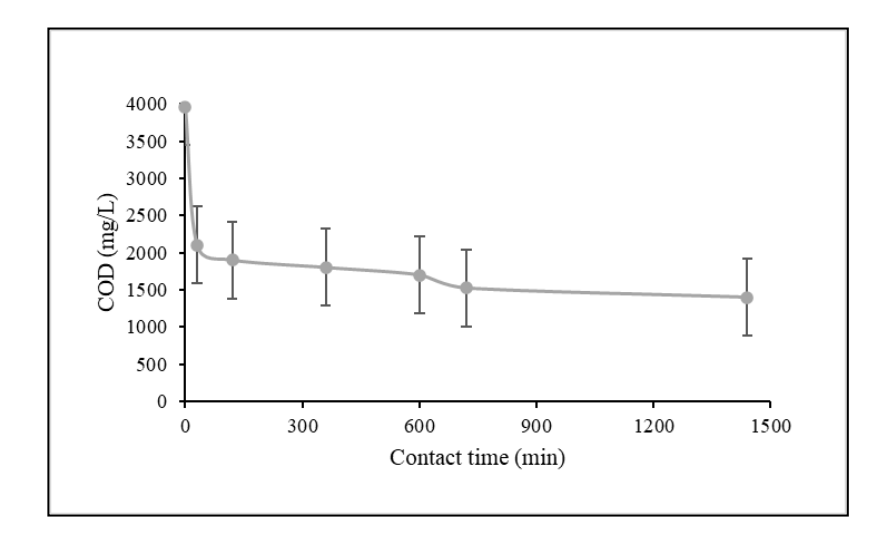


Figure 5. COD removal POMSE

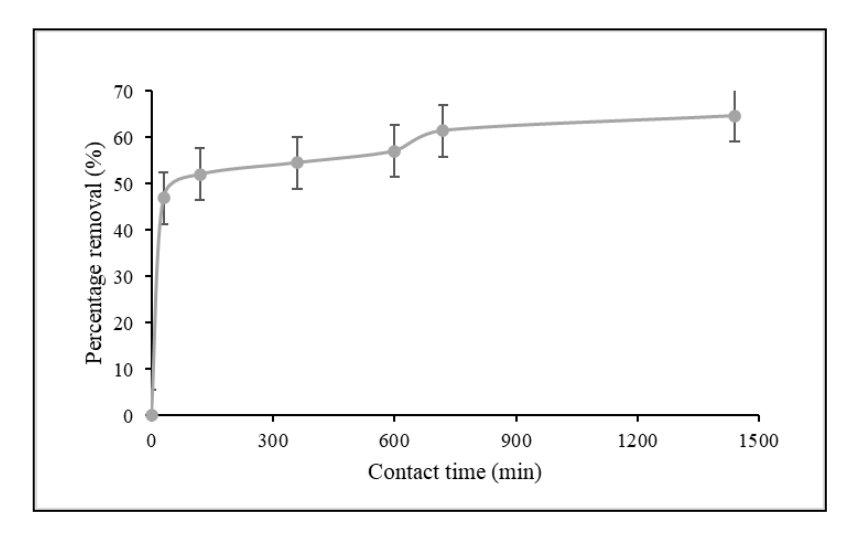


Figure 6. Percentage removal of COD from POMSE

Conclusion

The gasification process proves that other valuable and functional products (biochar) can be produced by using OPF, which is currently used as mulching and fertiliser. This study discovered that gasification biochar that was specifically produced from raw OPF has the potential to be used as adsorbents in wastewater application treatment. The biochar from the

gasification process can be used as soil conditioning and in wastewater treatment as an adsorbent due to its unique characteristic, low moisture content, low ash content and high fixed carbon content. The OPF biochar produced from this study has a large surface area and high total pore volume which can be potentially used as alternative adsorbent in the adsorption process. The high carbon content and the

presence of carbonyl compound and aromatic rings in the biochar provide active sites that aid the adsorption process. It was proven that OPF biochar can provide more than 50% removal of pollutants from the wastewater tested in this study compared to other biochar produced in other studies.

A further study should be done on the application of biochar as an adsorbent for wastewater application. Further research on the factors and the kinetic of adsorption using this gasification biochar should be conducted to gain more understanding on the mechanism involved in the adsorption process by using gasification biochar.

Acknowledgement

This research is supported by Short Term Grant - STRG (Grant no. STRG/NBR/STR16034) from Universiti Kuala Lumpur.

References

- Ghulam Kadir, A. P. (2020). Overview of the malaysian oil palm industry 2020. In Malaysian Palm Oil Board website. Access from https://www.mpob.gov. [Accessed Jun. 14, 2021].
- Tan, Z. Y. (2020). Green technology: Time to Tap Biomass. The Edge Markets. https://www.theedgemarkets.com/article/greentechnology-time-tap-biomass [Accessed Jun. 14, 2021].
- 3. Zwart, R. (2013). Sustainability in the cultivation of oil palm –issues and prospects for the industry. *Journal of Oil Palm and the Environment*, 4(5): 41-62.
- Malaysian Department of Environment (2009). Environmental quality (industrial effluent) regulations 2009. In Environmental Quality Act 1974 (pp. 4010–4059). Access from https://www.doe.gov.my/portalv1/wpcontent/uploads/2015/01/Environment al_Quality_Industrial_Effluent_Regulations_2009_--P.U.A_ 434-2009.pdf.
- Zainuri, N. Z., Hairom, N. H. H., Sidik, D. A. B., Desa, A. L., Misdan, N., Yusof, N. and Mohammad, A. W. (2018). Palm oil mill secondary effluent (POMSE) treatment via

- photocatalysis process in presence of ZnO-PEG nanoparticles. *Journal of Water Process Engineering*, 26:10-16.
- Zahrim, A. Y., Nasimah, A. and Hilal, N. (2014).
 Pollutants analysis during conventional palm oil mill effluent (POME) ponding system and decolourisation of anaerobically treated POME via calcium lactate-polyacrylamide. *Journal of Water Process Engineering*, 2014: 159-165.
- Ngeno, E. C., Orata, F., Baraza, L. D., Shikuku, V.
 O. and Kimosop, S. J. (2016). Adsorption of caffeine and ciprofloxacin onto pyrolitically derived water hyacinth biochar: isothermal, kinetic and thermodynamic studies. *Journal of Chemistry and Chemical Engineering*, 10(4): 185-194.
- 8. Sia, Y. Y., Tan, I. A. W. and Abdullah, M. O. (2017). Adsorption of colour, TSS and COD from palm oil mill effluent (POME) using acid-washed coconut shell activated carbon: Kinetic and mechanism studies. *MATEC Web of Conferences*, 87:1-7.
- 9. Chin, M. J., Poh, P. E., Tey, B. T., Chan, E. S. and Chin, K. L. (2013). Biogas from palm oil mill effluent (POME): Opportunities and challenges from Malaysia's perspective. *Renewable and Sustainable Energy Reviews*, 26: 717-726.
- 10. Mukherjee, I. and Sovacool, B. K. (2014). Palm oil-based biofuels and sustainability in Southeast Asia: A review of Indonesia, Malaysia, And Thailand. *Renewable and Sustainable Energy Reviews*, 37: 1-12.
- 11. Umar, M. S., Jennings, P. and Urmee, T. (2013). Strengthening the palm oil biomass renewable energy industry in Malaysia. *Renewable Energy*, 60; 107-115.
- Hansen, V., Müller-Stöver, D., Ahrenfeldt, J., Holm, J. K., Henriksen, U. B. and Hauggaard-Nielsen, H. (2015). Gasification biochar as a valuable by-product for carbon sequestration and soil amendment. *Biomass and Bioenergy*, 72: 300-308.
- 13. Shen, Y. (2015). Chars as carbonaceous adsorbents/catalysts for tar elimination during biomass pyrolysis or gasification. *Renewable and Sustainable Energy Reviews*, 43: 281-295.

- Hosseini, S. E., Wahid, M. A. and Ganjehkaviri, A. (2015). An overview of renewable hydrogen production from thermochemical process of oil palm solid waste in Malaysia. *Energy Conversion* and Management, 94: 415-429.
- Anukam, A., Mamphweli, S., Reddy, P., Meyer, E. and Okoh, O. (2016). Pre-processing of sugarcane bagasse for gasification in a downdraft biomass gasifier system: A comprehensive review. Renewable and Sustainable Energy Reviews, 66: 775-801.
- Couto, N., Rouboa, A., Silva, V., Monteiro, E. and Bouziane, K. (2013). Influence of the biomass gasification processes on the final composition of syngas. *Energy Procedia*, 36:596-606.
- 17. Huggins, T. M., Haeger, A., Biffinger, J. C. and Ren, Z. J. (2016). Granular biochar compared with activated carbon for wastewater treatment and resource recovery. *Water Research*, 94: 225-232
- Kearns, J., Anh, M. T. L., Reents, N. W., Shimabuku, K. K., Mahoney, R. B., Summers, R. S. and Knappe, D. R. U. (2014). Trace organic contaminant removal from drinking water using local char. 37th WEDC International Conference, 2014: pp. 1-6.
- Kaetzl, K., Lübken, M., Uzun, G., Gehring, T., Nettmann, E., Stenchly, K. and Wichern, M. (2019). On-farm wastewater treatment using biochar from local agro residues reduces pathogens from irrigation water for safer food production in developing countries. Science of the Total Environment, 682: 601-610.
- Thompson, K. A., Shimabuku, K. K., Kearns, J. P., Knappe, D. R. U., Summers, R. S. and Cook, S. M. (2016). Environmental comparison of biochar and activated carbon for tertiary wastewater treatment. *Environmental Science & Technology*, 50(20): 11253-11262.
- Zhang, F., Wang, X., Yin, D., Peng, B., Tan, C., Liu, Y., Tan, X. and Wu, S. (2015). Efficiency and mechanisms of Cd removal from aqueous solution by biochar derived from water hyacinth (*Eichornia* crassipes). Journal of Environmental Management, 153: 68-73.
- 22. Han, R., Wang, Y., Zhoa, X., Wang, Y., Xie, F., Cheng, J. and Tang, Mi. (2009). Adsorption of

- methylene blue by phoenix tree leaf powder in a fixed-bed column: Experiments and prediction of breakthrough curves. *Desalination*, 245(1–3): 284-297.
- 23. Enaime, G., Baçaoui, A., Yaacoubi, A. and Lübken, M. (2020). Biochar for wastewater treatment—conversion technologies and applications. *Applied Sciences*, 10: 1-29.
- 24. Wang, X., Guo, Z., Hu, Z. and Zhang, J. (2020). Recent advances in biochar application for water and wastewater treatment: A review. *PeerJ*, 8: 1-34.
- Oliveira, F. R., Patel, A. K., Jaisi, D. P., Adhikari, S., Lu, H. and Khanal, S. K. (2017). Environmental application of biochar: Current status and perspectives. *Bioresource Technology*, 246: 110-122.
- 26. Nsamba, H. K., Hale, S. E., Cornelissen, G. and Bachmann, R. T. (2014). Improved gasification of rice husks for optimized biochar production in a top lit updraft gasifier. *Journal of Sustainable Bioenergy Systems*, 4: 225-242.
- 27. James, R. A. M., Yuan, W. and Boyette, M. D. (2016). The effect of biomass physical properties on top-lit updraft gasification of woodchips. *Energies*, 9(4): 1-13.
- 28. You, S., Ok, Y. S., Chen, S. S., Tsang, D. C. W., Kwon, E. E., Lee, J. and Wang, C. H. (2017). A critical review on sustainable biochar system through gasification: energy and environmental applications. *Bioresource Technology*, 246: 242-253.
- 29. Mohan, D., Sarswat, A., Sik, Y. and Pittman, C. U. (2014). Organic and inorganic contaminants removal from water with biochar, a renewable, low cost and sustainable adsorbent a critical review. *Bioresource Technology*, 160: 191-202.
- Ahmad, M., Rajapaksha, A. U., Lim, J. E., Zhang, M., Bolan, N., Mohan, D., Vithanage, M., Lee, S. S. and Sik Ok, Y. (2014). Biochar as a sorbent for contaminant management in soil and water: A review. *Chemosphere*, 99: 19-33.
- 31. Rahman, A. A., Abdullah, N. and Sulaiman, F. (2014). Temperature effect on the characterization of pyrolysis products from oil palm fronds. *Advances in Energy Engineering*, 2: 14-21.

- 32. Sun, Y., Gao, B., Yao, Y., Fang, J., Zhang, M., Zhou, Y., Chen, H. and Yang, L. (2014). Effects of feedstock type, production method, and pyrolysis temperature on biochar and hydrochar properties. *Chemical Engineering Journal*, 240: 574-578.
- 33. Tran, H. and Yuan, C. (2016). Effect of pyrolyisis temperatures and times in adsorption of cadmium onto orange peel derived biochar. *Waste Management & Research*, 34(2): 129-138.
- 34. Tan, X., Liu, Y., Zeng, G., Wang, X., Hu, X. and Gu, Y. (2015). Application of biochar for the removal of pollutants from aqueous solutions. *Chemosphere*, 125: 70-85.
- 35. Mojiri, A., Ziyang, L., Tajuddin, R. M., Farraji, H. and Alifar, N. (2016). Co-treatment of landfill leachate and municipal wastewater using the ZELIAC/Zeolite constructed wetland system. *Journal of Environmental Management*, 166: 124-130.
- Lam, S. S., Liew, R. K., Cheng, C. K., Rasit, N., Ooi, C. K., Ma, N. L., Ng, J. H., Lam, W. H., Chong, C. T. and Chase, H. A. (2018). Pyrolysis production of fruit peel biochar for potential use in treatment of palm oil mill effluent. *Journal of Environmental Management*, 213: 400-408.
- 37. Angin, D. (2012). Effect of pyrolysis temperature and heating rate on biochar obtained from pyrolysis of safflower seed press cake. *Bioresource Technology*, 128: 593–597.
- 38. Usman, A. R. A., Abduljabbar, A., Vithanage, M., Ok, Y. S., Ahmad, M., Ahmad, M., Elfaki, J., Abdulazeem, S. S., & Al-Wabel, M. I. (2015). Biochar Production from Date Palm Waste: Charring Temperature Induced Changes in Composition and Surface Chemistry. *Journal of Analytical and Applied Pyrolysis*, 115: 392-400.
- Mahmood, W. M. F. W., Ariffin, M. A., Harun, Z., Ishak, N. A. I., Ghani, J. A. and Rahman, M. N. A. (2014). Characterisation and potential use of biochar from gasified oil palm wastes. *Journal of Engineering Science and Technology*, 45-54.
- Suárez-Hernández, L., Ardila-A, A. N. and Barrera-Zapata, R. (2017). Morphological And physicochemical characterization of biochar produced by gasification of selected forestry

- species. Revista Facultad de Ingeniería, 26(46): 123-130.
- Feng, D., Zhao, Y., Zhang, Y., Sun, S. and Gao, J. (2018). Steam gasification of sawdust biochar influenced by chemical speciation of alkali and alkaline earth metallic species. *Energies*, 11(1): 205.
- 42. Shen, Y. (2015). Chars as carbonaceous adsorbents/catalysts for tar elimination during biomass pyrolysis or gasification. *Renewable and Sustainable Energy Reviews*, 43: 281-295.
- 43. Park, J., Hung, I., Gan, Z., Rojas, O. J., Lim, K. H. and Park, S. (2013). Activated carbon from biochar: influence of its physicochemical properties on the sorption characteristics of phenanthrene. *Bioresource Technology*, 149: 383-389.
- 44. Liew, R. K., Nam, W. L., Chong, M. Y., Phang, X. Y., Su, M. H., Yek, P. N. Y., Ma, N. L., Cheng, C. K., Chong, C. T. and Lam, S. S. (2017). Oil palm waste: An abundant and promising feedstock for microwave pyrolysis conversion into good quality biochar with potential multi-applications. *Process Safety and Environmental Protection*, 2017: 1-13.
- 45. Parveen, S., Kaman, D., Ai, I., Tan, W., Lik, L. and Lim, P. (2016). Palm oil mill effluent treatment using coconut shell based activated carbon: adsorption equilibrium and isotherm. *MATEC Conference ENCON*, 2016: 1-6.
- 46. Majedi, Y., Alhilali, E., al Nehayan, M., Rashed, A., Ali, S. S., Al Rawashdeh, N., Thiemann, T. and Soliman, A. (2014). Treatment of dye-loaded wastewater with activated carbon from date palm leaf wastes. World Sustainability Forum, 2014: 1-12.
- 47. Abdulsalam, M., Man, H. C., Yunos, K. F., Abidin, Z. Z., Idris, A. I. and Hamzah, M. H. (2020). Augmented yeast-extract and diary-waste for enhancing bio-decolourization of palm oil mill effluent using activated sludge. *Journal of Water Process Engineering*, 36: 1-12.
- 48. Razali, N. and Kamarulzaman, N. Z. (2020). Chemical characterizations of biochar from palm oil trunk for palm oil mill effluent (POME) treatment. *Materials Today: Proceedings*, 31(1): 191-197.

- 49. Domingues, R. R., Trugilho, P. F., Silva, C. A., de Melo, I. C. N. A., Melo, L. C. A., Magriotis, Z. M. and Sánchez-Monedero, M. A. (2017). Properties of biochar derived from wood and high-nutrient biomasses with the aim of agronomic and environmental benefits. *PLoS ONE*, 12(5): 1-19.
- 50. Klasson, K. T. (2017). Biochar characterization and a method for estimating biochar quality from proximate analysis results. *Biomass and Bioenergy*, 96: 50-58.
- 51. Wijitkosum, S. and Jiwnok, P. (2019). Elemental composition of biochar obtained from agricultural waste for soil amendment and carbon sequestration. *Applied Sciences*, 9(19): 3980.
- 52. Wei, L., Huang, Y., Huang, L., Li, Y., Huang, Q., Xu, G., Müller, K., Wang, H., Ok, Y. S. and Liu, Z. (2020). The ratio of H/C is a useful parameter to predict adsorption of the herbicide metolachlor to biochars. *Environmental Research*, 184: 109324.
- 53. Griffith, S. M., Banowetz, G. M. and Gady, D. (2013). Chemical characterization of chars developed from thermochemical treatment of Kentucky bluegrass seed screenings. *Chemosphere*, 92(10): 1275-1279.
- 54. Ibrahim, I., Hassan, M. A., Abd-Aziz, S., Shirai, Y., Andou, Y., Othman, M. R., Ali, A. A. M. and Zakaria, M. R. (2017). Reduction of residual pollutants from biologically treated palm oil mill effluent final discharge by steam activated bioadsorbent from oil palm biomass. *Journal of Cleaner Production*, 141: 122-127.
- 55. Cibati, A., Foereid, B., Bissessur, A. and Hapca, S. (2017). Assessment of miscanthus × giganteus derived biochar as copper and zinc adsorbent: study of the effect of pyrolysis temperature, pH and hydrogen peroxide modification. *Journal of Cleaner Production*, 162: 1285-1296.
- An, H., Liu, Z., Cao, X., Teng, J., Miao, W., Liu, J., Li, R. and Li, P. (2017). Mesoporous lignite-coke as an effective adsorbent for coal gasification wastewater treatment. *Environmental Science: Water Research & Technology*, 3(1): 169-174.
- Gai, H., Guo, K., Xiao, M., Zhang, N., Li, Z., Lv,
 Z. and Song, H. (2018). Ordered mesoporous carbons as highly efficient absorbent for coal gasification wastewater a real case study based

- on the inner Mongolia autonomous coal gasification wastewater. *Chemical Engineering Journal*, 341: 471-482.
- 58. Xu, L., Wang, J., Zhang, X., Hou, D. and Yu, Y. (2015). Development of a novel integrated membrane system incorporated with an activated coke adsorption unit for advanced coal gasification wastewater treatment. *Colloids and Surfaces A: Physicochemical and Engineering Aspects*, 484: 99-107.
- 59. Lamaming, J., Hashim, R., Sulaiman, O., Peng Leh, C., Sugimoto, T. and Nordin, A. (2015). Cellulose nanocrystals isolated from oil palm trunk. *Carbohydrate Polymers*, 127: 202-208.
- Jahi, N., Ling, S., Othaman, R. and Ramli, S. (2015). Modification of oil palm plantation wastes as oil adsorbent for palm oil mill effluent (POME). Malaysian Journal of Analytical Sciences, 19: 31-40.
- 61. Liu, G., Li, X. and Campos, L. C. (2017). Role of the functional groups in the adsorption of bisphenol a onto activated carbon: Thermal modification and mechanism. *Journal of Water Supply: Research and Technology-Aqua*, 66(2): 105-115.
- 62. Sidik, S. M., Jalil, A. A., Triwahyono, S., Adam, S. H., Satar, M. A. H. and Hameed, B. H. (2012). Modified oil palm leaves adsorbent with enhanced hydrophobicity for crude oil removal. *Chemical Engineering Journal*, 203: 9-18.
- 63. Zainal, N. Ha., Jalani, N. F., Mamat, R. and Astimar, A. A. (2017). A review on the development of palm oil mill effluent (POME) final discharge polishing treatments. *Journal of Oil Palm Research*, 29(4): 528-540.
- 64. Bhalla, B., Saini, M. S. and Jha, M. K. (2013). Effect of Age and Seasonal Variations on Leachate Characteristics of Municipal Solid Waste Landfill. *International Journal of Research in Engineering and Technology*, 2(8): 223-232.

Malaysian Journal of Analytical Sciences (MJAS)



Published by Malaysian Analytical Sciences Society

ADSORPTION OF METHYLENE BLUE FROM AQUEOUS SOLUTIONS BY ACTIVATED CARBON PREPARED FROM BANANA TRUNK USING ZINC CHLORIDE ACTIVATION

(Penjerapan Metilena Biru daripada Larutan Akueus oleh Karbon Teraktif yang Disediakan dari Batang Pisang secara Pengaktifan Zink Klorida)

Zaidi Ab Ghani^{1*}, Muhammad Taufiq Hafizuddin R. Azemi¹, Mohd Hafiz Yaacob¹, Noor Hafizah Uyup¹, Lee Sin Ang¹, Nor Azliza Akbar²

¹Faculty of Applied Science, Universiti Teknologi MARA Cawangan Perlis, 02600 Arau Perlis, Malaysia. ²School of Civil Engineering, College of Engineering, Universiti Teknologi MARA Cawangan Pulau Pinang, 13500 Permatang Pauh, Pulau Pinang, Malaysia

*Corresponding author: zaidi433@uitm.edu.my

Received: 10 September 2021; Accepted: 18 December 2021; Published: 28 April 2022

Abstract

In this study, the banana trunk-derived activated carbon (BTAC) used was prepared via zinc chloride (ZnCl₂) activation. BTAC is used as an adsorbent to remove methylene blue (MB) from the aqueous solutions. The BET surface area, total pore volume and pore diameters of the BTAC were 1329.5 m²/g, 1.16 cm³/g and 3.8 nm, respectively. The effect of adsorbent dosage, initial concentration, contact time and solution pH were studied in batch experiments. The experimental data were analyzed by Langmuir, Freundlich, Temkin, and Dubinin-Radushkevich (D-R) adsorption isotherms model. Data analysis study via RMSE and χ^2 analyses suggested that Temkin isotherm model was the best fitted with the adsorption of MB on BTAC. The maximum monolayer adsorption of MB onto BTAC was calculated to be 217 mg/g. Kinetic parameters were evaluated based on pseudo-first-order (PFO), pseudo-second-order (PSO) and Weber–Morris intraparticle diffusion (IPD) kinetic models. The regression results showed that a PSO model is more accurately representing the adsorption kinetics. While the plot of q_t versus $t^{1/2}$ for the IPD model represented multi-linearity and proved that the adsorption processes occurred more than one step. Thermodynamics parameters were determined between temperatures of 25 to 40 °C. The ΔG° and ΔH° values were negative and the overall adsorption process was determined as spontaneous and exothermic. While the positive value of ΔS° proposed good affinity of the MB molecules toward the BTAC. The results from this study suggested that BTAC could be a viable adsorbent in managing higher concentrations of dyes from water and wastewater.

Keywords: adsorption, activated carbon, methylene blue, isotherm, kinetic

Abstrak

Dalam kajian ini, karbon teraktif daripada batang pisang (BTAC) yang digunakan telah disediakan melalui pengaktifan zink klorida (ZnCl₂). BTAC telah digunakan sebagai penjerap untuk menyingkirkan metilena biru (MB) daripada larutan akueus. Keluasan permukakaan BET, jumlah isipadu dan diameter liang pori bagi BTAC masing-masing adalah 1329.5 m²/g, 1.16 cm³/g

dan 3.8 nm. Kesan dos penjerap, kepekatan permulaan, masa kontak dan pH larutan dilakukan secara eksperimen kelompok. Data ekperimen telah dianalisa menggunakan model Langmuir, Freundlich, Temkin dan Dubinin–Radushkevich. Analisa data kajian melalui RMSE dan χ^2 mencadangkan bahawa model isoterma Temkin adalah yang paling sesuai dengan penjerapan MB pada BTAC. Penjerapan lapisan-mono maksima MB kepada BTAC dikira sebagai 217 mg/g. Parameter kinetik telah dinilai berdasarkan model kinetik pseudo-pertama (PFO), pseudo-kedua (PSO) dan resapan intrazarah (IPD) Weber–Morris. Hasil regresi menunjukkan bahawa model PSO lebih tepat mewakili kinetik penjerapan. Sementara plot q_t melawan $t^{1/2}$ untuk model IPD menunjukkan garisan linear yang pelbagai dan membuktikan bahawa proses penjerapan berlaku lebih daripada satu langkah. Parameter termodinamik telah ditentukan di antara suhu 25 hingga 40 °C. Nilai Δ G° dan Δ H° adalah negatif, maka keseluruhan proses penjerapan telah ditentukan sebagai spontan dan eksotermik. Sementara itu, nilai positif bagi Δ S° mencadangkan bahawa pertalian yang baik diantara molekul MB terhadap BTAC. Keputusan dari kajian ini mencadangkan bahawa BTAC mampu menjadi penjerap yang berkesan dalam menguruskan kepekatan pewarna yang lebih tinggi dari air dan air sisa.

Kata kunci: penjerapan, karbon teraktif, metilena biru, isoterma, kinetik

Introduction

Wastewater effluent that contains dyes is a typical and one of the major causes of environmental pollution. The presence of dyes in the industries effluent poses the most prominent problem since they are toxic and the recalcitrant nature of dyes [1]. Typical biological wastewater treatment plants cannot eliminate toxic pollutants such as dyes since they were purposely designed for organic and nutrient removal. Methylene blue (MB) is an example of dye that is commonly used in industry. MB is a heterocyclic aromatic chemical compound. Thus, MB is highly toxic, carcinogenic and its degradation process is difficult [2]. Therefore, MB containing effluent must be treated appropriately before discharge. Previously, various advanced oxidation methods have been introduced to treat dyes polluted water, such as ozonation [3], photocatalyst [4] and electrochemical treatment [5]. However, oxidation or degradation of dyes might contribute to the secondary pollutants. The other methods that have been employed include reverse osmosis [6], coagulationflocculation [7], membrane filtration [8], ion exchange[9] and adsorption [10]. Among these methods, adsorption is a well-known and applicable method of removing dyes contaminant water. In addition, the adsorption process has emerged as a costeffective, efficient, and environmentally friendly method of dye removal [11].

Recently, there are a variety of absorbents have been introduced to treat dyes such as bio-composite [12], nanoparticles [13], graphene oxide [14], forest wastes

[15], polystyrene foam [16] agriculture waste [17]. Based on the current scenario, activated carbon (AC) is the best adsorbent to treat textile effluent. Previously, the preparation of AC by using low-cost precursor from agriculture waste such as dates stone [18], ashitaba waste [19], banana peel [20], almond and walnut shells [21] have been employed extensively as a new precursor in the production of AC. Most of the mentioned researchers claimed that abundance and continuous availability of the agriculture biomass are the key motivation of their precursor selection. In addition, the treatment and reuse of agriculture waste should be implemented efficiently to obtain its valorization achieve sustainable waste management [22].

In Malaysia, biomass derived from agriculture such as banana plantation is gaining increasing attention. Banana widely planted in tropical country such as Malaysia, thus it is not surprising that it is the major biomass source. Instead of burning and disposing naturally as an organic fertilizer, a better way would be converting them into AC. Thus, this study used banana trunk as a precursor to prepare AC. During preparation of AC via chemical activation, the lignocellulosic precursor is treated primarily with a chemical agent, such as H₃PO₄, H₂SO₄, HNO₃, NaOH, KOH, or ZnCl₂. According to Lewoyehu [23], during the activation with ZnCl₂ the cellulosic material will be degraded, results in charring and aromatization of the carbon skeleton and creation of the pore structure. Hence,

produced AC with high surface area and good adsorption capacity.

However, in order to treat water-containing dye via adsorption requires a deeper understanding especially on the effectiveness of the adsorbent towards the adsorbate. Therefore, the objective of the present work is to introduce BTAC as an adsorbent and to examine its effectiveness in removing MB from aqueous solutions. The effect of adsorbent dosage, initial concentration, contact time and solution pH were studied in batch experiments. The experimental were analyzed by Langmuir, Freundlich, Temkin, and Dubinin-Radushkevich (D-R) adsorption isotherms model. Kinetic parameters, rate constants, equilibrium adsorption capacities, and related correlation coefficients were evaluated based on pseudo-first-order (PFO), pseudo-second-order (PSO) and Weber-Morris intraparticle diffusion (IPD) kinetic Thermodynamics parameters such as ΔG° , ΔH° , and ΔS° have also were evaluated.

Materials and Methods Materials

In this study, the adsorbent used was BTAC with particle size <215 um, which was obtained from our previous study [24]. The BTAC was prepared from the banana trunk and activated with ZnCl₂ at a temperature of 640 °C. All the chemicals used in this study were of analytical reagent grade unless otherwise stated. The adsorbate used is a cationic dye, namely methylene blue (Sigma Aldrich, Germany). The physicochemical information of BTAC and MB were shown in Table 1. MB adsorption data was used to obtain adsorption isotherms, kinetic and thermodynamic study. Stock solution of MB (1000 mg/L = 1000 ppm) was prepared by dissolving 1 g of MB into 1 L distilled water. The stock solution was further diluted with distilled water to obtain the desired concentrations of MB in the range of 75 to 125 mg/L.

Table 1. Physicochemical information of BTAC and MB[20]

Banana trunk derived activated carbon (BTAC)						
Textural properties		Ultimate anal	Ultimate analysis (wt.% dry basis)			
BET surface area (m ² /g)	1329.5 Carbon (wt%)		84.1			
Mesopore surface area (m ² /g)	1152.6	Hydrogen (wt%)	2.1			
Micropore surface area (m ² /g)	176.9	Nitrogen (wt%)	3.7			
Total pore volume (cm ³ /g)	Total pore volume (cm^3/g) 1.16		0.2			
Pore diameter (nm)	3.83	Oxygen (wt%)	9.9			
Physicochemical propert	ies	Proximate ana	Proximate analysis (wt.% dry basis)			
Bulk density (g/cm ³)	0.6	Volatile matter (w	rt%) 25.1			
Iodine number (mg/g)	819.03	Fixed carbon (wt	%) 74.7			
$\mathrm{pH}_{\mathrm{pzc}}$	3.7	Ash (wt%)	0.2			
	Meth	nylene blue (MB)				
		Commercial name	Methylene blue			
N _N		Chemical name	Methylthioninium chloride			
		Empirical formula	$C_{16}H_{18}CIN_3S$			
S+ N		Molar mass	319.85 g/mol			
		CAS number	61-73-4			
Structure formula of MB		$\lambda_{ m max}$	664 nm			

Batch adsorption study

The batch adsorption procedure was utilized to investigate the uptake of MB from aqueous solution onto BTAC. For the effect of adsorbent dosage, various dosage of BTAC ranging from 0.01 to 0.13 g was added into 250 mL Erlenmeyer flasks containing 100 mL of 150 mg/L MB concentration. The influence of initial concentration was explored using seven different concentrations from 50 to 150 mg/L MB solution. While the effect of contact time was determined from initial until equilibrium contact time is reached (5 to 360 min). The solution pH was varied from 5.0 to 8.0 with constant another adsorption parameter. The samples were then shaken at isothermal temperature (25 ±2 °C) at 125 rpm in an incubator shaker. Each experiment was conducted with two replications. Then, the samples were taken out and filtered through a 0.45 µm nylon membrane before analysis to minimize the adsorbent's interference. After that, the filtered solutions were analyzed for MB uptake analysis by UV-visible spectrophotometer at 664 nm, which is the maximum absorption peak of MB. The adsorption capacity of MB in the aqueous solution was calculated by using Eq. (1) as follows:

$$q_e = [(C_o - C_e)V] / M$$
 (1)

where C_e (mg/L) and C_o (mg/L) respectively represent the equilibrium and initial concentration of adsorbate, adsorbent mass is denoted by M (g), and solution volume is V (L). The isotherm parameters of the Langmuir and Freundlich, Temkin and Dubinin-Radushkevich models were investigated using batch experimental adsorption data at various C_o studied. For the kinetic studies, the experiments were carried out similarly as described above. Approximately 2 mL of MB solution was withdrawn at specific time intervals using a plastic syringe. The MB concentration in the liquid phase $(C_t, mg/g)$ was analysed as a function of contact time (t). The adsorption capacity (q_e) was calculated using Eq. (2):

$$q_t = [(C_o - C_t)V] / M$$
 (2)

where q_t is the amount of MB adsorbed per unit weight of adsorbent at any time t (mg/g); C_o and C_t are the initial and liquid-phase concentrations of the adsorbate solution at any time t (mg/L), respectively; V is the volume of the solution (L); and M is the weight of the sorbent used (g).

The thermodynamic studies were performed similarly as adsorption equilibrium study. The adsorption temperatures were varied from 25, 30, 35 and 40 °C (±2 °C). These experiments were carried out in incubator shaker at shaking rate of 125 rpm. The BTAC dosage and MB concentration was fixed at 0.05 g and 125 mg/L, respectively. The adsorption capacity of MB in the aqueous solutions was calculated by using Eq. (1). All isotherm, kinetic and thermodynamic studies were fitted with the experimental data using their linear equations which were shown in Table 2.

Table 2. The equations of isotherm, kinetic and thermodynamic studies

Parameters	Equation		Nomenclature
Langmuir	$C_e/q_e = 1/K_L q_m + C_e/q_m;$ $R_L = 1/(1 + K_L C_o)$	(3)	q _e = amount adsorbate quilibrium (mg/g)
Freundlich	$ln(q_e) = ln(K_F) + 1/n ln(C_e)$	(4)	q_t = amount adsorbate retained at time (mg/g) q_m = monolayer adsorption capacity (mg/g) t = time (min)
Temkin	$q_e = B \ln(K_T) + B \ln(C_e);$ $B = RT/b_T$	(5)	 k₁= PFO rate constant (1/min) k₂= PSO rate constant (g/mg.min) k_{ID}= IPD rate constant (mg/g/min^{0.5})
Dubinin- Radushkevich	$\begin{split} &\ln \left(\mathbf{q}_{e} \right) = \ln \left(\mathbf{q}_{s} \right) - \beta \epsilon^{2} \; ; \\ &\epsilon = RT \; ln \big[1 + 1/C_{e} \big] \; ; \\ &E = 1/\sqrt{2\beta} \end{split}$	(6)	C_i = thickness of the boundary layer (mg/g)
Pseudo first order (PFO)	$\ln(q_e - q_t) = \ln(q_e) - k_1 t$	(7)	C_i = thickness of the boundary layer (mg/g) K_L = Langmuir adsorption equilibrium constant (L/mg) C_e = equilibrium concentration (mg/L) C_o = initial concentration (mg/L)
Pseudo second order (PSO)	$t/q_t = (1/k_2 q_e^2) + (1/q_e)t$	(8)	R_L = separation factor $n = adsorption intensity \\ K_F$ = Freundlic adsorption capacity constant (L/g)
Intraparticle diffusion (IPD)	$q_t = k_{ID}t^{0.5} + C_i$	(9)	b_T = Temkin isotherm constant (mg/L) R = gas constant (8.314 J/mol.K) T = absolute temperature (K) q_s = DR adsorption capacity (mg/g) ϵ = Polanyi potential
Thermodynamic	$lnK_{D} = -\Delta G^{\circ}/RT$ $lnK_{D} = (\Delta S^{\circ}/R) - (\Delta H^{\circ}/RT);$ $\Delta G^{\circ} = \Delta H^{\circ} - T\Delta S^{\circ}$	(10)	β = constant related to adsorption energy (mol ² /kJ ²) E = free energy (kJ/mol) k_D = adsorption equilibrium constant (l/mg) ΔG° = free energy (kJ/mol) ΔH° = change in enthalpy (kJ/mol) ΔS° = change in entropy (J/mol.K)

Results and Discussion

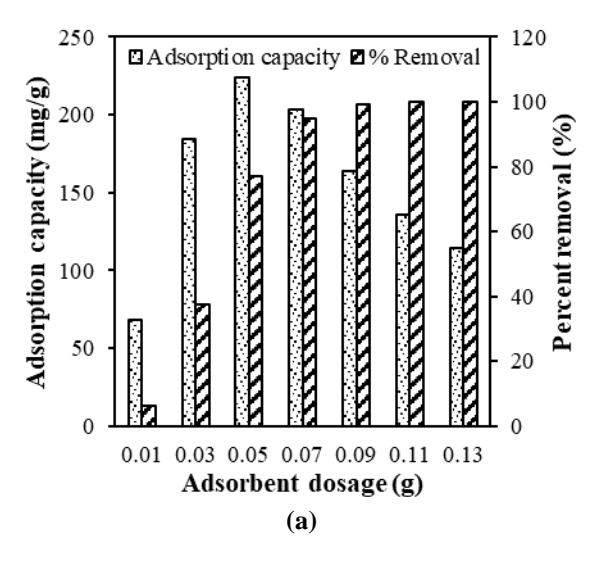
Effect of adsorption parameters on MB removal

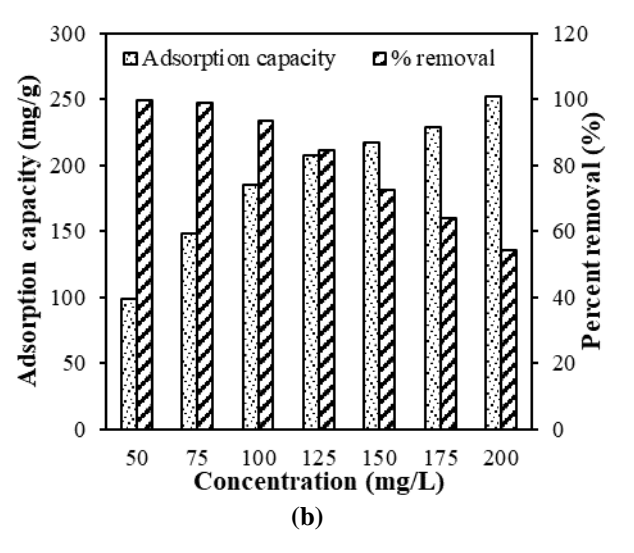
In this study, the preliminary experiments to explore the effect of several adsorption parameters were done by batch adsorption technique. For batch adsorption, the BTAC is mixed with the MB solution in an agitated vessel for specific time. The effects of adsorbent dosage, initial concentration, contact time and solution pH on adsorption efficiency were presented and described in the following subsections.

Effect of adsorbent dosage

Adsorbent dosage is an important parameter that affects the adsorption performance. This parameter is essential to observe the maximum adsorption with the minimum promising amount of adsorbent [25]. The effect of adsorbent dosage was studied by added different adsorbent dosage (0.01 to 0.13 g) into 100 mL of 150 mg/L MB concentrations under. Figure 1(a) shows the adsorption capacity and percentage removal of MB as a function of the BTAC dose. Adsorption capacity and percent removal of MB increased sharply as the BTAC dose increased from 0.01 to 0.05 g. However, an opposite trend was observed with the additional increased of BTAC dosage beyond 0.05 g. It was noticed that the adsorption capacity of MB start to reduce gradually from 224 to 115 mg/g. Similar trend reduction of adsorption capacity with additional increased in adsorbent dosage were observed by Xue, et al. [19], Muniyandi, et al. [10] and Fan, et al. [26].

While the percentage removal was further increased and reached approximately 100% and did not show any significant MB removal as the BTAC dosage beyond 0.09 g. The opposite relationship between adsorbent dosage and removal of the MB was explained by the existence of a greater number of available sorption sites on adsorbent surface as described by Saif Ur Rehman, et al. [27]. They claimed that the concentration of adsorbate is fixed against an increasing adsorbent dose. Thus, the MB per unit mass of BTAC decreased leaving a number of active sites uncovered at high dosage, subsequently leads to a low adsorption capacity. Hence, considering minimal dosage with the highest adsorption capacity, 0.05 g BTAC dosage was selected as the optimum adsorbent dosage and used for subsequent experiments to study the influence of initial concentration, contact time and solution pH.





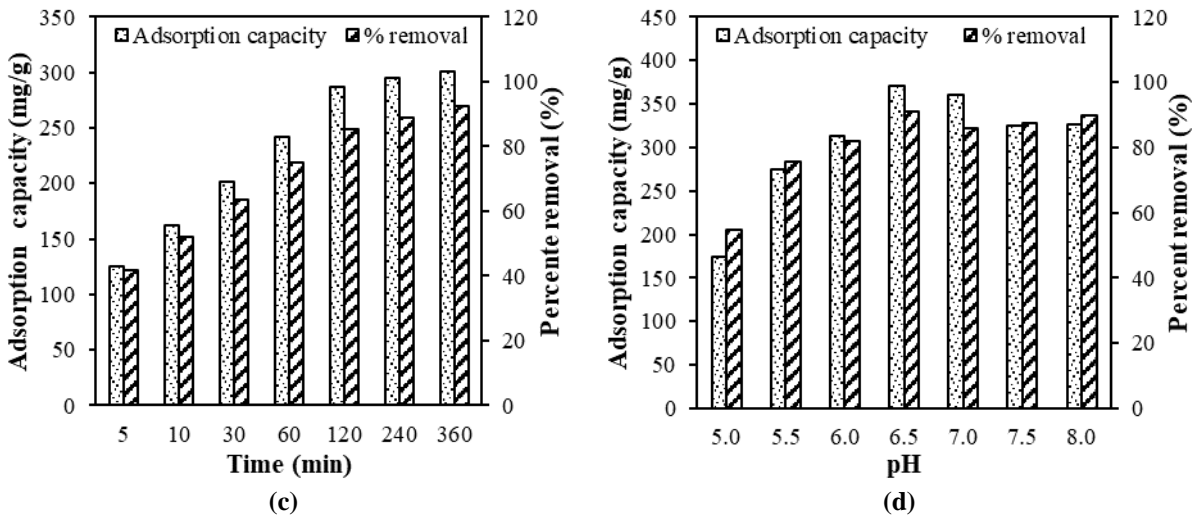


Figure 1. (a) effect of adsorbent dosage (b) effect of initial concentration, (c) effect of contact time and (d) effect of solution pH on the adsorption of MB dye

Effect of initial adsorbate concentration

Initial adsorbate concentration is another important parameter for adsorption study. Figure 1(b) shows an opposite trend of the adsorption capacity and percentage removal of MB as a function of initial MB concentration. Similar observation was reported previously for MB removal by using different type of adsorbent including modified lignocellulosic materials [28]. As per Figure 1(b), the adsorption capacity increased from 98 to 252 mg/g when the initial MB concentration increased from 50 to 200 mg/L. Higher adsorption capacity at high initial concentration is due to the generation of significant driving forces caused by a pressure gradient as explained by Benhouria et al. [29]. However, the percent MB removal gradually decreased from 99 to 54% for a similar increase in MB concentration. This observation related to the at low concentration [30]. This results clearly indicated that the adsorption process is highly dependent on the initial concentration of the solution. Based on the results, MB concentration of 125 mg/L was selected as an optimum concentration as the adsorption capacity was 207 mg/L with the percent removal of 83%, located in the middle of the graph. Thus, this initial concentration was adopted for the next experiment.

Effect of contact time

The influence of contact time (5 to 360 min) on adsorption capacity and MB percent removal is presented in Figure 1(c). Both adsorption capacity and percent removal increased as the function of contact time. When the contact time was approximately 360 min (6 h), the adsorption efficiency reached 92% with 301 mg/g adsorption capacity. It was noticed that the adsorptive removal of MB underwent two stages. During the first stage (within 60 min), the adsorption of MB increased quickly, followed by a slow adsorption stage during which adsorption capacity increased gradually. No further changed observed after 360 min which can be related to adsorption process reached the state of adsorbent-adsorbate equilibrium. This findings suggesting that high attraction existed between MB and the surface of the BTAC and the MB adsorption occurred mainly on the surface at the beginning as described by Li et al. [31]. However, with further extended the contact time, limited surface-active sites were accessible. Therefore, only a minor increase in the adsorption capacity and MB percent removal were observed and this finding mostly due to internal surface adsorption Maneerung et al. [32]. This finding suggested that significant contact time was needed for the adsorbate to diffuse into adsorption sites surface and internal pores of the adsorbent as mentioned by

Jawad et al. [33]. As no further improvement in term of adsorption capacity and MB percent removal were noticed after 360 min, therefore it was determined as an equilibrium contact time between MB and BTAC and was used as a contact time for isotherm study.

Effect of solution pH

The effect of pH on the removal of MB has been investigated. Solution pH was a key factor affecting ionic dyes (anionic or cationic) adsorption because the pH primarily influenced the surface charge on the adsorbent [34]. The adsorption experiment of MB onto BTAC was performed in 5.0 to 8.0 pH range, at controlled temperature of 30 °C for 360 min. Figure 1(d) shows the adsorption capacity and removal efficiency of MB by BTAC under different pH. It was notice that the adsorption capacity was lowest at pH 5.0 (174 mg/g) and the maximum adsorption capacity of the dye was achieved at pH 6.5 (371 mg/g). Similar trend was observed for percentage removal of MB. At the lowest pH (at pH 5.0) the MB removal efficiency was less than 60%. It showed that lower pH does not favour the uptake of cationic dye from the system and leads to electrostatic repulsion. This can be explained as dissolving MB in water results in having positively charged ions in the solution, thereby the positively charged surface of the adsorbent tends toward competing with the adsorption of the MB [35]. However, when the pH increased to 6.5, the MB removal efficiency increased up to 91% due to the decrease in electrostatic repulsion between the positively charged MB and the surface of the BTAC. While with further increase of pH to 7.0, removal efficiency reduced to 85% and no significant changes noticed as the pH increased from 7.0 to 8.0. According to Banerjee and Chattopadhyaya [36], change in pH affects the adsorptive process through the dissociation of functional groups on the adsorbent surface that tends to shift in equilibrium characteristics of the adsorption process. The present findings were supported by earlier reteaches who have reported the removal of MB onto waste carpets derived AC [34] and . Thus, the solution pH of 6.5 was selected as the optimum conditions for adsorption of MB on the surface of the investigated adsorbents.

Isotherm study

In order to study the adsorption behavior of MB in detail, the data for equilibrium adsorption isotherms were fitted into several isotherm models such as Langmuir, Freundlich, Temkin and Dubinin-Raduskevich. The parameters obtained in the isotherm equation and a determination coefficient (R2) were listed in Table 3. According to the linear regression (R²) analysis method, it was observed that the values of the correlation coefficients were slightly high (≥ 0.9300). Thus, it showed that the results fit these four models very well. Based on the value of R², the Langmuir isotherm model was the best fit with the adsorption equilibrium data with R²=0.9998. However, according to Misran et al. [2], R2 is not adequate to depict the applicability of the models to the experimental data. Hence, a comparison was exhibited between the calculated adsorption capacities at equilibrium (qe) from the applied models and the experimental values. Further analysis of the isotherm data based on root-mean-square error (RMSE) and chisquare (χ^2) analysis showed that the Temkin isotherm model given the lowest values for RMSE and χ^2 analyses. Therefore, Temkin isotherm model was selected as the best fits with the adsorption of MB onto BTAC since it demonstrates better agreement with the experimental data.

Based on the Langmuir isotherm model on the linear Eq. (3), the isotherm parameters, K_L and maximum adsorption capacity, qm can be determined from the slope of the plot C_e/q_e vs. C_e. In the conditions studied, the maximum adsorption capacity at monolayer coverage (q_m) was 217.4 mg/g. While the calculated R_L values for the selected range of concentration studied were in the range of 0.0045 to 0.0133. These values were greater than zero showing favorable adsorption of MB onto BTAC. Previous study, Ezechi et al. [37] and Fan et al. [26] claimed that for favorable adsorption, 0 $< R_L < 1$; unfavorable adsorption, $R_L > 1$; linear adsorption, R_L = 1; and adsorption process is irreversible if $R_L = 0$. For the Freundlich isotherm model, the values of n and K_F can be calculated from the plot of ln qe vs. ln Ce using Eq. (4). Based on the equation, the values of n and K_F were 6.9396 and 134.8

L/g, respectively, with $R^2 = 0.9797$. Temkin isotherm represents the quantity of heat needed for the adsorption by one layer of adsorbate on the surface of the adsorbent [38]. Temkin isotherm constants were determined from the slope and intercept from the plot q_e vs. ln C_e based on the linear Eq. (5). The value of the Temkin constant (B) was calculated to be 22.13 J/mol. The value of B was greater than 1 indicates an exothermic process [39]. While b_T and K_T were calculated to be 111.9 mg/L and 569.2 L/g, respectively. The positive value of b_T proved that the adsorption process was exothermic [35]. Ahmad et al. [40] also observed comparable results for the adsorption study of synthetic dyes removal using pomegranate peel AC. The Dubinin-Radushkevich adsorption isotherm is generally applied to express the adsorption mechanism with a Gaussian energy distribution onto a heterogeneous surface. Based on the Eq. (6), the theoretical saturation adsorption capacity (q_s) and k_{ad} values were calculated to be 172.2 mg/g

and 4×10⁻⁸ mol²/J², respectively. While the value of adsorption energy (E) was determined as 3.53 kJ/mol. The value of E was noticed less than 8 kJ/mol implying that removal of MB by BTAC involves physical adsorption as reported by Xue, et al. [19]. Magnitude of E is useful for estimating the mechanism of the adsorption reaction [38]. Based on the result, it can be concluded that strong physical interactions are the driving force of MB adsorption onto BTAC, an assumption supported as well by the great value of saturation adsorption capacity.

The q_m value of MB onto BTAC was then compared with the adsorption capacities of ACs as prepared by various agriculture waste as listed in Table 4. This comparison data clarified that the BTAC is a highly effective adsorbent due to its high surface area and good adsorption capacity for MB dye removal from aqueous solution.

Table 3. Langmuir, Freundlich, Temkin and Dubinin-Radushkevich constants for MB adsorption

Langmuir Fr		Freundlic	h	Temkin		Dubinin-Radı	Dubinin-Radushkevich	
q _m (mg/g)	217.4	n	6.9396	B (J/mol)	22.13	q _s (mg/g)	197.2	
$K_{L}\left(L/mg\right)$	1.4838	$K_{F}\left(L/g\right)$	134.8	$b_{T} (mg/L)$ $K_{T} (L/g)$	111.9 569.2	$ m k_{ad} (mol^2/J^2) m E (kJ/mol)$	4.0×10^{-8} 3.53	
\mathbb{R}^2	0.9998	\mathbb{R}^2	0.9797	\mathbb{R}^2	0.9671	\mathbb{R}^2	0.9304	
RMSE	23.22	RMSE	11.60	RMSE	7.72	RMSE	14.48	
χ^2	37.72	χ^2	4.58	χ^2	2.27	χ^2	5.74	

Table 4. Comparison of MB adsorption capacities by different activated carbon materials

Raw Materials	Surface Area (m²/g)	MB q _m (mg/g)	References
Banana trunk	1329.5	217.0	This study
Ashitaba biomass	1505.4	323.5	[19]
Sugarcane bagasse	709.3	136.5	[33]
Mangosteen peel	1832.0	871.5	[41]
Myristica fragrans shell	1462.0	346.8	[22]
Fox nutshell shell	2869	249.8	[42]

Kinetic study

In this study, pseudo-first order (PFO) and pseudosecond order (PSO) were used to examine the experimental adsorption data, such as the examination of the controlling mechanisms of the adsorption process (chemical reaction, diffusion control, and mass transfer). The parameter data of the PFO and PSO can be determined from the slope and intercept of plot ln (q_e-q_t) against t and plot t/q_t against t by the linear Eq. (7) and (8), respectively. The parameters obtained in the PFO and PSO equations, together with their R² and q_{e,cal} is listed in Table 3. It was found that the plots In (q_e- q_t) against t (Figure 2(a)) give a less linear relationship and subsequently contribute to the low R² values. In addition, the experimental and calculated values of qe showed a significant difference. These results indicate that the experimental data do not agree with PFO kinetic model.

On the other hand, plot t/q_t against t (Figure 2(b)) showed a linear relationship. The R^2 value (~0.999) for the PSO kinetic model was relatively higher than the PFO. Moreover, the $q_{e,cal}$ values derived from the PSO model were slightly close to the $q_{e,exp}$ value. Thus, these results suggest that the PSO model provided a good correlation for the adsorption of MB onto BTAC. Most previous studies also report PSO kinetics for adsorption, such as the adsorption of MB onto forest wastes [15], methyl orange onto pumpkin seed powder [43], and adsorption of reactive orange by iron oxide nanospheres [44]. The PSO kinetic model also verified that the chemisorption was the rate-controlling step over the whole adsorption process [45].

The IPD model was also tested because the PFO and PSO kinetic models cannot identify a diffusion

mechanism [46]. Intraparticle models parameters (k_{ID} and C) were calculated from the slope and intercept of plot q_t vs. $t^{1/2}$ and summarized in Table 5. As shown in Figure 2(c), plots of q_t vs. $t^{1/2}$ present multi-linearity, thus indicating that more than one step occurs during the adsorption of MB onto BTAC. Similar patterns have also been obtained by Kumar and Jena [42] and Bedin et al. [47]. According to Shin and Kim [46], the first portion is the fast adsorption or external surface adsorption stage, where adsorbate (MB molecules) migrates through the solution to the exterior surface of the adsorbent (BTAC) particles (Stage I). This portion was attributed to bulk diffusion. The second portion is the gradual adsorption stage, where MB molecules move within the particles (Stage II). This portion is due to intraparticle diffusion. The third portion is the final equilibrium stage, where the MB molecules are adsorbed at sites on the interior surface of BTAC (Stage III). Moreover, the observed multi-linearity also suggests that intraparticle diffusion is not the ratelimiting step [48]. It was observed from Table 5, the value of k_{ID1} and k_{ID2} increase with increasing MB concentration from 75 to 125 mg/L. In addition, at constant MB concentration, the values of k_{ID1} were found larger than k_{ID2}. In other words, the adsorption was rapidly at the initial stage and became slower beyond this stage and no more adsorption occurred when achieving the equilibrium. The magnitude in the C₁ pattern with the changes of adsorbate concentrations was not clearly observed. However, at the second stage, C2 values were noticed to decrease as the adsorbate concentration increase. The reason behind this due that higher adsorbent dosage will weaker the boundary layer effect.

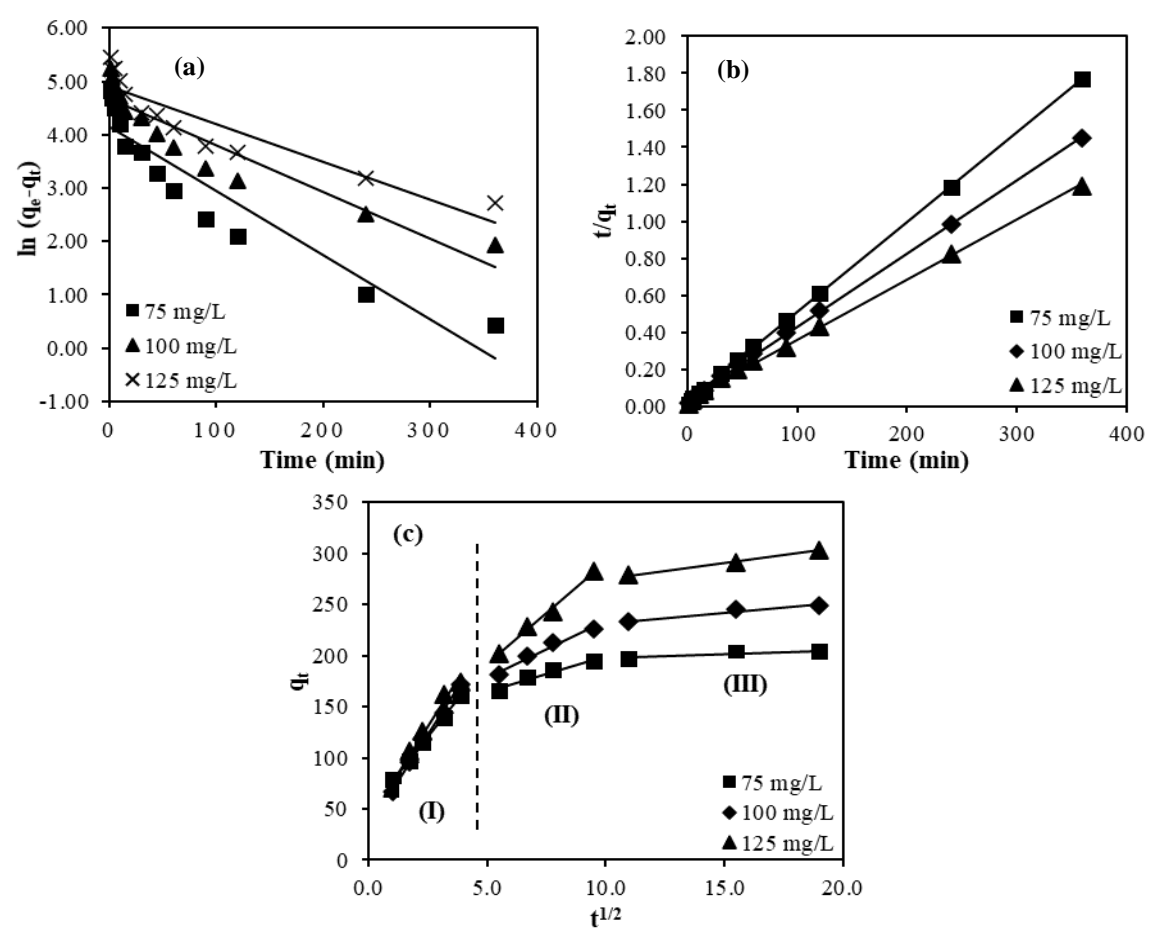


Figure 2. (a) PFO, (b) FSO and (c) IPD model for the adsorption of MB onto BTAC

Table 5. PFO, FSO and IPD parameters for adsorption of MB onto BTAC

Kinetic Model

Concentration	q _{e,exp}	Pseud	lo First Oro	der	P	Pseudo Second Order		
(mg/L)	(mg/g)	$q_{e,cal} \\ (mg/g)$	k ₁ (1/min)	\mathbb{R}^2	$\begin{array}{c} q_{e,cal} \\ (mg/g) \end{array}$	k ₂ (g/mg.min)	\mathbb{R}^2	
75 100	205.4 255.8	62.8 106.5	0.0121 0.0087	0.8841 0.8740	208.3 250.0	0.0010 0.0005	0.9998 0.9992	
125	316.2	135.4	0.0071	0.8345	312.5	0.0003	0.9984	
		Intra-Particle Diffusion Model						
Concentration (mg/L)	k _{ID1} (mg/g.min ^{0.5})	C ₁ (mg/g)	R	2	k_{ID2} (mg/g.min ^{0.5})	C ₂ (mg/g)	\mathbb{R}^2	
75	28.722	49.421	0.99	978	5.515	139.9	0.9565	
100	35.816	33.619	0.99	936	9.192	136.3	0.9710	
125	36.448	40.151	0.97	767	19.173	98.0	0.9957	

Thermodynamic study

The slope and the intercept of the plots of ln K_D versus 1/T using the Van't Hoff plot (figure not shown) are used to determine the ΔH° and ΔS° values. From the values of ΔH° and ΔS° , ΔG° can be calculated using Eq. 10. According to the data presented in Table 6, Gibbs free energy (ΔG°) values for MB were in between -25.83 and -26.34 kJ/mol as the temperature rose from 25 to 40 °C. These negative ΔG° values indicate that spontaneous sorption takes place. In addition, the value of ΔG° was observed to increase (less negative) with decreasing temperature, suggesting rapid and more spontaneous adsorption at lower temperatures. In addition, the calculated ΔH° value was -15.57 kJ/mol. The negative value of ΔH° for the adsorption process indicates that the adsorption was an

exothermic process [15]. Furthermore, these results indicate weak attraction forces between the adsorbate and the BTAC. The low value of ΔH° (less than 40 kJ/mol) implies loose bonding between the adsorbate molecules and the adsorbent surface. In the case of entropy (ΔS°), it was found to be 33.87 J/mol.K. The positive value of ΔS° resulted from the increased randomness due to the adsorption of MB, which suggested good affinity of the solute molecules toward the BTAC and increased randomness at the solid-solution interface during the fixation of MB molecules on the active site of the BTAC. A similar finding was also reported by Alver et al. [12] for the adsorption of methylene blue on magnetic alginate/rice husk biocomposite.

Table 6.	Thermody	znamic stu	idy for	adsor	ntion	of MB

Temperature	\mathbf{k}_{ad}	ΔG°	ΔH°	ΔS°
$^{\circ}\mathbf{C}$	(L/g)	(kJ/mol)	(kJ/mol)	(J/mol.K)
25	28.48	-25.83		
30	25.51	-26.00	15.57	33.87
35	23.54	-26.17	-15.57	
40	21.16	-26.34		

Conclusion

The present investigation revealed that BTAC is a promising adsorbent to remove MB from aqueous solutions. The equilibrium data fitted well to Langmuir, Freundlich, Temkin and Dubinin-Radushkevich isotherm models. Based on error analysis study via RMSE and χ^2 analyses, Temkin isotherm model was the best fitted with the adsorption of MB on BTAC. Maximum monolayer adsorption based on Langmuir was calculated to be 217.4 mg/g. Thermodynamic parameters such as free energy changes (ΔG°), enthalpy (ΔH°) and entropy (ΔS°) were evaluated between temperatures of 25 °C and 40 °C. The ΔG° was noticed progressively decrease from -25.83 to -26.34 kJ/mol as the temperature increase. The ΔH° and ΔS° values were found to be -15.57 kJ/mol and 33.87 J/mol.K respectively. The results showed that the overall adsorption process was exothermic and spontaneous. The findings from this study suggested

that BTAC could be a viable adsorbent in managing higher dye problems associated with textiles industries effluent.

Acknowledgement

This work was supported by Universiti Teknologi MARA (UiTM). Great appreciation goes to the Ministry of Higher Education (MOHE) and members of ASTeRN research interest group for providing support throughout the completion of this research.

References

1. Amran, F. and Zaini, M. A. A. (2021). Sodium hydroxide-activated empty Casuarina Isotherm, kinetics thermodynamics and congo methylene blue and red adsorption. Environmental *Technology* & Innovation, 23: 101727.

- Misran, E., Bani, O., Situmeang, E. M. and Purba, A. S. (2022). Banana stem based activated carbon as a low-cost adsorbent for methylene blue removal: Isotherm, kinetics, and reusability. *Alexandria Engineering Journal*, 61(3): 1946-1955.
- 3. Wu, J. and Upreti, S. R. (2015). Continuous ozonation of methylene blue in water. *Journal of Water Process Engineering*, 8: 142-150.
- Hoang, N. T. T., Tran, A. T. K., Hoang, M. H., Nguyen, T. T. H. and Bui, X. T. (2021). Synergistic effect of TiO₂/chitosan/glycerol photocatalyst on color and COD removal from a dyeing and textile secondary effluent. *Environmental Technology & Innovation*, 21: 101255.
- Singh, J. and Dhaliwal, A. S. (2022). Electrochemical and photocatalytic degradation of methylene blue by using rGO/AgNWs nanocomposite synthesized by electroplating on stainless steel. *Journal of Physics and Chemistry* of Solids, 160: 110358.
- Sahinkaya, E., Sahin, A., Yurtsever, A. and Kitis, M. (2018). Concentrate minimization and water recovery enhancement using pellet precipitator in a reverse osmosis process treating textile wastewater. *Journal of Environmental Management*, 222: 420-427.
- Dotto, J., Fagundes-Klen, M. R., Veit, M. T., Palacio, S. M. and Bergamasco, R. (2019). Performance of different coagulants in the coagulation/flocculation process of textile wastewater. *Journal of Cleaner Production*, 208: 656-665.
- 8. Gnanasekaran, G., Sudhakaran, M. S. P., Kulmatova, D., Han, J., Arthanareeswaran, G., Jwa, E. and Mok, Y. S. (2021). Efficient removal of anionic, cationic textile dyes and salt mixture using a novel CS/MIL-100 (Fe) based nanofiltration membrane. *Chemosphere*, 284: 131244.
- Sinha, A. K., Sasmal, A. K., Pal, A., Pal, D. and Pal, T. (2021). Ammonium phosphomolybdate [(NH₄) ₃PMo₁₂O₄₀] an inorganic ion exchanger for environmental application for purification of dye contaminant wastewater. *Journal of Photochemistry and Photobiology A:*

- Chemistry, 418: 113427.
- Muniyandi, M. and Govindaraj, P. (2021). Potential removal of Methylene Blue dye from synthetic textile effluent using activated carbon derived from Palmyra (Palm) shell. *Materials Today: Proceedings*, 47: 299-311.
- De Gisi, S., Lofrano, G., Grassi, M. and Notarnicola, M. (2016). Characteristics and adsorption capacities of low-cost sorbents for wastewater treatment: a review. Sustainable Materials and Technologies, 9: 10-40.
- 12. Alver, E., Metin, A. Ü. and Brouers, F. (2020). Methylene blue adsorption on magnetic alginate/rice husk bio-composite. *International Journal of Biological Macromolecules*, 154: 104-113.
- Rohaizad, A., Shahabuddin, S., Shahid, M. M., Rashid, N. M., Hir, Z. A. M., Ramly, M. M., ... and Aspanut, Z. (2020). Green synthesis of silver nanoparticles from *Catharanthus roseus* dried bark extract deposited on graphene oxide for effective adsorption of methylene blue dye. *Journal of Environmental Chemical Engineering*, 8(4): 103955.
- Arabpour, A., Dan, S. and Hashemipour, H. (2021). Preparation and optimization of novel graphene oxide and adsorption isotherm study of methylene blue. *Arabian Journal of Chemistry*, 14(3): 103003.
- 15. Gemici, B. T., Ozel, H. U. and Ozel, H. B. (2021). Removal of methylene blue onto forest wastes: Adsorption isotherms, kinetics and thermodynamic analysis. *Environmental Technology & Innovation*, 22: 101501.
- Li, W., Xie, Z., Xue, S., Ye, H., Liu, M., Shi, W. and Liu, Y. (2021). Studies on the adsorption of dyes, Methylene blue, Safranin T, and Malachite green onto Polystyrene foam. Separation and Purification Technology, 276: 119435.
- 17. Meili, L., Lins, P. V. S., Costa, M. T., Almeida, R. L., Abud, A. K. S., Soletti, J. I., ... and Erto, A. (2019). Adsorption of methylene blue on agroindustrial wastes: experimental investigation and phenomenological modelling. *Progress in Biophysics and Molecular Biology*, 141: 60-71.

- 18. Shamsabadi, A. S., Bazarganipour, M. and Tavanai, H. (2021). An investigation on the pore characteristics of dates stone based microwave activated carbon nanostructures. *Diamond and Related Materials*, 120: 108662.
- 19. Xue, H., Wang, X., Xu, Q., Dhaouadi, F., Sellaoui, L., Seliem, M. K., ... and Li, Q. (2022). Adsorption of methylene blue from aqueous solution on activated carbons and composite prepared from an agricultural waste biomass: A comparative study by experimental and advanced modeling analysis. *Chemical Engineering Journal*, 430: 132801.
- Khairiah, K., Frida, E., Sebayang, K., Sinuhaji, P. and Humaidi, S. (2021). Data on characterization, model, and adsorption rate of banana peel activated carbon (Musa Acuminata) for adsorbents of various heavy metals (Mn, Pb, Zn, Fe). *Data in Brief*, 39: 107611.
- Salem, S., Teimouri, Z. and Salem, A. (2020). Fabrication of magnetic activated carbon by carbothermal functionalization of agriculture waste via microwave-assisted technique for cationic dye adsorption. Advanced Powder Technology, 31(10): 4301-4309.
- Mariana, M., Mistar, E. M., Alfatah, T. and Supardan, M. D. (2021). High-porous activated carbon derived from *Myristica fragrans* shell using one-step KOH activation for methylene blue adsorption. *Bioresource Technology Reports*, 16: 100845.
- 23. Lewoyehu, M. (2021). Comprehensive review on synthesis and application of activated carbon from agricultural residues for the remediation of venomous pollutants in wastewater. *Journal of Analytical and Applied Pyrolysis*, 159: 105279.
- 24. Ab Ghani, Z., Yusoff, M. S., Zaman, N. Q., Zamri, M. F. M. A. and Andas, J. (2017). Optimization of preparation conditions for activated carbon from banana pseudo-stem using response surface methodology on removal of color and COD from landfill leachate. Waste Management, 62: 177-187.
- Olu-Owolabi, B. I., Diagboya, P. N. and Ebaddan, W. C. (2012). Mechanism of Pb²⁺ removal from aqueous solution using a nonliving moss biomass. *Chemical Engineering Journal*, 195:

- 270-275.
- 26. Fan, S., Wang, Y., Wang, Z., Tang, J., Tang, J. and Li, X. (2017). Removal of methylene blue from aqueous solution by sewage sludge-derived biochar: Adsorption kinetics, equilibrium, thermodynamics and mechanism. *Journal of Environmental Chemical Engineering*, 5(1): 601-611.
- 27. Saif Ur Rehman, M., Kim, I., Rashid, N., Adeel Umer, M., Sajid, M. and Han, J. I. (2016). Adsorption of brilliant green dye on biochar prepared from lignocellulosic bioethanol plant waste. *CLEAN–Soil, Air, Water*, 44(1): 55-62.
- 28. Manna, S., Roy, D., Saha, P., Gopakumar, D. and Thomas, S. (2017). Rapid methylene blue adsorption using modified lignocellulosic materials. *Process Safety and Environmental Protection*, 107, 346-356.
- Benhouria, A., Islam, M. A., Zaghouane-Boudiaf, H., Boutahala, M. and Hameed, B. H. (2015). Calcium alginate-bentonite-activated carbon composite beads as highly effective adsorbent for methylene blue. *Chemical Engineering Journal*, 270: 621-630.
- Pathania, D., Sharma, S. and Singh, P. (2017).
 Removal of methylene blue by adsorption onto activated carbon developed from *Ficus carica* bast. *Arabian Journal of Chemistry*, 10: S1445-S1451.
- 31. Li, Z., Wang, G., Zhai, K., He, C., Li, Q. and Guo, P. (2018). Methylene blue adsorption from aqueous solution by loofah sponge-based porous carbons. *Colloids and Surfaces A: Physicochemical and Engineering Aspects*, 538: 28-35.
- 32. Maneerung, T., Liew, J., Dai, Y., Kawi, S., Chong, C. and Wang, C. H. (2016). Activated carbon derived from carbon residue from biomass gasification and its application for dye adsorption: kinetics, isotherms and thermodynamic studies. *Bioresource technology*, 200: 350-359.

- 33. Jawad, A. H., Abdulhameed, A. S., Bahrudin, N. N., Hum, N. N. M. F., Surip, S. N., Syed-Hassan, S. S. A., .. and Sabar, S. (2021). Microporous activated carbon developed from KOH activated biomass waste: surface mechanistic study of methylene blue dye adsorption. *Water Science and Technology*, 84(8): 1858-1872.
- 34. Hassan, A. F. and Elhadidy, H. (2017). Production of activated carbons from waste carpets and its application in methylene blue adsorption: Kinetic and thermodynamic studies. *Journal of Environmental Chemical Engineering*, *5*(1): 955-963.
- 35. Miraboutalebi, S. M., Nikouzad, S. K., Peydayesh, M., Allahgholi, N., Vafajoo, L. and McKay, G. (2017). Methylene blue adsorption via maize silk powder: Kinetic, equilibrium, thermodynamic studies and residual error analysis. *Process Safety and Environmental Protection*, 106: 191-202.
- 36. Banerjee, S. and Chattopadhyaya, M. C. (2017). Adsorption characteristics for the removal of a toxic dye, tartrazine from aqueous solutions by a low cost agricultural by-product. *Arabian Journal* of Chemistry, 10: S1629-S1638.
- 37. Ezechi, E. H., bin Mohamed Kutty, S. R., Malakahmad, A. and Isa, M. H. (2015). Characterization and optimization of effluent dye removal using a new low cost adsorbent: Equilibrium, kinetics and thermodynamic study. *Process Safety and Environmental Protection*, 98: 16-32.
- 38. Abbas, M. and Trari, M. (2015). Kinetic, equilibrium and thermodynamic study on the removal of Congo Red from aqueous solutions by adsorption onto apricot stone. *Process Safety and Environmental Protection*, 98: 424-436.
- Nnadozie, E. C. and Ajibade, P. A. (2020). Adsorption, kinetic and mechanistic studies of Pb (II) and Cr (VI) ions using APTES functionalized magnetic biochar. *Microporous and Mesoporous Materials*, 309: 110573.
- 40. Ahmad, M. A., Puad, N. A. A. and Bello, O. S. (2014). Kinetic, equilibrium and thermodynamic studies of synthetic dye removal using pomegranate peel activated carbon prepared by microwave-induced KOH activation. Water

- Resources and industry, 6: 18-35.
- 41. Zhang, Z., Xu, L., Liu, Y., Feng, R., Zou, T., Zhang, Y., ... and Zhou, P. (2021). Efficient removal of methylene blue using the mesoporous activated carbon obtained from mangosteen peel wastes: Kinetic, equilibrium, and thermodynamic studies. *Microporous and Mesoporous Materials*, 315: 110904.
- 42. Kumar, A. and Jena, H. M. (2016). Removal of methylene blue and phenol onto prepared activated carbon from Fox nutshell by chemical activation in batch and fixed-bed column. *Journal of Cleaner Production*, 137: 1246-1259.
- 43. Subbaiah, M. V. and Kim, D. S. (2016). Adsorption of methyl orange from aqueous solution by aminated pumpkin seed powder: Kinetics, isotherms, and thermodynamic studies. *Ecotoxicology and Environmental Safety*, 128: 109-117.
- 44. Khosravi, M. and Azizian, S. (2014). Adsorption of anionic dyes from aqueous solution by iron oxide nanospheres. *Journal of Industrial and Engineering Chemistry*, 20(4): 2561-2567.
- 45. Zhu, C. S., Wang, L. P. and Chen, W. B. (2009). Removal of Cu (II) from aqueous solution by agricultural by-product: peanut hull. *Journal of Hazardous Materials*, 168(2-3): 739-746.
- Shin, H. S. and Kim, J. H. (2016). Isotherm, kinetic and thermodynamic characteristics of adsorption of paclitaxel onto Diaion HP-20. Process Biochemistry, 51(7): 917-924.
- 47. Bedin, K. C., Martins, A. C., Cazetta, A. L., Pezoti, O. and Almeida, V. C. (2016). KOH-activated carbon prepared from sucrose spherical carbon: Adsorption equilibrium, kinetic and thermodynamic studies for Methylene Blue removal. *Chemical Engineering Journal*, 286: 476-484.
- 48. Ghani, Z. A., Yusoff, M. S., Zaman, N. Q., Andas, J. and Aziz, H. A. (2017). Adsorptive removal of dissolved organic matter (DOM) in landfill leachate by iron oxide nanoparticles (FeONPs). *AIP Conference Proceedings*, 1892: 040016.

Malaysian Journal of Analytical Sciences (MJAS)



INITIATIVES IN UTILIZING NATURAL REAGENTS AND NATURAL MATERIALS FOR CHEMICAL ANALYSIS: TALENT AND CHALLENGE FOR ASEAN IN NEW NORMAL CHEMICAL ANALYSIS

(Inisiatif dalam Penggunaan Reagen Semulajadi dan Bahan Semulajadi bagi Analisis Kimia: Bakat dan Cabaran untuk ASEAN dalam Analisis Kimia Norma Baru)

Kanokwan Kiwfo^{1,2}, Pei Meng Woi^{3*}, Chalermpong Saenjum^{1,2,4}, Treethip Sukkho^{1,2,4}, Kate Grudpan^{1,2,5}

¹Center of Excellence for Innovation in Analytical Science and Technology ²Cluster of Excellence on Biodiversity-based Economic and Society (B.BES-CMU) Chiang Mai University, Chiang Mai 50200, Thailand ³Chemistry Department. Faculty of Science, Universiti Malaya, 50603 Kuala Lumpur, Malaysia ⁴Pharmaceutical Sciences, Faculty of Pharmacy ⁵Department of Chemistry, Faculty of Science Chiang Mai University, Chiang Mai 50200, Thailand

*Corresponding author: pmwoi@um.edu.my

Received: 19 September 2021; Accepted: 28 November 2021; Published: 28 April 2022

Abstract

This review explores the contributions of natural resources with diverse disciplines which offers the insights into the design of greener chemical analysis. The discussion was focused on the published works in our group where a diverse range of natural reagents used in the determination of various environmental analytes has been highlighted, aiming to discuss the initiatives and applicability of the usage of alternative natural reagents and substitute synthetic methods in optimizing analytical processes, which in turn would lead to cost-effective and time-efficient in handling analytes assay. By exploring the potential of natural reagents, the sustainability in green chemical analysis could be promised in coming near future, especially in convincing for the talent and challenge for ASEAN in this new normal chemical analysis.

Keywords: green analytical chemistry, natural reagent, natural material, local wisdom, sustainable chemistry

Abstrak

Ulasan ini membincangkan sumbangan reagen semula jadi dalam pelbagai disiplin ilmu yang dapat memberikan gambaran mengenai analisis kimia hijau. Perbincangan in fokus kepada penerbitan yang telah diterbitkan oleh kumpulan kami di mana beberapa jenis reagen semula jadi yang digunakan dalam penentuan pelbagai analit persekitaran akan diutamakan, bagi membincangkan inisiatif dan penerapan penggunaan reagen semulajadi alternatif dan kaedah sintetik gantian dalam mengoptimumkan proses analisis, supaya analisis dapat dikendalikan secara kos efektif dan cekap masa. Dengan menerokai potensi reagen semula jadi, kesinambungan dalam analisis kimia hijau akan dapat dijanjikan dalam masa terdekat terutamanya dapat memberikan keyakinan dalam bakat dan cabaran di ASEAN dari segi analisis kimia di norma baru ini.

Kata kunci: kimia analisis hijau, reagen semula jadi, bahan semula jadi, kebijaksaan tempatan, kimia kelestarian

Introduction

Green chemistry concept was first devised in the early of 1990s, which is practically about 30 years ago [1, 2]. This concept is laid on the foundation of twelve principles for green chemistry which can be described as ecological approaches in molecules and materials making, reactions, and processes that are meant to provide a safer human health with the effort in minimizing or removing the use and production of harmful constituents. Evolving from here, green analytical chemistry has adopted the green chemistry's twelve principles to focus on the development of analytical methodologies and techniques with greater commitment in preservation of the environment and safety of operators. These two concepts, the green chemistry, and the green analytical chemistry, are closely associated with sustainable chemistry, which is the scientific notion that strive for efficiency improvement in natural resources utilization as to fulfill the human needs and requirement for chemical products and services. Sustainable chemistry encompasses the design, manufacture and use of efficient, effective, and more environmentally benign and friendly on chemical products and processes. This also serves the United Nations Sustainable Development Goals (UN SDGs) on the universal call to act in protecting the planet by integrating balance in between development involving social, economic, and environmental sustainability [3].

Having said that, a global consensus on how to assess and appraise the greenness of an analytical method has not yet been achieved, but several green metric tools have been proposed towards this goal [4]. Apart from the development in experimental techniques and instrumentation designs, which both are crucial for quality improvements in chemical analyses; efforts and attempts are being made to reduce or minimizing the undesirable impact of chemical analyses on the environment, and to enable sustainable development principles being embedded and implemented within analytical laboratories. As shown in Figure 1, the current trend in analytical practices is depending on high-performance instruments which emphasize on sensitivity, selectivity, and precision. Such laboratory design and set-up always required skillful human resource, and utilize enormous amounts of chemicals, solvents, as well as energy [5]. The similar practice was applied in almost all academia institutions in developed countries as well as for the laboratories setting in industry, where most of them rely on highend instruments to generate most of the analytical information which applicable for process control, or environmental conditions assessment and evaluation [6]. Nevertheless, despite the capability of such designed-laboratories, there is an urgent need for simple indicator-type sensors in market that able to offer adequate precision and specificity, easy to handle thus do not require trained personnel, and while during operation, little or no waste generation thanks to volume minimization, which in return consume negligible amounts of energy or none, and still capable to obtain chemical information from the point-of-care, including on-site process analysis for the widest use. Such sensor characteristics would also link to costeffective operation.

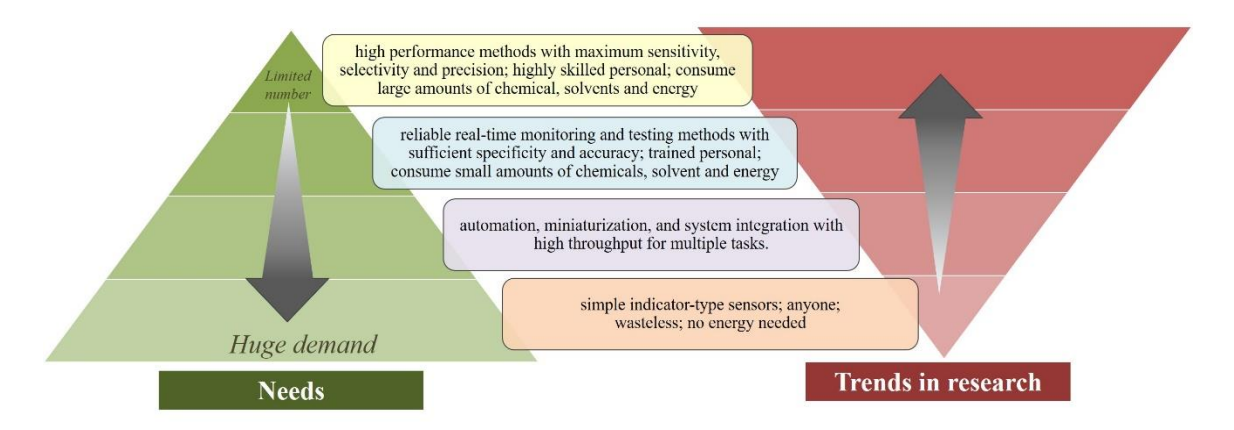


Figure 1. Comparison of the needs and trends in analytical chemistry. Reproduced with adaptation from [5]

Thus, one of the purposes of green analytical chemistry is to discover alternative reagents or substitutive synthetic methods which can reduce or minimize the usage of hazardous or poisonous chemicals. This suggestion may at first seem to be counteract to one of the best adhered principles of analytical chemistry, in which typically reagents of the highest purity grade are accounted for minimization of reagent blanks and impurities interferences. Nevertheless, in some cases there may be the possibility in replacing or substituting this highly purified reagents (which contributing to the costing in analysis) without compromising or bargaining the success of the assay determination. Under the typical condition of analytical experiments, a reagent is normally required in a small amount, or a crude extract which contains the essential active reagent are sufficient to get the analysis done. This is where the use of such natural reagents is highly desirable attributed to its simplicity in their preparation as well as the inherent or zero energy and chemical waste prevention. The ASEAN countries including Thailand and Malaysia are rich in natural resources. Utilizing a variety of natural resources existing in this region for health, chemicals, nutrient tests, and as natural dyes have been exercised as one of local wisdoms. Such wisdoms have long been employed in local peoples for improvement of life quality, for example using the fermented tea leaf like Miang as health supplement and snacks [7], which in return becomes the major source of income and tourism activities for one of the village in northern Thailand.

Natural dyeing craftsmanship in textile industry has been kept alive thanks to discovery of various extracts from local plant such as mangosteen tree (Garcinia dulcis) [8] which offers bright yellow color, indigo leaves (Indigofera tinctoria) which contributes the blue color and coconut barks which attributed to pinkish brown color [9]. A team of chemists, focusing on the development of green chemical analysis techniques, has adapted the wisdoms in modern chemical analyses. In many parts of Thailand alone, there has been some regional handling of guava leaves as the sign or as an indicator towards the presence of iron in ground water. The appearance of darker color of water upon contacts with the guava leaves helps local villagers in making some decisions (or "screening test", as for today term), such as whether the water is suitable for cloth washing, due to the strain that tends to deposited on the cloth, attributed to the iron presence in the water source; or it can lead to pre-treatment decisions such as applying alum into the ground water prior consumed for drinking or cooking use. This example of local wisdom has never been published nor any scientific explanation is available until Settheeworrarit et al. reported the investigation of natural guava (Psidium guajava L., Myrtaceae family) leaf extract as an alternative natural indicator for quantification of iron using the flow injection technique [10]. This is just one of the many examples which showcase on how the natural resources can work perfectly in applying chemical analysis in such green analytical approach.

From the Scopus database, trends in research works based on keywords "natural reagent" in "chemistry" have shown an increasing pattern as displays in Figure 2. This indicates an encouraging direction among analytical chemist in effort towards green analytical chemistry which adopted natural reagents as the active materials in performing assay testing. It is worth to notice that scientific articles contribution from our group are sharing the similar development. Different examples of the use of natural reagents for derivatization have been published as indicated by the used database. Natural reagents are consisted of extracts from various sources including the vegetables, plant-based, bacteria, or animals that required minimal treatment (extraction process) and among them, natural compounds contained in plants were able to distinguish themselves as the imperative key to green analytical chemistry initiatives.

Herein in this review, we have pin-pointed the published works done on natural reagents and materials, particularly in green analytical chemistry by our group to discuss its scientific potential as part of the ASEAN consortium efforts. The scope of discussion was designed to fortify the geographical advantages in this southern Asia region where each country is sharing the similar bioresources that could be explored further in various scientific exploration as well as collaboration and networking. One of the advantages of the reported works here is that it could help in shorten the needs of screening a vast range of natural compounds, hence open the opportunity to adopt the similar plant species for further exploration. A diverse range of natural reagents used for the determination of various environmental analytes has been highlighted, aiming to critically discussed the initiatives and applicability of the use of such alternative reagents and alternative synthetic methods in optimizing analytical processes, as a way to provide the required information in a manner that is environmentally friendly, prioritize sustainability with the least possible consumption of materials, energy, and generating less or zero waste along the way.

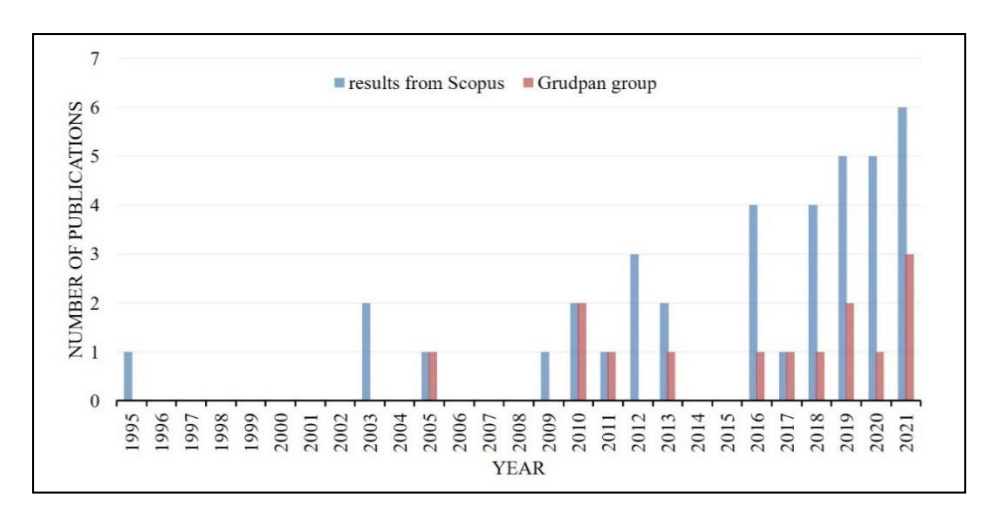


Figure 2. Number of publications obtained from Scopus database using the keywords of "natural reagent" () in chemistry and with "Grudpan" () (searched on 31 August 2021)

Natural reagents used in chemical analysis

Table 1 represents some natural reagents extracts which can be found in plants that grew in ASEAN countries. The tropical forests in this region offer a unique natural heritage which has been evolved for over a hundred million years, resulting in rich flora and

fauna with spectacular biodiversity. Currently, these are in much demand due to their efficacy, safety, and minimal side effects. Sample treatment which involves both the extraction of the analytes and the purification of the sample extract obtained, is still considered the bottleneck of the entire analytical procedure, despite

much progress on automation and miniaturization has been accomplished. It is still the most labor-intensive and time-consuming analytical step, accounting for 60-80% of the total analysis time. These steps can affect both, the accuracy and precision, and green analytical features of analytical methods. Extraction of plant materials can be done by various conventional and nonconventional extraction procedures including maceration, infusion, percolation, digestion, decoction, Soxhlet extraction, ultrasound-assisted extraction, turbo-extraction, countercurrent extraction, microwaveassisted extraction, ultrasound extraction, supercritical fluid extraction, solid-phase extraction, and column chromatography. Considering the aforementioned information, it is easy to imagine that substantial efforts have been made in recent years to simplify the overall sample preparation steps and to tailor it to the green analytical chemistry principles. Major efforts of scientists have been devoted to miniaturization of the extraction device; development of new sorbent materials with advanced properties; reduction and replacement or elimination of toxic and hazardous organic solvents; reduction of sample volume and extraction time, and maximizing extraction efficiency and selectivity, among others. The natural reagents reported here can be obtained in a greener approach of extraction which only involving the use of water and ethanol as the organic solvent. The extracted chemical species have shelf-life of up for weeks provided with proper storage in fridge, thus allowing repeatability of experiments easily without restriction in chemical stocks.

Based on previous reported works, the chemical species which are active to certain analytes are listed. These active compounds are operating on the principle of colorimetric, where upon interacts with target analyte, the color changes will provide information on types of analytes as well as its concentration range, by performing the image analyzing via open source (free) color applications such as ImageJ and Color Grab. It should be noticed that for an analyte detection, the coloration visualization may be attributed to presence of different ligands from the reagents active compounds that forming chelation or binding with the analyte itself. This explains the versatility of various

active compounds as they may obtain from different plants as of same species or family, yet capable to provide the equal analyte quantification. For instance, the anthocyanins species that active towards acidity measurement, can be obtained from butterfly pea, orchid and beetroot [11, 12]; iron can be quantified using phenolic compounds from green tea and guava leave [13, 14]. It is then of interest to explore which local plants would be use of in each analyte detection. By combining the efforts and intellectual of analytical chemists, natural products expertise, biologist, computational modeling, along with the advantages of ASEAN geographical, many plant species as natural reagents could be explored further. Such strategy one day may offer benefits in the possibility where we would be on self-reliance in using the reagents from the bioresources in our region, and with less dependent from the big chemical companies, thus affording the cost-effective in handling analytes assay; and timeefficiency where chemical delays arise from delivery would no longer be an issue.

Despite the detection limits and linear ranges are probably constrained by higher blank values originating from the reagents themselves, and the limitation of the detection systems used, yet the assay determination in analytical chemistry does not restrict to maximum sensitivity, rather to the applicability towards the targeted detection range. The trend of having high precision and sensitivity which restricted to advance instrument and highly trained personnel is not able to support the demand in analytical testing especially in those resources-limited countries. While most of these examples focus on agricultural, clinical or wastewater samples, which have higher analyte concentrations, the use of natural reagents for trace analytical purposes, e.g., in environmental waters, are possible to accomplish when the enhanced analytical control of flow injection-based or sequential injection analysis is utilized in combination with intrinsically sensitive detection methods such chemiluminescence. Thus, when applied with recognition of their limitations, natural reagents, especially when used in combination with flow-based systems, can offer an alternative approach to sustainable and greener analytical measurement.

Table 1. Natural regents obtained from plants used in chemical analysis

Analyte	Active Species	Common Name	Scientific Name	Ref.	Photo of the Plant	Availability
Acidity and iron	Anthocyanins	Butterfly pea flower	Clitoria ternatea L.	[11]		Introduced into: Cambodia, Laos, Myanmar, Thailand, Vietnam, Brunei Darussalam, Philippines, Singapore, Indonesia, commercial hybrid
	Anthocyanins	Orchid flower	Dendrobium Sonia			Commercial hybrid
	Anthocyanins	Beet root	Beta vulgaris subsp. Vulgaris			Introduced into: Vietnam, Thailand
	Phenolic compounds	Tea	Camellia sinensis (L.) Kuntze			Native to: Laos, Myanmar, Thailand, Vietnam Introduced into: Cambodia
Acidity	Anthocyanins	Butterfly pea flower	Clitoria ternatea L.	[12]		Introduced into: Cambodia, Laos, Myanmar, Thailand, Vietnam, Brunei Darussalam, Philippines, Singapore, Indonesia, commercial hybrid

Table 1 (cont'd). Natural regents obtained from plants used in chemical analysis

Analyte	Active Species	Common Name	Scientific Name	Ref.	Photo of the Plant	Availability
Benzoyl peroxide	β-carotene compound	Pumpkin	Cucurbita moschata Duchesne	[15]	rainenum)————————————————————————————————————	Introduced into: Thailand, Myanmar, Vietnam, Indonesia
Aluminum	Polyphenolic compounds	Indian almond leaf	Terminalia catappa L.	[16]		Native to: Cambodia, Myanmar, Philippines, Thailand, Vietnam, Brunei Darussalam, Indonesia, Malaysia, Singapore
Aluminum	Homo- isoflavonoid compounds	Heartwood of Indian radwwod/ Sappan tree	Caesalpinia sappan L.	[17]		Native to: Cambodia, Laos, Myanmar, Thailand, Vietnam Introduced into: Brunei Darussalam, Indonesia, Malaysia, Philippines, Singapore
Copper and acidity	Starch	Rice	Oryza sativa L.	[18]		Introduced into: Brunei Darussalam, Cambodia, Indonesia, Laos, Myanmar, Malaysia, Philippines, Singapore, Vietnam, Thailand
	Anthocyanins	Butterfly pea flower	Clitoria ternatea L.			Introduced into: Cambodia, Laos, Myanmar, Thailand, Vietnam, Brunei Darussalam, Philippines, Singapore, Indonesia, commercial hybrid

Table 1 (cont'd). Natural regents obtained from plants used in chemical analysis

Analyte	Active Species	Common Name	Scientific Name	Ref.	Photo of the Plant	Availability
Iron	Polyphenolic compounds	Guava leaf	Psidium guajava L.	[10]		Introduced into: Brunei Darussalam, Malaysia, Thailand, Singapore, Indonesia
Iron	Polyphenolic compounds	Green tea	Camellia sinensis (L.) Kuntze	[13]		Native to: Laos, Myanmar, Thailand, Vietnam Introduced into: Cambodia
Iron	Phenolic compounds	Guava leaves	Psidium guajava L.	[14]		Introduced into: Brunei Darussalam, Malaysia, Thailand, Singapore, Indonesia,
Iron	Phenolic compounds	Pomegranate Peels	Punica granatum L.	[19]		Introduced into: Laos, Thailand, Vietnam
Iron	Mimosine	Leucaena leaf	Leucaena leucocephala (Lam.) de Wit	[20]		Introduced into: Cambodia, Indonesia, Laos, Philippines, Thailand, Vietnam
Iron	Phenolic compounds	Betel nut	Areca catechu L.	[21]		Native to: Philippines Introduced into: Cambodia, Laos, Thailand, Vietnam, Malaysia, Brunei Darussalam, Indonesia

Analyte	Active Species	Common Name	Scientific Name	Ref.	Photo of the Plant	Availability
Nitrite	Phenolic compounds	Miang	Camellia sinensis var. assamica (J.W.Mast.) Kitam.	[22]		Native to: Laos, Myanmar, Thailand, Vietnam

Table 1 (cont'd). Natural regents obtained from plants used in chemical analysis

Natural reagents for green analytical procedures

Pertaining to the effective experimental measurement stage, greener analytical procedures and experimental setup are inherent to automated flow-based instrument setup, owing to their capability in reducing the consumption and needs of reagent and solvent and to the possibility of incorporating decontamination of wastes on-line. The development of flow-analysis-based techniques best suited in realizing such ideology. The flow analysis approach offers a feasible means of employing natural reagents for green chemical analysis.

Guava leaf extract is one of the widely studied natural reagent where its chemical compounds may serve as whitening essence, anti-bacterial, anti-pigmentation, and in diabetes prevention. Besides, guava leaf extract is an alternative natural compound used to identify ferrous (Fe²⁺) metal through flow injection method. In one of the reported works by Hartwell and her coworkers, by using a simple flow injection system, the scientific explanation behind the use of guava leaf extract as an alternative reagent to quantify iron(II) in water samples has been revealed. Chemical and physical properties of the extract, including its stability and ability to form chelation complexes with iron(II) and (III), respectively, spectroscopic characteristics, the appropriate solvent medium used for extraction, and its potential to be used for quantification of iron in water samples were tabulated in detail. Minimization on guava leaf extract consumption was achieved via using the modified reverse flow injection manifold with two lines, where the reagent was injected into the buffer solution which was later mixed with the flow of sample solution. Such in-situ design displayed a better

sensitivity and detection limit as compared to the conventional flow system. This is presumably attributed to higher amount and a concentrated iron solution are being introduced via pumping as compared to injection along the line. [10]

Some of the works discussed as follows, although were not registered in the above search (Table 1), they engaged with the deployment of natural reagent. A simple simultaneous quantification of two metals-iron and manganese in ground water via sequential injection spectrophotometry was reported by utilizing the astilbin crude which extracted from Smilax china L. root. This natural reagent can be found easily in one of those common plants that grown in many tropics and subtropics worldwide. The extraction was done with methanol solvent at room temperature and the solid astilbin was obtained after evaporation recrystallization steps. By dissolving the natural reagent with buffer solution, the mixtures were sequentially aspirated into the holding coil and the reactions with iron(III), manganese(II) and astilbin which took place in the flow cell was monitored by measuring absorbance change at the visible light wavelength. The applicability and simplicity setup which demonstrated in this work indicates that the proposed system and the easily obtained reagent are useful for ground water analysis. [23].

A simple and cost-effective analytical device for determination of ammonia which based on gas pervaporation and diffusion method is proposed [24]. This user-friendly device is consisted of a well microplate as a donor chamber and the butterfly pea flower extract was applied as natural indicator. The

butterfly pea flower which having an intense blue color flower is easily grown in the ASEAN region. In this reported work, the flower extract was immobilized on the paper as the acceptor sensor. The anthocyanin color pigments from this flower extract are strongly influenced by the degree of acidity upon contact which changed the structure of the pigment and displaying color changes accordingly to different pH values. Using the reagent immobilization method on paper allows the microliter-scale solution handling. Such principle can reduce the consumption of reagent and the analyte itself. On the reported work, the sample preparation started by converting the ammonium ion into ammonia by using the solution in alkalinity range. The next procedure is allowing the ammonia gas pervaporation and diffusion across the PTFE membrane into the natural indicator which has been pre-immobilized on the filter paper. The colorimetric change (color appearance) on the paper was then detected by either a smartphone camera or naked eye which offer the quantitative or semi-quantitative analysis, respectively. Such simple paper sensor was successfully applied for real samples in ammonia detection that are widely found in the swine farming wastewater and chemical fertilizer samples. On top of that, the developed ammonia sensor could concurrently perform triplicate runs of 18 samples in just 15 minutes, which in return can generate 72 samples in one-hour timeframe. This proposed device with pervaporation and diffusion method offers on-site assay and green chemical analysis with relatively high throughput while at the same time display the example of cost-efficiency.

Several extracts from natural sources- vegetables and plant-based, namely carrots, leaves and flowers of peacock plants (*Caesalpinia pulcherrima*) were acquired through maceration and boiling procedures by using ethanol and water as solvents. Such extracts are being tested to detect lead(II), the poison heavy metal which mainly found in agriculture or industrial ecosystem. After performing the screening using the reagents which have been prepared, the researchers from Indonesia discovered those which can form complexes between ligand compounds of plant extract

with lead(II), via the observation of color change, were only the flowers of the peacock plant (*Caesalpinia pulcherrima*). As such, the sequential injection analysis (SIA) system for determination of lead(II) in this work by employing the peacock flower extract as the natural reagent was developed. The discovery of using such natural reagent offers the advantages, once again, cost-effective and feasibility due to the easily available plant itself, inexpensive experimental setup, environmentally friendly, and the reagent can form the stable complex with the target lead ion [25].

In the recent published work, phenolic species of the guava leaf extract was used as natural reagent which responsible for chelation with the ferrous metal ions and leads to color formation. Such observation serves as a detection tool for the small and portable paperbased analytical devices (PADs) which can operate without any complicate supporting equipment, thus it is well-suited for point of care applications in places especially where budget is limited. The novel PAD reported here has been fabricated using a home-based printer with the design that able to complete replication test of iron analysis via a single run which in turn offers the versatility of having standards for calibration and duplicate or triplicate of sample analysis; concurrently under one analysis. Calibration plot in the concentration range from 0 to 20 ppm iron(III) was plotted based on the gray color intensity against iron concentration [26].

Natural materials used in chemical analysis

Various natural materials have been proposed for the use in chemical analysis, as represented in Table 2. They serve as platforms in colorimetric assays, in combining with the use of information technology (IT) devices including smartphone, webcam camera, and scanner, or via naked eyes, to perform the images analysis as the mode of detection. Such arrangements offer the benefits, such as easily accessible to local available materials, biodegradable, portable in terms of smartphones, and with simple fabrication (using homebased printer to complete the process). All the listed pros eventually will lead to cost-effective and user-friendly analytical applications.

Table 2. Natural materials used in chemical analysis

Material	Analyte	Reagent	Detection Principle	Detection Device	Advantages	Ref.
Paper	Ammonium	Alkaline solution and butterfly pea flower extract	Gas pervaporatio n, diffusion method and acid –base equilibrium	Smartphone	High sample through put, local available materials, biodegradable materials, portable	[24]
Paper and cotton cloth	Acidity	Red maple leaf extract	Acid-base equilibrium	Smartphone	Local available materials, biodegradable materials, portable	[27]
Paper	Iron, phosphate, water hardness	Iron: 1,10- phenanthroli ne/guava leaf extract phosphate: molybdenu m blue water hardness: Eriochrome black T and EDTA	Iron: complex formation reaction phosphate: complex formation reaction water hardness: complexome tric titration	Smartphone	Replication analysis of a sample within a single run, local available materials, biodegradable materials, portable	[26]
Cotton thread	Anionic surfactant	Methylene blue	Ion association	Smartphone	Local available materials, biodegradable materials, portable	[28]
Cotton	Total phenolic content and antioxidant capacity	Total phenolic content: Folin- ciocalteu antioxidant capacity : 2, 2- diphenyl-1- picryhydraz yl (DPPH)	Redox reaction	Smartphone	Local available materials, biodegradable materials, portable	[29]

Kiwfo et al: INITIATIVES IN UTILIZING NATURAL REAGENTS AND NATURAL MATERIALS FOR CHEMICAL ANALYSIS: TALENT AND CHALLENGE FOR ASEAN IN NEW NORMAL CHEMICAL ANALYSIS

Table 2 (cont'd). N	Natural materials	used in c	chemical	analysis
---------------------	-------------------	-----------	----------	----------

Material	Analyte	Reagent	Detection Principle	Detection Device	Advantages	Ref.
Noodle	Acidity and copper	Acidity: bromothymo l blue/ butterfly pea flower extract copper: starch and potassium iodide	Acidity: acid-base equilibrium copper: redox reaction and complex formation	Webcam camera/ scanner	Local available materials, biodegradable materials, self-indicating platform	[18]
Kaolin clay	Acidity	Phenolphtha lein/ thymol blue/ butterfly pea flower extract	Acid-base titration	Naked eye	Reusable, local available, materials, biodegradable materials	[12]

Natural reagents with synthetic materials

From the green analytical perspective, new analytical tools can be obtained via modification or combination of conventional molecules with synthetic materials and forming a kind of hybrid system. Such tactics set off a promising strategic way in getting synergistic and additive effect achieved from either the natural reagents or the synthetic materials. In the work reported by Rujiwatra et al., [22] miang (Camellia sinensis var. assamica) leaves from northern Thailand are being fermented and blended with silver (Ag) nanoparticles (NPs) which can be applied as colorimetric agents for nitrite determination. The working principle behind this work is depends on employing p-aminobenzoic acid as aiding reagent, and a camera phone as a detector to capture the color changes upon interaction of Ag-miang NPs with the target analyte. As an effort to design the synthesis route become more environmentally benign, crude water extracts of miang leaves, which are abundantly available locally throughout the year in two forms, i.e., non-fermented and fermented miang, were used as natural reagents. Unique color of AgNPs can be obtained via controlling the morphology and sizes of AgNPs itself. Thus, the Ag-miang nanocomposites in turn providing the rapid, simple, and selective tool for the determination of nitrite.

On another reported work by Rujiwatra et al., [30], the team has demonstrated a sustainable way of reducing the waste generation, which in turn offers the potential in minimizing the impact on the environment. Such approach is achieved via the consumption of crude water extract from the ground longan (Dimocarpus longan Lour) seeds industry in northern Thailand, which annually discarded in large amount. This untreated wastewater was being used as the natural reagent, serving as the starting material for the green synthesis of ZnO photocatalyst. By using the simple and rapid microwave synthesis, phytochemicals from longan seeds such as flavonoids, catechins, vitamins, proteins, and sugars can be employed as either the capping or reducing agents, or both at same time which driven the ZnO nanoparticles synthesis. Such green synthesis of ZnO nanoparticles can be employed further for wastewater treatment of the local textile dyeing industry and contributing to the circular economy in the region.

Natural reagents in new normal chemistry education

Covid-19 has deeply affected the education sector globally as it forced many schools and colleges to remain closed temporarily. For most science students, their hands-on experience working as a real scientist in school and university laboratory are limited during this lockdown period, whereas in some region, certain students are inaccessible to fully stocked and supported teaching lab owing to limited funding. Despite such scenarios have created many problems; one can harness it as an opportunity for profound changes in our practical education approach that will align our teaching laboratories with those where we conduct our research, by adopting green chemistry principles to the practice of science education lab work. We live in a golden age of easy-to-access instrumentation thanks to smartphones which can be used as detector in chemical analysis. The difficulties of having to set up a measurement almost from scratch, without technicians to prepare equipment and solutions, could help inculcate a spirit of improvisation. By combining these factors, lab-at-home teaching is ready in action. Some of the examples using natural reagents extracted from plants as alternative low-cost tools in teaching chemical analysis, especially in school laboratories that ought to operate within a stiff budget. In some of the universities in Thailand, the ready-to-use natural reagents were introduced in the academic year of 2019 in science and pharmaceutical science courses. They were also employed in lab-at-home sessions and Eworkshops. One of the examples was using the natural reagent kit for iron assay in water quality testing which adapted from Thai local wisdom using guava leaves. The kit was equipped with dry guava leaf powder that served as natural reagent in the assay, iron(III) standard and buffer solutions, sample vials, 96-wells microplate as reaction platform and a manual. The camera from smartphone was used as the detector to monitor the difference in color intensity of the reaction product which attributed by the reaction in between iron(III) and phenolic compounds in the natural reagent. Students from six different universities have received the kit via postage during the pandemic lock-down period and had benefits from this lab-at-home practice [31]. The initiative of using modern green chemical

analysis in the online classroom setting received great feedback from teachers and learners as the chemicals involved utilized locally available bioresource as the natural reagent for green analysis in chemistry education which supports the sustainable education in Thailand. The method is now being employed by an increasing number of institutions. The team has demonstrated that their experience in conducting this green analytical research can be incorporated into the new normal style of teaching [32].

Challenges in natural reagents application

Natural reagents hold great promise for addressing global humanitarian needs including the goals of sustainable development. The sources of natural reagents and their applications are numerous, yet they are still largely an untapped resource. Use of natural reagents as a source of greener and cheaper reagents for a range of analytical tasks should not be seen as an option just for the developing world, but as something that is equally applicable worldwide. Opportunity should be valued when a natural reagent can be legitimately substituted for a purified or synthetic material, without compromising the viability or quality of the analytical process. Despite not explored here, there is also great potential to utilize food grade or domestic chemicals in a range of analytical procedures, again without prejudice to analytical quality. However, most current developments are not immediately translatable to outside-the-lab scenarios which differ in terms of resource-accessible and resource-limited aspects. Resource-accessible settings include scenarios whereby technology is deployed with essentially unlimited access to resources and experienced personnel. Resource-limited settings refer to situations marked by limited or no access to resources and expertise, which unfortunately most part of ASEAN fall in this category. Such challenges necessitate the time constraints in accessing commercially available chemicals especially when dealing with the long duration of waiting period for procurement. The increasing prices of reagent grade chemicals may restrict the accessibility as well. For instance, when students extract an indicator from plant tissue, and applied in an acid base titration or extracting the acid phosphatase from potatoes and used in the study of

enzyme behavior and kinetics, costing of such experiments can be varied by 30 times as compared to procuring of 50 units acid phosphatase from a major US supplier which costs about \$60 dollar with ca. \$2 for a sack of potatoes. Students studying such fundamental analytical and biochemical behavior would gain an appreciation for the important role of natural product chemistry.

Conclusion

This mini review discusses the simple natural reagents and natural materials which were developed from a century-old local knowledge in the rural area, and through the combining with today technology, such phenomenon contributes to green chemistry, principally in green analytical chemistry aspect, leading to sustainable chemistry which could serves many goals of the United Nation Sustainable Development Goals (UN SDGs). Research of such direction has gained of interest as indicated by the increasing trends in publications. ASEAN is rich in bioresources, there are talent and challenges in development of utilizing natural reagents and natural materials for chemical analysis in new normal chemical analysis. To meet the talent and challenge, works across disciplines with networking would enhance the targets. Apart from analytical scientists, researchers in the other fields including, natural product, computational chemistry, chemometrics, other fields of chemistry, computer scientists etc. should work together. The work would reflect: Local issue- Global impact- Sustainable world.

Acknowledgement

The authors would like to thank the Thailand Research Fund (TRF) Distinguished Research Professor Award Grant (DPG6080002) and indirect support by Alexander von Humboldt Foundation (K. Grupdan); Universiti Malaya for RU SATU Grant ST022-2020 (P.M. Woi); Chiang Mai University (through Center of Excellence on Innovation in Analytical Science and Technology (I-ANALY-S-T), Cluster of Excellence on Biodiversity-based Economics and Society (B.BES-CMU) and postdoctoral fellowship grant (K. Kiwfo).

References

- 1. Anastas, P. and Eghbali, N. (2010). Green chemistry: principles and practice. *Chemical Society Reviews*, 39(1): 301-312.
- 2. Abdussalam-Mohammed, W., Qasem Ali, A. and Errayes, A. O. (2020). Green Chemistry: principles, applications, and disadvantages. *Chemical Methodologies*, 4(4): 408-423.
- 3. OECD (2021). Sustainable chemistry. Access from https://www.oecd.org/chemicalsafety/risk-management/sustainablechemistry.htm [Retrieved 13 September 2021].
- Gamal, M., Naguib, I. A., Panda, D. S. and Abdallah, F. F. (2021). Comparative study of four greenness assessment tools for selection of greenest analytical method for assay of hyoscine N-butyl bromide. *Analytical Methods*, 13(3): 369-380.
- 5. Koel, M. (2016). Do we need green analytical chemistry?. *Green Chemistry*, 18(4): 923-931.
- Chang, F., Zhang, X., Zhan, G., Duan, Y. and Zhang, S. (2021). Review of methods for sustainability assessment of chemical engineering processes. *Industrial & Engineering Chemistry Research*, 60(1): 52-66.
- Chinwong, D., Charaj, P., Panitsupakamol, P., Chankaew, T., Chinwong, S. and Saenjum, C. (2021). Local wisdom of miang lifestyle and community for sustainable development in Northern Thailand. Sustainability, 13: 7381.
- 8. Lim, T. K. (2012). Garcinia dulcis. In edible medicinal and non-medicinal plants: fruits. Springer Netherlands: pp. 35-40.
- 9. Purnama, H., Hidayati, N., Safitri, D. S. and Rahmawati, S. (2017). Effect of initial treatment in the preparation of natural indigo dye from Indigofera tinctoria. *AIP Conference Proceedings*, 1855(1): 020022.
- Settheeworrarit, T., Hartwell, S. K., Lapanatnoppakhun, S., Jakmunee, J., Christian, G. D. and Grudpan, K. (2005). Exploiting guava leaf extract as an alternative natural reagent for flow injection determination of iron. *Talanta*, 68(2): 262-26.

- 11. Grudpan, K., Hartwell, S. K., Wongwilai, W., Grudpan, S. and Lapanantnoppakhun, S. (2011). Exploiting green analytical procedures for acidity and iron assays employing flow analysis with simple natural reagent extracts. *Talanta*, 84(5): 1396-1400.
- 12. Kanna, M., Somnam, S., Wongwilai, W. and Grudpan, K. (2019). Towards green titration: Batchwise titration with reusable solid sorbed indicators. *Analytical Sciences*, 35(3): 347-350.
- 13. Pinyou, P., Kradtap Hartwell, S., Jakmunee, J., Lapanantnoppakhun, S. and Grudpan, K. (2010). Flow Injection determination of iron ions with green tea extracts as a natural chromogenic reagent. *Analytical Sciences*, 26(5): 619-623.
- Siriangkhawut, W., Ponhong, K. and Grudpan, K. (2019). A green colorimetric method using guava leaves extract for quality control of iron content in pharmaceutical formulations. *Malaysian Journal of Analytical Sciences*, 23(4): 595-603.
- 15. Supharoek, S.-A., Ponhong, K. and Grudpan, K. (2017). A green analytical method for benzoyl peroxide determination by a sequential injection spectrophotometry using natural reagent extracts from pumpkin. *Talanta*, 171, 236-241.
- analytical methodology using indian almond (*Terminalia Catappa L.*) leaf extract for Insain, P., Khonyoung, S., Sooksamiti, P., Lapanantnoppakhun, S., Jakmunee, J., Grudpan, K., Zajicek, K. and Kradtap Hartwell, S. (2013). Green determination of aluminum ion in waste water from ceramic factories. *Analytical Sciences*, 29(6): 655-659.
- Siriangkhawut, W., Khanhuathon, Y., Chantiratikul, P., Ponhong, K. and Grudpan, K. (2016). A green sequential injection spectrophotometric approach using natural reagent extracts from heartwood of *Ceasalpinia sappan Linn*. for Determination of Aluminium. *Analytical Sciences*, 32(3): 329-336.
- Kiwfo, K., Wongwilai, W., Paengnakorn, P., Boonmapa, S., Sateanchok, S. and Grudpan, K. (2018). Noodle based analytical devices for cost effective green chemical analysis. *Talanta*, 181: 1-5.

- Siriangkhawut, W., Didpinrum, P., Khanhuathon, Y., Ponhong, K. and Grudpan, K. (2020). Small-scale ultrasound-assisted extraction of phenolics from pomegranate peels and their application as a natural reagent for the colorimetric assay of iron. *Analytical Letters*, 53(6): 887-904.
- Kotchabhakdi, N., Seanjum, C., Kiwfo, K. and Grudpan, K. (2021). A simple extract of Leucaena leucocephala (Lam.) de Wit leaf containing mimosine as a natural color reagent for iron determination. *Microchemical Journal*, 162: 105860.
- 21. Weerasuk, B., Supharoek, S.-a., Grudpan, K. and Ponhong, K. (2021). Exploiting crude betel nut (*Areca catechu* Linn.) extracted solution as a natural reagent with sequential injection spectrophotometry for iron analysis in rice samples. *Journal of the Iranian Chemical Society*, 19: 741-751.
- 22. Tapala, W., Chankaew, C., Grudpan, K. and Rujiwatra, A. (2021). Silver-miang nanocomposites: A green, rapid and simple approach for selective determination of nitrite in water and meat samples. *Microchemical Journal*, 162: 105879.
- Ganranoo, L., Chokchaisiri, R. and Grudpan, K. (2019). Simple simultaneous determination of iron and manganese by sequential injection spectrophotometry using astilbin extracted from Smilax china L. root. *Talanta*, 191: 307-312.
- 24. Jaikang, P., Paengnakorn, P. and Grudpan, K. (2020). Simple colorimetric ammonium assay employing well microplate with gas pervaporation and diffusion for natural indicator immobilized paper sensor via smartphone detection. *Microchemical Journal*, 152: 104283.
- 25. Sabarudin, A. and Indrayani, D. O. (2019). Sequential Injection analysis for determination of lead(II) using extract of Caesalpinia pulcherrima as a natural reagent. IOP Conference Series. Materials Science and Engineering, 546(3): 032027.

- 26. Kiwfo, K., Woi, P. M., Saenjum, C. and Grudpan, K. (2022). New designs of paper based analytical devices (PADs) for completing replication analysis of a sample within a single run by employing smartphone. *Talanta*, 236: 122848.
- 27. Kiwfo, K., Wongwilai, W., Sakai, T. N. T., Murakami, H.P. P., Phojuang, K., Kotchabhakdi, N. and Grudpan, K. (2020). Simple natural material based microfluidic platforms with a smartphone detection employing natural reagent for acidity assay. *Journal Flow Injection Analysis*, 37(1): 9-12.
- 28. Sateanchok, S., Wongwilai, W., Kiwfo, K. and Grudpan, K. (2016). The assay of anionic surfactant employing thread based analytical device with mobile phone. *Journal Flow Injection Analysis*, 33(1): 5-7.
- 29. Sateanchok, S., Wangkarn, S., Saenjum, C. and Grudpan, K. (2018). A cost-effective assay for antioxidant using simple cotton thread combining paper based device with mobile phone detection. *Talanta*, 177: 171-175.

- 30. Chankaew, C., Tapala, W., Grudpan, K. and Rujiwatra, A. (2019). Microwave synthesis of ZnO nanoparticles using longan seeds biowaste and their efficiencies in photocatalytic decolorization of organic dyes. *Environmental Sciene Pollution Research International*, 26(17): 17548-17554.
- 31. Kiwfo, K., Yeerum, C., Issarangkura Na Ayutthaya, P., Kesonkan, K., Suteerapataranon, S., Panitsupakamol, P., Chinwong, D., Paengnakorn, P., Chinwong, S., Kotchabhakdi, N., Saenjum, C., Vongboot, M. and Grudpan, K. (2021). Sustainable Education with local-wisdom based natural reagent for green chemical analysis with a smart device: experiences in Thailand. *Sustainability*, 13(20): 11147.
- 32. Center, C. C. A. R. (2021). CMU researcher creates green innovation in chemical analysis from century-old wisdom of the Fang people. Access from https://www.cmu.ac.th/en/article/7b2719e8-86bc-4d0c-9205-9b4a40647597

Malaysian Journal of Analytical Sciences (MJAS)



Published by Malaysian Analytical Sciences Society

OPTIMISATION OF THE EXTRACTION METHOD OF RED Christia vespertilionis LEAVES TO YIELD BIOACTIVE PHYTOCHEMICAL AS MONITORED BY GAS CHROMATOGRAPHY-MASS SPECTROMETRY

(Pengoptimuman Kaedah Pengekstrakan Pada Daun Merah *Christia vespertilionis* untuk Menentukan Fotokimia Bioaktif Melalui Kromatografi Gas-Spektrometri Jisim)

Izzah Farhah Zambari¹, Sitti Rahma Abdul Hafid², Nur Airina Muhamad^{1*}

¹Institute of Biological Sciences, Faculty of Science, Universiti Malaya, 50603 Kuala Lumpur, Malaysia. ²Nutrition Unit, Product Development and Advisory Services Division, Malaysian Palm Oil Board, 43000 Kajang, Selangor, Malaysia.

*Corresponding author: nurairina@um.edu.my

Received: 31 August 2021; Accepted: 30 December 2021; Published: 28 April 2022

Abstract

Christia vespertilionis (L. f.) Bakh. f. is well-known for treating various contagious diseases. This plant has been recognised among researchers and locals to have anti-inflammatory properties and has thus become popular for treating cancer. Two types of *C. vespertilionis* are acknowledged which are green and red. The green *C. vespertilionis* has been widely studied by many researchers, however just a few have studied the red type. This study was carried out to optimise the extraction method of red *C. vespertilionis* leaves by different extraction techniques (maceration and Soxhlet extraction) and solvents (methanol and ethanol) to yield bioactive phytochemicals using gas chromatography-mass spectrometry (GC-MS). The components were identified through GC-MS via comparisons as guided by the National Institute of Standards and Technology Mass Spectral Library 2011 (NIST 11, version 2.0g). According to the four (4) samples of red *C. vespertilionis* leaves using maceration of methanol (RMM), maceration of ethanol (RME), Soxhlet extraction of methanol (RSM), and Soxhlet extraction of ethanol (RSE), seventy-one (71) bioactive phytochemicals were identified. Eleven (11) major bioactive phytochemicals (abundance of > 4%) were identified namely, acetic acid, butyl ester; 1-butanol, 3-methyl-, acetate; heptanoic acid, propyl ester; hexanoic acid, 3-oxo-, ethyl ester; phenol, 3,5-bis(1,1-dimethylethyl)-; 1-octadecene; 4-O-methylmannose; .alpha.-d-mannofuranoside, methyl; 2-undecene, 9-methyl-, (E)-; n-hexadecanoic acid; and 1-octadecanol. Only seven (7) out of eleven (11) compounds were reported to have biological activities. Among those samples, RSM was the most effective using correlation coefficient between abundance (%) and retention time (minute(s)) with a significant difference at *P* < 0.05.

Keywords: Christia vespertilionis, gas chromatography-mass spectrometry, phytochemicals, maceration, Soxhlet extraction

Abstrak

Christia vespertilionis (L. f.) Bakh. f. dikenali secara meluas dalam merawat pelbagai penyakit berjangkit. Tumbuhan ini diakui di kalangan penyelidik dan penduduk tempatan tentang kelebihannya sebagai salah satu ubat tradisional yang mempunyai sifat

anti-radang serta digunakan secara meluas dalam merawat barah. Terdapat dua jenis *C. vespertilionis* iaitu jenis hijau dan merah. *C. vespertilionis* hijau telah banyak dikaji oleh penyelidik dan hanya sedikit yang dikaji untuk jenis merah. Kajian ini dijalankan untuk mengoptimumkan kaedah pengekstrakan daun *C. vespertilionis* merah dengan teknik pengekstrakan yang berbeza (pengekstrakan maserasi dan Soxhlet) dan pelarut (metanol dan etanol) untuk menentukan fitokimia bioaktif melalui kromatografi gas-spektrometri jisim (GC-MS). Komponen tersebut dikenal pasti melalui GC-MS dengan membuat perbandingan dari data rujukan Institut Piawaian dan Teknologi Nasional 2011 (NIST11-MS, version 2.0g). Berdasarkan 4 sampel daun merah *C. vespertilionis* melalui maserasi metanol (RMM), maserasi etanol (RME), pengekstrakan Soxhlet methanol (RSM) dan pengekstrakan Soxhlet etanol (RSE), tujuh puluh satu (71) sebatian fitokimia dikenal pasti. Sebelas (11) sebatian fitokimia utama (> 4 % kawasan puncak) juga dikenalpasti seperti asid asetik, butil ester; 1-butanol, 3-metil-, asetat; asid heptanoik, propil ester; asid heksanoik, 3-okso-, etil ester; fenol, 3,5-bis (1,1-dimetiletil)-; 1-oktadekena; 4-O-metilmanos; .alpha.-d-manofurosida, metil; 2-undekena, 9-metil-, (E)-; asid n-heksadekanoik dan 1-oktadekanol. Hanya tujuh (7) daripada sebelas (11) sebatian yang dilaporkan mempunyai aktiviti biologi. Di antara sampel tersebut, RSM adalah yang paling berkesan dengan menggunakan pekali korelasi antara kebanyakan (%) dan masa pengekalan (min) dengan perbezaan yang signifikan pada *P* < 0.05.

Kata kunci: Christia vespertilionis, kromatografi gas-spektrometri jisim, fitokimia, maserasi, pengekstrakan Soxhlet

Introduction

Christia vespertilionis (L. f.) Bakh. f. is a family of Fabaceae that is known as butterfly wing because of its shape, which is similar to that of a butterfly wing. This plant possesses the ability to cure several diseases due to it having various biological activities such as anticancer, anti-inflammatory, anti-proliferative and antiplasmodial properties [1, 2, 3]. In Malaysia, C. vespertilionis leaves are consumed by cancer patients and have gained great popularity among Malaysians, including researchers who are keen to explore and discover the real potential of this plant.

C. vespertilionis is known to potentially exhibit various bioactive secondary compounds that can be used in food and pharmaceutical areas [4]. Previous studies revealed the presence of bioactive secondary compounds in C. vespertilionis such as alkaloid, phenol, fatty acid, triterpene and alcohol [2]. The aerial part of C. vespertilionis is revealed to contain corynoxidine and palmitine [2]. C. vespertilionis also possesses great anti-proliferative activities in MTC cells and is excellent in anti-plasmodial activities using aqueous-methanol extracts [1,2]. Other studies showed that C. vespertilionis extract has a high inhibition on cancer cells such as human medullary thyroid carcinoma and human intestinal neuroendocrine tumours [5]. In addition, C. vespertilionis exhibits moderately as an anti-malaria which is against the 3D7 malaria parasite and literally can be used for malaria treatment [6].

Today, people have developed high interest in traditional plants, as a substitute for synthetic drugs. Plant comes from nature and safe to use. It is also low cost and has less negative side effects [7]. However, the World Health Organization (WHO) has noted that inappropriate practices of using traditional plants for treatment can have dangerous effects. Therefore, further study is necessary to ascertain the efficacy and safety of plants for human consumption. While many studies of C. vespertilionis have been conducted, there is no study available on bioactive phytochemicals of red C. vespertilionis leaves using gas chromatographymass spectrometry (GC-MS). GC-MS is one of the techniques that separates individual compounds in the form of a mass spectrum and measurement of the abundance of chromatography [8]. Identification of compounds in GC-MS is achieved by comparing mass spectrum of sample with the reference National Institute of Standards and Technology Mass Spectral Library 2011 (NIST11-MS) based on matching system.

Prior to that, before GC-MS, red *C. vespertilionis* leaves need to undergo extraction to separate the target products from the raw materials. Currently, solvent extraction is widely used in natural plants and herb medicines. Selection of solvent is also a crucial part for solvent extraction. The solvent with a shorter differences of polarity value to the polarity of the solute, is expected to perform better. As regarding the technique of extraction, there are two commonly used methods namely as maceration and Soxhlet extraction.

These methods were most of the time given acceptable results, however Soxhlet can be time-consuming although requires a small amount of sample compared to maceration. Therefore, this research aims to optimise the extraction method of red *C. vespertilionis* leaves in different extraction techniques (maceration and Soxhlet extraction) and solvents (methanol and ethanol) to yield bioactive phytochemicals using GC-MS.

Materials and Methods

Plant material

Red *C. vespertilionis* was collected from Floranika Nursery Sungai Buloh, Selangor (Malaysia), located at a latitude and longitude of 3° 13' 6.7764" N, 101° 34' 18.1704" E, respectively. The voucher specimen was authenticated by Dr Yong Kien Thai from Plant Taxonomy, Rimba Ilmu, University of Malaya. The voucher specimen of red *C. vespertilionis* (KLU 50025) was placed at the herbarium of the University of Malaya, and left to air-dry for 7 to 8 days. Leaves were ground with a blender to obtain coarse powder for extraction and were kept in a closed jar until further use.

Maceration

1 g of dried leaves powder of red *C. vespertilionis* was immersed into a 100 ml of methanol, MeOH (Merck, Germany), and absolute ethanol, EtOH (VWR Chemicals, American) in a 250 ml conical flask, separately. The samples were left in a water bath at 40 °C for 48 hours. The extracts were filtered and evaporated with rotary evaporator at 45 °C until they were concentrated. The extracts were filtered again to remove any solid particles and kept tightly closed in a microcentrifuge tube at 4 °C until further use.

Soxhlet extraction

1 g of dried leaves powder of red *C. vespertilionis* was extracted with 200 ml of MeOH (Merck, Germany), and absolute EtOH (VWR Chemicals, American) using a Soxhlet apparatus, separately. The samples were left in a water bath at 40 °C for 48 hours. The extracts were filtered and evaporated using a rotary evaporator at 45 °C until they were concentrated. The extracts were filtered again to remove any solid particles and kept

tightly closed in a microcentrifuge tube at 4 °C until further use.

Gas chromatography-mass spectrometry analysis

Samples were diluted to 500 ppm with the respective solvents into 1.5 ml vials. The GC-MS analysis was done at the IPPP Central Laboratory Facilities, University Malaya, Kuala Lumpur, Malaysia. Model of GCMS-QP2010 Ultra (Shimadzu, Tokyo, Japan) was used for the GC-MS analysis. This model is a single quadrupole gas chromatograph-mass spectrometer that produces stable and affordable analyses for complex compounds. 0.5 µl of the sample was auto-injected into the system. The system was supplied with a capillary column of RTX5MS with length x diameter of 30.0 m \times 0.25 mm and a 0.25 μ m of thickness. The injection temperature was set to 200 °C which possessed a splitless injection mode. The initial temperature was 50 °C (3 minutes) with an accelerating rate of 10 °C (1 minute) to 300 °C (10 minutes). Helium gas was used with 47.8 cm/second of linear velocity. Electron ionisation (EI) mode at 70 eV with a spectral range of 35 m/z-500 m/z was performed for mass spectra results. The ion source temperature was fixed at 150 °C and the interface temperature was at 230 °C with a solvent cut-off time of 3 minutes. The start time was set at 3.0 minutes and the final time was adjusted at 33 minutes. The total flow programmed was 21.6 ml/minute with a column flow of 1.69 ml/minute. The compounds were determined based interpretation of mass spectrum with standard reference spectral using the National Institute of Standards and Technology Mass Spectral Library 2011 (NIST11) version 2.0g databases.

Statistical analysis

The correlation between abundance and retention time of the sample was determined using GraphPad Prism 8.0.2, where Pearson's correlation coefficient test was conducted and the difference was considered statistically significant when P < 0.05. Chemical structure drawing was applied on the website: https://chemwriter.com/.

Results and Discussion

GC-MS chromatogram and bioactive phytochemicals

GC-MS is important to identify bioactive phytochemicals in a complex compound using a technique of separation in a GC system and measuring on a mass spectrometer that comes with an electron ionisation (EI) ion source. There are two electron ionisation (EI) main spectrum library: main and replicate with a total of 212,961 and 30,932 mass spectra, respectively. NIST11-MS library has a total of 346,757 retention index for 70,835 compounds that were extracted based on column type, column class, data type and program type [9]. Through GC-MS analysis showed seventy-one (71) phytochemicals from four (4) samples that consist of major and minor compounds. Major compounds consisted of an abundance larger than 4% [10] as shown in Table 3. The conditions of the samples were shown in Table 1.

Bioactive phytochemicals of the samples were presented in Table 2 and the GC-MS chromatogram of the abundance of samples shown in Figure 1. GC-MS analysis for RMM resulted in a total of sixteen (16) peaks (according to Figure 1(a) and Table 2). There are three (3) major compounds, namely: acetic acid, butyl ester (81.967%); 1-butanol, 3-methyl-, acetate (4.246%) and 4-O-methylmannose (7.778%). RME resulted in a total of thirty (30) peaks (according to Figure 1(b) and Table 2). There were seven (7) major compounds, namely: 1-butanol, 3-methyl-, acetate (27.414%); heptanoic acid, propyl ester (5.700%);

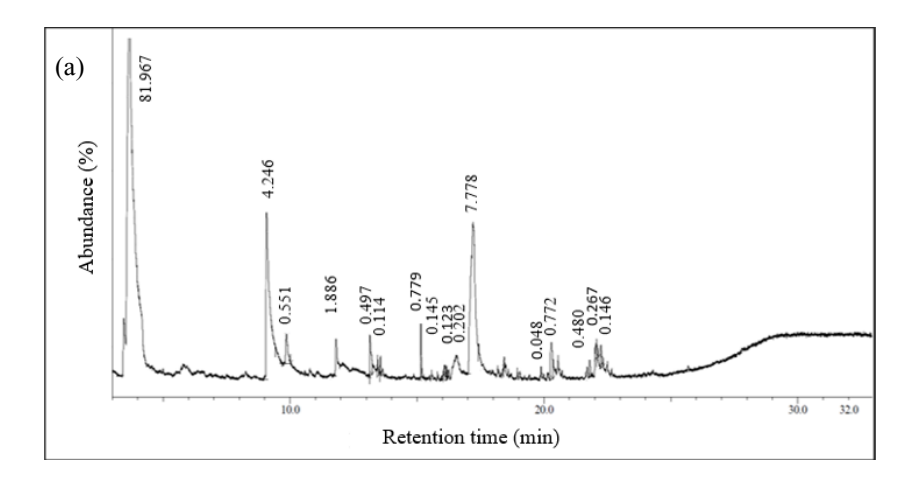
phenol, 3,5-bis(1,1-dimethylethyl)- (6.232%); 1-octadecene (6.079%); .alpha.-d-mannofuranoside, methyl (10.247%); 2-undecene, 9-methyl-, (E)-(5.505%) and 1-octadecanol (4.152%).

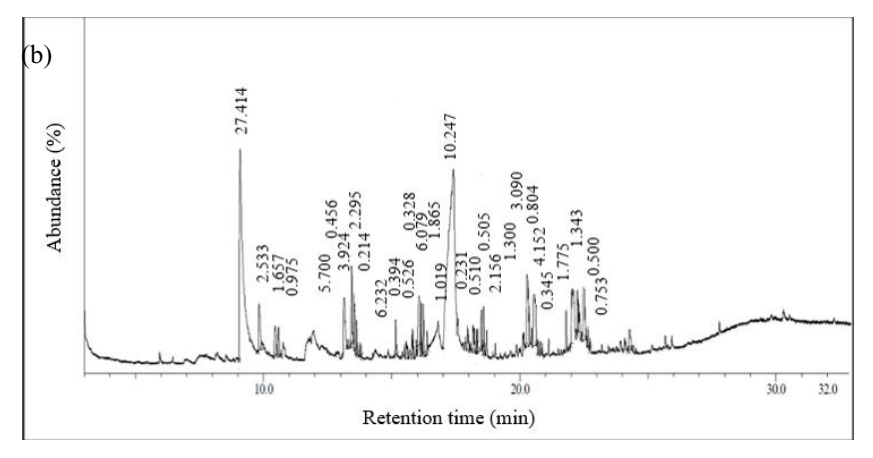
Furthermore, RSM resulted in a total of thirty-three (33) peaks (according to Figure 1(c) and Table 2). Five (5) major compounds were identified, namely: acetic acid, butyl ester (11.655%); 1-butanol, 3-methyl-, acetate (31.037%); hexanoic acid, 3-oxo-, ethyl ester (5.549%); 4-O-methylmannose (21.491%) and n-hexadecanoic acid (4.465%). Lastly, RSE resulted in a total of thirty-seven (37) peaks (according to Figure 1(d) and Table 2). Four (4) major compounds comprised: 1-butanol, 3-methyl-, acetate (6.414%); phenol, 3,5-bis(1,1-dimethylethyl)- (5.950%); 4-O-methylmannose (4.085%) and n-hexadecanoic acid (8.733%).

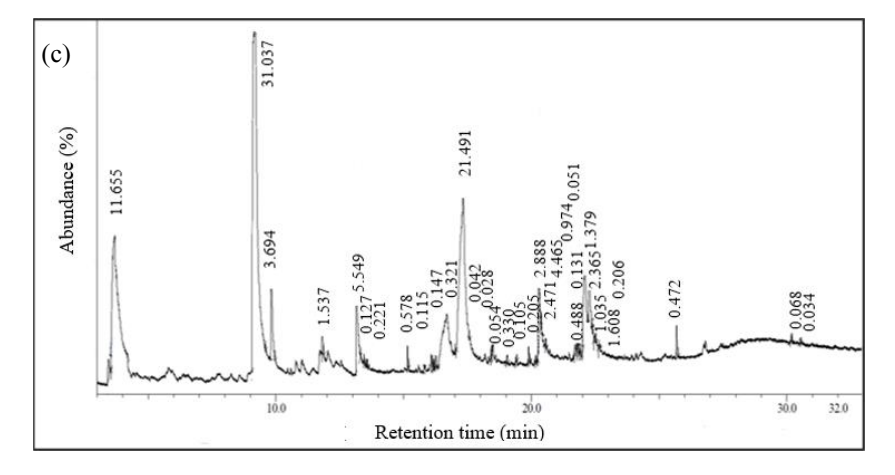
Previous study found other major compounds on red *C. vespertilionis* leaves extract such as 10-undecenoic acid (5.00%), 6-methylheptyl-2-propenoate (4.96%), 2-(2-benzothiazolylthio)-1-(3,5-dimethylpyrazolyl)-ethanone (2.70%), tetrahydro-2-methyl-thiophene (61.77%) and phytol (8.59%) [11]. Another study also found that *C. vespertilionis* leaves methanolic extract exhibited hexadecanoic acid (4.87 %), 9,12,15-octadecatrienoic acid (7.82%), phytol (6.97%), 2-propenoic acid (8.75%) and cyclododecane (7.04%) [12]. These previous study outcomes also can be found in Table 2 such as 9,12,15-octadecatrienoic acid, phytol and hexadecanoic acid.

Table 1. Conditions of samples

Plant	Technique	Solvent	Sample Code	Temperature (°C)	Time (hours)
		MeOH	RMM		
Rad	Maceration	EtOH	RME	40	48
Red C. vespertilionis	Soxhlet extraction	МеОН	RSM	< 64.7	5
	Soxinct extraction	EtOH	RSE	< 78.37	. J







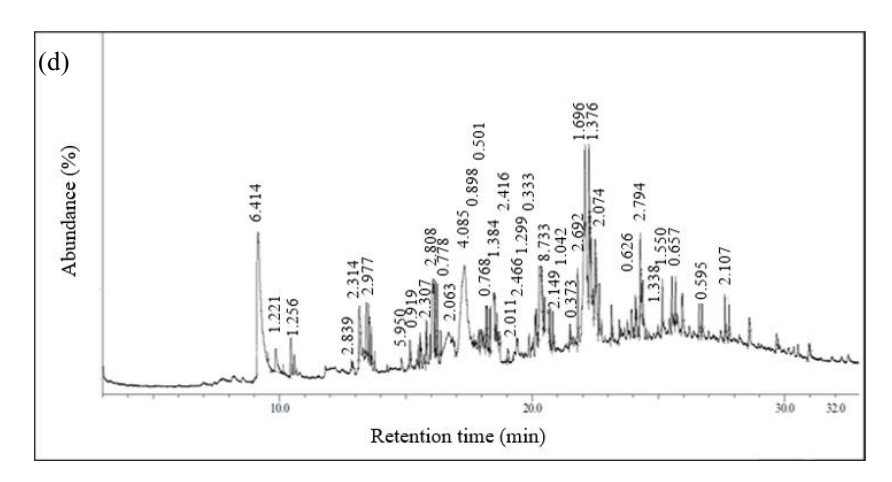


Figure 1. GC-MS chromatogram abundance (%) versus retention time (min) of a) red *C. vespertilionis* methanolic leaves extract in maceration (RMM); b) red *C. vespertilionis* ethanolic leaves extract in maceration (RME); c) red *C. vespertilionis* methanolic leaves extract in Soxhlet extraction (RSM); d) red *C. vespertilionis* ethanolic leaves extract in Soxhlet extraction (RSE)

Table 2. Phytochemicals compounds found in red C. vespertilionis leaves based on abundance and retention time

				Abundance (%)				
	Bioactive Phytochemicals	Retention	Macera	ation	Soxhlet			
		Time (min)	MeOH (RMM)	EtOH (RME)	MeOH (RSM)	EtOH (RSE)		
1	Acetic acid, butyl ester	3.683	81.967	-	11.655	-		
2	1-butanol, 3-methyl-, acetate	9.179	4.246	27.414	31.037	6.414		
3	4H-pyran-4-one, 2,3-dihydro-3,5-dihydroxy-6-methyl-	9.815	0.551	2.533	3.694	1.221		
4	1-dodecene	10.459	-	-	-	1.256		
5	3-tetradecene, (Z)-	10.461	-	1.657	-	-		
6	Dodecane	10.590	-	0.975	-	-		
7	1,3-diisobutyrin, trimethylsilyl	11.817	1.886	-	1.537	-		
8	Heptanoic acid, propyl ester	13.140	0.497	5.700	-	-		
9	Hexanoic acid, 3-oxo-, ethyl ester	13.160	-	0.456	5.549	2.839		
10	1-tridecene	13.446	0.114	3.924	-	-		
11	1-tetradecene	13.449	-	-	0.127	2.314		
12	Tetradecane	13.555	-	2.295	0.221	2.977		
13	Cyclotetradecane	13.775	-	0.214	-	-		
14	Phenol, 3,5-bis(1,1-dimethylethyl)-	15.150	0.779	6.232	0.578	5.950		
15	2-hexyl-1-octanol	15.570	-	0.394	-	-		
16	1-octanol, 2-butyl-	15.801	-	0.526	-	-		
17	1-hexadecene	16.072	0.145	0.328	-	-		

Table 2 (cont'd). Phytochemicals compounds found in red *C. vespertilionis* leaves based on abundance and retention time

		.		Abundance (%)			
	Bioactive Phytochemicals	Retention	Macera			xhlet	
		Time (min)	MeOH (RMM)	EtOH (RME)	MeOH (RSM)	EtOH (RSE)	
18	1-octadecene	16.077	-	6.079	-	0.919	
19	1-heptadecene	16.079	-	-	0.115	2.307	
20	Pentadecane	16.162	0.123	1.865	-	-	
21	Nonadecane	16.167	-	-	-	2.808	
22	Hexadecane	16.170	0.202	-	0.147	-	
23	Dichloroacetic acid, 4-hexadecyl ester	16.253	-	-	-	0.778	
24	2-undecene, 3-methyl-, (Z)-	16.254	-	1.019	-	2.063	
25	1,2-benzenedicarboxylic acid, mono(2-ethylhexyl) ester	16.269	-	-	0.321	-	
26	4-O-methylmannose	17.404	7.778	-	21.491	4.085	
27	.alphad-mannofuranoside, methyl	17.421	-	10.247	-	-	
28	1-hexanol, 5-methyl-2-(1-methylethyl)-	17.958	-	0.231	-	-	
29	Cyclohexane, 2-butyl-1,1,3-trimethyl-	18.173	-	-	-	0.898	
30	1-decanol, 2-hexyl-	18.176	-	0.510	0.042	0.501	
31	1-pentadecene, 2-methyl-	18.214	-	-	-	0.768	
32	Cyclopropane, 1-methyl-1-(1-methylethyl)-2-nonyl-	18.400	-	-	-	1.384	
33	2-undecene, 9-methyl-, (E)-	18.430	-	5.505	-	-	
34	1-heneicosanol	18.431	-	2.156	-	2.416	
35	4,5-heptadien-2-ol, 3,3,6-trimethyl-	18.435	-	-	0.028	-	
36	n-heneicosane	18.501	-	-	-	2.011	
37	Undecane, 3-methylene-	18.594	-	-	-	2.466	
38	Tridecane, 3-methylene-	18.595	-	1.300	-	1.299	
39	2-pentadecanone, 6,10,14-trimethyl-	19.039	-	-	0.054	0.333	
40	1,2-benzenedicarboxylic acid, bis(2-methylpropyl) ester	19.392	-	-	0.330	-	
41	Hexadecanoic acid, methyl ester	19.895	-	-	0.105	-	
42	Heptacosanoic acid, methyl ester	19.900	-	-	0.205	-	
43	1-eicosanol	20.282	-	-	2.888	-	
44	Methyl di-tert-	20.284	-	-	2.471	-	
45	butylhydroxyhydrocinnamate n-hexadecanoic acid	20.291	0.772	3.090	4.465	8.733	
46	Dibutyl phthalate	20.392	0.772	5.050	0.974	-	
47	Octacosanol	20.558	<u>-</u>	0.804	U.J/T	2.149	
48	1-octadecanol	20.561	0.048	4.152	_	2.1 4 9	
49	3-eicosene, (E)-	20.562	0.070	4. 132	0.051	-	

Table 2 (cont'd). Phytochemicals compounds found in red *C. vespertilionis* leaves based on abundance and retention time

		.		Abunda	ance (%)		
	Bioactive Phytochemicals	Retention Time (min)	Macera		Soxhlet		
		Time (min)	MeOH (RMM)	EtOH (RME)	MeOH (RSM)	EtOH (RSE)	
50	Heneicosane, 11-(1-ethylpropyl)-	20.607	-	-	-	1.042	
51	1-docosene	20.816	-	0.345	-	-	
52	1-tetradecanol	21.502	-	-	-	0.373	
53	Phytol	21.798	0.480	1.775	0.488		
54	1,1,1,3,5,7,7,7-octamethyl-3,5-bis- (trimethylsiloxy)-tetrasiloxane	21.808	-	-	-	2.692	
55	Methyl 9-methyltetradecanoate	21.901	-	-	0.131	-	
56	9,12,15-octadecatrienoic acid, methyl ester, (Z,Z,Z)-	22.090	-	-	1.379	-	
57	9,12,15-octadecatrienoic acid, (Z,Z,Z)-	22.092	0.267	1.343	2.365	1.696	
58	Tetradecyl trifluoroacetate	22.253	-	-	1.035	-	
59	Octadecanoic acid	22.255	0.146	0.500	1.608	1.376	
60	1-tetracosanol	22.498	-	-	-	2.074	
61	2,4-pentadien-1-ol, 3-pentyl-, (2Z)-	22.659	-	-	0.206	-	
62	9-(3,3-dimethyloxiran-2-yl)-2,7-dimethylnona-2,6-dien-1-ol	22.660	-	0.753	-	-	
63	1-dodecanol, 2-octyl-	24.091	-	-	-	0.626	
64	Heptasiloxane, hexadecamethyl-	24.377	-	-	-	2.794	
65	Hexacosane	25.151	-	-	-	1.338	
66	Diisooctyl phthalate	25.679	-	-	0.472	1.550	
67	Docosane	25.954	-	-	-	0.657	
68	Eicosane	26.730	-	-	-	0.595	
69	Squalene	27.788	-	-	-	2.107	
70	Cholesta-4,6-dien-3-ol, (3.beta.)-	30.174	-	-	0.068	-	
71	.alphatocopheryl acetate	30.522	-	-	0.034	-	
	Quantity of identified compound		16	30	33	37	

Optimisation of extraction

Correlation was used between abundance and retention time of the sample in GC-MS for all compounds found. Maceration using MeOH (RMM) was significantly high at P < 0.011 (Figure 2). When using EtOH (RME), the significant difference was at P < 0.049. In Soxhlet, the significant difference was high in MeOH (RSM) with P < 0.009 and there was no significant difference in (RSE) which was at P < 0.104. The smaller the P value, the more significant it is. A total of

seventy-one (71) abundance were analysed for each sample. The results indicated that significant difference between abundance and retention time increased when using Soxhlet extraction particularly in MeOH.

Extraction methods using different solvents play an important role to exhibit bioactive phytochemicals. Based on Figure 2, abundances of compounds are exhibited more when using Soxhlet extraction and MeOH. A previous study stated that the polarity of MeOH could be the reason for the high exhibition of

compounds [13]. Other study stated that using MeOH produces high bioactive phytochemicals particularly compounds that cure inflammation which is extracted from the branches of *S. buxifolia* [14]. It was also revealed that MeOH is a solvent that is more effective in extracting secondary metabolite compounds from *M. viridis* than any other plants in the Lamiaceae family [15].

The technique of extraction is also one of the factors that contribute to the effectiveness of bioactive phytochemicals attribution. Based on Figure 2, more compounds were exhibited using Soxhlet extraction as compared to maceration. Soxhlet extraction offered

more efficiency and was less time-consuming as compared to maceration. Other researches obtained similar results in *Nepeta leucophylla* and *Potentilla atrosanguinea* aerial parts when using Soxhlet extraction where it exhibited significantly higher, and attained maximum percentage yields than maceration [4, 16]. Therefore, for red *C. vespertilionis* leaves, Soxhlet extraction obtained highest compounds attribution as compared to the maceration technique. Overall, red *C. vespertilionis* leaves work efficiently using Soxhlet extraction and MeOH as a solvent.

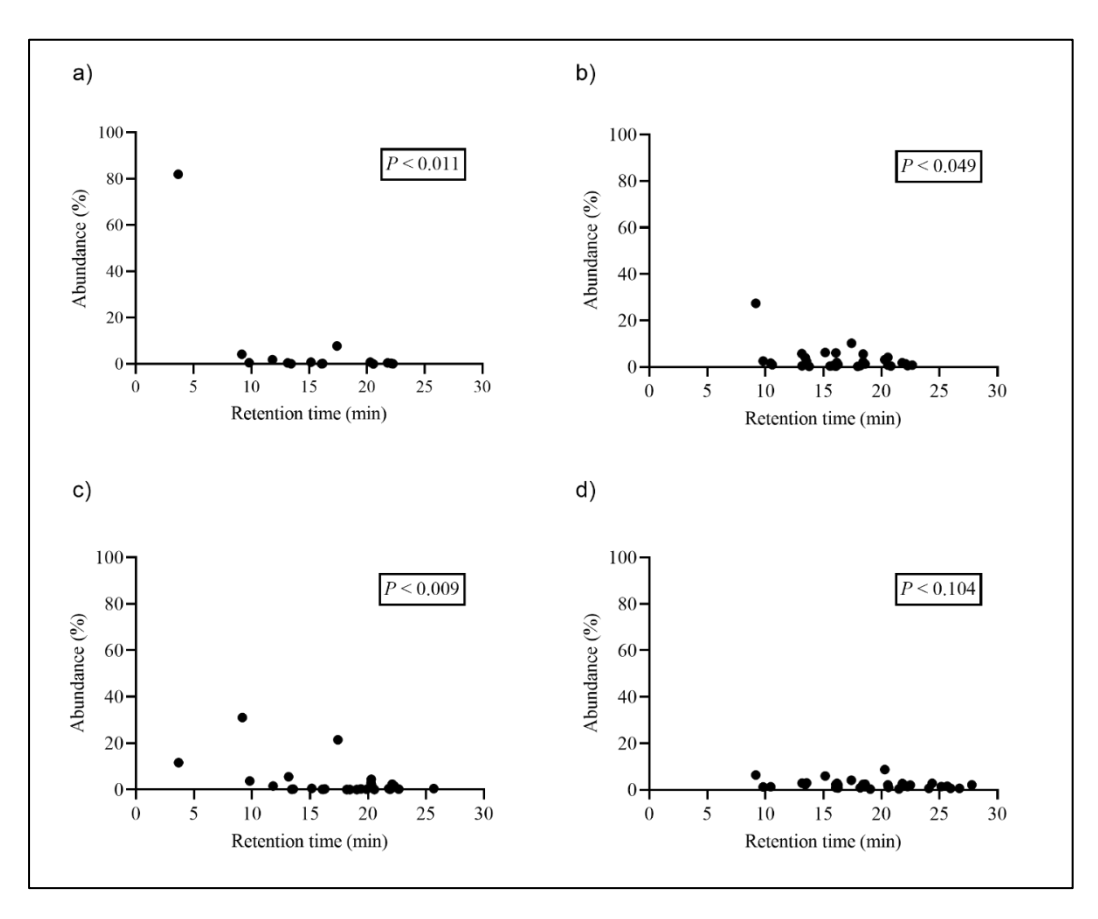


Figure 2. Correlation between abundance (%) versus retention time (min) of a) RMM b) RME c) RSM and d) RSE

Major bioactive phytochemicals

Four (4) samples (RMM, RME, RSM and RSE) of *C. vespertilionis* leaves extract, detected seventy-one (71) bioactive phytochemicals, which consisted of major

and minor compounds using GC-MS, as presented in Table 2. The abundance presented for each sample is shown in Figure 1. Through this analysis, it was found that eleven (11) major compounds achieved higher than

4 % of the abundance from all of samples as presented in Table 3.

The eleven (11) major bioactive phytochemicals were acetic acid, butyl ester (81.967%), 1-butanol, 3-methyl, acetate (31.037%), heptanoic acid, propyl ester (5.700%), hexanoic acid, 3-oxo-, ethyl ester (5.549%), phenol, 3,5-bis(1,1-dimethylethyl)- (6.232%), 1-octadecene (6.079%), 4-O-methylmannose (21.491%), alpha.-d-mannofuranoside, methyl (10.247%), 2-undecene, 9-methyl-, (E)- (5.505 %), n-hexadecanoic acid (8.733%), and 1-octadecanol (4.152%).

The n-hexadecanoic acid and 1-octadecanol possessed anti-inflammatory activities [17,18]. The antimicrobial agent was revealed by 1-butanol, 3-methyl-, acetate, [19]. Ethyl acetate root extract of *C. vespertilionis* showed the highest total phenolic content that is responsible for good anti-inflammatory and antimicrobial properties [20,21]. Meanwhile, 1-octadecene possessed anti-cancer property [22, 23]. Based on the previous study, *C. vespertilionis* extract has viability against various cell lines such as WRL68 (normal liver), CRL 2522 (fibroblast), HepG2 (liver carcinoma), MCF-7 (breast cancer) and HaCaT (keratinocyte) with the IC50 values of 1.93, 1.51, 1.63,

1.74 and 1.22 mg/ml, respectively [24]. Four (4) compounds had antibacterial activities that included n-hexadecanoic acid, 4-O-methylmannose, 1-octadecene and phenol, 3,5-bis(1,1-dimethylethyl)- [23, 24, 26-30].

Most of the compounds possessed anti-oxidants, including 1-octadecanol, n-hexadecanoic acid and 1octadecene [18, 23, 26, 31]. C. vespertilionis ethyl acetate: methanol extract has significantly exhibited the highest DPPH scavenging activity with the IC50 value of 0.549 ± 0.02 mg/mL [32]. Acetic acid, butyl ester was the most abundant compounds that is beneficial as an antifungal and antitumour [33]. C. vespertilionis inhibited tumour growth and increase survival time of mice induced with S180 AND H22 tumour cells [34]. Another known compound was phenol, 3,5-bis(1,1dimethylethyl)- which acts as an antiseptic, disinfectant and flavourant [24, 29]. No biological activity was reported for heptanoic acid, propyl ester; hexanoic acid, 3-oxo-, ethyl ester; .alpha.-d-mannofuranoside, methyl and 2-undecene, 9-methyl-, (E)-. Therefore, only seven (7) out of eleven (11) major compounds were reported their biological activities.

Table 3. Major bioactive phytochemicals of red C. vespertilionis leaves

		Abundance (%)									
	Name of Compound/ Chemical Classes	Rt (Min)	Mace	ration	Sox	hlet	Formula	MW	Structure	Biological Properties	
	Chemical Classes (IVIII		MeOH (RMM)	EtOH (RME)	MeOH (RSM)	EtOH (RSE)	_				
1	Acetic acid, butyl ester (Carboxylic acid ester)	3.683	+ 81.967	-	+ 11.655	-	$C_{16}H_{12}O_2$	116		Antifungal, Antitumor [33]	
2	1-butanol, 3-methyl-, acetate (Carboxylic acid ester)	9.179	+ 4.246	+ 27.414	+ 31.037	+ 6.414	C7H14O2	130		Antimicrobia [19]	
3	Heptanoic acid, propyl ester (fatty acid ester)	13.140	-	+ 5.700	-	-	$C_{10}H_{20}O_2$	172		No activity reported	

Table 3 (cont'd). Major bioactive phytochemicals of red C. vespertilionis leaves

				Abunda	nce (%)					
	Name of Compound/ Chemical Classes	Rt (Min)	Mace			hlet	Formula	MW	Structure	Biological Properties
			MeOH (RMM)	EtOH (RME)	MeOH (RSM)	EtOH (RSE)	_		-	
4	Hexanoic acid, 3-oxo-, ethyl ester (fatty acid ester)	13.160	=	-	+ 5.549	-	C ₈ H ₁₄ O ₃	158		No activity reported
5	Phenol, 3,5-bis(1,1-dimethylethyl)-(phenolic ester)	15.150	-	+ 6.232	-	+ 5.950	C ₁₄ H ₂₂ O	206	↓ H	Antiseptic, disinfectant, flavouring, antibacterial [24,29
6	1-octadecene (Alkene hydrocarbon)	16.077	-	+ 6.079	-	-	C ₁₈ H ₃₆	252		Antibacterialal, antioxidant, anticancer [22, 23, 26]
7	4-O-methylmannose (aliphatic ether alcohol)	17.404	+ 7.778	-	+ 21.491	+ 4.085	$C_7H_{14}O_6$	194	H-O H	Antibacterial [27, 2
3	alphad-mannofuranoside, methyl (methyl mannoside)	17.421	-	+ 10.247	-	-	$C_7H_{14}O_6$	194	HO OH	No activity reported
)	2-undecene, 9-methyl-, (E)-(hydrocarbon)	18.430	-	+ 5.505	-	-	C ₁₂ H ₂₄	168		No activity reported
0	n-hexadecanoic acid (fatty acid)	20.291	-	-	+ 4.465	+ 8.733	C ₁₆ H ₃₂ O ₂	256	, common	Anti-inflammatory, antibacterial, antioxidant [17, 30 31].
1	1-octadecanol (fatty alcohol)	20.561	-	+ 4.152	-	-	C ₁₈ H ₃₈ O	270.5		Anti-inflammatory antioxidant [18].
	Total of major compounds		3	7	5	4				

Conclusion

This study revealed that red *C. vespertilionis* leaves have various bioactive compounds that has high potential to treat diseases. Red *C. vespertilionis* leaves possessed biological activities of anti-inflammatory, antitumour, anticancer, antibacterial, antimicrobial, antioxidant and antifungal properties. The compounds were greatly exhibited from Soxhlet extraction and MeOH as a solvent. Conclusively, this study achieved success in identifying bioactive phytochemicals of red *C. vespertilionis* leaves in different techniques and solvents. Further study needs to be done to isolate bioactive phytochemicals and investigate its biological activities. A comparison to green *C. vespertilionis* needs to be analysed to observe the differences in terms of bioactive phytochemicals and biological activities.

Acknowledgement

The authors are thankful to the University of Malaya for the financial support on the research project through Research University of Faculty Programme Grant Scheme (GPF006B-2018). Appreciation to Institute of Biological Sciences and Infra Analysis Laboratory for the opportunity to use laboratories and infrastructures to perform this research.

References

- Nguyen-Pouplin, J., Tran, H., Phan, T. A., Dolecek, C., Farrar, J., Tran, T. H., Caron, P., Bodo, B. and Grellier, P. (2007). Antimalarial and cytotoxic activities of ethnopharmacologically selected medicinal plants from South Vietnam. Journal Ethnopharmacology, 109: 417-427.
- Hofer, D., Schwach, G., Tabrizi-Wizsy, N.G., Sadjak, A., Sturm, S., Stuppner, H. and Pfragner, R. (2013). *Christia vespertilionis* plant extracts as novel antiproliferative agent against human neuroendocrine tumor cells. *Oncology Reports*, 6(29): 2219-2226.
- Osman, M. S., Ghani, Z. A., Ismail, N. F., Razak, N. A., Jaapar, J. and Ariff, M. A. (2017). Qualitative comparison of active compounds between red and green *Mariposa Christia*

- vespertillonis leaves extracts. AIP Conference Proceedings, 1885(020282): 1-6.
- Sharma, A. and Cannoo, D.S. (2016). Effect of extraction solvents/techniques on polyphenolic contents and antioxidant potential of the aerial parts of *Nepeta leucophylla* and the analysis of their phytoconstituents using RP-HPLC-DAD and GC-MS. *RSC Advance*, 6: 78151-78160.
- 5. Bunawan, H., Bunawan, S. N. and Baharum, S. N. (2015). The red butterfly wing (*Christia vespertilionis*): A promising cancer cure in Malaysia. *International Journal of Pharmacy and Pharmaceutical Sciences* 7(8): 1.
- Mohd Yasin, Z. N., Zakaria, M. A., Nik Mat Zin, N. N. I., Ibrahim, N., Mohamad, F. S., Mat Desa, W. N. S., Sul'ain, M. D. and Abu Bakar, N. (2020). Biological activities and GCMS analysis of the methanolic extract of *Christia vespertilionis* (L.F.) Bakh. F. leaves. *Asian Journal of Medicine and Biomedicine* 4(1): 1-11.
- 7. Haida, Z. and Hakiman, M. (2019). A review of therapeutics potentials of *Clinacanthus nutans* as source for alternative medicines. *Sains Malaysiana*, 48(12): 2683-2691.
- 8. Yusufzai, S. K., Khan, M. S., Hanry, E. L., Rafatullah, M. and Elison, B. (2019). GC-MS analysis of chemical constituents and *in vitro* antioxidant activity of the organic extracts from the stem of *Bridelia stipularis*. *Sains Malaysiana*, 48(5): 999-1009.
- NIST/NIH/EPA Mass Spectral Library, Standard Reference Database 1, NIST 11. (2011). Standard Reference Data Program, National Institute of Standards and Technology. Gaithersburg, MD, USA.
- 10. Abd Rahim, E. N. A., Ismail, A., Omar, M. N., Rahmat, U. N. and Wan Ahmad, W. A. N. (2018). GC-MS analysis of phytochemical compounds in *Syzygium polyanthum* leaves extracted using ultrasound-assisted method. *Pharmacognosy Journal*, 10(1): 110-119.

- Mohd Yasin, Z. N., Zakaria, M. A., Nik Mat Zin, N. N.I., Ibrahim, N., Mohamad, F. S., Mat Desa, W. N. S., Sul'ain, M. D. and Abu Bakar, N. (2020). Biological activities and chemical compositions of the methanol extract of *Christia vespertilionis* leaves. *Asian Journal of Medicine and Biomedicine* 4(2): 78-88.
- 12. Sidek, M. M., Ismail, N. Z., Zain, N. N. M. and Arsad, H. (2019). Cytotoxicity activity of *Christia vespertilionis* leaves extracts against Hela cells and the detection of compounds by GC-MS. *Journal of Biological & Scientific Opinion*, 7(6): 71-78.
- 13. Gami, B. and Parabia, F. (2011). Screening of methanol & acetone extract for antimicrobial activity of some medicinal plants species of Indian folklore. *International Journal Research Pharmaceutical Sciences*, 2(1): 69-75.
- 14. Truong, D-H., Nguyen, D-H., Ta, N.T.A., Bui, A.V., Do, T.H. and Nguyen, H.C. (2019). Evaluation of the use of different solvents for phytochemical constituents, antioxidants, and in vitro anti-inflammatory activities of *Severinia buxifolia*. *Journal of Food Quality*, 2019: 8178294.
- Karunaratne, U. K. P. R. and Karunaratne, M. M. S. C. (2012). Evaluation of methanol, ethanol and acetone extracts of four plant species as repellents against *Callosobruchus maculatus* (Fab.). *Vidyodaya Journal of Science* 17: 1-8.
- Kalia, K., Sharma, K., Singh, H.P. and Singh, B. (2008). Effects of extraction methods on phenolic contents and antioxidant activity in aerial parts of *Potentilla atrosanguinea* L. and quantification of its phenolic constituents by RP-HPLC. *Journal Agriculture Food Chemistry*, 56: 10129-10134.
- Aparna, V., Dileep, K. V., Mandal, P. K., Karthe, P., Sadasivan, C. and Haridas, M. (2012).
 Antiinflammatory property of n-hexadecanoic acid: Structural evidence and kinetic assessment.
 Chemical Biology Drug Design, 80(3): 434-439.
- 18. Singab, A. N., El-Taher, E. M. M., Elgindi, M. R and Kassem, M-S. (2015). *Phoenix roebelenii* O'Brien DNA profiling, bioactive constituents, antioxidant and hepatoprotective activities. *Asian Pacific Journal Tropical Disease*, 5(7): 552-558.

- Mitchell, A. M., Strobel, G. A., Moore, E., Robison, R. and Sears, J. (2010). Volatile antimicrobials from *Muscodor crispans*, A novel endophytic fungus. *Microbiology*, 156: 270-277.
- 20. Chew, Y. L., Chan, E. W. L., Tan, P. L., Lim, Y. Y., Stanslas, J. and Goh, J. K. (2011). Assessment of phytochemical content, polyphenolic composition, antioxidant and antibacterial activities of Leguminosae medicinal plants in Peninsular Malaysia. *BMC complementary and Alternative Medicine*, 11(1): 12.
- Lee, J. J., Yazan, L. S., Kassim, N. K., Che Abdullah, C. A., Esa, N., Lim, P. C. and Tan, D.C. (2020). Cytotoxic activity of *Christia vespertilionis* root and leaf extracts and fractions against breast cancer cell lines. *Molecules*, 25(2610):1-18.
- 22. Lee, Y. S., Kang, M. H., Cho, S. Y. and Jeong, C. S. (2007). Effects of constituents of *Amomum xanthioides* on gastritis in rats and on growth of gastric cancer cells. *Achieve Pharmaceutical Research*, 30(4): 436-443.
- Belakhdar, G., Benjouad, A. and Abdennebi, E.H. (2015). Determination of some bioactive chemical constituents from *Thesium humile* Vahl. *Journal Materials Environmental Sciences*, 6(10): 2778-2783.
- 24. Duke J. (2002). American Agricultural Research Service-Phytochemical & Ethnobotanical Database. Available at: http://www.ars-grin.gov/duke/index.html [accessed on 09 December 2019].
- 25. Mutalib, N. A. and Latip, N. A. (2019). Synergistic interactions between *Christia vespertilionis* leaves extract and chemotherapy drug cyclophosphamide on WRL-68 Cell Line. Asian Journal of Pharmaceutical Research and Development, 7(3): 109-113.
- 26. Mishra, P. M. and Sree, A. (2007). Antibacterial activity and GCMS analysis of the extract of leaves of *Finlaysonia obovata* (a mangrove plant). *Asian Journal Plant Sciences*, 6(1): 168-172.

- Kumar, P. R. Z. A. and Bhaskar, A. (2012). Phytochemical evaluation by GC-MS and *in vitro* antioxidant activity of *Punica granatum* fruit rind extract. *Journal of Chemical and Pharmaceutical Research*, 4(6): 2869-2873.
- Suman, T., Chakkaravarthi, K. and Elangomathavan, R. (2013). Phyto-chemical profiling of *Cleistanthus collinus* leaf extracts using GC-MS analysis. *Research Journal Pharmaceutical and Technology*, 6(11): 1173-1177.
- 29. Igwe, K. K., Okafor, P. N. and Ijeh, I. I. (2015). GC-MS analysis of phytocomponents in *Vernonia amygdalina*. *Del* leaves and its contractile potential in mammary tissue in female albino Wistar rats. *Journal of Agriculture and Veterinary Science*, 8(11): 25-30.
- 30. Johannes, E., Litaay, M. and Syahribulan. (2016). The bioactivity of hexadecanoic acid compound isolated from hydroid *Aglaophenia cupressina* lamoureoux as antibacterial agent against *Salmonella* typhi. *International Journal Biological Medicinal Research*, 7(2): 5469-5472.
- 31. Gavamukulya, Y., Abou-Elella, F., Wamunyokoli, F. and El-Shemy, H. A. (2015). GC-MS analysis

- of bioactive phytochemicals present in ethanolic extracts of leaves of *Annona muricata*: A further evidence for its medicinal diversity. *Pharmacognosy Journal*, 7(5): 300-304.
- 32. Shukri, N. S. S. M., Perumal, V., Balan, T., Murugesu, S., Khatib, A., Saleh, M. S. M, Hin, L.W., Darus, K. A., Zailani, I.A. and Zahidi, F. A. H. M. (2019). The screening of antioxidant activities and FTIR analysis of *Christia vespertilionis* leaves extracts. *International Journal of Research in Pharmaceutical Sciences*, 10(1): 1713.
- 33. Guo, L., Wu, J., Han, T., Cao, T., Rahman, K. and Qin, L. (2008). Chemical composition, antifungal and antitumor properties of ether extracts of *Scapania verrucosa* Heeg. and its endophytic fungus *Chaetomium fusiforme*. *Molecules*, 13: 2114-2125.
- 34. Wu, X. Y., Tang, A. C. and Lu, Q. Y. (2012). Study on antitumor effect of the extract from *Christia vespertilionis in vivo. Chinese Journal of Experimental Traditional Medical Formulae*, 8: 202-204.

Malaysian Journal of Analytical Sciences (MJAS) Published by Malaysian Analytical Sciences Society



ESSENTIAL MINERALS AND HEAVY METALS ANALYSIS OF PENANG ASSAM LAKSA USING ATOMIC ABSORPTION SPECTROMETRY, FLOW INJECTION MERCURY SYSTEM, AND INDUCTIVELY COUPLED PLASMA OPTICAL EMISSION SPECTROMETRY

(Analisis Mineral Penting dan Logam Berat Asam Laksa Pulau Pinang Menggunakan Spektrometri Penyerapan Atom dn Spektrometri Pancaran Optik Induktif Gabungan Plasma)

Phang Hui Lee^{1,2}, Koo Pooi Ling², Lim Gin Keat^{2*}, Oo Chuan Wei², Tan Kean Chye³

¹Jabatan Perubatan Forensik. Hospital Pulau Pinang. 1, Jalan Tull, George Town, 10450 George Town, Pulau Pinang, Malaysia ²School of Chemical Sciences, Universiti Sains Malaysia, 11800 USM, Penang, Malaysia ³Department of Family Medicine, RCSI and UCD Malaysia Campus, 4, Jalan Sepoy Lines, 10450 George Town, Pulau Pinang, Malaysia

*Corresponding author: limgk@usm.my

Received: 9 November 2021; Accepted: 10 February 2022; Published: 28 April 2022

Abstract

Penang Assam Laksa is a sour, fish-based soup popular in Malaysian street food. The content of heavy metals (Cd, Hg, and Pb) as well as essential minerals (Fe, Ca, Na, and K) in ready-to-eat Penang Assam Laksa food samples collected from five stalls over three different days was determined using flame atomic absorption spectrometry (FAAS), a Flow Injection Mercury System (FIMS), and inductively coupled plasma optical emission spectrometry (ICP-OES) after a wet-digestion procedure. Statistical analyses such as Student's t-test and an inter-day precision study were conducted on the obtained results. The wet-digestion procedure was found to be effective, with recoveries above 85%. Meanwhile, an inconsistency in element content was observed for food samples collected on different days. Based on Student's t-test, both FAAS and ICP-OES were suitable for detecting and quantifying heavy metals and essential minerals in the food samples.

Keywords: Penang Assam Laksa, heavy metal, essential minerals, street food

Abstrak

Asam Laksa Pulau Pinang adalah sup masam yang berasaskan ikan. Kandungan logam berat (Cd, Hg, Pb) serta mineral penting (Fe, Ca, Na, K) dalam Asam Laksa Pulau Pinang (makanan sedia dimakan) yang dikumpul dari lima gerai terpilih pada tiga hari berbeza telah ditentukan menggunakan FAAS (spektrometri penyerapan atom nyalaan), FIMS (sistem merkuri suntikan aliran) dan ICP-OES (spektrometri pancaran optik induktif gabungan plasma) selepas prosedur pencernaan basah. Analisis statistik seperti *Ujian-t* pelajar dan kajian ketepatan antara hari telah dijalankan ke atas keputusan yang diperolehi. Prosedur pencernaan Phang et al: ESSENTIAL MINERALS AND HEAVY METALS ANALYSIS OF PENANG ASSAM LAKSA USING ATOMIC ABSORPTION SPECTROMETRY, FLOW INJECTION MERCURY SYSTEM, AND INDUCTIVELY COUPLED PLASMA OPTICAL EMISSION SPECTROMETRY

basah didapati merupakan kaedah yang berkesan dalam mencerna sampel makanan dengan pemulihan lebih daripada 85%. Sementara itu, ketidakselarasan kandungan unsur diperhatikan daripada sampel makanan yang dikumpul pada hari yang berbeza. Berdasarkan *Ujian-t* pelajar, kedua-dua FAAS dan ICP-OES sesuai untuk pengesanan dan penentuan logam berat dan mineral penting dalam sampel makanan.

Kata kunci: Asam Laksa Pulau Pinang, logam berat, mineral penting, makanan jalanan

Introduction

Food is a fundamental requirement for sustaining life. The rapid acceleration of the human population has led to the creation of various kinds of foods, including street foods, which are defined as ready-to-eat foods and beverages that are prepared and/or sold by street vendors [1]. Generally, street foods are rich in macromicro-nutrients. Macro-nutrients carbohydrates, fats, and proteins are needed in relatively large amounts, as they provide energy to the human body, while micro-nutrients in food comprise vitamins and inorganic minerals such as calcium (Ca), potassium (K), and iron (Fe). Essential minerals are present in small quantities but play significant roles in human biology, especially as catalysts for enzymatic activities [2-5]. For example, sodium (Na) and K are common electrolytes that drive the transmission of signals along nerves as well as maintain water balance, while Fe is a principal component in hemoglobin production, which is responsible for oxygen transportation [6-8] in blood. Either inadequate or excessive intake of essential minerals will adversely affect human health. Hypocalcemia, also known as low blood calcium levels may result in tetany, whereas hypercalcemia may lead to kidney-stone formation (nephrolithiasis) [7].

Street foods can readily become contaminated with heavy metals such as cadmium (Cd), lead (Pb), and mercury (Hg) due to environmental pollution, which is all the more common in modern times [9]. Heavy metals are substances that occur naturally and are often present in the environment at trace levels [10]. Heavy metals have caused widespread concern due to their tendency to accumulate in selective human tissues (liver, brain, and kidney) and not decay over time. These characteristics will eventually lead to various types of disorders, such as peripheral neuropathy and different cancers9. Previous studies have shown that

humans are exposed to heavy metals via the ingestion of contaminated food and beverages [3, 9, 10]. Hence, is has become necessary to perform food analysis in order to assess food quality and safety.

Food analysis is a challenging task in analytical chemistry; the presence of heavy metals and essential minerals in trace quantities, as well as the complex nature of food matrices, have only increased its difficulty. Proper and efficient sample preparation followed by a highly sensitive instrumental analysis is often required to obtain quality element-content data in food [11]. There are numerous types of sample digestion methods that have been successfully employed in determining element content in diverse samples. Dry-ashing and wet-digestion procedures are well established methods, and their efficiency has been reported in previous studies. Dry ashing is known to be effective in digesting organic materials in food samples, but it is time-consuming and prone to losses due to volatilization and/or retention problems [9, 12, 13]. Wet digestion is relatively simple, rapid, and inexpensive compared to dry ashing. This procedure benefits from small sample quantities and greater flexibility, as the sample weight and digestion conditions can be changed accordingly.

In recent years, numerous analytical techniques have been developed for determining element content in food samples. These techniques include neutron activation analysis (NAA), voltammetry, atomic absorption spectrometry (AAS), inductively coupled plasma optical emission spectrometry (ICP-OES), and inductively coupled plasma mass spectrometry (ICP-MS) [4, 9, 10, 14, 15, 16]. Among these techniques, AAS (including flame atomic absorption spectrometry, FAAS, and graphite furnace atomic absorption spectrometry, GFAAS), ICP-OES, and ICP-MS [4, 15] are well established as mainstays in food analysis

because of their rapidity and effectiveness in detecting and quantifying elements in samples at extremely low concentrations [4, 10, 11, 16]. In addition, flow injection analysis (FIA) using devices such as the Flow Injection Mercury System (FIMS) is also employed, as it combines the advantages of flow injection and atomic absorption measurement into a compact Hg analyzer [17].

In Malaysia, Penang is well known as a food paradise due to its wide variety of street foods. These foods reflect the multicultural makeup of the state, which has citizens of Chinese, Malay, and Indian descent. One of the most famous Penang street foods is Penang Assam Laksa, which is a broth made of shredded fish (Kembung fish or mackerel) and finely sliced vegetables [cucumber, onions, red chilies, pineapples, lettuce, fresh mint, and torch ginger (in Malay: bunga kantan)][18]. An increased interest in street foods has led to public concern about their safety and quality, owing to their socioeconomic importance as well as nutritional value. However, there is a paucity of proper studies and data on this kind of fresh, ready-to-eat food, as most studies focus on raw, uncooked foods or commercialized food products. Thus, there is a need to perform a proper scientific study to obtain a general picture of the nutritional content of Penang Assam Laksa. Such information can help prove the safety of the food and increase confidence among consumers.

This study mainly aimed to detect the essential minerals (Ca, Fe, Na, and K) and heavy metals (Hg, Cd, and Pb) in Penang Assam Laksa by using FAAS, FIMS, and ICP-OES. The safety of the food was further assessed by comparing the element content obtained from collected food samples to the permissible levels stated in Malaysia Food Act 1983 and Food Regulations 1985 [19], as well as the recommended dietary allowance (RDA) from U.S. Dietary Guideline 2010 [18]. Finally, a simple comparative study was performed to evaluate the agreement between the results provided by these two different groups of techniques.

Materials and Methods

Chemicals and Standards

Concentrated nitric acid (HNO₃, 65%, Merck, USA) and hydrogen peroxide (H₂O₂, 35%, Hmbg, India) were purchased from local chemical suppliers. Commercial 1000-ppm standard stock solutions (Perkin Elmer Laboratory preparation, USA) containing elements of interest were used to prepare working standard solutions, all of which were freshly prepared prior to analysis. Ultrapure water was produced by a Milli-Q System (Millipore, Bedford, MA, USA) and used for solution preparation as well as sample digestion.

Sample Collection and Handling

Fifteen food samples (Penang Assam Laksa) were purchased from five selected areas throughout Penang Island on three different days, all of which were cooked and ready-to-eat. Upon purchasing, the solid ingredients (sliced vegetables and noodles) and the broth of the samples were packed separately with leak-proof nylon bags. During sample preparation, the solid ingredients were soaked in the broth and left for 20 min. After that, the mixture was filtered, and the broth was collected for further treatment.

Wet Digestion of Samples

The wet-digestion procedure performed in this work was adopted from a study by Salau and Hassan [5]. Three 5-mL aliquots of previously filtered broth samples were transferred to three conical flasks. Ten mL of HNO $_3$ was added to the sample and left overnight (24 h) in a fume hood. The following day, further digestion was carried out by adding a mixture of HNO $_3$ and H $_2$ O $_2$. Details about the procedure and its steps are summarized in Table 1. The solutions were filtered with white filter papers (WHATMAN, qualitative filter papers, 125-mm diameter) and then refiltered with a syringe filter. Then, the filtered solutions were diluted with ultrapure water to 100 mL and transferred into polyethylene sample bottles and kept in a refrigerator.

Ultrapure water HNO₃ added H₂O₂ added Heating Time Step added (mL) (mL) (mL) (°C) (min) 1 10 Overnight 2 5 2 30 100 3 4 10 100 30 4 30 5 2 100 30

10

Table 1. Wet digestion procedure for samples

Recovery Study

5

Standard solutions containing the elements of interest were prepared at three different concentrations: 6.00, 8.00, and 10.00 ppm, except for those of Hg, which were prepared at 0.10, 0.15, and 0.20 ppm. Five-mL samples of the prepared food were spiked with 0.5 mL of the standard solutions. The spiked samples were prepared in triplicate at each concentration. Simultaneously, unspiked blank solutions containing 5 mL of food sample and 0.5 mL of ultrapure water were prepared as well. These spiked and unspiked samples then went through the digestion procedure as described above before subsequent instrumental analysis.

30

Instrumental Analysis

A Perkin Elmer AAnalyst 400, a Perkin Elmer FIMS 100, and a Perkin Elmer Optima 8000 were used for FASS, FIMS, and ICP-OES analyses of the target elements, respectively. All the instruments were equipped with WinLab 32 computer software for data acquisition. For every target element, calibration was performed prior to instrumental analysis. The calibration curves for all elements were plotted as absorbance intensity against concentration in ppm (with the exception of ppb for Hg analysis) using Microsoft Excel, and correlation coefficients, R², for all curves were determined. Working standard solutions of certain concentrations were prepared accordingly by diluting the 1000-ppm standard stock solutions. The standard stock solutions were drawn by using micropipette. Samples collected on Days 1 and 2 were run on instruments at the same time, while samples

collected on Day 3 were run separately with a new calibration cycle. The concentrations of the working standards for each element remained unchanged for the first and second runs.

20

100

Statistical Analysis

2

Student's t-test was performed by means of Excel in order to determine whether the two methods (FAAS/FIMS and ICP-OES) gave significantly different results. Meanwhile, an inter-day precision study was conducted for the samples collected on different days by expressing the repeatability in terms of relative standard deviation (RSD).

Results and Discussion Recovery and Efficiency of Wet Digestion **Procedure**

The accuracy and efficiency of the wet digestion procedure performed on the spiked samples at three different concentration levels were evaluated in triplicate. The average recovery (%) of all target elements is presented in Table 2, which shows that the recoveries for all the target elements were satisfactory more than 85% of the elements were recovered from the spiked samples. In FAAS, the highest digestion efficiency was achieved for Cd at 96.1%, whereas Pb exhibited the lowest efficiency at 86.3%. In contrast, Hg exhibited the highest average recovery percentage in ICP-OES (94.5%). Based on this recovery assay, the efficiency of the digestion procedure used in this work was confirmed.

Table 2.	Average recovery	v for all	targeted	elements

Elements	Average Recovery (%)				
	FAAS/FIMS	ICP-OES			
Hg	91.6	94.5			
Cd	96.1	85.8			
Pb	86.3	91.7			
Fe	94.0	90.3			
Ca	91.7	91.1			
Na	93.5	93.5			
K	94.1	86.9			

Instrumental Analysis of Studied Foods

Linearity of Analysis: Every elemental analysis carried out via FAAS, FIMS, and ICP-OES consisted of two calibration cycles, as the food samples were run in two batches. All the calibration curves exhibited linearity, with R^2 values greater than 0.99, except for Hg via ICP-OES, as well as K and Na via FAAS, which gave slightly lower R^2 values. As an overall observation, all the calibration curves demonstrated a linear response within a particular range. It was noted that both calibration cycles for the elements generated different regression equations and R^2 values, but these differences were quite small and negligible, as they did not possess any significant meaning.

Detection of Essential Minerals in Studied Food Samples: The mineral-content ranges of the food samples were compared to the RDA for minerals according to U.S. Dietary Guideline 2010, as shown in Table 3. Since the RDA values stated in the guideline are in units of mg/day, for ease of comparison, an assumption was made wherein the mineral content presented in the Tables 3 and 4 under this section is normalized as that in 250-mL samples. Adequate Fe intake is crucial to prevent anaemia [2]. It was noted that the order of Fe content for each sample collected at different locations showed the same pattern for the three different collection days. The highest detected Fe content was 1.98 mg/L by FAAS and 1.51 mg/L ICP-OES. According to U.S. Dietary Guideline 2010 [8], adult females and males are recommended to take

approximately 18.00 mg and 8.00 mg of Fe per day, respectively. In general, all the studied food samples were considered to have adequate levels of Fe for an adult male older than 19 years. However, the Fe content was insufficient for an adult female because they experience the Fe losses associated with physiological processes (menstruation) [8].

Calcium is the most abundant cation in the human body. According to U.S. Dietary Guideline 2010 [8], an adult is recommended to take 1.00×10^3 mg of Ca daily as an upper intake level (UL). From Table 3, the highest detected Ca content was 3.25×10^2 mg/L (FAAS) and 2.61×10^2 mg/L (ICP-OES). The high Ca content in the studied food samples was most probably due to mackerel, the main ingredient of the food samples, since it was reported in a previous study that mackerel contains high levels of Ca, ranging from 1.60×10^3 to 1.80×10^3 mg/L [20]. All the studied food samples were considered to have adequate Ca levels for an adult older than 19 years.

For Na, adequate intake (AI) levels are used instead of RDA, since the latter could not be determined. The determined Na concentration of all the studied food samples approached the AI level and was less than the UL. The highest Na levels were 1.23×10^3 mg/L (FAAS) and 1.44×10^3 mg/L (ICP-OES). The Na content in the studied food samples was most likely due to salt (sodium chloride), which is added to enhance taste. Based on the obtained results, the

Phang et al: ESSENTIAL MINERALS AND HEAVY METALS ANALYSIS OF PENANG ASSAM LAKSA USING ATOMIC ABSORPTION SPECTROMETRY, FLOW INJECTION MERCURY SYSTEM, AND INDUCTIVELY COUPLED PLASMA OPTICAL EMISSION SPECTROMETRY

studied food samples were considered to have adequate Na levels. However, the consumption of Penang Assam Laksa is advised to be reduced in order to avoid excessive Na intake.

Potassium is important for building muscle as well as metabolizing proteins and carbohydrates [8]. The highest concentration of K was detected at 1.52×10^3

mg/L and 6.67×10^2 mg/L for FAAS and ICP-OES, respectively. The AI level for K established by U.S. Dietary Guideline 2010 is approximately 4.70×10^3 mg/day; all the studied samples were considered to have sufficient K, most likely because of the mackerel - the main ingredient of the broth [21].

Table 3. Ranges of Fe, Ca, Na, and K contents in the studied food samples detected by FAAS and ICP-OES (assuming 250 mL of broth per serving unit)

Element	O	ntration Detected g/L)	Recommended Dietary Allowance		
	FAAS	ICP-OES	-		
Fe	5.48 × 10 ⁻¹ to 1.98	5.57 × 10 ⁻¹ to 1.51	18.00 mg per day (female above 19 y.o.) 8.00 mg per day (male above 19 y.o.)		
Ca	3.96×10 to 3.25×10^2	1.18×10^2 to 2.61×10^2	1.00×10^3 mg per day (male and female above 19 y.o.) Adequate Intakes		
Na	7.32×10^2 to 1.23×10^3	$6.87 \times 10^2 \text{ to}$ 1.44×10^3	1.50×10^3 mg per day (male and female above 19 y.o.)		
K	1.92×10^2 to 1.52×10^3	1.44×10^2 to 6.67×10^2	4.70×10^3 mg per day (male and female above 19 y.o.)		

^{*}All values are expressed as a mean in ppm or mg/L

Detection of Heavy-Metal Contents in Studied Food Samples: The concentration of heavy metals detected in all food samples was tabulated and compared to the permissible levels stated in Malaysia Food Act 1983 and Food Regulations 1985 [19], as seen in Table 4.

Cadmium affects cell proliferation, differentiation, and apoptosis; it also inhibits both cellular respiration and oxidative phosphorylation at low concentrations [22]. In this study, Cd was not detectable via ICP-OES for all samples, while it was detectable via FAAS. This observation does not lead to the conclusion that the samples were free of Cd. Instead, the results only suggest that Cd was undetectable in ICP-OES, as FAAS was able to give readings. Basically, the Cd

content in the studied food samples ranged from 7.80×10^{-2} to 2.85×10^{-1} mg/L (in FAAS determination). This concentration level was relatively low and did not exceed the permissible level stated in Malaysia Food Act 1983 and Food Regulations 1985 [19], which is 1.00 mg/L.

The FIMS used in this study was a dedicated Hg system coupled with a high-sensitivity Hg detector [17]. This instrument was designed purposely for Hg quantification with an extremely low detection limit (as suggested by the user manual of the instrument) of less than 5.00×10^{-6} mg/L, as compared to the much higher 5.10×10^{-3} mg/L for ICP-OES. In other words, ICP-OES is not sensitive enough to detect Hg at trace

^{*} y.o. = years old

^{*} Recommended dietary allowance and adequate intakes (Source: US DA & US DHS 2010)[8]

levels; thus, it yielded no readings or measurements in this study. The Hg detected in most of the food samples was present at trace amounts ranging from 9.00×10^{-4} to 8.10×10^{-3} mg/L, lower than the permissible level of 5.00×10^{-2} mg/L as stated in Malaysian Food Act 1985 [12]. Meanwhile, Hg was undetectable in a few samples.

The Pb levels in the food samples were significantly higher than those of Cd and Hg. According to Malaysia Food Act 1983 and Food Regulations 1985 [19], the

permissible level of Pb in food is 2.00 mg/L. Unfortunately, the majority of the samples contained excessive Pb levels, which possibly originated from the raw ingredients used to prepare the foods, such as fish, spices, and vegetables. This finding is of great concern, as Pb was classified as a "human carcinogen" by International Agency for Research on Cancer (IARC) in 1993 [23]. Excessive Pb intake can cause severe brain and kidney damage. Moreover, a high intake of (or exposure to) Pb may cause miscarriages in pregnant women [10, 24].

Table 4. Ranges of Cd, Hg, and Pb contents in the studied food samples detected by FAAS/FIMS and ICP-OES (assuming 250 mL of broth per serving unit)

Elements	Range of Concer (mg	tration Detected	Permissible Level in Malaysia
	FAAS/FIMS	ICP-OES	-
Cd	7.80×10^{-2} to 2.85×10^{-1}	n.d.	1.00 mg/L
Hg	9.00×10^{-4} to 8.10×10^{-3}	n.d.	$5.00 \times 10^{-2} \text{mg/L}$
Pb	2.87 to 5.26	1.27 to 5.04	2.0 mg/L

^{*}All values are expressed as a mean in ppm or mg/L

Statistical Testing

Student's *t*-test: The results provided (Table 5) by the two types of analytical instruments, FAAS/FIMS and ICP-OES, were compared using Student's *t*-test. There was no significant difference (at a confidence level of 95%) in the results of essential minerals as determined by FAAS and ICP-OES. However, there was a significant difference found in the heavy-metal results. This indicated that both FAAS and ICP-OES were suitable for the detection and quantification of essential

minerals in food samples. For heavy metals, both analytical instruments failed to show a good correlation between the obtained results. Perhaps this was associated with the trace levels of heavy metals in the food samples and the sensitivities of the instruments. Thus, the suitability of an instrument in detecting and quantifying heavy metals in food samples is dependent upon its detection limit.

^{*}n.d = non-detectable

^{*}Permissible Level in Malaysia (Source: Malaysia Food Act 1983 and Food Regulations 1985, 2017 [19]

Phang et al: ESSENTIAL MINERALS AND HEAVY METALS ANALYSIS OF PENANG ASSAM LAKSA USING ATOMIC ABSORPTION SPECTROMETRY, FLOW INJECTION MERCURY SYSTEM, AND INDUCTIVELY COUPLED PLASMA OPTICAL EMISSION SPECTROMETRY

Elements	t-calculated	t-critical	Result
Fe	1.24		No Significant difference
Ca	1.67		No Significant difference
Na	1.91		No Significant difference
K	1.25	2.15	No Significant difference
Cd	11.2		Significant difference
Hg	3.18		Significant difference
Pb	8.11		Significant difference

Table 5. Summary of Student's *t*-test for all targeted elements

Inter-day Precision Study

An inter-day precision study was performed in order to assess the consistency of the determined content of minerals and heavy metals in the studied food samples. Sample collection was repeated on three different days at selected locations. The precision of repeatability is expressed as %RSD. In general, the acceptable level for %RSD is less than 10%[8]. Overall, almost all the elements exhibited a %RSD value above 10%, which suggests the inconsistency of the content of heavy metals and minerals for samples collected on different days. The variability of the element content is most likely a result of the ingredients comprising the food samples. However, it is difficult to ascertain the exact cause for such variation, as there are a wide variety of factors involved.

Conclusion

The heavy metals (Cd, Hg, and Pb) and essential minerals (Fe, Ca, Na, and K) present in Penang Assam Laksa collected from different areas were successfully characterized by using both FAAS/FIMS and ICP-OES. Cadmium and mercury were detected in Penang Assam Laksa at trace levels, whereas lead was found at levels higher than those permitted by Malaysian Food Act 1983 and Food Regulations 1985. Most of the Penang Assam Laksa contained adequate levels of iron, calcium, potassium, and sodium. As determined by Student's *t*-test, both FAAS and ICP-OES can be satisfactorily used in the detection and quantification of minerals, while an inter-day precision test showed variability of the element content in food samples

collected on different days. Moreover, the wetdigestion procedure was efficient and suitable for digesting the food samples. In general, this work represents the first scientific study on the element content in Penang Assam Laksa, one of the most famous street foods in Penang. However, the findings stated above cannot be generalized to all Penang Assam Laksa samples, as this study just focused on five selected locations. Instead, this work serves as valuable direction for other researchers in the field. Further studies are needed in order to provide a full picture of the nutritional content in Penang Assam Laksa.

Acknowledgments

The authors would like to acknowledge participating local hawker stalls for supporting this research.

References

- Food and Agriculture Organization. (1997). Street Foods: Report of an FAO technical meeting on street foods. Calcutta, India: Food and Agriculture Organization.
- 2. Tuzen, M., and Soylak, M. (2007). Evaluation of trace element contents in canned foods marketed from Turkey. *Food Chemistry*, 102(4): 1089-1095.
- 3. Damastuti E., Syahfitri W. Y. N., Santoso M. and Lestiani D. D. (2012). Assessment of trace element daily intake based on consumption rate of foodstuffs in Bandung City. *Atom Indonesia*, 38(1): 29-34.

^{*}Student's t-test performed at a 95% confidence interval

- Jignesh, S., Vineeta, K., Abhay, S. and Vilasrao, K. (2012). Analytical methods for estimation of metals. *International Journal of Research in Pharmacy and Chemistry*, 2(1): 146-163.
- 5. Salau, R. B. and Hassan, M. N. (2014). Evaluation and analysis of dietary essential mineral micronutrients in selected Malaysian foods using FAAS and ICP-MS. *Modern Applied Science*, 8(6): 103-111.
- 6. World Health Organization (1996). Trace elements in health and nutrition. Geneva: WHO.
- Tee, E. S. and Rodolfo, F. F. (2005). Recommended dietary allowances: Homogenization in Southeast Asia. International Life Sciences Institute, Southeast Region (ILSI SEA Region).
- U.S. Department of Agriculture and U.S. Department of Human Services. (2010). Dietary Guidelines for Americans. 7th Edition. Washington, DC.
- Zukowska, J. and Biziuk, M. (2008). Methodological evaluation of method for dietary heavy metal intake. *Journal of Food Science*, 73(2): 1-9.
- Das, S. K., Grewal, A. S. and Banerjee, M. (2011).
 A brief review: Heavy metal and their analysis.
 International Journal of Pharmaceutical Sciences Review and Research, 11(1): 13-18.
- Korn, M. D. G. A., Morte, E. S. D. B., Santos, D. C. M. B. D., Castro, J. T., Barbosa, J. T. P., Teixeira, A. P., Fernandes, A. P., Welz, B., Santos, W. P. C. D., Santos, E. B. G. N. D. and Korn, M. (2008). Sample preparation for determination of metals in food samples using spectroanalytical methods A review. *Applied Spectroscopy Reviews*, 43(2): 67-92.
- Tuzen, M., Sari, H., Narin, I. and Soylak, M. (2004). Comparison of microwave, dry and wet digestion procedures for the determination of trace metal contents in spice samples produced in Turkey. *Journal of Food and Drug Analysis*, 12(3): 254-258.
- Momen, A. A., Georage, A. Z., Anthemidis, A. N. and Stratis, J. A. (2006). Investigation of four digestion procedures for multi-element determination of toxic and nutrient elements in

- legumes by inductively coupled plasma-optical emission spectrometry. *Analytica Chimica Acta*, 565(1): 81-88.
- 14. Kira, C. S. and Maihara, V. A. (2007). Determination of major and minor elements in dairy products through inductively coupled plasma optical emission spectrometry after wet partial digestion and neutron activation analysis. *Food Chemistry*, 100(1): 390-395.
- 15. Luo, Y., Zhang, B., Chen, M., Wang, J., Zhang, X., Gao, W. Y. and Huang, J. F. (2010). Rapid and simultaneous determination of essential minerals and trace elements in human milk by improved flame atomic absorption spectroscopy (FAAS) with microwave digestion. *Journal of Agricultural and Food Chemistry*, 58(17): 9396-9400.
- Boutakhrit, K., Crisci, M., Bolle, F. and Loca, J. V. (2011). Comparison of four analytical techniques based on atomic spectrometry for the determination of total tin in canned foodstuffs. Food Additives and Contaminants, 28(2): 1-18.
- 17. Perkin Elmer (2011). Exceptional performance for challenging mercury analyses. Perkinelmer, Inc.
- Khor, S. (2015). Penang Laksa isn't the only laksa out there. You need to try them all. like really. SAYS. https://says.com/my/lifestyle/let-s-talkabout-laksa. [Access online 27 March 2020].
- Malaysia Food Act 1983 and Food Regulations 1985 (2017). Warta Kerajaan Malaysia. Kuala Lumpur: Ministry of Health Malaysia.
- Yuvarani, T., Anuradha, V., and Praveena, A. (2013). Analysis of antioxidants, minerals and vitamins composition between male and female Indian mackerel Rastrelliger Kanagurta. *International Journal of Food, Agriculture and Veterinary Sciences*, 3(1): 76-81.
- Nurnadia, A. A., Azrina, A., Amin, I., Mohd Yunus, A. S. and Mohd Izuan, E. H. (2013). Mineral contents of selected marine fish and shellfish from the west coast of Peninsular Malaysia. *International Food Research Journal*, 20(1): 431-437.
- Mehrdad, R. R., Mehravar, R. R., Sohrab, K. and Ali, A. M. (2017). Cadmium toxicity and treatment: An update. *Caspian Journal of Internal Medicine*, 8(3): 135-145.

- Phang et al: ESSENTIAL MINERALS AND HEAVY METALS ANALYSIS OF PENANG ASSAM LAKSA USING ATOMIC ABSORPTION SPECTROMETRY, FLOW INJECTION MERCURY SYSTEM, AND INDUCTIVELY COUPLED PLASMA OPTICAL EMISSION SPECTROMETRY
- 23. Salama, A. K., and Radwan, M. A. (2005). Heavy metals (Cd, Pb) and trace elements (Cu, Zn) contents in some foodstuffs from the Egyptian market. *Journal of Agricultural Sciences*, 17(1): 34-42.
- 24. Jarup, L. (2003). Hazards of heavy metal contamination. *British Medical Bulletin*, 68: 167-182.